CHANGES IN SNOW, MONSOON AND SNOW-MONSOON RELATIONSHIP IN THE WARMING CLIMATE

EDITED BY: Song Yang, Xiaoming Hu, Sergio Antonio Sejas and Renguang Wu
PUBLISHED IN: Frontiers in Earth Science

frontiers Research Topics

frontiers

ISSN 1664-8714
ISBN 978-2-88976-173-9
DOI 10.3389/978-2-88976-173-9

About Frontiers

Frontiers is more than just an open-access publisher of scholarly articles: it is a pioneering approach to the world of academia, radically improving the way scholarly research is managed. The grand vision of Frontiers is a world where all people have an equal opportunity to seek, share and generate knowledge. Frontiers provides immediate and permanent online open access to all its publications, but this alone is not enough to realize our grand goals.

Frontiers Journal Series

The Frontiers Journal Series is a multi-tier and interdisciplinary set of open-access, online journals, promising a paradigm shift from the current review, selection and dissemination processes in academic publishing. All Frontiers journals are driven by researchers for researchers; therefore, they constitute a service to the scholarly community. At the same time, the Frontiers Journal Series operates on a revolutionary invention, the tiered publishing system, initially addressing specific communities of scholars, and gradually climbing up to broader public understanding, thus serving the interests of the lay society, too.

Dedication to Quality

Each Frontiers article is a landmark of the highest quality, thanks to genuinely collaborative interactions between authors and review editors, who include some of the world's best academicians. Research must be certified by peers before entering a stream of knowledge that may eventually reach the public - and shape society; therefore, Frontiers only applies the most rigorous and unbiased reviews.
Frontiers revolutionizes research publishing by freely delivering the most outstanding research, evaluated with no bias from both the academic and social point of view. By applying the most advanced information technologies, Frontiers is catapulting scholarly publishing into a new generation.

What are Frontiers Research Topics?

Frontiers Research Topics are very popular trademarks of the Frontiers Journals Series: they are collections of at least ten articles, all centered on a particular subject. With their unique mix of varied contributions from Original Research to Review Articles, Frontiers Research Topics unify the most influential researchers, the latest key findings and historical advances in a hot research area! Find out more on how to host your own Frontiers Research Topic or contribute to one as an author by contacting the Frontiers Editorial Office: frontiersin.org/about/contact

CHANGES IN SNOW, MONSOON AND SNOW-MONSOON RELATIONSHIP IN THE WARMING CLIMATE

Topic Editors:
Song Yang, Sun Yat-sen University, China
Xiaoming Hu, Sun Yat-sen University, China
Sergio Antonio Sejas, Science Systems and Applications, Inc., United States
Renguang Wu, Zhejiang University, China

Citation: Yang, S., Hu, X., Sejas, S. A., Wu, R., eds. (2022). Changes in Snow, Monsoon and Snow-Monsoon Relationship in the Warming Climate. Lausanne: Frontiers Media SA. doi: 10.3389/978-2-88976-173-9

Table of Contents

frontiers | Frontiers in Earth Science

EDITORIAL
published: 26 April 2022
doi: 10.3389/feart.2022.906982

Editorial: Changes in Snow, Monsoon and Snow-Monsoon Relationship in the Warming Climate

Renguang Wu[1]*, *Xiaoming Hu*[2], *Song Yang*[2] and *Sergio Antonio Sejas*[3]

[1]School of Earth Sciences, Zhejiang University, Hangzhou, China, [2]School of Atmospheric Sciences, Sun Yat-sen University, Zhuhai, China, [3]Science Systems and Applications, Inc., Lanham, MA, United States

Keywords: snow, monsoon, snow-monsoon relationship, warming climate, changes

Editorial on the Research Topic

Changes in Snow, Monsoon and Snow-Monsoon Relationship in the Warming Climate

Monsoons affect a large percent of the world's population. Snow cover modulates land surface conditions and consequently the land-sea thermal contrast. Thus, snow over the land is an important factor for monsoon variations. In a warming climate, both snow and monsoon are subject to notable changes. The snow-monsoon relationship has also experienced changes in the past. Improved understanding of the factors responsible for the changes in snow over various regions and in different components of monsoon, and the physical reasons for the changes in snow-monsoon relationship will help to alleviate monsoon-related adverse impacts on societal development.

This special issue "Changes in Snow, Monsoon and Snow-Monsoon Relationship in the Warming Climate" includes articles that address the impacts of snow cover on Asian climate and changes in the snow-monsoon relationship in a warming climate. Papers range from the impacts of the Tibetan Plateau and Eurasian snow cover on the winter atmospheric circulation and East Asian winter monsoon to summer precipitation and extremes. Papers also consider the regulation of solar activity on the Tibetan Plateau snow variations and their impacts on summer precipitation in China and evaluate the ability of coupled models in simulating the Eurasian snow and its relationship with atmospheric circulation.

Three papers in this special issue are focused on the impacts of the Tibetan Plateau snow changes. Chen et al. analyzed the role of eastern Tibetan Plateau autumn-winter snow cover in the variability of the northern component of the East Asian winter monsoon. Song et al. documented the linkage of the spring Tibetan Plateau snow to summer precipitation in China. Wang et al. examined the impact of summer western Tibetan Plateau snow cover on East Asian summer precipitation. Four papers are focused on the impacts of Eurasian snow on winter atmospheric circulation. Yang and Fan analyzed the influence of November Siberian snow on the out-of-phase Siberian High change in December and January and the responsible physical mechanism. Sun et al. documented the connection of diverse winter Siberian high variation modes with preceding autumn and simultaneous winter Eurasian snow cover. Zhang and Sun revealed the impacts of central Siberian October snow cover on spring extreme precipitation in southern China. Yao et al. identified the relation of summer compound hot and dry extreme days in China to the preceding winter Northern Hemisphere snow.

Four papers revealed that the effects of snow on climate have experienced interdecadal changes. Chen et al. identified an interdecadal weakening in the relationship of the northern component of East Asian winter monsoon to autumn-winter Tibetan Plateau snow cover in the mid-1990's. Yang and Fan unraveled the intensified impact of spring Siberian snow on the out-of-phase December-January Siberian high relation after 2000. Song et al. showed that the linkage of Tibetan Plateau snow

Edited and reviewed by:
Yuqing Wang,
University of Hawaii at Manoa,
United States

***Correspondence:**
Renguang Wu
renguang@zju.edu.cn

Specialty section:
This article was submitted to Atmospheric Science, a section of the journal Frontiers in Earth Science

Received: *29 March 2022*
Accepted: *04 April 2022*
Published: *26 April 2022*

Citation:
Wu R, Hu X, Yang S and Sejas SA (2022) Editorial: Changes in Snow, Monsoon and Snow-Monsoon Relationship in the Warming Climate. Front. Earth Sci. 10:906982. doi: 10.3389/feart.2022.906982

to summer precipitation in China was regulated by the solar activity. Wang et al. found that the influence of summer western Tibetan Plateau snow on East Asian precipitation had decreased after the early 2000's due to the reduction of Tibetan Plateau snow cover variability.

The paper by Sun et al. evaluated the model simulation of the relationship of the Eurasian snow to Siberian high variation. They showed that the models needed to capture the snow pattern properly in order to simulate the influence of snow on the Siberian high variation realistically. Zhang and Sun, and Yao et al. revealed evidence for the role of snow in the occurrence of extreme events.

With the increase in global temperature, the domain and variability of snow cover are likely to undergo continuous changes. While snow cover over land may continue to play a role in the climate variability in different regions and different seasons, the key regions of snow and the magnitude of snow influence may change under a warming climate, as indicated by several articles in this special issue. For future projections of snow and its impacts using climate models, there exist uncertainties related to the ability of models in capturing the realistic snow distribution and the spatial pattern of snow variability. Efforts are needed in the future to improve the simulations of the distribution and variability of continental and regional snow and understanding of the physical processes of snow impacts on climate variability in various regions and seasons.

AUTHOR CONTRIBUTIONS

RW drafted the manuscript. All the authors contributed to the revising of the manuscript.

Conflict of Interest: Author SS is employed by Science Systems and Applications, Inc., Lanham, USA.

The remaining authors declare that the research was conducted in the absence of any commercial or financial relationships that could be construed as a potential conflict of interest.

frontiers in Earth Science

ORIGINAL RESEARCH
published: 14 June 2021
doi: 10.3389/feart.2021.708567

Improvement in the Prediction of Summer Precipitation in the North China–Hetao Region Using the Tropospheric Temperature Over the Tibetan Plateau in Spring

Dan Chen[1,2], *Sulan Nan*[3]*, *Ge Liu*[3], *Changyan Zhou*[1], *Renrui Shi*[1], *Yinhuan Ao*[2] *and Xiang Li*[4]

[1]*Institute of Plateau Meteorology, China Meteorological Administration/Heavy Rain and Drought-Flood Disasters in Plateau and Basin Key Laboratory of Sichuan Province, Chengdu, China,* [2]*Key Laboratory for Land Surface Process and Climate Change in Cold and Arid Regions, Chinese Academy of Sciences, Lanzhou, China,* [3]*State Key Laboratory of Severe Weather, Chinese Academy of Meteorological Sciences, Beijing, China,* [4]*Sichuan Meteorological Observation and Data Center, Chengdu, China*

OPEN ACCESS

Edited by:
Xiaoming Hu,
Sun Yat-Sen University, China

Reviewed by:
Yuxiang Zhu,
China Meteorological Administration, China
Tuantuan Zhang,
Sun Yat-Sen University, China

***Correspondence:**
Sulan Nan
nansl@cma.gov.cn

Specialty section:
This article was submitted to Atmospheric Science, a section of the journal Frontiers in Earth Science

Received: *12 May 2021*
Accepted: *02 June 2021*
Published: *14 June 2021*

Citation:
Chen D, Nan S, Liu G, Zhou C, Shi R, Ao Y and Li X (2021) Improvement in the Prediction of Summer Precipitation in the North China–Hetao Region Using the Tropospheric Temperature Over the Tibetan Plateau in Spring. Front. Earth Sci. 9:708567. doi: 10.3389/feart.2021.708567

We investigated the relationship between the spring tropospheric temperature over the Tibetan Plateau (TPT) and summer precipitation in eastern China on an interannual timescale using the monthly mean ERA-Interim reanalysis dataset, the HadISST dataset and the daily mean precipitation dataset for China. We found that there is a significant positive correlation between the spring TPT and summer precipitation in the North China–Hetao region. The relationship is manifested in the context of the East Asia–Pacific pattern teleconnection. In the high spring TPT index years, the geopotential height anomalies over East Asia and the western North Pacific present a negative phase of the East Asia–Pacific pattern teleconnection in the subsequent summer. This circulation pattern is beneficial for the water vapor transport from the western Pacific to inland, which further transport to the North China–Hetao region from the Yangtze River–Yellow rivers region. Anomalous upward motion occurs in the North China–Hetao region, which increases precipitation. The East Asian subtropical westerly jet shifts further north and the South Asian high weakens and shrinks westward. These conditions all favor an increase in precipitation over the North China–Hetao region. The spring TPT plays an important part in the prediction of summer precipitation in the North China–Hetao region. The improvement in the use of the spring TPT to predict summer precipitation in the North China–Hetao region is examined by comparing the prediction equations with and without the prediction factor of the spring TPT on the basis of the sea surface temperatures in key regions. After considering the impact of the spring TPT, the explanatory variance of the prediction equation for precipitation in the North China–Hetao region increases by 17.3%.

Keywords: Thermal condition of the Tibetan Plateau, Precipitation in the North China-Hetao region, East Asia-Pacific pattern teleconnection, Climate prediction, EAST Asian subtropical westerly jet, South Asian high

INTRODUCTION

The Tibetan Plateau is located in the mid-to low latitudes of the Eurasian continent and is the highest plateau in the world. The thermal and dynamic effects of the Tibetan Plateau have an important impact on the Asian monsoon and precipitation in this region (Yanai et al., 1992; Wu et al., 2007; Liu et al., 2012; Wang et al., 2014; Jiang and Ting, 2017). The surface sensible heat over the Tibetan Plateau in spring is closely related to the timing of the onset of the Indian summer monsoon, with a strong (weak) surface sensible heat favoring an earlier (later) onset of the monsoon (Zhang et al., 2015). Duan et al. (2005) showed that the sensible heat over the Tibetan Plateau can be a predictor of precipitation in the valley between the Yangtze and Huaihe rivers. Weakening of the sensible heat flux over the Tibetan Plateau in spring can lead to an increase in summer precipitation in South China and a decrease in precipitation in northern and northeastern China (Duan et al., 2013). Zhao and Chen (2001) showed that the heat source over the Tibetan Plateau in spring is indicative of summer precipitation in eastern China. Latent heating over the Tibetan Plateau has an essential role in enhancing the East Asia summer monsoon circulation, intensifying the monsoon in East Asia and leading to drier conditions in central Asia (He et al., 2019). Early winter and spring snow anomalies on the Tibetan Plateau have a significant impact on the distribution of summer precipitation in China (Chen and Wu, 2000; Wang et al., 2017).

Changes in the global sea surface temperature (SST) also have an important impact on precipitation and the atmospheric circulation in eastern China. Convective activities tend to be weaker around South China Sea and the Philippines in the developing stage of El Niño. Meanwhile, the SST in the western tropical Pacific tends to be colder in summer and the western Pacific subtropical high shifts southward. As a consequence, drought conditions occur in the Indo-China peninsula and South China and there may be flooding in the area from the Yangtze River valley to the Huaihe River valley. The opposite conditions are seen in the decaying stage of El Niño (Huang and Wu, 1989). Zhang et al. (2018) showed that the phase transition from La Niña to El Niño is an important precursor of prolonged spring–summer drought in northern China. El Niño can also significantly affect precipitation in China during its mature phase, with a positive precipitation anomaly occurring over the Yangtze River valley in the northern summer and a negative precipitation anomaly developing over southern and northern China (Zhang et al., 1999). Xu et al. (2019) indicated that precipitation over southern China is enhanced (suppressed) during the eastern (central) Pacific El Niño, which can be attributed to different atmospheric responses in the western North Pacific and South China Sea during the two types of ENSO (El Niño-Southern Oscillation).

The SST in the North Pacific Ocean also play an important role in drought/flood conditions in northern China. The SST anomaly over the North Pacific can intensify the western North Pacific subtropical high and increase the transport of water vapor from the tropical ocean, which favors heavy precipitation over North China (Li et al., 2017). The warm phase of the Pacific interdecadal oscillation usually corresponds to drought in northern China (Qian and Zhou, 2014).

There are strong interactions between the thermal condition of the Tibetan Plateau and the global SST. In spring and summer, the heating anomaly over the Tibetan Plateau can modulate tropical and mid-latitude air–sea interactions and affect the development of the tropical ENSO (Nan et al., 2009; Zhou et al., 2009). The SST in the tropical central and eastern Pacific in early winter and spring can also affect precipitation and the soil moisture content on the Tibetan Plateau in the same period, further modulating the local surface air temperature during the following summer (Liu et al., 2015). The tripolar SST anomaly in the North Atlantic can stimulate a stable Rossby wave train propagating downstream, which strengthens westerly winds over the Tibetan Plateau and intensifies the transfer of sensible heat from the surface of the Tibetan Plateau to the atmosphere (Cui and Wang, 2009). The thermal forcing of the Tibetan Plateau can be modulated by the SST anomaly in the North Atlantic in March and April and altered by the Indian Ocean SST anomaly in May on an interannual timescale (Zhao et al., 2018). The positive Tibetan Plateau heating anomalies can induce significant responses in the atmospheric circulation over the northern Indian Ocean, characterized by easterly anomalies in the upper troposphere as a result of the enhanced South Asian high and lower level southwesterly anomalies from the heat pump effect (Zhao et al., 2019). Hu and Duan (2015) indicated that Indian Ocean SST and thermal heating by the Tibetan Plateau are closely related in summer and are both important to the interannual variability of the East Asian monsoon. Jiang et al. (2019) pointed out that on the interannual scales, the snow depth over the eastern Tibetan Plateau is affected by ENSO, while the snow depth over the central western Tibetan Plateau is affected by Indian Ocean dipole.

These studies indicate that both the thermal condition of the Tibetan Plateau and the global SST have important indicative influences on the climate of eastern China, and there exist strong interaction between the thermal condition of the Tibetan Plateau and the global SST. However, the thermal effect of the Tibetan Plateau is seldom considered in actual forecasts for many reasons, including the reliability and timeliness of data. Previous research has shown that many variables can reflect the thermal condition of the Tibetan Plateau, such as the snow cover, the sensible and latent heat fluxes and the atmospheric heat source. However, it is also well known that there are deficiencies in the reliability of data for these variables and the quality of the data is severely affected by the local environment. The variabilities of some of these variables are inconsistent—for example, the variations in the sensible heat and the latent heat of condensation are often opposite in summer. Recent studies have introduced the tropospheric temperature over the Tibetan Plateau (TPT) to represent the thermal condition of the Tibetan Plateau, which has a good regional coherence and reflects a synthesis of various physical processes (Nan et al., 2009, Nan et al., 2019, Nan et al., 2021).

This paper focuses on the impact of the spring TPT on summer precipitation in eastern China and constructs prediction equations to study the improvement in the thermal

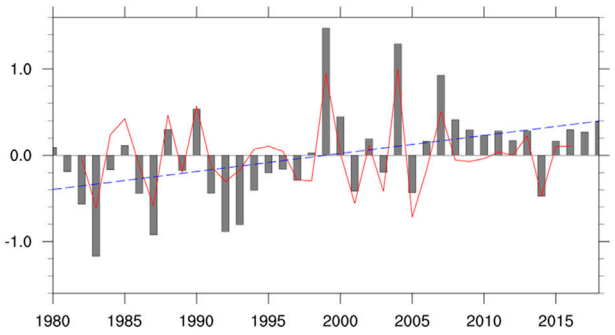

FIGURE 1 | Normalized spring TPT index time series during the time period 1980–2018 (gray columns) and its interannual component (red solid line, for signals below the nine-year period obtained by the high-pass filter) and linear trend (blue dashed line). The TPT index is the vertically (500–200 hPa) and regionally (25°N–45°N, 65°E–105°E) averaged air temperature over the Tibetan Plateau.

condition of the Tibetan Plateau as a predictor of summer precipitation in this region. *Data and Methods* describes the data and methods used in this study. *Relationship Between the Spring TPT and Summer Precipitation in Eastern China* presents the relationship between the spring TPT and summer precipitation in eastern China. Physical mechanism responsible for the relation between the spring TPT and summer precipitation in the North China–Hetao region further investigates the physical mechanism responsible for the relation between the spring TPT and summer precipitation in the North China–Hetao region. *Prediction of Summer Precipitation in the North China–Hetao Region Using the Spring* TPT shows how the spring TPT and SST can predict summer precipitation in the North China–Hetao region and *Summary and Discussion* presents our discussion and conclusions.

DATA AND METHODS

We used the European Centre for Medium-Range Weather Forecasts (ECMWF) ERA-Interim reanalysis dataset from 1980–2018 with a horizontal resolution of (1.5° × 1.5°) (Simmons et al., 2007). The variables include the geopotential height, the zonal and meridional winds, the vertical velocity, the specific humidity and the vertical integral of the water vapor flux. We also used the monthly mean SST provided by the Hadley Center with a horizontal resolution of (1° × 1°) (Rayner et al., 2003) and the daily mean precipitation data from >2000 stations in the latest version (V3) of surface climatological data compiled by the China National Meteorological Information Center.

We focused on the interannual scale and used the high-pass filter and signals with a period <9 years to represent the interannual variation signals. We used correlation analysis, partial correlation analysis and composite analysis to examine the relations among the TPT, SST and precipitation in eastern China. The prediction equations for summer precipitation in the North China–Hetao region were established by stepwise regression analysis with the SST and TPT as prediction factors. The seasons were defined according to the usual meteorological seasons (spring, March–May; summer, June–August). Student's *t*-test was used to assess the statistical significance.

RELATIONSHIP BETWEEN THE SPRING TPT AND SUMMER PRECIPITATION IN EASTERN CHINA

Temporal Variation of the Spring TPT

We selected the TPT index to represent the thermal condition of the Tibetan Plateau, which is defined as the vertically (500–200 hPa) and regionally (25–45°N, 65–105°E) averaged temperature (Nan et al., 2009, Nan et al., 2019, Nan et al., 2021). **Figure 1** shows the time series of the spring TPT during the period 1980–2018. It shows a significant upward linear trend of 0.2°C/decade (>99% significance level). The TPT also has a clear interannual variation accounting for 52.7% of the total variability of the covariance. This study is focused on the relation between the spring TPT and summer precipitation in eastern China on an interannual timescale and the TPT index and other variables were filtered through a nine-point high-pass filter.

Relationship Between the Spring TPT and Summer Precipitation in the North China–Hetao Region

Figure 2 shows a correlation map of the spring TPT index with the summer 2000-station precipitation in China for the time period 1980–2018. It is characterized by a negative–positive–negative–positive pattern from north to south in eastern China. Significantly negative correlations are seen in northeast China and

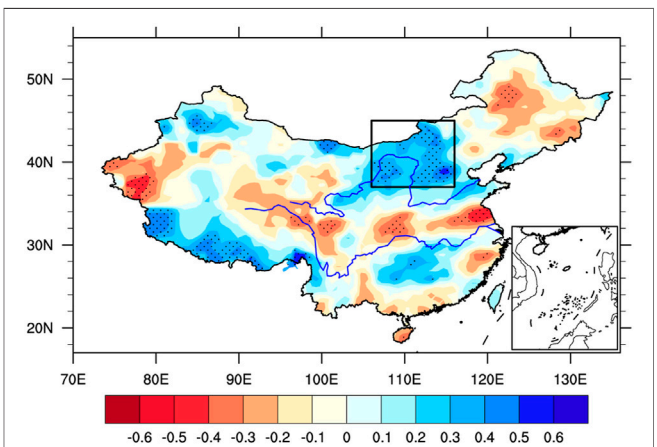

FIGURE 2 | Correlation map of the spring TPT index with the 2000–station summer precipitation in China on an interannual timescale for the time period 1980–2018. The box represents the North China–Hetao region (37°N–45°N, 106°E–116°E). The stippled areas are significant at the 95% confidence level.

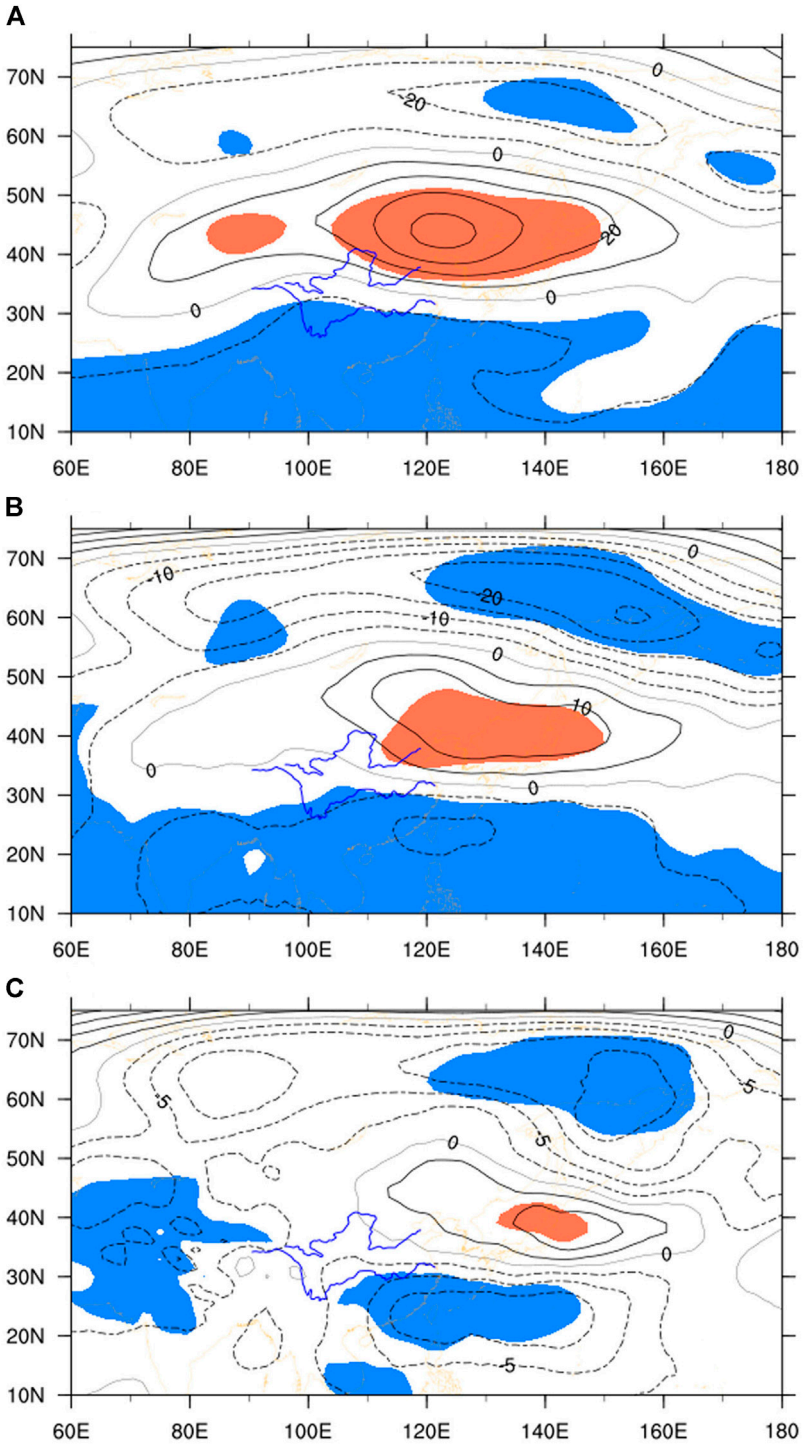

FIGURE 3 | Composite differences in **(A)** 200, **(B)** 500, and **(C)** 850 hPa geopotential high anomalies (m) between the high and low spring TPT index cases. The shaded areas are significant at the 90% confidence level.

the Yangtze–Huaihe river valleys. Significantly positive correlations mainly appear in the North China–Hetao region and the south of the middle reaches of the Yangtze River valley. This indicates that when the spring TPT is high, precipitation in northeast China and the Yangtze–Huaihe river valleys tends to be less than normal and precipitation in the North China–Hetao region and the south of the middle reaches of the Yangtze River valley tends to be greater than normal in the subsequent summer. The significantly positive

correlation region in the North China–Hetao region is large-scale, which is useful and popular in actual prediction. Below, this study focuses on relationship between the spring TPT and summer precipitation in the North China–Hetao region. The summer precipitation in the North China–Hetao region (as shown in the box in **Figure 2**) has a correlation coefficient of 0.41 (>97% confidence level) with the spring TPT index on an interannual timescale.

PHYSICAL MECHANISM RESPONSIBLE FOR THE RELATION BETWEEN THE SPRING TPT AND SUMMER PRECIPITATION IN THE NORTH CHINA–HETAO REGION

East Asia–Pacific Pattern Teleconnection

We examine the variations in the atmospheric circulation associated with the spring TPT by composite analysis, based on the inter-annual time series in **Figure 1** (red solid line). Six high (1985, 1988, 1990, 1999, 2004, and 2007) and six low (1983, 1987, 2001, 2003, 2005, and 2014) spring TPT index years are selected, in which the fluctuations of the TPT index exceed one standard deviation. **Figure 3** indicates the composite differences in the anomalous geopotential high between high and low spring TPT index cases in the upper, mid-and lower troposphere. There is a meridional negative–positive–negative pattern of geopotential height anomalies over East Asia and the western Pacific in the high spring TPT index years, with negative values over South China and the lower latitudes of the western North Pacific and to the north of the Okhotsk Sea and positive values at mid-latitudes over East Asia. This pattern is similar to the negative phase of the East Asia–Pacific pattern (EAP) (Huang and Li, 1987; Nitta, 1987) and shows an equivalent barotropic feature over the whole troposphere. The EAP is an important teleconnection affecting both the East Asian summer monsoon and precipitation (Chen and Zhai, 2015; Li et al., 2018; Hu et al., 2020). Its negative phase can cause a decrease in precipitation in the Yangtze–Huaihe river basin and an increase in precipitation in the Yellow river basin (Huang and Li, 1987; Huang, 1992; Wang et al., 2018). These results are in agreement with the relation between the spring TPT and summer precipitation (**Figure 3**), indicating that the spring TPT can affect summer precipitation in eastern China through the EAP teleconnection.

In the negative phase of the EAP, an anomalous cyclone appears around the Okhotsk Sea, which is not conducive to the southward movement of cold air from mid-to high latitudes to northern China. An anomalous anticyclone controls the mid-latitudes of East Asia. The North China–Hetao region is located on the southern and southwestern flanks of the anomalous anticyclone. An anomalous cyclone appears in South China and the lower latitudes of the western Pacific. Between the anomalous anticyclone at the mid-latitudes of East Asia and the anomalous cyclone at the lower latitudes of the western Pacific, anomalous easterly winds flow from the western North Pacific to inland East Asia and diverge from the Yangtze–Yellow river region to the North China–Hetao region and South China (**Figures 4A–C**). These anomalous circulations favor the transport of more water vapor from the western Pacific to the North China–Hetao region and South China, increasing of precipitation in these regions (**Figure 4D**).

Figure 5A shows the composite differences in the summer 500hPa vertical velocity between the high and low spring TPT index cases. In the high spring TPT index years, significant positive anomalies appear between the Yangtze and Yellow rivers, indicating anomalous descending motion, which is also seen in the latitude–height cross-section of the composite differences in vertical velocity along 106–116°E (**Figure 5B**). Such anomalous descending motion favors a decrease in precipitation between the Yangtze and Yellow rivers. At the same time, significant negative anomalies of vertical velocity appear throughout the troposphere over the North China–Hetao region between 36 and 45°N, suggesting anomalous ascending motion (**Figures 5A,B**) and favoring an increase in precipitation in this region. The distribution of anomalous vertical velocity in the North China–Hetao and the Yangtze–Yellow river regions associated with the high spring TPT (**Figure 5**) corresponds well with the anomalous distribution of precipitation in **Figure 2**.

East Asian Subtropical Westerly Jet and South Asian High

In the composite differences of the 200 hPa horizontal winds (**Figure 4A**), anomalous westerly winds prevail between the anomalous cyclone in northeast Asia and the anomalous anticyclone at mid-latitudes over East Asia. **Figure 6A** shows the composite differences in the 200 hPa zonal wind between high and low spring TPT index cases. The region of northeast Asia from east of Lake Baikal to the Okhotsk Sea between 50 and 65°N and the mid-latitude region over East Asia between 30 and 40°N are covered by significant positive and negative anomalies, respectively. These regions are controlled in the climatology by the westerly jet. These zonal wind anomalies therefore indicate an increase in westerly winds in northeast Asia and a decrease in westerly winds at mid-latitudes in East Asia, implying a northward shift of the East Asian subtropical westerly jet.

Figure 6B shows the axes of the westerly jet in the high and low TPT index cases. The axis of the westerly jet shifts further north in the high TPT index cases than in the low TPT index cases, especially in East Asia. Previous studies have indicated that the position of the East Asian subtropical westerly jet in summer has an important impact on the East Asian summer monsoon and further influences summer precipitation in China (Yu et al., 2004; Wang and Zou, 2016; Xuan et al., 2018). When the East Asian subtropical westerly jet is abnormally north, precipitation increases abnormally in northern China and the Hetao area (Kuang and Zhang, 2006). This implies that the TPT probably links with the

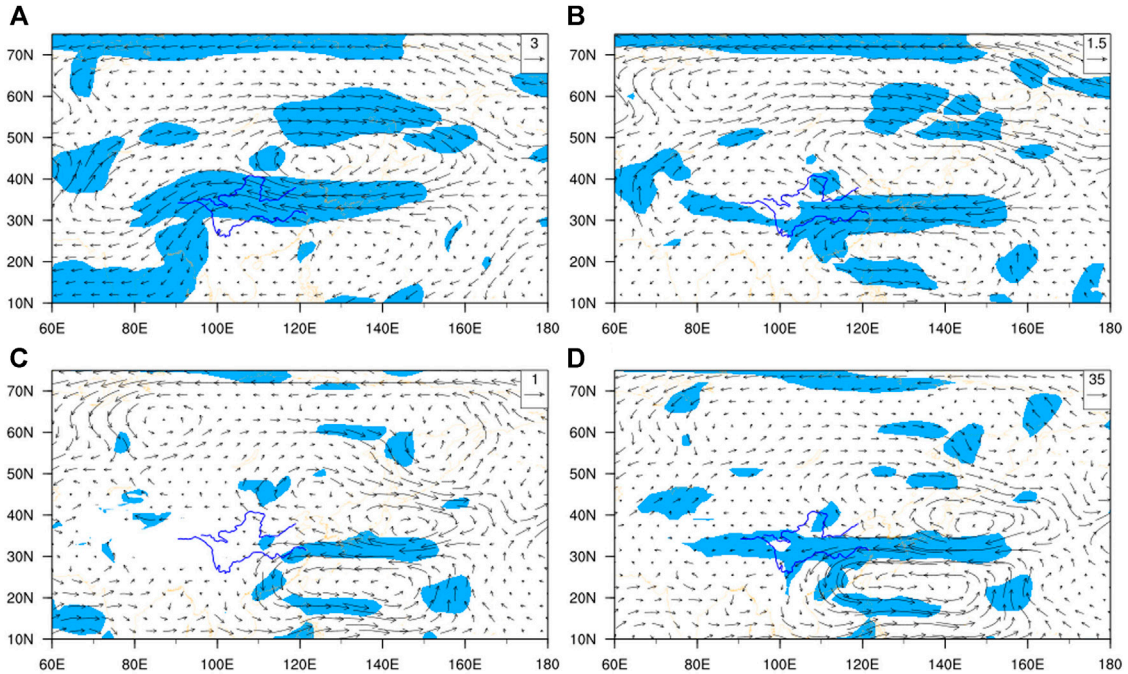

FIGURE 4 | Composite differences in **(A)** 200, **(B)** 500, and **(C)** 850 hPa wind vector anomalies (m s^{-1}) and **(D)** the vertical integral of water vapor transport anomalies (kg m^{-1} s^{-1}) between the high and low spring TPT index cases. The shaded areas are significant at the 95% confidence level.

anomaly of precipitation in the North China–Hetao region via modulating the position of the East Asian subtropical westerly jet.

In the composite difference of the 200 hPa geopotential height between the high and low spring TPT index cases (**Figure 3A**), significant negative anomalies cover the lower latitudes from the western Pacific to East and South Asia, implying that the anomaly in the South Asian high corresponds to the high spring TPT. **Figure 7** presents the composites for the 200 hPa geopotential high for the high and low spring TPT index cases. In the high spring TPT index years (**Figure 7A**), the area of the South Asian high above 12.5 km is clearly smaller in summer than in the low spring TPT index years (**Figure 7B**). The most eastern points of the 12.5 km contour line are located near 120 and 135°E in the high and low spring TPT index cases, respectively—that is, the South Asian high weakens and shrinks westward in the high TPT index years compared with the low spring TPT index years. Previous research has indicated that the weakening and westward shrinking of the South Asian high can induce floods in northern China (Huang and Qian, 2004; Huang et al., 2006). The change in the atmospheric thermal condition over the Tibetan Plateau is therefore also probably related to the anomaly in precipitation over northern China by the change in the position of the South Asian high.

In general, when the spring TPT is high, the East Asian subtropical westerly jet moves northward and the South Asian high weakens and shrinks westward. These conditions favor an increase in precipitation in the North China–Hetao region.

PREDICTION OF SUMMER PRECIPITATION IN THE NORTH CHINA–HETAO REGION USING THE SPRING TPT

The above study shows that the spring TPT is closely related to summer precipitation in the North China–Hetao region, which makes it possible to use the spring TPT to improve the prediction of summer precipitation in the region. Previous studies have also concluded that SST anomalies are the main interannual prediction signals of summer precipitation in eastern China (Huang and Wu, 1989; Zhu et al., 2015). Therefore, we tries to study the improvement of the thermal condition of the Tibetan Plateau for summer precipitation prediction in the North China–Hetao region, by introducing the thermal factor of the Tibetan Plateau into the prediction equation on the basis of the SST factors.

We used partial correlation analysis to determine the areas of high correlation in which the SSTs are closely related to regional precipitation in the North China–Hetao region, but independent of the TPT. The SSTs in these high-correlation areas were then used to predict the regional precipitation in summer. Based on the effect of SSTs in these high-correlation regions, we evaluated the improvement in the use of the spring TPT for the prediction of summer precipitation in the North China–Hetao region by comparing the prediction results for regional precipitation before

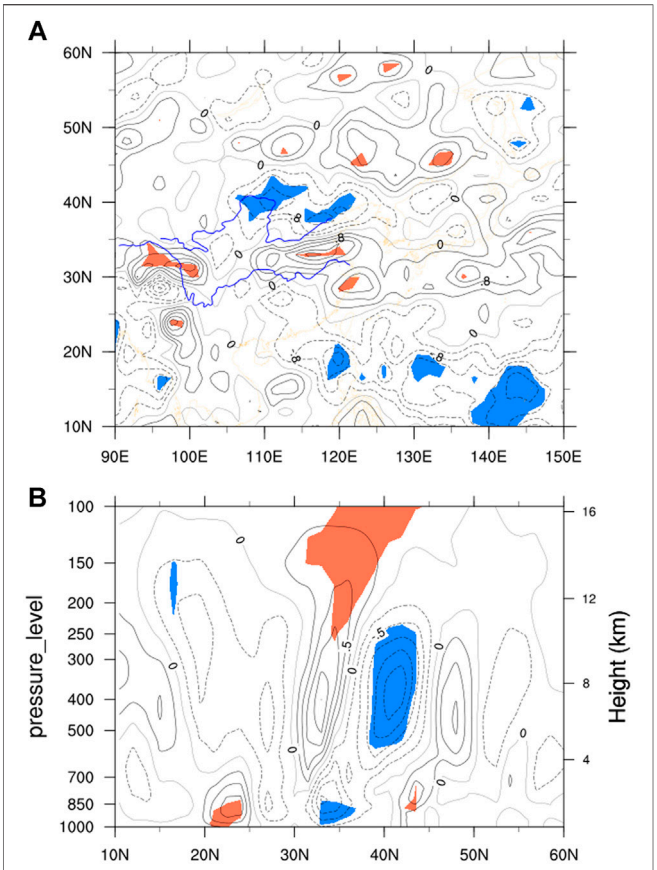

FIGURE 5 | Composite differences in **(A)** the 500 hPa vertical velocity anomalies (10^{-2} Pa s) and **(B)** the latitude-height cross-section of vertical velocity anomalies along 106°E–116°E (10^{-2} Pa s) between the high and low spring TPT index cases. The shaded areas are significant at the 95% confidence level.

and after considering the prediction factor of the spring TPT (**Figure 8**; **Table 1**).

Figure 8A shows the partial correlation map between summer precipitation in the North China–Hetao region and the SST in the previous spring, with the effect of the spring TPT removed in each grid. Significant negative values covering a large area appear at mid- to high latitudes over the North Pacific (MHNP) and the tropical central Pacific (TCP) and positive values are seen in the tropical eastern Pacific (TEP) and the eastern Indian Ocean (EIO). The standardized and regionally averaged SSTs in these regions are used as the basic prediction factors. There are also other significant areas of correlation over the oceans, but these areas are small and therefore the SSTs in these regions were not selected as prediction factors.

We constructed prediction **Eq. 1** for summer precipitation in the North China–Hetao region using stepwise regression. The SST in the tropical eastern Pacific was eliminated and only the SSTs in the MHNP, TCP and EIO were selected as significant prediction factors for summer precipitation in the North China–Hetao region. The correlation coefficient between the regressed and observed summer precipitation time series in the North China–Hetao region (**Figure 8B**) is 0.52, above the 99% confidence level (**Table 1**). The explanatory variance of prediction factors for precipitation in the North China–Hetao region is 26.6%.

After introducing the spring TPT factor, we obtained prediction **Eq. 2** for summer precipitation in the North China–Hetao region. The SSTs in the TCP and EIO are still significant prediction factors and the SST in the MHNP is eliminated. The correlation coefficient between the regressed and observed precipitation time series increases to 0.66, exceeding the 99% confidence level (**Table 1**). The explanatory variance of the spring TPT and SSTs in the TCP and EIO for summer precipitation in the North China–Hetao region reaches 43.9%, which is 17.3% more than that of the SSTs in the MHNP, TCP and EIO for the precipitation in this region.

Figure 8B shows the variations in the observed and fitted summer precipitation in the North China–Hetao region. The fitting value, using both spring TPT and SSTs in the TCP and EIO as prediction factors, is closer to the observed precipitation than the fitting value considering only the effect of SSTs.

Stepwise regression fitting equation:

$$P_{NH} = -0.13 - 6.4SST_{MHNP} - 12.2SST_{TCP} + 13.7SST_{EIO} \quad (1)$$

$$P_{NH} = -0.08 - 16.9SST_{TCP} + 16.4SST_{EIO} + 11.2TPT \quad (2)$$

Where P_{NH} is the summer precipitation in the North China–Hetao region, SST_{MHNP} is the SST of the MHNP in spring, SST_{TCP} is the SST of the TCP in spring, SST_{EIO} is the SST of the EIO and TPT is the tropospheric temperature over the Tibetan Plateau in spring.

The spring TPT therefore plays an important part in the prediction of summer precipitation in the North China–Hetao

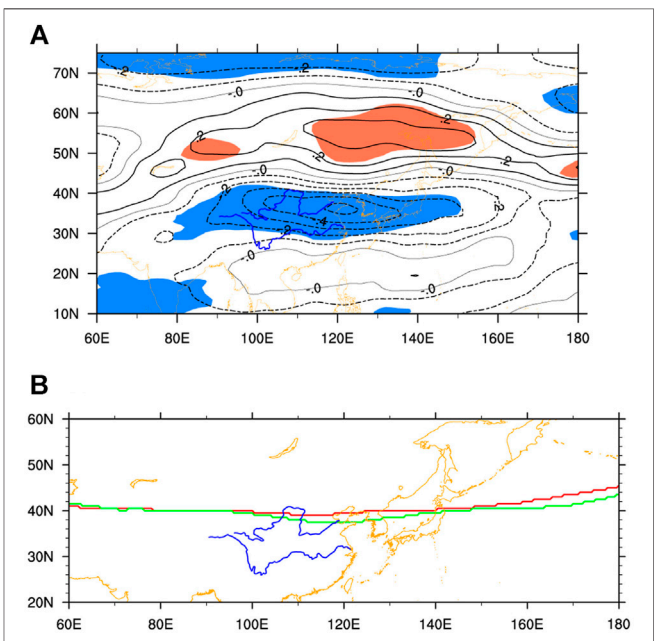

FIGURE 6 | (A) Composite differences in the 200 hPa zonal wind anomalies (m s^{-1}) between the high and low spring TPT index cases. **(B)** Axes of the westerly jet in the high (red) and low (green) TPT index cases. The shaded areas in part **(A)** are significant at the 95% confidence level.

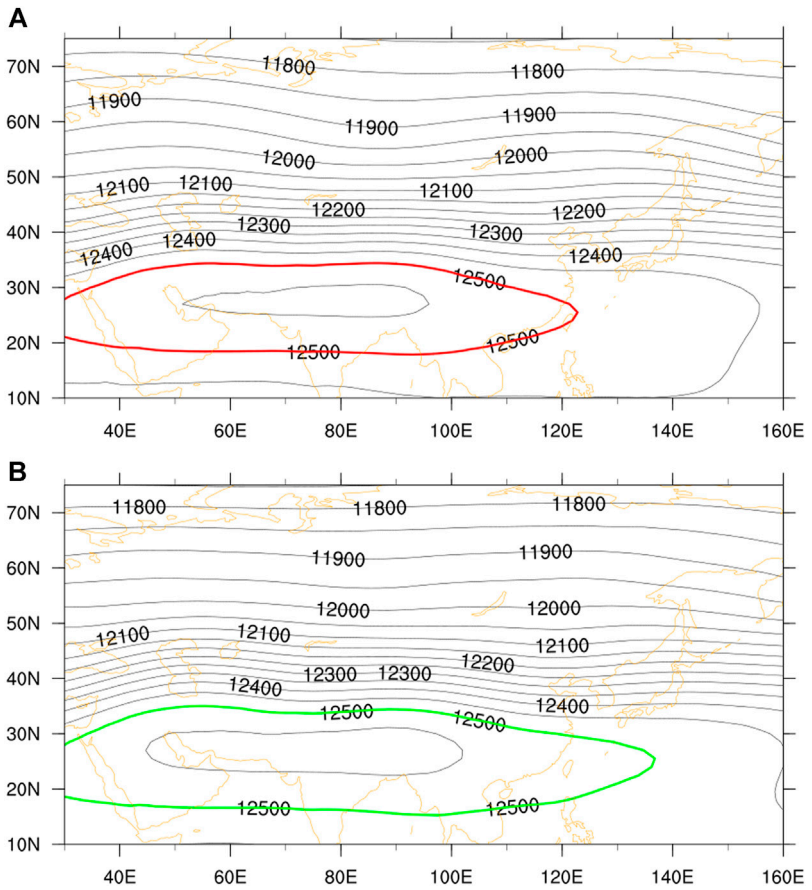

FIGURE 7 | Composite in the 200 hPa geopotential high (m) for the **(A)** high and **(B)** low spring TPT index cases.

region. After introducing the effect of the TPT on the basis of the SST, the prediction skill for summer precipitation in this region increased by 17.3%. Therefore the role of the spring TPT should not be ignored in short-term predictions of summer precipitation in the North China–Hetao region.

SUMMARY AND DISCUSSION

Using the monthly mean ERA-Interim reanalysis dataset, the HadISST dataset and the daily mean precipitation dataset for the time period 1980–2018, we investigated the relationship between the springtime TPT and summer precipitation over eastern China on an interannual timescale. There was a significant correlation of negative–positive–negative–positive from northeast China to South China between the spring TPT and precipitation in eastern China, with significant positive correlation in the North China–Hetao region and South China and negative correlation in northeast China and the Yangtze–Yellow river region. This indicates that, associated with a high (low) spring TPT, precipitation in the North China–Hetao region and South China tends to be more (less) than normal, whereas the precipitation in northeast China and the Yangtze–Yellow river region tends to be less (more) than normal in the subsequent summer. Precipitation in the North China–Hetao region has a correlation coefficient of 0.41 with the spring TPT index, exceeding the 97% confidence level.

The relationship between the spring TPT and precipitation in the North China–Hetao region was considered in the context of the EAP teleconnection. In the high spring TPT index years, the geopotential height anomalies in East Asia and the western North Pacific present a negative phase of the EAP teleconnection in the subsequent summer, characterized by negative anomalies over South China and the lower latitudes of the western Pacific and the mid-to high latitudes north of the Okhotsk Sea and by positive anomalies in the mid-latitudes of East Asia. Under this background, anomalous easterly winds prevail between the anomalous anticyclone at mid-latitudes in East Asia and the western Pacific and the anomalous cyclone in South China and the lower latitudes of the western Pacific, which brings more water vapor inland from the western Pacific and a divergence from the Yangtze–Yellow river region to the North China–Hetao region. Anomalous upward (downward) motion occurs in the North China–Hetao (Yangtze–Yellow river) region, favoring an increase (decrease) in precipitation in the North China–Hetao (Yangtze–Yellow river) region. Under the background of the negative phase of the EAP teleconnection, anomalous westerly

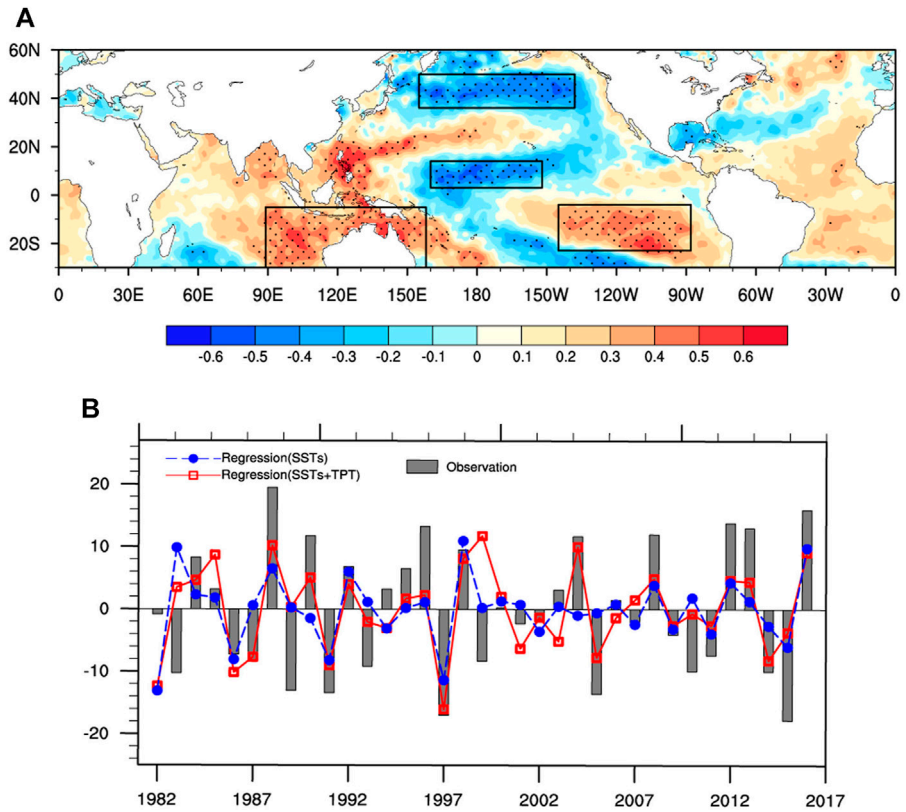

FIGURE 8 | (A) Partial correlation coefficient between summer precipitation in the North China–Hetao region and the preceding spring SST after removal of the impact of the spring TPT. **(B)** Times series of the observed and regressed anomalous summer precipitation over the North China–Hetao region (mm). The shaded areas in part **(A)** are significant at the 95% confidence level.

TABLE 1 | Stepwise regression of summer precipitation in the North China–Hetao region.

	SST in MHNP	SST in TCP	SST in TEP	SST in EIO	TPT	*R* (observed, fitted)
1	−6.4	−12.2	/	13.7	—	0.52**
2	/	−16.9	/	16.4	11.2	0.66**

*Note: the prediction factors are the previous spring SSTs and TPT. The range of each sea area is shown in **Figure 8a**. — represent the prediction factor which has not being introduced. / represent the prediction factor which has being eliminated by stepwise regression. ** Above the 99% confidence level.*

winds prevail between the anomalous cyclone over the Okhotsk Sea and the anomalous anticyclone at mid-latitudes in East Asia and the western Pacific in the subsequent summer, indicating a northward shift in the East Asian subtropical westerly jet. The South Asia high weakens and shrinks westward. These conditions all favor an increase in precipitation in the North China–Hetao region.

The improvement in the use of the spring TPT to predict summer precipitation in the North China–Hetao region was examined by comparing the prediction equations without and with the prediction factor of the spring TPT on the basis of the SSTs, which have high correlations with precipitation in the North China–Hetao region. We first established a prediction equation for precipitation in the North China–Hetao region based on the prediction factor of SSTs in the MHNP, TCP, and EIO. The correlation coefficient between the regressed and observed summer precipitation time series is 0.52. The spring TPT was then introduced as a prediction factor for precipitation in the North China–Hetao region. Another prediction equation was then established based on the prediction factors of the spring TPT and SSTs in the TCP and EIO. The correlation coefficient between the predicted and observed precipitation was improved to 0.66. After considering the impact of the spring TPT, the explanatory variance of the prediction equation for precipitation in the North China–Hetao region increased by 17.3%.

This study focused on the impact and prediction of the spring TPT for precipitation in the subsequent summer in eastern China on interannual scales. The actual forecasts cover various

timescales. It is worth investigating further how to apply this interannual link to the prediction of actual precipitation.

This study examined the improvement in the prediction of summer precipitation in the North China–Hetao region using the spring TPT on the basis of the SSTs. Previous research has shown that many variables can affect the precipitation of North China–Hetao region, such as the snow cover (Yang and Xu, 1994) and the sea ice concentration (Li and Zeng, 2008). The multiple factors should be explored in the future to improve the prediction skill for the precipitation in the North China–Hetao region.

DATA AVAILABILITY STATEMENT

Publicly available datasets were analyzed in this study. This data can be found here: https://apps.ecmwf.int/datasets/, https://www.metoffice.gov.uk/hadobs/.

AUTHOR CONTRIBUTIONS

DC: Methodology, Data curation, Writing-Original draft preparation; SN: Conceptualization, Writing-Reviewing and Editing; CZ: Writing-Reviewing and Editing; RS: Investigation; GL: Writing-Reviewing and Editing; YA: Writing-Reviewing and Editing; XL: Data collection.

FUNDING

This work was jointly sponsored by the National Natural Science Foundation of China (41775084); Opening Found of Key Laboratory of Land Surface Process and Climate Change in Cold and Arid Regions, Chinese Academy of Sciences (LPCC2019007); Key Special Projects of National Key R and D Program of China (2018YFC1505706); National Natural Science Foundation of China (42075045) and the Basic Research Fund of Chinese Academy of Meteorological Sciences (2019Z008; 2021Z007).

REFERENCES

Chen, L., and Wu, R. (2000). Interannual and Decadal Variations of Snow Cover over Qinghai-Xizang Plateau and Their Relationships to Summer Monsoon Rainfall in China. *Adv. Atmos. Sci.* 17, 18–30. doi:10.1007/s00376-000-0040-7

Chen, Y., and Zhai, P. (2015). Synoptic-scale Precursors of the East Asia/Pacific Teleconnection Pattern Responsible for Persistent Extreme Precipitation in the Yangtze River Valley. *Q.J.R. Meteorol. Soc.* 141, 1389–1403. doi:10.1002/qj.2448

Cui, Y., and Wang, C. (2009). Comparison of Sensible and Latent Heat Fluxes during the Transition Season over the Western Tibetan Plateau from Reanalysis Datasets. *Prog. Nat. Sci.* 19 (6), 719–726. doi:10.1016/j.pnsc.2008.11.001

Duan, A., Liu, Y., and Wu, G. (2005). Heating Status of the Tibetan Plateau from April to June and Rainfall and Atmospheric Circulation Anomaly over East Asia in Midsummer. *Sci. China Ser. D-earth Sci.* 48 (2), 250–257. doi:10.1360/02yd0510

Duan, A., Wang, M., Lei, Y., and Cui, Y. (2013). Trends in Summer Rainfall over China Associated with the Tibetan Plateau Sensible Heat Source during 1980-2008. *J. Clim.* 26 (1), 261–275. doi:10.1175/JCLI-D-11-00669.1

He, C., Wang, Z., Zhou, T., and Li, T. (2019). Enhanced Latent Heating over the Tibetan Plateau as a Key to the Enhanced East Asian Summer Monsoon Circulation under a Warming Climate. *J. Clim.* 32 (11), 3373–3388. doi:10.1175/JCLI-D-18-0427.1

Hu, J., and Duan, A. (2015). Relative Contributions of the Tibetan Plateau thermal Forcing and the Indian Ocean Sea Surface Temperature basin Mode to the Interannual Variability of the East Asian Summer Monsoon. *Clim. Dyn.* 45, 2697–2711. doi:10.1007/s00382-015-2503-7

Hu, P., Feng, G., Dogar, M. M., Cheng, J., and Gong, Z. (2020). Joint Effect of East Asia-Pacific and Eurasian Teleconnections on the Summer Precipitation in North Asia. *J. Meteorol. Res.* 34 (3), 559–574. doi:10.1007/s13351-020-9112-z

Huang, R. H. (1992). The East Asia/Pacific Pattern Teleconnection of Summer Circulation and Climate Anomaly in East Asia. *J. Meteorol. Res* 6, 25–37.

Huang, R. H., and Li, W. J. (1987). Influence of the Heat Source Anomaly over the Western Tropical Pacific on the Subtropical High over East Asia (in Chinese). Proc. Int. Conf. on the General Circulation of East Asia. April 10-15, 1987, Chengdu, China. 40–45. Available at: https://www.ixueshu.com/document/946e317b94c48768256dff31f1b37dc5318947a18e7f9386.html

Huang, R., and Wu, Y. (1989). The Influence of ENSO on the Summer Climate Change in China and its Mechanism. *Adv. Atmos. Sci.* 6, 21–31. doi:10.1007/BF02656915

Huang, Y., and Qian, Y. (2004). Relationship between South Asian High and Characteristic of Precipitation in Mid-and Lower-Reaches of Yangtze River and North China (In Chinese). *Plateau Meteorol.* 23 (1), 68–74. doi:10.3321/j.issn:1000-0534.2004.01.010

Huang, Y., Qian, Y., and Wan, Q. (2006). Simulation and Analysis about the Effects of Geopotential Height Anomaly in Tropical and Subtropical Region on Droughts or Floods in the Yangtze River Valley and North China. *J. Meteor Res.* 20 (4), 426–436. doi:10.1016/S1872-2032(06)60022-X

Jiang, X., and Ting, M. (2017). A Dipole Pattern of Summertime Rainfall across the Indian Subcontinent and the Tibetan Plateau. *J. Clim.* 30, 9607–9620. doi:10.1175/JCLI-D-16-0914.1

Jiang, X., Zhang, T., Tam, C. Y., Chen, J., Lau, N. C., Yang, S., et al. (2019). Impacts of ENSO and IOD on Snow Depth over the Tibetan Plateau: Roles of Convections over the Western North Pacific and Indian Ocean. *J. Geophys. Res. Atmos.* 124, 11961–11975. doi:10.1029/2019JD031384

Kuang, X., and Zhang, Y. (2006). Impact of the Position Abnormalities of East Asian Subtropical Westerly Jet on Summer Precipitation in Middle-Lower Reaches of Yangtze River (In Chinese). *Plateau Meteor*, 25 (3), 266–277. doi:10.3321/j.issn:1000-0534.2006.03.004

Li, F., and Zeng, Q. (2008). Statistical Prediction of East Asian Summer Monsoon Rainfall Based on SST and Sea Ice Concentration. *J. Meteorol. Soc. Jpn.* 86 (1), 237–243. doi:10.2151/jmsj.86.237

Li, H.-X., Chen, H.-P., and Wang, H.-J. (2017). Influence of North Pacific SST on Heavy Precipitation Events in Autumn over North China. *Atmos. Oceanic Sci. Lett.* 10 (1), 21–28. doi:10.1080/16742834.2017.1237256

Li, H., Zhai, P., Chen, Y., and Lu, E. (2018). Potential Influence of the East Asia-Pacific Teleconnection Pattern on Persistent Precipitation in South China: Implications of Atypical Yangtze River Valley Cases. *Weather Forecast.* 33 (1), 267–282. doi:10.1175/WAF-D-17-0011.1

Liu, G., Zhao, P., Chen, J., and Yang, S. (2015). Preceding Factors of Summer Asian-Pacific Oscillation and the Physical Mechanism for Their Potential Influences. *J. Clim.* 28 (7), 2531–2543. doi:10.1175/JCLI-D-14-00327.1

Liu, Y., Wu, G., Hong, J., Dong, B., Duan, A., Bao, Q., et al. (2012). Revisiting Asian Monsoon Formation and Change Associated with Tibetan Plateau Forcing: II. Change. *Clim. Dyn.* 39 (5), 1183–1195. doi:10.1007/s00382-012-1335-y

Nan, S., Zhao, P., Chen, J., and Liu, G. (2021). Links between the thermal Condition of the Tibetan Plateau in Summer and Atmospheric Circulation and Climate Anomalies over the Eurasian Continent. *Atmos. Res.* 247, 105212. doi:10.1016/j.atmosres.2020.105212

Nan, S., Zhao, P., and Chen, J. (2019). Variability of Summertime Tibetan Tropospheric Temperature and Associated Precipitation Anomalies over the Central-Eastern Sahel. *Clim. Dyn.* 52 (3-4), 1819–1835. doi:10.1007/s00382-018-4246-8

Nan, S., Zhao, P., Yang, S., and Chen, J. (2009). Springtime Tropospheric Temperature over the Tibetan Plateau and Evolutions of the Tropical Pacific SST. *J. Geophys. Res.* 114 (D10). doi:10.1029/2008JD011559

Nitta, T. (1987). Convective Activities in the Tropical Western Pacific and Their Impact on the Northern Hemisphere Summer Circulation. *J. Meteorol. Soc. Jpn.* 65, 373–390. doi:10.2151/jmsj1965.65.3_373

Qian, C., and Zhou, T. (2014). Multidecadal Variability of North China Aridity and its Relationship to PDO during 1900-2010. *J. Clim.* 27 (3), 1210–1222. doi:10.1175/JCLI-D-13-00235.1

Rayner, N. A., Parker, D. E., Horton, E. B., Folland, C. K., Alexander, L. V., Rowell, D. P., et al. (2003). Global Analyses of Sea Surface Temperature, Sea Ice, and Night marine Air Temperature since the Late Nineteenth century. *J. Geophys. Res.* 108 (D14), 4407. doi:10.1029/2002JD002670

Simmons, A., Uppala, S., Dee, D., and Kobayashi, S. (2007). ERA Interim: New ECMWF Reanalysis Products from 1989 Onwards. *ECMWF Newsl.* 110, 25–35. Available at: https://www.researchgate.net/publication/255267047_ERAInterim_New_ECMWF_reanalysis_products_from_1989_onwards

Wang, C., Yang, K., Li, Y., Wu, D., and Bo, Y. (2017). Impacts of Spatiotemporal Anomalies of Tibetan Plateau Snow Cover on Summer Precipitation in Eastern China. *J. Clim.* 30 (3), 885–903. doi:10.1175/JCLI-D-16-0041.1

Wang, L., Wang, C., and Guo, D. (2018). Evolution Mechanism of Synoptic-Scale EAP Teleconnection Pattern and its Relationship to Summer Precipitation in China. *Atmos. Res.* 214, 150–162. doi:10.1016/j.atmosres.2018.07.023

Wang, S., and Zuo, H. (2016). Effect of the East Asian Westerly Jet's Intensity on Summer Rainfall in the Yangtze River Valley and its Mechanism. *J. Clim.* 29 (7), 2395–2406. doi:10.1175/JCLI-D-15-0259.1

Wang, Z., Duan, A., and Wu, G. (2014). Time-lagged Impact of spring Sensible Heat over the Tibetan Plateau on the Summer Rainfall Anomaly in East China: Case Studies Using the WRF Model. *Clim. Dyn.* 42, 2885–2898. doi:10.1007/s00382-013-1800-2

Wu, G., Liu, Y., Zhang, Q., Duan, A., Wang, T., Wan, R., et al. (2007). The Influence of Mechanical and thermal Forcing by the Tibetan Plateau on Asian Climate. *J. Hydrometeor* 8, 770–789. doi:10.1175/JHM609.1

Xu, K., Huang, Q.-L., Tam, C.-Y., Wang, W., Chen, S., and Zhu, C. (2019). Roles of Tropical SST Patterns during Two Types of ENSO in Modulating Wintertime Rainfall over Southern China. *Clim. Dyn.* 52 (1/2), 523–538. doi:10.1007/s00382-018-4170-y

Xuan, S., Zhang, Q., Sun, S., and Shi, C. (2018). Contrast in the East Asian Subtropical westerly Jet and its Association with Precipitation in China between Early Summer and Midsummer. *Met. Apps* 25 (1), 119–127. doi:10.1002/met.1675

Yanai, M., Li, C., and Song, Z. (1992). Seasonal Heating of the Tibetan Plateau and its Effects on the Evolution of the Asian Summer Monsoon. *J. Meteorol. Soc. Jpn.* 70 (1), 319–351. doi:10.2151/jmsj1965.70.1B_319

Yang, S., and Xu, L. (1994). Linkage between Eurasian winter Snow Cover and Regional Chinese Summer Rainfall. *Int. J. Climatol.* 14 (7), 739–750. doi:10.1002/joc.3370140704

Yu, R., Wang, B., and Zhou, T. (2004). Tropospheric Cooling and Summer Monsoon Weakening Trend over East Asia. *Geophys. Res. Lett.* 31, L22212. doi:10.1029/2004GL021270

Zhang, L., Wu, P., Zhou, T., and Xiao, C. (2018). ENSO Transition from La Niña to El Niño Drives Prolonged Spring-Summer Drought over North China. *J. Clim.* 31 (9), 3509–3523. doi:10.1175/JCLI-D-17-0440.1

Zhang, R., Sumi, A., and Kimoto, M. (1999). A Diagnostic Study of the Impact of El Niño on the Precipitation in China. *Adv. Atmos. Sci.* 16, 229–241. doi:10.1007/BF02973084

Zhang, Y., Li, Z., and Liu, B. (2015). Interannual Variability of Surface Sensible Heating over the Tibetan Plateau in Boreal spring and its Influence on the Onset Time of the Indian Summer Monsoon. *Chin. J. Atmos. Sci. (In Chinese)* 39 (6), 1059–1072. doi:10.3878/j.issn.1006-9895.1410.14226

Zhao, P., and Chen, L. (2001). Climatic Features of Atmospheric Heat Source/sink over the Qinghai-Xizang Plateau in 35 Years and its Relation to Rainfall in China. *Sci. China Ser. D-earth Sci.* 44 (9), 858–864. doi:10.1007/BF02907098

Zhao, Y., Duan, A., and Wu, G. (2018). Interannual Variability of Late-spring Circulation and Diabatic Heating over the Tibetan Plateau Associated with Indian Ocean Forcing. *Adv. Atmos. Sci.* 35, 927–941. doi:10.1007/s00376-018-7217-4

Zhao, Y., Duan, A., Wu, G., and Sun, R. (2019). Response of the Indian Ocean to the Tibetan Plateau thermal Forcing in Late spring. *J. Clim.* 32 (20), 6917–6938. doi:10.1175/JCLI-D-18-0880.1

Zhou, X., Zhao, P., Chen, J., Chen, L., and Li, W. (2009). Impacts of Thermodynamic Processes over the Tibetan Plateau on the Northern Hemispheric Climate. *Sci. China Ser. D-earth Sci.* 52, 1679–1693. doi:10.1007/s11430-009-0194-9

Zhu, Y., Wang, H., Ma, J., Wang, T., and Sun, J. (2015). Contribution of the Phase Transition of Pacific Decadal Oscillation to the Late 1990s' Shift in East China Summer Rainfall. *J. Geophys. Res. Atmos.* 120 (17), 8817–8827. doi:10.1002/2015JD023545

Conflict of Interest: The authors declare that the research was conducted in the absence of any commercial or financial relationships that could be construed as a potential conflict of interest.

frontiers in Earth Science

ORIGINAL RESEARCH
published: 07 July 2021
doi: 10.3389/feart.2021.699358

Impact of Autumn-Winter Tibetan Plateau Snow Cover Anomalies on the East Asian Winter Monsoon and Its Interdecadal Change

Zhang Chen[1]*, *Renguang Wu*[2,3,4] and *Zhibiao Wang*[3]

[1]Plateau Atmosphere and Environment Key Laboratory of Sichuan Province, School of Atmospheric Sciences, Chengdu University of Information Technology, Chengdu, China, [2]Department of Atmospheric Sciences and Key Laboratory of Geoscience Big Data and Deep Resource of Zhejiang Province, School of Earth Sciences, Zhejiang University, Hangzhou, China, [3]Center for Monsoon System Research, Institute of Atmospheric Physics, Chinese Academy of Sciences, Beijing, China, [4]Southern Marine Science and Engineering Guangdong Laboratory (Zhuhai), Zhuhai, China

The present study investigates the impacts of autumn-winter Tibetan Plateau (TP) snow cover anomalies on the interannual variability of the East Asian winter monsoon (EAWM). It is found that the northern component of EAWM is significantly associated with October-November-December-January (ONDJ) snow cover anomalies over the eastern TP, whereas the TP snow cover changes have little impact on the southern component of EAWM. However, the relationship of the northern component of EAWM to ONDJ TP snow cover experienced an obvious change in the mid-1990s. During 1979–1998, due to the high persistence of TP snow anomalies from autumn to winter, extensive ONDJ TP snow cover anomalies have a prominent influence on atmospheric circulation over Asia and the North Pacific, with more TP snow cover followed by an enhanced Siberian high and a deepened Aleutian low in winter, resulting in stronger EAWM. During 1999–2016, TP snow cover anomalies have a weak persistence. The atmospheric circulation anomalies display a different distribution. As such, there is a weak connection between the northern component of EAWM and the TP snow cover anomalies during this period.

Keywords: East asian winter monsoon, tibetan plateau snow cover, persistence of snow cover anomalies, interdecadal change, aleutian low

OPEN ACCESS

Edited by:
Yuqing Wang,
University of Hawaii at Manoa,
United States

Reviewed by:
Yunyun Liu,
National Climate Center, China
Chenghai Wang,
Lanzhou University, China

***Correspondence:**
Zhang Chen
chenzhang@cuit.edu.cn

Specialty section:
This article was submitted to Atmospheric Science, a section of the journal Frontiers in Earth Science

Received: *23 April 2021*
Accepted: *28 June 2021*
Published: *07 July 2021*

Citation:
Chen Z, Wu R and Wang Z (2021) Impact of Autumn-Winter Tibetan Plateau Snow Cover Anomalies on the East Asian Winter Monsoon and Its Interdecadal Change. Front. Earth Sci. 9:699358. doi: 10.3389/feart.2021.699358

INTRODUCTION

The Tibetan Plateau (TP) is the highest plateau on earth with an average altitude over 4,000 m above sea level. Due to its high elevation, the TP is covered by snow in most of the year (Wang C. et al., 2017). As an important lower boundary condition, snow anomalies may change the surface energy budget and hydrological cycle, and induce both local and remote atmospheric responses (Barnett et al., 1989; Yasunari et al., 1991).

The impacts of the TP snow cover on global climate have received considerable attention. Numerous studies investigated the relationship between the TP snow cover and the Indian summer monsoon (e.g., Blanford 1884; Fasullo 2004; Zhao and Moore 2004) and the East Asian summer monsoon (e.g., Wu and Qian 2003; Wu and Kirtman 2007; Xiao and Duan 2016; Wang et al., 2018). The snow cover anomalies over the TP can also influence surface air temperature (SAT) variations over North America (e.g., Lin and Wu 2011; Qian et al., 2019; Wang et al., 2020), but the linkage

between them is not stationary (e.g., Qian et al., 2019; Wang et al., 2020). Qian et al. (2019) showed that the connection between the TP autumn snow cover and the North America winter SAT is weakened after the mid-1990s. Wang et al. (2020) detected that the impact of the TP snow cover on the North America SAT in spring experienced a weakening in the mid-2000s. In addition, observational and numerical studies suggest that the TP snow anomaly can trigger near-global atmospheric circulation patterns, such as the Pacific-North American (PNA)-like teleconnection (e.g., Lin and Wu 2011; Wu et al., 2011; Liu et al., 2017) and the Western Pacific-like teleconnection (e.g., Liu et al., 2020).

Most of previous studies are concentrated on the impacts of the TP snow on summer monsoon. The effects of snow cover anomalies over the TP on the East Asian winter monsoon (EAWM) are rarely studied. The EAWM is one of the most active components in the global climate system during boreal winter, and it exerts large impacts on the Asia-Pacific winter climate (e.g., Lau and Chang 1987). Thus, it is valuable to investigate whether and how the TP snow cover anomalies influence the EAWM variability, and whether the relationship between the TP snow and EAWM has experienced interdecadal changes in the past? Furthermore, previous studies have demonstrated that the EAWM variability is dominated by two distinct components: the northern (mid-latitude) and southern (low-latitude) components (e.g., Wang et al., 2010; Liu et al., 2012; Chen et al., 2014a) and the two components have notably different circulation systems and factors (e.g., Liu et al., 2012, 2013; Chen et al., 2014a, 2014b; Chen et al., 2019). Additionally, climate anomalies associated with the two components of EAWM are also different. Chen et al. (2014a) found that when the northern component of EAWM is strong, significant cooling occurs over northwest and northeast China and significant warming is confined to southwestern China. However, when only the southern component of EAWM is strong, significant warming is observed in northeast China and the surface air anomalies are small over other regions of China. Therefore, to better understand the TP snow cover-related EAWM variability, it is necessary to consider the two components of the EAWM separately.

DATA AND METHODS

The original weekly Northern Hemisphere snow cover data are acquired from the National Snow and Ice Data Center (NSIDC) (Brodzik and Armstrong 2013) (http://nsidc.org/data/). The data spans the period from October 1966 to December 2017, with a spatial resolution of 25 km. We have converted the raw snow cover data to monthly mean on regular $1^{\circ} \times 1^{\circ}$ grids for our analyses. The monthly mean atmospheric data used in this study are from the National Centers for Environmental Prediction-Department of Energy (NCEP-DOE) Reanalysis-2, spanning the time period from 1979 to present (Kanamitsu et al., 2002) (https://www.esrl.noaa.gov/psd/). The variables include winds and geopotential heights at pressure levels, sea level pressure (SLP), surface air temperature (SAT), surface latent heat flux, surface sensible heat flux, upward and downward shortwave radiation, upward and downward longwave radiation and precipitation rate. The resolution of the NCEP-DOE reanalysis data is $2.5^{\circ} \times 2.5^{\circ}$ for pressure level variables. The surface variables have a resolution of T62. The period of analysis in this study is from 1979 to 2016, and the winter of 1979 refers to the three months from December 1979 to February 1980. Since we focus on the interannual variability, all the variables are filtered by a 9-years high-pass Lanczos filter (Duchon 1979).

Following Chen et al. (2014a), we used area-mean 1000hPa meridional wind anomalies in December-January-February (DJF) over the regions of 10°–25°N, 105°–135° E (hereinafter, Sindex) and 35°–55°N, 110°–125°E (hereinafter, Nindex) to represent the southern and northern components of the EAWM variability, respectively. Note that these two indices have been multiplied by -1 so that a positive (negative) value of the index corresponds to a strong (weak) EAWM. The Aleutian low index is defined as the regionally averaged winter SLP anomaly over the region 30°–50°N, 160°–210°E. The Pacific-North American pattern (PNA) index is produced by the Climate Prediction Center (CPC, https://www.cpc.ncep.noaa.gov/).

The total atmospheric column heat source (Q_1) defined by Zhao and Chen (2001) is applied to examine the effect of snow cover anomalies on the atmosphere. Q_1 is calculated as follows:

$$Q_1 = \mathrm{SH} + R_{net} + LP \quad (1)$$

SH denotes sensible heat flux at the surface, R_{net} refers to the net radiation in the atmospheric column, and LP represents the condensation-released latent heat.

RESULTS

Relationship Between the Tibetan Plateau Snow Cover and East Asian winter monsoon

To explore the relationship between autumn-winter TP snow cover and the two components of the EAWM variability during 1979–2016, a correlation analysis was performed for October-November-December-January (ONDJ) TP snow cover anomalies with respect to the winter Nindex and Sindex separately (**Figures 1A,B**). The Nindex displays a significantly positive correlation with snow cover in the eastern TP (**Figure 1A**), whereas the Sindex shows a weak correlation over almost the whole TP (**Figure 1B**). Based on the distribution of significant correlation coefficients, we choose the region of 31°–37°N and 86°–98°E (denoted by the box in **Figure 1A**) as a key region to analyze the influence of TP snow cover anomalies on EAWM variability. The selected key region also shows a large standard deviation of the interannual variation of snow cover in ONDJ (figure not shown).

To illustrate why we focus on the TP snow cover in ONDJ, area-mean snow cover anomalies in the TP key region are constructed for months from September to the following February. Then, we calculate the month-to-month correlation

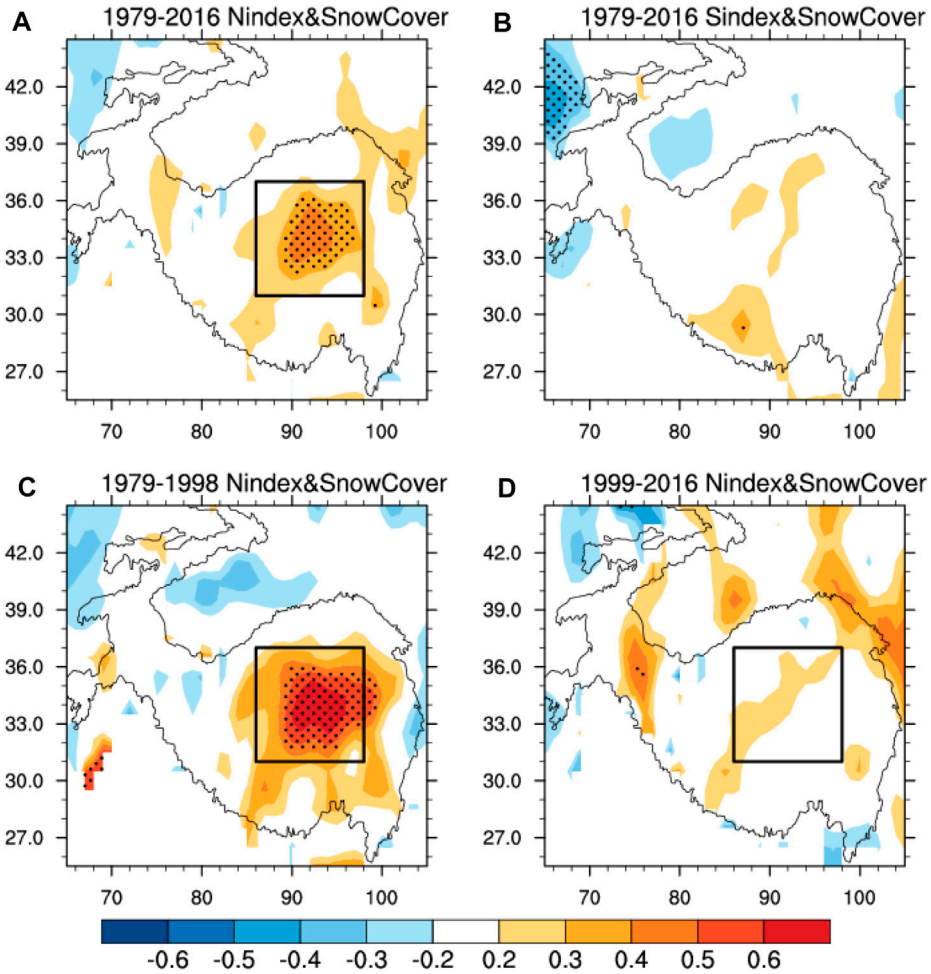

FIGURE 1 | Correlation coefficients between the ONDJ snow cover anomalies over the Tibetan Plateau and the Nindex during 1979–2016 **(A)**, 1979–1998 **(C)**, and 1999–2016 **(D)**, and those between the ONDJ snow cover anomalies over the Tibetan Plateau and the Sindex during 1979–2016 **(D)**. The dotted regions represent the correlation coefficients significant at the 95% confidence level. The box denotes the key region over the Tibetan Plateau that is used to define the SCI.

TABLE 1 | Correlation coefficients between the neighboring month snow cover from September to February of the following year in the selected key region over the eastern TP for 1979–2016. Symbol "*", "**" and "***" denote correlation coefficients significant at the 90, 95 and 99% confidence level.

	Oct	Nov	Dec	Jan	Feb
Sep	0.29*	0.25	−0.03	0.19	0.20
Oct		0.65***	0.23	0.12	0.18
Nov			0.57***	0.20	0.46***
Dec				0.60***	0.31*
Jan					0.35**

coefficients between those area-mean snow cover anomalies (**Table 1**). The correlation coefficient between September and October is significant at the 90% confidence level and that between January and February is significant at the 95% confidence level. The other correlation coefficients between October and November, between November and December, and between December and January are all significant at the 99% confidence level. This implies a month-to-month persistence of snow cover anomalies during September through January, consistent with previous studies (e.g., Wang et al., 2019). According to the magnitude of 1-month lag correlation coefficient, we combine the snow cover anomalies in the four months of October, November, December and January in analyzing the TP snow cover influences.

An ONDJ TP snow cover index (SCI) is defined as area-mean ONDJ snow cover anomalies over the key region to represent the TP snow cover variation. During 1979–2016, the correlation coefficient of Nindex and Sindex with ONDJ TP SCI is 0.42 and 0.07, respectively, with the former reaching the 99% confidence level. This indicates that there is a close relationship between the ONDJ TP snow cover anomaly and the northern component of EAWM, but the TP snow cover has a weak effect on the southern component of EAWM.

Similar domains have been used in previous studies in defining snow cover indices to study the relationship between the TP snow

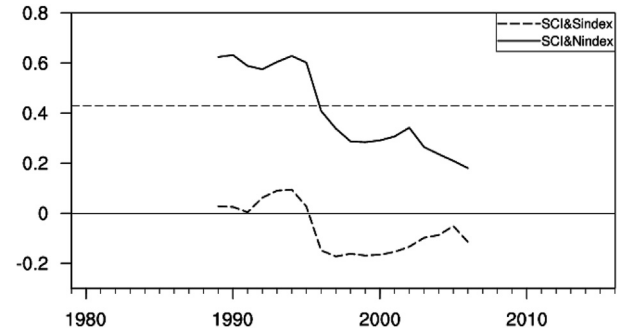

FIGURE 2 | The 21-years sliding correlation between the ONDJ TP SCI and the Nindex (solid line) and Sindex (dashed line) of EAWM. The years are labeled based on the central year of the 21-years window. The horizontal dashed lines indicate correlation coefficient the 95% confidence level.

cover and climate. Qian et al. (2019) calculated an area mean SCI in the region of 27.5°–36.0°N and 88.5°–100.5°E based on the spatial distribution of both climatological mean snow amount and the standard deviation of interannual variation of snow cover in autumn. According to the loading of the first EOF mode of autumn-winter mean snow cover, Wang et al. (2019) used area mean snow cover anomalies averaged over the central eastern region as an SCI. In the present study, we choose the region based on the distribution of significant correlation between the northern component of EAWM and the ONDJ TP snow cover.

The statistical relationship between the ONDJ TP snow cover and EAWM variations appears unsteady. The changing relationship is illustrated in **Figure 2** that displays the sliding correlation between the ONDJ TP SCI and the Nindex and Sindex of the EAWM with a 21-years window. The SCI-Nindex correlation remains significant positive before the mid-1990s, but it weakens dramatically around the mid-1990s and becomes insignificant after the mid-1990s (**Figure 2**, solid line). In contrast, the SCI-Sindex correlation is weak and insignificant during the period of analysis though its magnitude shows changes (**Figure 2**, dashed line). This result reconfirms that the southern component of EAWM does not have an obvious relationship to the TP snow cover during 1979–2016. Thus, we focus on the effects of the TP snow cover on the northern component of EAWM in the following analysis.

To understand the interdecadal changes in the ONDJ TP snow cover-northern component of EAWM connection, we separate the analysis period (1979–2016) into two subperiods, 1979–1998 as the high correlation period and 1999–2016 as the low correlation period. These two epochs are selected because the difference of the correlation achieves large contrast between the neighboring periods. The correlation coefficient between the ONDJ TP SCI and Nindex is 0.57 and 0.22, respectively, for the above two subperiods. Only the former exceeds the 99% confidence level. The changing relationship between the ONDJ TP snow cover and the northern component of EAWM can be verified by the spatial distributions of correlation coefficients between the ONDJ TP snow cover anomalies and Nindex during 1979–1998 and 1999–2016 as shown in **Figures 1C,D**. Apparently, the correlation with the Nindex is significant positive over the eastern TP during 1979–1998 (**Figure 1C**), but becomes weak during 1999–2016 (**Figure 1D**).

Processes Connecting the Tibetan Plateau Snow Cover to East Asian Winter Monsoon During 1979–1998

Previous studies pointed out that the impacts of snow on climate in local and remote regions are through modulating local atmospheric column heating (e.g., Xiao and Duan 2016; Wang et al., 2018; Qian et al., 2019). In this section, in order to understand the plausible physical processes that link the ONDJ TP snow cover to the northern component of EAWM for the period 1979–1998, we illustrate first the concurrent influence of TP snow cover anomalies on local atmospheric thermal condition. Then, we analyze the winter atmospheric circulation anomalies associated with the ONDJ TP snow cover anomalies and document their role in connecting the TP snow cover and EAWM variability.

Figure 3 presents anomalies of surface heat fluxes as well as anomalies of SAT and Q_1 obtained by regression on SCI. Positive TP snow cover anomalies in the key region are accompanied by increased upward shortwave radiation flux (USWR, **Figure 3A**), which is attributed to the snow-albedo effect. Upward longwave radiation (ULWR) is reduced (**Figure 3B**) following the land surface temperature decrease (figure not shown), which is attributed to the absorption of less shortwave radiation by the land surface. Upward sensible heat flux (SHF) decreases notably (**Figure 3C**) due to the snow interception of heat exchange and the decrease of surface temperature. Latent heat flux (LHF) anomalies are small (**Figure 3D**). As a consequence, positive snow cover anomalies cool the near-surface air (**Figure 3E**). Corresponding to more snow cover, significant negative Q_1 anomalies are observed over the eastern Plateau (**Figure 3F**). The correlation coefficient between SCI and area-mean Q_1 in the same domain as the SCI in ONDJ is -0.69, exceeding the 99% confidence level. These results confirm the cooling effect of more snow cover on local atmospheric column.

The cooling effect directly modulates the upper-level atmospheric state, which, in turn, may induce atmospheric circulation changes in remote regions. **Figure 4** shows 500 hPa geopotential height, SLP, and 850 hPa wind anomalies in winter obtained by regression against the ONDJ TP SCI during 1979–1998. Corresponding to more snow cover over the eastern Plateau, negative height anomalies dominate the coastal East Asia and the northern North Pacific, and large positive height anomalies are observed over northern Eurasia and North America (**Figure 4A**). Such a circulation anomaly pattern indicates a deepened East Asian trough and an enhanced ridge around the Ural Mountains. When the SCI is high, significant positive SLP anomalies are seen around the Lake Baikal and significant negative SLP anomalies occur over the northern North Pacific, reflecting an enhanced Siberian high and a deepened Aleutian low (**Figure 4B**). Previous modeling studies revealed that the autumn-winter TP snow cover is closely associated with the winter Aleutian low variability (e.g.,

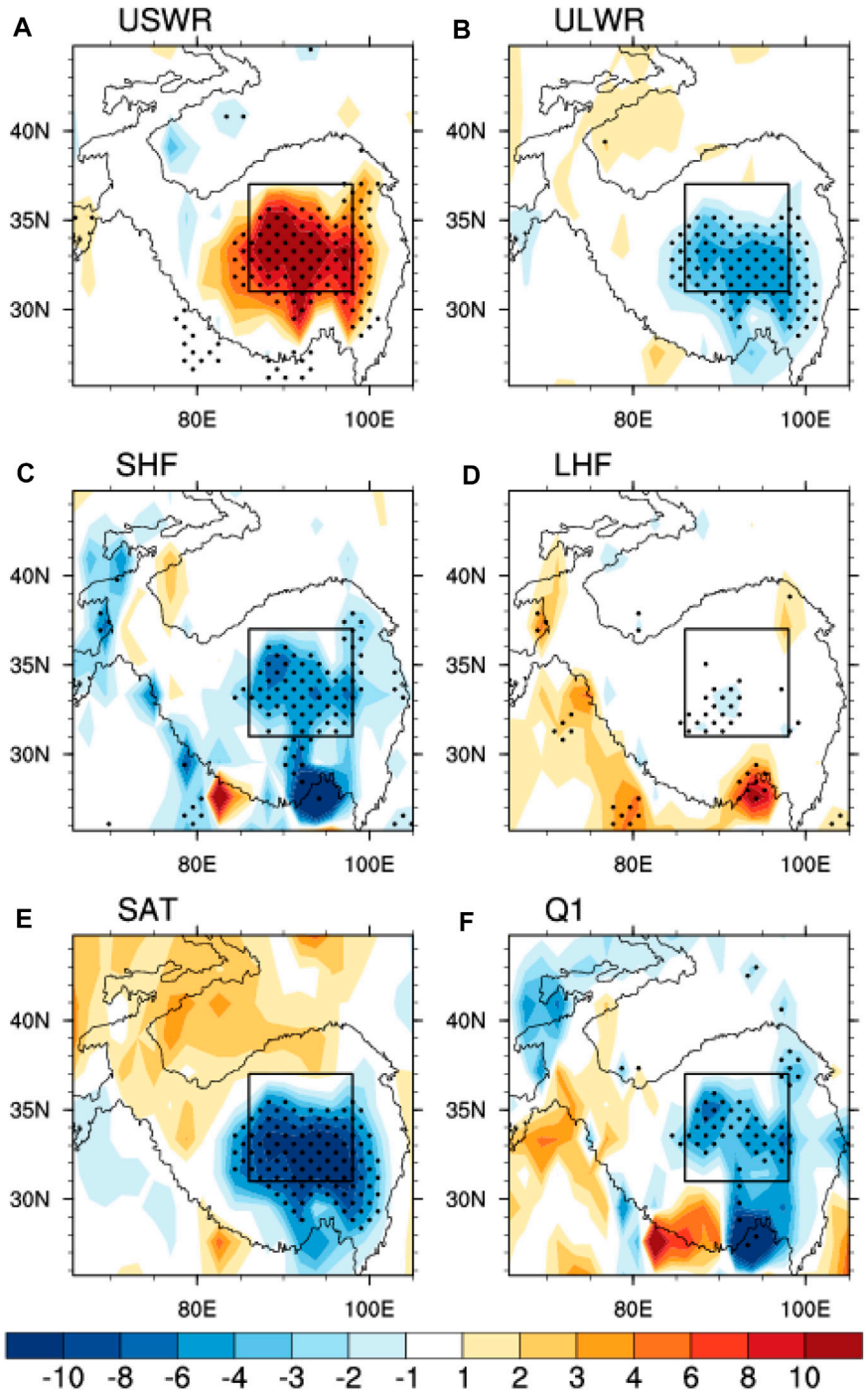

FIGURE 3 | Interannual anomalies of **(A)** upward shortwave radiation flux (Wm^{-2}), **(B)** upward longwave radiation flux (Wm^{-2}), **(C)** sensible heat flux (Wm^{-2}), **(D)** latent heat flux (Wm^{-2}), **(E)** surface air temperature (×10, °C), and **(F)** Q_1 (Wm^{-2}) in ONDJ obtained by regression on the ONDJ TP SCI for the period 1979–1998. The dotted regions denote that anomalies are significant at the 95% confidence level. The box denotes the key region over the Tibetan Plateau that is used to define the SCI.

Yasunari et al., 1991; Walland and Simmonds 1996). Corresponding to the deepened Aleutian low, an anomalous cyclone is seen over the northern North Pacific (**Figure 4C**). The contrast of SLP anomalies over the Eurasian continent and the Aleutian low enhances the zonal gradient of SLP over East Asia, indicating a stronger EAWM. Indeed, significant northerly wind anomalies prevail over the coast of East Asia (**Figure 4C**). We have performed a regression analysis of winter atmospheric circulation with respect to ONDJ area-mean Q_1 in the selected TP key region (figures not shown). The results are generally similar

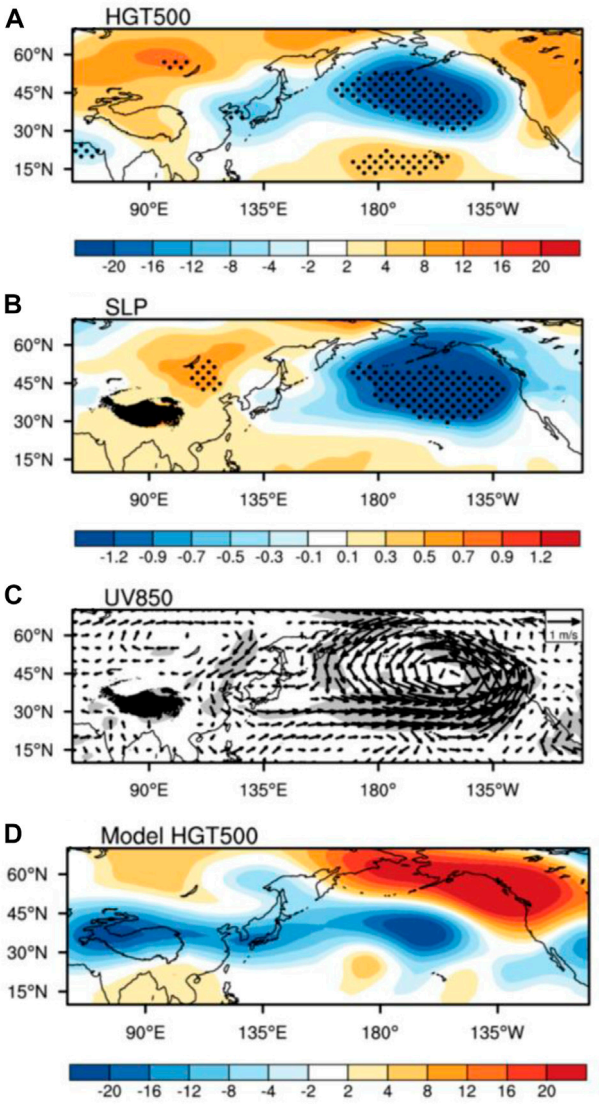

FIGURE 4 | Interannual anomalies of winter **(A)** 500°hPa geopotential height (m), **(B)** SLP (hPa) and (c) 850°hPa wind (ms^{-1}) obtained by regression on the ONDJ TP SCI for the period 1979–1998. (d) Difference of winter 500°hPa geopotential height (m) between the sensitivity experiment and control experiment based on the last 14-years simulations of the CAM model. The wind vector scale is shown on the top-right corner in **(C)**. The dotted regions in **(A, B)** and the shaded regions in **(C)** denote that anomalies of geopotential height in **(A)**, SLP in **(B)** and either u wind or v wind in (C) are significant at the 95% confidence level.

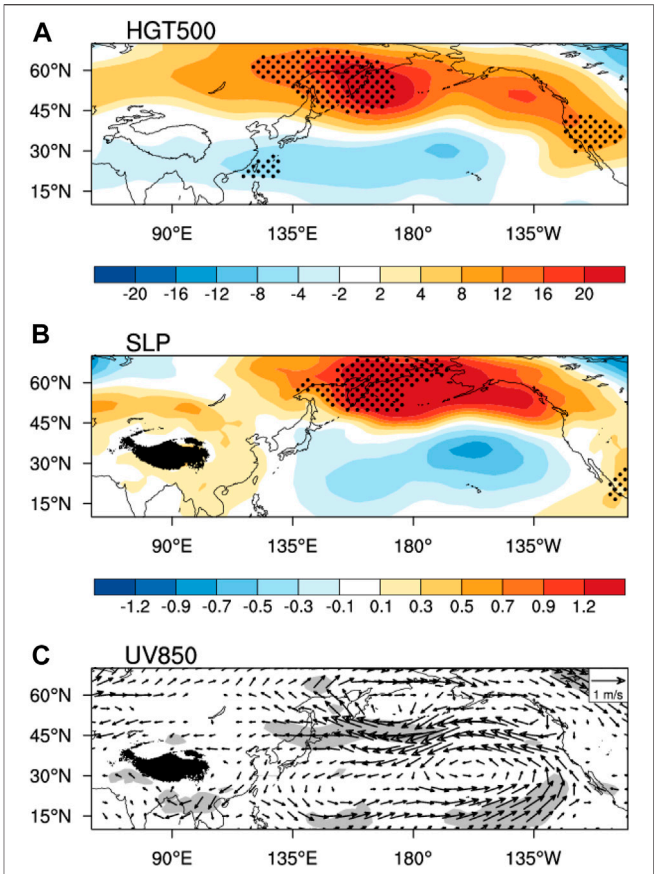

FIGURE 5 | As in **Figure 4**, but for 1999–2016.

to those shown in **Figure 4**. This confirms that snow cover anomalies modulate the atmospheric circulation in local and remote regions through changing local atmospheric column thermal state.

To confirm the role of the TP ONDJ snow cover anomalies on EAWM variations, we perform numerical experiments using the Community Atmospheric Model of version 5.0 (CAM5). The model is developed by the National Center for Atmospheric Research (Eaton 2011) with an approximately 1.9° × 2.5° latitude-longitude spatial resolution and 31 vertical levels. We perform one control experiment and one sensitivity experiment. In all experiments the model is integrated for 15°years. Since the albedo effect is the main way that snow cover affects the atmospheric variation, the albedo in the sensitivity experiment is set as 0.9 of that in the control experiment over the eastern Tibetan Plateau (see the box in **Figure 1C**) in ONDJ to represent the influence of positive TP snow cover anomalies. The model response derived as the difference between the sensitivity and control experiment displays negative height anomalies over the TP and the mid-latitude North Pacific and positive height anomalies over the northern Siberia, high-latitude North Pacific and Northern America (**Figure 4D**). The above distribution of height anomalies indicates an enhanced ridge around the Ural Mountains and a deepened East Asian trough, which agrees with that obtained in the observations (**Figure 4A** vs. **Figure 4D**).

Based on the above analyses, we propose the following processes connecting ONDJ snow cover anomalies over the eastern TP to winter Asian climate anomalies. The snow cover anomalies over the eastern TP have a significant cooling effect on local atmospheric column. The atmospheric cooling stimulates anomalous atmospheric circulation over East Asia and the North Pacific regions, leading to changes in the Aleutian low, the Siberian high, Ural ridge, and the East Asian trough. Chen et al. (2014a) pointed out that the northern component of

TABLE 2 | As in **Table 1**, but for 1979–1998.

	Oct	Nov	Dec	Jan	Feb
Sep	0.20	0.01	0.01	0.09	0.02
Oct		0.66***	0.23	0.33	0.51**
Nov			0.74***	0.54**	0.54**
Dec				0.75***	0.31
Jan					0.51**

TABLE 3 | As in **Table 1**, but for 1999–2016.

	Oct	**Nov**	**Dec**	**Jan**	**Feb**
Sep	0.34	0.36	–0.06	0.27	0.32
Oct		0.65***	0.27	–0.07	–0.11
Nov			0.32	–0.20	0.36
Dec				0.37	0.33
Jan					0.14

EAWM is mainly affected by the above mentioned mid-latitude circulation systems. Thus, the ONDJ TP snow cover anomalies impose an impact on the northern component of the EAWM variability in 1979–1998.

Note that the spatial distribution of the atmospheric circulation anomalies in **Figure 4A** shows a PNA-like structure over the North Pacific through North America. In fact, previous observational and numerical studies have already demonstrated that autumn and winter positive TP snow cover anomalies can lead to a remote equivalent barotropic PNA response in winter (e.g., Lin and Wu 2011; Wu et al., 2011; Liu et al., 2017). Liu et al. (2017) suggested that the PNA responses result mainly from the eastward propagation of Rossby wave energy forced by TP snow forcing and winter transient eddy feedback.

Why Is the Relationship Between the Tibetan Plateau Snow Cover and EAWM Weak During 1999–2016?

To understand how anomalous TP snow cover influences the EAWM variation differently between 1979–1998 and 1999–2016, the same analysis is conducted for 1999–2016. During 1999–2016, when the SCI is high, the most prominent characteristic of both the 500 hPa height and SLP anomalies is a meridional dipole structure over the North Pacific, with positive and negative anomalies located north and south of approximately 45°N, respectively (**Figures 5A,B**). Positive height and SLP anomalies also extend westward to Asia (**Figures 5A,B**). Overall, there is no obvious change in the intensity of the East Asian trough (**Figure 5A**), the Siberian high and the Aleutian low (**Figure 5B**) in winter. Anomalous anticyclone and cyclone are present over the high-latitude and mid-latitude North Pacific, respectively (**Figure 5C**). The wind anomalies along the coast of East Asia are weak (**Figure 5C**), indicating a normal EAWM. Thus, the connection of the ONDJ TP snow cover with the EAWM variability is weak during 1999–2016.

In comparison, the influence of ONDJ TP snow cover on large-scale atmospheric circulation over the North Pacific is distinctly different between 1979–1998 and 1999–2016. Extensive more autumn-winter TP snow generates a PNA-like atmospheric response and induces a deepened Aleutian low in winter during 1979–1998 (**Figures 4A,B**). However, the PNA response is absent and there are no obvious anomalies in the intensity of the Aleutian low during 1999–2016 (**Figures 5A,B**). The correlation coefficient of winter PNA and Aleutian low index with the ONDJ SCI during 1979–1998 is 0.45 and −0.55, respectively, both exceeding the 95% confidence level, and that during 1999–2016 is −0.22 and −0.10, respectively, both of which are insignificant.

Why cannot the ONDJ TP snow anomalies trigger a winter PNA response and a deepened Aleutian low during 1999–2016? Liu et al. (2017) found that with TP snow cover anomalies in autumn or winter only, the winter PNA response is nearly absent or noticeably reduced, and the most significant PNA response requires persistent TP snow forcing from autumn to winter. To explore the persistence of TP snow cover anomalies in the two periods, we calculated the month-to-month snow cover correlation coefficient for the two epochs, respectively. In the former period, except for the correlation coefficient between September and October, the other correlation coefficients between neighboring month snow cover anomalies are all significant (**Table 2**). This means that the TP snow cover anomalies have a high persistence from October to February during 1979–1998, which is favorable for generating a robust PNA-like response in winter (**Figures 4A,B**). However, in the latter period, only the correlation coefficient between October and November is significant, the other correlation coefficients are all insignificant (**Table 3**). Thus, the persistence of TP snow cover anomalies is weak during 1999–2016. As a consequence, TP snow forcing in autumn or winter does not produce a PNA-like winter response during this period (**Figures 5A,B**).

SUMMARY

The present study investigates the impacts of the autumn-winter TP snow cover anomalies on the two components of the EAWM variability on the interannual time scale. A close relationship is identified between the ONDJ snow cover anomalies in the eastern TP and the northern component of the EAWM variability. However, the southern component of EAWM does not appear to be related to the autumn-winter TP snow cover anomalies. The relationship of the northern component of EAWM to the anomalous ONDJ TP snow cover experienced an obvious change in the mid-1990s. The relationship is strong and statistically significant before the mid-1990s, whereas the connection is weak and insignificant after the mid-1990s. Thus, the target period (1979–2016) is divided into two subperiods, 1979–1998 as the high correlation period and 1999–2016 as the low correlation period.

During 1979–1998, the TP snow cover anomalies have high persistence from October to February. Extensive more autumn-winter snow cover over the eastern TP induces persistent cooling

in local atmospheric column and has a prominent influence on downstream atmospheric circulation over Asia and the North Pacific. The remote atmospheric responses in winter are mainly characterized by an enhanced Siberian high and a deepened Aleutian low, which result in stronger EAWM. During 1999–2016, due to weak persistence of TP snow cover anomalies from autumn to winter, the winter PNA-like response is nearly absent and the atmospheric circulation anomalies are relatively weak over East Asia. Thus, the connection between the northern component of EAWM and the ONDJ TP snow cover is weak during this period. For the recent two winters (2018/19 and 2019/20), the snow cover on the Tibetan Plateau is extremely above normal, while the value of Nindex is 0.12 and −1.62, respectively, for 2018/19 and 2019/20 winters, which is consistent with the weak statistical relationship during 1999–2016. Note that the percent variance of northern component of EAWM variability explained by ONDJ TP SCI is about 32% during 1979–1998. In addition, the northern component of EAWM is also affected by other factors, such as autumn Arctic sea ice concentration change (Chen et al., 2014b) and summer North Atlantic SST anomalies (Chen et al., 2019).

The analysis of Wang et al. (2019) illustrated that the opposite-sign sea surface temperature (SST) anomalies in the eastern North Pacific and western North Atlantic play an important role in the formation of snow cover anomalies over the central eastern TP in autumn. The SST anomalies in these regions may excite a wave train that extends to the TP and causes anomalous circulation and vertical motion, leading to anomalous snowfall over the eastern TP. It is worthy to note that the spatial distribution of atmospheric circulation anomalies over the North Pacific in **Figures 5A,B** shows a North Pacific Oscillation/western Pacific (WP)-like structure. Previous studies have already reported that the TP snow cover anomalies can lead to a WP-like response (e.g., Wang Z. et al., 2017; Liu et al., 2020). Why did the ONDJ TP snow forcing trigger a winter PNA response in 1979–1998 but a WP response in 1999–2016? Additionally, why is the persistence of TP snow cover anomalies from autumn to winter strong in 1979–1998 but weak in 1999–2016? Further studies are needed to address the above issues.

DATA AVAILABILITY STATEMENT

The original contributions presented in the study are included in the article/supplementary material, further inquiries can be directed to the corresponding author.

AUTHOR CONTRIBUTIONS

CZ and WR designed this manuscript; CZ and WZ performed the data analysis; CZ drafted the manuscript; WR performed manuscript review and editing.

FUNDING

This study is supported by the National Natural Science Foundation of China grants (41705051, 41530425, 41775080, and 41721004), Scientific Research Fund of Chengdu University of Information Technology (KYTZ201726), and the China Postdoctoral Science Foundation Grant (2019M660762, and 2020T130640).

REFERENCES

Barnett, T., Düenil, L., Schlese, U., Roeckner, E., and Latif, M. (1989). The Effect of Eurasian Snow Cover on Regional and Global Climate Variations. *J. Atmos. Sci.* 46, 661–686. doi:10.1175/1520-0469(1989)0462.0.CO;2

Blanford, H. F. (1884). On the Connection of the Himalaya Snowfall with Dry Winds and Seasons of Drought in India. *Proc. Roy. Soc. Lond.* 37, 3–22. doi:10.1098/rspl.1884.0003

Brodzik, M., and Armstrong, R. (2013). Data from: Northern Hemisphere EASE-Grid 2.0 Weekly Snow Cover and Sea Ice Extent, Version 4. National Snow and Ice Data Center. Available at: https://doi.org10.5067/P7O0HGJLYUQU.

Chen, Z., Wu, R., and Chen, W. (2014a). Distinguishing Interannual Variations of the Northern and Southern Modes of the East Asian winter Monsoon. *J. Clim.* 27, 835–851. doi:10.1175/JCLI-D-13-00314.1

Chen, Z., Wu, R., and Chen, W. (2014b). Impacts of Autumn Arctic Sea Ice Concentration Changes on the East Asian winter Monsoon Variability. *J. Clim.* 27, 5433–5450. doi:10.1175/JCLI-D-13-00731.1

Chen, Z., Wu, R., and Wang, Z. (2019). Impacts of Summer North Atlantic Sea Surface Temperature Anomalies on the East Asian Winter Monsoon Variability. *J. Clim.* 32, 6513–6532. doi:10.1175/JCLI-D-19-0061.1

Duchon, C. E. (1979). Lanczos Filtering in One and Two Dimensions. *J. Appl. Meteorol.* 18, 1016–1022. doi:10.1175/1520-0450(1979)018<1016:LFIOAT>2.0.CO;2

Eaton, B. (2011). *User's Guide to the Community Atmosphere Model CAM-5.1.* NCAR. Available at: http://www.cesm.ucar.edu/models/cesm1.0/cam/docs/ug5_1/ug.html.

Fasullo, J. (2004). A Stratified Diagnosis of the Indian Monsoon-Eurasian Snow Cover Relationship. *J. Clim.* 17, 1110–1122. doi:10.1175/1520-0442(2004)017<1110:asdoti>2.0.co;2

Kanamitsu, M., Ebisuzaki, W., Woollen, J., Yang, S. K., Hnilo, J. J., Fiorino, M., et al. (2002). NCEP-DOE AMIP-II Reanalysis (R-2). *Bull. Amer. Meteorol. Soc.* 83, 1631–1643. doi:10.1175/bams-83-11-1631(2002)083<1631:nar>2.3.co;2

Lau, K. M., and Chang, C. P. (1987). "Planetary Scale Aspects of winter Monsoon and Teleconnections," in *Monsoon Meteorology*. Editors C. P. Chang and T. N. Krishnamurti (New York: Oxford University Press).

Lin, H., and Wu, Z. (2011). Contribution of the Autumn Tibetan Plateau Snow Cover to Seasonal Prediction of North American winter Temperature. *J. Clim.* 24, 2801–2813. doi:10.1175/2010JCLI3889.1

Liu, G., Ji, L. R., Sun, S. Q., and Xin, Y. F. (2013). A Discussion on the East Asian winter Monsoon index-differences between the East Asian winter Monsoon at the Mid-high Latitudes and that at the Low Latitudes (**In Chinese**). *Chin. J. Atmos. Sci.* 37, 755–764. doi:10.3878/j.issn

Liu, G., Ji, L. R., Sun, S. Q., and Xin, Y. F. (2012). Low- and Mid-high Latitude Components of the East Asian winter Monsoon and Their Reflecting Variations in winter Climate over Eastern China. *Atmos. Ocean. Sci. Lett.* 5, 195–200. doi:10.1080/16742834.2012.11446985

Liu, S., Wu, Q., Ren, X., Yao, Y., Schroeder, S. R., and Hu, H. (2017). Modeled Northern Hemisphere Autumn and winter Climate Responses to Realistic Tibetan Plateau and Mongolia Snow Anomalies. *J. Clim.* 30, 9435–9454. doi:10.1175/JCLI-D-17-0117.1

Liu, S., Wu, Q., Schroeder, S. R., Yao, Y., Zhang, Y., Wu, T., et al. (2020). Near-Global Atmospheric Responses to Observed Springtime Tibetan Plateau Snow Anomalies. *J. Clim.* 33, 1691–1706. doi:10.1175/JCLI-D-19-0229.1

Qian, Q., Jia, X., and Wu, R. (2019). Changes in the Impact of the Autumn Tibetan Plateau Snow Cover on the Winter Temperature over North America in the Mid-1990s. *J. Geophys. Res. Atmos.* 124, 10321–10343. doi:10.1029/2019JD030245

Walland, D. J., and Simmonds, I. (1996). Modelled Atmospheric Response to Changes in Northern Hemisphere Snow Cover. *Clim. Dyn.* 13, 25–34. doi:10.1007/s003820050150

Wang, B., Wu, Z., Chang, C. P., Liu, J., Li, J., and Zhou, T. (2010). Another Look at Interannual-To-Interdecadal Variations of the East Asian winter Monsoon: the Northern and Southern Temperature Modes. *J. Clim.* 23, 1495–1512. doi:10.1175/2009JCLI3243.1

Wang, C., Yang, K., Li, Y., Wu, D., and Bo, Y. (2017a). Impacts of Spatiotemporal Anomalies of Tibetan Plateau Snow Cover on Summer Precipitation in Eastern China. *J. Clim.* 30, 885–903. doi:10.1175/JCLI-D-16-0041.1

Wang, Z., Wu, R., Chen, S., Huang, G., Liu, G., and Zhu, L. (2018). Influence of Western Tibetan Plateau Summer Snow Cover on East Asian Summer Rainfall. *J. Geophys. Res. Atmos.* 123, 2371–2386. doi:10.1002/2017JD028016

Wang, Z., Wu, R., Duan, A., and Qu, X. (2020). Influence of Eastern Tibetan Plateau spring Snow Cover on North American Air Temperature and its Interdecadal Change. *J. Clim.* 33, 5123–5139. doi:10.1175/JCLI-D-19-0455.1

Wang, Z., Wu, R., and Huang, G. (2017b). Low-frequency Snow Changes over the Tibetan Plateau. *Int. J. Climatol* 38, 949–963. doi:10.1002/joc.5221

Wang, Z., Wu, R., Zhao, P., Yao, S. L., and Jia, X. (2019). Formation of Snow Cover Anomalies over the Tibetan Plateau in Cold Seasons. *J. Geophys. Res. Atmos.* 124, 4873–4890. doi:10.1029/2018JD029525

Wu, Q., Hu, H., and Zhang, L. (2011). Observed Influences of Autumn-Early winter Eurasian Snow Cover Anomalies on the Hemispheric PNA-like Variability in winter. *J. Clim.* 24, 2017–2023. doi:10.1175/2011JCLI4236.1

Wu, R., and Kirtman, B. P. (2007). Observed Relationship of spring and Summer East Asian Rainfall with winter and spring Eurasian Snow. *J. Clim.* 20, 1285–1304. doi:10.1175/JCLI4068.1

Wu, T. W., and Qian, Z. A. (2003). The Relation between the Tibetan winter Snow and the Asian Summer Monsoon and Rainfall: An Observational Investigation. *J. Clim.* 16, 2038–2051. doi:10.1175/1520-0442(2003)016<2038:TRBTTW>2.0.CO;2

Xiao, Z., and Duan, A. (2016). Impacts of Tibetan Plateau Snow Cover on the Interannual Variability of the East Asian Summer Monsoon. *J. Clim.* 29, 8495–8514. doi:10.1175/JCLI-D-16-0029.1

Yasunari, T., Kitoh, A., and Tokioka, T. (1991). Local and Remote Responses to Excessive Snow Mass over Eurasia Appearing in the Northern Spring and Summer Climate. *J. Meteorol. Soc. Jpn.* 69, 473–487. doi:10.2151/jmsj1965.69.4_473

Zhao, H., and Moore, G. W. K. (2004). On the Relationship between Tibetan Snow Cover, the Tibetan Plateau Monsoon and the Indian Summer Monsoon. *Geophys. Res. Lett.* 31, L14204. doi:10.1029/2004GL020040

Zhao, P., and Chen, L. (2001). Climatic Features of Atmospheric Heat Source/sink over the Qinghai-Xizang Plateau in 35 Years and its Relation to Rainfall in China. *Sci. China Ser. D-earth Sci.* 44, 858–864. doi:10.1007/bf02907098

Conflict of Interest: The authors declare that the research was conducted in the absence of any commercial or financial relationships that could be construed as a potential conflict of interest.

frontiers in Earth Science

ORIGINAL RESEARCH
published: 29 September 2021
doi: 10.3389/feart.2021.748484

Strengthened Impacts of November Snow Cover Over Siberia on the Out-of-phase Change in the Siberian High Between December and January Since 2000 and Implication for Intraseasonal Climate Prediction

*Hongqing Yang and Ke Fan**

School of Atmospheric Sciences, Sun Yat-sen University, and Southern Marine Science and Engineering Guangdong Laboratory (Zhuhai), Zhuhai, China

OPEN ACCESS

Edited by:
Renguang Wu,
Zhejiang University, China

Reviewed by:
Lei Song,
Institute of Atmospheric Physics, (CAS), China
Ruowen Yang,
Yunnan University, China

***Correspondence:**
Ke Fan
fanke@mail.iap.ac.cn

Specialty section:
This article was submitted to Atmospheric Science, a section of the journal Frontiers in Earth Science

Received: *28 July 2021*
Accepted: *30 August 2021*
Published: *29 September 2021*

Citation:
Yang H and Fan K (2021) Strengthened Impacts of November Snow Cover Over Siberia on the Out-of-phase Change in the Siberian High Between December and January Since 2000 and Implication for Intraseasonal Climate Prediction. Front. Earth Sci. 9:748484. doi: 10.3389/feart.2021.748484

This study investigates the out-of-phase change in the Siberian High (SH) between December and January (stronger than normal in December and weaker than normal in January, and vice versa). The results show that the monthly reversal frequency of the SH between December and January increases significantly after 2000 from 30% (1981–2000) to 63% (2001-2019). Correspondingly, the influence of November snow cover over Siberia on the phase reversal of the SH has intensified after 2000. The reasons may be as follows. Higher snow depth over Siberia (SSD) in November corresponds to stronger diabatic cooling and increased snow accumulation over Siberia in November and December, which may strengthen the SH in December via the positive feedback of snow albedo. The dynamic mechanisms between the higher SSD in November and weaker SH in January are further investigated from the perspective of troposphere–stratosphere interaction. Such anomalously higher SSD with strong upward heat flux induces the upward-propagating wave activity flux in November and December over the Urals and Siberia, leading to a weaker and warmer stratospheric polar vortex in January. Subsequently, the anomalies of the stratospheric polar vortex signal propagate downwards, giving rise to a negative Arctic Oscillation–like structure in the troposphere and a weakening of the SH in January. This mechanism can be partly reproduced in CMIP6. Additionally, the variability of the September–October Arctic sea ice mainly leads to coherent variations of the SH in December and January via the eddy–mean flow interaction before 2000. Furthermore, the preceding November snow cover over Siberia enhances the intraseasonal prediction skill for the winter SH after 2000. Meanwhile, considering the previous November SSD, the prediction accuracy for the out-of-phase change in the SH between December and January increases from 16% (outputs of the NCEP's Climate Forecast System, version 2) to 75%.

Keywords: November snow cover over Siberia, phase reversal, Siberian high, troposphere-stratosphere interaction, intraseasonal climate prediction

INTRODUCTION

The Siberian high (SH), a center of seasonal activity, is formed in the lower troposphere over Eurasia during the wintertime as a result of surface radiative cooling and large-scale descending motion (Ding and Krishnamurti, 1987; Sahsamanoglou et al., 1991; Xie et al., 1992). As one of the main components of the East Asian winter monsoon (EAWM), the winter SH exerts a significant influence on the variability of Eurasian surface air temperature (SAT) and precipitation during the wintertime (Lu and Chang, 2009; Hasanean et al., 2013; Iqbal et al., 2013; Lei and Wu, 2017; Riaz and Iqbal, 2017). In the context of global warming, extreme climate events occur more frequently in winter over Eurasia. For instance, the SH rapidly strengthened during late January and early February, triggering an extreme cold event in Asia from 17 January to February 1, 2012 (Wu et al., 2017). Hence, improving our understanding of the variability of the winter SH is important for the prediction of Eurasian climate.

Some studies have revealed that the winter SH is affected by the internal variability of the atmosphere and underlying variation. Zeng et al. (2015) revealed that the location of the North Atlantic storm track is strongly related to the winter SH. Besides, the decrease in the Arctic sea-ice concentration (SIC) in the preceding September can strengthen the winter SH via the eddy–mean flow interaction (Wu et al., 2011). Li and Lan (2017) pointed out that a warmer sea surface temperature (SST) in the North Atlantic noticeably intensifies the Ural blocking ridge, resulting in a stronger winter SH. Cohen et al. (2001) investigated the connection between the Eurasian snow-cover extent (SCE) and variabilities of the SH. Based on these significant factors and relatively low prediction skill of the winter SH, a highly efficient prediction model was constructed (Yang and Lu, 2014; Yang and Fan, 2021). Although the wintertime average SH is very important, it is easy for it to mask the characteristics of intraseasonal variation, meaning intraseasonal predictions of the SH are more challenging.

Chang and Lu (2012) indicated that the SH exhibits out-of-phase relationships between November and December–January since 1979. They suggested that this intraseasonal phase reversal may be related to the relatively lower frequency of Pacific and Ural blocking events during a positive Arctic Oscillation (AO) phase. Moreover, Lu et al. (2019) further traced the reversal response of the SH in November and December–January to preceding autumn sea-ice variations. There is a significant positive (negative) correlation between the November (December–January) SH and the previous September Arctic SIC via eddy energy and wave activity flux (WAF). Additionally, the intraseasonal variabilities of the SH in the upper-level troposphere are linked to the blocking ridge with Atlantic-origin and Pacific-origin Rossby waves (Takaya and Nakamura, 2005a; Takaya and Nakamura, 2005b; Lei et al., 2018). Yang et al. (2021) found that a difference exists in the prediction skill for the monthly SH during November–February. The Climate Forecast System, version 2 (CFSv2), can skillfully predict the SH only in November, the reason for which is that CFSv2 can reproduce the connections between the SH and both the regional snow cover and thermodynamic process in November. However, these studies mainly focused on the December–January average SH, paying little attention to monthly reversals of the SH in December and January.

Sahsamanoglou et al. (1991) showed that the intensity and variability of the SH are strongest in December and January. Recent studies have shown that the East Asian winter SAT exhibits variability reversals in December and January–February (Hu et al., 2005; Huang and Hu, 2006; Zuo et al., 2015; Xu et al., 2018). Hu et al. (2005) indicated that the relationship between the polar vortex and extratropical SAT displays near opposite tendencies between early winter (November–December) and late winter (February–March). Another study, meanwhile, indicated that the interannual and decadal trends of the SAT reversal also exist in China (Huang and Hu, 2006). Besides, Zuo et al. (2015) revealed an out-of-phase variation in the relationship between the winter AO and southern China SAT anomalies in December and January–February. For instance, warmer conditions in the prior December and a colder January were accompanied by a reversal in the phase of the AO in 2015 over China (Si et al., 2016). Dai et al. (2019) pointed out that the out-of-phase change between December and January–February over Northeast China may be attributable to the variability of the SIC in the preceding November over the Davis Strait–Baffin Bay and Barents–Kara Sea regions via Arctic-midlatitude tropospheric and stratospheric processes. Besides, when the reversal of the East Asian SAT exhibited relatively colder anomalies in the previous December and warmer anomalies in January–February of 2015, the SH indices in December, January and February were 0.7, −1.3 and −0.6, which demonstrated an out-of-phase SH in December and January in 2015 (Xu et al., 2018). Therefore, the monthly reversal of the SH in December and January is worthy of discussion towards improving the intraseasonal prediction of the Eurasian climate.

The winter SH is a vital characteristic of the EAWM. Some studies have indicated that the intraseasonal variations of the EAWM might be affected by certain atmospheric circulation systems, including geopotential height anomalies related to the AO (Si et al., 2016), blocking high activities over the North Pacific (Si et al., 2014), and the polar vortex of the Northern Hemisphere (Wang et al., 2013). Besides, the connections between El Niño–Southern Oscillation (ENSO) and the EAWM can be found on seasonal and intraseasonal time scales (Li, 1990; Zhang et al., 1996; Webster et al., 1998; Li et al., 2021). Tian and Fan (2020) pointed out that the prediction skill for the EAWM in early winter (November–December) is higher than in late winter (January–February), due to the weakening relationship between ENSO and the EAWM in late winter. As the Arctic warming has reached rates that are double that of the global average, the influence of the Arctic on the mid-to-high latitude climate has been strengthened (Francis and Vavrus, 2012; Kug et al., 2015). Meanwhile, the EAWM serves as a crucial bridge connecting the Arctic sea-ice

concentration (ASIC) and intraseasonal SAT over East Asia (Xu et al., 2018; Dai et al., 2019).

Wegmann et al. (2015) revealed that the decline in sea-ice cover over the Barents–Kara Seas serves as a moisture source for the increasing Siberian snow cover. Meanwhile, the Eurasian snow cover is closely associated with the Eurasian climate on different time scales (Gong et al., 2007; Li and Wang, 2014; Ao and Sun, 2016; Li et al., 2020). Snow cover variations over Eurasia impact the atmospheric circulation through thermal and dynamic effects. From the thermal perspective, the simultaneous Eurasian snow cover can directly affect local atmospheric circulations through surface radiative effects (Cohen and Rind, 1991; Chen and Sun, 2003; Jeong et al., 2011). And from the dynamical perspective, as a major source of vertical WAF, the Siberian snow cover during autumn can influence the following-winter AO, East Asian precipitation, and predominate modes of Eurasian SAT via troposphere–stratosphere interaction (Cohen et al., 2001; Cohen et al., 2010; Han and Sun, 2020). The extreme cold events in 2010 had a significant connection with the preceding autumn snowpack and stratospheric polar vortex (Cohen et al., 2010). Furthermore, the November snow cover plays an important role in the intraseasonal climate over Eurasia. Northern Eurasian snow cover in November, linked to stationary planetary waves, demonstrates a significant impact on the warm Arctic–cold Eurasia pattern during the following January (Xu et al., 2017). Meanwhile, November snow depth (SD) plays an important role in intraseasonal precipitation in southern China during 6–15 January (Li et al., 2020).

Due to the frequent occurrence of monthly climate transitions in December and January over East Asia, this study further investigates the intraseasonal reversal of the SH between December and January and its connections with Siberian snow cover. The possible physical mechanisms underlying this link are also revealed from snow-related thermal and dynamical effects to improve the prediction skill for the winter SH and Eurasian SAT on the intraseasonal timescale.

The remainder of the paper is structured as follows. The data and methods used are described in *Data and Methods Section 2. Month-To-Month Variability of the Siberian High and Their Imapct on Eurasian Climate* reveals the out-of-phase variations of the SH in December and January and their impact on Eurasian SAT and precipitation. In *Reversal Response of November Snow Cover over the Siberia to the December and January Siberian High*, the explicit linkage and physical mechanisms between the out-of-phase variation of the SH and November snow cover after 2000 are discussed. Meanwhile, results based on CMIP6 are also illustrated in this section, to verify the physical mechanisms. *Connection Between Autumn Arctic Sea-Ice Concentration and a Coherent December and January Siberian High* demonstrates the relationship between the autumn Arctic SIC and coherent variability of the SH in December and January before 2000. A preliminary application of November SD in the intraseasonal prediction of the SH is presented in *Intrarseasonal prediction of the Siberian High in December and January Based on Siberian snow depth and Arctic Sea-Ice Concentration*. And finally, a summary and some further discussion are provided in *Conclusion and Discussion*.

DATA AND METHODS

Data

The atmospheric reanalysis data from National Centers for Environmental Prediction/National Center for Atmospheric Research (NCEP/NCAR) were obtained, including the monthly mean SLP, SAT, geopotential height, zonal and meridional wind, at a resolution of 2.5° × 2.5° (Kalnay et al., 1996). The surface heat flux was also adopted, as the sum of surface sensible and latent heat flux, using the NCEP/NCAR data, compiled on a Gaussian grid. Meanwhile, the daily mean geopotential height with 17 levels was adopted to analyze the vertical propagation of the stratospheric polar vortex signal.

The monthly SD data used in this study were derived from the ECMWF (European Center for Medium-Range Weather Forecasts) interim reanalysis datasets, with a horizontal resolution of 1° × 1°, for the period 1980–2019 (Dee et al., 2011). Meanwhile, the observing SD data were provided by the Canadian Meteorological Centre (CMC), on a 706 × 706 cell grid from 1998 (Brown and Brasnett, 2010, updated anually). To facilitate the analysis, the SD was interpolated onto a 1° ×1 ° regular grid. The SCE data in the Northern Hemisphere, on an 89 × 89 cell grid, were obtained from the Rutgers University Global Snow Lab (Robinson et al., 1993). These data were then interpolated onto a 2.5° × 2.5° regular grid for further analysis. The monthly averaged SIC data were taken from the Met Office Hadley Center for Climate Prediction and Research, at a resolution of 1° × 1° (Rayner, 2003). The monthly averaged precipitation data are provided by GPCP (Huffman et al., 1997). In addition, outputs from the historical-simulation experiments of four models (BCC-CSM2, CanESM5, CESM2 and MIROC-ES2L) from phase 6 of the Coupled Model Intercomparison Project (CMIP6) were employed to test the physical mechanisms between the reversed SH and preceding November Siberian snow cover (Eyring et al., 2016). The selection of the CMIP6 models was primarily driven by their capability of reproducing the increase in the reversal frequency of the SH between December and January after the year 2000. To examine the prediction skill for SH reversal between December and January in November, CFSv2, an atmosphere-ocean-sea ice-land model, is released in November, which means the CFSv2-predicted data are employed at a 1-month lead for the December SH and at a 2-months lead for the January SH (Saha et al., 2014). The CFSv2 data are interpolated from the resolution of 1° × 1° onto a 2.5° × 2.5° grid. The linear trends of all data were removed prior to analysis.

In this study, we focus on the monthly variability of the SH in December and January. The intensity index of the winter SH (SHI) is defined as the normalized regional-averaged SLP (40°–60°N, 70°–120°E) to describe the monthly variability of the SH in midwinter (Gong and Ho, 2002). The midwinter period is defined as December in the previous year and January (DJ) in the current year. In this study, the midwinter seasons of 1981–2019 are used. When the SH in each midwinter (DJ) presents a

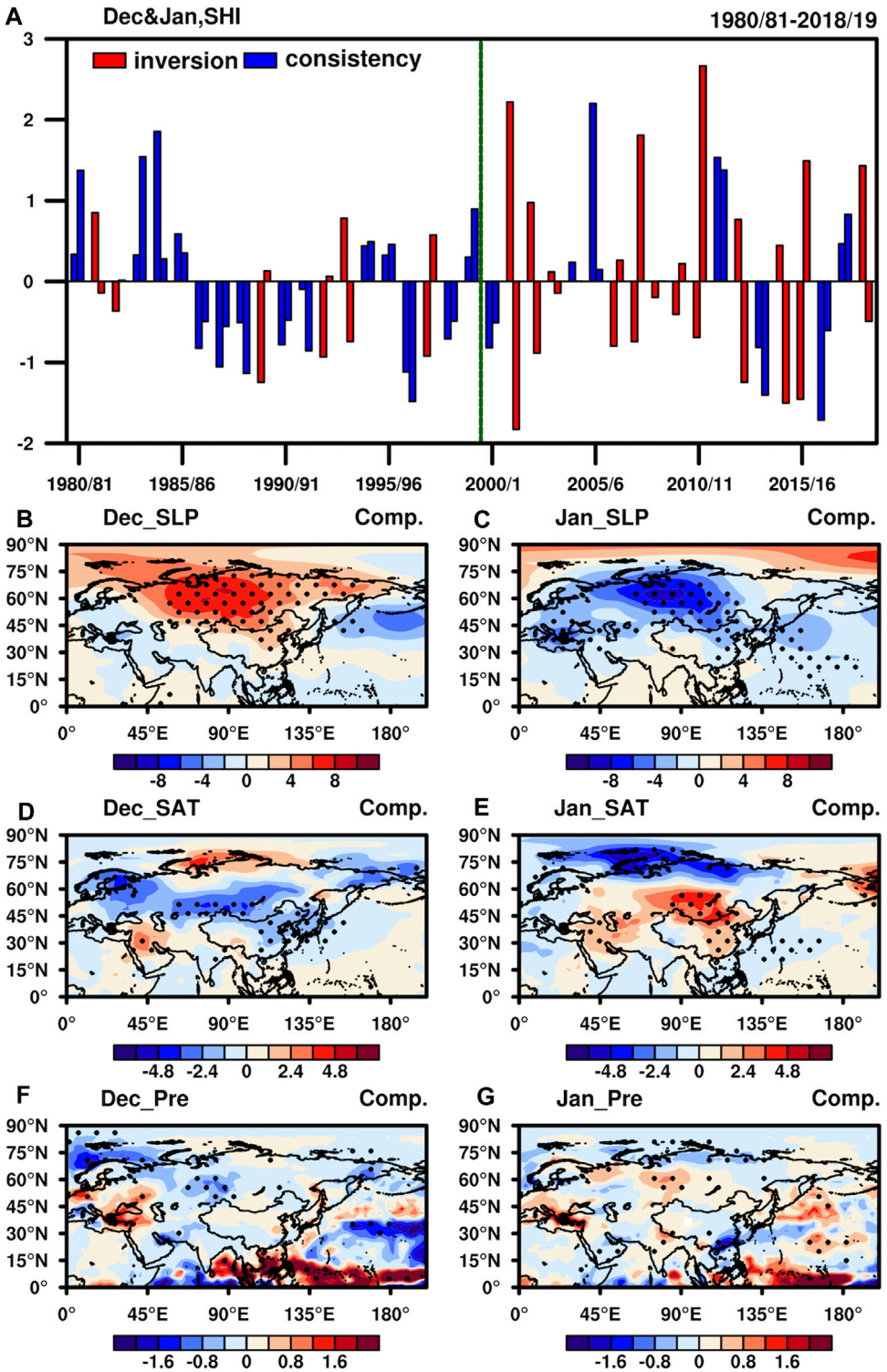

FIGURE 1 | (A) Siberian high intensity index (SHI) in each midwinter month (December, January) during 1980/81–2018/19. Composite spatial patterns of variables between SH_{+-} and SH_{-+} for (B, D, F) December and (C, E, G) January during 1980/81–2018/19: **(B, C)** sea level pressure (SLP, units: hPa); **(D, E)** surface air temperature (SAT, units: °C); **(F, G)** precipitation (units: mm/day). Years of other reversal types of SH are shaded by red bars, and consistent types are shaded by blue bars in (A). Dotted regions in (B–G) are statistically significant at the 90% confidence level, based on the *t*-test.

TABLE 1 | Temporal correlation coefficient (TCC) and reversal frequency of the Siberian high intensity index between December and January.

Period	TCC	Reversal frequency
1980/81–2018/19	−0.07	46% (18/39)
1980/81–1999/2000	0.39*	30% (6/20)
2000/01–2018/19	−0.30	63% (12/19)

positive–negative pattern (SH_{+-}, anomalously warmer than normal in December and colder than normal in January), this study records it (SH_{+-}) as the positive phase of this event. Correspondingly, a negative–positive pattern (SH_{-+}) event of the SH in midwinter is recorded as the negative phase of this event.

Methods

Composite difference analysis and one-dimension linear regression were applied to discuss the relationship and its linkage between the November SD and December and January SH. The *t*-test was used to verify the statistical significance of the linear regression and composite difference analysis results.

The stratosphere–troposphere interaction was diagnosed by the vertical and zonal components of Plumb (1985)'s WAF:

$$F_x = \frac{P}{2a^2 \cos\Phi}\left[\left(\frac{\partial\psi'}{\partial\lambda}\right) - \psi'\frac{\partial^2\psi''}{\partial\lambda^2}\right] \quad (1)$$

$$F_z = \frac{2p\Omega^2 \sin^2\Phi}{N^2 a}\left(\frac{\partial\psi'}{\partial\lambda}\frac{\partial\psi'}{\partial z} - \psi'\frac{\partial^2\psi'}{\partial\lambda\partial z}\right) \quad (2)$$

In these equations, P is pressure/1,000 hPa; a is the mean radius of the Earth; Ω is the angular velocity of rotation; ψ' is the perturbation geostrophic stream function; λ and Φ are longitude and latitude, respectively; primes indicate the departure from the zonal mean; $z = -H\ln P$, where H is a constant scale height (H = 8,000 in this paper).

Fourier transformation was also used, to obtain the zonal wavenumber-1 component of variable y, as follows:

$$y = A_0 + \sum_{k=1}^{n/2} A_k \cdot \sin(kx - \varphi_k) \quad (3)$$

where k is the wavenumber; A is the wave amplitude; x is the longitudinal distance; and φ is the phase.

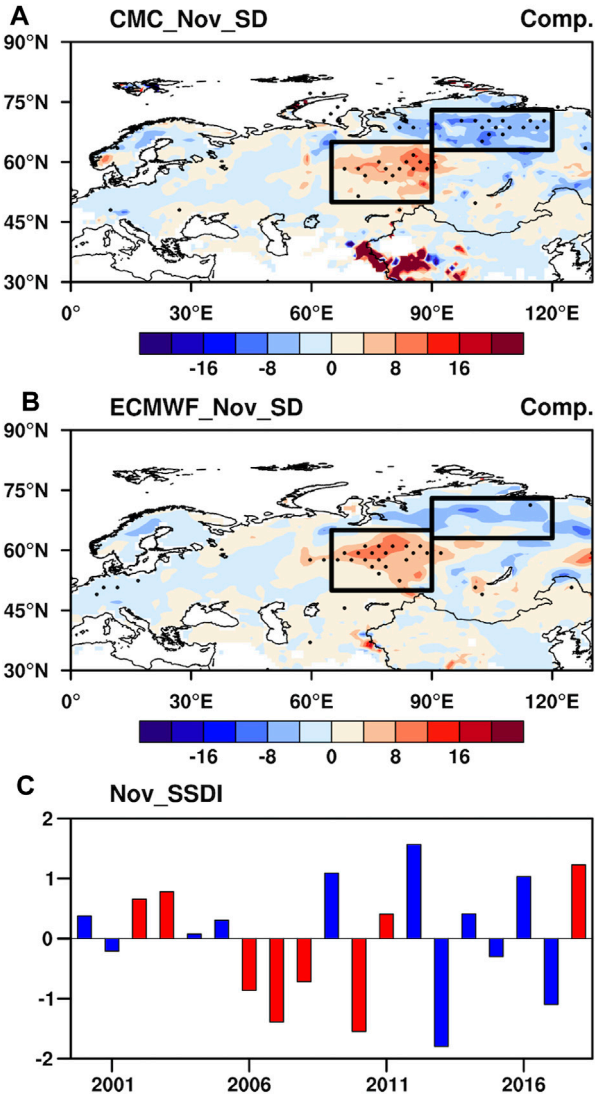

FIGURE 2 | Composite spatial patterns of snow depth (SD, units: mm) in the previous November between SH_{+-} and SH_{-+} for two datasets during 2000/01–2018/9: **(A)** Canadian Meteorological Centre (CMC) data; **(B)** ECMWF (European Center for Medium-Range Weather Forecasts) interim reanalysis data. **(C)** Normalized time-series of Siberian snow depth index (SSDI) based on CMC. Dotted regions in **(A, B)** are statistically significant at the 90% confidence level, based on the *t*-test. The black rectangle represents the key area of Siberian snow depth (SSD) [(50°–65°N, 65°–90°E), (63°–73°N, 90°–120°E)] in **(A,B)**. Years of heaviest (lightest) SSD corresponding to SH_{+-} (SH_{-+}) are shaded by red bars in **(C)**.

RESULTS

Month-To-Month Variability of the Siberian High and Their Impact on Eurasian Climate

The monthly SH intensity in midwinter (DJ) during 1980/81–2018/19 is depicted in **Figure 1A**. There are 18 years in which the SHI demonstrates reverse variations (red bars in **Figure 1A**) between December and January during the past 39 years. The composite difference in SLP in December and January between eight SH_{+-} years (1981/82, 1993/94, 2001/02, 2002/03, 2003/04, 2012/13, 2014/15, 2018/19) and ten SH_{-+} years (1982/83, 1989/90, 1992/93, 1997/98, 2006/07, 2007/08, 2008/09, 2009/10, 2010/11, 2015/16) further confirms the transition is significant over the entire SH region (**Figures 1B,C**). This out-of-phase phenomenon has a pronounced influence on the SAT reversal between December and January over East China and Mongolia (**Figures 1D,E**). Under the circumstances, while the precipitation over the Urals increases in December, it correspondingly decreases over the Urals in January, and vice versa (**Figures 1F,G**). Hence, the out-of-phase variation of the SH exerts a noticeable effect on the East Asian climate.

We can see that 12 transitions occurred after 2000, whereas only 6 reversals occurred before 2000. Correspondingly, the monthly reversal frequency of the SH significantly increases after 2000 from 30% (1980/81–1999/2000) to 63% (2001–2019). The temporal correlation coefficient (TCC) of the SHI between December and January is −0.30 during 2000/01–2018/19 and 0.39 (significant at the 10% significance level) during 1980/81–1999/2000 (**Table 1**). In addition, a singular value decomposition (SVD) analysis between the December and January SH was applied to reveal the spatial structure of their coupled relationship (figure not shown). The first SVD mode (SVD1) can explain 90% of the covariance and has an out-of-phase pattern with the maximum amplitudes in the Lake Baikal region during 2000/01–2018/19. However, SVD1 can explain 85% of the covariance and presents a coherent pattern with the different maximum amplitudes in the Lake Baikal (December) and Balkhash (January) regions during 1980/81–1999/2000. Therefore, this study focuses on the out-of-phase variation of the SH after 2000 and reveals its possible causes.

Reversal Response of November Snow Cover over the Siberia to the December and January Siberian High

Features and Importance of November Snow Cover Over the Siberia

Jeong et al. (2011) indicated that an increase in Eurasian snow cover in late autumn intensifies the surface radiation cooling, strengthening the winter SH. However, many researchers have presented that the anomalous Eurasian snow cover in autumn can generate variations of AO-like circulation during winter (Saito et al., 2001; Gong et al., 2003; Lu et al., 2020). Hence, autumnal Eurasian snow cover may be connected to SH reversal in December and January after 2000.

Climatologically, the snow cover expands southwards from September to January. The Eurasian SCE (50°–80°N, 30°–150°E) is nearly 90% in the north of 50°N in November, which causes little variability in wintertime (Wu and Kirtman, 2007). Thus, the SD can be used to describe the temporal evolution of snow and the interannual variability from November to the following winter. The composite differences of SD in the preceding November between SH_{+-} years and SH_{-+} years are examined for the period 2000–2018. The most significant positive SD anomalies over western Siberia and negative SD anomalies over northern Siberia occur in November, based on the CMC dataset (**Figure 2A**). Meanwhile, the composite difference in the November SD presents similar results from ECMWF (**Figure 2B**). This means that the November snow cover anomalies over Siberia in the previous November might be attributable to SH_{+-}/SH_{-+} events after 2000.

SVD analysis was performed to examine the main coupled modes of covariability of the November SD between western and northern Siberia. In SVD1, the two regions are in reverse mode, which is also reflected in the composite results (figure not shown). The correlation coefficient of the expansion time-series between the two areas is 0.75 (significant at the 0.1% level). Furthermore, the percentage variance explained by SVD1 is 73.26%, indicating the November SD over western and northern Siberia shows coherent variations. Therefore, the Siberian SD (SSD) index (SSDI) is defined as the normalized and detrended area-averaged SD difference between western Siberia (50°–65°N, 65°–90°E) and northern Siberia (63°–73°N, 90°–120°E).

TABLE 2 | The SH reversal years in December and January and the SSD anomalous years in preceding November during 2000/01 -2018/19.

SHI_{+-}	2001/02; 2002/03; 2003/04; 2012/13; 2014/15; 2018/19
SHI_{-+}	2006/07; 2007/08; 2008/09; 2009/10; 2010/11; 2015/16
SSD_H	**2002, 2003,** 2009, **2012,** 2016, **2018**
SSD_L	**2006, 2007, 2008, 2010**, 2013/14, 2017/18
SSD_H–SHI_{+-}	**2002/03; 2003/04; 2012/13; 2018/19**
SSD_L–SHI_{-+}	**2006/07; 2007/08; 2008/09; 2010/11**

To further confirm the linkage between anomalous SSD and SH reversal in December and January, the six heaviest (2002/03, 2003/04, 2009/10, 2012/13, 2016/17, 2018/19) and six lightest (2006/07, 2007/08, 2008/09, 2010/11, 2013/14, 2017/18) years of SSD in the previous November were selected based on them exceeding ±0.5 standard deviations (**Table 2**). Pertinently, the four heaviest (four lightest) SSD years correspond to four SH_{+-} (four SH_{-+}) years. We denote these eight events as SSD_H–SHI_{+-} (2002/03, 2003/4, 2012/13, 2018/19) or SSD_L–SHI_{-+} (2006/07, 2007/08, 2008/09, 2010/11) for the following discussion (**Table 2**). Notably, the previous November SSD is significantly correlated with January SH, with a correlation coefficient of −0.43 (exceeding the 90% confidence level) during 2000/01–2018/19. The TCC between the November SSDI and December SHI is 0.32 which demonstrates a contrary effect compared with the January SH. Thus, we may infer that the out-of-phase change in the SH between December and January increases after 2000, which may be attributable to SSD anomalies.

Mechanisms

To systematically explore the mechanism of the reverse response between December and January from long-term trends and extreme anomalous conditions, linear regression and composite difference results were considered together. Linear regression on the preceding November SSD was employed to investigate the snow cover–related atmospheric circulation. Meanwhile, the connected preceding and current atmospheric circulation of the SH reversal in the context of anomalous snow cover was also used, to investigate the composite difference analysis results between SSD_H–SHI_{+-} and SSD_L–SHI_{-+}.

December Siberian High

Due to higher albedo and lower thermal conductivity, the snow albedo feedback (SAF) exerts an important impact on global climate change sensitivity and regional climate change over the heavily populated Northern Hemisphere continental regions (Bony et al., 2006; Soden and Held, 2006). Hall and Qu (2006) pointed out that SAF is appropriate to reveal short-term climate

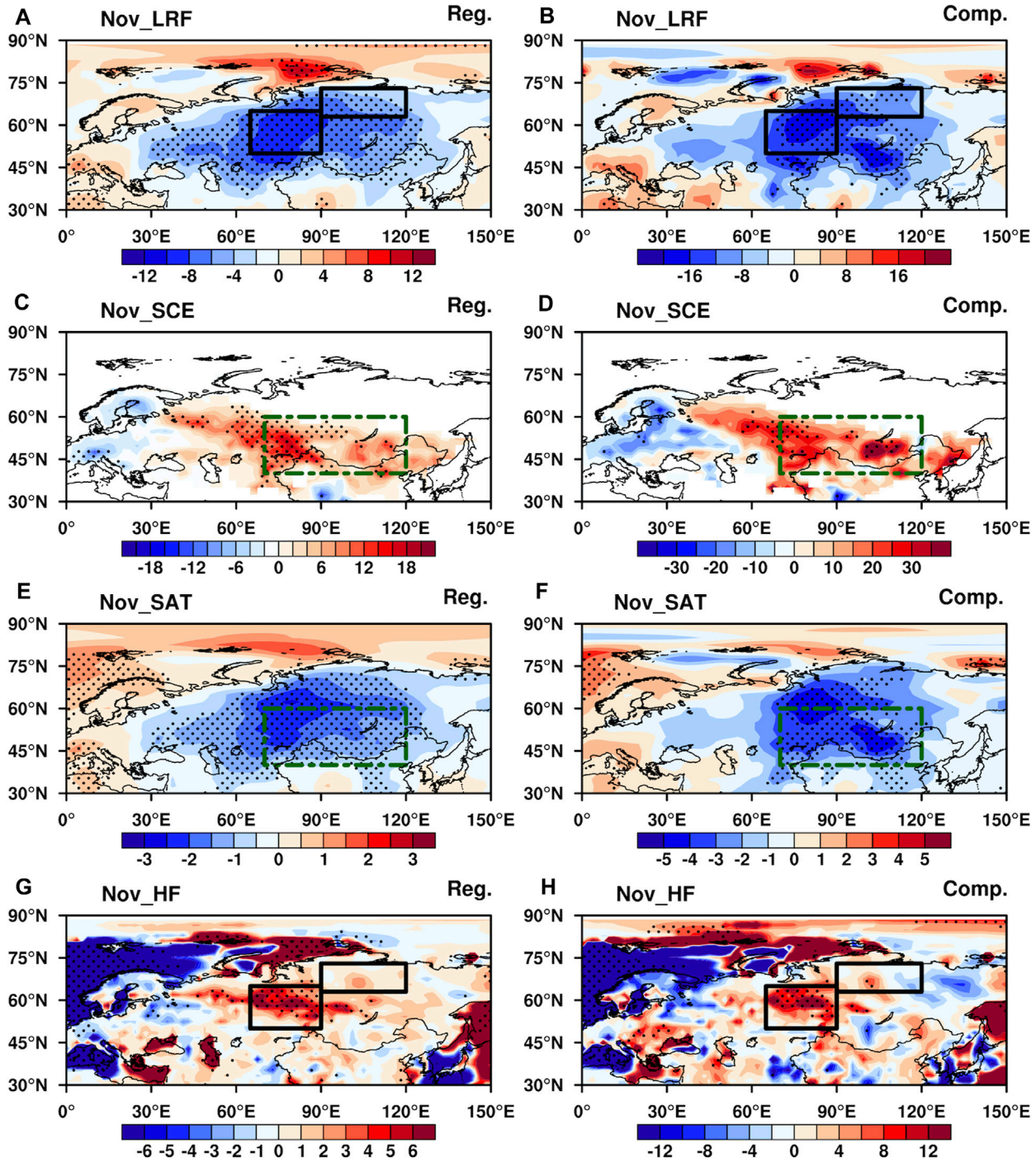

FIGURE 3 | (A, C, E, G) Regression of variables on the Siberian snow depth index (SSDI) and (B, D, F, H) results of composite differences in variables between SSD_H–SHI_{+-} and SSD_L–SHI_{-+} in November during 2000–2018: **(A, B)** upward long-wave radiation flux (units: W m^{-2}); **(C, D)** snow cover extent (SCE; units: %); **(E, F)** surface air temperature (SAT; units: °C); **(G, H)** heat flux (units: W m^{-2}). Dotted regions are statistically significant at the 90% confidence level, based on the *t*-test. The black rectangle represents the key area of Siberian snow depth (SSD) [(50°–65°N, 65°–90°E), (63°–73°N, 90°–120°E)] in (A, B, G, H). The green dotted rectangle represents the key area of the Siberian high (SH) (40°–60°N, 70°–120°E) in (C–F).

change as follows. With the melting of snow, darker ground is exposed, which leads to more absorption of solar radiation. More longwave radiation can alter the warmer regional SAT and the cloudiness, which then results in a warmer condition and strong absorption of shortwave radiation. Thus, the snow cover further decreases.

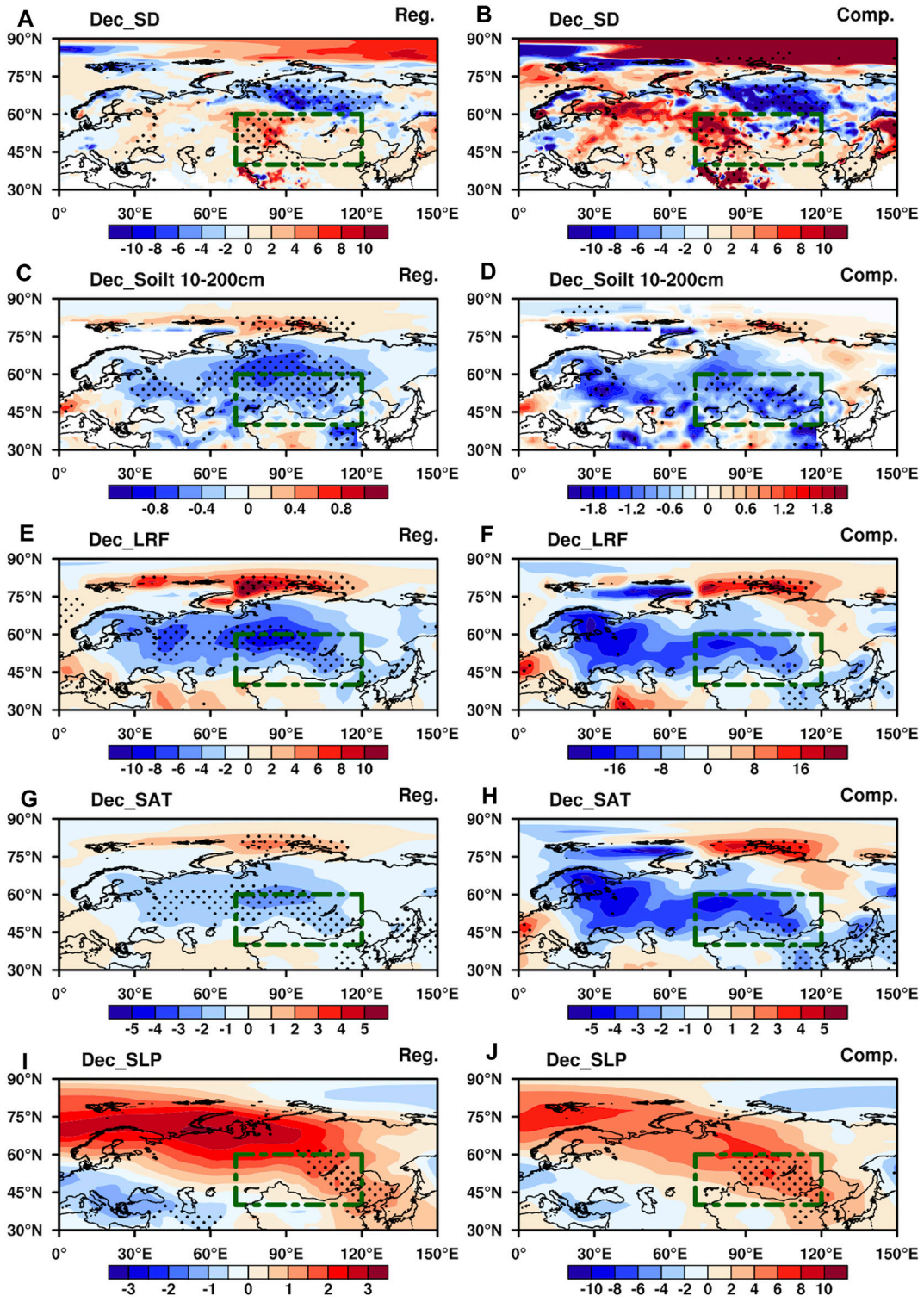

FIGURE 4 | (A, C, E, G, I) Regression of variables in December on the November SSDI and (B, D, F, H, J) results of composite differences in variables in December between SSD_H–SHI_{+-} and SSD_L–SHI_{-+} in December during 2000–2018: **(A, B)** SD (units: mm); **(C, D)** 10-200 cm soil temperature (units: K); **(E, F)** upward long-wave radiation flux (units: W m^{-2}); **(G, H)** SAT (units: °C); **(I, J)** SLP (units: hPa). Dotted regions are statistically significant at the 90% confidence level, based on the *t*-test. The green dotted rectangle represents the key area of the SH (40°–60°N, 70°–120°E).

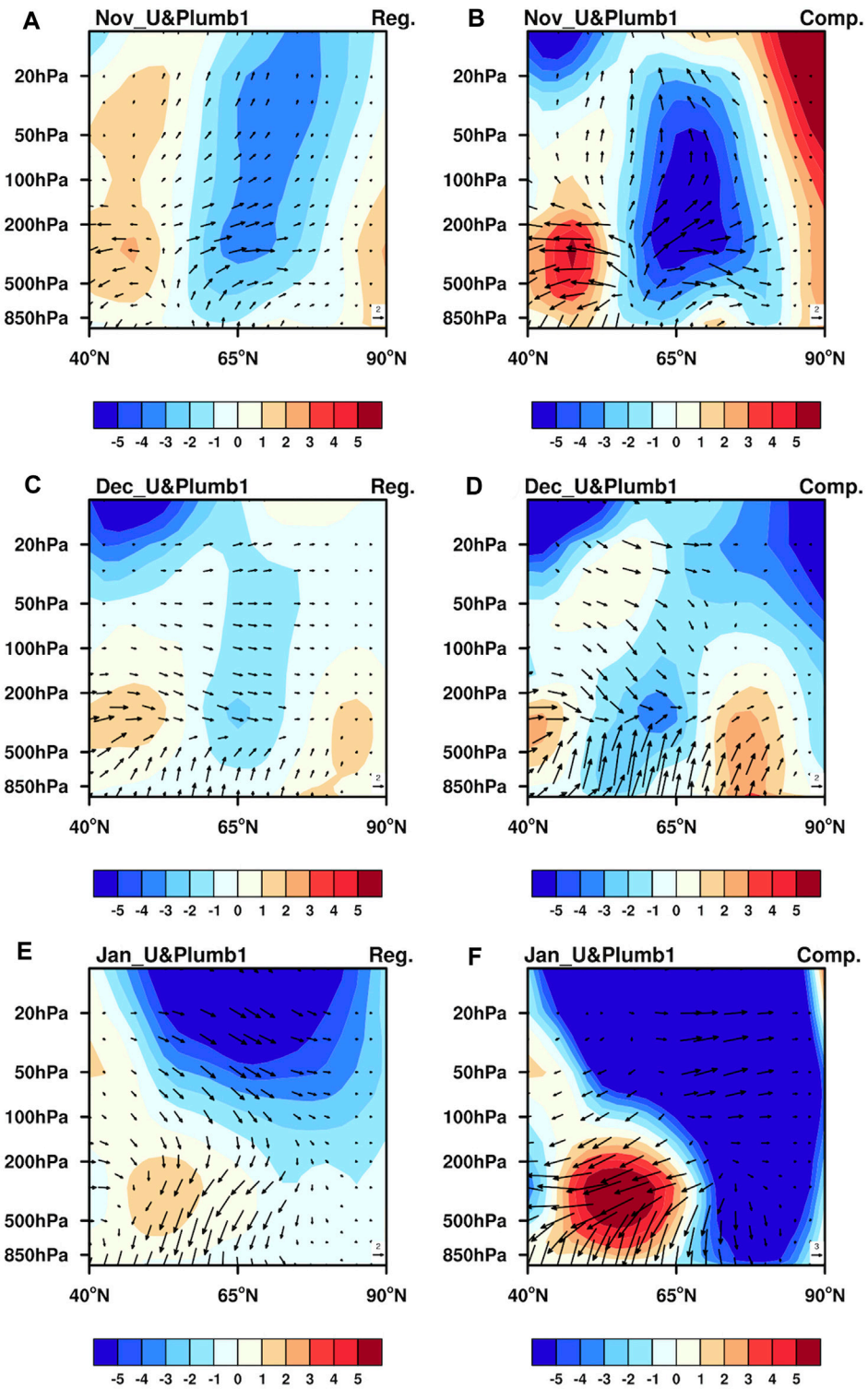

FIGURE 5 | (A, C, E) Regressions of zonal wind (shading; units: m s^{-1}) anomalies and the associated wavenumber-1 wave activity flux (WAF; vectors; units: m^2 s^{-2}) for November to January on the November SSDI and (B, D, F) results of composite differences between SSD_{H}–SHI_{+-} and SSD_{L}–SHI_{-+} during 2000/01–2018/19: **(A, B)** November (averaged between 65°E and 90°E); **(C, D)** December (averaged between 65°E and 90°E); **(E, F)** January (averaged between 90°E and 120°E).

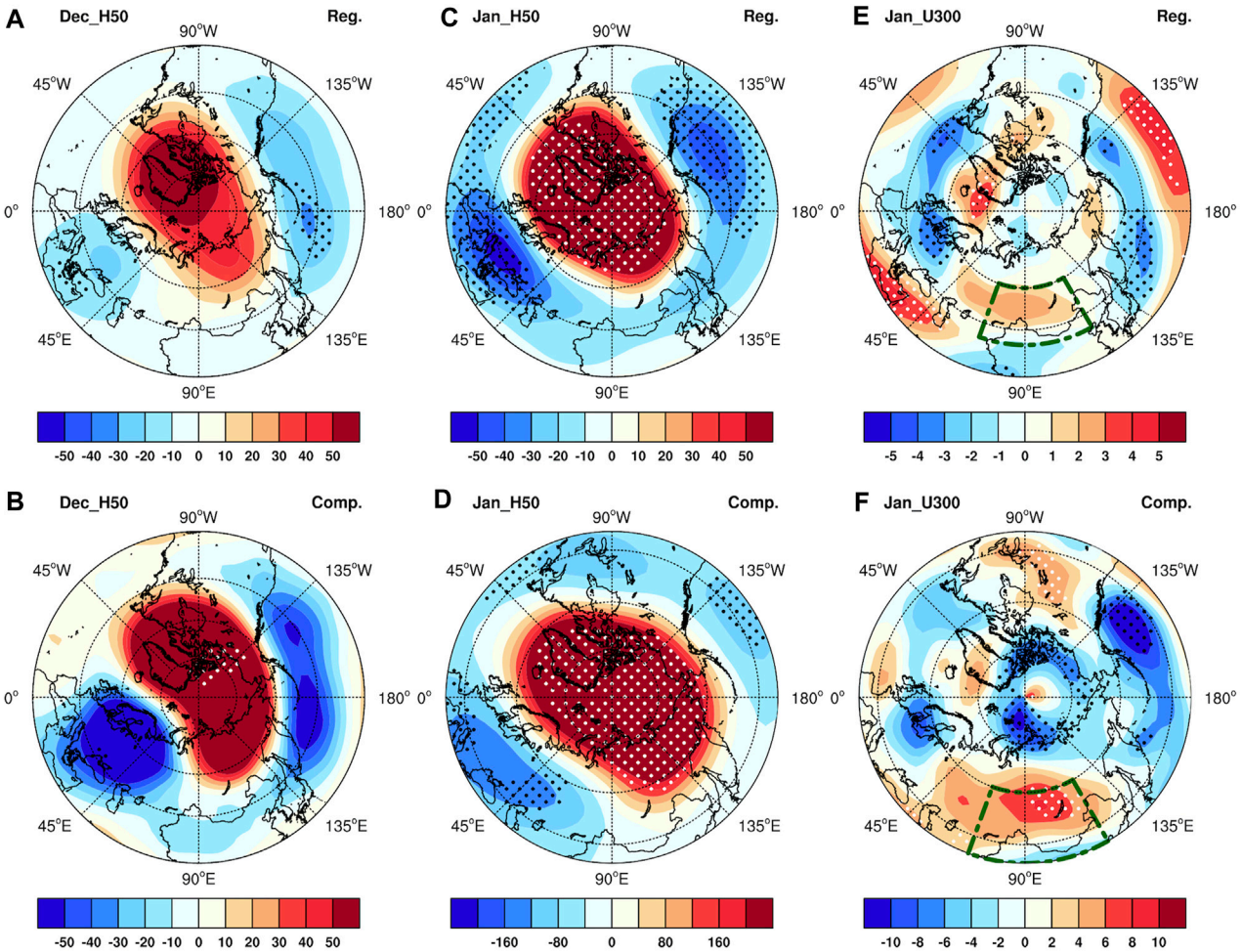

FIGURE 6 | (A, C, E) Regressions of variables on the November SSDI and (B, D, F) results of composite differences between SSD_H–SHI_{+-} and SSD_L–SHI_{-+} during 2000/01–2018/19: **(A, B)** December geopotential height at 50 hPa (units: gpm); **(C, D)** January geopotential height at 50 hPa (units: gpm); **(E, F)** January zonal wind at 300 hPa (units: gpm). Dotted regions are statistically significant at the 90% confidence level, based on the *t*-test. The green dotted rectangle represents the key area of the SH (40°–60°N, 70°–120°E) in **(E, F)**.

Based on the theory of SAF, the response November snow cover to the following December SH is discussed. When the November snowpack deepens with high snow albedo over Siberia (figure not shown), the significant radiative cooling strengthens over Northwest Eurasia, extending from west of the Urals to eastern Siberia in November (**Figures 3A,B**). Land–atmosphere coupling coincides significantly with the SSD variability center over the Siberian region along 40°–70°N, while Siberia is mainly located in the snow transition regions at the southern edge of the snow-covered region along 40°–60°N. Hence, with markedly lower SAT in November, the SCE increases in the west of Siberia and south of Lake Baikal (**Figures 3C,D**), which leads to a stronger radiative cooling (**Figures 3E,F**). Correspondingly, the SD increases over Siberia in the following December (**Figures 4A,B**), leading to a coherently lower soil temperature mode over Siberia from deep to shallow layers, especially in the anomalous SSD–SH years (**Figures 4C,D**). As the surface soil temperature (0–10 cm) tends to be decreased, the atmospheric absorption of longwave radiation flux weakens. Ding and Krishnamurti (1987) indicated that the effect of adiabatic cooling on the development of high pressure in Siberia. However, there is a balance between adiabatic heating and diabatic heating below 500 hPa, which makes the heat distribution in Siberia mainly is affected by radiative cooling. Therefore, the radiative cooling over Siberia tends to be further intensified (**Figures 4E,F**). This condition could result in more accumulation of cold air masses over Siberia (**Figures 4G,H**). Subsequently, the December SH can be strengthened (**Figures 4I,J**).

January Siberian High

Various studies have indicated the cross-month impact of autumn SCE via the tropospheric and stratospheric response (Wagner, 1973; Cohen and Rind, 1991; Xu et al., 2017; Han and Sun, 2021). Meanwhile, the autumn SCE has also been applied to develop prediction models of the winter SAT of the extratropical

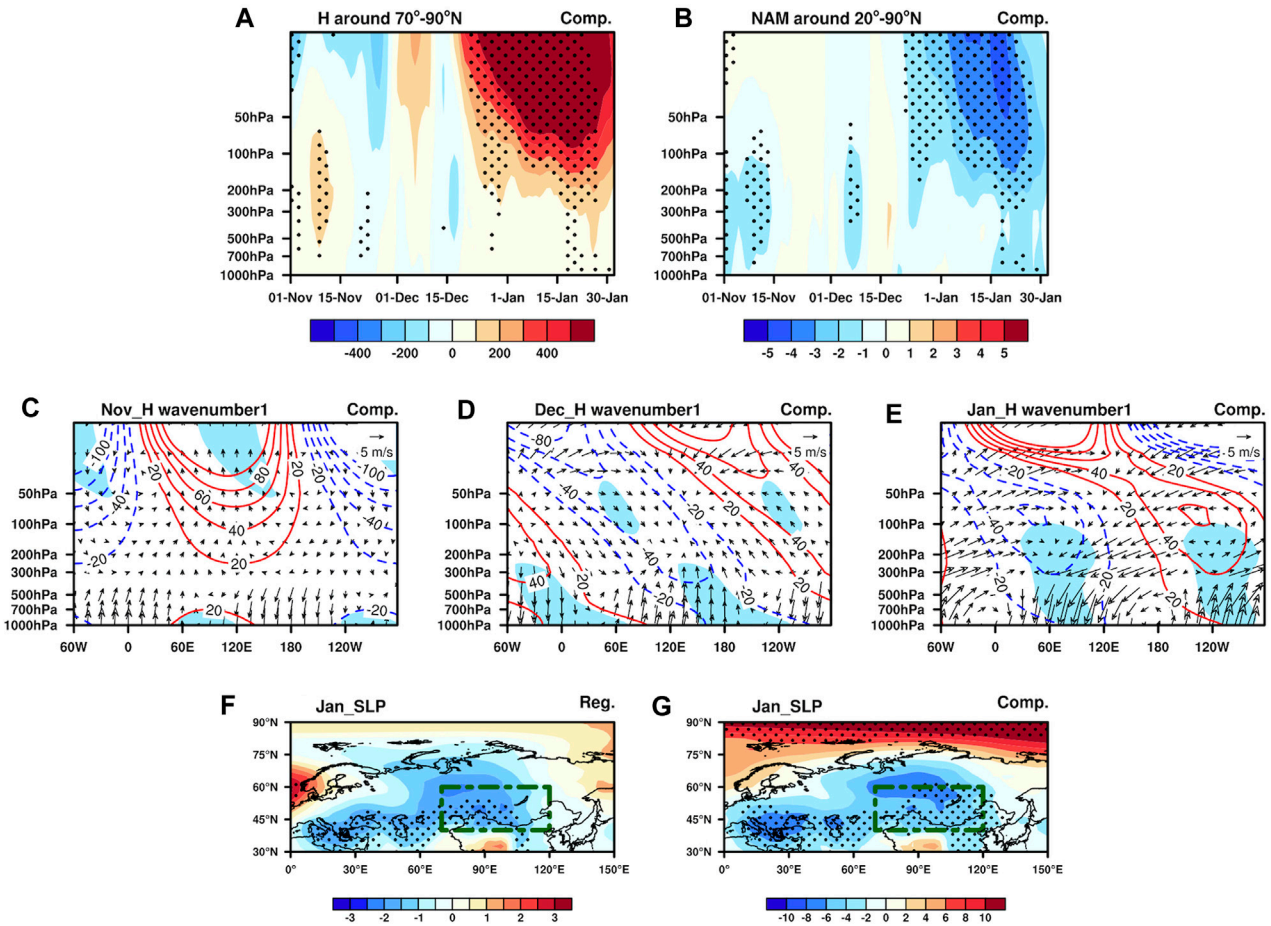

FIGURE 7 | Composite spatial patterns of variables between SSD_H–SHI_{+-} and SSD_L–SHI_{-+} during 2000/01–2018/19: **(A)** time–pressure cross-section in the area-averaged geopotential height anomalies (units: gpm) in the region poleward of 70°N; **(B)** time–latitude cross-sections of the meridional component of Northern Annular Mode index (the normalized time coefficient of the first EOF mode of zonal-mean (20°–90°N) geopotential height anomaly); (C–E) zonal wavenumber-1 distribution of geopotential height (contour, units: gpm) and WAF (vectors, units: $m^2\ s^{-2}$) along a section at 50°–70°N in **(C)** November, **(D)** December and **(E)** January.; **(F)** Regression of variables on the SSDI and **(G)** results of composite differences in January SLP between SSD_H–SHI_{+-} and SSD_L–SHI_{-+}; Dotted (A, B, F, G) and shaded (C–E) regions are statistically significant at the 90% confidence level, based on the *t*-test.

Northern Hemisphere (Cohen and Fletcher, 2007). Ringler and Cook (1999) showed that diabatic heating can influence the interannual variations of WAF. With strong surface radiation cooling, the upward WAF enhances (Plumb, 1985). That means the vertical WAF is concentrated on the region where the highest gradient in SAT and heat flux. Besides, the Eurasian continent, especially the area around Siberia, is the major source of vertical WAF. Thus, we further discuss how the November snowpack relates to January atmospheric circulation from the perspective of troposphere–stratosphere interaction.

The planetary wave is a viable physical variable to reveal the response between the stratosphere and troposphere. Research has shown that the climatological-mean Northern Hemispheric stationary waves over the middle latitudes propagate upwards from the lower troposphere. Meanwhile, when planetary waves propagate across the tropopause, they divided into two branches. One continues to propagate upwards along the polar waveguide into the stratosphere, while the other propagates southwards into the troposphere along the low-latitude waveguide (Dickinson, 1968). Xu et al. (2017) found that zonal wavenumber-1 plays a dominant role in connecting the October northern Eurasian SCE and following January Eurasian SAT.

When the SSD deepens in November with high albedo and low heat conductivity, the surface radiation cooling strengthens (**Figures 3A,B** and **Figure 4E,F**). This causes the November upward heat flux to increase, especially over western Siberia (**Figures 3G,H**). Eliassen and Palm (1960) indicated that heat flux can be used not only to describe its poleward transportation but also to represent upwelling tropospheric wave energy into the lower stratosphere. Correspondingly, the upward WAF originates and propagates from the troposphere to the stratosphere in November over western Siberia with the strong temperature gradient in 65°–90°E (**Figures 5A,B**). With the SD further increasing, the upward propagation is still in December. the monthly increment of Siberian snow cover from November to January is 27.7, 5.5 and 0.2%, which represents the

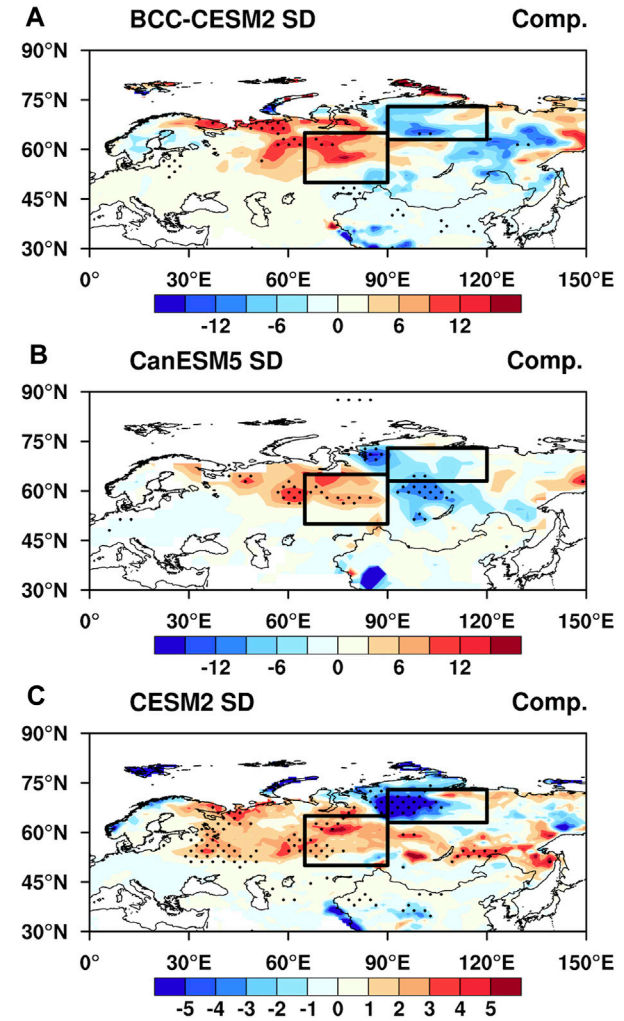

FIGURE 8 | Composite spatial patterns of SD (units: mm) in November between SH_{+-} and SH_{-+} in each model during 2000–2018: **(A)** first group of BCC-CSM2; **(B)** thirteenth group of CanESM5; **(C)** ensemble (seventh to ninth group) of CESM2. Dotted regions are statistically significant at the 90% confidence level, based on the *t*-test. The black rectangle represents the key area of SSD [(50°–65°N, 65°–90°E), (63°–73°N, 90°–120°E)].

difference of month-to-month variation (defined as the current month of SCE minus that of the previous month). However, the monthly increment of December snow cover is much smaller compared with that in November, resulting in weak surface heat flux anomaly. The upward WAF from the tropopause to the upper stratosphere relatively weakens in that month (**Figures 5C,D**).

Scott and Polvani (2006) indicated that the variability of stratospheric polar vortex is influenced by radiative cooling and wave, like a cycle. With the stratospheric polar vortex becoming warm and weak from December to January (**Figures 6A–D**), the upward wave propagation is suppressed. The anomalies of the stratospheric polar vortex signal propagate downwards in January (**Figures 7E,F**). Some research also presented that the influence of anomalous stratospheric signals on tropospheric surface weather via AO anomalies propagation downwards (Baldwin and Dunkerton, 1999; Black, 2002). Large amplitude AO anomaly in the stratosphere affects storm track, tropospheric jet, and then surface weather (Kidston et al., 2015). To further present the downward propagation and influence of the anomalous signal of SSD-related stratospheric polar vortex, **Figures 7A,B** show the time–pressure cross-section of composite differences of the area-averaged geopotential height anomalies in the region poleward of 70°N and the Northern Annular Mode index [NAM index, defined by the normalized time coefficient of the first EOF mode of zonal-mean (20°–90°N) geopotential height anomaly (Baldwin and Dunkerton, 2001)] on the daily scale. The polar vortex anomalous signal can extend from stratosphere to troposphere (**Figure 7A**). Meanwhile, the anomalously negative Arctic Oscillation–like pattern of downward propagation may make the easterlies anomaly over polar and the westerlies over Northern Eurasia at 300 hPa, which hinder the cold air masses accumulation over Siberia in January (**Figures 6E,F**, **7B**) (Zeng et al., 2015). Thus, the SH weakens in January (**Figures 7F,G**).

In years of both Siberian reversal and SSD anomalies, the troposphere–stratosphere coupling over Siberia can also be analyzed over Eurasia. The temporal evolution of the zonal wavenumber-1 structure of geopotential height and WAF along the strong heat flux anomalous area at 50°–70°N is presented in **Figures 7C–E** during November–January. As the SSD is higher, the significantly negative anomalies over the northern Atlantic extend from the upper stratosphere to the surface in November and tilt eastwards with height due to the quasi-geostrophic linear dynamics (Charney and Drazin, 1988). Positive anomalies develop from the Siberian stratosphere to the East Asian and Pacific troposphere. The upward WAF is concentrated over western Siberia with the strong temperature gradient in 65°–90°E (**Figure 7C**). However, the troposphere–stratosphere interaction is weaker over Siberia (70°–120°E) in December, which may be influenced by the smaller monthly increment of December Siberian snow cover. Meanwhile, the upward WAF concentrates on troposphere and lower stratosphere in December (**Figure 7D**). In January, a close troposphere–stratosphere connection can be found with a downward propagation of the stratospheric polar vortex signal, which has a weak projection on the weak East Asian trough and Ural high (**Figure 7E**). The strong troposphere–stratosphere interaction and relatively tropospheric circulation may induce a weak SH in January (**Figures 7F,G**).

Validation by Model Simulation

To test whether numerical models can reproduce the reverse response of the SH to November snow cover, the historical simulation experiments from CMIP6 were used for the period 1985–2014. Specifically, we selected the first group of historical simulation experiments of 27 models that contain SLP, SD and Hgt50. Based on the limited prediction skill for the SH in wintertime (Yang et al., 2021), there are only four models (BCC-CSM2, CanESM5, CESM2, MIROC-ES2L) that can reproduce the frequency of SH reversal after 2000 being 15% higher than that before 2000.

To further verify the physical mechanisms, we examine the snow cover response in the preceding November between

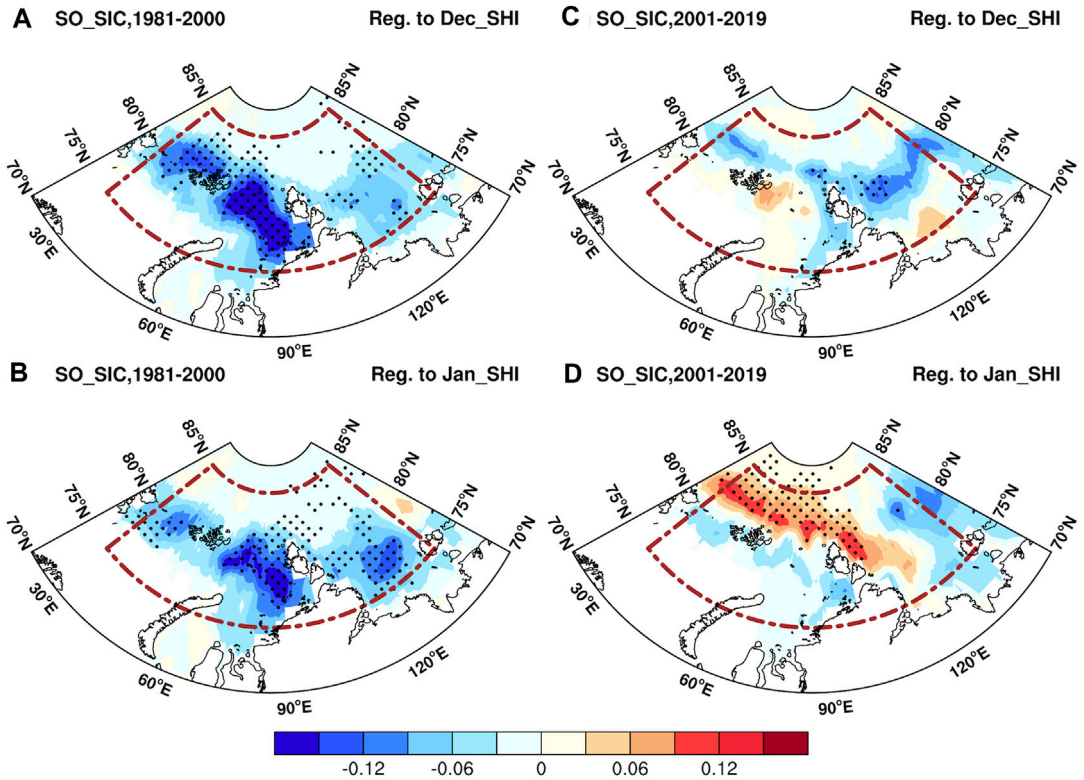

FIGURE 9 | Regressions of September–October sea-ice concentration (SIC) on the **(A)** December and **(B)** January Siberian high intensity index (SHI), separately, during 1980/81–1999/2000. **(C–D)** As in (A–B) but during 2000/01–2018/19. Dotted regions are statistically significant at the 90% confidence level, based on the *t*-test. The brown rectangle represents the key area of SIC over the Barents to Laptev Sea [BLSIC, (75°–85°N, 30°–140°E)].

SHI_{+-} and SHI_{-+} using 3–30 groups of historical simulation experiments from the four models that can reproduce the reversal decadal variations. The results show that the first group of BCC-CSM2 and the thirteenth group of CanESM5 can partly reproduce the November SSD anomalies over Siberia while the SH reversal occurs (**Figures 8A,B**). Furthermore, the seventh to the ninth group from CESM2 also partly present the SSD anomalies in November. The simple ensemble CESM2 model (averaged seventh to ninth group results) can reproduce significant November SD anomalies over western and eastern Siberia in the reversal years (**Figure 8C**). The stratospheric polar vortex is relatively warmer and weaker in December and January in the above experiments (figure not shown). Thus, the reversal response of SSD to the SH in December and January can be partly reproduced in some of the simulation experiments, especially in CESM2.

Connection Between Autumn Arctic Sea-Ice Concentration and a Coherent December and January Siberian High

Wu et al. (2011) indicated a relationship between autumn sea ice and the winter SH via changes in the thermal gradient between the Arctic and mid-to-high latitudes. Lu et al. (2019) revealed the impact of September–October ASIC on the intraseasonal reversal of the November and December–January SH during 1979–2015. It is suggested that the reduction in September SIC can persist into November and induce upward surface heat flux anomalies, which can enhance the transportation of eddy energy and WAF to mid-to-high latitudes. This benefits the development of the storm track over northeastern Europe in November. On the contrary, decreased heat flux anomalies and suppressed eddy energy hinder the growth of the storm track in December–January, which weakens storm track activities and Ural blocking. The accelerated westerlies prevent the transportation of cold air masses from the Arctic to Siberia, leading to less accumulation in the region (Chang and Lu, 2012; Zeng et al., 2015). The winter SH tends to be mainly weakened in December–January. The researchers also consider that the SH in December and January exhibits consistent variations.

Based on the connection between SH and SIC, we further explore its relationships between the September–October SIC and SH in December and January respectively during 1981–2000 and 2001–2019. As **Figures 9A,B** shown, the September–October SIC around the Barents to Laptev Sea has a significantly negative correlation with the SH in December and January during 1981–2000. However, the negative correlation of sea ice around the Barents Sea in the period of 2001–2019 is weak (**Figures 9C,D**). Meanwhile, we found that the September–October Barents Sea SIC in the north of 80°N has

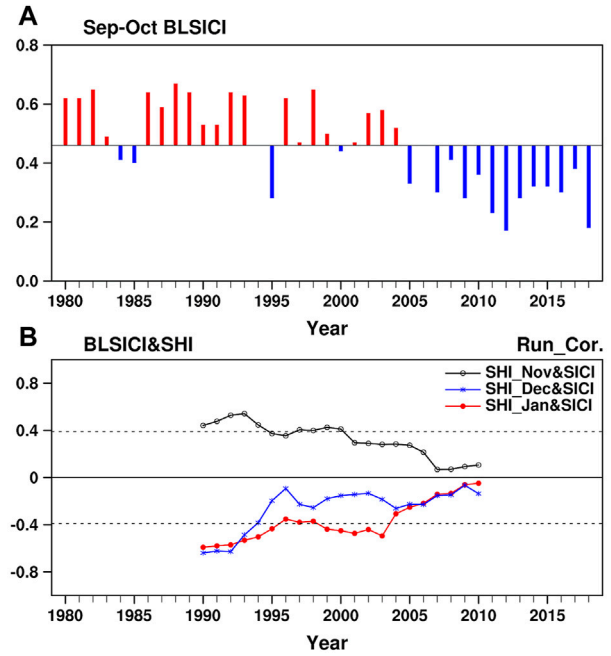

FIGURE 10 | (A) Time-series of BLSICI in September–October [area-averaged (75°–85°N, 30°–140°E) Arctic sea-ice concentration] during 1980/81–2018/19. **(B)** The 19-years sliding correlation coefficients between September–October BLSICI and the SHI in November (black line), December (blue line) and January (red line) separately, during during 1980/81–2018/19. Dotted lines denote correlations above the 90% confidence level.

TABLE 3 | The correctly predicted SH reverse year based on CFSv2 outputs and SSD-scheme.

CFSv2 outputs	SHI_{+-}	2012/13
	SHI_{-+}	2006/07
SSD-scheme	SHI_{+-}	2002/03; 2003/04; 2012/13; 2018/19
	SHI_{-+}	2006/07; 2007/08; 2008/09; 2010/11; 2015/2016

a reverse impact on the SH between December and January. Moreover, the time series of SIC over the Barents to Laptev Sea [BLSIC, (75–85°N, 30–140°E)] demonstrates a decline in recent years (**Figure 10A**). The 19-years sliding correlation is decreased in the connection between the September–October BLSIC and the out-of-phase variation of the SH in November and December–January after 2004 (**Figure 10B**). Therefore, the intraseasonal reversal of the SH in midwinter increasing after 2000 may be attributable to the gradually diminishing SIC.

Intraseasonal Prediction of the Siberian High in December and January Based on Siberian Snow Depth and Arctic Sea-Ice Concentration

The prediction skill for the SH in December and January are evaluated using CFSv2 outputs releasing in November. The TCC of the SHI of the December and January SHI between the observation and CFSv2 outputs is 0.01 and 0.09 (not significant at the 10% level), respectively, during 1983–2019. Meanwhile, the predicted reversal frequency of the SH in December and January is 16% after 2000, which is smaller than observed. The CFSv2 only predicted the reverse phenomenon in 2006/07 and 2012/13 (**Table 3**). Thus, the prediction skill for the SH in December and January is poor, and the intraseasonal reversal cannot be predicted well. Our analysis indicates that the consistent SH before 2000 and its reversal after 2000 in midwinter are mainly acted on by the September–October ASIC and November SSD, respectively. Hence, we further examine their importance in the intraseasonal prediction of the SH by taking the observed September–October ASIC and November SSD to construct an intraseasonal prediction model.

The linear-regression SIC-scheme shows a high prediction skill for the December and January SH before 2000. The TCC of the SHI between the observation and cross-validation results is 0.58 and 0.51 in December and January before 2000, respectively. Meanwhile, linear-regression SSD-scheme is established using November SSD. The predicted reversal frequency can be promoted from 16% (CFSv2 outputs) to 75% (SSD-scheme) after 2000. Therefore, the snow cover over Siberia in the previous November is an important potential factor for predicting the intraseasonal reversal.

CONCLUSION AND DISCUSSION

The intraseasonal variation of the SH during December–January is documented in this study. It is found that the reversal of the SH_{+-}/SH_{-+} only exists in 6 years during 1981–2000; nevertheless, the out-of-phase frequency rises rapidly to 12 years during 2001–2019. Therefore, strengthened impacts of November snow cover over Siberia on the out-of-phase change in the SH between December and January since 2000 are discussed, accompanied by the thermal feedback and dynamical coupling of the November SSD.

From the thermal perspective, with the higher SSD, the snow albedo increases over Siberia, which tends to results in strong radiation cooling and a lowering of the SAT over Siberia in the preceding November. Meanwhile, the SCE increases over Siberia in November, which causes deeper snow accumulation in the following December. Thus, the surface cooling anomalies can persist to December and intensify the SH in that month. From the dynamical perspective, the surface heat flux is an important variable to generate and propagate WAF. In the context of higher SSD, the higher heat flux increases over western Siberia in November, which triggers upward propagation of WAF from the troposphere to the stratosphere during November–December. Due to the anomalously upward planetary waves, the stratospheric polar vortex weakens and warms in December–January. The troposphere–stratosphere coupling is closer in January under the SSD anomalies. Hence, the anomalies of the stratospheric polar vortex signal propagate downwards, hindering the development of Ural blockings and the East Asian trough in January. With the anomalously downward negative Arctic Oscillation–like signal, the

westerlies correspondingly intensify over Siberia and reduces over polar in January. Therefore, the SH in January weakens relatively. The physical mechanisms also exist in the lower SSD. In addition, some historical simulation experiments of the BCC-CSM2, CanESM5 and CESM2 models from CMIP6 can also partly reproduce the connection between the November SSD and SH reversal in midwinter. Some research has indicated that the autumnal ASIC is significant for the winter SH, which may be a reason behind the SH reversal in November and December–January via eddy–mean flow interaction. Moreover, we found that the linkage becomes weak and insignificant after 2000. The diminishing Arctic sea ice may have induced the coherent variation of the SH in December and January to have decreased after 2000.

Based on the poor prediction skill for the SH in real-time global climate models, the observed SSD in November and the ASIC in September–October were employed to construct intraseasonal prediction models during 2001–2019 and 1981–2000. The prediction accuracy for the out-of-phase change in the SH between December and January increases from 16% (CFSv2 outputs) to 75% (SCE-scheme) after 2000. The TCC of the SHI between the observation and cross-validation results of ASIC-scheme is 0.58 and 0.51 in December and January before 2000, respectively (significant at the 10% level).

This study only demonstrates the role of snow cover for the intraseasonal SH reversal in midwinter. More factors, including the SST over the subtropical Northwest Pacific and the SIC in the Southern Hemisphere, will be further explored and considered in future work. Besides, this study mainly considers the relationship between the SH and SD using observing snow depth from CMC. As ECWMF interim datasets add the assimilation of the satellite-based NOAA/NESDIS daily snow cover to the snow depth after 2003, the sources of snow depth have difference in 2001–2003 and 2003–2018. This difference may make the SD anomalies between SH_{+-} and SH_{-+} over the Northern Siberia is not significant compared to results from CMC. If more reliable snow depth data before 2000 is available, the relationship between the SH and SD will be further explored before 2000.

In addition, not only does the transition frequency of the SH in December and January after 2000, but reversal of the SH is more evident after 2000. It might be due to the variability of November snow cover and global warming. Firstly, the variability of November snow cover over Eurasia (50°–80°N, 30°–150°E) increases from 3.2 (1980–1999) to 3.9 (2000–2018) over Eurasia, especially over Siberia (40°–60°N, 70°–120°E) from 8.4 to 9.5. These changes may cause more complex land-air feedbacks, making the intraseasonal variabilities of the SH strengthening in following winter. Secondly, the Arctic amplification with global warming has coincided with a period of ostensibly more frequent extreme weather events across the Northern Hemisphere mid-latitudes, including severe winters (Cohen et al., 2014). Thus, as mainly connecting system of East Asian climate, the intraseasonal variabilities of the SH gradually intensify in the context of Global warming and Arctic amplification (Wu et al., 2017). As the location of the Siberian high has an important influence on the Eurasian climate, the intraseasonal variations of the location of the SH need to be investigated in the future work.

DATA AVAILABILITY STATEMENT

We are grateful to the National Centers for Environmental Prediction/National Center for Atmospheric Research for providing the reanalysis data (https://psl.noaa.gov/data/gridded/data.ncep.reanalysis.html) and NCEP Climate Forecast System, version 2 data (http://iridl.ldeo.columbia.edu/SOURCES/. NOAA/.NCEP/.EMC/.CFSv2/), the Met Office Hadley Centre for providing monthly sea-ice cover data (https://www.metoffice.gov.uk/hadobs/hadisst/data/download.html), the Rutgers Global Snow Lab for providing monthly snow cover extent data (https://climate.rutgers.edu/snowcover/), the ECMWF (European Center for Medium-Range Weather Forecasts) interim (https://www.ecmwf.int/en/forecasts/datasets/browse-reanalysis-datasets) and the Canadian Meteorological Centre (CMC) (https://doi.org/10.5067/W9FOYWH0EQZ3) for snow depth, and the phase 6 of the Coupled Model Intercomparison Project (CMIP6) for simulated sea level pressure and snow depth data (https://esgf-node.llnl.gov/search/cmip6/).

AUTHOR CONTRIBUTIONS

Conceptualization: KF Data curation: HY Formal analysis: HY Funding acquisition: KF Investigation: HY Methodology: KF Project Administration: KF Resources: HY Supervision: KF Validation: KF Writing original draft: HY Writing review and editing: KF.

FUNDING

This study was supported by National Natural Science Foundation of China (NSFC) (Grants 41730964、42088101) and the Innovation Group Project of Southern Marine Science and Engineering Guangdong Laboratory (Zhuhai) (No 311021001).

REFERENCES

Ao, J., and Sun, J. (2016). Connection between November Snow Cover over Eastern Europe and winter Precipitation over East Asia. *Int. J. Climatol.* 36 (5), 2396–2404. doi:10.1002/joc.4484

Baldwin, M. P., and Dunkerton, T. J. (1999). Propagation of the Arctic Oscillation from the Stratosphere to the Troposphere. *J. Geophys. Res.* 104 (30), 937–946. doi:10.1029/1999jd900445

Baldwin, M. P., and Dunkerton, T. J. (2001). Stratospheric Harbingers of Anomalous Weather Regimes. *Science* 294 (5542), 581–584. doi:10.1126/science.1063315

Black, R. X. (2002). Stratospheric Forcing of Surface Climate in the Arctic Oscillation. *J. Clim.* 15 (3), 268–277. doi:10.1175/1520-0442(2002)015<0268:Sfosci>2.0.Co;2

Bony, S., Colman, R., Kattsov, V. M., Allan, R. P., Bretherton, C. S., Dufresne, J.-L., et al. (2006). How Well Do We Understand and Evaluate Climate Change Feedback Processes? *J. Clim.* 19 (15), 3445–3482. doi:10.1175/jcli3819.1

Brown, R. D., and Brasnett, B. (2010). *Canadian Meteorological Centre (CMC) Daily Snow Depth Analysis Data*. Version 1. Boulder, Colorado: NASA National Snow and Ice Data Center Distributed Active Archive Center. doi:10.5067/W9FOYWH0EQZ3

Chang, C.-P., and Lu, M.-M. (2012). Intraseasonal Predictability of Siberian High and East Asian Winter Monsoon and its Interdecadal Variability. *J. Clim.* 25 (5), 1773–1778. doi:10.1175/Jcli-D-11-00500.1

Charney, J. G., and Drazin, P. G. (1961). Propagation of Planetary-Scale Disturbances from the Lower into the Upper Atmosphere. *J. Geophys. Res.* 66 (3), 83–109. doi:10.1029/JZ066i001p00083

Chen, H., and Sun, Z. (2003). The Effects of Eurasian Snow Cover Anomaly on Winter Atmospheric General Circulation Part I. Observational Studies. *Chin. J. Atmos. Sci.* 27 (3), 304–316. doi:10.3878/j.issn.1006-9895.2003.03.02

Cohen, J., and Fletcher, C. (2007). Improved Skill of Northern Hemisphere winter Surface Temperature Predictions Based on Land-Atmosphere Fall Anomalies. *J. Clim.* 20 (16), 4118–4132. doi:10.1175/JCLI4241.1

Cohen, J., Foster, J., Barlow, M., Saito, K., and Jones, J. (2010). Winter 2009-2010: A Case Study of an Extreme Arctic Oscillation Event. *Geophys. Res. Lett.* 37 (17), a–n. doi:10.1029/2010gl044256

Cohen, J., and Rind, D. (1991). The Effect of Snow Cover on the Climate. *J. Clim.* 4 (7), 689–706. doi:10.1175/1520-0442(1991)004<0689:Teosco>2.0.Co;2

Cohen, J., Saito, K., and Entekhabi, D. (2001). The Role of the Siberian High in Northern Hemisphere Climate Variability. *Geophys. Res. Lett.* 28 (2), 299–302. doi:10.1029/2000gl011927

Cohen, J., Screen, J. A., Furtado, J. C., Barlow, M., Whittleston, D., Coumou, D., et al. (2014). Recent Arctic Amplification and Extreme Mid-latitude Weather. *Nat. Geosci.* 7 (9), 627–637. doi:10.1038/NGEO2234

Dai, H., Fan, K., and Liu, J. (2019). Month-to-Month Variability of Winter Temperature over Northeast China Linked to Sea Ice over the Davis Strait-Baffin Bay and the Barents-Kara Sea. *J. Clim.* 32 (19), 6365–6384. doi:10.1175/jcli-d-18-0804.1

Dee, D. P., Uppala, S. M., Simmons, A. J., Berrisford, P., Poli, P., Kobayashi, S., et al. (2011). The ERA-Interim Reanalysis: Configuration and Performance of the Data Assimilation System. *Q.J.R. Meteorol. Soc.* 137 (656), 553–597. doi:10.1002/qj.828

Dickinson, R. E. (1968). Planetary Rossby Waves Propagating Vertically through Weak Westerly Wind Wave Guides. *J. Atmos. Sci.* 25 (6), 984–1002. doi:10.1175/1520-0469(1968)025<0984:Prwpvt>2.0.Co;2

Ding, Y., and Krishnamurti, T. N. (1987). Heat Budget of the Siberian High and the Winter Monsoon. *Mon. Wea. Rev.* 115 (10), 2428–2449. doi:10.1175/1520-0493(1987)115<2428:hbotsh>2.0.co;2

Eliassen, A., and Palm, E. (1960). On the Transfer of Energy in Stationary Mountain Waves. *Geophy Publ.* 22, 1–23.

Eyring, V., Bony, S., Meehl, G. A., Senior, C. A., Stevens, B., Stouffer, R. J., et al. (2016). Overview of the Coupled Model Intercomparison Project Phase 6 (CMIP6) Experimental Design and Organization. *Geosci. Model. Dev.* 9 (5), 1937–1958. doi:10.5194/gmd-9-1937-2016

Francis, J. A., and Vavrus, S. J. (2012). Evidence Linking Arctic Amplification to Extreme Weather in Mid-latitudes. *Geophys. Res. Lett.* 39 (6), a–n. doi:10.1029/2012gl051000

Gong, D.-Y., and Ho, C.-H. (2002). The Siberian High and Climate Change over Middle to High Latitude Asia. *Theor. Appl. Climatology* 72 (1-2), 1–9. doi:10.1007/s007040200008

Gong, G., Cohen, J., Entekhabi, D., and Ge, Y. (2007). Hemispheric-scale Climate Response to Northern Eurasia Land Surface Characteristics and Snow Anomalies. *Glob. Planet. Change* 56 (3-4), 359–370. doi:10.1016/j.gloplacha.2006.07.025

Gong, G., Entekhabi, D., and Cohen, J. (2003). Modeled Northern Hemisphere winter Climate Response to Realistic Siberian Snow Anomalies. *J. Clim.* 16 (23), 3917–3931. doi:10.1175/1520-0442(2003)016<3917:Mnhwcr>2.0.Co;2

Hall, A., and Qu, X. (2006). Using the Current Seasonal Cycle to Constrain Snow Albedo Feedback in Future Climate Change. *Geophys. Res. Lett.* 33 (3), L03502. doi:10.1029/2005gl025127

Han, S., and Sun, J. (2021). Connection between the November Snow Cover over Northeast Asia and the Following January Precipitation in Southern China. *Int. J. Climatol* 41 (4), 2553–2567. doi:10.1002/joc.6974

Han, S., and Sun, J. (2020). Potential Contribution of winter Dominant Atmospheric Mode over the Mid-latitude Eurasia to the Prediction of Subsequent spring Arctic Oscillation. *Int. J. Climatol* 40 (6), 2953–2963. doi:10.1002/joc.6376

Hasanean, H. M., Almazroui, M., Jones, P. D., and Alamoudi, A. A. (2013). Siberian High Variability and its Teleconnections with Tropical Circulations and Surface Air Temperature over Saudi Arabia. *Clim. Dyn.* 41 (7-8), 2003–2018. doi:10.1007/s00382-012-1657-9

Hu, Y., Tung, K. K., and Liu, J. (2005). A Closer Comparison of Early and Late-winter Atmospheric Trends in the Northern Hemisphere. *J. Clim.* 18 (16), 3204–3216. doi:10.1175/jcli3468.1

Huang, J., and Hu, Y. (2006). Trennds of winter Temperatures in China. *Acta Meteorologica Sinica* 64 (5), 614–621. doi:10.3321/j.issn:0577-6619.2006.05.008

Huffman, G. J., Adler, R. F., Arkin, P., Chang, A., Ferraro, R., Gruber, A., et al. (1997). The Global Precipitation Climatology Project (GPCP) Combined Precipitation Dataset. *Bull. Amer. Meteorol. Soc.* 78 (1), 5–20. doi:10.1175/1520-0477(1997)078<0005:Tgpcpg>2.0.Co;2

Iqbal, M. J., Riaz, S. M. F., and Ghauri, B. M. K. (2013). Impact of Siberian High on Rainfall Variability over Northern Part of Indo-Pak Region. *Arab J. Geosci.* 6 (8), 3087–3092. doi:10.1007/s12517-012-0598-2

Jeong, J.-H., Ou, T., Linderholm, H. W., Kim, B.-M., Kim, S.-J., Kug, J.-S., et al. (2011). Recent Recovery of the Siberian High Intensity. *J. Geophys. Res.* 116 (D23), a–n. doi:10.1029/2011jd015904

Kalnay, E., Kanamitsu, M., Kistler, R., Collins, W., Deaven, D., and Gandin, L. (1996). The NCEP/NCAR 40-year Reanalysis Project. *Bull. Am. Meteorol. Soc.* 77, 437–441. doi:10.1175/1520-0477(1996)077<0437:TNYRP>2.0.CO;2

Kidston, J., Scaife, A. A., Hardiman, S. C., Mitchell, D. M., Butchart, N., Baldwin, M. P., et al. (2015). Stratospheric Influence on Tropospheric Jet Streams, Storm Tracks and Surface Weather. *Nat. Geosci.* 8 (6), 433–440. doi:10.1038/ngeo2424

Kug, J. S., Jeong, J. H., Jang, Y. S., Kim, B. M., Folland, C. K., Min, S. K., et al. (2015). Two Distinct Influences of Arctic Warming on Cold winters over North America and East Asia. *Nat. Geosci.* 8 (10), 759–762. doi:10.1038/ngeo2517

Lei, S., and Wu, R. (2017). Processes for Occurrence of strong Cold Events over Eastern China. *J. Clim.* 30 (22), 9247–9266. doi:10.1175/JCLI-D-16-0857.1

Lei, S., Wu, R., and Yang, J. (2018). Relative Contributions of Synoptic and Intraseasonal Variations to strong Cold Events over Eastern China. *Clim. Dyn.* 50, 4619–4634. doi:10.1007/s00382-017-3894-4

Li, C. (1990). Interaction between Anomalous winter Monsoon in East Asia and EI Nino Events. *Adv. Atmos. Sci.* 7 (1), 36–46. doi:10.1007/BF02919166

Li, D., and Lan, L. (2017). Relationship between the Intensity of the Siberian High and the SST Anomaly in the North Atlantic. *Trans. Atmos. Sci.* 40 (1), 13–24. doi:10.13878/j.cnki.dqkxxb.20151218001

Li, F., and Wang, H. (2014). Autumn Eurasian Snow Depth, Autumn Arctic Sea Ice Cover and East Asian winter Monsoon. *Int. J. Climatology* 34 (13), 3616–3625. doi:10.1002/joc.3936

Li, H., Fan, K., He, S., Liu, Y., Yuan, X., and Wang, H. (2021). Intensified Impacts of Central Pacific ENSO on the Reversal of December and January Surface Air Temperature Anomaly over China since 1997. *J. Clim.* 34 (5), 1601–1618. doi:10.1175/jcli-d-20-0048.1

Li, J., Li, F., and Wang, H. (2020). Subseasonal Prediction of winter Precipitation in Southern China Using the Early November Snowpack over the Urals. *Atmos. Oceanic Sci. Lett.* 13 (6), 534–541. doi:10.1080/16742834.2020.1824547

Lu, M. M., and Chang, C. P. (2009). Unusual Late-Season Cold Surges during the 2005 Asian Winter Monsoon: Roles of Atlantic Blocking and the Central Asian Anticyclone. *J. Clim.* 22 (19), 5205–5217. doi:10.1175/2009jcli2935.1

Lu, Z., Li, F., Orsolini, Y. J., Gao, Y., and He, S. (2020). Understanding of European Cold Extremes, Sudden Stratospheric Warming, and Siberian Snow Accumulation in the Winter of 2017/18. *J. Clim.* 33 (2), 527–545. doi:10.1175/jcli-d-18-0861.1

Lu, Z. Z., He, S., Li, F., and Wang, H. J. (2019). Impacts of the Autumn Arctic Sea Ice on the Intraseasonal Reversal of the Winter Siberian High. *Adv. Atmos. Sci.* 36, 173–188. doi:10.1007/s00376-017-8089-8

Plumb, R. A. (1985). On the 3-dimensional Propagation of Sattionary Waves. *J. Atmos. Sci.* 42 (3), 217–229. doi:10.1175/1520-0469(1985)042<0217:Ottdpo>2.0.Co;2

Rayner, N. A. (2003). Global Analyses of Sea Surface Temperature, Sea Ice, and Night marine Air Temperature since the Late Nineteenth century. *J. Geophys. Res.* 108 (D14), 4407. doi:10.1029/2002JD002670

Riaz, S. M. F., and Iqbal, M. J. (2017). Singular Value Decomposition Analysis for Examining the Impact of Siberian High on winter Precipitation Variability over South Asia. *Theor. Appl. Climatology* 130 (3-4), 1189–1194. doi:10.1007/s00704-016-1948-x

Ringler, T. D., and Cook, K. H. (1999). Understanding the Seasonality of Orographically Forced Stationary Waves: Interaction between Mechanical and thermal Forcing. *J. Atmos. Sci.* 56 (9), 1154–1174. doi:10.1175/1520-0469(1999)056<1154:Utsoof>2.0.Co;2

Robinson, D. A., Dewey, K. F., and Heim, R. R. (1993). Global Snow Cover Monitoring: an Update. *Bull. Am. Meteorol. Soc.* 74 (9), 1689–1696. doi:10.1175/1520-0477(1993)074<1689:Gscmau>2.0.Co;2

Saha, S., Moorthi, S., Wu, X. R., Wang, J., Nadiga, S., Tripp, P., et al. (2014). The NCEP Climate Forecast System Version 2. *J. Clim.* 27 (6), 2185–2208. doi:10.1175/Jcli-D-12-00823.1

Sahsamanoglou, H. S., Makrogiannis, T. J., and Kallimopoulos, P. P. (1991). Some Aspects of the Basic Characteristics of the Siberian Anticyclone. *Int. J. Climatology* 11 (8), 827–839. doi:10.1002/joc.3370110803

Saito, K., Cohen, J., and Entekhabi, D. (2001). Evolution of Atmospheric Response to Early-Season Eurasian Snow Cover Anomalies. *Monthly Weather Rev.* 129 (11), 2746–2760. doi:10.1175/1520-0493(2001)129<2746:Eoarte>2.0.Co;2

Scott, R. K., and Polvani, L. M. (2006). Internal Variability of the winter Stratosphere. Part I: Time-independent Forcing. *J. Atmos. Sci.* 63 (11), 2758–2776. doi:10.1175/jas3797.1

Si, D., Li, Q., Liu, Y., Wang, Z., Yuan, Y., and Wang, D. (2014). Possible Causes for the Anomalous Weak East Asian Winter Monsoon in 2013/2014. *Meteorol. Monthly* 40 (7), 891–897. doi:10.7519/j.issn.1000-0526.2014.07.014

Si, D., Ma, L., Wang, P., Wang, Y., Nie, Y., and Sun, L. (2016). Anomalous Activity of Arctic Oscillation in winter 2015/16 and its Impact on Temperature in China. *Meteorol. Monthly* 42 (7), 892–897. doi:10.7519/j.issn.1000-0526.2016.07.013

Soden, B. J., and Held, I. M. (2006). An Assessment of Climate Feedbacks in Coupled Ocean-Atmosphere Models. *J. Clim.* 19 (14), 3354–3360. doi:10.1175/jcli3799.1

Takaya, K., and Nakamura, H. (2005a). Geographical Dependence of Upper-Level Blocking Formation Associated with Intraseasonal Amplification of the Siberian High. *J. Atmos. Sci.* 62 (12), 4441–4449. doi:10.1175/jas3628.1

Takaya, K., and Nakamura, H. (2005b). Mechanisms of Intraseasonal Amplification of the Cold Siberian High. *J. Atmos. Sci.* 62 (12), 4423–4440. doi:10.1175/Jas3629.1

Tian, B., and Fan, K. (2020). Different Prediction Skill for the East Asian winter Monsoon in the Early and Late winter Season. *Clim. Dyn.* 54 (3-4), 1523–1538. doi:10.1007/s00382-019-05068-6

Wagner, A. J. (1973). The Influence of Average Snow Depth on Monthly Mean Temperature Anomaly. *Monthly Weather Rev.* 101 (8), 624–626. doi:10.1175/1520-0493(1973)101<0624:tioasd>2.3.co;2

Wang, D., Zhou, B., Sun, C., Yuan, Y., Liu, Y., and Wang, P. (2013). Features and Possible Causes for East Asian Winter Monsoon in 2012/2013. *Meteorol. Monthly* 39 (7), 930–937. doi:10.7519/j.issn.1000-0526.2013.07.014

Webster, P. J., Magana, V. O., Palmer, T. N., Shukla, J., Tomas, R. A., Yanai, M., et al. (1998). Monsoons: Processes, Predictability, and the Prospects for Prediction. *J. Geophys. Research-Oceans* 103 (C7), 14451–14510. doi:10.1029/97jc02719

Wegmann, M., Orsolini, Y., Vazquez, M., Gimeno, L., Nieto, R., Bulygina, O., et al. (2015). Arctic Moisture Source for Eurasian Snow Cover Variations in Autumn. *Environ. Res. Lett.* 10 (5), 054015. doi:10.1088/1748-9326/10/5/054015

Wu, B., Su, J., and Zhang, R. (2011). Effects of Autumn-winter Arctic Sea Ice on winter Siberian High. *Chin. Sci. Bull.* 56 (30), 3220–3228. doi:10.1007/s11434-011-4696-4

Wu, B. Y., Yang, K., and Francis, J. A. (2017). A Cold Event in Asia during January-February 2012 and its Possible Association with Arctic Sea Ice Loss. *J. Clim.* 30 (19), 7971–7990. doi:10.1175/Jcli-D-16-0115.1

Wu, R., and Kirtman, B. P. (2007). Observed Relationship of spring and Summer East Asian Rainfall with winter and spring Eurasian Snow. *J. Clim.* 20 (7), 1285–1304. doi:10.1175/jcli4068.1

Xie, A., Lu, Y., and Chen, S. (1992). The Evolution of Siberian High Prior to the Outbreak of Cold Air. *Chin. J. Atmos. Sci.* 16 (6), 677–685. doi:10.3878/j.issn.1006-9895.1992.06.05

Xu, X., He, S., Li, F., and Wang, H. (2017). Impact of Northern Eurasian Snow Cover in Autumn on the Warm Arctic–Cold Eurasia Pattern during the Following January and its Linkage to Stationary Planetary Waves. *Clim. Dyn.* 50 (5-6), 1993–2006. doi:10.1007/s00382-017-3732-8

Xu, X., Li, F., He, S., and Wang, H. (2018). Subseasonal Reversal of East Asian Surface Temperature Variability in Winter 2014/15. *Adv. Atmos. Sci.* 35 (6), 737–752. doi:10.1007/s00376-017-7059-5

Yang, H., and Fan, K. (2021). A Hybrid Ensemble Canonical Correlation Prediction Model of the Winter Siberian High. *J. Geophys. Research-Atmospheres* 126 (4), e2020JD033780. doi:10.1029/2020jd033780

Yang, H., Fan, K., Tian, B., and Hua, W. (2021). Why Is the November Siberian High Intensity More Predictable by NCEP-CFSv2 Model?. *Chin. J. Atmos. Sci.* 45 (4), 697–712. doi:10.3878/j.issn.1006-9895.2009.20106

Yang, S., and Lu, R. (2014). Predictability of the East Asian winter Monsoon Indices by the Coupled Models of ENSEMBLES. *Adv. Atmos. Sci.* 31 (6), 1279–1292. doi:10.1007/s00376-014-4020-8

Zeng, D., Zhu, W., Ma, X., Gu, P., Liu, M., and Gao, J. (2015). North Atlantic Storm Track and its Infulence on Siberian High in winter. *Trans. Atmos. Sci.* 38 (2), 232–240. doi:10.13878/j.cnki.dqkxxb.20121003001

Zhang, R. H., Sumi, A., and Kimoto, M. (1996). Impact of El Nino on the East Asian Monsoon: A Diagnostic Study of the 86/87 and 91/92 Events. *J. Meteorol. Soc. Jpn.* 74 (1), 49–62. doi:10.2151/jmsj1965.74.1_49

Zuo, J., Ren, H., and Li, W. (2015). Contrasting Impacts of the Arctic Oscillation on Surface Air Temperature Anomalies in Southern China between Early and Middle-To-Late Winter. *J. Clim.* 28 (10), 4015–4026. doi:10.1175/jcli-d-14-00687.1

Conflict of Interest: The authors declare that the research was conducted in the absence of any commercial or financial relationships that could be construed as a potential conflict of interest.

Publisher's Note: All claims expressed in this article are solely those of the authors and do not necessarily represent those of their affiliated organizations, or those of the publisher, the editors and the reviewers. Any product that may be evaluated in this article, or claim that may be made by its manufacturer, is not guaranteed or endorsed by the publisher.

frontiers in Earth Science

ORIGINAL RESEARCH
published: 11 November 2021
doi: 10.3389/feart.2021.762348

Precipitation Changes in Semi-arid Regions in East Asia Under Global Warming

Xiaodan Guan[1,2]*, *Kaiwei Zhu*[2], *Xiaoqian Huang*[2], *Xinrui Zeng*[2] and *Yongli He*[1,2]

[1]Collaborative Innovation Center for Western Ecological Safety, Lanzhou University, Lanzhou, China, [2]College of Atmospheric Sciences, Lanzhou University, Lanzhou, China

The semi-arid regions of East Asia are located in the transition area between regions dominated by the monsoon system and by westerly winds; their interaction is the key to understand precipitation changes, especially in the summer. Our results show that the enhancement of both the monsoon and westerly winds occurs in wet years, leading to stronger convergence and more rainfall. Weakening of both the monsoon and westerly winds occurs in dry years and results in less rainfall. Such interaction between the monsoon and westerlies is not constant; the boundary of their effects is changing all the time. As the monsoon strengthens, it shifts to the west in wet years and covers most of the semi-arid regions, and the negative effect of the El Niño-Southern Oscillation (ENSO) system on precipitation in the semi-arid regions becomes obvious. However, westward expansion has not been evident over the past 70 years in historic data. In the future, the monsoon will obviously expand westward, and the precipitation over the Loess Plateau will gradually increase as the monsoon boundary expand westward until the end of the 21st century. This change indicates that more rainfall will occur in the semi-arid regions of East Asia, which could dramatically change the ecological environment, especially over the Loess Plateau.

Keywords: precipitation, loess plateau, monsoon, westerly wind, enso

OPEN ACCESS

Edited by:
Renguang Wu,
Zhejiang University, China

Reviewed by:
Lin Wang,
Institute of Atmospheric Physics (CAS), China
Yunting Qiao,
Sun Yat-sen University, China

***Correspondence:**
Xiaodan Guan
guanxd@lzu.edu.cn

Specialty section:
This article was submitted to Atmospheric Science, a section of the journal Frontiers in Earth Science

Received: *21 August 2021*
Accepted: *15 October 2021*
Published: *11 November 2021*

Citation:
Guan X, Zhu K, Huang X, Zeng X and He Y (2021) Precipitation Changes in Semi-arid Regions in East Asia Under Global Warming. Front. Earth Sci. 9:762348. doi: 10.3389/feart.2021.762348

INTRODUCTION

The semi-arid area is broadly defined as the ratio of annual precipitation (P) to potential evapotranspiration (PET), in terms of the aridity index (AI), between one fifth and one half (Middleton and Thomas, 1997; Feng and Fu, 2013; Huang et al., 2016b; Zhu et al., 2021). In 2000, it covered ~15% of the earth's land surface and supported 14.4% of the global population (Safriel and Adeel 2005), and the area will continue to expand in the future (Huang et al., 2016b). The typical semi-arid region in East Asia (30–60°N, 80–140°E) is the largest semi-arid region in the middle latitudes of the Northern Hemisphere (Guan et al., 2015; Huang et al., 2016a), and the most representative underlying surface of this semi-arid region is the Loess Plateau of China (Chen et al., 2016). This area is thought to be largely constrained by water availability, and it has the characteristics of a dry climate, scarce vegetation, and poor soil and water conservation ability and is sensitive to precipitation (Sala and Lauenroth, 1982; Austin et al., 2004; Li et al., 2009; Yang et al., 2020). Because of the presence of loess, landslide disasters occur easily under heavy precipitation, whereas environmental degradation occurs under a lack of precipitation (Huang et al., 2016b). Because of this loess characteristic in China, the government has adopted a series of policies to prevent land desertification and soil erosion

(Zhang and Liu, 2005) to recover the ecological environment and reduce the occurrence of disasters. Such artificial regulation can improve the regional climate to a large extent, but measures should be taken according to local conditions and climate change. According to current studies, Northwest China is getting wet, which seems beneficial for ecological system development (Zhang et al., 2021). However, disasters caused by more precipitation are increasing and are contributing to large economic losses and threats to life security.

The semi-arid region of East Asia is located in the transition zone between the monsoon region and the westerly region (Wang et al., 2017). It is under the joint influence of the westerly wind and the East Asian summer monsoon (EASM; Xing and Wang, 2017; Yan et al., 2021). The westerly wind can bring water vapour from upstream sources, such as the Atlantic Ocean, Mediterranean Sea, and Arabian Sea. (Huang et al., 2015), while the EASM delivers water vapour from the Indian Ocean and the Pacific Ocean to the semi-arid region (Ding and Chan, 2005; Zhang and Zhou, 2015). Both systems can greatly influence precipitation over the semi-arid regions of East Asia (Sun and Ding, 2010; Chen et al., 2019). The semi-arid region over East Asia has a northeast-southwest orientation, and it is parallel to and close to the northwesternmost edge of the EASM. The edge of the EASM can be properly represented by the 2 mm day^{-1} (300 mm a^{-1}) precipitation isoline, which has a clearer physical significance from the perspective of climate, ecology and geography than other definitions. (Wang et al., 2012; Chen et al., 2018). Therefore, the precipitation of semi-arid region over East Asia is sensitive to the domain of the EASM (Chen et al., 2018). Hence, studying the impact of the EASM on precipitation in the semi-arid region over East Asia is of great significance for predicting precipitation in the semi-arid region and for making decisions regarding ecological protection and economic development in countries in semi-arid regions.

This paper explores the mechanism of precipitation changes in the semi-arid region of East Asia in response to changes in the EASM and the changes in the future. The data and methods are introduced in the second section. The detailed effects on precipitation changes from EASM and westerly winds, even the role of the El Niño-Southern Oscillation (ENSO) in the process, are illustrated in the third section. The fourth section presents the discussion and conclusions.

DATASETS AND METHODS

In this study, the gauge-based gridded precipitation dataset from the Global Precipitation Climatology Centre (GPCC) was used to analyze the precipitation variation in the semi-arid regions of East Asia, which has a spatial resolution of 0.5° by 0.5° and covers the period from 1891 to 2019 (https://opendata.dwd.de/climate_environment/GPCC/html/fulldata-monthly_v2020_doi_download.html). Compared with other precipitation datasets, GPCC's new global precipitation climatology V.2020 is more suitable for estimating

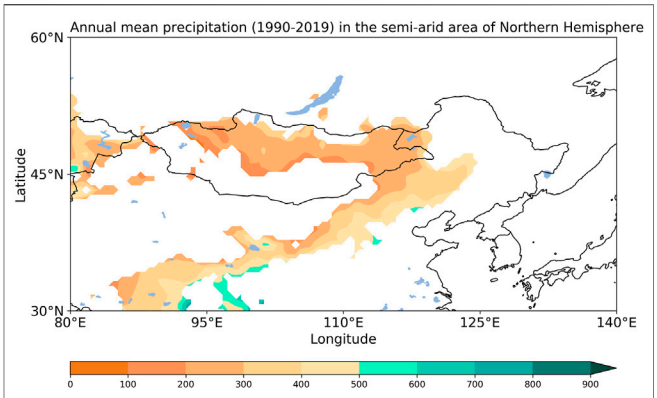

FIGURE 1 | Annual mean precipitation in the semi-arid area of East Asia during 1990–2019 (units: mm).

precipitation in the semi-arid regions of East Asia owing to its much denser station network (Schneider et al., 2014).

The HadISST 1.1 monthly average SST dataset is from the Met Office Hadley Centre (https://www.metoffice.gov.uk/hadobs/hadisst/data/download.html), which has a spatial resolution of 1° by 1° and ranges from 1870 to present (Rayner et al., 2003). The AI (aridity index) dataset used in this study is the same as that used in Huang et al. (2020), which has a spatial resolution of 0.5° by 0.5° and covers the period from 1948 to 2016.

We use the monthly geopotential height and wind at the 850 hPa pressure level to explain the mechanism of precipitation change in the semi-arid regions of East Asia. These variables are obtained from the 20th Century Reanalysis V3 dataset, which has a spatial resolution of 1° by 1° over the period of 1836–2015 (https://psl.noaa.gov/data/gridded/data.20thC_ReanV3.html).

The self-calibrating Palmer Drought Severity Index (PDSI) is available from the Climate Explorer (http://climexp.knmi.nl/select.cgi?id=someone@somewhere&field=scpdsi), which has a spatial resolution of 0.5° by 0.5° and covers the period from 1901 to 2017. The gross primary production (GPP) is provided by National Tibetan Plateau Data Center (http://data.tpdc.ac.cn), which has a spatial resolution of 0.05° by 0.05° and covers the period from 1982 to 2018 (Wang et al., 2021).

To assess the performances of the edge of the monsoon in the future, we used outputs from 18 Coupled Model Intercomparison Project Phase 6 (CMIP6) models. The CMIP6 experiments include simulations of the 21st-century climate under new greenhouse gas (GHG) emission scenarios (referred to as shared socioeconomic pathways (SSPs); Riahi et al., 2017). The SSPs are based on five narratives describing alternative socioeconomic developments, including sustainable development, regional rivalry, inequality, fossil fuel development, and middle-of-the-road development (Riahi et al., 2017).

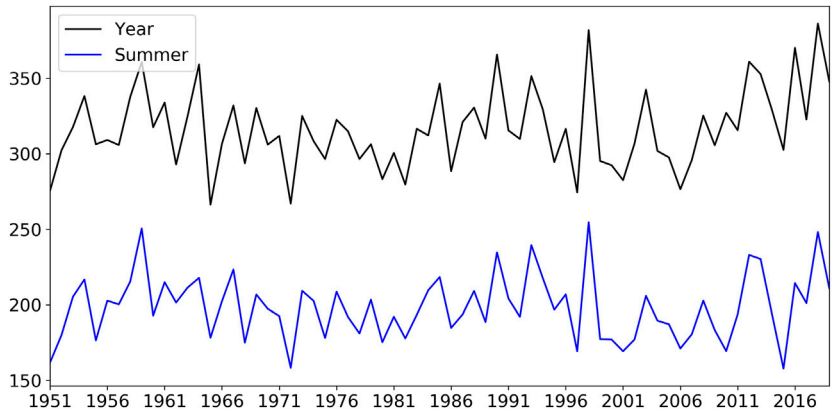

FIGURE 2 | Time series of weighted-average annual (black curve) and summer (blue curve) precipitation in the semi-arid area of East Asia during 1951–2019 (units: mm).

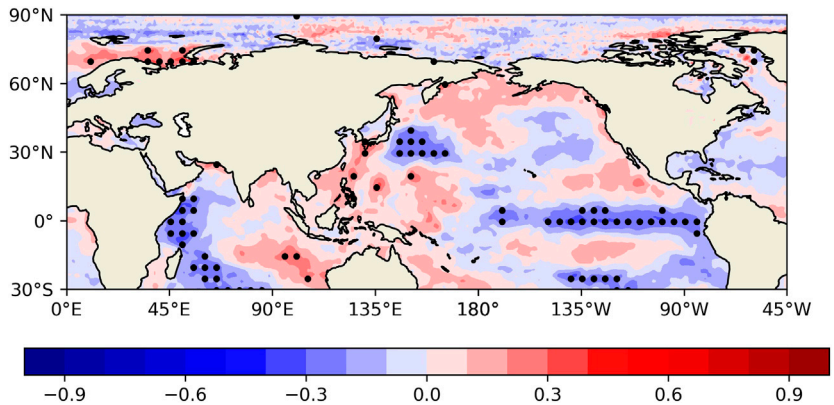

FIGURE 3 | Correlation coefficient between SST and precipitation in semi-arid regions in East Asia. Stippling denotes the region with statistical significance at the 90% confidence level based on Student's t-test.

RESULT

Precipitation Change in the Semi-arid Regions Over East Asia and the Relevant Mechanism

Figure 1 shows the spatial distributions of precipitation in the semi-arid regions in East Asia. The semi-arid regions of China and Kazakhstan have an annual mean precipitation between 300 and 500 mm, and Mongolia has an annual mean precipitation in the range of 100–300 mm. These semi-arid areas are all less affected by monsoons, have limited water vapour input, and thus generally receive little precipitation, with few spatial differences (Huang et al., 2012). The time series of annual precipitation and summer precipitation are shown in **Figure 2**. The summer mean precipitation accounts for 63% of the annual precipitation, and the correlation coefficient between them is as high as 0.874 ($p < 0.01$). Therefore, the annual precipitation over semi-arid regions of East Asia is primarily determined by summer precipitation on both amplitude and variability.

As summer precipitation dominates the variability in annual precipitation in the semi-arid regions of East Asia, understanding the summer precipitation variation is a positive step toward predicting the precipitation in these regions. To preliminarily investigate the factors affecting summer precipitation over semi-arid regions in East Asia, we calculated the correlation coefficient between summer precipitation and sea surface temperature (SST). The SST in the tropical east-central Pacific, western Indian Ocean, and northwestern Pacific has negative correlation patterns, and the Barents Sea and East China Sea have positive patterns that passed the significance test at 90% (**Figure 3**). These oceanic activities can influence precipitation in semi-arid regions in East Asia through atmospheric circulation. This shows that the SST factors are mainly related to the monsoon route and the sea basin where ENSO occurs, so the monsoon and ENSO may have a great impact on the precipitation over semi-arid regions in East Asia.

To further explore the ocean effect on the precipitation changes in the semi-arid areas of East Asia, we selected wet and dry years to compare the different monsoon and ENSO

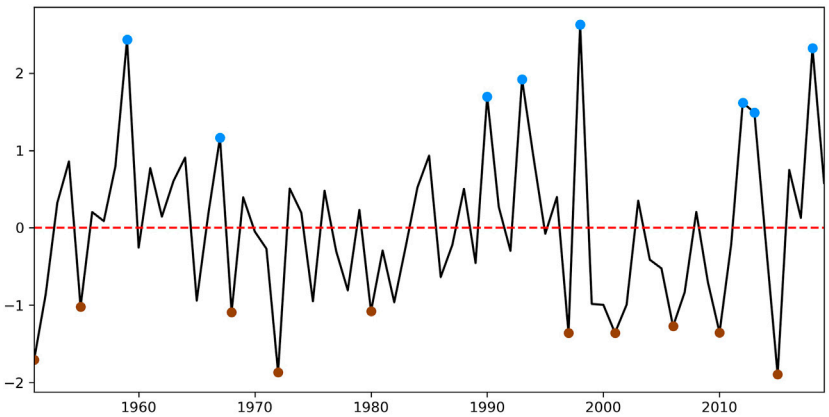

FIGURE 4 | Time series of summer precipitation anomalies (normalized) in the semi-arid regions of East Asia. The blue dots represent wet years, and the brown dots represent dry years.

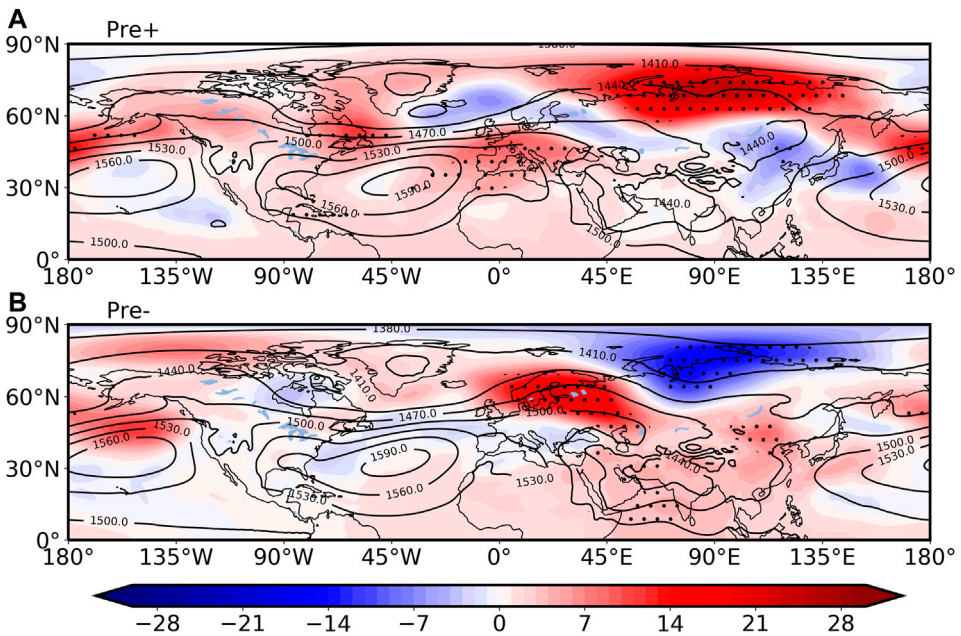

FIGURE 5 | 850 hPa summer geopotential height field anomalies (shaded) and 850 hPa summer mean geopotential height field (contours) composite for wet **(A)** and dry **(B)** years in the semi-arid regions of East Asia (units: gpm). Stippling denotes the region with statistical significance at the 90% confidence level based on Student's t-test.

behaviours. Periods with precipitation greater than one standard deviation are defined as wet years, and periods with precipitation less than one standard deviation are defined as dry years (**Figure 4**). The wet years in the past 70 years are 1959, 1967, 1990, 1993, 1998, 2012, 2013, and the dry years are 1951, 1955, 1968, 1972, 1980, 1997, 2001, 2006, 2010, 2015. From the composited 850 hPa geopotential height field for positive (wet) years and negative (dry) years (**Figure 5**), we found that there is a negative anomaly center over the East Asia continent during wet years, which spatially corresponds to the Mongolian low (**Figure 5A**). The anomaly center and mean field center basically coincide and pass the significance test at 90%. The negative geopotential height anomaly center, on the one hand, can greatly enhance the Mongolian low, which enhances upstream westerly wind transport; on the other hand, it can enhance the summer pressure difference between land and sea, enhancing monsoon transport (**Figure 6A**). As a result, the strengthening of the monsoon causes the edge of the monsoon to shift westward, and the monsoon region covers most of the semi-arid regions in East Asia (**Figure 6A**). Wet and warm

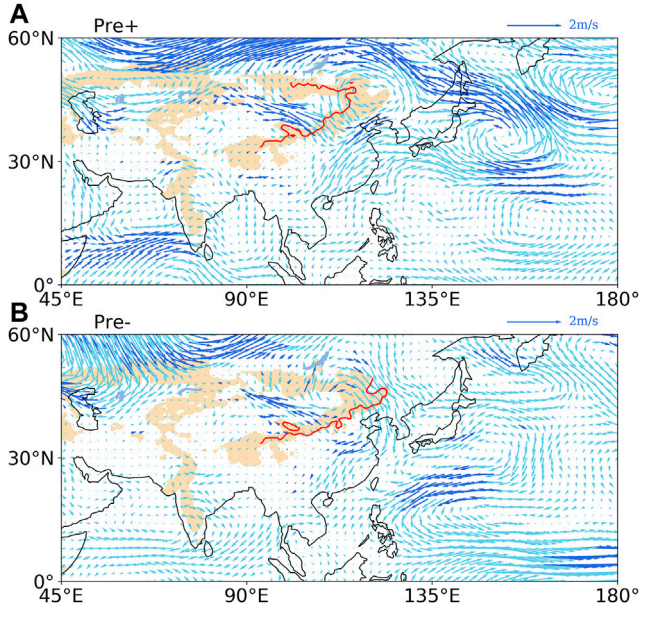

FIGURE 6 | 850 hPa summer wind composite for wet **(A)** and dry **(B)** years in the semi-arid regions of East Asia (units: m/s). The brown areas represent semi-arid areas of East Asia. The red curve represents the edge of the East Asian monsoon. The dark blue arrow denotes the region with statistical significance at the 90% confidence level based on Student's t-test.

monsoon southwesterlies, meeting cold air from the northwest over the semi-arid regions, generate strong convergence anomalies, which enhance the updraft and favour more precipitation (**Figure 6A**).

During dry years, a positive geopotential height anomaly center is located at the Mongolian low, and a negative geopotential height anomaly center is located northwest of the Mongolian low (**Figure 5B**). This geopotential height anomaly distribution weakens the Mongolian low and causes southeast wind anomalies from the semi-arid regions of East Asia (**Figure 6B**), which is in the opposite direction to the westerlies, thereby weakening them. The positive geopotential height anomalies over the East Asian continent and the negative geopotential height anomalies over the surrounding sea weaken the summer pressure difference between land and sea (**Figure 5B**). Thus, the monsoon anomalies move in the opposite direction, greatly weakening the monsoon (**Figure 6B**). The weakening of the monsoon occurs as the edge of the monsoon moves back, right on the eastern edge of the semi-arid regions (**Figure 6B**). The monsoon does not reach the semi-arid regions, and the westerly winds are weakened, which results in a decrease in precipitation in the semi-arid regions.

To further explore the effect of ENSO and the monsoon on precipitation, we calculated the correlation coefficients among precipitation, the Niño 3.4 index, the monsoon index and the westerly index to reveal their relationships (**Figure 7**). The monsoon index is defined as the U_{850} in (5°–15°N, 90°–130°E) minus U_{850} in (22.5°–32.5°N, 110°–140°E) (Wang and Fan, 1999) to measure the strength of the EASM, it can capture the three-dimensional circulation and total variance of the precipitation over East Asia (Wang et al., 2008; Huang et al., 2018). The westerly index proposed by Li et al. (2008) (the difference of the geopotential height at 500 hPa between 35°N and 50°N over 70°–110°E) is a good indicator of the westerly strength over East Asian middle latitude. **Figure 7A** shows that the monsoon index has an obvious negative effect (r = −0.86) on the precipitation in the wet years and passed 99% of the significance test when the monsoon edge crossed the semi-arid region of East Asia. However, the correlation coefficient decreases to −0.21 and is not significant when we do not distinguish between dry years and wet years (**Figure 7A**). This means that only when the edge of the monsoon crosses the semi-arid regions can the monsoon affect the precipitation of the semi-arid regions. The effect of ENSO on precipitation can also be inferred through the same calculation. The direct relationship between Niño 3.4 and precipitation is not significant, but Niño 3.4 has an obvious positive effect (r = 0.30) on the monsoon index, which has the ability to change precipitation over semi-arid regions. Therefore, ENSO has a negative effect on the precipitation of the semi-arid region of East Asia when the edge of the monsoon crosses the semi-arid regions of East Asia. **Figure 7D** shows that the westerly index is positively correlated with the precipitation in semi-arid regions over East Asia and passed 95% of the significance test, which means westerly wind favors the increased precipitation in this region.

Effects of Monsoon Edge Changes on Semi-arid Regions Over East Asia in the Future

The historic decadal change in the monsoon edge shows that the decadal monsoon edge over the past 70 years exhibits obvious oscillations near the middle area of semi-arid regions. Although there was obvious deviation in the 2000s, the decadal change in the edge has not led to a robust western or eastern trend (**Figure 8**). However, in future scenarios (**Figure 9**), the monsoon edges in ACCESS-CM2, CESM2-WACCM, CMCC-CM2-SR5, CMCC-ESM2, FIO-ESM-2–0, INM-CM4-8, INM-CM5-0, MIROC6, and TaiESM1 exhibit obvious westward expansion, and most of them cover the entire semi-arid region. The monsoon edges in AWI-CM-1-1-MR, EC-Earth3-Veg, EC-Earth3-Veg-LR, GFDL-ESM4, MPI-ESM1-2-HR, MPI-ESM1-2-LR, and MRI-ESM2-0 expand westward, except for the middle part of the monsoon edges. The monsoon edges in CanESM5 and IPSL-CM6A-LR also expand westward, but the monsoon edges near the Tibetan Plateau expand in the opposite direction. Accordingly, the edge of the monsoon in half of the models exhibits obvious westward expansion, and all the models show that the edge has a general tendency to extend westward with increasing emissions of GHGs; the more GHGs are emitted, the greater the westward spread of the monsoon

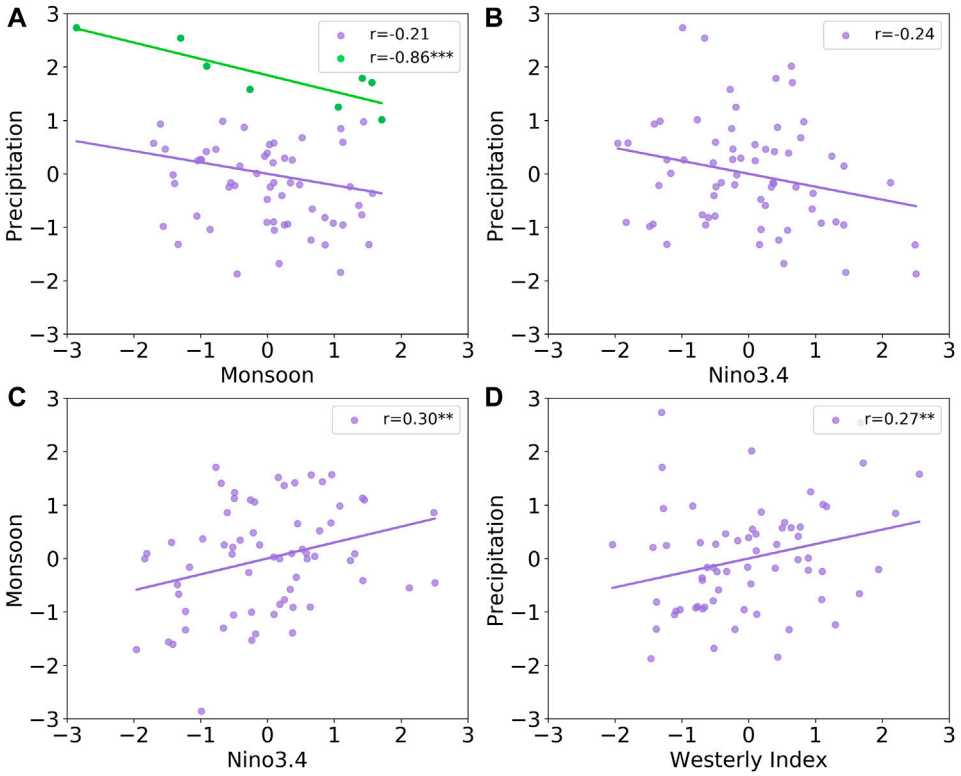

FIGURE 7 | Correlation coefficients between precipitation and the monsoon index **(A)**, precipitation and Niño 3.4 **(B)**, and Niño 3.4 and the monsoon index **(C)**. The green dots in **(A)** represent the years when the monsoon edge crossed the semi-arid regions. Two asterisks denote statistical significance at the 95% confidence level based on Student's t-test. Three asterisks denote statistical significance at the 99% confidence level based on Student's t-test.

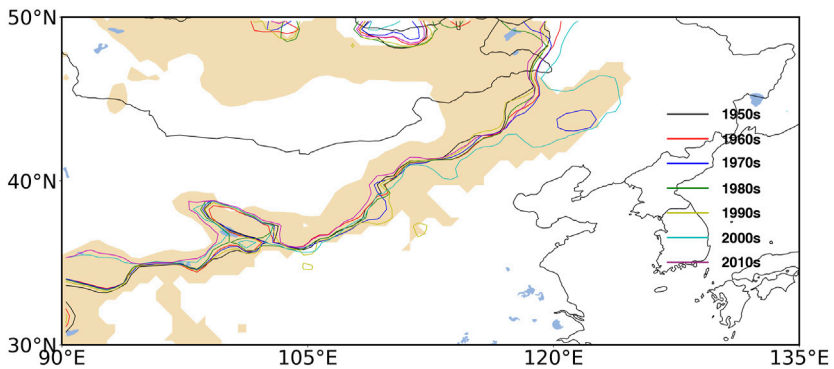

FIGURE 8 | The decadal monsoon edge in the past 70 years. The brown areas represent semi-arid areas.

edge. Due to the increase in the control area of the East Asia summer monsoon in the future, its influence on the semi-arid regions of East Asia will also be enhanced, which will lead to an increase in precipitation in the semi-arid regions.

As precipitation changes in semi-arid regions, both aridity and ecology exhibit sensitive responses. The Palmer drought severity index (PDSI) distribution increases in wet years and decreases in dry years, especially in the northern part of the semi-arid regions. This shows that semi-arid regions will become wetter (drier) when precipitation increases (decreases), and the northern part of the semi-arid region is more sensitive to precipitation variation. Meanwhile, precipitation can

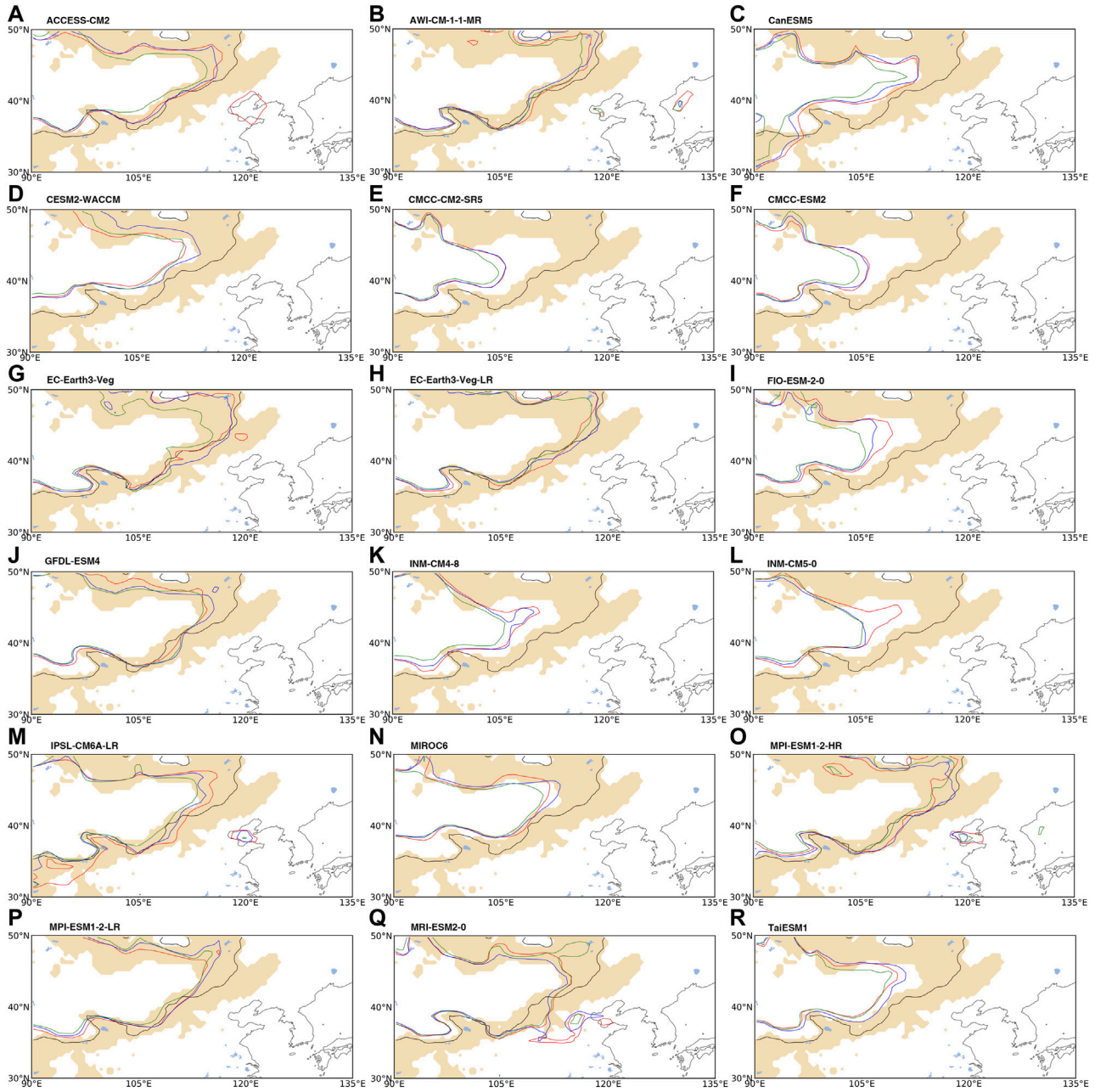

FIGURE 9 | The decadal monsoon edge simulated by the models in the future. The brown areas represent semi-arid areas. The black curve represents the mean monsoon edge for 2011–2019. The red, blue, and green curves represent the mean monsoon edges for 2091–2100 under SSP126, SSP245, and SSP585, respectively.

obviously affect ecological conditions (**Figure 10**). The gross primary production (GPP) in wet years shows a consistent variation with precipitation, especially in the eastern drylands. The most obvious increase in GPP occurs in the northeastern part of the semi-arid region, which is sensitive to monsoon changes (**Figure 11A**). This result indicates that vegetation growth is closely associated with precipitation in this region (**Figures 10**, **11**). According to the monsoon edges in the different scenarios in the future, the westward expansion of the monsoon edge will turn the semi-arid regions of East Asia wet and green. The area that turns wet and green will be even larger under the high-emission scenario. In addition, more areas in the semi-arid regions of East Asia will be influenced by ENSO via the monsoon.

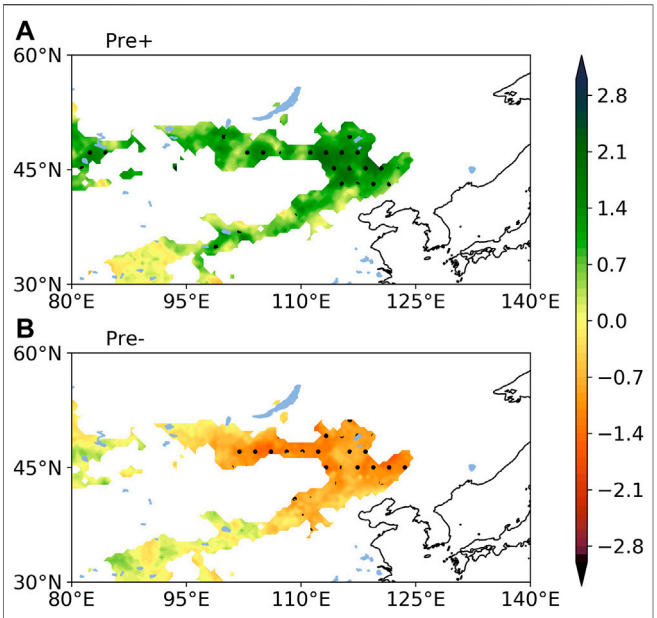

FIGURE 10 | PDSI composite for wet **(A)** and dry **(B)** years in the semi-arid regions of East Asia. Stippling denotes the region with statistical significance at the 90% confidence level based on Student's t-test.

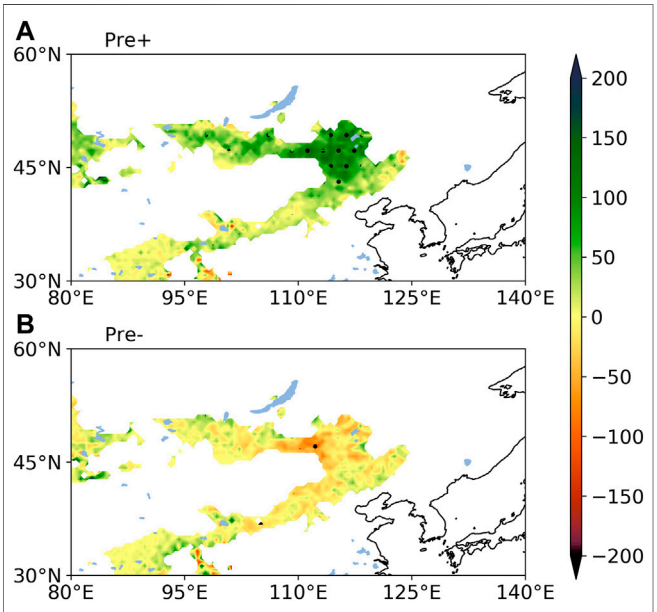

FIGURE 11 | GPP composite for wet **(A)** and dry **(B)** years in the semi-arid regions of East Asia (units: g C m^{-2}). Stippling denotes the region with statistical significance at the 90% confidence level based on Student's t-test.

CONCLUSIONS AND DISCUSSION

In this study, we investigate the key role of the monsoon on precipitation in the semi-arid regions of East Asia under global warming. The characteristics of annual precipitation in the semi-arid regions can be basically reflected by summer precipitation because in terms of amount, the summer mean precipitation accounts for 63% of the annual precipitation, and in terms of variation, the correlation coefficient between them is as high as 0.874. Therefore, exploring the causes of summer precipitation variation is the key to understanding precipitation in the semi-arid regions of East Asia. During wet years, there is a negative pressure anomaly center at 850 hPa in the Mongolian low, which strengthens the Mongolian low and leads to the strengthening of the westerly wind. Simultaneously, the anomalous low pressure, combined with the anomalous high pressure at sea, enhances the sea-land pressure difference in summer and strengthens the summer monsoon. The coincidence of an enhanced monsoon and enhanced westerly winds over the semi-arid regions results in increased precipitation. The coincidence of a weak monsoon and weak westerly winds results in low precipitation in dry years. In addition, we found that ENSO has a negative effect on precipitation in semi-arid regions when the monsoon is strong enough to expand into the inner semi-arid regions of East Asia.

The decadal monsoon edge in the past 70 years has an obvious oscillation near the middle area of semi-arid regions, which has not obviously led to a robust western or eastern trend. However, in the future, the monsoon edge has a tendency to extend westward with the increased emission of GHGs. Westward spread of the monsoon edge will take place in the high-emissions scenario. Such westward extension of the edge of the monsoon will result in more precipitation. Meanwhile, as the frequency of El Niño increases and the intensity of El Niño-induced atmospheric anomalies under greenhouse warming increases (Cai et al., 2015; Hu et al., 2021), the climate in the semi-arid regions of East Asia may be greatly changed by ENSO. In addition, monsoon expansion will turn the semi-arid regions of East Asia wet and green. As a typical underlying surface of the semi-arid region of East Asia, the Loess Plateau will undergo great ecological changes in the future, and more investigation is needed.

DATA AVAILABILITY STATEMENT

We thank all the institutions providing data for this research. The precipitation dataset is from GPCC (https://opendata.dwd.de/climate_environment/GPCC/html/fulldata-monthly_v2020_doi_download.html). The AI dataset used in this study is provided by Huang et al. (2020) (https://www.sciencedirect.com/science/article/pii/S1470160X20305884). The 20th Century Reanalysis V3 data are provided by the NOAA/OAR/ESRL PSD, Boulder, Colorado, United States, from their website at https://psl.noaa.gov/data/gridded/data.20thC_ReanV3.html, the HadISST 1.1 monthly average SST dataset is from the Met Office Hadley Centre (https://www.metoffice.gov.uk/hadobs/hadisst/data/download.html), the self-calibrating PalmerDrought Severity Index is available from the Climate Explorer (http://climexp.knmi.nl/select.cgi?id=someone@somewhere&field=scpdsi), the gross primary production is provided by National Tibetan Plateau Data Center (http://data.tpdc.ac.cn/), and the phase 6 of the Coupled Model Intercomparison Project (CMIP6) for simulated sea level

pressure and snow depth data (https://esgf-node.llnl.gov/search/cmip6/).

AUTHOR CONTRIBUTIONS

XG contributed to conception and design of the study. KZ organized the database. KZ, XH, and XZ performed the statistical analysis. XG and KZ wrote the first draft of the manuscript. XH, XZ, and YH wrote sections of the manuscript. All authors contributed to manuscript revision, read, and approved the submitted version.

FUNDING

This work is supported by National Natural Science Foundation of China (42041004, 41722502), the "Innovation Star" Project for Outstanding Postgraduates of Gansu Province (2021CXZX-103, 2021CXZX-102), the Strategic Priority Research Program of Chinese Academy of Sciences (Grant No. XDA2006010301), and the Fundamental Research Funds for the Central Universities (lzujbky-2019-kb30).

ACKNOWLEDGMENTS

We thank all the institutions providing data for this research. The precipitation dataset is from GPCC. The AI dataset used in this study is provided by Huang et al. (2020). The 20th Century Reanalysis V3 data are provided by the NOAA/OAR/ESRL PSD, Boulder, Colorado, United States, from their website at https://psl.noaa.gov/data/gridded/data.20thC_ReanV3.html. Thanks to the help of the two reviewers and the editor.

REFERENCES

Austin, A. T., Yahdjian, L., Stark, J. M., Belnap, J., Porporato, A., Norton, U., et al. (2004). Water Pulses and Biogeochemical Cycles in Arid and Semiarid Ecosystems. *Oecologia* 141 (2), 221–235. doi:10.1007/s00442-004-1519-1

Cai, W., Santoso, A., Wang, G., Yeh, S.-W., An, S.-I., Cobb, K. M., et al. (2015). ENSO and Greenhouse Warming. *Nat. Clim Change* 5 (9), 849–859. doi:10.1038/nclimate2743

Chen, F., Chen, J., Huang, W., Chen, S., Huang, X., Jin, L., et al. (2019). Westerlies Asia and Monsoonal Asia: Spatiotemporal Differences in Climate Change and Possible Mechanisms on Decadal to Sub-orbital Timescales. *Earth-Science Rev.* 192, 337–354. doi:10.1016/j.earscirev.2019.03.005

Chen, F., Yuan, Y., Zhang, T., and Linderholm, H. W. (2016). Annual Precipitation Variation for the Southern Edge of the Gobi Desert (China) Inferred from Tree Rings: Linkages to Climatic Warming of Twentieth century. *Nat. Hazards* 81 (2), 939–955. doi:10.1007/s11069-015-2113-z

Chen, J., Huang, W., Jin, L., Chen, J., Chen, S., and Chen, F. (2018). A Climatological Northern Boundary index for the East Asian Summer Monsoon and its Interannual Variability. *Sci. China Earth Sci.* 61 (1), 13–22. doi:10.1007/s11430-017-9122-x

Feng, S., and Fu, Q. (2013). Expansion of Global Drylands under a Warming Climate. *Atmos. Chem. Phys.* 13 (19), 10081–10094. doi:10.5194/acp-13-10081-2013

Guan, X., Huang, J., Guo, R., and Lin, P. (2015). The Role of Dynamically Induced Variability in the Recent Warming Trend Slowdown over the Northern Hemisphere. *Sci. Rep.* 5 (1), 1–10. doi:10.1038/srep12669

Hu, K., Huang, G., Huang, P., Kosaka, Y., and Xie, S.-P. (2021). Intensification of El Niño-Induced Atmospheric Anomalies under Greenhouse Warming. *Nat. Geosci.* 14 (6), 377–382. doi:10.1038/s41561-021-00730-3

Huang, B., Cubasch, U., and Li, Y. (2018). East Asian Summer Monsoon Representation in Re-analysis Datasets. *Atmosphere* 9 (6), 235. doi:10.3390/atmos9060235

Huang, J., Guan, X., and Ji, F. (2012). Enhanced Cold-Season Warming in Semi-arid Regions. *Atmos. Chem. Phys.* 12 (12), 5391–5398. doi:10.5194/acp-12-5391-2012

Huang, J., Ji, M., Xie, Y., Wang, S., He, Y., and Ran, J. (2016a). Global Semi-arid Climate Change over Last 60 Years. *Clim. Dyn.* 46 (3-4), 1131–1150. doi:10.1007/s00382-015-2636-8

Huang, J., Yu, H., Guan, X., Wang, G., and Guo, R. (2016b). Accelerated Dryland Expansion under Climate Change. *Nat. Clim Change* 6 (2), 166–171. doi:10.1038/nclimate2837

Huang, J., Yu, H., Han, D., Zhang, G., Wei, Y., Huang, J., et al. (2020). Declines in Global Ecological Security under Climate Change. *Ecol. Indicators* 117, 106651. doi:10.1016/j.ecolind.2020.106651

Huang, W., Feng, S., Chen, J., and Chen, F. (2015). Physical Mechanisms of Summer Precipitation Variations in the Tarim Basin in Northwestern China. *J. Clim.* 28 (9), 3579–3591. doi:10.1175/JCLI-D-14-00395.1

Li, W. L., Wang, K. L., Fu, S. M., and Jiang, H. (2008). The Interrelationship between Regional westerly index and the Water Vapor Budget in Northwest China (In Chinese). *J. Glaciol. Geocryol.* 30 (1), 28–34.

Li, Z., Liu, W.-z., Zhang, X.-c., and Zheng, F.-l. (2009). Impacts of Land Use Change and Climate Variability on Hydrology in an Agricultural Catchment on the Loess Plateau of China. *J. Hydrol.* 377 (1-2), 35–42. doi:10.1016/j.jhydrol.2009.08.007

Middleton, N., and Thomas, D. (1997). *World Atlas of Desertification*. New York: Oxford Univ. Press.

Rayner, N. A., Parker, D. E., Horton, E. B., Folland, C. K., Alexander, L. V., Rowell, D. P., et al. (2003). Global Analyses of Sea Surface Temperature, Sea Ice, and Night marine Air Temperature since the Late Nineteenth century. *J. Geophys. Res.* 108 (D14). doi:10.1029/2002JD002670

Riahi, K., Van Vuuren, D. P., Kriegler, E., Edmonds, J., O'Neill, B. C., Fujimori, S., et al. (2017). The Shared Socioeconomic Pathways and Their Energy, Land Use, and Greenhouse Gas Emissions Implications: An Overview. *Glob. Environ. Change* 42, 153–168. doi:10.1016/j.gloenvcha.2016.05.009

Sala, O. E., and Lauenroth, W. K. (1982). Small Rainfall Events: An Ecological Role in Semiarid Regions. *Oecologia* 53, 301–304. doi:10.1007/BF00389004

Schneider, U., Becker, A., Finger, P., Meyer-Christoffer, A., Ziese, M., and Rudolf, B. (2014). GPCC's New Land Surface Precipitation Climatology Based on Quality-Controlled *In Situ* Data and its Role in Quantifying the Global Water Cycle. *Theor. Appl. Climatol.* 115 (1), 15–40. doi:10.1007/s00704-013-0860-x

Sun, Y., and Ding, Y. (2010). A Projection of Future Changes in Summer Precipitation and Monsoon in East Asia. *Sci. China Earth Sci.* 53 (2), 284–300. doi:10.1007/s11430-009-0123-y

Wang, B., and Fan, Z. (1999). Choice of South Asian Summer Monsoon Indices. *Bull. Amer. Meteorol. Soc.* 80 (4), 629–638. doi:10.1175/1520-0477(1999)080<0629:cosasm>2.0.co;2

Wang, B., Liu, J., Kim, H.-J., Webster, P. J., and Yim, S.-Y. (2012). Recent Change of the Global Monsoon Precipitation (1979-2008). *Clim. Dyn.* 39 (5), 1123–1135. doi:10.1007/s00382-011-1266-z

Wang, B., Wu, Z., Li, J., Liu, J., Chang, C.-P., Ding, Y., et al. (2008). How to Measure the Strength of the East Asian Summer Monsoon. *J. Clim.* 21 (17), 4449–4463. doi:10.1175/2008JCLI2183.1

Wang, L., Chen, W., Huang, G., and Zeng, G. (2017). Changes of the Transitional Climate Zone in East Asia: Past and Future. *Clim. Dyn.* 49 (4), 1463–1477. doi:10.1007/s00382-016-3400-4

Wang, S., Zhang, Y., Ju, W., Qiu, B., and Zhang, Z. (2021). Tracking the Seasonal and Inter-annual Variations of Global Gross Primary Production during Last Four Decades Using Satellite Near-Infrared Reflectance Data. *Sci. Total Environ.* 755, 142569. doi:10.1016/j.scitotenv.2020.142569

Xing, W., and Wang, B. (2017). Predictability and Prediction of Summer Rainfall in the Arid and Semi-arid Regions of China. *Clim. Dyn.* 49 (1), 419–431. doi:10.1007/s00382-016-3351-9

Yan, X., Liu, J., Rühland, K. M., Smol, J. P., and Chen, F. (2021). Climate Change as the Dominant Driver of Recent Ecological Changes in a Semi-arid alpine lake from the Chinese Loess Plateau. *J. Paleolimnol.* 1-19. doi:10.1007/s10933-020-00167-5

Yang, F., He, Q., Huang, J., Mamtimin, A., Yang, X., Huo, W., et al. (2020). Desert Environment and Climate Observation Network over the Taklimakan Desert. *Bull. Am. Meteorol. Soc.* 102 (6), E1172–E1191. doi:10.1175/BAMS-D-20-0236.1

Yihui, D., and Chan, J. C. L. (2005). The East Asian Summer Monsoon: an Overview. *Meteorol. Atmos. Phys.* 89 (1), 117–142. doi:10.1007/s00703-005-0125-z

Zhang, L., and Zhou, T. (2015). Drought over East Asia: a Review. *J. Clim.* 28 (8), 3375–3399. doi:10.1175/JCLI-D-14-00259.1

Zhang, Q., Yang, J., Wang, W., Ma, P., Lu, G., Liu, X., et al. (2021). Climatic Warming and Humidification in the Arid Region of Northwest China: Multi-Scale Characteristics and Impacts on Ecological Vegetation. *J. Meteorol. Res.* 35 (1), 113–127. doi:10.1007/s13351-021-0105-3

Zhang, X.-C., and Liu, W.-Z. (2005). Simulating Potential Response of Hydrology, Soil Erosion, and Crop Productivity to Climate Change in Changwu Tableland Region on the Loess Plateau of China. *Agric. For. Meteorology* 131 (3-4), 127–142. doi:10.1016/j.agrformet.2005.05.005

Zhu, K., Guan, X., Huang, J., Wang, J., Guo, S., and Cao, C. (2021). Precipitation over Semi-arid Regions of North Hemisphere Affected by Atlantic Multidecadal Oscillation. *Atmos. Res.* 262, 105801. doi:10.1016/j.atmosres.2021.105801

Conflict of Interest: The authors declare that the research was conducted in the absence of any commercial or financial relationships that could be construed as a potential conflict of interest.

Publisher's Note: All claims expressed in this article are solely those of the authors and do not necessarily represent those of their affiliated organizations, or those of the publisher, the editors and the reviewers. Any product that may be evaluated in this article, or claim that may be made by its manufacturer, is not guaranteed or endorsed by the publisher.

frontiers in Earth Science

ORIGINAL RESEARCH
published: 12 November 2021
doi: 10.3389/feart.2021.785601

Impact of October Snow Cover in Central Siberia on the Following Spring Extreme Precipitation Frequency in Southern China

Mengqi Zhang[1] *and Jianqi Sun*[1,2,3]*

[1]Nansen-Zhu International Research Center, Institute of Atmospheric Physics, Chinese Academy of Sciences, Beijing, China, [2]Collaborative Innovation Center on Forecast and Evaluation of Meteorological Disasters, Nanjing University of Information Science and Technology, Nanjing, China, [3]University of Chinese Academy of Sciences, Beijing, China

Spring extreme precipitation poses great challenges to agricultural production and economic development in southern China. From the perspective of prediction, the relationship between spring extreme precipitation frequency (SEPF) in southern China and preceding autumn snow cover over Eurasia is investigated. The results indicate that the southern China SEPF is significantly correlated with October snow cover in central Siberia. Corresponding to reduced October snow cover, the vertical propagation of planetary waves is suppressed, which leads to a strengthened stratospheric polar vortex from October to following December. The signal of the anomalous stratospheric polar vortex propagates downward to the surface, contributing to a positive North Atlantic Oscillation (NAO)-like pattern in December. The southwesterlies in the northern Eurasia-eastern Arctic associated with the positive NAO induce sea ice loss in the Barents–Kara seas in January–February, which then tends to enhance the vertical propagation of planetary waves by constructively interfering with the climatological wavenumber-1 component. Therefore, the stratosphere polar vortex is significantly weakened in spring, which further contributes to a negative Arctic Oscillation (AO)-like pattern in the troposphere. The negative spring AO is related to an anomalous cyclone in East Asia, which induces upward motion and moisture convergence in southern China, consequently providing favorable dynamic and moisture conditions for extreme precipitation in the region. The snow cover signal in central Siberia in the preceding October provides a potential source for the prediction of spring extreme precipitation variability in southern China with two seasons in advance.

Keywords: snow cover, spring extreme precipitation, southern China, prediction, sea ice

OPEN ACCESS

Edited by:
Renguang Wu,
Zhejiang University, China

Reviewed by:
Shangfeng Chen,
Institute of Atmospheric Physics (CAS), China
Bingyi Wu,
Fudan University, China

***Correspondence:**
Jianqi Sun
sunjq@mail.iap.ac.cn

Specialty section:
This article was submitted to Atmospheric Science, a section of the journal Frontiers in Earth Science

Received: *29 September 2021*
Accepted: *28 October 2021*
Published: *12 November 2021*

Citation:
Zhang M and Sun J (2021) Impact of October Snow Cover in Central Siberia on the Following Spring Extreme Precipitation Frequency in Southern China. Front. Earth Sci. 9:785601. doi: 10.3389/feart.2021.785601

INTRODUCTION

Southern China is a major rice-producing region in East Asia and has a dense population and developed industry, making it vulnerable to extreme precipitation events. Spring is the rice-seeding season in southern China. Floods and droughts associated with anomalous precipitation and extreme precipitation events in spring can influence agricultural activity and rice production in the region. Therefore, it is of great importance to better understand and predict the variabilities of spring precipitation and extreme precipitation events in southern China.

Although the precipitation amount in spring in southern China is less than that in summer, it can still contribute to more than 30% of the annual total precipitation and has strong variability (Feng and Li, 2011). Efforts have been made to explore possible mechanisms for spring precipitation variability in southern China, revealing several influencing factors, including the East Asian jet stream (Wen et al., 2007; Wang et al., 2011), western Pacific subtropical high (Wang et al., 2000; Zhang et al., 2009), polar vortex (Wang et al., 2002), North Atlantic Oscillation (NAO; Xin et al., 2006; Sun and Yang, 2012), sea surface temperature (SST) anomalies in the North Atlantic (You and Jia, 2018; Jia et al., 2019) and tropical Indian-Pacific Oceans (Wu et al., 2003; Xie et al., 2009; Feng and Li, 2011; Sun and Yang, 2012; Chen et al., 2014), etc.

Compared with spring mean precipitation, extreme precipitation tends to be more destructive to the ecosystem, social economy, and agricultural activity and production. Recent studies have begun to focus on the variability and influencing factors of spring precipitation extremes in southern China from a climatic perspective. For example, Huang et al. (2015) indicated that the southern China spring persistent rainfall frequency is positively related to the strong East Asian subtropical jet–weak East Asian polar front jet configuration. Li et al. (2018) suggested that there are two branches of water vapor transport in association with spring persistent rainfall in southern China: One is westerlies over the southern Tibetan Plateau, and the other is southwesterlies over the western North Pacific. Shen and Chen (2018) pointed out that the out-of-phase change in surface sensible heat between mid-latitude Eurasia and Southeast Asia is significantly correlated with the out-of-phase change in spring extreme precipitation frequency between northern China and southern China. A recent study by Gu et al. (2021) suggested that spring consecutive cloudy-rainy events in southern China exhibit considerable interdecadal variation, which is related to the Pacific Decadal Oscillation (PDO). Zhang et al. (2021) revealed that anomalous sea ice in the Davis Strait–Baffin Bay region in the preceding winter has a delayed impact on spring extreme precipitation events in southern China.

Eurasian snow cover is an important influencing factor and prediction source for the Northern Hemisphere climate (Saito et al., 2001; Cohen et al., 2007; Cohen and Fletcher, 2007; Cohen and Jones, 2011; Cohen et al., 2014; Orsolini et al., 2016). Anomalous Eurasian snow cover affects the local energy budget by changing surface albedo and snowmelt-related soil moisture anomalies, which further influence the climate remotely by exciting Rossby wave anomalies (Barnett et al., 1989; Yim et al., 2010; Zhang et al., 2019). Stratosphere-troposphere interaction is an important pathway whereby autumn Eurasian snow impact on subsequent winter atmospheric circulations (Cohen et al., 2007; Cohen et al., 2014; Ao and Sun, 2015; Han and Sun, 2018; Xu et al., 2018). Specifically, increased (decreased) October Eurasian snow cover enhances (suppresses) the upward propagation of planetary waves, which further weakens (strengthens) the stratospheric polar vortex and induces a negative (positive) Arctic Oscillation (AO)/NAO in the following winter (Gong et al., 2003; Cohen et al., 2007; Fletcher et al., 2009; Garfinkel et al., 2010; Smith et al., 2011; Cohen et al., 2014). Some studies have suggested a linkage between spring Eurasian snow cover and southern China spring precipitation variability (Wu and Kirtman, 2007; Zuo et al., 2012; Jia et al., 2018). Then, it is natural to ask whether the preceding Eurasian snow cover influences the southern China spring extreme precipitation frequency (SEPF). If so, the snow cover information could provide sources for the seasonal prediction of SEPF variability in southern China. Therefore, from the perspective of prediction, this study investigates the relationship between the southern China SEPF and Eurasian snow cover in the preceding autumn and the related physical processes.

DATA AND METHODS

In this study, we use daily precipitation observations from 839 meteorological stations in China provided by the National Meteorological Information Center of the China Meteorological Administration. There are 569 stations in East China (east of 105°E) after eliminating the stations with missing values of more than 5 days during spring (March–May) in any year from 1979 to 2017. Following previous studies (e.g., Zhai et al., 2005), an extreme precipitation day is identified at a station when the station's daily precipitation amount is larger than the 90th percentile of precipitation on all rainy days (daily precipitation≥0.1 mm) in spring during 1979–2017. The extreme precipitation frequency indicates the number of extreme precipitation days.

The Northern Hemisphere weekly snow cover dataset is provided by the Rutgers University Global Snow Lab (GSL, Robinson et al., 2012), which has been available since 1967 on an 88 × 88 grid. The weekly data are converted to monthly data for analysis. The monthly atmospheric circulation datasets are obtained from the National Centers for Environmental Prediction and National Center for Atmospheric Research (NCEP–NCAR) from 1948 to the present with a 2.5 ° × 2.5 ° horizontal resolution (Kalnay et al., 1996). The monthly Arctic sea ice concentration dataset is obtained from the Hadley Centre Sea Ice and SST dataset version 1 (HadISST1), from 1870 to the present with a resolution of 1 ° × 1 ° (Rayner et al., 2003). The monthly mean AO and NAO indices are extracted from the Climate Prediction Center (https://www.cpc.ncep.noaa.gov/products/precip/CWlink/daily_ao_index/ao.shtml and https://www.cpc.ncep.noaa.gov/products/precip/CWlink/pna/nao.shtml), which spans the period from 1950 to the present.

The research period of this study is 1979–2017, and all variables are available during the period. To obtain the interannual component, a 9-years high pass filter is applied to all variables using the Flourier transform. The statistical significance is estimated according to the two-tailed Student's

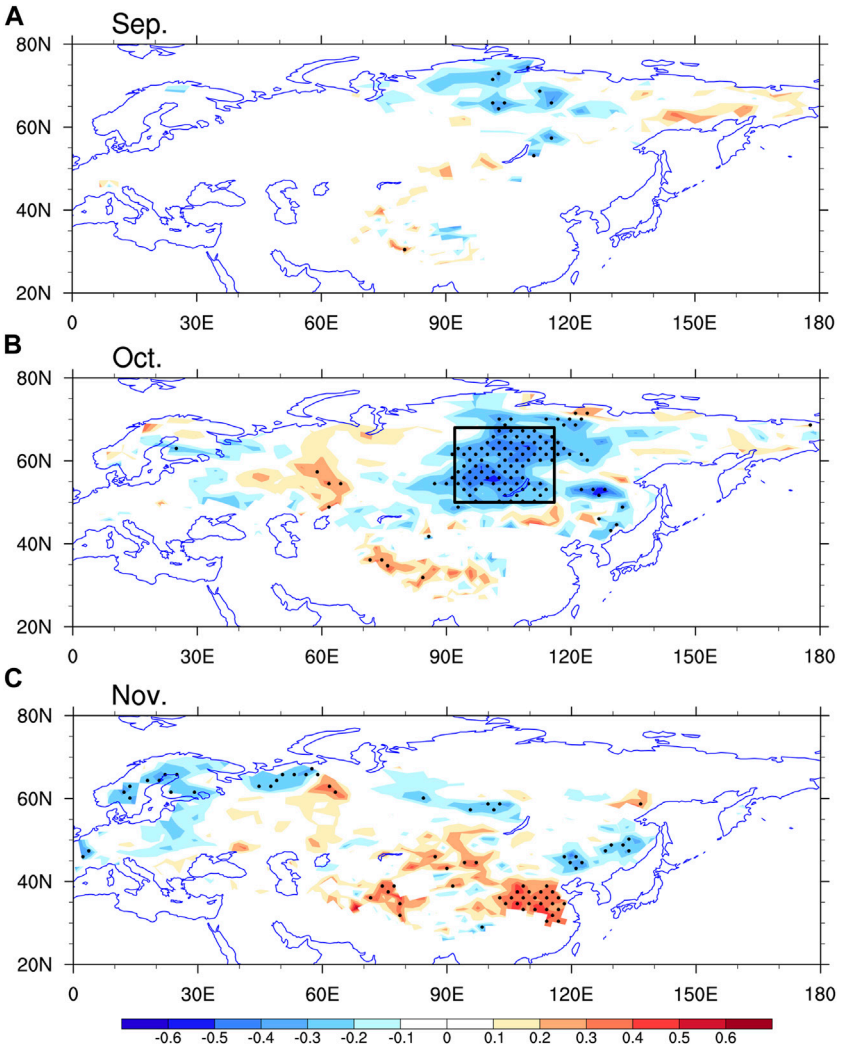

FIGURE 1 | Correlation coefficients of snow cover in **(A)** September, **(B)** October and **(C)** November with SC_SEPI during 1979–2017. Stippled regions indicate that the anomalies are significant at the 90% confidence level. The box in **(B)** indicates the region used to define the SNOWI.

t test. The zonal wavenumber-1 disturbance is obtained by zonal Fourier harmonics.

RESULTS

Relationship Between Southern China Spring Extreme Precipitation Frequency and Eurasian Snow Cover in the Preceding Autumn

Recently, Zhang et al. (2021) performed an empirical orthogonal function (EOF) analysis on the interannual SEPF variability in East China (east of 105°E) during 1979–2017. The EOF1 mode accounts for 16.2% of the total variance and generally shows consistent variability of SEPF in East China, with a large-value center in southern China (20°–30°N, 110°–125°E). The EOF2 mode accounts for 10.8% of the total variance and shows a south-north dipole structure of SEPF variability between central East China (29°–38°N, 105°–125°E) and southeastern coast of China (20°–27°N, 110°–120°E; figure not shown). The EOF1 and EOF2 can be well separated from each other and from the remaining modes, based on North et al. (1982). This study focuses on the first mode of interannual SEPF variability in East China. Based on the study by Zhang et al. (2021), a southern China spring extreme precipitation frequency index (SC_SEPI) is defined as area-average SEPF anomalies over 20°–30°N, 110°–125°E. The correlation coefficient between PC1 and SC_SEPI is 0.94 during 1979–2017, which indicates that the SEPF variability in southern China is the major feature of that in East China.

To investigate the connection between the interannual variabilities in the southern China SEPF and Eurasian snow cover in the preceding autumn, **Figure 1** examines the correlations of Eurasian snow cover in the preceding September to November with SC_SEPI.

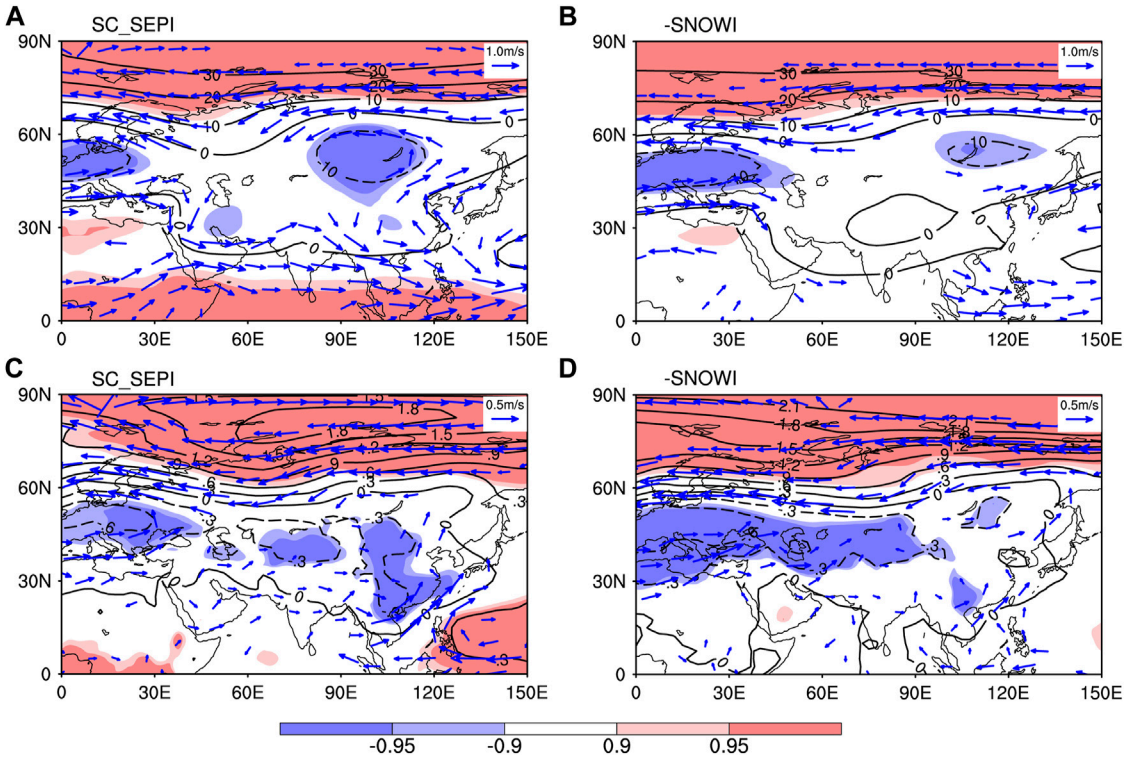

FIGURE 2 | Regressions of spring **(A)** 200 hPa geopotential height (m) and wind (ms^{-1}) and **(C)** sea level pressure (SLP; hPa) and 850 hPa wind (ms^{-1}) against the SC_SEPI during 1979–2017. **(B)** and **(D)** are the same as **(A)** and **(C)** but for negative October SNOWI. Light and dark shaded regions indicate that the anomalies are significant at the 90 and 95% confidence levels, respectively. Wind vectors that are significant at the 90% confidence level are shown.

Significantly large-scale negative correlations are observed in October in central Siberia. However, correlations are negligible in the region in September and November. This is reasonable since large snow cover variabilities appear in mid- to high-latitude Eurasia in October, whereas the variabilities are weak in the region in September and November (Han and Sun, 2018). Furthermore, a snow cover index (SNOWI) is defined as snow cover anomalies averaged over 50°–68°N, 92°–116°E (**Figure 1B**). The SC_SEPI is closely related to the October SNOWI, with a correlation coefficient of -0.65 during 1979–2017, which is significant at the 99% confidence level. Besides the snow cover signals over central Siberia, significant decrease in snow cover can also be seen over north Europe and a marked dipole snow cover anomaly pattern can be detected in East Asia. This result indicates that the November snow cover anomalies over the aforementioned two regions might also have lagged influence in the SEPF variability in southern China, which will be explored in details in our future studies. The role of the largest-scale signal of snow cover over central Siberia is focused in this study.

We further analyze the spring atmospheric circulation anomalies associated with the SC_SEPI and negative October SNOWI. As shown in **Figure 2**, the spring large-scale atmospheric circulation anomalies associated with the two indices share similar features, with significant positive sea level pressure (SLP) and geopotential height anomalies in the polar region, as well as negative anomalies in mid-latitude Eurasia, resembling the negative phase of AO. The correlation coefficients of the spring AO index with the SC_SEPI and October SNOWI are −0.42 and 0.52 during 1979–2017, respectively, and both are significant at the 99% confidence level. These results suggest that the spring AO may play an important role in linking the preceding October snow cover in central Siberia and SEPF in southern China.

Corresponding to more southern China SEPF, there is a quasi-barotropic anomalous cyclone in East Asia, with southerlies prevailing in southern China (**Figures 2A,C**). Such atmospheric circulation anomalies favor more water vapor transport from low latitudes to southern China and lead to moisture convergence in the region (**Figure 3A**). Meanwhile, significant upward motion anomalies dominate southern China (**Figure 3C**). The anomalous moisture and vertical motion conditions associated with the negative October SNOWI bear a resemblance to those associated with SC_SEPI (**Figures 3B,D**). The similarity between atmospheric circulation anomalies associated with the reduced October snow cover in central Siberia and SEPF in southern China further confirms the close relationship between the two.

Physical Processes Connecting October Snow Cover in Central Siberia and Spring Extreme Precipitation Frequency in Southern China

To investigate the possible physical processes that link the preceding October snow cover in central Siberian and SEPF in

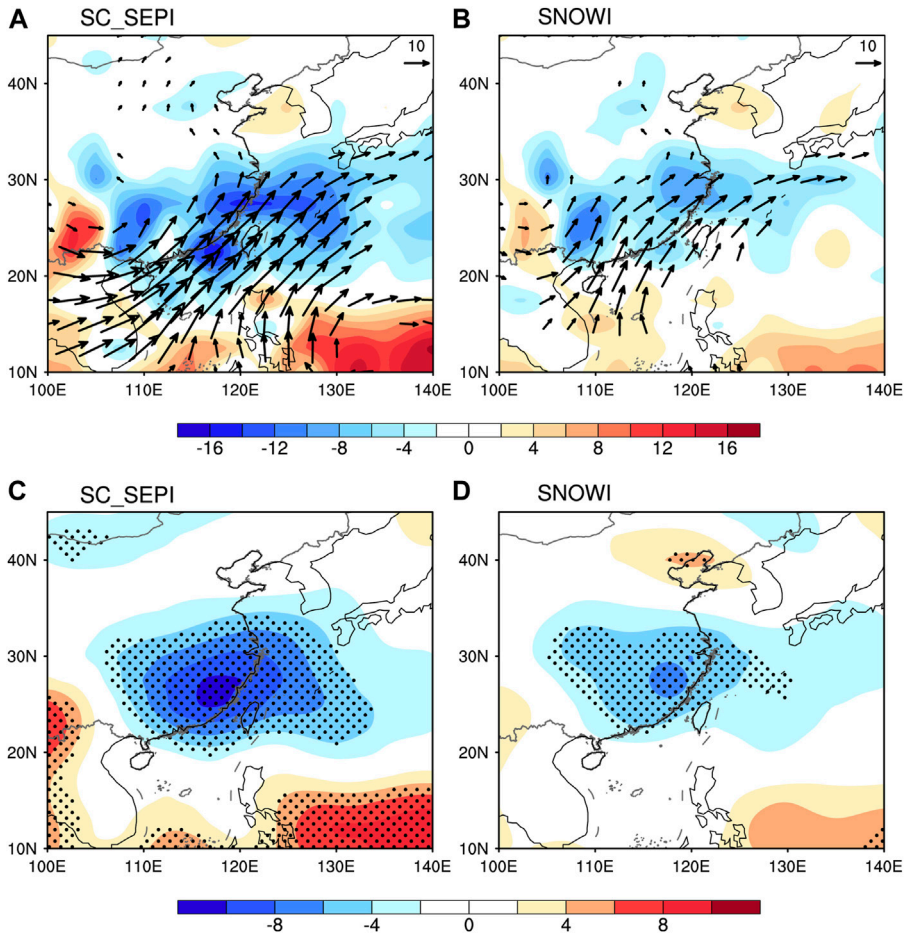

FIGURE 3 | Regressions of spring **(A)** vertically integrated water vapor flux (vectors; $kgm^{-1}\ s^{-1}$) and its divergence (shading; $10^{-6}\ kgm^{-2}s^{-1}$) and **(C)** 500 hPa vertical velocity ($10^{-3}\ Pas^{-1}$) against the SC_SEPI during 1979–2017. **(B)** and **(D)** are the same as **(A)** and **(C)** but for negative October SNOWI. Stippled regions indicate that the anomalies are significant at the 95% confidence level. Vectors that are significant at the 90% confidence level are shown.

southern China, the temporal evolution of anomalous atmospheric circulations associated with the October SNOWI are examined in this section. Previous observational and modeling studies connected October Eurasian snow cover with the following winter climate through troposphere–stratosphere interactions (Gong et al., 2003; Cohen et al., 2007; Peings et al., 2012; Cohen et al., 2014; Han and Sun, 2018; Xu et al., 2018). Therefore, we hypothesize that October central Siberian snow cover could also affect atmospheric circulation in the following seasons by modulating the vertical component of wave activity fluxes (WAFs) from the troposphere to the stratosphere. To test this hypothesis, **Figure 4** shows the 50 hPa vertical stationary wave activity flux (Plumb, 1985) anomalies regressed against the negative October SNOWI and its long-term climatology in October. Climatologically, there is strong upward propagation of WAFs located in the mid- to high-latitude Eurasia-North Pacific. Corresponding to the negative October SNOWI, significantly anomalous downward WAFs occur in a large-scale area of mid-to high latitude Eurasia, with a center in the area with reduced snow cover. The negative October SNOWI-related downward WAF anomalies weaken the upward WAFs of the climatological mean, which tends to suppress the vertical propagation of planetary waves.

The enhanced/suppressed vertical propagation of planetary waves favors weakened/strengthened stratospheric polar vortex anomalies (e.g., Gong et al., 2003; Cohen et al., 2007; Fletcher et al., 2009; Kim et al., 2014). Therefore, along with the suppressed vertical propagation of planetary waves, the polar vortex becomes stronger from October to December, as shown in **Figure 5**. Previous studies suggested that the anomalous stratospheric polar vortex could persist and further propagate downward, forming an anomalous AO (NAO)-like pattern in weeks to months (Baldwin and Dunkerton, 2001). As a result, a positive NAO-like pattern occurs in December following the reduced October snow cover in central Siberia. The correlation coefficient between the October SNOWI and the following December NAO index is −0.46 during 1979–2017, which is significant at the 99% confidence level. The above results

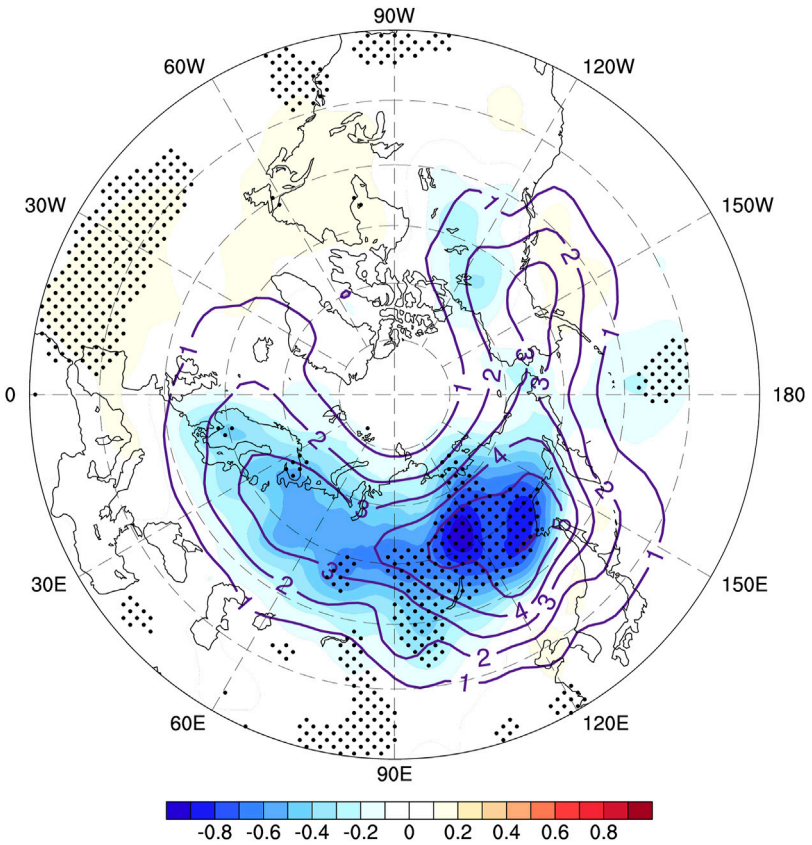

FIGURE 4 | Regression of October vertical wave activity flux (WAF) anomalies (shading; 10^{-3} m^2s^{-2}) at 50 hPa against the negative October SNOWI during 1979–2017. Contours denote the climatological mean of 50 hPa vertical WAFs in October. Stippled regions indicate that the anomalies are significant at the 90% confidence level.

indicate that anomalous preceding October snow cover in central Siberia can lead to an anomalous December NAO through troposphere–stratosphere interactions.

Figures 6A,C exhibits the anomalous Arctic sea ice concentration (SIC), surface air temperature (SAT) and surface winds in December regressed against the negative October SNOWI. Corresponding to NAO-like atmospheric circulation anomalies associated with reduced October snow cover in central Siberia, significant southwesterlies prevail the region from the North Atlantic to northern Eurasia-eastern Arctic in December, which transports warm air masses to the northern Eurasia-eastern Arctic and leads to significantly increased SAT in the region. Consequently, sea ice is reduced in the Barents–Kara seas. The SIC and SAT anomalies could persist and strengthen in the following January–February (**Figures 6B,D**). Therefore, the January–February SIC index (SICI; SIC anomalies averaged over 69°–75°N, 20°–58°E) is significantly correlated with the October SNOWI, with a correlation of 0.46, exceeding the 99% confidence level.

Figures 7A,B examines the regressed January–February 500 hPa geopotential heights against the negative October SNOWI and negative January–February SICI. The atmospheric circulation anomalies in association with changes in snow cover and SIC show similar features, indicating that the SIC anomalies in the Barents–Kara seas could play an important role in the influence of October snow cover in central Siberia in the following January–February atmospheric circulations. The atmospheric circulations associated with the SNOWI and SICI show a zonal wavenumber-1 structure, from the perspective of hemispheric atmospheric variability. **Figures 7C,D** further exhibits the zonal wavenumber-1 components of geopotential height at 500 hPa regressed upon the negative October SNOWI and negative January–February SICI. The atmospheric circulation anomalies in **Figures 7C,D** are very similar to those in **Figures 7A,B**, with a pattern correlation coefficient of 0.61/0.69, which is significant at the 99% confidence level. These results imply that the October snow cover in central Siberia and January–February Barents–Kara seas SIC mainly influence the zonal wavenumber-1 atmospheric circulation.

The anomalous wavenumber-1 components associated with the SNOWI and SICI are approximately in phase with the climatology of zonal wavenumber-1 atmospheric circulation, as shown in **Figures 7C–F**. The constructive interference of wavenumber-1 disturbance with the background state tends to enhance the upward wave activity propagation and further weakens the polar vortex (Garfinkel and Hartmann, 2008;

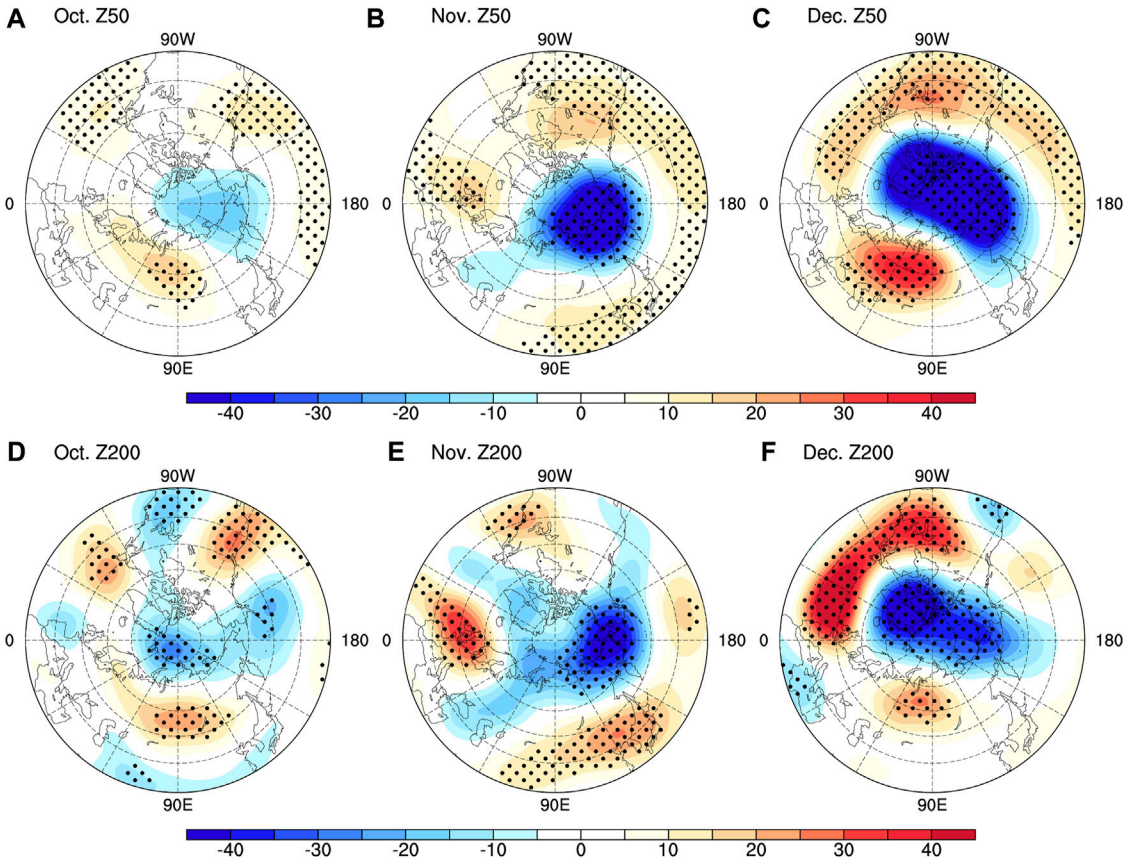

FIGURE 5 | Regressions of **(A–C)** 50 hPa geopotential height (m) and **(D–F)** 200 hPa geopotential height (m) in October, November and December against the negative October SNOWI during 1979–2017. Stippled regions indicate that the anomalies are significant at the 90% confidence level.

Smith et al., 2010; Han and Sun, 2019). The above results indicate that anomalous October snow cover in central Siberia could induce a zonal wavenumber-1 disturbance during the following January–February by changing the SIC in the Barents–Kara seas, which could further enhance vertically propagating planetary waves by constructively interfering with the climatological wavenumber-1 component. These results are consistent with previous studies that suggested that decreased sea ice cover in the Barents–Kara seas could weaken the stratospheric polar vortex by modulating vertically propagating planetary waves (Kim et al., 2014; Nakamura et al., 2015; Nath et al., 2016).

To further confirm the January–February anomalous vertically propagating planetary waves in response to reduced October snow cover in central Siberia, **Figure 8** depicts the January–February 50 hPa vertical WAFs regressed against the negative October SNOWI. Large-scale upward WAFs are found in mid- to high-latitude Eurasia and the North Pacific, coinciding with the large value of the climatological mean, which likely strengthens the upward propagation of planetary waves. Therefore, the stratosphere polar vortex is significantly weakened in spring, which can propagate downward and form a negative AO-like pattern in the troposphere (**Figure 9**). These results indicate that the October central Siberian snow cover is linked to the following spring AO-like circulation anomalies through stratosphere-troposphere interaction processes.

The above results suggest a close relationship between the preceding October snow cover in central Siberia and SEPF in southern China. The snow cover signals with a two-season lead could provide useful information for the prediction of the southern China SEPF. **Figure 10A** calculates the correlations between observed and hindcasted SEPF in East China. The hindcast of SEPF is based on the following fomula:

$$SEPF(i, j, t) = EOF1(i, j) \times PC1(t),$$

where EOF1 is the observed leading mode of SEPF in East China (east of 105°E) during 1979–2017, and PC1 is the hindcasted time series based on the October SNOWI using leave-one-out cross-validation method. There are generally positive correlations in East China, with large-scale significant signals in southern China. **Figure 10B** further estimates the prediction value of October SNOWI for the SC_SEPI through the leave-one-out cross-validation method. The result indicates that the hindcasted SC_SEPI based on the October SNOWI could generally capture the variability in observation, with a correlation coefficient of 0.61 between the two, which is significant at the 99% confidence level. This suggests that the preceding October

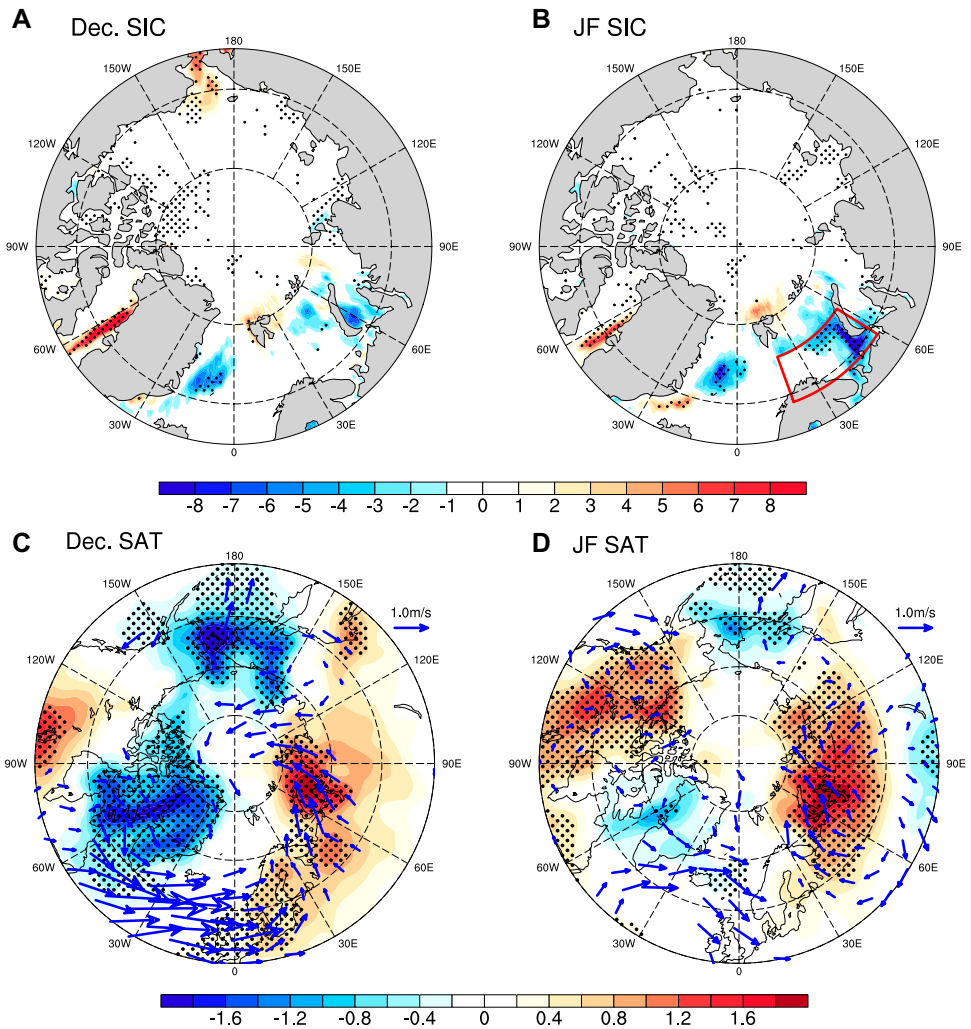

FIGURE 6 | Regressions of December **(A)** Arctic sea ice concentration (SIC; %) and **(C)** surface air temperature (SAT; °C) and surface winds (m s^{-1}) against the negative October SNOWI during 1979–2017. **(B)** and **(D)** are the same as **(A)** and **(C)**, but for January–February. Stippled regions indicate that the anomalies are significant at the 90% confidence level. Wind vectors that are significant at the 90% confidence level are shown. The box in **(B)** indicates the region used to define the SICI.

central Siberian snow cover could serve as a predictor for the southern China SEPF.

CONCLUSION AND DISCUSSION

Spring extreme precipitation in southern China significantly disrupts spring sowing and could cause heavy economic losses. The results of this study indicate that the southern China SEPF is negatively correlated with the central Siberian snow cover in the preceding October. This cross-seasonal relationship provides a possibility for predicting southern China spring extreme precipitation variability with two seasons in advance.

The October snow cover in central Siberia is linked to the southern China SEPF through stratosphere-troposphere interactions. Specifically, reduced October snow cover suppresses vertically propagating planetary waves from the troposphere to the stratosphere and further strengthens the stratospheric polar vortex from October to December. The strengthened stratospheric polar vortex signals propagate downward to the surface, forming a positive NAO-like structure in December. Corresponding to the NAO-like circulation anomalies, southwesterlies prevail in the North Atlantic and northern Eurasia-eastern Arctic, which bring warm air masses to the northern Eurasia-eastern Arctic and lead to local SAT warming. As a result, sea ice cover is reduced in the Barents–Kara seas, which further persists into the following January–February. The reduced SIC in the Barents–Kara seas further strengthens the upward propagation of Rossby waves by constructively interfering with the climatological wavenumber-1 component. Consequently, the stratospheric polar vortex is significantly weakened in spring and further contributes to a negative AO-like structure at the surface. The spring AO-like circulation anomalies are related to

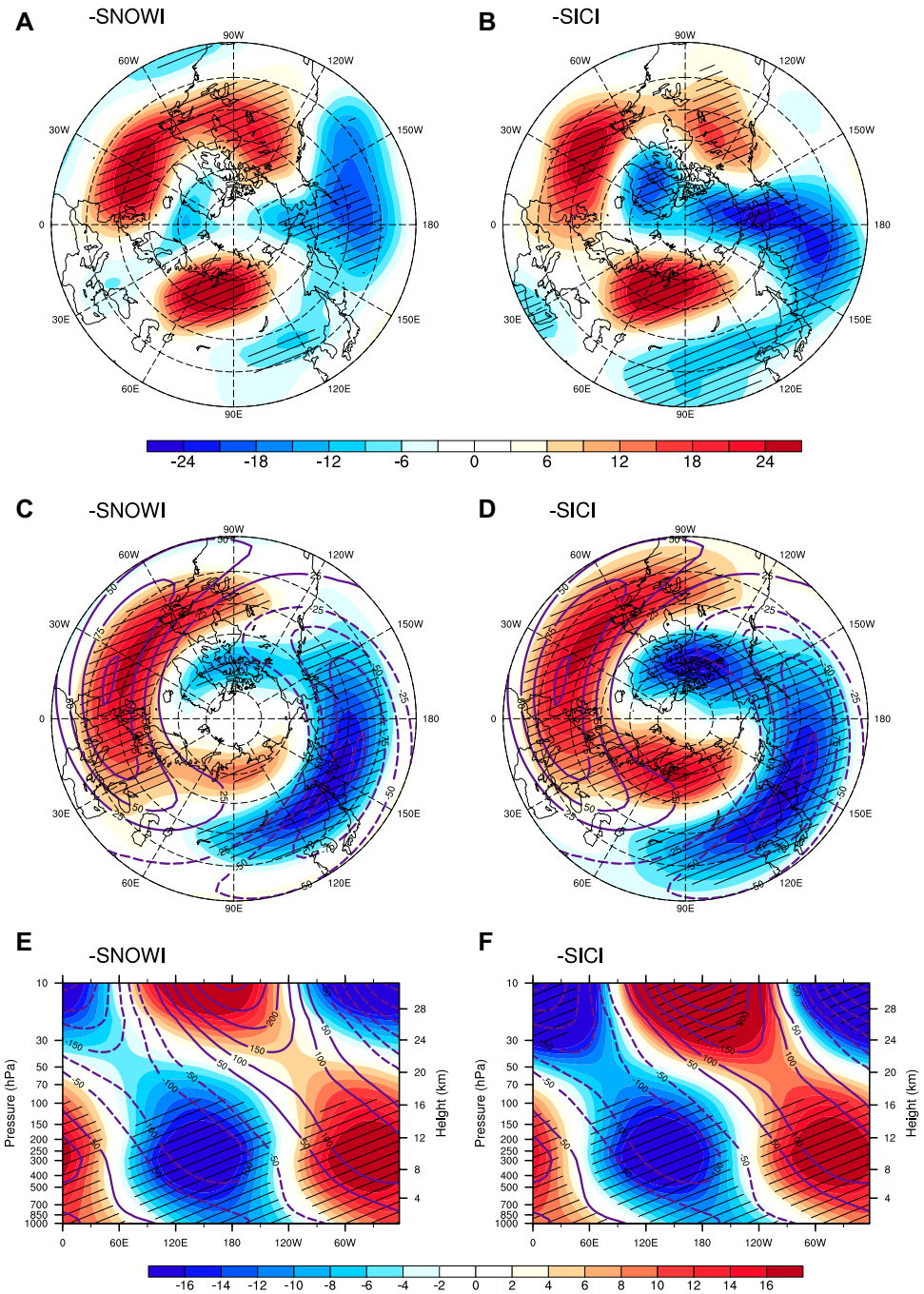

FIGURE 7 | Regressions of 500 hPa geopotential height (m) in January–February against the **(A)** negative October SNOWI and **(B)** negative January–February SICI during 1979–2017. **(C,D)** and **(E,F)** are the same as **(A,B)** but for the zonal wavenumber-1 component of geopotential height at 500 hPa (shading; m) and longitude-pressure sections of the zonal wavenumber-1 component of geopotential height along 50°N (shading; m). Contours in **(C–F)** denote the climatological zonal wavenumber-1 component of geopotential height (m). Regions with hatched patterns indicate that the anomalies are significant at the 90% confidence level.

an anomalous cyclone in East Asia, which induces upward motion and moisture convergence in southern China, providing favorable conditions for extreme precipitation in the region. Through the above processes, decreased (increased) October central Siberian snow cover can lead to increased (decreased) spring extreme precipitation frequency in southern China.

Previous studies indicated that the troposphere–stratosphere interaction is important in the seasonal-delayed relationship between climate systems over the Northern Hemispheric mid-

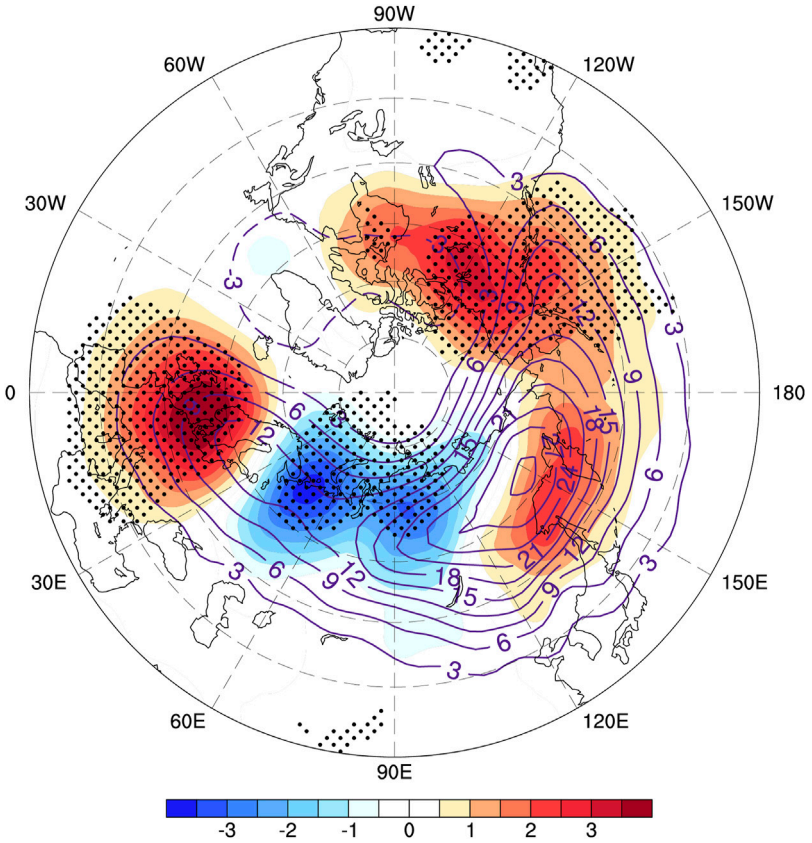

FIGURE 8 | Regression of January–February vertical WAF anomalies (shading; 10^{-3} m^2s^{-2}) at 50 hPa against the negative October SNOWI during 1979–2017. Contours denote the climatological mean of 50 hPa vertical WAFs. Stippled regions indicate that the anomalies are significant at the 90% confidence level.

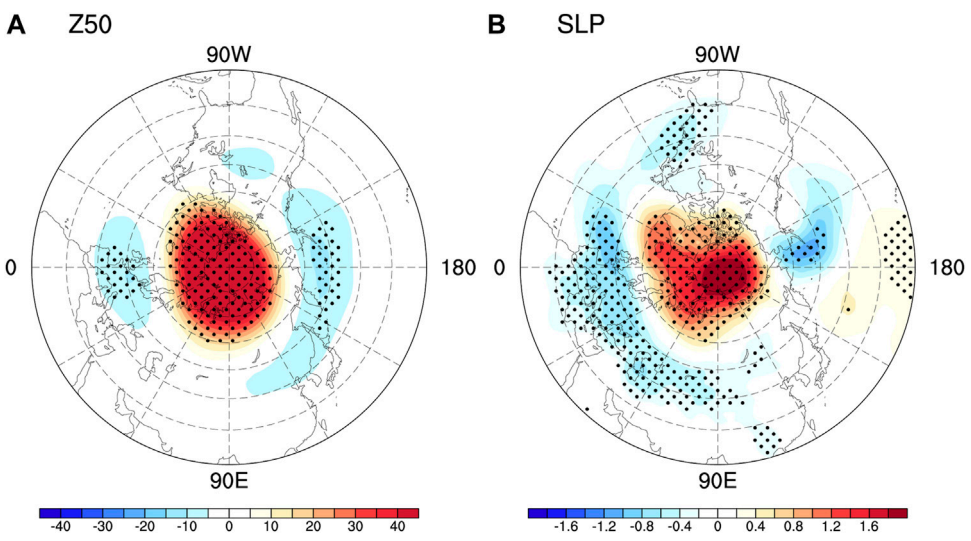

FIGURE 9 | Regressions of spring **(A)** 50 hPa geopotential height (m) and **(B)** SLP (hPa) against the negative October SNOWI during 1979–2017. Stippled regions indicate that the anomalies are significant at the 90% confidence level.

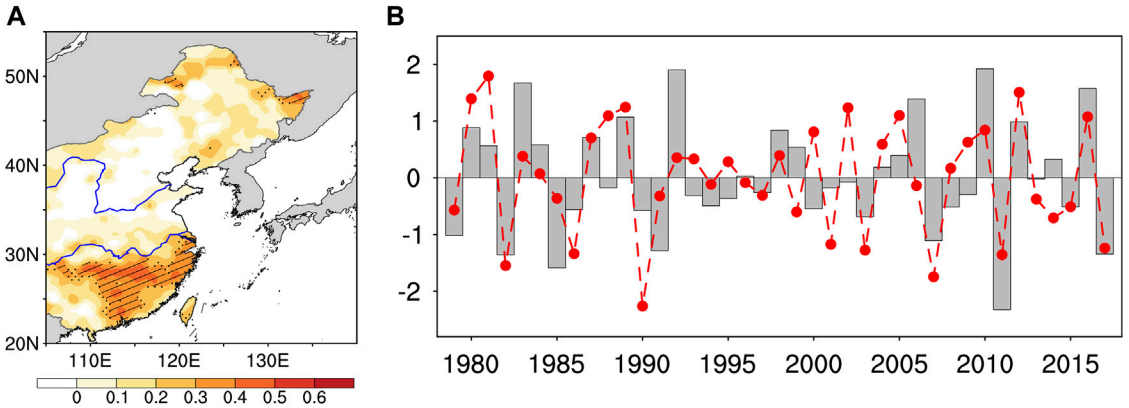

FIGURE 10 | (A) Distribution of temporal correlation coefficient of SEPF in East China between the observation and hindcast. Regions with stippled and hatched patterns indicate that the correlations are significant at the 90 and 95% confidence levels, respectively. **(B)** Time series of the normalized SC_SEPI (bars) and the hindcasted SC_SEPI calculated using the leave-one-out cross-validation method based on the preceding October SNOWI (red line).

to high-latitude, in particular in the delayed impact of Eurasian snow cover and sea ice (e.g., Gong et al., 2003; Cohen et al., 2007; Peings et al., 2012; Cohen et al., 2014; Kim et al., 2014; Nakamura et al., 2015; Han and Sun, 2018; Xu et al., 2018; Ding and Wu, 2021). In this study, we find that the stratosphere-troposphere interaction also play important role in the influence of preceding October central Siberian snow cover on spring extreme precipitation frequency southern China, which is a possible physical way. In addition, previous studies also suggested that the air-sea interaction over the North Atlantic region plays an important role in prolonging impact of the NAO on the following circulation anomalies (e.g., Chen et al., 2020a; Chen et al., 2020b; Wu and Chen, 2020). In particular, Wu and Chen (2020) indicated that both the North Atlantic SST anomalies and Arctic sea ice anomalies are important in linking preceding winter and following spring SAT anomalies over Eurasia. Therefore, the North Atlantic SST might also play a role in linking the October snow cover and following spring extreme precipitation frequency in southern China through the tropospheric processes, which needs to be investigated in our future study.

This study revealed a cross-seasonal relationship between preceding October snow cover in central Siberia and spring extreme precipitation frequency in southern China. The October SNOWI shows significant skill in predicting the SC_SEPI, with a correlation coefficient of 0.61, explaining 37% of the total variance. However, there are still 63% of the variance missed. In addition, from **Figure 10**, we can also see that the October SNOWI cannot well predict SEPF in some extreme years (e.g., 1983, 1992, and 2006), which indicates that the SEPF in these years could be controlled by other factors. Thus, other influencing factors need to be investigated in the future to further improve the prediction skill of southern China SEPF.

DATA AVAILABILITY STATEMENT

The original contributions presented in the study are included in the article/Supplementary Material, further inquiries can be directed to the corresponding author.

AUTHOR CONTRIBUTIONS

JS and MZ designed this manuscript; MZ wrote the first draft of the manuscript; JS performed manuscript review and editing. Both authors discussed the results together and provided critical feedback to the manuscript.

FUNDING

This research was supported by the National Natural Science Foundation of China (41825010 and 42105018) and Dragon 5 Cooperation 2020-2024 (59376).

REFERENCES

Ao, J., and Sun, J. (2015). Connection between November Snow Cover over Eastern Europe and winter Precipitation over East Asia. *Int. J. Climatol.* 36, 2396–2404. doi:10.1002/joc.4484

Baldwin, M. P., and Dunkerton, T. J. (2001). Stratospheric Harbingers of Anomalous Weather Regimes. *Science* 294, 581–584. doi:10.1126/science.1063315

Barnett, T. P., Dümenil, L., Schlese, U., Roeckner, E., and Latif, M. (1989). The Effect of Eurasian Snow Cover on Regional and Global Climate Variations. *J. Atmos. Sci.* 46, 661–686. doi:10.1175/1520-0469(1989)046<0661:teoesc>2.0.co;2

Chen, J., Wen, Z., Wu, R., Chen, Z., and Zhao, P. (2014). Interdecadal Changes in the Relationship between Southern China winter-spring Precipitation and ENSO. *Clim. Dyn.* 43, 1327–1338. doi:10.1007/s00382-013-1947-x

Chen, S., Wu, R., Chen, W., and Li, K. (2020b). Why Does a Colder (Warmer) winter Tend to Be Followed by a Warmer (Cooler) Summer over Northeast Eurasia? *J. Clim.* 33, 7255–7274. doi:10.1175/jcli-d-20-0036.1

Chen, S., Wu, R., and Chen, W. (2020a). Strengthened Connection between Springtime North Atlantic Oscillation and North Atlantic Tripole SST

Pattern since the Late 1980s. *J. Clim.* 33, 2007–2022. doi:10.1175/jcli-d-19-0628.1

Cohen, J., Barlow, M., Kushner, P. J., and Saito, K. (2007). Stratosphere-Troposphere Coupling and Links with Eurasian Land Surface Variability. *J. Clim.* 20, 5335–5343. doi:10.1175/2007jcli1725.1

Cohen, J., and Fletcher, C. (2007). Improved Skill of Northern Hemisphere winter Surface Temperature Predictions Based on Land-Atmosphere Fall Anomalies. *J. Clim.* 20, 4118–4132. doi:10.1175/jcli4241.1

Cohen, J., and Jones, J. (2011). A New index for More Accurate winter Predictions. *Geophys. Res. Lett.* 38, L21701. doi:10.1029/2011GL049626

Cohen, J., Screen, J. A., Furtado, J. C., Barlow, M., Whittleston, D., Coumou, D., et al. (2014). Recent Arctic Amplification and Extreme Mid-latitude Weather. *Nat. Geosci* 7, 627–637. doi:10.1038/ngeo2234

Ding, S., and Wu, B. (2021). Linkage between Autumn Sea Ice Loss and Ensuing spring Eurasian Temperature. *Clim. Dyn.* 57, 2793–2810. doi:10.1007/s00382-021-05839-0

Feng, J., and Li, J. (2011). Influence of El Niño Modoki on spring Rainfall over south China. *J. Geophys. Res.* 116, D13102. doi:10.1029/2010JD015160

Fletcher, C. G., Hardiman, S. C., Kushner, P. J., and Cohen, J. (2009). The Dynamical Response to Snow Cover Perturbations in a Large Ensemble of Atmospheric GCM Integrations. *J. Clim.* 22, 1208–1222. doi:10.1175/2008jcli2505.1

Garfinkel, C. I., and Hartmann, D. L. (2008). Different ENSO Teleconnections and Their Effects on the Stratospheric Polar Vortex. *J. Geophys. Res.* 113, D18114. doi:10.1029/2008jd009920

Garfinkel, C. I., Hartmann, D. L., and Sassi, F. (2010). Tropospheric Precursors of Anomalous Northern Hemisphere Stratospheric Polar Vortices. *J. Clim.* 23, 3282–3299. doi:10.1175/2010jcli3010.1

Gong, G., Entekhabi, D., and Cohen, J. (2003). Modeled Northern Hemisphere winter Climate Response to Realistic Siberian Snow Anomalies. *J. Clim.* 16, 3917–3931. doi:10.1175/1520-0442(2003)016<3917:mnhwcr>2.0.co;2

Gu, L., Sun, J., Yu, S., and Zhang, M. (2021). Footprints of Pacific Decadal Oscillation in the Interdecadal Variation of Consecutive Cloudy-Rainy Events in Southern China. *Atmos. Res.* 257, 105609. doi:10.1016/j.atmosres.2021.105609

Han, S., and Sun, J. (2018). Impacts of Autumnal Eurasian Snow Cover on Predominant Modes of Boreal winter Surface Air Temperature over Eurasia. *J. Geophys. Res.* 123, 10057–10072. doi:10.1029/2018jd028443

Han, S., and Sun, J. (2019). Potential Contribution of winter Dominant Atmospheric Mode over the Mid-latitude Eurasia to the Prediction of Subsequent spring Arctic Oscillation. *Int. J. Climatol.* 40, 2953–2963. doi:10.1002/joc.6376

Huang, D.-Q., Zhu, J., Zhang, Y.-C., Wang, J., and Kuang, X.-Y. (2015). The Impact of the East Asian Subtropical Jet and Polar Front Jet on the Frequency of spring Persistent Rainfall over Southern China in 1997-2011. *J. Clim.* 28, 6054–6066. doi:10.1175/jcli-d-14-00641.1

Jia, X., Cao, D., Ge, J., and Wang, M. (2018). Interdecadal Change of the Impact of Eurasian Snow on spring Precipitation over Southern China. *J. Geophys. Res.* 123, 10073–10089. doi:10.1029/2018jd028612

Jia, X., You, Y., Wu, R., and Yang, Y. (2019). Interdecadal Changes in the Dominant Modes of the Interannual Variation of Spring Precipitation over China in the Mid-1980s. *J. Geophys. Res. Atmos.* 124, 10676–10695. doi:10.1029/2019jd030901

Kalnay, E., Kanamitsu, M., Kistler, R., Collins, W., Deaven, D., Gandin, L., et al. (1996). The NCEP/NCAR 40-year Reanalysis Project. *Bull. Amer. Meteorol. Soc.* 77, 437–471. doi:10.1175/1520-0477(1996)077<0437:tnyrp>2.0.co;2

Kim, B.-M., Son, S.-W., Min, S.-K., Jeong, J.-H., Kim, S.-J., Zhang, X., et al. (2014). Weakening of the Stratospheric Polar Vortex by Arctic Sea-Ice Loss. *Nat. Commun.* 5, 4646. doi:10.1038/ncomms5646

Li, P., Zhou, T., and Chen, X. (2018). Water Vapor Transport for spring Persistent rains over southeastern China Based on Five Reanalysis Datasets. *Clim. Dyn.* 51, 4243–4257. doi:10.1007/s00382-017-3680-3

Nakamura, T., Yamazaki, K., Iwamoto, K., Honda, M., Miyoshi, Y., Ogawa, Y., et al. (2015). A Negative Phase Shift of the winter AO/NAO Due to the Recent Arctic Sea-ice Reduction in Late Autumn. *J. Geophys. Res. Atmos.* 120, 3209–3227. doi:10.1002/2014jd022848

Nath, D., Chen, W., Zelin, C., Pogoreltsev, A. I., and Wei, K. (2016). Dynamics of 2013 Sudden Stratospheric Warming Event and its Impact on Cold Weather over Eurasia: Role of Planetary Wave Reflection. *Sci. Rep.* 6, 24174. doi:10.1038/srep24174

North, G. R., Bell, T. L., Cahalan, R. F., and Moeng, F. J. (1982). Sampling Errors in the Estimation of Empirical Orthogonal Functions. *Mon. Wea. Rev.* 110, 699–706. doi:10.1175/1520-0493(1982)110<0699:seiteo>2.0.co;2

Orsolini, Y. J., Senan, R., Vitart, F., Balsamo, G., Weisheimer, A., and Doblas-Reyes, F. J. (2016). Influence of the Eurasian Snow on the Negative North Atlantic Oscillation in Subseasonal Forecasts of the Cold winter 2009/2010. *Clim. Dyn.* 47, 1325–1334. doi:10.1007/s00382-015-2903-8

Plumb, R. A. (1985). On the Three-Dimensional Propagation of Stationary Waves. *J. Atmos. Sci.* 42, 217–229. doi:10.1175/1520-0469(1985)042<0217:ottdpo>2.0.co;2

Rayner, N. A., Parker, D. E., Horton, E. B., Folland, C. K., Alexander, L. V., Rowell, D. P., et al. (2003). Global Analyses of Sea Surface Temperature, Sea Ice, and Night marine Air Temperature since the Late Nineteenth century. *J. Geophys. Res.* 108, 4407. doi:10.1029/2002JD002670

Robinson, D., Estilow, T., and Cdr Program, N. O. A. A. (2012). *NOAA Climate Data Record (CDR) of Northern Hemisphere (NH) Snow Cover Extent (SCE), Version 1. [indicate Subset Used]*. Washington, D.C., United States: NOAA National Centers for Environmental Information. doi:10.7289/V5N014G9

Saito, K., Cohen, J., and Entekhabi, D. (2001). Evolution of Atmospheric Response to Early-Season Eurasian Snow Cover Anomalies. *Mon. Wea. Rev.* 129, 2746–2760. doi:10.1175/1520-0493(2001)129<2746:eoarte>2.0.co;2

Shen, D., and Chen, H. (2018). Possible Linkage between spring Extreme Precipitation over east China and Surface Sensible Heat Flux over the Eurasian Continent (In Chinese). *Clim. Environ. Res.* 23, 103–112. doi:10.3878/j.issn.1006-9585.2017.16226

Smith, K. L., Fletcher, C. G., and Kushner, P. J. (2010). The Role of Linear Interference in the Annular Mode Response to Extratropical Surface Forcing. *J. Clim.* 23, 6036–6050. doi:10.1175/2010jcli3606.1

Smith, K. L., Kushner, P. J., and Cohen, J. (2011). The Role of Linear Interference in Northern Annular Mode Variability Associated with Eurasian Snow Cover Extent. *J. Clim.* 24, 6185–6202. doi:10.1175/jcli-d-11-00055.1

Sun, C., and Yang, S. (2012). Persistent Severe Drought in Southern China during winter-spring 2011: Large-Scale Circulation Patterns and Possible Impacting Factors. *J. Geophys. Res.* 117, D10112. doi:10.1029/2012JD017500

Wang, B., Wu, R., and Fu, X. (2000). Pacific-east Asian Teleconnection: How Does ENSO Affect East Asian Climate? *J. Clim.* 13, 1517–1536. doi:10.1175/1520-0442(2000)013<1517:peathd>2.0.co;2

Wang, H., Xue, F., and Zhou, G. (2002). The spring Monsoon in south China and its Relationship to Large-Scale Circulation Features. *Adv. Atmos. Sci.* 19, 651–664. doi:10.1007/s00376-002-0005-0

Wang, L., Chen, W., Feng, R., and Liang, J. (2011). The Seasonal March of the North Pacific Oscillation and its Association with the Interannual Variations of China's Climate in Boreal winter and spring (In Chinese). *Chin. J. Atmos. Sci.* 35, 393–402. doi:10.3878/j.issn.1006-9895.2011.03.01

Wen, Z., Wu, N., Feng, Y., Lin, L., Yuan, Z., and Chen, B. (2007). A Quantitative Diagnosis for the Mechanisms of spring Droughts in South China (In Chinese). *Chin. J. Atmos. Sci.* 31, 1223–1236.

Wu, R., and Chen, S. (2020). What Leads to Persisting Surface Air Temperature Anomalies from Winter to Following Spring over Mid- to High-Latitude Eurasia? *J. Clim.* 33, 5861–5883. doi:10.1175/jcli-d-19-0819.1

Wu, R., Hu, Z.-Z., and Kirtman, B. P. (2003). Evolution of ENSO-Related Rainfall Anomalies in East Asia. *J. Clim.* 16, 3742–3758. doi:10.1175/1520-0442(2003)016<3742:eoerai>2.0.co;2

Wu, R., and Kirtman, B. P. (2007). Observed Relationship of Spring and Summer East Asian Rainfall with Winter and Spring Eurasian Snow. *J. Clim.* 20, 1285–1304. doi:10.1175/jcli4068.1

Xie, S.-P., Hu, K., Hafner, J., Tokinaga, H., Du, Y., Huang, G., et al. (2009). Indian Ocean Capacitor Effect on Indo-Western Pacific Climate during the Summer Following El Niño. *J. Clim.* 22, 730–747. doi:10.1175/2008jcli2544.1

Xin, X., Yu, R., Zhou, T., and Wang, B. (2006). Drought in Late spring of South China in Recent Decades. *J. Clim.* 19, 3197–3206. doi:10.1175/jcli3794.1

Xu, X., He, S., Li, F., and Wang, H. (2018). Impact of Northern Eurasian Snow Cover in Autumn on the Warm Arctic-Cold Eurasia Pattern during the Following January and its Linkage to Stationary Planetary Waves. *Clim. Dyn.* 50, 1993–2006. doi:10.1007/s00382-017-3732-8

Yim, S.-Y., Jhun, J.-G., Lu, R., and Wang, B. (2010). Two Distinct Patterns of spring Eurasian Snow Cover Anomaly and Their Impacts on the East Asian Summer Monsoon. *J. Geophys. Res.* 115, D22113. doi:10.1029/2010JD013996

You, Y., and Jia, X. (2018). Interannual Variations and Prediction of spring Precipitation over China. *J. Clim.* 31, 655–670. doi:10.1175/jcli-d-17-0233.1

Zhai, P., Zhang, X., Wan, H., and Pan, X. (2005). Trends in Total Precipitation and Frequency of Daily Precipitation Extremes over China. *J. Clim.* 18, 1096–1108. doi:10.1175/jcli-3318.1

Zhang, J., Zhou, T., Yu, R., and Xin, X. (2009). Atmospheric Water Vapor Transport and Corresponding Typical Anomalous spring Rainfall Patterns in China (In Chinese). *Chin. J. Atmos. Sci.* 33, 121–134. doi:10.3878/j.issn.1006-9895.2009.01.11

Zhang, M., Sun, J., and Gao, Y. (2021). Possible Influence and Prediction Value of Preceding winter Sea Ice Variability over the Davis Strait–Baffin Bay for Changes in spring Extreme Precipitation Frequency over East China (In Chinese). *Earth Sci. Front.*. doi:10.13745/j.esf.sf.2021.9.60

Zhang, R., Sun, C., Zhang, R., Li, W., and Zuo, J. (2019). Role of Eurasian Snow Cover in Linking Winter-Spring Eurasian Coldness to the Autumn Arctic Sea Ice Retreat. *J. Geophys. Res. Atmos.* 124, 9205–9221. doi:10.1029/2019jd030339

Zuo, Z., Zhang, R., Wu, B., and Rong, X. (2012). Decadal Variability in Springtime Snow over Eurasia: Relation with Circulation and Possible Influence on Springtime Rainfall over China. *Int. J. Climatol.* 32, 1336–1345. doi:10.1002/joc.2355

Conflict of Interest: The authors declare that the research was conducted in the absence of any commercial or financial relationships that could be construed as a potential conflict of interest.

The reviewer (SC) declared a shared affiliation, with several of the authors (MZ, JS) to the handling editor at the time of the review

frontiers in Earth Science

ORIGINAL RESEARCH
published: 25 November 2021
doi: 10.3389/feart.2021.787971

Decreasing Influence of Summer Snow Cover Over the Western Tibetan Plateau on East Asian Precipitation Under Global Warming

Zhibiao Wang[1], Renguang Wu[2,3], Zhang Chen[4], Lihua Zhu[4], Kai Yang[5], Kui Liu[1] and Yiya Yang[6]*

[1]Center for Monsoon System Research, Institute of Atmospheric Physics, Chinese Academy of Sciences, Beijing, China, [2]School of Earth Sciences, Zhejiang University, Hangzhou, China, [3]Southern Marine Science and Engineering, Guangdong Laboratory (Zhuhai), Zhuhai, China, [4]Plateau Atmosphere and Environment Key Laboratory of Sichuan Province, School of Atmospheric Sciences, Chengdu University of Information Technology, Chengdu, China, [5]Key Laboratory of Arid Climate Resource and Environment of Gansu Province, Research and Development Center of Earth System Model, College of Atmospheric Sciences, Lanzhou University, Lanzhou, China, [6]Beijing Weather Forecast Center, Beijing, China

OPEN ACCESS

Edited by:
Bin Yu,
Environment and Climate Change (Canada), Canada

Reviewed by:
Shengping He,
University of Bergen, Norway
Maoqiu Jian,
Sun Yat-sen University, China

***Correspondence:**
Renguang Wu
renguang@zju.edu.cn

Specialty section:
This article was submitted to Atmospheric Science, a section of the journal Frontiers in Earth Science

Received: *01 October 2021*
Accepted: *08 November 2021*
Published: *25 November 2021*

Citation:
Wang Z, Wu R, Chen Z, Zhu L, Yang K, Liu K and Yang Y (2021) Decreasing Influence of Summer Snow Cover Over the Western Tibetan Plateau on East Asian Precipitation Under Global Warming. Front. Earth Sci. 9:787971. doi: 10.3389/feart.2021.787971

In recent years, some studies emphasized the influence of western Tibetan Plateau summer snow on the East Asian summer precipitation. With the temperature rise in the past decades, the snow cover over the western Tibetan Plateau in summer has significantly decreased. This raises the question whether the impact of the Tibetan Plateau snow has changed. The present study identifies a prominent change in the influence of the western Tibetan Plateau snow cover on the East Asian summer precipitation. Before the early 2000's, positive precipitation anomalies extend from the southeastern Tibetan Plateau through the Yangtze River to Japan and Korea and negative anomalies cover southeast China corresponding to more Tibetan Plateau snow cover. After the early 2000's, with the reduction of snow cover variability, below-normal and above-normal summer precipitation occurs over northern China-Mongolia and northeast Asia, respectively, corresponding to more Tibetan Plateau snow cover. The change in the influence of the Tibetan Plateau snow on the East Asian summer precipitation is associated with an obvious change in the atmospheric circulation anomaly pattern. Before the early 2000's, the wind anomalies display a south-north contrast pattern with anomalous convergence along the Yangtze River. After the early 2000's, an anomalous cyclone occupies Northeast China with anomalous southerlies and northerlies over northeast Asia and northern China, respectively. The Tibetan Plateau snow cover variation after the early 2000's is associated with the northeast Indian summer precipitation. The model experiments confirm that the weakened influence of summer western Tibetan Plateau snow cover on the East Asian atmospheric circulation and precipitation with the reduced snow cover anomalies.

Keywords: tibetan plateau summer snow cover, east asian summer precipitation, global warming, northeast indian precipitation, weakened influence

INTRODUCTION

Snow is an important component in the global energy budget and hydrological cycle (Barnett et al., 1989; Yasunari et al., 1991). The snow variations have a significant influence on the climate system and modulate regional weather and climate (Cohen and Rind, 1991; Brown, 2000; Wu and Kirtman, 2007; Ding et al., 2009; Wu et al., 2014; Schlögl et al., 2018; Wang et al., 2019; Zhang et al., 2020). On the other hand, the change of snow is affected by the atmosphere, especially the air temperature (Karl et al., 1993; Wang et al., 2018a). With rapid global warming in the past decades, the snow cover has declined over most areas of Earth (Bormann et al., 2018).

Due to the high altitude, the average air temperature over the Tibetan Plateau is lower than the surrounding regions. Most areas of the Tibetan Plateau are covered by snow in cold seasons, and there are still snow covered regions with higher altitudes in the summer, especially the western and southern parts of the Tibetan Plateau (Wang et al., 2018a). Since Blanford. (1884) found the relationship between northwest Indian summer precipitation and the winter-spring snow on the Himalayas, a large number of studies have analyzed the influence of the Tibetan Plateau snow on regional weather and climate (Chen and Wu, 2000; Lin and Wu, 2011; Xiao and Duan, 2016; Wang et al., 2017; Li et al., 2018; Qian et al., 2019; Wang et al., 2020; You et al., 2020; Jia et al., 2021). These studies found the impact of cold season snow over the Tibetan Plateau on East Asian, Indian, Eurasian, and North Americna climate variability. However, due to lack of effective long-term observation snow data, the effect of summer snow over the Tibetan Plateau on climate has been neglected for a long time.

In recent years, the high-resolution long-term snow cover data over the whole Tibetan Plateau have been gradually accumulated (Estilow et al., 2015). The influence of summer snow cover on regional climate has been emphasized by some studies. For instance, the Tibetan Plateau snow anomalies modulate the East Asian summer precipitation (Wu et al., 2012; Liu et al., 2014; Wang et al., 2018b) and influence Eurasian heatwave frequency (Wu et al., 2016). However, the Tibetan Plateau has experienced an obvious temperature rise in the past few decades (Wang et al., 2008; Zhong et al., 2019), and the summer snow cover has decreased largely over the Tibetan Plateau (Wang et al., 2018a). Under the background of the rapid decrease of summer snow cover over the Tibetan Plateau, whether the relationship between the Tibetan Plateau snow cover and East Asia summer precipitation variations has changed in the past decades is a problem worthy of study. This has important implication as the changes of summer precipitation over East Asia have an important impact on the region (Wang et al., 2001; Wu and Wang 2002).

Our analysis has identified an obvious change in the relationship between the summer Tibetan Plateau snow cover and East Asian precipitation. The present study presents evidence for the change in the relationship and explores the plausible reasons of the change. The rest of this study is organized as follows. We describe data and methods in **section 2**. In **section 3**, we present the change in the relationship between the western Tibetan Plateau summer snow cover and East Asian summer precipitation. In **section 4**, we analyze the effect of northeast Indian summer precipitation on the relationship between the snow cover and East Asian precipitation in the early 2000s. The summary and discussion are provided in **section 5**.

DATA AND METHODS

This study used the Northern Hemisphere snow cover data of version 4 (Brodzik and Armstrong, 2013), which spans the time period from October 1966 to December 2020. The present analysis only uses the data for the period 1973—2020 as the snow cover data before 1973 is less reliable. The data were acquired from the National Snow and Ice Data Center (NSIDC) (https://nsidc.org/data/NSIDC-0046/versions/4). We converted the weekly EASE-Grid 2.0 projection at a 25-km spatial resolution data to monthly mean on regular 1 × 1 grids.

The monthly precipitation was obtained from the University of East Anglia Climate Research Unit (CRU) of version 4.05 (http://www.cru.uea.ac.uk/data/) (Harris et al., 2014). The CRU data have a spatial resolution of 0.5 × 0.5 and are available from 1901 to 2020.

The NCEP/NCAR reanalysis 1 data (Kalnay et al., 1996) provide monthly mean geopotential heights and winds at pressure levels from 1948 to the present. The pressure level variables are on regular 2.5 × 2.5 grids. The NCEP-DOE reanalysis variables were obtained from the NOAA/OAR/ESRL Physical Science Department (https://psl.noaa.gov/data/).

This study focused on the relationship between the western Tibetan Plateau summer snow cover and the East Asian summer precipitation on interannual time scales. Summer refers to June-July-August (JJA) in the present study. The component of the interannual signal was obtained by a 9-years high pass Gaussian filter. Linear regression, partial regression, sliding correlation, and correlation analysis were used in the study. The significance level of regression and correlation analysis was estimated using the Student's *t*-test.

The Community Atmospheric Model version 5.0 (CAM5), the atmospheric component of the Community Earth System Model (CESM), is adopted in this study to examine the response of atmospheric circulation and precipitation to albedo changes caused by snow cover. The CAM5 is developed by the National Center for Atmospheric Research (Neale et al., 2010) Atmosphere Model Working Group. The model has a 1.9 × 2.5 finite volume grid and 31 vertical levels.

RESULTS

Changes in the Relationship Between Snow Cover and Precipitation

The snow cover over the Tibetan Plateau in summer is mainly located in the high altitude region of the western and southern parts, and the values of snow cover in the western part are larger than in the southern part (**Figure 1A**, shaded). The interannual variations of snow cover in the western part are more prominent than in the southern part (**Figure 1A**, contour). The large

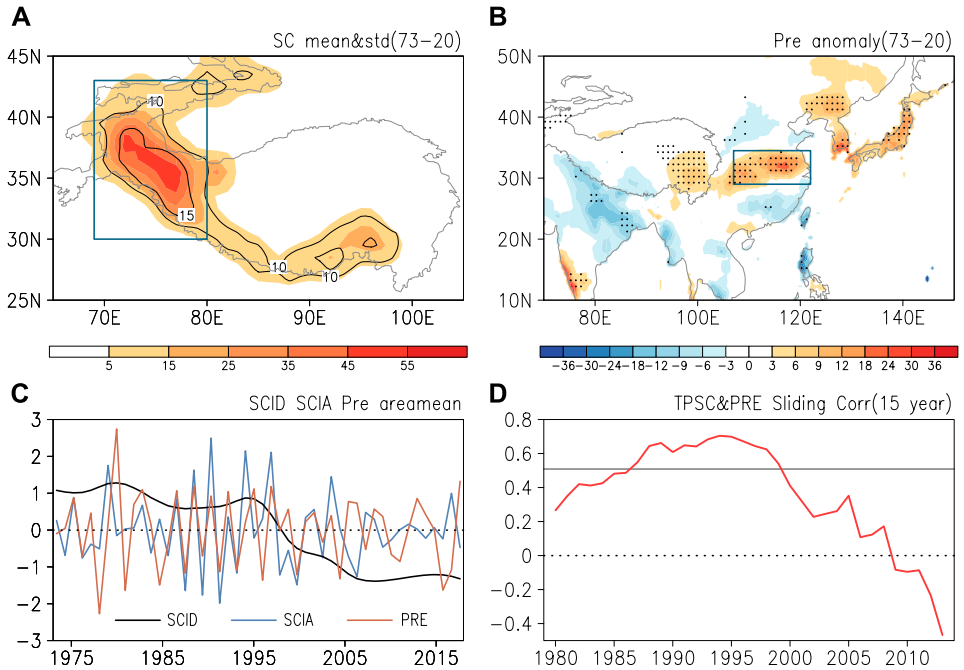

FIGURE 1 | (A) Climatological mean (shading, %) and interannual standard deviation (contour, %) of snow cover (SC) in summer over the Tibetan Plateau for the period 1973—2020. **(B)** Anomalies of summer precipitation (Pre) (mm/month) obtained by linear regression against the western Tibetan Plateau summer snow cover index for the period 1973—2020. **(C)** Standardized area-mean interannual (SCIA) (blue line) and interdecadal (SCID) (black line) summer snow cover anomalies over the western Tibetan Plateau, and interannual East Asian summer precipitation (Pre) (brown line) anomalies for the period 1973—2020. **(D)** Sliding correlation coefficients between the interannual western Tibetan Plateau summer snow cover index (TPSC) and interannual East Asian summer precipitation index (Pre) with a 15-years moving window for the period 1973—2020. The dotted regions in **(B)** denote anomalies significant at the 95% confidence level. The gray line in **(D)** denotes the 15-years sliding correlation coefficient significant at the 95% confidence level. The box covered area in **(A)** denotes the domain (30°N-43°N, 69°E-80°E) of western Tibetan Plateau, same in other figures. The box covered area in **(B)** denotes the domain (29°N-34.5°N, 107°E-122°E) used to calculate the East Asian summer precipitation index. Curves in **(A)** and **(B)** denote the elevation of 3000 m over the Tibetan Plateau region, same in other figures.

variation of the western Tibetan Plateau snow cover has an obvious influence on East Asian precipitation in summer (Wang et al., 2018b). We use the area mean of interannual western (Domain: 30°N-43°N, 69°E-80°E) snow cover anomalies as an index (**Figure 1C**, blue line) to reexamine the above relationship. Corresponding to more snow cover in the western Tibetan Plateau, positive precipitation anomalies are observed in central China, Japan, and Korean Peninsula, and negative anomalies exist in southeast China, north China, and the northeastern part of India (**Figure 1B**).

With the significant warming, the summer snow cover over the western Plateau displays an obvious decrease in the past decades (**Figure 1C**, black line). Would this affect the relationship between western Plateau summer snow cover and East Asian summer precipitation? To address this issue, we use the area mean central China (Domain: 29°N-34.5°N, 107°E-122°E) interannual precipitation anomalies as an index to represent the East Asian summer precipitation (**Figure 1C**, brown line). We calculate the sliding correlation between the snow cover index and the precipitation index. Their correlation coefficient is large before the middle 1990's, but experiences a continue decrease after that (**Figure 1D**). The result indicates that the relationship between two indexes is unstable.

To illustrate the change in the relationship between the western Tibetan Plateau snow cover and the East Asian precipitation in summer, we divide the 1973—2020 period into two sub-periods (1973—2001 and 2001—2020) to analyze the relationship, respectively. The selection of the year 2001/2002 as the changing point is based on the following two considerations. One is the change of standardized western Plateau snow cover interdecadal anomalies from positive to negative (**Figure 1C**, black line). The other is the large drop of the sliding correlation between the two indexes (**Figure 1D**).

For the period 1973—2001, the snow cover distribution and interannual variation are similar to the whole period, but the values are obviously larger than the whole period (**Figures 1A**, **Figure 2A**). Corresponding to more snow cover in the western Tibetan Plateau, the distribution of precipitation anomalies is also similar to the whole period, but with a larger value (**Figures 1B**, **Figures 2C**). At the upper level, cyclonic anomalies are observed over the western Tibetan Plateau, anticyclonic anomalies extend from the eastern part of the Tibetan Plateau to the subtropical western North Pacific, and cyclonic anomalies are distributed from northeast China to east of Japan (**Figure 3A**). The circulation anomalies at the lower level (**Figure 3C**) are similar to those at upper level over East Asia and western

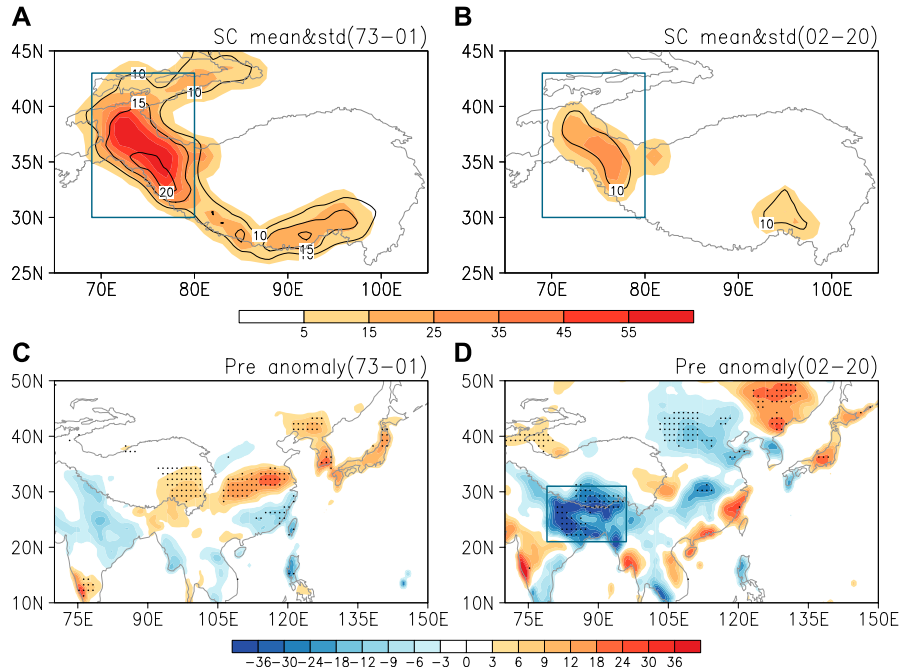

FIGURE 2 | Climatological mean (shading, %) and interannual standard deviation (contour, %) of snow cover over the Tibetan Plateau for the period **(A)** 1973—2001 and **(B)** 2002—2020. Anomalies of summer precipitation (Pre) (mm/month) obtained by linear regression against the western Tibetan Plateau summer snow cover index for the period **(A)** 1973—2001 and **(B)** 2002—2020. The dotted regions in **(C)** and **(D)** denote anomalies significant at the 95% confidence level. The box covered area in **(D)** denotes the domain (21°N-31°N, 79°E-96°E) of northeast Indian region.

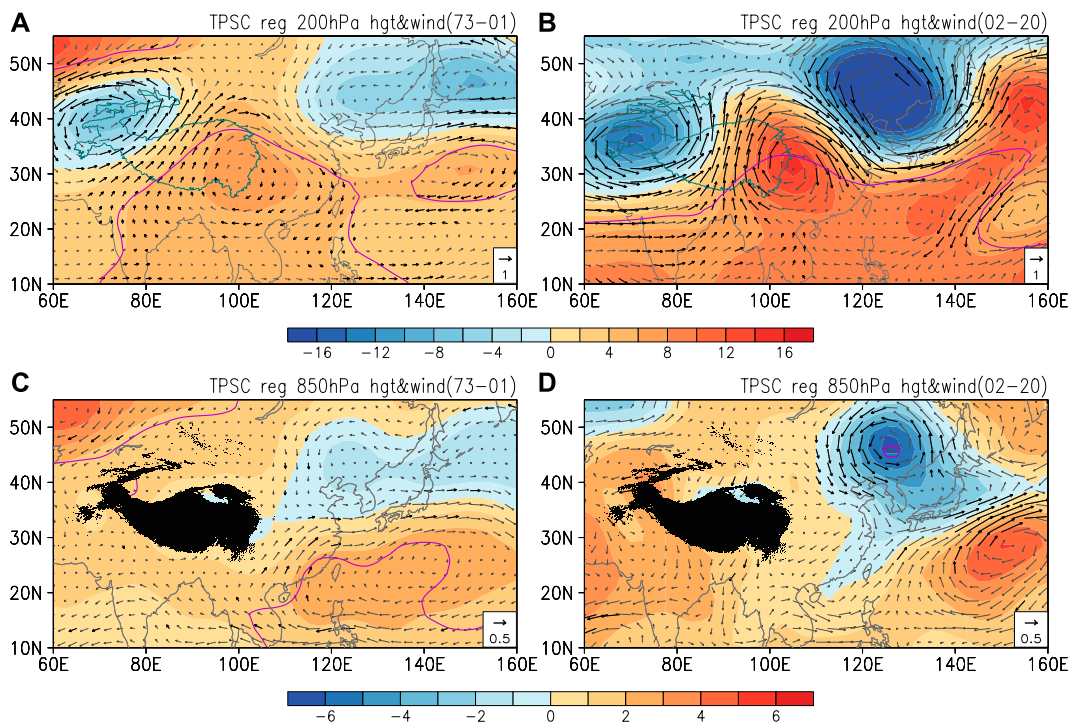

FIGURE 3 | Anomalies of **(A, B)** 200 hPa and **(C, D)** 850 hPa geopotential height (hgt) (shading, gpm) and wind (vector, m/s) in summer obtained by linear regression against the western Tibetan Plateau summer snow cover index for the period **(A, C)** 1973—2001 and **(B, D)** 2002—2020. The scale for winds is shown at the bottom-right corner. The black vectors denote wind anomalies significant at the 95% confidence level. The purple contours denote geopotential height anomalies significant at the 95% confidence level.

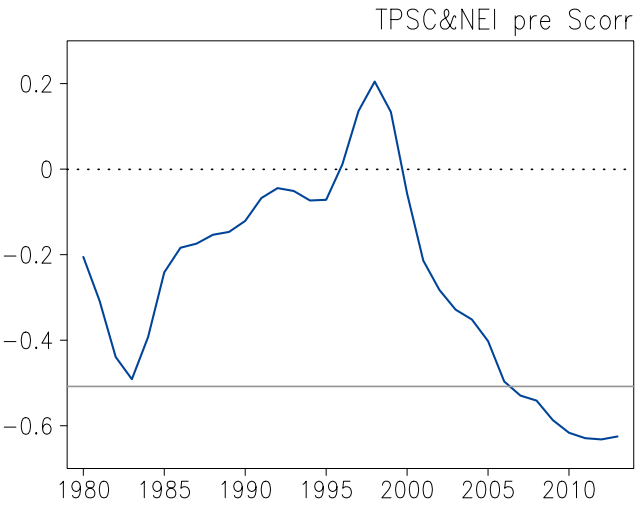

FIGURE 4 | Sliding correlation coefficient between the interannual western Tibetan Plateau summer snow cover index (TPSC) and interannual northeast Indian summer precipitation index (NEI pre) with a 15-years moving window for the period 1973—2020. The gray line denotes the 15-years sliding correlation coefficient significant at the 95% confidence level.

North Pacific, indicative of a barotropic vertical structure. Anomalous wind convergence extends from the eastern Tibetan Plateau to east Japan (**Figure 3C**), corresponding to positive precipitation anomalies (**Figure 2C**).

For the period 2002—2020, the area of snow cover anomalies shrinks and the anomalous value declines, mainly located in part of western and southeast Plateau, and its interannual variation also decreases obviously (**Figure 2B**). Corresponding to positive snow cover anomalies in the western Tibetan Plateau, precipitation anomalies are completely different from those in the previous period. Negative precipitation anomalies are distributed in northern China-Mongolia and in northeast India, and positive anomalies are distributed in southeast coast of China and part of northeast Asia (**Figure 2D**). At upper level, cyclonic anomalies are distributed over the western Plateau and northeast Asia regions, and anticyclonic anomalies are observed over the eastern Plateau to central China and eastern Japan (**Figure 3B**). At the lower level, cyclonic anomalies are distributed over the northeast Asia region (**Figure 3D**). The southerly and northerly wind anomalies over the northeast and southwest part of the anomalous cyclone correspond to positive and negative precipitation anomalies, respectively (**Figures 2D**, **Figures 3D**). Anticyclonic anomalies are seen over the subtropical western Pacific with a northwest shift of the location with the altitude (**Figures 3B,D**).

Influence of Northeast Indian Precipitation Anomalies

During the period 2002—2020, while the snow cover anomalies over the Tibetan Plateau are reduced obviously, atmospheric circulation and precipitation anomalies over East Asia have increased, which seems to be a puzzle. At the same period,

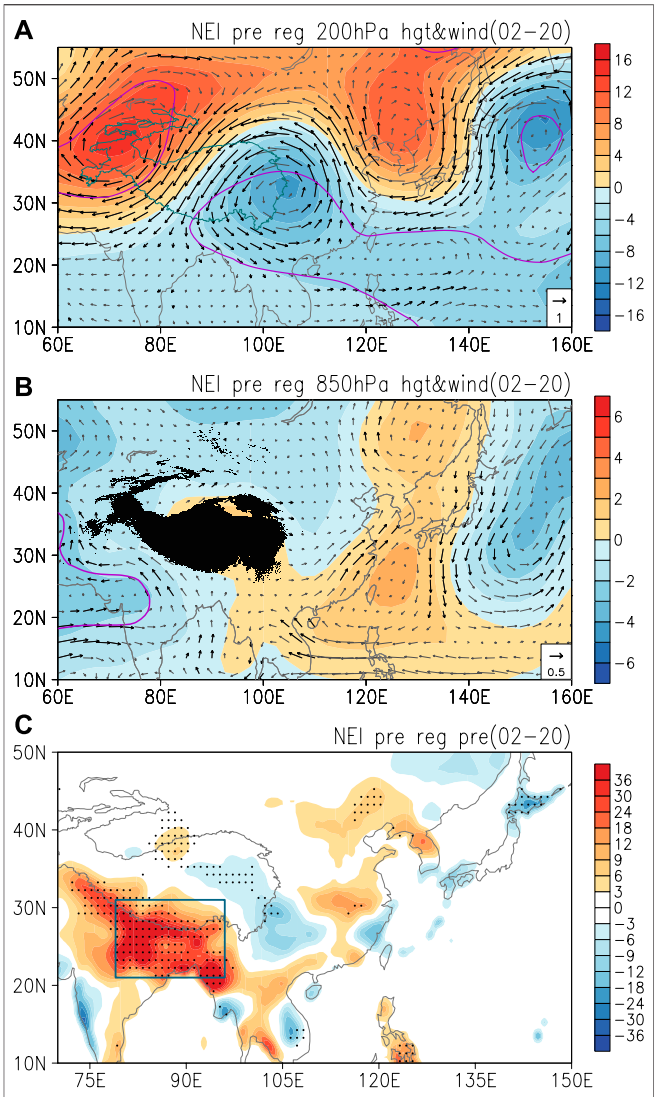

FIGURE 5 | Anomalies of **(A)** 200 hPa and **(B)** 850 hPa geopotential height (hgt) (shading, gpm) and wind (vector, m/s) in summer obtained by linear regression against the northeast Indian summer precipitation index for the period 2002—2020. **(C)** Anomalies of summer precipitation (pre) (mm/month) obtained by linear regression against the northeast Indian summer precipitation index for the period 2002—2020. The scale for winds is shown at the bottom-right corner. The black vectors in **(A, B)** denote wind anomalies significant at the 95% confidence level. The purple contours in **(A, B)** denote geopotential height anomalies significant at the 95% confidence level. The dotted regions in **(C)** denote precipitation anomalies significant at the 95% confidence level.

obvious precipitation anomalies are observed over northeast India. Previous studies indicated that the north Indian summer precipitation anomalies have a significant effect on East Asian summer precipitation variations (Wu 2002; Wei et al., 2015; Wu 2017). Would the northeast Indian precipitation anomalies have an effect on the Tibetan Plateau snow cover and East Asian precipitation during the period 2002—2020? We perform the following analysis to answer this question.

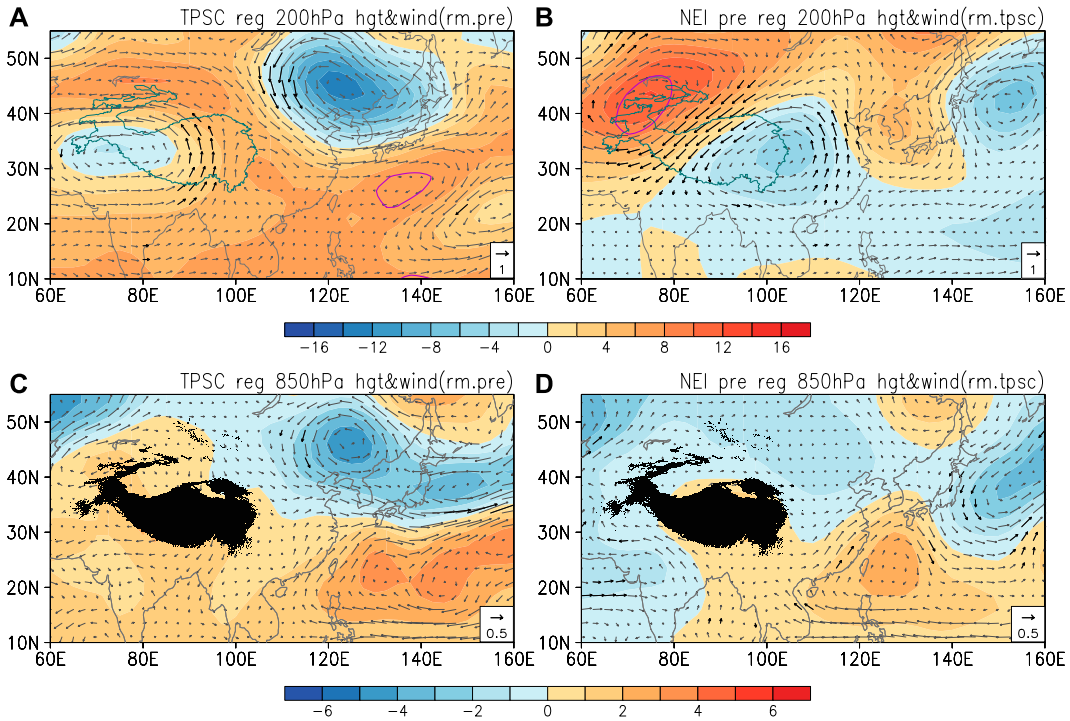

FIGURE 6 | Anomalies of **(A, B)** 200 hPa and **(C, D)** 850 hPa geopotential height (hgt) shading, gpm) and wind (vector, m/s) in summer obtained by linear regression against the **(A, C)** western Tibetan Plateau summer snow cover index and **(B, D)** northeast Indian summer precipitation index for the period 2002—2020 with the **(A, C)** northeast Indian summer precipitation signal and **(B, D)** western Tibetan Plateau summer snow cover signal removed. The scale for winds is shown at the bottom-right corner. The black vectors denote wind anomalies significant at the 95% confidence level. The purple contours denote geopotential height anomalies significant at the 95% confidence level.

First, we analyzed correlations between the Tibetan Plateau summer snow cover index and northeast Indian summer precipitation index (**Figure 2D**, box covered area, domain: 21°N-31°N, 79°E-96°E). The correlation coefficient is −0.12 and −0.56, respectively, in the period 1973—2001 and 2002—2020. The correlation coefficient in the second period is significant at the 95% confidence level. The sliding correlation shows that the negative correlation between the two indices continues to increase after the eary 2000's (**Figure 4**). The result confirms that the Tibetan Plateau snow cover and the northeast Indian precipitation in summer have a significant negative correlation for the second period.

To illustrate whether the northeast Indian precipitation anomalies influence the East Asian precipitation and the western Tibetan Plateau snow cover changes for the period 2002—2020, we regressed the geopotential height and wind anomalies at 200 hPa and 850 hPa, precipitation and snow cover anomalies against the northeast Indian summer precipitation index. The above-normal precipitation over the northeast India is accompanied by anomalous heating that induces an anomalous lower-level cyclone over the Arabian Sea and western India and an anomalous upper-level anticyclone to the west of the Tibetan Plateau (**Figures 5A,B**), which is consistent with Rodwell and Hoskins. (1996). The perturbed atmosphere in turn induces downstream atmospheric circulation anomalies extending to East Asia. Corresponding to positive northeastern Indian precipitation anomalies, anticyclonic anomalies are observed over northeast Asia, and cyclonic anomalies are distributed over the eastern Tibetan Plateau and east of Japan at the upper level (**Figure 5A**). At the lower level, there are anticyclonic anomalies off the coast of eastern China and over northeast Asia, and cyclonic anomalies exist east of Japan (**Figure 5B**). The above circulation anomalies are very similar to those obtained by regression against the western Tibetan Plateau snow cover index except for opposite anomalies (**Figures 3B,D** and **Figures 5A,B**). The precipitation anomalies also have similar (opposite) features (**Figure 2D** and **Figure 5C**). Above normal northeast Indian precipitation is also accompanied by reduced snow cover over the western Tibetan Plateau (figure not shown). The results further illustrate the negative relationship between the Tibetan Plateau snow cover and northeast Indian precipitation.

To examine the effect of northeast Indian precipitation anomalies in the change of the relationship between the western Tibetan Plateau summer snow cover and East Asian precipitation around the early 2000's, we perform a partial regression analysis. After removing the northeast Indian precipitation signal, corresponding to positive snow cover anomalies, weak cyclonic anomalies exist over the southwestern Tibetan Plateau, cyclonic anomalies are located over Northeast China, positive geopotential heights anomalies

extend southern China to subtropical western North Pacific at the upper level (**Figure 6A**). The distribution of circulation anomalies at the upper-level displays differences from the pattern against the snow cover index in the second period (**Figures 3A**, **Figures 6B**), but somewhat similarity to the pattern against the snow cover index in the first period with lower significance of circulation anomalies (**Figures 3A**, **Figures 6A**). At the lower level, the circulation anomalies over East Asia are also similar to the pattern against the snow cover index in the first period (**Figures 3C**, **Figures 6C**). The above analysis implies that when the northeast Indian precipitation signal is removed the influence of the western Tibetan Plateau snow cover anomalies on the East Asian atmospheric circulation in the second period is similar to the first period, but the influence is weakened. However, after removing the northeast Indian precipitation signal, the precipitation anomalies over eastern China and northeast Asia are similar to those when the signal is not removed, but the magnitude of precipitation anomalies decreases (**Figures 2D**, **Figures 7A**). When the snow cover signal is removed, the circulation anomalies at both the upper and lower levels are similar to those when the signal is not removed, but the level of significance decreases (**Figures 5A,B** and **Figures 6B,D**), and the precipitation anomalies are weak over East Asia (**Figure 7B**). From the above analysis, we can conclude that with the snow cover variation reduced in the second period, the influence of summer western Tibetan Plateau snow cover on the East Asian atmospheric circulation and precipitation becomes weaker, the snow cover anomalies are influenced by the precipitation changes over the northeast India, and especially the atmospheric circulation anomalies which are related to the Tibetan Plateau snow cover anomalies are mainly affected by the northeast Indian precipitation change.

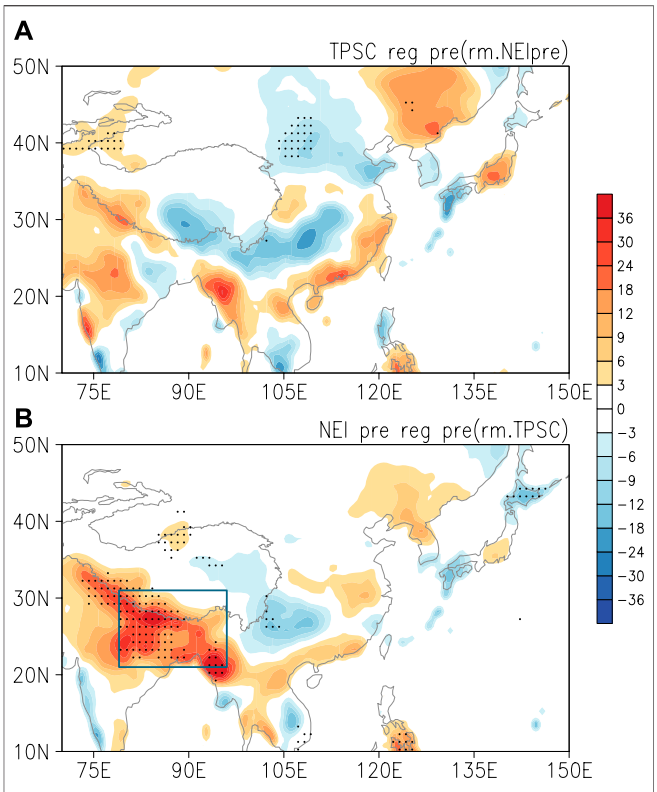

FIGURE 7 | Anomalies of summer precipitation (pre) (mm/month) obtained by linear regression against the **(A)** western Tibetan Plateau summer snow cover index and **(B)** northeast Indian summer precipitation index for the period 2002—2020 with the **(A)** northeast Indian summer precipitation signal and **(B)** western Tibetan Plateau summer snow cover signal removed. The dotted regions in **(A)** and **(B)** denote anomalies significant at the 95% confidence level.

Model Simulation for the Different Snow Cover Status

To verify the influence of more and less snow cover anomalies over the western Tibetan Plateau on East Asian precipitation changes, we perform numerical experiments using CAM5. One control run and two forcing runs are conducted in the study. In the control run, which serves as a reference for the forcing runs, climatological monthly SST for the period 1981—2010 is specified in the global oceans and the surface albedo is calculated by the model itself. In the forcing runs, the surface albedo is calculated by the model itself except for the western Tibetan Plateau in summer. Over the western Tibetan Plateau in summer, when the albedo is lower than 0.8, it is reset to a fixed value of 0.8 in the high albedo forcing run to represent features of more snow over the western Tibetan Plateau (**Figure 8A**), and when the albedo is higher than 0.3, it is reset to a fixed value of 0.3 in the low albedo forcing run to represent features of less snow over the western Tibetan Plateau (**Figure 8B**). The albedo over 0.8 is nearly fresh snow surface albedo, and less than 0.3 is nearly dry bare ground surface albedo (Cohen and Rind, 1991). In all the experiments, the model is integrated for 15 years. The differences of geopotential height, wind, and total precipitation in summer between forcing runs and control run averaged for the last 14 years represent the model response to more and less snow over the western Tibetan Plateau.

In the higher albedo forcing run, at the upper level, cyclonic anomalies exist over the western Plateau and northeast Asian regions, and anticyclonic anomalies are observed over the eastern Plateau region (**Figure 8C**). The pattern of circulation anomalies is similar to that against the snow cover index for the period 1973—2001 (**Figures 3A**, **Figure 8C**). At the lower level, positive geopotential height anomalies are distributed north of the Plateau and over eastern Japan (**Figure 8E**). The precipitation anomalies display a spatial pattern similar to the observations, but the positive anomalies over East Asia shift northward compared to the observations (**Figures 2C**, **Figure 8G**). In the lower albedo forcing run, both the atmospheric circulation and precipitation anomalies are weaker than those in the higher albedo forcing. The upper-level circulation response at the mid- and low-latitude is weak, and positive geopotential height anomalies are distributed north and northeast of the Tibetan Plateau (**Figure 8D**). At the lower level, weak positive geopotential height anomalies exist in most areas of the continent, and cyclonic anomalies are located off the east coast of China (**Figure 8F**). Weak positive precipitation anomalies are distributed over the eastern Plateau and North China, and negative precipitation anomalies

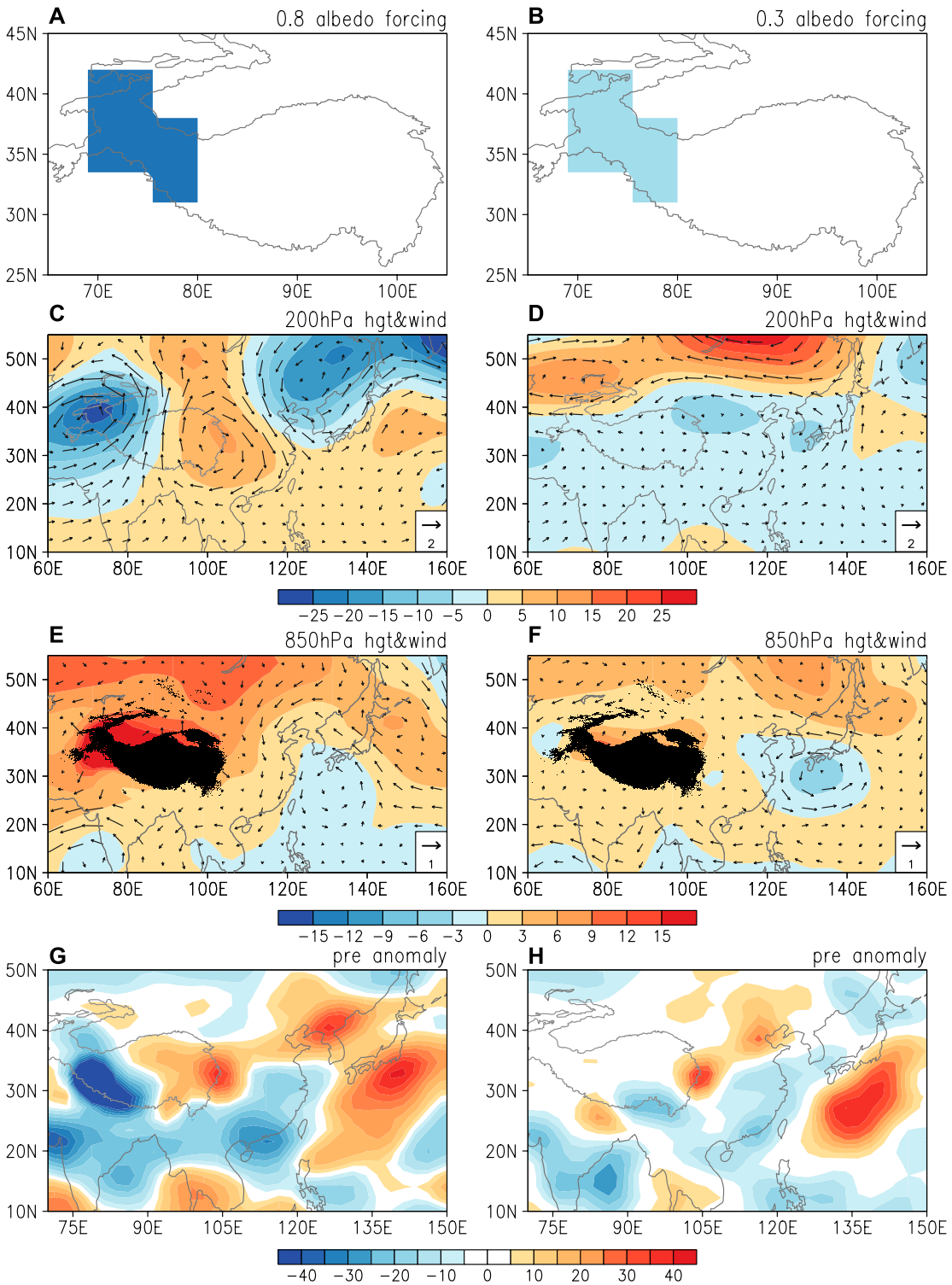

FIGURE 8 | Model **(A)** higher and **(B)** lower albedo forcing pattern. The model response of **(C, D)** 200hPa and **(E, F)** 850hPa geopotential height (hgt) (shading, gpm) and wind (vector, m/s) and **(G, H)** precipitation (pre) (mm/month) to **(C, E, G)** higher and **(D, F, H)** lower albedo forcing. The scale for winds in **(C–F)** is shown at the bottom-right corner.

extend from southern to eastern China (**Figure 8H**). The model results further illustrate that after the snow cover is reduced over the western Tibetan Plateau, its influence on the atmospheric circulation and precipitation over East Asia is also weakened.

SUMMARY AND DISCUSSIONS

The snow cover over the Tibetan Plateau has an important influence on regional and global climate. Most of the previous studies mainly concerned the impacts of cold season snow anomalies. The effect of summer snow cover anomalies over the Tibetan Plateau has been neglected. In recent years, some papers emphasized the effects of summer Tibetan Plateau snow cover changes on regional climate, especially on the East Asian summer precipitation. With the significant warming over the Tibetan Plateau, the snow cover over the Plateau has an obvious decreasing trend, accompanied by a reduced variability. The present study addresses the question whether the influence of the Tibetan Plateau snow cover changes on the East Asian precipitation has changed with the snow decrease by conducting the statistical analysis and model simulation.

The snow cover over the Tibetan Plateau in summer has an obvious connection with the summer precipitation over East Asia. However, their relationship has a significant decrease in the past decades from the obvious positive correlation before the early 2000s. Then, we divide the 1973—2020 period into two sub-periods, 1973—2001 and 2002—2020, to analyze the changes of influence of more and less snow conditions over the western Tibetan Plateau on East Asian summer precipitation.

In the first period, positive snow cover anomalies over the western Tibetan Plateau induce cyclonic anomalies over the western Tibetan Plateau and northeast Asia to eastern Japan, and anticyclonic anomalies over the eastern Tibetan Plateau to the subtropical western North Pacific at the upper level, similar to the previous study (Wang et al., 2018b). The circulation anomalies have a barotropic vertical structure over East Asia. The circulation anomalies cause positive precipitation anomalies from the eastern Tibetan Plateau through the Yangtze River to Japan, and negative precipitation anomalies over southern China.

In the second period, with the snow cover decrease over the western Tibetan Plateau, the variability of snow cover is also reduced. However, corresponding to positive snow cover anomalies, more significant cyclonic anomalies are observed over the western Tibetan Plateau and northeast Asian regions, and anticyclonic anomalies exist over the eastern Tibetan Plateau and eastern Japan at the upper level. The barotropic vertical structure is observed over East Asia region as well. The negative precipitation anomalies are distributed over northern China-Mongolia and northeast India, positive anomalies are observed over the coastal area of southeast China and part of northeast Asia. The precipitation anomalies over northeast India are very significant.

Our analysis reveals a significant negative relationship between the snow cover over the western Tibetan Plateau and northeast Indian precipitation in the second period. Corresponding to positive northeast Indian precipitation anomalies, the circulation anomalies are very similar to those against the snow cover index. Partial regression analysis indicates that the influences of the Tibetan Plateau snow cover anomalies on atmospheric circulation over East Asia are largely modulated by the northeast Indian summer precipitation changes.

The CAM5 experiments verify the observational results. With the higher albedo forcing, the response of upper-level atmospheric circulation and precipitation over East Asia is similar to the observations related to the snow cover index in the first period. With the lower albedo forcing, there is a significant reduction of atmospheric circulation and precipitation response over East Asia compared with the higher albedo forcing. So, the model simulation further illustrates the change in the influence of the western Tibetan Plateau snow cover on the East Asian precipitation following the decrease of snow cover under global warming.

The present analysis revealed that the influence of the summer western Tibetan Plateau snow cover on East Asian atmospheric circulation and precipitation changes depends upon the magnitude of snow cover variability. Reduced snow cover may be accompanied by a different atmospheric circulation and precipitation response over East Asia, resulting in changes in the relationship between the Tibetan Plateau snow cover and East Asian summer climate. This indicates an effect of global warming on the Tibetan Plateau snow impacts.

The East Asian atmospheric circulation changes subject to influences of other factors, e.g., the sea surface temperature (SST) anomalies in the tropical Indo-Pacific region. It is possible that the Tibetan Plateau snow cover-East Asian precipitation relationship may be modulated by the tropical Indo-Pacific SST anomalies. Further investigation is needed to understand the contribution of the SST forcing and its cooperation with the Tibetan Plateau snow effects in the East Asian climate variability.

DATA AVAILABILITY STATEMENT

The original contributions presented in the study are included in the article/Supplementary Material, further inquiries can be directed to the corresponding author.

AUTHOR CONTRIBUTIONS

Conceptualization: RW, ZW Data curation: ZW Formal analysis: ZW, RW, ZC, LZ, KY, KL, and YY Funding acquisition: RW, ZW Investigation: ZW Methodology: RW, ZW Project Administration: RW, ZW Resources: ZW Supervision: RW Validation: ZW, RW Writing original draft: ZW, RW Writing review and editing: ZW, RW, ZC, LZ, KY, KL, and YY.

FUNDING

This study is supported by the National Natural Science Foundation of China grants (42105028, 41721004 and 41775080), the China Postdoctoral Science Foundation (2019M660762, and 2020T130640).

REFERENCES

Barnett, T. P., Dümenil, L., Schlese, U., Roeckner, E., and Latif, M. (1989). The Effect of Eurasian Snow Cover on Regional and Global Climate Variations. *J. Atmos. Sci.* 46 (5), 661–686. doi:10.1175/1520-0469(1989)046<0661:teoesc>2.0.co;2

Blanford, H. F. (1884). II. On the Connexion of the Himalaya Snowfall with Dry Winds and Seasons of Drought in India. *Proc. R. Soc. Lond.* 37 (232-234), 3–22. doi:10.1098/rspl.1884.0003

Bormann, K. J., Brown, R. D., Derksen, C., and Painter, T. H. (2018). Estimating Snow-Cover Trends from Space. *Nat. Clim Change* 8 (11), 924–928. doi:10.1038/s41558-018-0318-3

Brodzik, M., and Armstrong, R., 2013: Northern Hemisphere EASE-Grid 2.0 Weekly Snow Cover and Sea Ice Extent, version 4. National Snow and Ice Data Center, (Accessed on August 21, 2021).

Brown, R. D. (2000). Northern Hemisphere Snow Cover Variability and Change, 1915-97. *J. Clim.* 13 (13), 2339–2355. doi:10.1175/1520-0442(2000)013<2339:nhscva>2.0.co;2

Chen, L., and Wu, R. (2000). Interannual and Decadal Variations of Snow Cover over Qinghai-Xizang Plateau and Their Relationships to Summer Monsoon Rainfall in China. *Adv. Atmos. Sci.* 17 (1), 18–30. doi:10.1007/s00376-000-0040-7

Cohen, J., and Rind, D. (1991). The Effect of Snow Cover on the Climate. *J. Clim.* 4 (7), 689–706. doi:10.1175/1520-0442(1991)004<0689:teosco>2.0.co;2

Ding, Y., Sun, Y., Wang, Z., Zhu, Y., and Song, Y. (2009). Inter-decadal Variation of the Summer Precipitation in China and its Association with Decreasing Asian Summer Monsoon Part II: Possible Causes. *Int. J. Climatol.* 29 (13), 1926–1944. doi:10.1002/joc.1759

Estilow, T. W., Young, A. H., and Robinson, D. A. (2015). A Long-Term Northern Hemisphere Snow Cover Extent Data Record for Climate Studies and Monitoring. *Earth Syst. Sci. Data* 7 (1), 137–142. doi:10.5194/essd-7-137-2015

Harris, I., Jones, P. D., Osborn, T. J., and Lister, D. H. (2014). Updated High-Resolution Grids of Monthly Climatic Observations - the CRU TS3.10 Dataset. *Int. J. Climatol.* 34 (3), 623–642. doi:10.1002/joc.3711

Jia, X., Zhang, C., Wu, R., and Qian, Q. (2021). Influence of Tibetan Plateau Autumn Snow Cover on Interannual Variations in spring Precipitation over Southern China. *Clim. Dyn.* 56 (3), 767–782. doi:10.1007/s00382-020-05497-8

Kalnay, E., Kanamitsu, M., Kistler, R., Collins, W., Deaven, D., Gandin, L., et al. (1996). The NCEP/NCAR 40-year Reanalysis Project. *Bull. Amer. Meteorol. Soc.* 77 (3), 437–471. doi:10.1175/1520-0477(1996)077<0437:tnyrp>2.0.co;2

Karl, T. R., Groisman, P. Y., Knight, R. W., and Heim, R. R. (1993). Recent Variations of Snow Cover and Snowfall in North America and Their Relation to Precipitation and Temperature Variations. *J. Clim.* 6 (7), 1327–1344. doi:10.1175/1520-0442(1993)006<1327:rvosca>2.0.co;2

Li, W., Guo, W., Qiu, B., Xue, Y., Hsu, P. C., and Wei, J. (2018). Influence of Tibetan Plateau Snow Cover on East Asian Atmospheric Circulation at Medium-Range Time Scales. *Nat. Commun.* 9 (1), 4243–4249. doi:10.1038/s41467-018-06762-5

Lin, H., and Wu, Z. (2011). Contribution of the Autumn Tibetan Plateau Snow Cover to Seasonal Prediction of North American winter Temperature. *J. Clim.* 24 (11), 2801–2813. doi:10.1175/2010jcli3889.1

Liu, G., Wu, R., Zhang, Y., and Nan, S. (2014). The Summer Snow Cover Anomaly over the Tibetan Plateau and its Association with Simultaneous Precipitation over the Mei-Yu-Baiu Region. *Adv. Atmos. Sci.* 31 (4), 755–764. doi:10.1007/s00376-013-3183-z

Neale, R. B., Chen, C. C., Gettelman, A., Lauritzen, P. H., Park, S., Williamson, D. L., et al. (2010). Description of the NCAR Community Atmosphere Model (CAM 5.0). *NCAR Tech. Note Ncar/tn-486+ STR* 1 (1), 1–12.

Qian, Q., Jia, X., and Wu, R. (2019). Changes in the Impact of the Autumn Tibetan Plateau Snow Cover on the Winter Temperature over North America in the Mid-1990s. *J. Geophys. Res. Atmos.* 124 (19), 10321–10343. doi:10.1029/2019jd030245

Rodwell, M. J., and Hoskins, B. J. (1996). Monsoons and the Dynamics of Deserts. *Q.J R. Met. Soc.* 122 (534), 1385–1404. doi:10.1002/qj.49712253408

Schlögl, S., Lehning, M., and Mott, R. (2018). How Are Turbulent Sensible Heat Fluxes and Snow Melt Rates Affected by a Changing Snow Cover Fraction. *Front. Earth Sci.* 6, 154. doi:10.3389/feart.2018.00154

Wang, B., Bao, Q., Hoskins, B., Wu, G., and Liu, Y. (2008). Tibetan Plateau Warming and Precipitation Changes in East Asia. *Geophys. Res. Lett.* 35 (14), 1–5. doi:10.1029/2008gl034330

Wang, B., Wu, R., and Lau, K.-M. (2001). Interannual Variability of the Asian Summer Monsoon: Contrasts between the Indian and the Western North Pacific-East Asian Monsoons*. *J. Clim.* 14 (20), 4073–4090. doi:10.1175/1520-0442(2001)014<4073:ivotas>2.0.co;2

Wang, C., Yang, K., Li, Y., Wu, D., and Bo, Y. (2017). Impacts of Spatiotemporal Anomalies of Tibetan Plateau Snow Cover on Summer Precipitation in Eastern China. *J. Clim.* 30 (3), 885–903. doi:10.1175/jcli-d-16-0041.1

Wang, M., Jia, X. J., Ge, J. W., and Qian, Q. F. (2019). Changes in the Relationship between the Interannual Variation of Eurasian Snow Cover and spring SAT over Eastern Eurasia. *J. Geophys. Res. Atmos.* 124 (2), 468–487. doi:10.1029/2018jd029077

Wang, Z., Wu, R., Chen, S., Huang, G., Liu, G., and Zhu, L. (2018b). Influence of Western Tibetan Plateau Summer Snow Cover on East Asian Summer Rainfall. *J. Geophys. Res. Atmos.* 123 (5), 2371–2386. doi:10.1002/2017jd028016

Wang, Z., Wu, R., Duan, A., and Qu, X. (2020). Influence of Eastern Tibetan Plateau spring Snow Cover on North American Air Temperature and its Interdecadal Change. *J. Clim.* 33 (12), 5123–5139. doi:10.1175/jcli-d-19-0455.1

Wang, Z., Wu, R., and Huang, G. (2018a). Low-frequency Snow Changes over the Tibetan Plateau. *Int. J. Climatol* 38 (2), 949–963. doi:10.1002/joc.5221

Wei, W., Zhang, R., Wen, M., Kim, B.-J., and Nam, J.-C. (2015). Interannual Variation of the South Asian High and its Relation with Indian and East Asian Summer Monsoon Rainfall. *J. Clim.* 28 (7), 2623–2634. doi:10.1175/jcli-d-14-00454.1

Wu, R. (2002). A Mid-latitude Asian Circulation Anomaly Pattern in Boreal Summer and its Connection with the Indian and East Asian Summer Monsoons. *Int. J. Climatol.* 22 (15), 1879–1895. doi:10.1002/joc.845

Wu, R., and Kirtman, B. P. (2007). Observed Relationship of spring and Summer East Asian Rainfall with winter and spring Eurasian Snow. *J. Clim.* 20 (7), 1285–1304. doi:10.1175/jcli4068.1

Wu, R., Liu, G., and Ping, Z. (2014). Contrasting Eurasian spring and Summer Climate Anomalies Associated with Western and Eastern Eurasian spring Snow Cover Changes. *J. Geophys. Res. Atmospheres* 119 (12), 7410–7424. doi:10.1002/2014jd021764

Wu, R. (2017). Relationship between Indian and East Asian Summer Rainfall Variations. *Adv. Atmos. Sci.* 34 (1), 4–15. doi:10.1007/s00376-016-6216-6

Wu, R., and Wang, B. (2002). A Contrast of the East Asian Summer Monsoon–ENSO Relationship between 1962–77 and 1978–93. *J. Clim.* 15 (22), 3266–3279. doi:10.1175/1520-0442(2002)015<3266:acotea>2.0.co;2

Wu, Z., Li, J., Jiang, Z., and Ma, T. (2012). Modulation of the Tibetan Plateau Snow Cover on the ENSO Teleconnections: From the East Asian Summer Monsoon Perspective. *J. Clim.* 25 (7), 2481–2489. doi:10.1175/jcli-d-11-00135.1

Wu, Z., Zhang, P., Chen, H., and Li, Y. (2016). Can the Tibetan Plateau Snow Cover Influence the Interannual Variations of Eurasian Heat Wave Frequency. *Clim. Dyn.* 46 (11), 3405–3417. doi:10.1007/s00382-015-2775-y

Xiao, Z., and Duan, A. (2016). Impacts of Tibetan Plateau Snow Cover on the Interannual Variability of the East Asian Summer Monsoon. *J. Clim.* 29 (23), 8495–8514. doi:10.1175/jcli-d-16-0029.1

Yasunari, T., Kitoh, A., and Tokioka, T. (1991). Local and Remote Responses to Excessive Snow Mass over Eurasia Appearing in the Northern spring and Summer Climate. *J. Meteorol. Soc. Jpn. Ser.* 69 (4), 473–487. doi:10.2151/jmsj1965.69.4_473

You, Q., Wu, T., Shen, L., Pepin, N., Zhang, L., Jiang, Z., and AghaKouchak, A. (2020). Review of Snow Cover Variation over the Tibetan Plateau and its

Influence on the Broad Climate System. *Earth-Science Rev.* 201, 103043. doi:10.1016/j.earscirev.2019.103043

Zhang, R., Sun, C., Zhu, J., Zhang, R., and Li, W. (2020). Increased European Heat Waves in Recent Decades in Response to Shrinking Arctic Sea Ice and Eurasian Snow Cover. *NPJ Clim. Atmos. Sci.* 3 (1), 1–9. doi:10.1038/s41612-020-0110-8

Zhong, L., Ma, Y., Xue, Y., and Piao, S. (2019). Climate Change Trends and Impacts on Vegetation Greening over the Tibetan Plateau. *J. Geophys. Res. Atmospheres* 124 (14), 7540–7552. doi:10.1029/2019JD030481

Conflict of Interest: The authors declare that the research was conducted in the absence of any commercial or financial relationships that could be construed as a potential conflict of interest.

Publisher's Note: All claims expressed in this article are solely those of the authors and do not necessarily represent those of their affiliated organizations, or those of the publisher, the editors and the reviewers. Any product that may be evaluated in this article, or claim that may be made by its manufacturer, is not guaranteed or endorsed by the publisher.

frontiers in Earth Science

ORIGINAL RESEARCH
published: 26 November 2021
doi: 10.3389/feart.2021.761311

Diverse Inter-Annual Variations of Winter Siberian High and Link With Eurasian Snow in Observation and BCC-CSM2-MR Coupled Model Simulation

Chenghu Sun[1,2]*, *Jinqing Zuo*[3], *Xiaohui Shi*[1], *Xiangwen Liu*[3] and *Haiwen Liu*[4]

[1]Chinese Academy of Meteorological Sciences, Beijing, China, [2]Collaborative Innovation Center on Forecast and Evaluation of Meteorological Disasters, Nanjing University of Information Science & Technology, Nanjing, China, [3]Laboratory for Climate Studies, National Climate Center, China Meteorological Administration, Beijing, China, [4]Department of Aviation Meteorology, Civil Aviation University of China, Tianjin, China

An observational study illustrates that three distinct modes of winter Siberian high variability exist in observations at the inter-annual time scale. In this paper, we compare the connection between these diverse Siberian high variation modes with pre-autumn and simultaneous Eurasian snow cover in an observation and BCC-CSM2-MR coupled climate model run under pre-industrial conditions from the CMIP6 project. Our analyses indicate that the inter-annual variation of observed Siberian high modes do have a connection with pre-autumn and simultaneous Eurasian snow cover anomalies, but the BCC-CSM2-MR coupled climate model does not capture the observed diverse Eurasian snow–Siberian high relationships well. The BCC-CSM2-MR coupled climate model can partly reproduce the observed Siberian high variation modes, but fail to capture the spatial distribution and statistics of boreal fall and winter Eurasian snowpack, which is a key facet of simulated diverse Siberian high variability irrespective of the influence of Eurasian snow cover.

Keywords: Siberian high, diverse inter-annual variation, Eurasian snow, CMIP6, BCC-CSM2-MR coupled model

OPEN ACCESS

Edited by:
Renguang Wu,
Zhejiang University, China

Reviewed by:
Shangfeng Chen,
Institute of Atmospheric Physics (CAS), China
Kunhui Ye,
Uppsala University, Sweden

***Correspondence:**
Chenghu Sun
sunch@cma.gov.cn

Specialty section:
This article was submitted to Atmospheric Science, a section of the journal Frontiers in Earth Science

Received: *19 August 2021*
Accepted: *01 November 2021*
Published: *26 November 2021*

Citation:
Sun C, Zuo J, Shi X, Liu X and Liu H (2021) Diverse Inter-Annual Variations of Winter Siberian High and Link With Eurasian Snow in Observation and BCC-CSM2-MR Coupled Model Simulation. Front. Earth Sci. 9:761311. doi: 10.3389/feart.2021.761311

INTRODUCTION

The Siberian high (SH) is the most conspicuous pressure system found in the Northern Hemisphere during wintertime (Lydolf, 1977). The strong radiative cooling over the Eurasian snow cover forms a cold-core high-pressure system in the lower troposphere over the Mongolia plateau (e.g., Cohen et al., 2001; Gong and Ho, 2002; Panagiotopoulos et al., 2005). A stronger SH could result in a higher frequency of cold surges over East Asia to decrease the temperature and generate heavy snow (Ding and Krishnamurti, 1987; Ding, 1990). Thus, SH is a primary factor of determining strength of the East Asian Winter Monsoon (EAWM) circulation. Previous studies have found that the variation of SH intensity is impacted by a number of factors, such as the Arctic Oscillation (AO), North Atlantic Oscillation (NAO), high-pressure ridge around the Ural mountains (Joung and Hitchman, 1982; Takaya and Nakamura, 2005a, Takaya and Nakamura, 2005b; Wang B. et al., 2010; Sun et al., 2016), Eurasian snow cover (Foster et al., 1983; Cohen and Fletcher, 2007; Cohen et al., 2012; Ghatak et al., 2012), and sea surface temperature (SST) anomalies in the North Atlantic. (e.g., Li, 2004; Li and Lan, 2017). Among them, interaction between the snow cover and the overlying atmospheric circulation remains a challenging issue (Henderson et al., 2018).

Snow is an important component of the hydroclimate system. Variations of snow cover can modulate radiative, moisture, and heat exchanges between the atmosphere and land surface. Physically, snow cover could affect the atmospheric circulation through altering surface albedo and soil moisture during the melting process (Hahn and Shukla 1976; Groisman et al., 1994; Barnett et al., 1989; Cohen and Rind, 1991; Dutra et al., 2011; Mu and Zhou., 2015; Zhang et al., 2017; Henderson et al., 2018). Therefore, the interaction between snow in local and remote atmospheric dynamics has been an interesting research subject (e.g., Henderson et al., 2018). Previous studies have found that the inter-annual variation of Eurasian snow cover is influenced by atmospheric circulation such as weather pattern, NAO, the mid-latitude Rossby wave train, and Arctic moisture transportation (e.g., Clark et al., 1999; Bulygina et al., 2009; Henderson and Leathers, 2010; Zuo et al., 2011; Wegmann et al., 2015; Ye et al., 2015; Ye and Lau, 2016; Ye and Wu, 2017; Sun et al., 2019). Other studies have suggested that the Eurasian snow has sufficient potential to alter the large-scale atmospheric circulation in the following winter, which affects sea level pressure (SLP) over vast areas of Northern Eurasia to exert impact on SH intensity (Cohen and Entekhabi, 1999; Cohen et al., 2001, 2007; Saito et al., 2001; Fletcher et al., 2009; Orsolini and Kvamstø, 2009; Luo and Wang, 2019). Recent results have shown that the inter-annual variation in SH exhibits three dominant modes (e.g., Jia et al., 2018; Liu et al., 2019; Zhu et al., 2019), the uniform mode, the north–south dipole mode, and the east–west dipole mode. These modes have diverse spatial features and thus different impact on East Asian winter climate. However, the connection between the spatial variations in SH and Eurasian snow anomalies in pre-autumn and simultaneous winter has received little attention and remains unclear.

The Eurasian snow–mid-latitude circulation (e.g., AO and SH) relationship has been reproduced in modeling experiments forced with Eurasian snow cover anomalies (e.g., Gong et al., 2003; Cohan and Fletcher. 2007; Fletcher., 2009; Allen and Zender 2010, 2011; Peings et al., 2012). Modeling experiment success, however, arises only when prescribing the observed snow variability, while the coupled models cannot reproduce the snow–mid-latitude circulation relationship with internally generated snow anomalies (e.g., Hardiman et al., 2008; Allen and Zender 2011; Furtado et al., 2015). For example, Furtado et al. (2015) demonstrated that coupled CMIP5 models are unable to reproduce the snow–AO dynamical links, echoing similar results from Hardiman et al. (2008) for the CMIP3 models. They claimed that the coupled CMIP5 models underestimate the variability of October Eurasian snow cover and thus do not simulate lagged winter atmospheric responses to October Eurasian snow cover variability. However, along with improvement of model physics and resolution, whether the state-of-the-art climate model can reproduce the snow–mid-latitude circulation relationship remains unclear.

In this study, we intend to examine the connection between Eurasian snow anomalies with diverse winter SH modes of inter-annual variability in observations during 1979–2019 and the BCC-CSM2-MR coupled climate model simulations. BCC-CSM2-MR is a coupled climate model developed by the Beijing Climate Center (BCC). This model participates in the current Coupled Model Inter-comparison Project, CMIP6, and the sub-seasonal to seasonal (S2S) prediction project and also provides routine seasonal forecasts (Liu et al., 2019; Liu et al., 2021; Zhu et al., 2021). The evaluation indicates that BCC-CSM2-MR shows better performance in the tropospheric air temperature and circulation in East Asia and Indian monsoon region (e.g., Wu et al., 2019; Kumar and Sarthi, 2021). Whether this newly developed climate model of BCC has any ability to reproduce the observed snow–mid latitude circulation connection in winter is still unknown, and the associated evaluated results are important to further improve the seasonal prediction skill of the BCC climate system model. We attempt to address the following issues: the lead-concurrent relationship between Eurasian snow anomalies and the diverse winter SH modes in observations at an inter-annual timescale during 1979–2019, and whether the lead-concurrent relationship can be captured by the BCC-CSM2-MR coupled climate model.

The observation and BCC-CSM2-MR coupled climate model datasets applied in the study are described in **Section 2**. In **Section 3**, we depict the major inter-annual variation modes of SH and explore their relationships with Eurasian snow cover conditions. In **Section 4**, we further explore the simulated inter-annual variations of SH in the BCC-CSM2-MR coupled climate model, their possible relationships with simulated snow, and the possible causes for the lack of snow–SH connection in the BCC-CSM2-MR coupled climate model. The summary of results is presented in **Section 5**.

DATA, METHOD, AND COUPLED MODEL OUTPUT

The observational dataset used for comparison with model output is the ERA5 (Hersbach., 2020). The monthly mean values from 1979 to 2019 of several atmospheric variables such as geopotential height, surface air temperature, sea level pressure (SLP), snow fall, and snow depth are studied with a focus on the boreal winter season (i.e., December–January–February). Version 4 of the Northern Hemisphere EASE-Grid 2.0 snow cover (Brodzik and Armstrong 2013) used in this study is obtained from the National Snow and Ice Data Center (http://nsidc.org/data/) with the original weekly data at a grid cell size of 25 km × 25 km, which has been converted to monthly mean with 1 × 1 spatial resolution, and the newly released GlobSnow v3.0 Northern Hemisphere snow water equivalent dataset for the period of 1979–2018 is also used (Luojus et al., 2021). The AO, East Atlantic/Western Russia (EA/WR), and Polar/Eurasia (POLEUR) teleconnection indices are provided by the Climate Prediction Center (CPC). The seasonal means are calculated from monthly values, and anomalies are computed relative to the means of entire periods. To retain the inter-annual variability, the 9-year low-pass components using the Gaussian-type filter is removed for all variables. The SH intensity index (SBI) is defined after Gong et al. (2001). The North's significance test is used to determine the confidence level of statistics in Empirical Orthogonal Function (EOF) analysis (North et al., 1982).

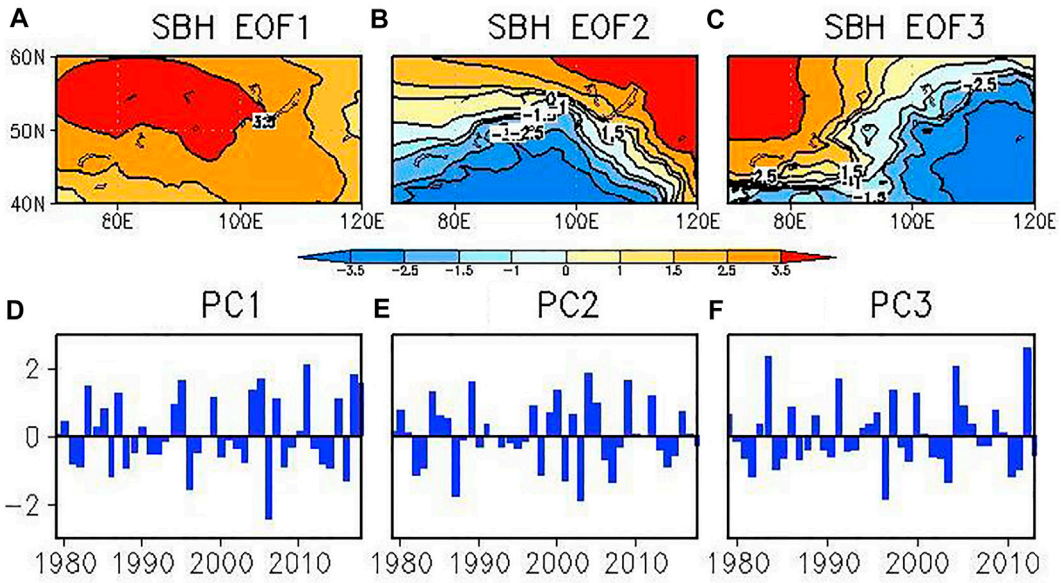

FIGURE 1 | Spatial patterns and corresponding principal components of the first **(A,D)**, second **(B,E)**, and third **(C,F)** EOF mode of winter-mean SLP in the Siberian high domain (40–60°N, 70–120°E) in 1979–2019 for ERA5 Reanalysis.

Singular value decomposition analysis (SVD) is employed for identifying the temporal co-variability between two climatic spatial fields (Bretherton et al., 1992), and the Monte Carlo approach (Czaja and Frankignoul, 2002) is used to evaluate the significance of statistics in the SVD method. To estimate the transient eddy response of mid-latitude circulation to snow cover anomalies, the synoptic eddy vorticity feedback to the anomalous low-frequency flow is analyzed as Lau and Holopainen (1984).

Simulations from the BCC-CSM2-MR model are used to diagnose the presence of the modeled Eurasian snow–SH mechanism. The BCC-CSM2-MR model is an atmosphere–land–ocean–sea ice coupled model. The atmosphere component is the BCC Atmospheric General Circulation Model version 3 with T106 triangular truncation (resolution of approximate 110 km) and 46 vertical hybrid sigma/pressure layers, top at 1.459 hPa. The land component is the BCC Atmosphere and Vegetation Interaction Model version 2 with T106 horizontal resolution and 10 soil layers. The ocean component is the GFDL Modular Ocean Model version 4 with varying horizontal resolutions of 1/3° (at the equator) to 1° (at the pole), and the sea-ice component is the GFDL Sea Ice Simulator with the same resolution as the ocean component. All components are coupled at a frequency of 30 min without any flux adjustment. Details of the BCC-CSM2-MR model and its general performance have been documented in Wu et al. (2019).

Similar to Furtado et al. (2015), we select the coupled climate model output from a pre-industrial control (piControl) scenario (i.e., prescribed, non-evolving greenhouse gas concentrations and aerosols mimicking conditions prior to 1850 are the primary forcings) for analysis in this work. The advantages of choosing piControl scenario over other simulations are its long integrations (600 years of model output) and its exclusion of anthropogenic effects that could influence the studied relationship. Model atmospheric variables analyzed are identical to those from observations.

TABLE 1 | Correlation coefficient of Siberian High intensity index (SHI), AO, POLEUR, and EAWR teleconnection indices with the PCs of SH modes. The bold italic font indicates the value exceeding the 95% confidence level.

ACC	SHI	AO	POLEUR	EAWR
SH-PC1	**0.90**	/	/	**0.50**
SH-PC2	−0.06	**−0.40**	**/**	/
SH-PC3	−0.10	/	**−0.39**	**/**

DIVERSE SH INTER-ANNUAL VARIATION MODES AND THEIR CONNECTIONS WITH EURASIAN SNOW COVER IN OBSERVATIONS

Figure 1 depicts the first three leading EOF modes of wintertime sea level pressure anomalies over the SH domain (40°N–60°N, 60°E–120°E) for the 1979–2019 period. The first leading EOF mode (referred to as SH-EOF1, hereafter) accounts for about 65% of the total variance, which is characterized by a uniform variation over the whole SH region to represent the intensity variation of SH (**Table 1**). The second leading EOF mode (SH-EOF2) accounts for about 14.1% of the total variance, and its horizontal structure shows a north–south seesaw pattern in SLP anomalies. The third leading EOF mode (SH-EOF3) shows a

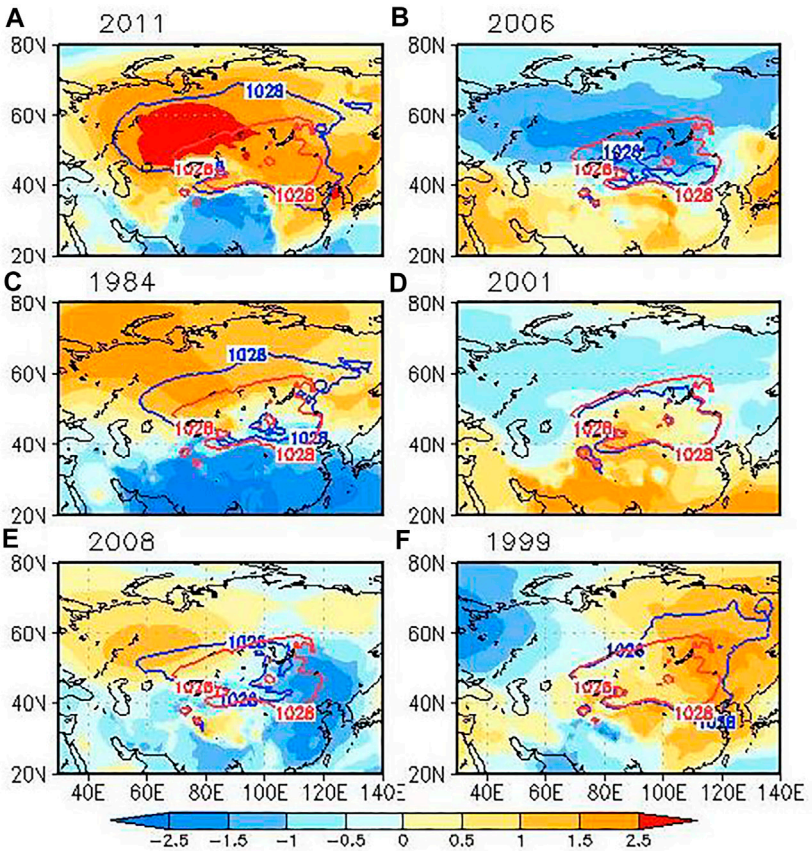

FIGURE 2 | The distribution of the 1,028-hPa SLP contour in typical cases of the SH-EOF1 mode (blue line; **A,B**), the SH-EOF2 mode (blue line; **C,D**), and the SH-EOF3 mode (blue line; **E,F**). The climate mean 1,028-hPa SLP contour is represented by the red line and the standardized anomalies of SLP are shaded.

west–east seesaw pattern, which accounts for about 10.2% of the total variance. The three SH-EOF modes are well distinguished from each other according to the rule of North et al. (1982). **Figures 1D–F** display the principal components (PC) of the three SH EOF modes, and they exhibit notable interannual variations during the 1979–2019 period.

To further illustrate diverse features of the three SH-EOF modes, the typical anomaly SH cases for each mode are shown in **Figure 2**. The SH defined by the outline of 1,028 hPa SLP (Liu and Zhu, 2020) is quite similar to that defined by 1,030 hPa as Wu and Wang (2002) except for the discontinuation of the climatological 1,030 hPa contour over the SH domain. **Figures 2A,B** show a typical case in positive (negative) phase of the SH-EOF1 mode; that is, the enhanced (weakened) SH is notable along with enlarged (shrinked) SH extension in 2011 (2006). For the typical cases of the SH-EOF2 mode in 1984 (**Figure 2C**) and 2001 (**Figure 2D**), it represents northward or southward shift of the SH, respectively. In contrast, for the typical cases of SH-EOF3 mode in 2008 (**Figure 2E**) and 1999 (**Figure 2F**), it shows a westward displacement and eastward stretch of the SH, respectively.

Figure 3 displays the wintertime upper- and low-level large-scale tropospheric circulation associated with the SH-EOF modes. The SLP anomalies associated with the SH-EOF1 mode are characterized by positive anomalies over a broad region from the Arctic to the Siberian plateau, implying a stronger-than-normal Siberian–Mongolian high (**Figure 3A**). Consistently, positive 500-hPa geopotential height anomalies extend southward from the Arctic to the Ural Mountains (**Figure 3B**). In the mid-latitudes, two major negative anomaly centers are located in the central Europe and northeastern East Asia, separately. This distribution of geopotential height anomalies resembles the EA/WR teleconnection pattern as indicated by Chen et al. (2019), and the SH-PC1 has a correlation coefficient of 0.50 with the EA/WR index (**Table 1**), which is significant at the 95% confidence level. The EA/WR like pattern is accompanied by an upper-level blocking ridge over the Ural Mountains and a deepened trough off the east coast of East Asia, providing favorable dynamical conditions for the southward intrusion of mid–high latitude cold air into East Asia (e.g., Wu and Chan, 1997; Wang B. et al., 2010; Wang L. et al., 2010).

For the SH EOF2 (**Figure 3C**), the associated positive SLP anomalies occupy a broad region from the Arctic to the northern Siberian plateau and opposite anomalies occur over the southern Siberian plateau. For the winter 500-hPa geopotential height field

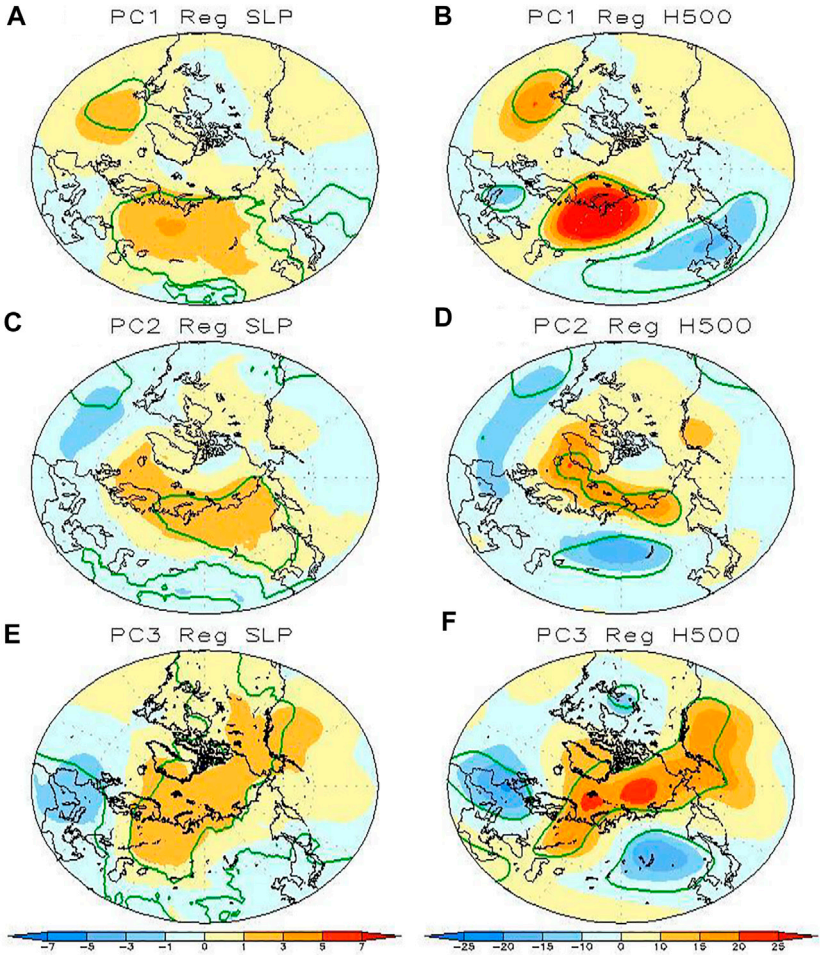

FIGURE 3 | Regressed anomalies of DJF **(A)** SLP (shading, units: hPa), **(B)** 500 hPa geopotential height (shading, units: m) onto the PC1 index, **(C,D)** onto the PC2 index, and **(E,F)** onto the PC3 index. The green line indicates the value significantly exceeding the 95% confidence level.

(**Figure 3D**), negative anomalies are evident over most of the Eurasian continent and opposite anomalies over the Arctic Ocean, the pattern of which is similar to the negative phase of AO to some extent (e.g., Chen et al., 2014, 2016). The correlation coefficient between the SH-PC2 and AO index is approximately −0.40, exceeding significance at the 95% confidence level (see **Table 1**). Comparison of **Figures 3C,D** indicates that the atmospheric circulation anomalies associated with the SH-EOF2 exhibits a notable baroclinic structure in the mid–high latitude.

The SLP variation associated with the SH-EOF3 mode is characterized by a west–east dipole pattern, with positive anomalies over the western Siberian plateau and the Arctic Ocean and opposite anomalies over the eastern Siberian plateau (**Figure 3E**). The west–east dipole pattern is also clearly observed in the 500-hPa geopotential height field (**Figure 3F**), with a mild ridge over the western Siberian plateau and a trough over the Lake Baikal, which resembles the POLEUR teleconnection pattern (see **Table 1**).

Moreover, relationships between the surface air temperature anomalies and the three SH-EOF modes in winter are examined. Associated with variation of the SH-EOF1 mode, warming signal exceeding 1.0°C occurs over the Arctic and northern edge of the Eurasian continent and cold anomalies spread in the high-mid latitude Eurasian continent (**Figure 4A**). Associated with variation of the SH EOF2 mode, the appearance of warm surface air temperature anomalies is confined to the Arctic region, and cold anomalies exceeding −1.0°C dominate the mid-high latitude of the Eurasian continent (**Figure 4B**). Associated with the SH EOF3 mode (**Figure 4C**), cold temperature anomalies cover most of the mid-latitude of the Eurasian continent, whereas the milder warm temperature anomalies occur over the region to the south of 40°N and stretch northwestward to Lake Baikal.

There are several possible physical mechanisms in the Eurasian snow cover–SH connection: (1) The thermodynamical pathway: the expansion of the Eurasian snow cover in late autumn can persist into winter and cause a strong radiative cooling above the snow-covered surface over the Eurasian continent, which cools the surface and increases surface pressure to enhance the SH (e.g., Ding 1990; Cohen et al., 2001;

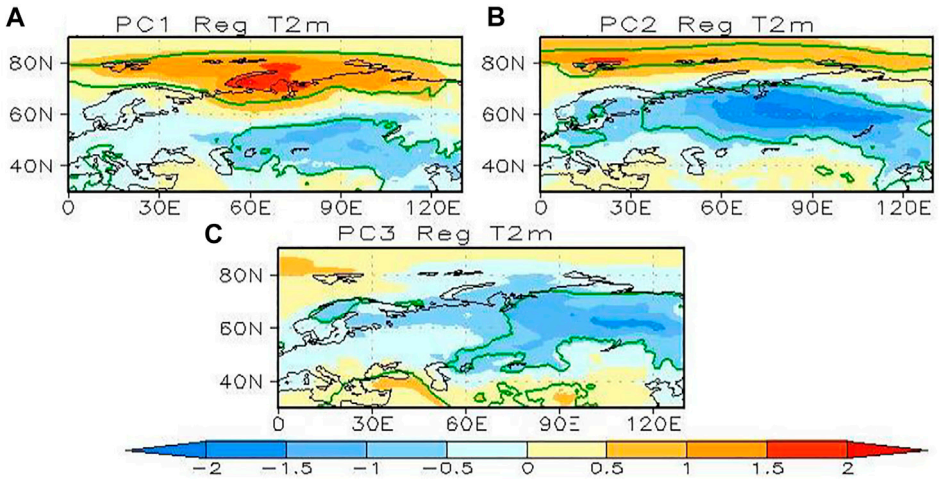

FIGURE 4 | Regressed anomalies of DJF T2m (shading, units: C) onto the **(A)** PC1, **(B)** PC2, and **(C)** PC3 index. The green line indicates the value significantly exceeding the 95% confidence level.

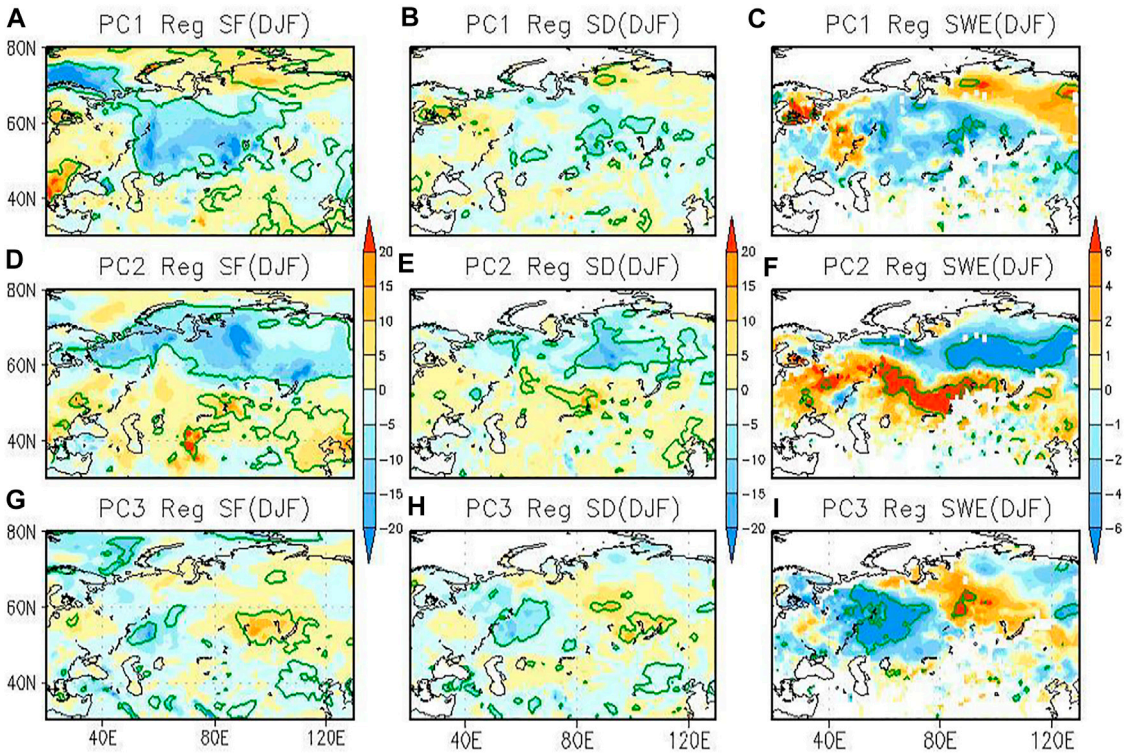

FIGURE 5 | Regressed anomalies of DJF **(A)** snow fall (shading, units: mm), **(B)** snow depth (shading, units: mm), and **(C)** snow water equivalent (shading, units: mm) onto PC1, **(D–F)** onto PC2, and **(G–I)** onto PC3. The green line indicates the value significantly exceeding the 95% confidence level.

Cohen et al., 2007; Jeong et al., 2011; Luo and Wang, 2019). (2) The troposphere–stratosphere interaction pathway: previous studies have suggested that the lower tropospheric anomalies associated with pre-autumn snow anomalies can amplify the downstream standing wave pattern and enhance the vertical wave propagation into the polar stratosphere through troposphere–stratosphere interaction to affect the mid-latitude circulation (e.g., AO) in late winter, which can also modulate SH variation (e.g., Henderson et al., 2018). Besides, several studies also found that the snow cover feedbacks start from radiative and

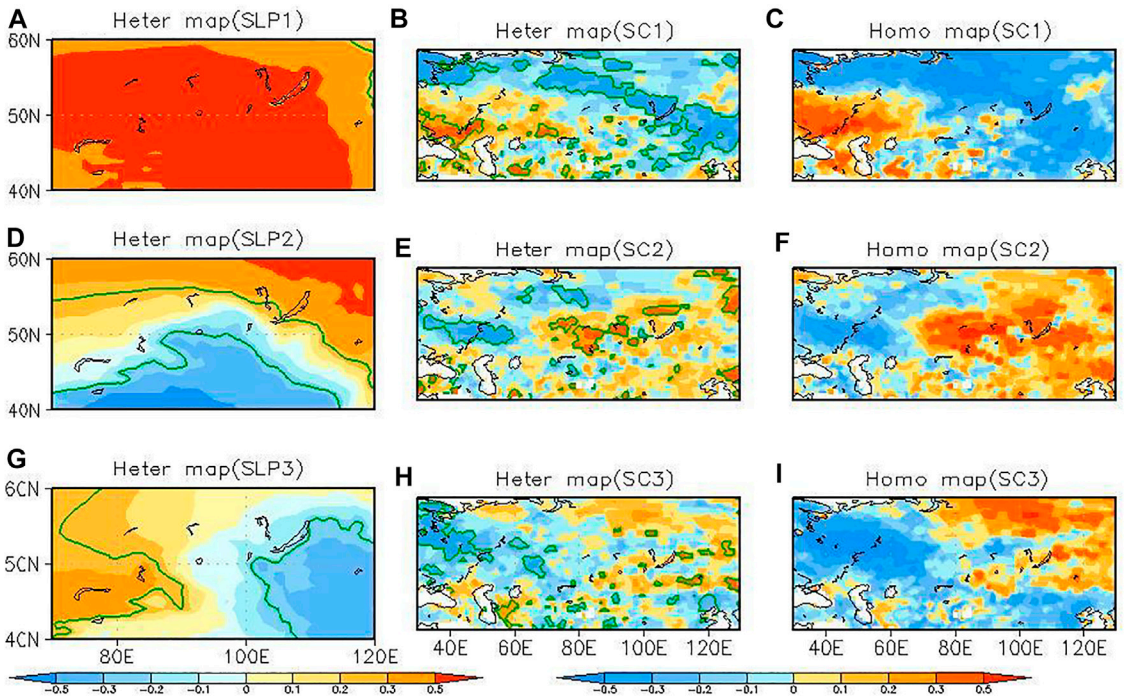

FIGURE 6 | Heterogeneous correlation coefficient maps of DJF SLP **(A)**, ON snow cover **(B)**, and homogeneous map of ON snow cover **(C)** in the first SVD mode of observations. **(D–F)** For the second SVD mode, **(E–F)** for the third SVD mode. The green line indicates the value significantly exceeding the 90% confidence level.

thermodynamical processes and then are amplified by the internal dynamics of the climate system (Clark et al., 1999; Cohen et al., 2007). The strong transient eddy forcing is important for connection of extratropical response to mid-latitude snow anomalies, which may impact the SH variation (Deser et al., 2007; Fletcher et al., 2009; Wu B. et al., 2011).

To examine the connection between the three SH modes and Eurasian snow cover variations, we present regression of their corresponding PCs onto the snowfall, snow depth, and snow water equivalent (SWE) anomalies in simultaneous winter. Associated with variation of the SH-EOF1 mode (**Figures 5A–C**), the less snow is observed over most areas of the Siberian plateau to the north of 45°N, in which the positive surface pressure anomalies are located (see **Figures 3A,B**), while more snow is over the region to its south, especially to the south of Lake Baikal where it is under the control of negative pressure anomalies. These features indicate that the SH-EOF1 mode dominates the local snow variations in simultaneous winter. Similar results are obtained for the EOF2 (**Figures 5D–F**) and EOF3 (**Figures 5G–I**) modes.

Furthermore, we detect the connection between pre-autumn snow anomalies and the three SH-EOF modes by applying the SVD method as Wu et al. (2011b). **Figure 6** displays the first three pairs of coupled SVD pattern of DJF SLP over the SH domain and (October–November) ON Eurasian snow cover anomalies for the period of 1979–2019. The first leading SVD mode describes decreased ON snow cover over most of the Eurasian continent, especially over the northern and eastern Siberian plateau, and increased snow cover over the southwestern Eurasia continent collated with a uniform enhanced SLP over the whole Siberian region as the SH-EOF1 mode (**Figures 6A–C**). The second most important pair of coupled SVD patterns is characterized by increased ON snow cover over the eastern Eurasian continent and decreased snow cover over the western part co-varying with a northward shift of SH as the SH-EOF2 mode (**Figures 6D–F**). The third pair of coupled SVD patterns is characterized by increased ON snow cover over the northeastern Eurasian continent and decreased snow cover over the western part co-varying with a westward shift of SH as the SH-EOF3 mode (**Figures 6G–I**).

To reveal the physical connection among the above-mentioned three leading SVD modes, we firstly analyze the possible influence of SVD SC1 snow cover mode on the ON, DJF snow depth, and H500 synoptic eddy-vorticity forcing by regressing the expansion coefficient time series of SVD-SC1 onto them. The features in **Figures 6B,C** are also evident in snow depth anomalies of later autumn and the following winter (**Figures 7A,B**). The distribution pattern of snow anomalies modulates the mid-latitude circulation resembled to EA/WR teleconnection pattern through synoptic eddy-vorticity response (**Figure 7C**), which further modulates the occurrence of the SH-EOF1 mode as in **Figures 3A,B**; **Table 1**. With the influence of the SVD-SC2 mode (**Figures 6E,F**), previous studies have found that the positive snow cover anomalies over the eastern Siberian plateau would force negative AO phase through troposphere–stratospheric circulation interaction. As AO-like response has been well studied, we will only examine the associated evolution of circulation in troposphere and

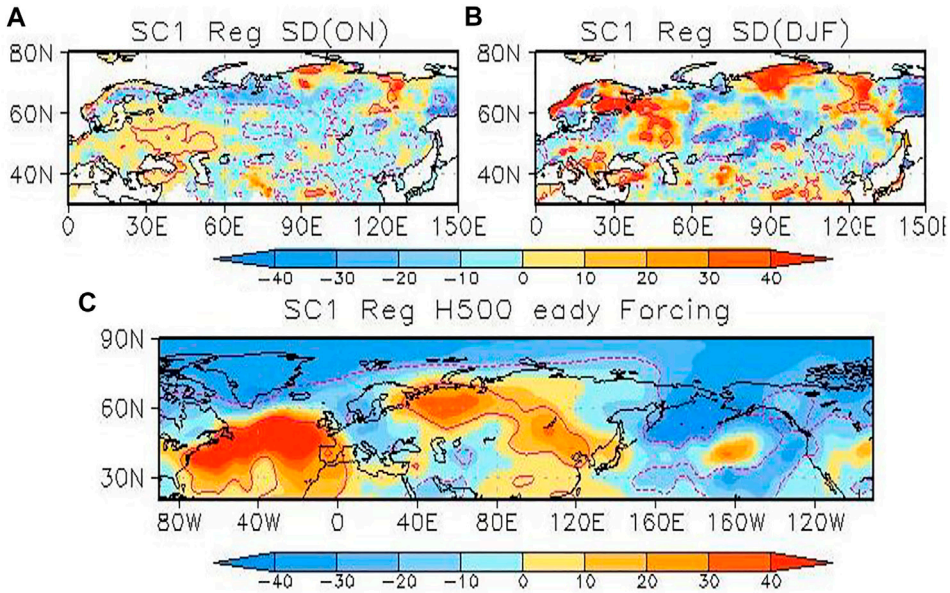

FIGURE 7 | Regressed anomalies of ON **(A)**, **(B)** DJF snow depth (shading, units: mm), and **(C)** H500 synoptic eddy-vorticity forcing onto expansion coefficient time series of snow cover in the first SVD mode. The red line indicates the value significantly exceeding the 90% confidence level.

stratosphere to illustrate the possible connections. **Figure 8** displays the regressed maps of ON and DJF 50-hPa geopotential height upon the time series of SVD-SC2 expansion coefficient. In ON, the 50-hPa geopotential height anomalies show a dipole-like structure (**Figure 8A**), with development of positive height anomalies over the North Atlantic–North American sector. In the following winter (**Figure 8B**), the above circulation structures remain visible at the middle and high latitudes. The above spatial distribution of stratospheric circulation changes is collocated with a wave 1 pattern. At H500 (**Figures 8C,D**), the blocking-type ridge is developed in the Ural Mountain region in later autumn, and it has been documented that the frequent and persistent episodes of blocking in the Ural Mountain region are likely to contribute to vertical planetary wave propagation with wavenumber-1 and wavenumber-2 components (Charney and Drazin 1961; Garfinkel et al., 2010; Mori et al., 2014). With enhanced propagation of the vertical wave into the polar stratosphere trough troposphere–stratospheric circulation interaction in the following winter, it finally affects the mid-latitude circulation as AO (**Figure 8D**) and further modulates the SH EOF-2 mode as in **Figures 3C,D**; **Table 1**. With the influence of the SVD-SC3 mode (**Figures 6H,I**), the enhanced snow cover over the northeastern Siberian Plateau and less snow cover over the Ural region persists from later autumn into winter (**Figures 9A,B**), and it modulates the mid-latitude circulation resembling the POLEUR teleconnection pattern through synoptic eddy-vorticity forcing response (**Figure 9C**), which further impacts the occurrence of SH-EOF 3 mode as in **Figures 3E,F**; **Table 1**.

Previous studies have found the linkage between Eurasian snow cover and the intensity of SH through both thermodynamic and troposphere–stratospheric circulation interaction pathway; however, the possible influence of snow cover on the spatial variation of SH received little attention. Our statistical analysis indicates that the possible connections between pre-autumn snow cover and three different types of SH variation mode is mainly through the transient eddy response mechanism and troposphere–stratospheric circulation interaction. In simultaneous winter, we find that the SH variation modes act to force the anomaly distribution of Eurasian snow cover.

SH AND EURASIAN SNOW CONNECTION IN BCC-CSM2-MR COUPLED SIMULATIONS

To examine whether the BCC-CSM2-MR coupled climate model has any ability to reproduce the observed Eurasian snow–SH connection, this section explores the diverse SH variation modes and their connections with the Eurasian snow cover in the 599-year piControl simulation from this model. **Figure 10** depicts the first three leading EOF modes of simulated winter SLP anomalies over the SH domain (40°N–60°N, 60°E–120°E) for the model years from 1850 to 2448. These three simulated EOF modes can be separated from each other according to the criterion of North et al. (1982). The simulated EOF1 mode accounts for 57.6% of the total variance (**Figure 10A**), which is characterized by a uniform variation in SLP over the whole region as that of observation. The simulated EOF2 mode accounts for 21.6% of the total variance (**Figure 10B**), and its horizontal structure depicts a northeast–southwest seesaw pattern in SLP variations, which is different from the observed EOF2 mode (i.e., the north–south seesaw pattern). The simulated EOF3 mode accounts for approximately 10.4% of the total variance (**Figure 10C**), and it

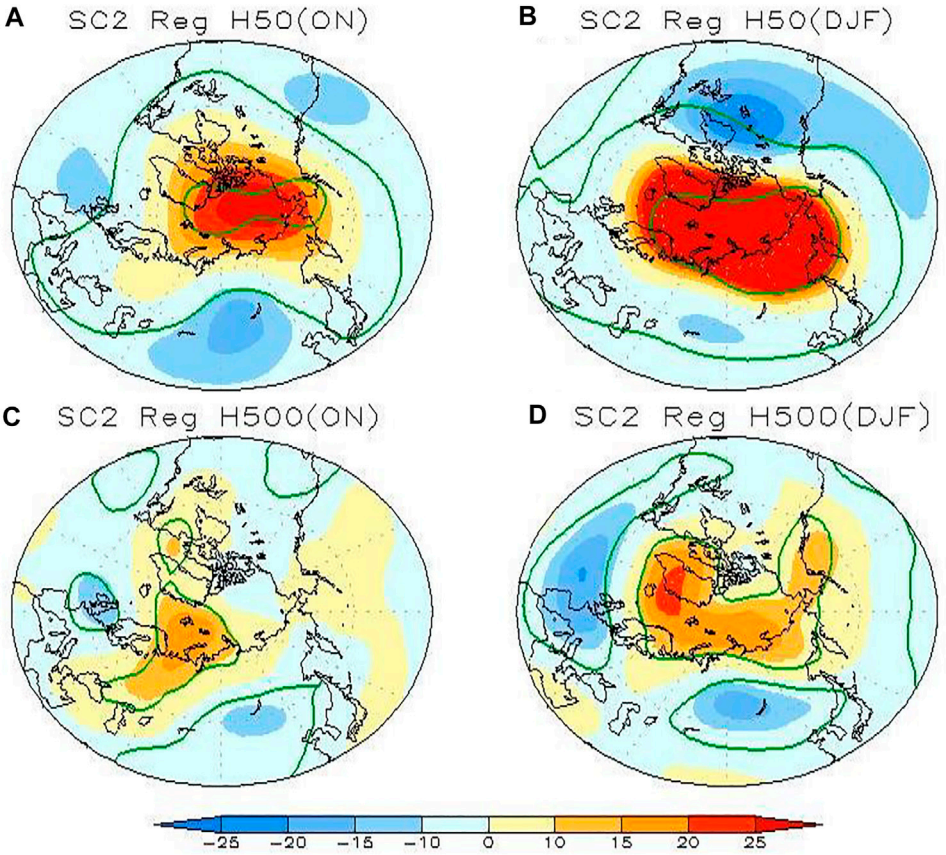

FIGURE 8 | Regressed anomalies of ON **(A)**, **(B)** DJF H50 geopotential height (shading, units: m), ON **(C)** and DJF **(D)** H500 geopotential height onto expansion coefficient time series of snow cover in the second SVD mode. The red line indicates the value significantly exceeding the 90% confidence level.

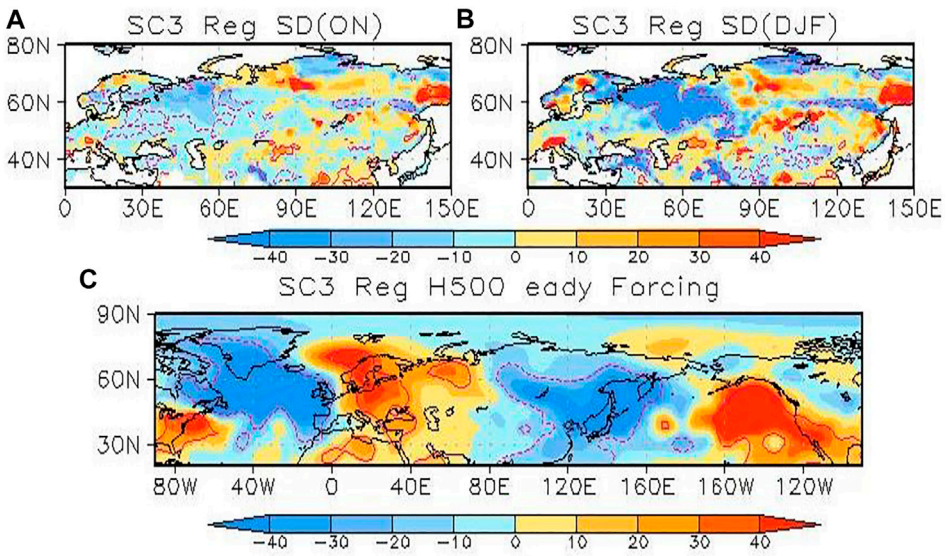

FIGURE 9 | Regressed anomalies of ON **(A)**, **(B)** DJF snow depth (shading, units: mm), and **(C)** H500 synoptic eddy-vorticity forcing onto expansion coefficient time series of snow cover in the third SVD mode. The red line indicates the value significantly exceeding the 90% confidence level.

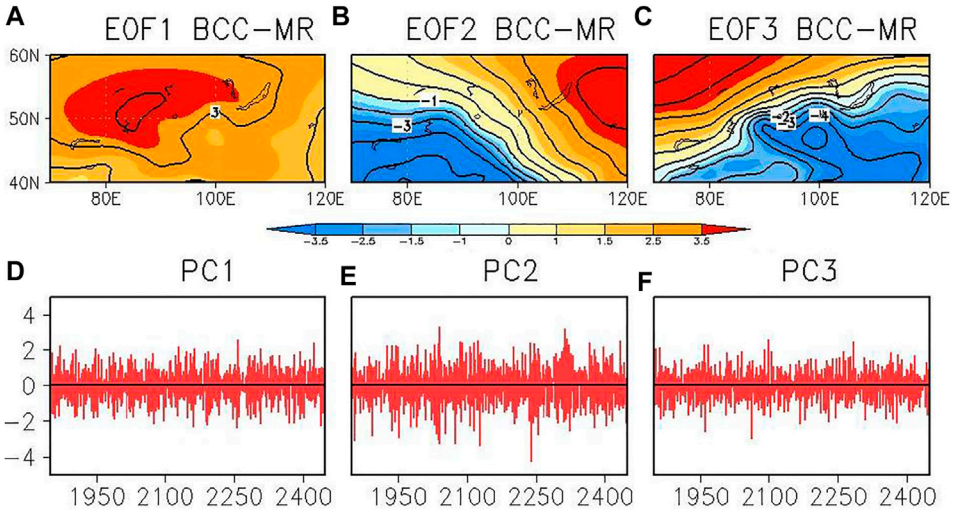

FIGURE 10 | Spatial patterns and corresponding principal components of the first **(A,D)**, second **(B,E)**, and third **(C,F)** EOF mode of winter-mean SLP in the Siberian high domain (40–60°N, 70–120°E) from the BCC-CSM2-MR model.

is characterized by a northwest–southeast seesaw pattern, which partly resembles the observed SH-EOF3 mode (i.e., the west–east seesaw pattern).

Figure 11 displays the large-scale tropospheric circulation associated with the abovementioned simulated SH modes in winter. Associated with variation in the simulated EOF1 mode (**Figure 11A**), positive SLP anomalies occurs over a broad region from the Arctic to the Siberian plateau as in the observation (**Figure 3A**). The simulated 500-hPa geopotential height anomalies show a wavy pattern over mid-high latitudes, with alternating positive and negative height centers of action over Central Europe, the northern Siberian plateau, and the northeastern East Asia (**Figure 11B**), the pattern of which is similar to that in observation (**Figure 3B**). Associated with variation in the simulated EOF2 mode, a similar east–west dipole pattern is observed in the SLP and 500-hPa geopotential height anomaly fields over the Eurasian continent (**Figures 11C,D**). The SLP and 500-hPa geopotential height anomalies associated with the simulated EOF3 mode both show a wavy pattern over the Eurasian mid–high latitudes (**Figure 11E**), with alternating positive and negative anomalies over southeastern Europe, the northern Siberian plateau–Arctic Ocean, and northeastern Asia. It is noticed that the overall structure of the 500-hPa geopotential height anomaly bears similarity between the simulated EOF1 and EOF3 modes, except that the latter shifts more northward to the higher latitude (**Figure 11F**).

Figure 12 shows relationships between the three simulated EOF modes and surface air temperature anomalies in winter. Associated with variation in the simulated EOF1 mode (**Figure 12A**), warming temperature anomalies between 0.5°C and 1.5°C occur over the Arctic and the northern edge of Eurasia, and cold anomalies occur over the Eurasian mid-latitudes, the pattern of which bears resemblance to that in observation (**Figure 4A**). For the simulated EOF2 mode, mild warm temperature anomalies of approximately 0.5°C appear over the Arctic region, while cold anomalies of approximately −0.5°C to−1.0°C occur over the northwestern Eurasian continent and extend eastward to Lake Baikal (**Figure 12B**). The pattern of surface air temperature anomalies associated with the simulated EOF3 mode is similar to that associated with the simulated EOF1 mode, but the warm temperature anomalies between 1°C and 1.5°C are confined to the Barents–Kara Sea and cold anomalies exceeding −1.0°C lie in central Siberia for the simulated EOF3 mode (**Figure 12C**).

Associated with variations in the simulated EOF1 mode (**Figures 13A–C**), reduced snow occurs over most of the Eurasian continent to the north of 40°N and increased snow to the south in winter. For the simulated EOF2 mode (**Figures 13D–F**), increased snow occurs over the southwestern Eurasian continent, while reduced snow is observed over central Siberia. The pattern of snow anomalies associated with the simulated EOF3 mode (**Figures 13G–I**) bears resemblance to that associated with the simulated EOF1 mode, with reduced snow over the northern Eurasia and increased snow to the south. Comparison of **Figures 11**, **13** indicates the direct modulation of atmospheric circulation on the underlying snow variations in the model simulation during winter, which is consistent with the observational result.

To examine the connection between precursory snow signal in late autumn over the Eurasian continent and SH in the following winter, an SVD analysis is also applied to the simulated ON snow cover and DJF SLP anomalies (**Figure 14**). It is indicated that the precursory snow signals for the three simulated SH modes are rather weak, with few areas exceeding significance at the 95% confidence level. In other words, the BCC-CSM2-MR coupled climate model cannot reproduce the observed autumn snow–winter SH connection. To verify whether the poor connection between the simulated SH in winter and Eurasian snow anomalies in the

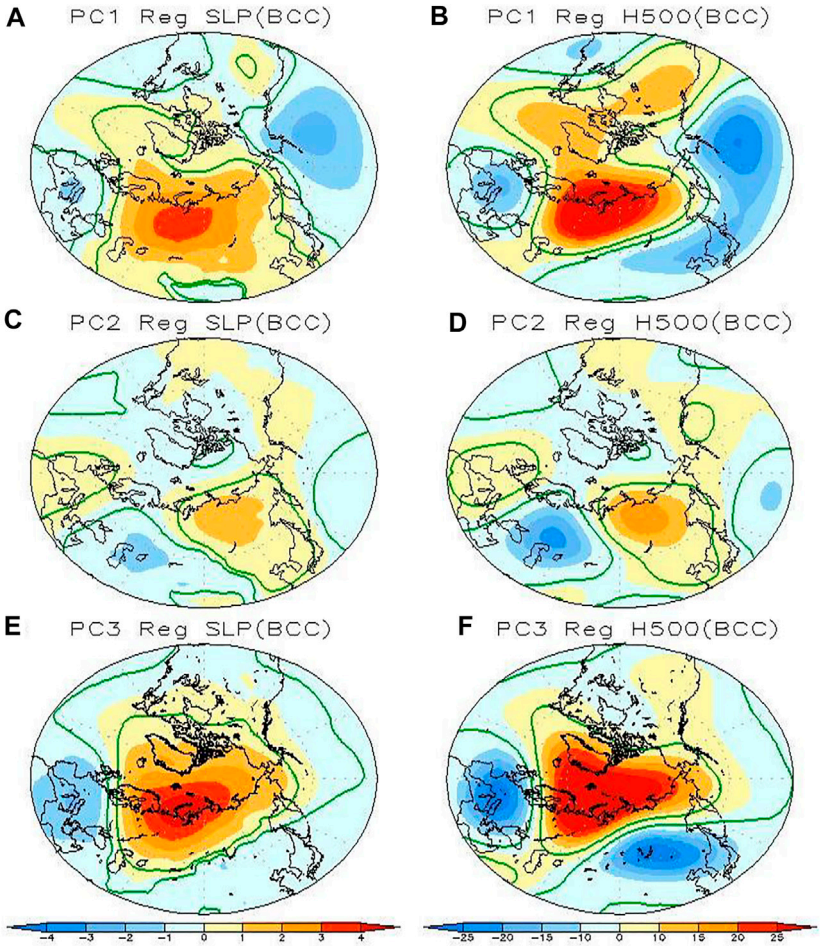

FIGURE 11 | Regressed anomalies of DJF **(A)** SLP (shading, units: hPa), **(B)** 500 hPa geopotential height (shading; units: m) onto the PC1, **(C,D)** PC2, and **(E,F)** PC3 index from the BCC-CSM2-MR model. The green line indicates the value significantly exceeding the 95% confidence level.

preceding autumn is stable, the 599-year expansion coefficient time series of the SVD modes are divided into 14 41-year subintervals and then the correlation coefficient between the expansion coefficient time series of the winter SLP and autumn snow cover anomalies is calculated for each subinterval (see **Figure 15**). It is found that insignificant correlation coefficient is observed for most of the subintervals, confirming the poor ability of the BCC-CSM2-MR model to reproduce the observed autumn snow–winter SH connection.

Previous studies have revealed that the poor relationship between Eurasian snow cover and winter AO variability in the CMIP5 coupled simulations may be attributed to the underestimation of snow cover and its inter-annual variability in the model (Derkson and Brown, 2012; Furtado et al., 2015). **Figure 16** presents the climatological late autumn snow cover fraction and snow depth in the observation (**Figures 16A,B**) and BCC-CSM2-MR simulations (**Figures 16C,D**). The spatial extent of snow cover fraction has notable differences between the observation and simulation (**Figures 16A,C**). In particular, the observation shows higher fraction (nearly 10%–20% higher) of snow cover over the northern Siberia and the mid-latitude belts between 40 and 50°N over Eurasia. Difference in snow depth between the observation and simulations is also evident; that is, the BCC-CSM2-MR model generally overestimates the snow depth over the area to the north of 50°N (**Figures 16B,D**).

The spatial pattern of standard deviation of snow cover fraction between the simulation and observation is rather different (**Figures 16E,G**). The standard deviation is generally overestimated over the region from Eastern Europe to the central Siberian plateau and underestimated over the eastern Siberian plateau in the simulations. The standard deviation of the simulated snow depth is generally overestimated when compared to the observation (**Figures 16F,H**). It is also noted that the SVD modes of autumn snow cover in observation and model simulation are rather different (**Figures 6**, **14**). The snow deficiency may be related to precipitation generation and/or land-surface parameterizations for accumulating snowfall in the model. Poor snowfall and snow cover representation in the BCC-CSM2-MR model results in weak or incorrect dynamical responses in the atmosphere. Future modeling studies should focus on assessing this snow cover/snowfall issue.

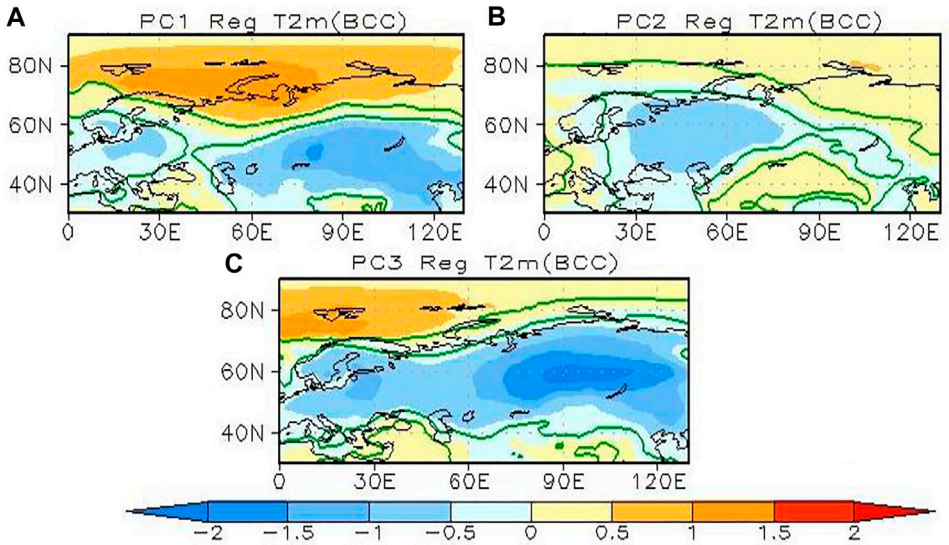

FIGURE 12 | Regressed anomalies of DJF T2m (shading, units: °C) onto the simulated **(A)** PC1, **(B)** PC2, and **(C)** PC3 index from the BCC-CSM2-MR model. The green line indicates the value significantly exceeding the 95% confidence level.

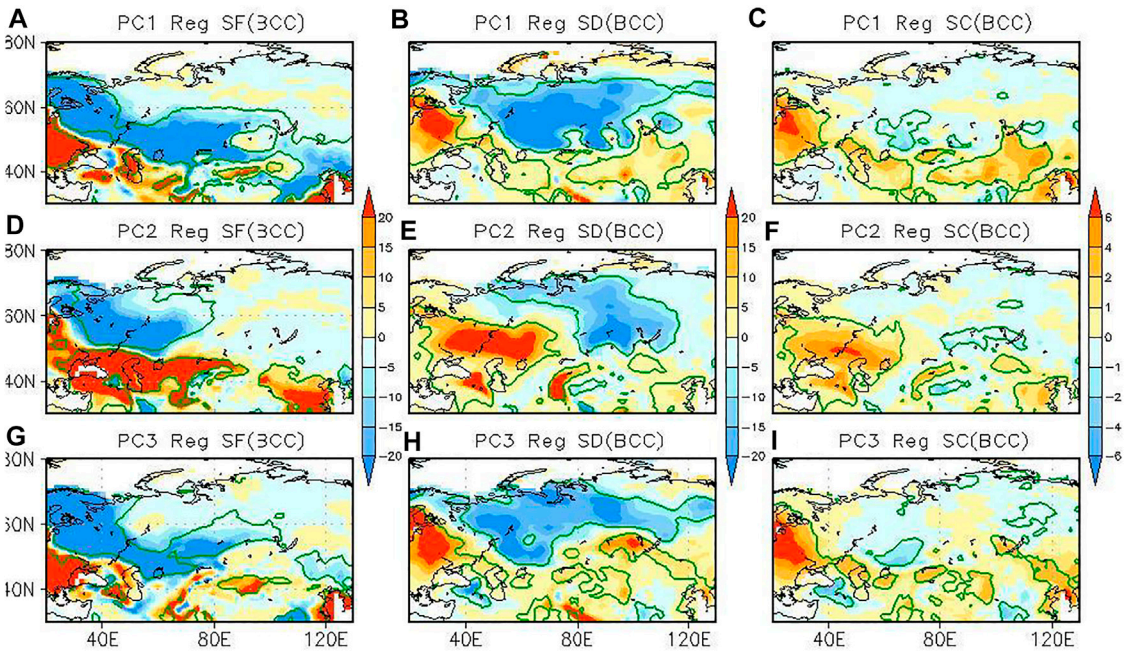

FIGURE 13 | Regressed anomalies of DJF **(A)** snow fall (shading, units: mm), **(B)** snow depth (shading; units: mm), and **(C)** snow cover (shading; units: %) onto the PC1 index, **(D–F)** onto the PC2 index, and **(G–I)** onto PC3 index from BCC-CSM2-MR simulations. The green line indicates the value significantly exceeding the 95% confidence level.

SUMMARY AND DISCUSSION

In this paper, we compared the connection between diverse SH inter-annual variation modes with pre-autumn and simultaneous winter Eurasian snow cover in observations and the BCC-CSM2-MR coupled climate model simulations under pre-industrial conditions from the CMIP6 project. Observational evidence shows that inter-annual variability of the winter SH exhibits three distinct modes, the uniform mode, the north–south dipole mode, and the west–east dipole mode, during 1979–2019. For the connection between the observed SH modes with simultaneous Eurasian snow anomalies in winter,

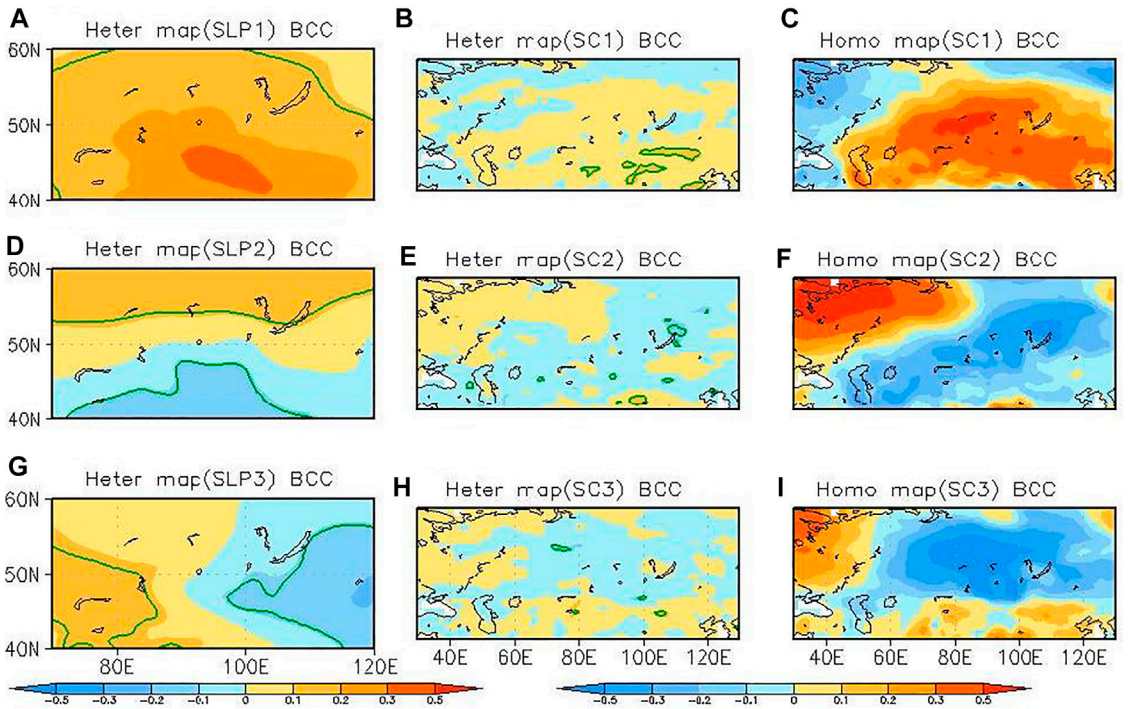

FIGURE 14 | Heterogeneous correlation coefficient maps of DJF SLP **(A)**, ON snow cover **(B)**, and homogeneous map of ON snow cover **(C)** in the first SVD mode of BCC-CSM2-MR simulations. **(D–F)** For the second SVD mode, **(D–F)** for the third SVD mode. The green line indicates the value significantly exceeding the 90% confidence level.

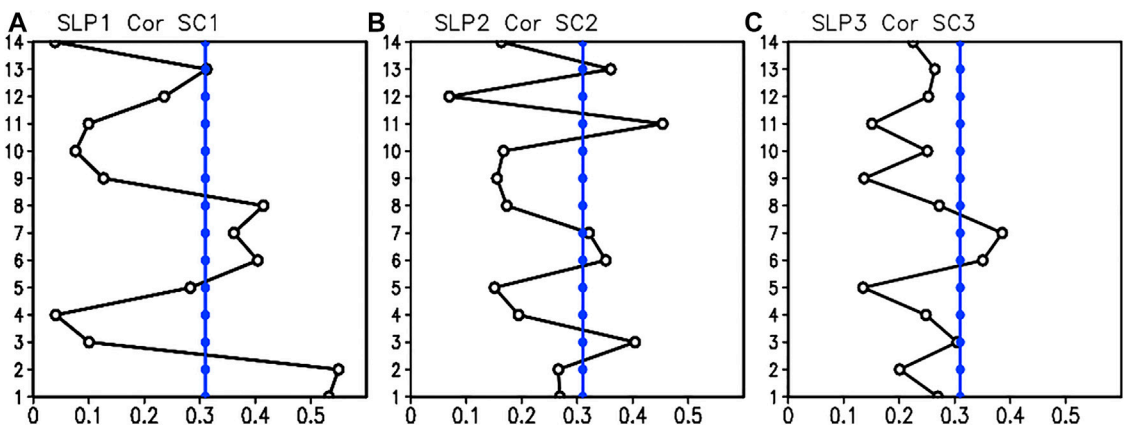

FIGURE 15 | The correlation coefficient between expansion coefficient time series of DJF SLP and ON snow cover in the first **(A)**, second **(B)**, and third **(C)** SVD mode for individual 41-year subintervals. The blue line indicates the value significantly exceeding the 95% confidence level.

the results imply that the SH modes actually force the variation in snowpack. Moreover, different spatial distribution of precursory Eurasian snowpack anomalies in the preceding autumn can be detected for the different SH modes in winter, and the possible physical connection between the autumn Eurasian snow and winter SH variations is found through transient eddy forcing response and troposphere–stratospheric interaction.

Moreover, it is found that the BCC-CSM2-MR models can capture the observed uniform mode of the SH well, but fail to reproduce the other two SH modes (i.e., the north–south and west–east dipole modes) in winter. The simulated SH-EOF1 mode features a uniform pattern over the Siberian region as that in observation. The simulated SH-EOF2 mode shows a northeast–southwest dipole pattern, which is different from the observed north–south dipole mode. The simulated SH-

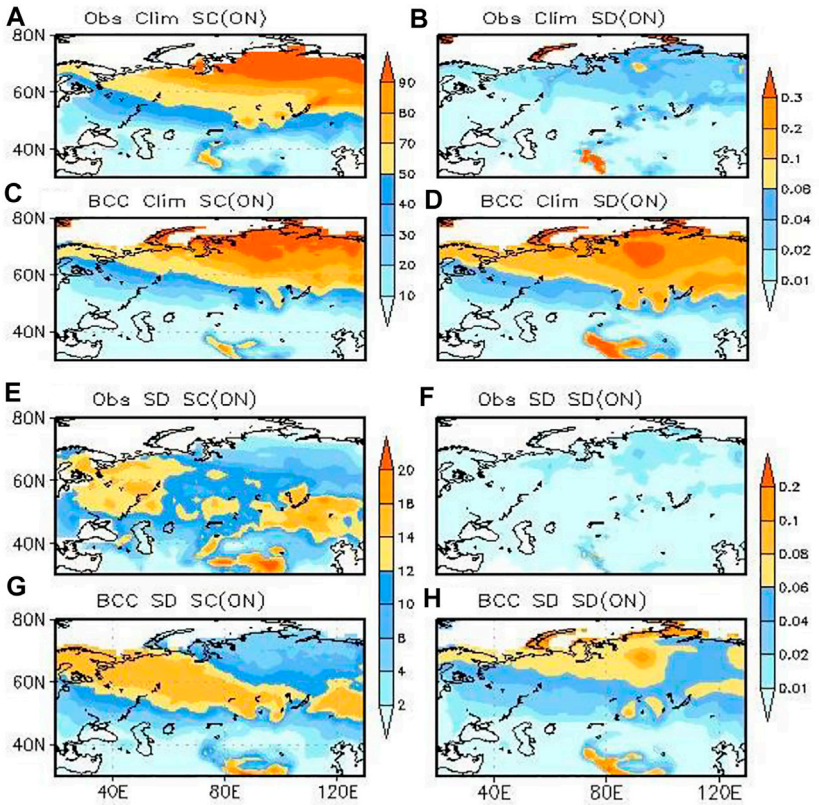

FIGURE 16 | The climatological ON mean **(A)** fractional snow cover (units: %), **(B)** snow depth (units: m) of observation, the simulated **(C)** fractional snow cover (units: %), and **(D)** snow depth (units: m) from BCC-CSM2-MR simulations. The standard deviation of ON mean **(E)** fractional snow cover (units: %), **(F)** snow depth (units: m) of observation, the simulated standard deviation of **(G)** fractional snow cover (units: %), and **(H)** snow depth (units: m) from BCC-CSM2-MR simulations.

EOF3 mode shows a northwest–southeast dipole pattern, whereas the observed SH-EOF3 mode features a west–east dipole pattern. Also, the BCC-CSM2-MR model cannot reproduce the observed diverse connections between the winter SH and preceding autumn Eurasian snow variations, which is possibly related to the poor ability of the model in simulating the Eurasian snow cover fraction and snow depth. Since the autumn Eurasian snow cover anomalies play an important role in modulating the winter SH and thus East Asian winter monsoon variability, the poor performance of BCC-CSM2-MR in simulating the autumn snow–winter SH connections may affect the seasonal prediction skill of East Asian winter monsoon and surface climate.

In this study, we just explored the possible statistic connection between three types of SH modes with precursory and simultaneous Eurasian snow anomalies in observations and BCC-CSM2-MR coupled model simulations as Furtado et al. (2015). Further studies are still required to systematically understand how different Eurasian snow distributions modulate the diverse SH modes. Moreover, this study diagnosed the presence of the Eurasian snow–SH connection in the state-of-the-art BCC-CSM-MR model participating in CMIP6, while the performance of other CMIP6 models remains unclear. Furtado et al. (2015) demonstrated that the CMIP5 coupled models underestimate the variability of October Eurasian snow cover and thus cannot simulate lagged winter atmospheric responses to the October Eurasian snow cover variability. Jiang et al. (2020) revealed that current CMIP6 models still underestimate the strength of the East Asian winter monsoon when compared to the CMIP5 models. However, whether the biases are related to the poor performance of the model in simulating the snow–SH connections are needed to be explored in future works.

As a word of caution, this study just focused on examining the connections between the Eurasian snow cover anomalies and the diverse SH modes, and their relationships may be influenced by other external forcings. For example, recent studies have indicated that Arctic sea ice and North Atlantic SST anomalies can exert substantial impacts on the atmospheric circulation and climate anomalies over Eurasia (e.g., Mori et al., 2014; Wu et al., 2013; Sun et al., 2016; Chen and Wu, 2018). It is also worth mentioning that the observational result derived from the uncoupled ERA5 reanalysis is affected by both forced variability and internal variability, while the model output used in this study only includes unforced variability. Further analysis by using coupled reanalysis data is needed to interpret model performances in capturing the possible connections.

DATA AVAILABILITY STATEMENT

The original contributions presented in the study are included in the article/**Supplementary Material**. Further inquiries can be directed to the corresponding author.

AUTHOR CONTRIBUTIONS

All authors have made a substantial, direct, and intellectual contribution to the work, and approved it for publication.

FUNDING

This research is supported by the National Key Research and Development Program of China (Grant No. 2019YFC1510104), the National Natural Science Foundation of China (Grant No. 41975102), the Basic Scientific Research and Operation Foundation of CAMS (2021Z004 and 2021Z007), and the joint fund of the State Key Program of National Natural Science of China and the Civil Aviation Administration of China (U2033207).

ACKNOWLEDGMENTS

The authors thank the reviewers whose constructive comments are helpful for improving the overall quality of the paper.

SUPPLEMENTARY MATERIAL

The Supplementary Material for this article can be found online at: https://www.frontiersin.org/articles/10.3389/feart.2021.761311/full#supplementary-material

REFERENCES

Allen, R. J., and Zender, C. S. (2010). Effects of continental-scale Snow Albedo Anomalies on the Wintertime Arctic Oscillation. *J. Geophys. Res.* 115, D23105. doi:10.1029/2010JD014490

Allen, R. J., and Zender, C. S. (2011). Forcing of the Arctic Oscillation by Eurasian Snow Cover. *J. Clim.* 24 (24), 6528–6539. doi:10.1175/2011JCLI4157.1

Barnett, T. P., Dümenil, L., Schlese, U., Roeckner, E., and Latif, M. (1989). The Effect of Eurasian Snow Cover on Regional and Global Climate Variations. *J. Atmos. Sci.* 46, 661–686. doi:10.1175/1520-0469(1989)046<0661:teoesc>2.0.co;2

Bretherton, C. S., Smith, C., and Wallace, J. M. (1992). An Intercomparison of Methods for Finding Coupled Patterns in Climate Data. *J. Clim.* 5, 541–560. doi:10.1175/1520-0442(1992)005<0541:aiomff>2.0.co;2

Brodzik, M., and Armstrong, R. (2013). *Northern Hemisphere EASE-Grid 2.0 Weekly Snow Cover and Sea Ice Extent, Version 4.* Boulder: NASA National Snow and Ice Data Center. doi:10.5067/P7O0HGJLYUQU

Bulygina, O. N., Razuvaev, V. N., and Korshunova, N. N. (2009). Changes in Snow Cover over Northern Eurasia in the Last Few Decades. *Environ. Res. Lett.* 4, 045026. doi:10.1088/1748-9326/4/4/045026

Charney, J., and Drazin, P. (1961). Propagation of planetaryscale disturbances from the lower into the upper atmosphere. *J. Geophys. Res.* 66, 83–109. doi:10.1029/JZ066i001p00083

Chen, S., and Wu, R. (2018). Impacts of Early Autumn Arctic Sea Ice Concentration on Subsequent spring Eurasian Surface Air Temperature Variations. *Clim. Dyn.* 51 (7-8), 2523–2542. doi:10.1007/s00382-017-4026-x

Chen, S., Wu, R., and Liu, Y. (2016). Dominant Modes of Interannual Variability in Eurasian Surface Air Temperature during Boreal spring. *J. Clim.* 29, 1109–1125. doi:10.1175/jcli-d-15-0524.1

Chen, S., Wu, R., Song, L., and Chen, W. (2019). Interannual Variability of Surface Air Temperature over Mid-high Latitudes of Eurasia during Boreal Autumn. *Clim. Dyn.* 53, 1805–1821. doi:10.1007/s00382-019-04738-9

Chen, S., Yu, B., and Chen, W. (2014). An Analysis on the Physical Process of the Influence of AO on ENSO. *Clim. Dyn.* 42, 973–989. doi:10.1007/s00382-012-1654-z

Clark, M. P., Serreze, M. C., and Robinson, D. A. (1999). Atmospheric Controls on Eurasian Snow Extent. *Int. J. Climatol.* 19, 27–40. doi:10.1002/(sici)1097-0088(199901)19:1<27:aid-joc346>3.0.co;2-n

Cohen, J., Barlow, M., Kushner, P. J., and Saito, K. (2007). Stratosphere-Troposphere Coupling and Links with Eurasian Land Surface Variability. *J. Clim.* 20, 5335–5343. doi:10.1175/2007JCLI1725.1

Cohen, J., and Entekhabi, D. (1999). Eurasian Snow Cover Variability and Northern Hemisphere Climate Predictability. *Geophys. Res. Lett.* 26, 345–348. doi:10.1029/1998GL900321

Cohen, J., and Fletcher, C. (2007). Improved Skill of Northern Hemisphere Winter Surface Temperature Predictions Based on Land-Atmosphere Fall Anomalies. *J. Clim.* 20, 4118–4132. doi:10.1175/JCLI4241.1

Cohen, J., and Rind, D. (1991). The Effect of Snow Cover on the Climate. *J. Clim.* 4, 689–706. doi:10.1175/1520-0442(1991)004<0689:teosco>2.0.co;2

Cohen, J., Furtado, J., Barlow, J., Alexeev, V., and Cherry, J. (2012). Arctic warming, increasing snow cover and widespread boreal winter cooling. *Environ. Res. Lett.* 7, 014007. doi:10.1088/1748-9326/7/1/014007

Cohen, J., Saito, K., and Entekhabi, D. (2001). The Role of the Siberian High in Northern Hemisphere Climate Variability. *Geophys. Res. Lett.* 28, 299–302. doi:10.1029/2000GL011927

Czaja, A., and Frankignoul, C. (2002). Observed impact of Atlantic SST anomalies on the North Atlantic Oscillation. *J. Clim.* 15, 606–623. doi:10.1175/1520-0442(2002)015<0606:OIOASA>2.0.CO;2

Derksen, C., and Brown, R. (2012). Spring Snow Cover Extent Reductions in the 2008-2012 Period Exceeding Climate Model Projections. *Geophys. Res. Lett.* 39, a–n. doi:10.1029/2012GL053387

Deser, C., Tomas, R., and Peng, S. (2007). The transient atmospheric circulation response to North Atlantic SST and sea ice anomalies. *J. Clim.* 20, 4751–4767. doi:10.1175/JCLI4278.1

Ding, Y. H. (1990). Buildup, Air-Mass Transformation and Propagation of Siberian High and its Relations to Cold Surge in East-Asia. *Meteorol. Atmos. Phys.* 44 (1–4), 281–292.

Ding, Y., and Krishnamurti, T. N. (1987). Heat Budget of the Siberian High and the winter Monsoon. *Mon. Wea. Rev.* 115, 2428–2449. doi:10.1175/1520-0493(1987)115<2428:hbotsh>2.0.co;2

Dutra, E., Schär, C., Viterbo, P., and Miranda, P. M. A. (2011). Land-atmosphere Coupling Associated with Snow Cover. *Geophys. Res. Lett.* 38 (15), L15707. doi:10.1029/2011gl048435

Fletcher, C. G., Kushner, P. J., Hall, A., and Qu, X. (2009). Circulation Responses to Snow Albedo Feedback in Climate Change. *Geophys. Res. Lett.* 36, L09702. doi:10.1029/2009GL038011

Foster, J., Owe, M., and Rango, A. (1983). Snow Cover and Temperature Relationships in North America and Eurasia. *J. Clim. Appl. Meteorol.* 22, 460–469. doi:10.1175/1520-0450(1983)022<0460:scatri>2.0.co;2

Furtado, J., Cohen, J., Butler, A., Riddle, E., and Kumar, A. (2015). Eurasian snow cover variability and Northern Hemisphere climate predictability. *Clim. Dyn.* 45, 2591–2605. doi:10.1007/s00382-015-2494-4

Garfinkel, C., Hartmann, D., and Sassi, F. (2010). Tropospheric precursors of anomalous Northern Hemisphere stratospheric polar vortices *J. Clim.* 23, 3282–3299. doi:10.1175/2010JCLI3010.1

Ghatak, D., Deser, C., Frei, A., Gong, G., Phillips, A., Robinson, D. A., et al. (2012). Simulated Siberian snow cover response to observed Arctic sea ice loss, 1979–2008. *J. Geophys. Res.* 117, D23108. doi:10.1029/2012JD018047

Gong, D., Wang, S., and Zhu, J. (2001). East Asian winter monsoon and Arctic Oscillation *Geophys. Res. Lett.* 28, 2073–2076. doi:10.1029/2000GL012311

Gong, D. Y., and Ho, C. H. (2002). Can the Arctic Oscillation Impact the East Asian Summer Monsoon? *CLIVAR Exchanges* 7, 18–20.

Gong, G., Entekhabi, D., and Cohen, J. (2003). Modeled Northern Hemisphere Winter Climate Response to Realistic Siberian Snow Anomalies. *J. Clim.* 16, 3917–3931. doi:10.1175/1520-0442(2003)016<3917:mnhwcr>2.0.co;2

Groisman, P. Y., Karl, T. R., Knight, R. W., and Stenchikov, G. L. (1994). Changes of Snow Cover, Temperature, and Radiative Heat Balance over the Northern Hemisphere. *J. Clim.* 7, 1633–1656. doi:10.1175/1520-0442(1994)007<1633:coscta>2.0.co;2

Hahn, D. G., and Shukla, J. (1976). An Apparent Relationship between Eurasian Snow Cover and Indian Monsoon Rainfall. *J. Atmos. Sci.* 33, 2461–2462. doi:10.1175/1520-0469(1976)033<2461:aarbes>2.0.co;2

Hardiman, S. C., Kushner, P. J., and Cohen, J. (2008). Investigating the Ability of General Circulation Models to Capture the Effects of Eurasian Snow Cover on winter Climate. *J. Geophys. Res.* 113, D21123. doi:10.1029/2008jd010623

Henderson, G. R., and Leathers, D. J. (2009). European Snow Cover Extent Variability and Associations with Atmospheric Forcings. *Int. J. Climatol.* 30, a–n. doi:10.1002/joc.1990

Henderson, G. R., Peings, Y., Furtado, J. C., and Kushner, P. J. (2018). Snow-atmosphere Coupling in the Northern Hemisphere. *Nat. Clim Change* 8, 954–963. doi:10.1038/s41558-018-0295-6

Hersbach, H., Bell, B., Berrisford, P., Hirahara, S., Horányi, A., Sabater, J. M., et al. (2020). The ERA5 Global Reanalysis. *Q.J.R. Meteorol. Soc.* 146, 1999–2049. doi:10.1002/qj.3803

Jeong, J.-H., Ou, T., Linderholm, H. W., Kim, B.-M., Kim, S.-J., Kug, J.-S., et al. (2011). Recent Recovery of the Siberian High Intensity. *J. Geophys. Res.* 116, a–n. doi:10.1029/2011jd015904

Jia, B., Wang, Y., Huang, S., Nan, Y., and Zhou, X. (2018). Variations of Siberian High Position under Climate Change: Impacts on winter Pollution over north China. *Atmos. Environ.* 189, 227–234. doi:10.1016/j.atmosenv.2018.06.045

Jiang, D., Hu, D., Tian, Z., and Lang, X. (2020). Differences between CMIP6 and CMIP5 Models in Simulating Climate over China and the East Asian Monsoon. *Adv. Atmos. Sci.* 37, 1102–1118. doi:10.1007/s00376-020-2034-y

Joung, C. H., and Hitchman, M. H. (1982). On the Role of Successive Downstream Development in East Asian Polar Air Outbreaks. *Mon. Wea. Rev.* 110, 1224–1237. doi:10.1175/1520-0493(1982)110<1224:otrosd>2.0.co;2

Kumar, P., and Sarthi, P. P. (2021). Intraseasonal Variability of Indian Summer Monsoon Rainfall in CMIP6 Models Simulation. *Theor. Appl. Climatol* 145, 687–702. doi:10.1007/s00704-021-03661-6

Lau, N.-C., and Holopainen, E. O. (1984). Transient Eddy Forcing of the Time-Mean Flow as Identified by Geopotential Tendencies. *J. Atmos. Sci.* 41, 313–328. doi:10.1175/1520-0469(1984)041<0313:tefott>2.0.co;2

Li, D., and Lan, L. (2017). Relationship between the Intensity of the Siberian High and the SST Anomaly in the North Atlantic. *Trans. Atmos. Sci.* 40, 13–24. doi:10.13878/j.cnki.dqkxxb.20151218001

Li, S. (2004). Impact of Northwest Atlantic SST Anomalies on the Circulation over the Ural Mountains during Early winter. *J. Meteorol. Soc. Jpn.* 82, 971–988. doi:10.2151/jmsj.2004.971

Liu, B., and Zhu, C. (2020). Diverse Impacts of the Siberian High on Surface Air Temperature in Northeast China during Boreal winter. *Int. J. Climatol.* 40, 594–603. doi:10.1002/joc.6199

Liu, X., Li, W., Wu, T., Li, T., Gu, W., Bo, Z., et al. (2019). Validity of Parameter Optimization in Improving MJO Simulation and Prediction Using the Sub-seasonal to Seasonal Forecast Model of Beijing Climate Center. *Clim. Dyn.* 52 (7–8), 3823–3843. doi:10.1007/s00382-018-4369-y

Liu, X., Yao, J., Wu, T., Zhang, S., Xu, F., Zhang, F., et al. (2021). Development of Coupled Data Assimilation with the BCC Climate System Model: Highlighting the Role of Sea-Ice Assimilation for Global Analysis. *J. Adv. Model. Earth Syst. (James)* 13, e2020MS002368. doi:10.1029/2020ms002368

Luo, X., and Wang, B. (2019). How Autumn Eurasian Snow Anomalies Affect East Asian winter Monsoon: a Numerical Study. *Clim. Dyn.* 52, 69–82. doi:10.1007/s00382-018-4138-y

Luojus, K., Pulliainen, J., Takala, M., Lemmetyinen, J., Mortimer, C., Derksen, C., et al. (2021). GlobSnow v3.0 Northern Hemisphere Snow Water Equivalent Dataset. *Sci. Data* 8, 163. doi:10.1038/s41597-021-00939-2

Lydolf, P. E. (1977). *Climates of the Soviet Union*. Amsterdam: Elsevier, 443.

Mori, M., Watanabe, M., Shiogama, H., Inoue, J., and Kimoto, M. (2014). Robust Arctic Sea-Ice Influence on the Frequent Eurasian Cold winters in Past Decades. *Nat. Geosci* 7, 869–873. doi:10.1038/ngeo2277

Mu, S. N., and Zhou, G. Q. (2015). Mechanism for the Correlation of winter Fresh Snow Extent over Northern Eurasia and Summer Climate Anomalies in China: The Important Role of Eurasian winter Fresh Snow Extent (In Chinese). *Chin. J. Atmos. Sci.* 39, 169–191.

North, G., Bell, T., Cahalan, F., and Moeng, J. (1982). Sampling errors in the estimation of empirical orthogonal functions. *Mon. Wea. Rev.* 110, 699–706. doi:10.1175/1520-0493(1982)110<0699:SEITEO>2.0.CO;2

Orsolini, Y. J., and Kvamstø, N. G. (2009). Role of Eurasian Snow Cover in Wintertime Circulation: Decadal Simulations Forced with Satellite Observations. *J. Geophys. Res.* 114, D19108. doi:10.1029/2009jd012253

Panagiotopoulos, F., Shahgedanova, M., Hannachi, A., and Stephenson, D. B. (2005). Observed Trends and Teleconnections of the Siberian High: a Recently Declining center of Action. *J. Clim.* 18 (9), 1411–1422. doi:10.1175/jcli3352.1

Peings, Y., Saint-Martin, D. S., and Douville, H. (2012). A Numerical Sensitivity Study of the Influence of Siberian Snow on the Northern Annular Mode. *J. Clim.* 25, 592–607. doi:10.1175/jcli-d-11-00038.1

Saito, K., Cohen, J., and Entekhabi, D. (2001). Evolution of Atmospheric Response to Early-Season Eurasian Snow Cover Anomalies. *Mon. Wea. Rev.* 129, 2746–2760. doi:10.1175/1520-0493(2001)129<2746:eoarte>2.0.co;2

Sun, C., Yang, S., Li, W., Zhang, R., and Wu, R. (2016). Interannual Variations of the Dominant Modes of East Asian winter Monsoon and Possible Links to Arctic Sea Ice. *Clim. Dyn.* 47, 481–496. doi:10.1007/s00382-015-2851-3

Sun, C., Zhang, R., Li, W., Zhu, J., and Yang, S. (2019). Possible Impact of North Atlantic Warming on the Decadal Change in the Dominant Modes of winter Eurasian Snow Water Equivalent during 1979-2015. *Clim. Dyn.* 53, 5203–5213. doi:10.1007/s00382-019-04853-7

Takaya, K., and Nakamura, H. (2005b). Geographical Dependence of Upper-Level Blocking Formation Associated with Intraseasonal Amplification of the Siberian High. *J. Atmos. Sci.* 62, 4441–4449. doi:10.1175/jas3628.1

Takaya, K., and Nakamura, H. (2005a). Mechanisms of Intraseasonal Amplification of the Cold Siberian High. *J. Atmos. Sci.* 62, 4423–4440. doi:10.1175/jas3629.1

Wang, B., Wu, Z., Chang, C.-P., Liu, J., Li, J., and Zhou, T. (2010). Another Look at Interannual-To-Interdecadal Variations of the East Asian Winter Monsoon: The Northern and Southern Temperature Modes. *J. Clim.* 23, 1495–1512. doi:10.1175/2009jcli3243.1

Wang, L., Chen, W., Zhou, W., and Chan, J. C. L. (2010). Effect of the Climate Shift Around Mid-1970s on the Relationship between Wintertime Ural Blocking Circulation and East Asian Climate. *Int. J. Climatology* 30, 153–158. doi:10.1002/joc.1876

Wegmann, M., Orsolini, Y., Vázquez, M., Gimeno, L., Nieto, R., Bulygina, O., et al. (2015). Arctic Moisture Source for Eurasian Snow Cover Variations in Autumn. *Environ. Res. Lett.* 10, 054015. doi:10.1088/1748-9326/10/5/054015

Wu, B., Su, J., and Zhang, R. (2011a). Effects of Autumn-winter Arctic Sea Ice on winter Siberian High. *Chin. Sci. Bull.* 56, 3220–3228. doi:10.1007/s11434-011-4696-4

Wu, B., and Wang, J. (2002). Winter Arctic Oscillation, Siberian High and East Asian winter Monsoon. *Geophys. Res. Lett.* 29, 1–3. doi:10.1029/2002gl015373

Wu, B., Zhang, R., Arrigo, R., and Su, J. (2013). On the Relationship between Winter Sea Ice and Summer Atmospheric Circulation over Eurasia. *J. Clim.* 26, 5523–5536. doi:10.1175/JCLI-D-12-00524.1

Wu, M. C., and Chan, J. C. L. (1997). Upper-level Features Associated with winter Monsoon Surges over south China. *Mon. Wea. Rev.* 125, 317–340. doi:10.1175/1520-0493(1997)125<0317:ulfaww>2.0.co;2

Wu, Q., Hu, H., and Zhang, L. (2011b). Observed Influences of Autumn-Early winter Eurasian Snow Cover Anomalies on the Hemispheric PNA-like Variability in winter. *J. Clim.* 24, 2017–2023. doi:10.1175/2011jcli4236.1

Wu, T., Lu, Y., Fang, Y., Xin, X., Li, L., Li, W., et al. (2019). The Beijing Climate Center Climate System Model (BCC-CSM): the Main Progress from CMIP5 to CMIP6. *Geosci. Model. Dev.* 12, 1573–1600. doi:10.5194/gmd-12-1573-2019

Ye, K., and Lau, N.-C. (2016). Influences of Surface Air Temperature and Atmospheric Circulation on winter Snow Cover Variability over Europe. *Int. J. Climatol.* 37, 2606–2619. doi:10.1002/joc.4868

Ye, K., and Wu, R. (2017). Autumn Snow Cover Variability over Northern Eurasia and Roles of Atmospheric Circulation. *Adv. Atmos. Sci.* 34, 847–858. doi:10.1007/s00376-017-6287-z

Ye, K., Wu, R., and Liu, Y. (2015). Interdecadal Change of Eurasian Snow, Surface Temperature, and Atmospheric Circulation in the Late 1980s. *J. Geophys. Res. Atmos.* 120, 2738–2753. doi:10.1002/2015JD023148

Zhang, R., Zhang, R., and Zuo, Z. (2017). Impact of Eurasian spring Snow Decrement on East Asian Summer Precipitation. *J. Clim.* 30, 3421–3437. doi:10.1175/jcli-d-16-0214.1

Zhu, H. X., Chen, W., Feng, T., et al. (2019). Interannual Variations of Siberian High during Boreal winter and its Influence on East Asian Temperature. *Plateau Meteorology* 38 (4), 685–692.

Zhu, X., Liu, X., Huang, A., Zhou, Y., Wu, Y., and Fu, Z. (2021). Impact of the Observed SST Frequency in the Model Initialization on the BSISO Prediction. *Clim. Dyn.* 57, 1097–1117. doi:10.1007/s00382-021-05761-5

Zuo, Z., Zhang, R., Wu, B., and Rong, X. (2011). Decadal Variability in Springtime Snow over Eurasia: Relation with Circulation and Possible Influence on Springtime Rainfall over China. *Int. J. Climatol.* 32, 1336–1345. doi:10.1002/joc.2355

Conflict of Interest: The authors declare that the research was conducted in the absence of any commercial or financial relationships that could be construed as a potential conflict of interest.

frontiers in Earth Science

ORIGINAL RESEARCH
published: 06 December 2021
doi: 10.3389/feart.2021.772202

Modulation of Atlantic Multidecadal Oscillation on the Interdecadal Variation of South Asian High and Somali Jet in Summer

Wenjing Shi[1,2,3]*, *Qingzhe Wang*[1], *Ziniu Xiao*[2]*, *Wei Cheng*[3,4]* and *Wei Duan*[5]

[1]CSSC Marine Technology Co. Ltd., Beijing, China, [2]State Key Laboratory of Numerical Modeling for Atmospheric Sciences and Geophysical Fluid Dynamics (LASG), Institute of Atmospheric Physics, Chinese Academy of Sciences, Beijing, China, [3]State Key Laboratory of Geo–Information Engineering, Xi'an, China, [4]Beijing Institute of the Applied Meteorology, Beijing, China, [5]Meteorological Science Institute of Yunnan Province, Kunming, China

OPEN ACCESS

Edited by:
Song Yang,
Sun Yat-sen University, China

Reviewed by:
Jia Liang,
Nanjing University of Information Science and Technology, China
Xue Xu,
Guizhou University, China

***Correspondence:**
Wenjing Shi
shiwenjing_005@163.com
Ziniu Xiao
xiaozn@lasg.iap.ac.cn
Wei Cheng
chengw@mail.iap.ac.cn

Specialty section:
This article was submitted to Atmospheric Science, a section of the journal Frontiers in Earth Science

Received: 07 September 2021
Accepted: 29 October 2021
Published: 06 December 2021

Citation:
Shi W, Wang Q, Xiao Z, Cheng W and Duan W (2021) Modulation of Atlantic Multidecadal Oscillation on the Interdecadal Variation of South Asian High and Somali Jet in Summer. Front. Earth Sci. 9:772202. doi: 10.3389/feart.2021.772202

As two important components of the Asian summer monsoon system, the intensities of South Asian High (SAH) and Somali jet (SMJ) in summer exhibit both interannual and decadal variabilities. On the interdecadal timescale, the temporal evolution of the SAH intensity is in phase with that of the SMJ intensity. By comparison, we find that both of them evolve synchronously with the Atlantic Multidecadal Oscillation (AMO), with AMO cold/warm phases corresponding to the weakening/strengthening of SAH and SMJ. Further diagnoses indicate that the interdecadal variabilities of the SAH and SMJ intensities in summer may be modulated by the AMO phase. Mechanistically, this modulation appears to be achieved *via* an interdecadal Silk Road pattern (SRP)-like wave train along the Asian westerly jet and Matsuno–Gill tropical atmospheric response. The cold SST anomaly over extratropical North Atlantic related to the AMO firstly induces an anomalous high over Western Europe and produces a well-organized wave train between 30°N and 60°N. The anomalous Iranian Plateau low along with the wave train path leads to a weakened SAH. Besides, the AMO-related cold SST anomalies over tropical North Atlantic cool the tropical tropospheric atmosphere through the moist adjustment process and produce a Matsuno–Gill-like atmospheric response covering the tropical Indian Ocean. Due to the Matsuno–Gill response, subsidence motion anomalies over the central tropical Indian Ocean corresponding to a result in increased lower-level divergence and upper-level convergence are excited over the tropical Indian Ocean. Finally, the tropical Indian Ocean divergence in the lower troposphere leads to the weakened summer SMJ, and the tropical Indian Ocean convergence in the upper troposphere results in the decrease and northward displacement of SAH in summer.

Keywords: South Asian High, somali jet, Atlantic multidecadal oscillation, interdecadal variability, silk road pattern, extratropical and tropical North Atlantic SSTs

INTRODUCTION

The Atlantic Multidecadal Oscillation (AMO) is a prominent basin-scale mode of multidecadal variability in North Atlantic sea surface temperatures (SSTs). Bjerknes (1964) first found the consistent variations of SSTs and sea level pressures (SLPs) in 30°–50°N of the North Atlantic during 1920–1960, with a gradually warming trend. Subsequently, Folland and Parker (1990) revealed that the North Atlantic SSTs gradually entered into a cooling stage from 1960 to 1980. After 1990, the North Atlantic SSTs were warming up again (Delworth and Mann, 2000; Kerr, 2000). Kerr (2000) formally defined this multidecadal variability in North Atlantic SSTs as the AMO. The AMO showed two leading periodicities of about 60–80 and 10–30 years with different regimes (Lin et al., 2019), which have an important impact on global climate, regional climate, and even El Niño–Southern Oscillation (ENSO) (Knight et al., 2006; Li and Bates, 2007; Feng and Hu, 2008; Li et al., 2008; Luo et al., 2011).

The AMO influence on the Indian summer monsoon (ISM) has been investigated by several recent studies based on observations and models. The positive phase of the AMO could induce increased summer rainfall in central and southern Indian, intensified ISM, and late withdrawal of the ISM (Goswami et al., 2006; Sutton and Hodson, 2007; Li et al., 2008; Wang et al., 2009). Despite an overall consistency of the AMO influence on the ISM in previous studies, there are still some disputes about the magnitude of the forcing and the responsible mechanism. Based on observations, Goswami et al. (2006) proposed that a positive-phase AMO induces atmospheric responses like the summer North Atlantic Oscillation (NAO) pattern, leading to warming over the Eurasian continent and intensifying thermal contrast between the Indian subcontinent and the tropical Indian Ocean and consequently stronger ISM. Feng and Hu (2008) suggested a different mechanism in which the AMO exerts its impact by changing surface thermal status over the Tibetan Plateau rather than the summer NAO. Through Atmospheric General Circulation Model (AGCM), Li et al. (2008) and Wang et al. (2009) also suggested that the AMO influences the India Summer Rainfall (ISR) *via* an increased meridional gradient of the tropospheric temperatures and intensification of the monsoonal low-level jet, but no significant NAO-like responses. Luo et al. (2011) viewed that the AMO influence on ISR is achieved through a propagating Rossby wave train from the North Atlantic across South Asia, which leads to enhanced South Asian High (SAH) and consequently a strengthening of the ISM.

In addition to the impact on the ISM, the AMO also has a certain modulation effect on summer precipitation in East Asia. The AMO warm phase is conducive to the enhancement of the East Asian summer monsoon (EASM) and the increase of precipitation in the Yangtze River Basin (Lu et al., 2006; Li et al., 2008). The warm AMO-related North Atlantic SSTs are favorable for the earlier onset of Meiyu, and the cold SSTs over North Atlantic in preceding winter and spring are related to the later onset of Meiyu (Xu et al., 2001). Wang and Li (2019) also pointed out that the turning of summer eastern China precipitation in the early 1990s is related to the AMO with its impact mainly concentrated in low-latitude regions.

The circumglobal teleconnection (CGT) pattern is a leading circulation mode over the Northern Hemisphere (NH) during boreal summer, which is propagating around the hemisphere along the subtropical upper-tropospheric westerly jet (Ding and Wang, 2005). The wave train propagating over the Eurasian continent (Lu et al., 2002) or the Silk Road pattern (SRP) (Enomoto, 2004) is considered to be a portion of the CGT. Recent studies found that the AMO has a considerable impact on this teleconnection pattern. Using five AGCMs driven by specified AMO-related SST anomalies (SSTAs) in the North Atlantic, Lin et al. (2016) verified that the interdecadal component of the CGT (ID-CGT) should be excited, at least partially, by the AMO-related SSTAs, and ID-CGT plays a role in linking the AMO and NH summer land surface air temperature (SAT) perturbations on the interdecadal timescale. Based on the 20CR data, Wu et al. (2016) also indicated that, during boreal summer, AMO-related SSTAs are associated with a wave train-like teleconnection pattern located along the NH westerly jet.

As two of the most important components of the Asian summer monsoon system, SAH and Somali jet (SMJ) have influence on the weather and climate in the Asian regions (e.g., Krishnamurti and Bhalme, 1976; Cadet and Desbois, 1981; Halpern and Woiceshyn, 2001; Huang and Qian, 2004; Lei and Yang, 2008; Watanabe and Yamazaki, 2014; Wei et al., 2014). The SAH is a large-scale anticyclone circulation system over the Tibetan Plateau and its adjacent regions in summer. In addition to the polar vortex, the SAH is suggested to be the strongest and most stable atmospheric circulation system in the upper troposphere (100 hPa) of NH (Mason and Anderson, 1963; He et al., 2006; Liu et al., 2009). On the other hand, the SMJ is a low-level cross-equatorial flow (CEF) at the strategic fulcrum of the Indian Ocean, characterized by southeasterly trade winds in the Southern Hemisphere, a strong and narrow CEF off the coast of Somalia, and southwesterly winds over the Arabian Sea (Simpson, 1921; Joseph and Raman, 1966; Findlater, 1969; Krishnamurti and Bhalme, 1976; Qian et al., 1987; Chakraborty et al., 2009; Pu and Cook, 2010). This low-level current is most prominent in summer and has its maximum wind speed center at approximately 925 hPa (Pu and Cook, 2010; Xiao et al., 2015). These two important atmospheric circulation systems of the NH in summer change not only interannually but also interdecadally (Zhang et al., 2000; Shi et al., 2007; Boos and Emanuel, 2009; Pu and Cook, 2010; Zhu, 2012; Yang et al., 2013; Jia and Liu, 2020). As Shi et al. (2007) investigated, the strength of the SMJ increased, on average, by 0.25 m s^{-1} per decade during 1948–2004. Zhu (2012) demonstrated that the low-level (925-hPa) Somali CEFs showed a strong upward trend, with two marked increases in strength in the late 1970s and the late 1990s. Moreover, Zhang et al. (2000) pointed out that the mutation of the SAH strength in the late 1970s is consistent with that of the Pacific SSTs. Yang et al. (2013) also suggested that the interdecadal transition of the SAH intensity occurred in the late 1970s, which was associated with the anomalies of the surface sensible heat flux in the plateau (especially in the northwest of the plateau). Actually, on the interdecadal timescale, the temporal evolution of the SAH is synchronous with that of the SMJ during 1951–2010 characterized by one-wave type. When the SMJ is weak (strong), the summertime SAH is also weak (strong) and

TABLE 1 | Datasets used in this study.

Dataset	Resolution	Pressure levels	Period of record
JRA-55 reanalysis	1.25° × 1.25°	37 (1,000–1 hPa)	1958–2021
NCEP/NCAR reanalysis	2.5° × 2.5°	17 (1,000–10 hPa)	1948–2021
20CRv3 reanalysis	1° × 1°	28 (1,000–1 hPa)	1836–2015
ERA-20c reanalysis	1° × 1°	37 (1,000–1 hPa)	1900–2010
HadISST1.1	1° × 1°	Surface	1870–2021

Note. JRA-55, Japanese 55-year Reanalysis; NCEP/NCAR, National Centers for Environmental Prediction/National Center for Atmospheric Research; 20CRv3, Twentieth Century Reanalysis dataset, version 3; ERA-20c, European Centre for Medium-Range Weather Forecasts 20th-century reanalysis.

retreats westward (advances eastward) (Shi et al., 2017). As mentioned above, the AMO plays an important role in components of the Asian summer monsoon system, e.g., ISM, EASM, and ID-CGT. However, it remains unclear whether the AMO, as one of the most important interdecadal atmospheric signals, has dominant modulation impact on the interdecadal variabilities of the SAH and SMJ in summer. This topic is focused on in this study. The *Data and Methods* section describes the data and methods used in this study. The *Interdecadal Variations of the South Asian High, Somali Jet, and Atlantic Ocean Sea Surface Temperature in Summer* section presents the interdecadal variation of the SAH and SMJ intensities, as well as their linkages with the AMO. The *Modulation Mechanism of the Summer South Asian High and Somali jet by the Atlantic Multidecadal Oscillation on an Interdecadal Timescale* section further investigates the modulation mechanism of the AMO phase-related SSTAs on the SAH and SMJ interdecadal variabilities in summer *via* an interdecadal SRP-like wave train along the Asian westerly jet and Matsuno–Gill-like tropical atmospheric response. The *Summary* section provides a summary of key findings in this study.

DATA AND METHODS

In order to satisfy the requirements of the decadal variability analyses, several long-term monthly mean atmospheric reanalysis datasets are used in this study, including the National Centers for Environmental Prediction (NCEP)/National Center for Atmospheric Research (NCAR) reanalysis dataset (Kalnay et al., 1996, https://psl.noaa.gov/data/gridded/data.ncep.reanalysis.html), the Japanese 55-year Reanalysis (JRA-55) dataset (Kobayashi et al., 2015, http://search.diasjp.net/en/dataset/JRA55), the European Centre for Medium-Range Weather Forecasts (ECMWF) 20th-century reanalysis (ERA-20c) dataset (Poli et al., 2013, https://apps.ecmwf.int/datasets/data/era20c–moda/levtype=pl/type=an/), and the Twentieth Century Reanalysis dataset, version 3 (20CRv3; Compo et al., 2011, https://psl.noaa.gov/data/gridded/data.20thC_ReanV3.html). The variables include horizontal wind, geopotential height, vertical velocity, air temperature, specific humidity, and relative vorticity at pressure levels, SLP and SAT. In addition, the monthly mean SST data are obtained from the Version 1.1 Hadley Center Global Sea Ice and Sea Surface Temperature (HadISST1.1; Rayner et al., 2003) dataset that is available online from the United Kingdom Met Office (http://www.metoffice.gov.uk/hadobs/HadISST1.1/). The resolution, pressure level, and record period of these data are given in **Table 1**.

The summer is defined as the average of June, July, and August (JJA). The SMJ strength index (SMJI) is defined to check the SMJ strength variation. Following Dai and Xiao (2014), the SMJI is calculated by area weighted averaging the 925-hPa meridional wind over the region of (equator; 40°–55°E), where the SMJ is generally located. The intensity of the SAH (SAHI) is defined as the sum of differences between the geopotential height at each point and the characteristic one (i.e., 16,600 gpm) over the SAH region (10°S–50°N, 30°W–180°E) following the method proposed in Zhang et al. (2002, 2005). The area of the SAH (SAHA) is computed by counting the points at which the geopotential height is equal to or greater than the characteristic height of 16,600 gpm in the region (Zhou et al., 2006). The SRP pattern is defined as the first empirical orthogonal function (EOF) mode of the summer mean 200-hPa meridional wind over the domain (20°–60°N, 30°–130°E; Kosaka et al., 2009), and the SRP index is defined as the normalized first principal component accordingly. Following Ting et al. (2009), the AMO index is defined as area-averaged SSTAs in the North Atlantic (0°–60°N, 80°W–0°) with the linear trend signal removed through regression analysis. To maintain consistency and for easy comparisons among the datasets with consideration for their different temporal coverages, the analysis periods of this study are the overlapping periods of different datasets (i.e., 1958–2010 for JRA-55, 1948–2010 for NCEP/NCAR, and 1900–2010 for 20CRv3 and ERA-20c). Since we focus on the decadal variability, the linear trend signals in all statistical analysis datasets are removed to isolate the contribution of the trends from that of natural variability (Nan et al., 2009). The interdecadal component of a variable is extracted using a 9-year Gaussian low-pass filter. The statistical significance of composite is evaluated based on a two-tailed Student's t-test, and the effective degree of freedom (N_{dof}) is evaluated as follows (Zhou and Zheng, 1999):

$$N_{dof} = (N-2)\frac{f_p}{f_n}, \qquad f_n = \frac{1}{2\Delta}, \quad f_p = \frac{1}{N_l\Delta} - \frac{1}{N_h\Delta} \tag{1}$$

where N is the sample size and Δis the sample spacing. N_h and N_l represent the maximum and minimum sample sizes passed in the filtering process, respectively. f_n and f_p are the Nyquist frequency

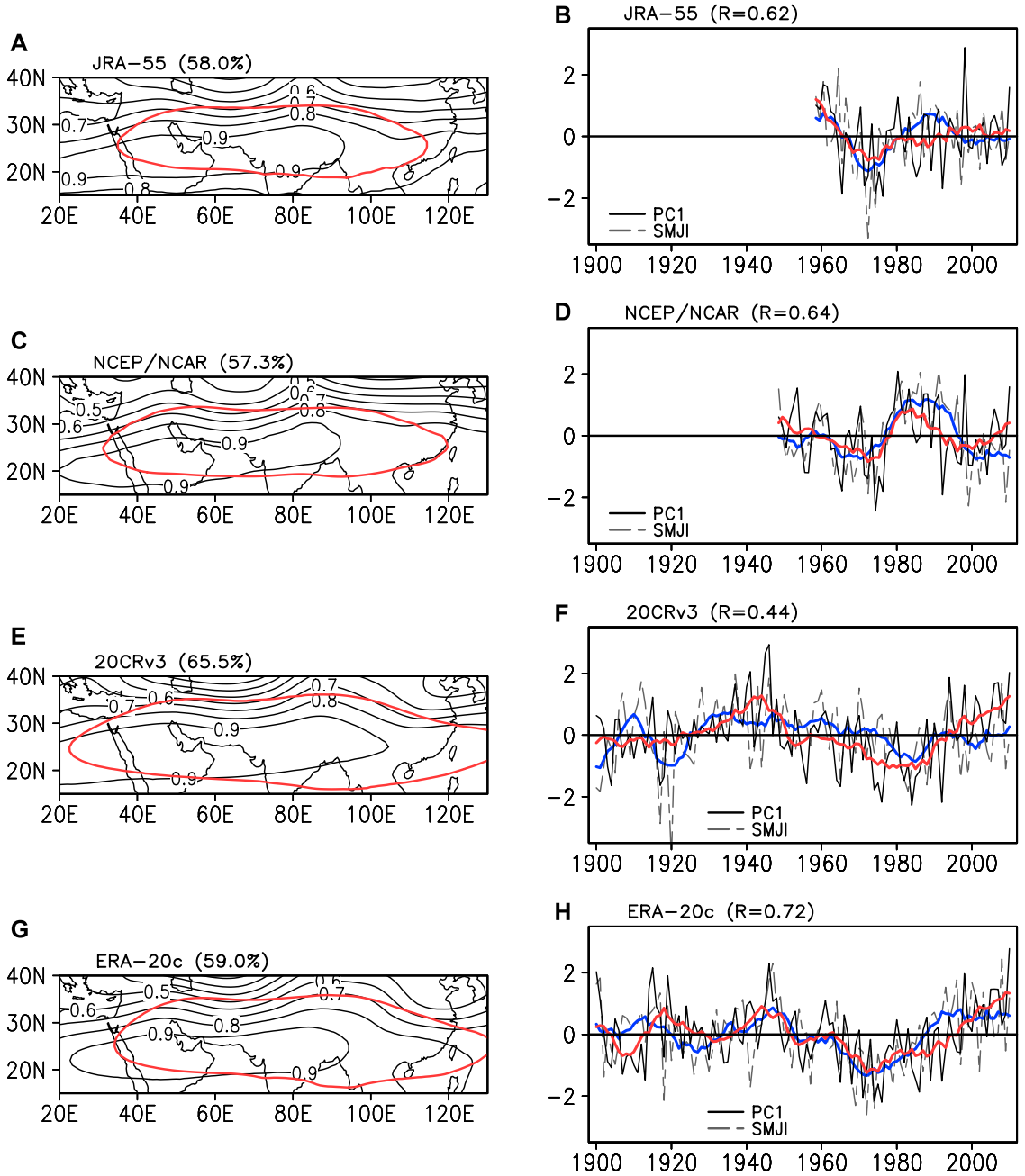

FIGURE 1 | Spatial pattern of the first EOF for the summer geopotential height anomalies (gpm) at 200 hPa in the **(A)** JRA-55, **(C)** NCEP/NCAR, **(E)** 20CRv3, and **(G)** ERA-20c datasets. The red contour denotes climatological location of the summer SAH featured by the 12,500 gpm (for the JRA-55, NCEP/NCAR, and 20CRv3 datasets) and 12,400 gpm (for the ERA-20c dataset) contours. Contour intervals are 0.1 gpm. The normalized time series of the SMJI (gray dashed line) and the principal component time series of the first EOF (PC1; black solid line) with their 9-year running averaged components, respectively, denoted by blue and red solid lines in the **(B)** JRA-55, **(D)** NCEP/NCAR, **(F)** 20CRv3, and **(H)** ERA-20c datasets. EOF, empirical orthogonal function; JRA-55, Japanese 55-year Reanalysis; NCEP/NCAR, National Centers for Environmental Prediction/National Center for Atmospheric Research; 20CRv3, Twentieth Century Reanalysis dataset, version 3; ERA-20c, European Centre for Medium-Range Weather Forecasts 20th-century reanalysis; SAH, South Asian High; SMJI, Somali jet strength index.

and the pass bandwidth of the frequency, respectively. In this study, the wave-activity flux for stationary Rossby waves is analyzed to investigate the propagation direction of wave energy as proposed by Takaya and Nakamura (2001). Its horizontal components in pressure coordinates are as follows:

$$W = \frac{1}{2|\bar{\mathbf{u}}|}\left\{\begin{array}{l}\bar{u}\left(\Psi_x^2 - \Psi'\Psi'_{xx}\right) + \bar{v}\left(\Psi'_x\Psi'_y - \Psi'\Psi'_{xy}\right)\\ \bar{u}\left(\Psi'_x\Psi'_y - \Psi'\Psi'_{xy}\right) + \bar{v}\left(\Psi_y^2 - \Psi'\Psi'_{yy}\right)\end{array}\right\} \quad (2)$$

Here, overbars and primes denote mean states and deviations from the mean states, respectively; subscripts x and y represent

TABLE 2 | Correlation coefficients between the PC1 and SAHI index in the different datasets.

JRA-55	NCEP/NCAR	20CRv3	ERA-20c
0.96	0.85	0.92	0.87

Note. All of the correlation coefficients exceed the 99.9% confidence level based on two-tailed Student's t-test.
PC1, the first principal component of the 200-hPa geopotential height. JRA-55, Japanese 55-year Reanalysis. NCEP/NCAR, National Centers for Environmental Prediction/National Center for Atmospheric Research; 20CRv3, Twentieth Century Reanalysis dataset, version 3; ERA-20c, European Centre for Medium-Range Weather Forecasts 20th-century reanalysis.

zonal and meridional gradients; $\mathbf{u} = (u, v)$denotes horizontal wind velocity; Ψ represents eddy stream functions.

INTERDECADAL VARIATIONS OF THE SOUTH ASIAN HIGH, SOMALI JET, AND ATLANTIC OCEAN SEA SURFACE TEMPERATURES IN SUMMER

Variations of the South Asian High, Somali Jet, and Atlantic Multidecadal Oscillation Indices

We first examine the variability of the SAH, SMJ, and AMO on the interdecadal timescale using four reanalysis datasets from 1958 to 2010 for JRA-55, 1948–2010 for NCEP/NCAR, and 1900–2010 for 20CRv3 and ERA-20c. Following previous studies (Wei et al., 2014, 2015), the dominant modes of the 200-hPa geopotential height anomalies over (15°–40°N; 20°–130°E), where the main body of the SAH is generally located, extracted by the EOF technique are usually used to examine the SAH variation. **Figure 1** shows the first EOF (EOF1) modes and the corresponding principal component (PC1) time series of the summer 200-hPa geopotential height anomalies from four reanalysis datasets. Spatial patterns of the EOF1 show same-sign geopotential height anomalies over the considered area and seem obviously consistent in four reanalysis datasets (**Figures 1A,C,E,G**). The EOF1s of the JRA-55, NCEP/NCAR, 20CRv3, and ERA-20c account for 58%, 57.3%, 65.6%, and 59% of the total variances, respectively. The correlation coefficients between the PC1 and the normalized SAHI index are calculated in **Table 2** for the different datasets. The two time series are highly consistent with each other in four datasets with all of the correlation coefficients exceeding 0.8. Thus, the EOF1 represents the variation of the SAH strength.

Before any analysis is performed, the consistency of the SAH and SMJ strength variabilities represented by the different datasets is checked by calculating the correlation coefficients of the PC1 and SMJI time series among the datasets (**Table 3**). Almost all of the correlation coefficients exceed the 95% confidence level based on two-tailed Student's t-test, except for the correlation coefficients of the SMJI index between the NCEP/NCAR and 20CRv3 dataset. The SAH strength variability in the ERA-20c dataset is highly consistent with that in the JRA-55 and 20CRv3 datasets, with all the correlation coefficients on the order of 0.75 or higher during their overlapping periods. In contrast, the SMJ strength variability is less consistent among the different datasets with only the correlation coefficients between the ERA-20c and JRA-55 datasets for the period of 1958–2010 exceeding 0.7. Therefore, the ERA-20c datasets during the period of 1900–2010 is used throughout this study except where otherwise stated explicitly. As evidenced by **Figures 1B,D,F,H**, the remarkable interdecadal variabilities of the SAH and SMJ strength are clearly seen by PC1 and SMJI time series. Except for the 20CRv3 dataset, almost all of the correlation coefficients between the 9-year running averaged component of the PC1 and those of the SMJI in the different datasets are on the order of 0.6, exceeding the 99% confidence level. The time series of the SMJI on the interdecadal timescale is in phase with that of the PC1 as shown by the 9-year running averaged component of the PC1 and SMJI. Our previous work also verified the positive correlation between SMJ strength and South Asian High on interdecadal timescale, when the SMJ strength is weak (strong), the summertime South Asian High is also weak (strong) and retreats westward (advances eastward) (Shi et al., 2017). As revealed by previous studies, the synchronous variability of the SAH and SMJ strength could be achieved *via* the upper-level tropical easterly jet across the Indian subcontinent (Ashfaq et al., 2009; Hu et al., 2010; Ren et al.,

TABLE 3 | Correlation coefficients of the SMJI and PC1 indexes among the different datasets for the periods 1958–2010, 1948–2010, and 1900–2010.

	SMJI index			PC1 index		
1958–2010	NCEP/NCAR	20CRv3	ERA-20c	NCEP/NCAR	20CRv3	ERA-20c
JRA-55	0.56	0.45	0.78	0.81	0.74	0.88
NCEP/NCAR	—	0.21	0.36	—	0.48	0.64
20CRv3	—	—	0.57	—	—	0.83
1948–2010	20CRv3	ERA–20c		20CRv3	ERA–20c	
NCEP/NCAR	0.22	0.31		0.51	0.65	
20CRv3	—	0.53		—	0.82	
1900–2010	ERA–20c			ERA–20c		
20CRv3	0.28			0.75		

Note. PC1, the first principal component of the 200-hPa geopotential height. SMJI, Somali jet strength index; NCEP/NCAR, National Centers for Environmental Prediction/National Center for Atmospheric Research; 20CRv3, Twentieth Century Reanalysis dataset, version 3; ERA-20c, European Centre for Medium-Range Weather Forecasts 20th-century reanalysis; JRA-55, Japanese 55-year Reanalysis.

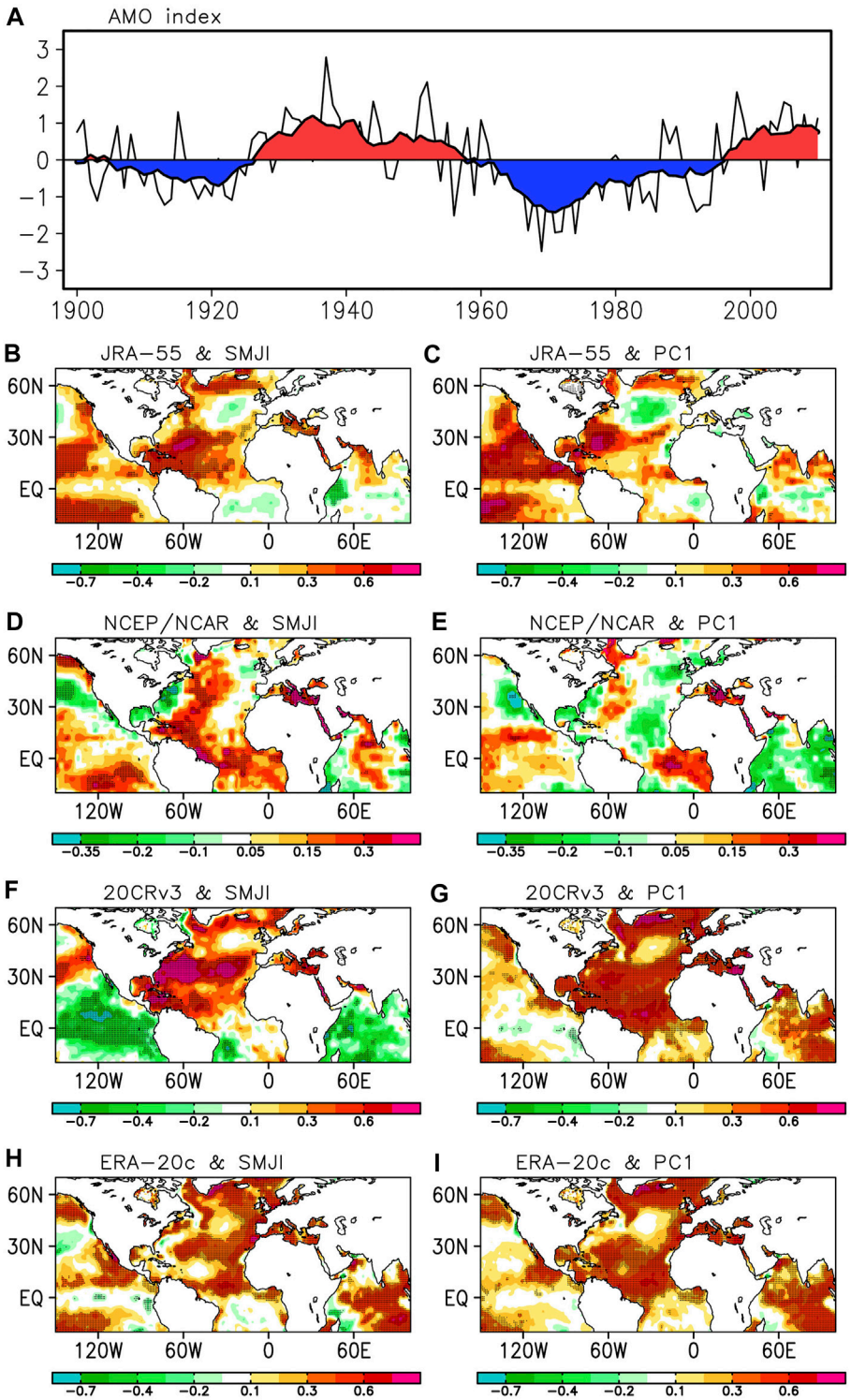

FIGURE 2 | (A) Normalized summer AMO index (black solid line) time series and its interdecadal component (thick line with filled colors) during the time period 1900–2010. Regressions of the summer SST (units: K) interdecadal component onto the interdecadal component of the summer **(B,D,F,H)** SMJI and **(C,E,G,I)** PC1 from the **(B,C)** JRA-55, **(D,E)** NCEP/NCAR, **(F,G)** 20CRv3, and **(H,I)** ERA-20c datasets. Black dots indicate the 95% confidence levels based on two-tailed Student's t-test. AMO, Atlantic Multidecadal Oscillation; SST, sea surface temperature; SMJI, Somali jet strength index; JRA-55, Japanese 55-year Reanalysis; NCEP/NCAR, National Centers for Environmental Prediction/National Center for Atmospheric Research; 20CRv3, Twentieth Century Reanalysis dataset, version 3; ERA-20c, European Centre for Medium-Range Weather Forecasts 20th-century reanalysis.

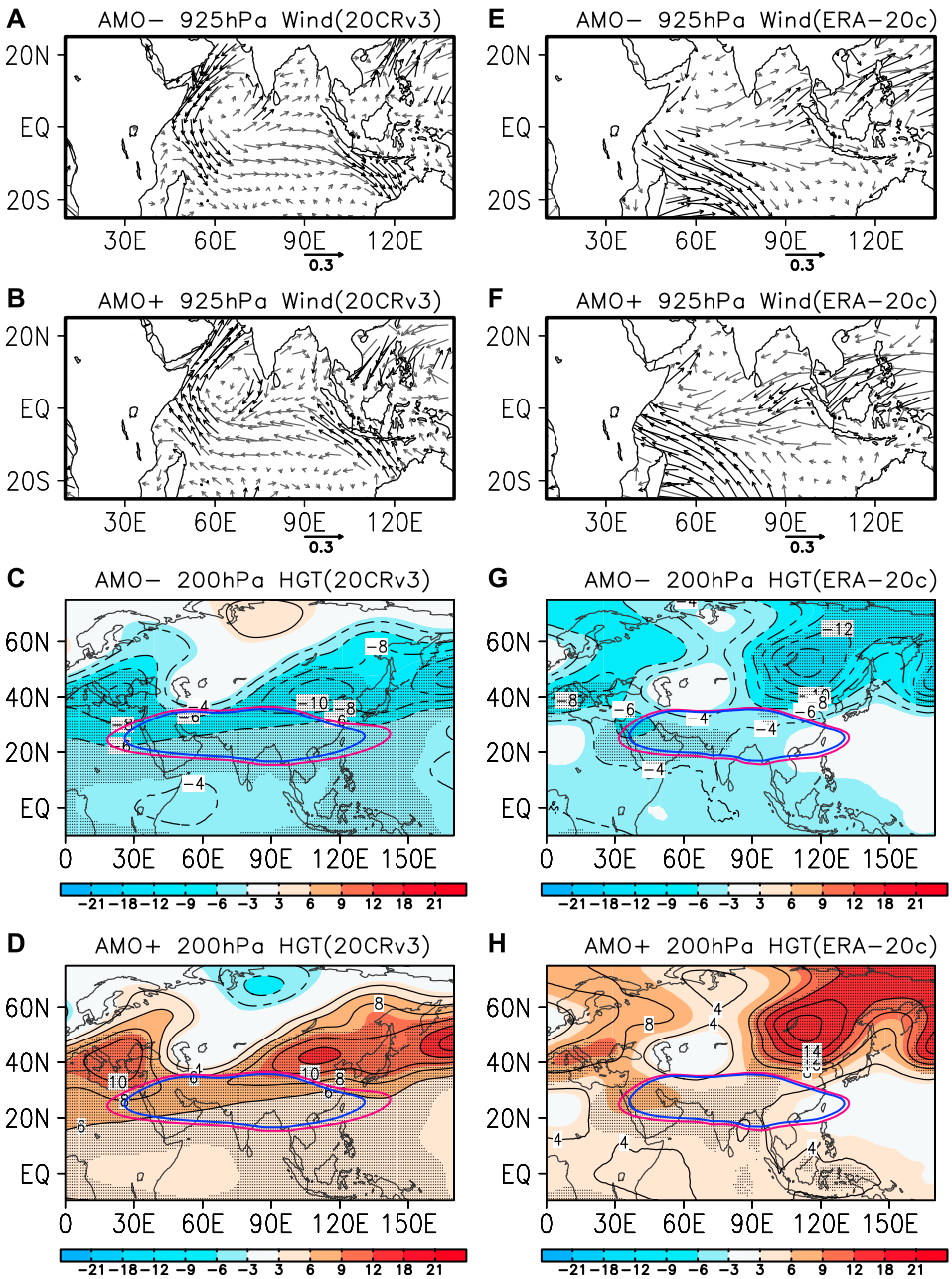

FIGURE 3 | A composite of the summer **(A,B,E,F)** 925-hPa wind anomalies (unit: m s^{-1}) and **(C,D,G,H)** 200-hPa geopotential height anomalies (gpm) during **(A,E,C,G)** AMO− and **(B,F,D,H)** AMO+ from the **(A–D)** 20CRv3 and **(E–H)** ERA-20c datasets. The blue and pink solid contour denotes composites of the 12,500 gpm (for the 20CRv3 dataset) or 12,400 gpm (for the ERA-20c dataset) contour at 200 hPa during AMO− or AMO+ periods in summer. Contour intervals are ±4, ±6, ±8, ±10, ±12, and ±14 gpm **(C,D)** and ±4, ±8, ±10, ±12, ±14, and ±16 gpm **(G,H)**. Dots and black bold vectors denote values that attained the 95% significance level. AMO, Atlantic Multidecadal Oscillation; 20CRv3, Twentieth Century Reanalysis dataset, version 3; ERA-20c, European Centre for Medium-Range Weather Forecasts 20th-century reanalysis.

2014; Shi et al., 2017). A stronger summer SAH changes the upper-level wind circulations and leads to the anomalous easterly flow over the south of the SAH location (represents a stronger upper-level tropical easterly jet). Thus, anomalous lower-level westerly flow over the Arabian Sea occurs *via* the meridional circulation of the ISM and leads to a strengthening of the SMJ.

The AMO is one of the two leading modes of the internally generated interdecadal variability of the climate system (the other is the Interdecadal Pacific Oscillation) (Liu, 2012). It has considerable impacts on the summer monsoon system. As previous studies investigated, the AMO-related SSTAs show a basin-wide warming/cooling in the North Atlantic, with tropical and extratropical branches centered over the tropical North

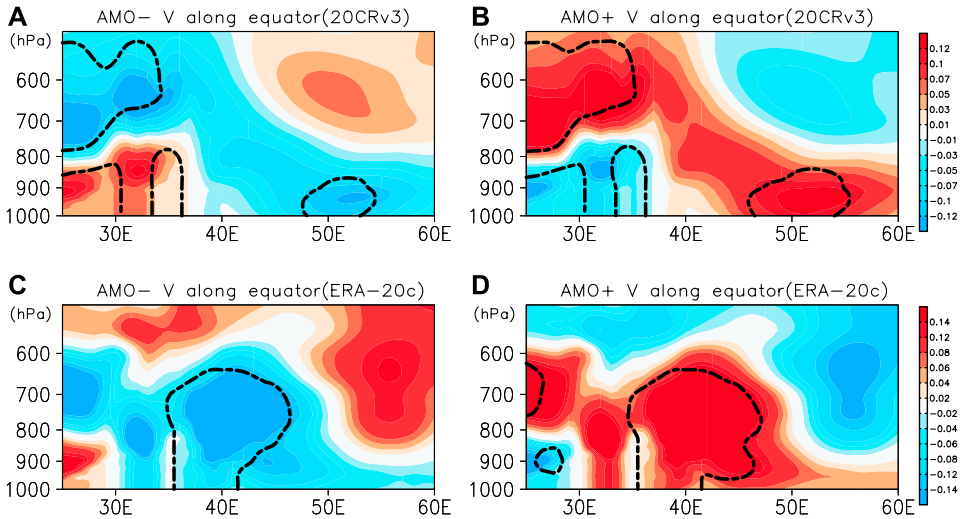

FIGURE 4 | A composite of the zonal mean meridional wind anomalies (unit: m s^{-1}) below 500 hPa along the equator in summer during **(A,C)** AMO− and **(B,D)** AMO + periods from the **(A,B)** 20CRv3 and **(C,D)** ERA-20c datasets. Areas covered by dashed contours denote values that attained the 90% significance level. AMO, Atlantic Multidecadal Oscillation; 20CRv3, Twentieth Century Reanalysis dataset, version 3; ERA-20c, European Centre for Medium-Range Weather Forecasts 20th-century reanalysis.

TABLE 4 | Composite values of the summer SAHI (unit: gpm) and SAHA (unit: grids) in warm/cold AMO phase, as well as their difference from the 20CRv3 and ERA-20c datasets during the period of 1900–2010.

	SAHI (gpm)			SAHA (grids)		
	AMO−	AMO+	Difference	AMO−	AMO+	Difference
20CRv3	**665,803.4**	**797,125.1**	**131,321.7**	8,124.73	8,883.73	**759.01**
ERA-20c	56,521.36	71,839.3	**15,317.94**	1,300.87	1,475.19	**174.32**

Note. The bold data denote values that attained the 95% significance level.
SAHI, intensity of the South Asian High; SAHA, South Asian High area; AMO, Atlantic Multidecadal Oscillation; 20CRv3, Twentieth Century Reanalysis dataset, version 3; ERA-20c, European Centre for Medium-Range Weather Forecasts 20th-century reanalysis.

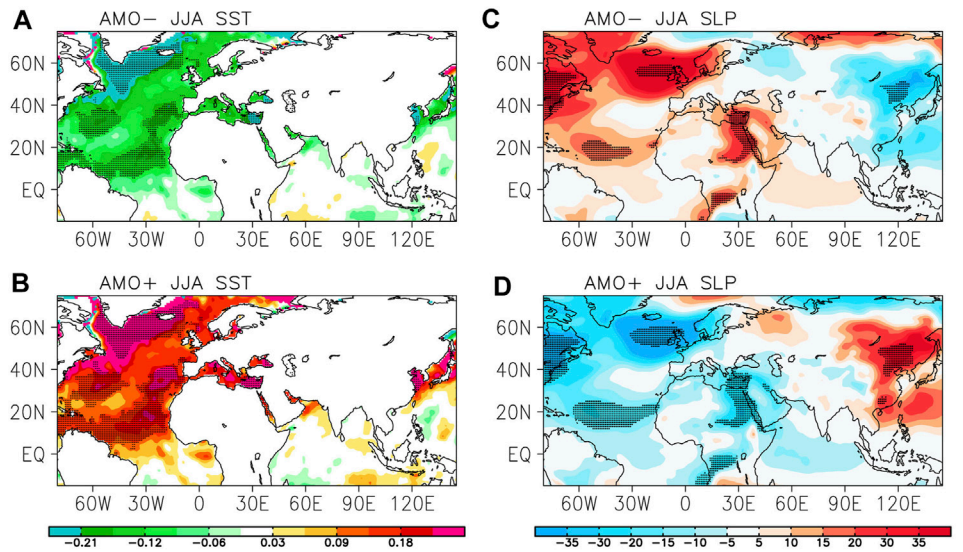

FIGURE 5 | A composite of the summer **(A,B)** SST anomalies (unit: °C) and **(C,D)** sea level pressure anomalies (Pa) over the northern Atlantic Ocean during **(A,C)** AMO− and **(B,D)** AMO+ periods from the ERA-20c dataset during the period 1900–2010. Dots denote values that attained the 95% significance level. SST, sea surface temperature; AMO, Atlantic Multidecadal Oscillation; ERA-20c, European Centre for Medium-Range Weather Forecasts 20th-century reanalysis.

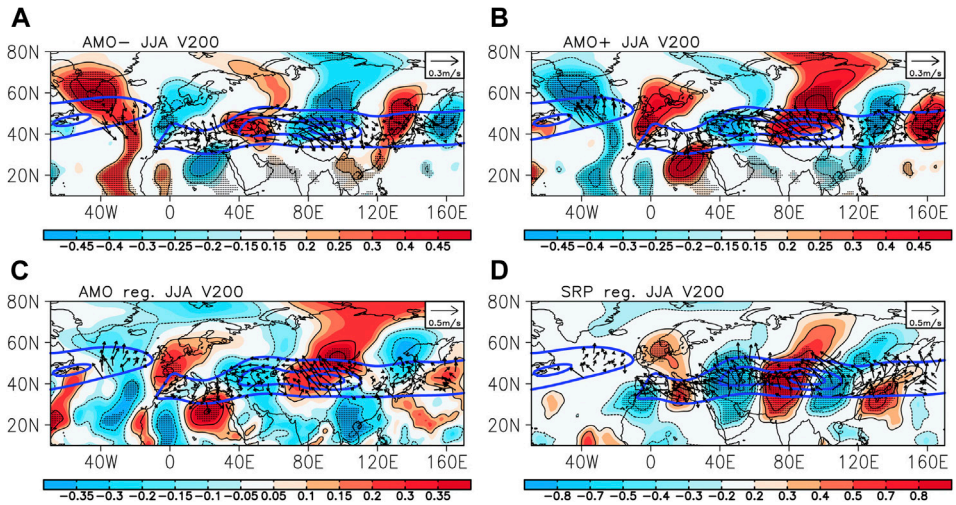

FIGURE 6 | A composite of the 200-hPa meridional wind (V200) anomalies (color shading; unit: m s^{-1}) and the horizontal component of the wave activity flux (arrow; unit: m^2 s^{-2}) in summer during **(A)** AMO− and **(B)** AMO+ periods. Regressions of the interdecadal component of the summer 200-hPa meridional wind anomalies (color shading; units: m s^{-1}) and horizontal wave activity fluxes (arrow; unit: m^2 s^{-2}) onto the interdecadal component of the summer **(C)** AMO and **(D)** SRP index from the ERA-20c datasets during the period 1900–2010. The blue solid contours are climatological 200-hPa zonal wind in summer (units: m s^{-1}). Contour intervals are ±0.2, ±0.4, and ±0.6 m s^{-1} **(A,B,D)** and ±0.1, ±0.3, and ±0.5 m s^{-1} **(C)**. Dots denote values that attained the 90% significance level. AMO, Atlantic Multidecadal Oscillation; SRP, Silk Road pattern; ERA-20c, European Centre for Medium-Range Weather Forecasts 20th-century reanalysis.

Atlantic and Labrador Sea, respectively (e.g., Sutton and Hodson, 2005; Gastineau and Frankignoul, 2015). **Figures 2B–I** show regressions of the interdecadal SST component onto the interdecadal component of the SMJI and PC1 in summer from the different datasets. The AMO-like regression SST patterns are seen from the northern Atlantic Ocean in the JRA-55, 20CRv3, and ERA-20c datasets. In contrast, the AMO-like SSTAs are much weaker in the NCEP/NCAR dataset than those in the other datasets. This analysis reveals a positive correlation of the AMO with the SAHI and SMJI in an interdecadal timescale. A remarkable feature of the AMO index in the latest 100 years is that the AMO has experienced three cold–warm phase turnings, with the turning points in near mid-1920s, 1960s, and mid-1990s (**Figure 2A**). Comparing **Figures 1F,H** and **Figure 2A**, it is easy to find that these three indices (PC1, SMJI, and AMO) evolve almost synchronously on multidecadal timescales, with the two AMO cold phases (AMO−) for a period of 59 years (1900–1925 and 1963–1995) corresponding to the weak phases for the SAH and SMJ, and the two warm AMO phases (AMO+) for 52 years (1926–1962 and 1996–2010) corresponding to the strong phases for the SAH and SMJ.

Variations of the Wind and Geopotential High Fields

In the following, we further conduct a composite analysis of the summer 925-hPa wind anomalies, 200-hPa geopotential height anomalies, and zonal mean meridional wind anomalies below 500 hPa along equator for AMO− years (1900–1925 and 1963–1995) and AMO+ years (1926–1962 and 1996–2010). The blue and pink solid contours in **Figure 3** represent the composited ridge lines (i.e., 12,500- or 12,400-gpm contours of the 200-hPa geopotential height) of the summer SAH for the AMO− and AMO+ years, respectively. **Figures 3E,F** show that significant northwesterly/southeasterly anomalies appear over the western Indian Ocean between 0° and 25°S for AMO−/AMO+ years in the ERA-20c dataset, indicating marked weakening/strengthening of the SMJ in the AMO cold/warm phase. This is also announced by northerly/southerly wind anomalies for the AMO−/AMO+ phase from the ERA-20c dataset at 40°E below 600 hPa, which is the domain region of the SMJ, with its maximum center occurring between 800 and 700 hPa (**Figures 4C,D**). The significant northerly/southerly anomalies from the Arabian Sea to the Southern Indian Ocean are also seen from the 925–hPa wind anomalies composite of the 20Rv3 dataset (**Figures 3A,B**). The northerly/southerly wind anomalies exceeding 90% confidence level for AMO−/AMO+ phase in the 20CRv3 dataset are also found at 50°E below 800 hPa. Furthermore, associated with the AMO cold/warm phase, large-scale negative/positive geopotential height anomalies at 200 hPa are seen from **Figures 3C,D,G,H** with significant values over Northeast Asia and the Mediterranean Sea and extending from the Arabian Peninsula to the Bay of Bengal. In comparison, the significant height anomaly area from the 20CRv3 dataset, which extends from the Northern Africa to the northwestern Pacific Ocean is substantially larger than that from the ERA-20c dataset. The above evidences indicate that when the AMO is in the cold (warm) phase, the summer SAH tends to weaken and shrink (intensify and expand) as revealed by the composited ridge lines and the composites of the SAH intensity and area calculated in **Table 4**. The quantitative analyses in **Table 4** clearly show that the differences of the SAH area and intensity between the warm and cold AMO phases from both 20CRv3 and ERA-20c datasets are significant and exceed the 95% confidence level.

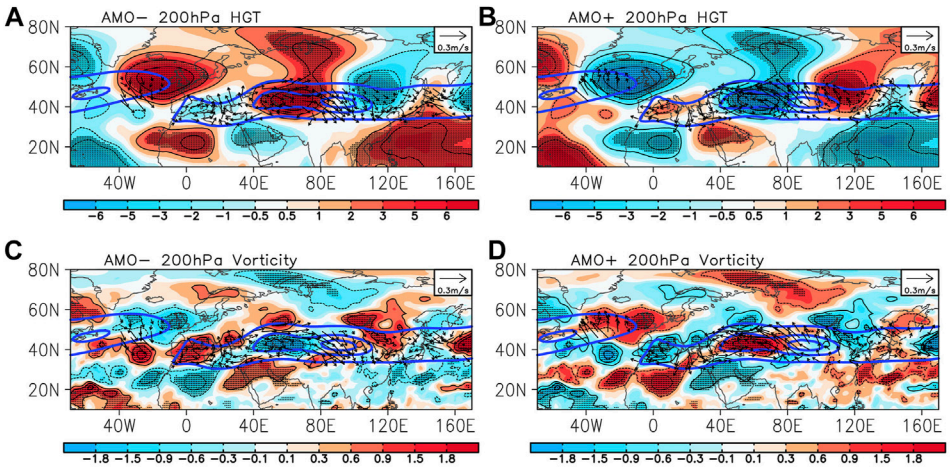

FIGURE 7 | A composite of **(A,B)** the departure from zonal mean 200-hPa geopotential height (HGT) anomalies (color shading; unit: gpm) and **(C,D)** the 200-hPa relative vorticity anomalies (color shading; unit: 10^{-6} s^{-1}) with the horizontal wave activity flux (arrow; unit: m^2 s^{-2}) in summer during **(A)** AMO− and **(B)** AMO+ periods from the ERA-20c datasets during the period 1900–2010. The blue solid contours are climatological 200-hPa zonal wind in summer (units: m s^{-1}). Contour intervals are ±2, ±4, and ±6 gpm **(A,B)** and ±0.6, ±1.2, and ±1.8 × 10^{-6} s^{-1} **(C,D)**. Dots denote values that attained the 90% significance level. AMO, Atlantic Multidecadal Oscillation; ERA-20c, European Centre for Medium-Range Weather Forecasts 20th-century reanalysis.

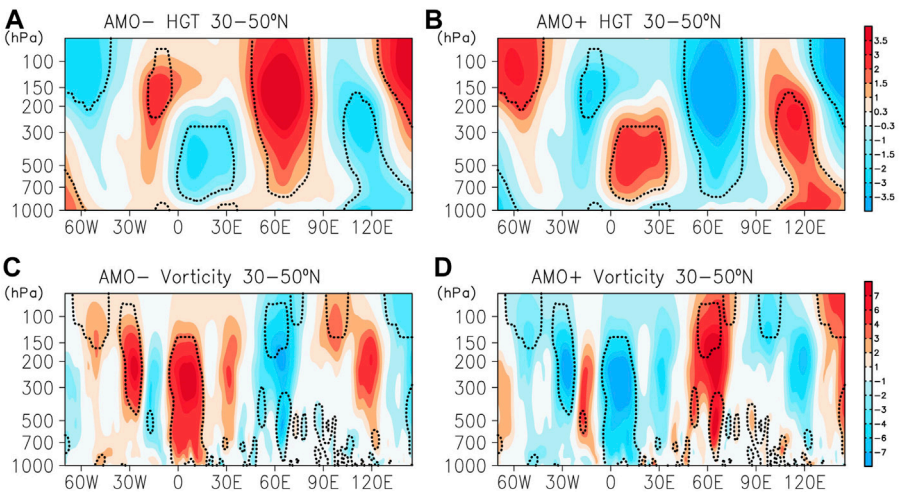

FIGURE 8 | A composite of the **(A,B)** zonal mean (30°–50°N) geopotential height anomalies (departures from zonal means; unit: gpm) and **(C,D)** the relative vorticity anomalies (color shading; unit: 10^{-6} s^{-1}) in summer during **(A,C)** AMO− and **(B,D)** AMO+ periods from the ERA-20c dataset during the period 1900–2010. Areas covered by dotted contours denote values that attained the 90% significance level. AMO, Atlantic Multidecadal Oscillation; ERA-20c, European Centre for Medium-Range Weather Forecasts 20th-century reanalysis.

MODULATION MECHANISM OF THE SUMMER SOUTH ASIAN HIGH AND SOMALI JET BY THE ATLANTIC MULTIDECADAL OSCILLATION ON AN INTERDECADAL TIMESCALE

The previous section illustrated that the interdecadal variabilities of the SAH and SMJ in summer were closely associated with the AMO. In the following, we extend our investigation into how the variations of the SAH and SMJ on the interdecadal timescale are modulated by the AMO phase.

Interdecadal Silk Road Pattern-Like Wave Train

To investigate the effects of the AMO phases on the intensity of the SAH and SMJ on the interdecadal timescale, a composite

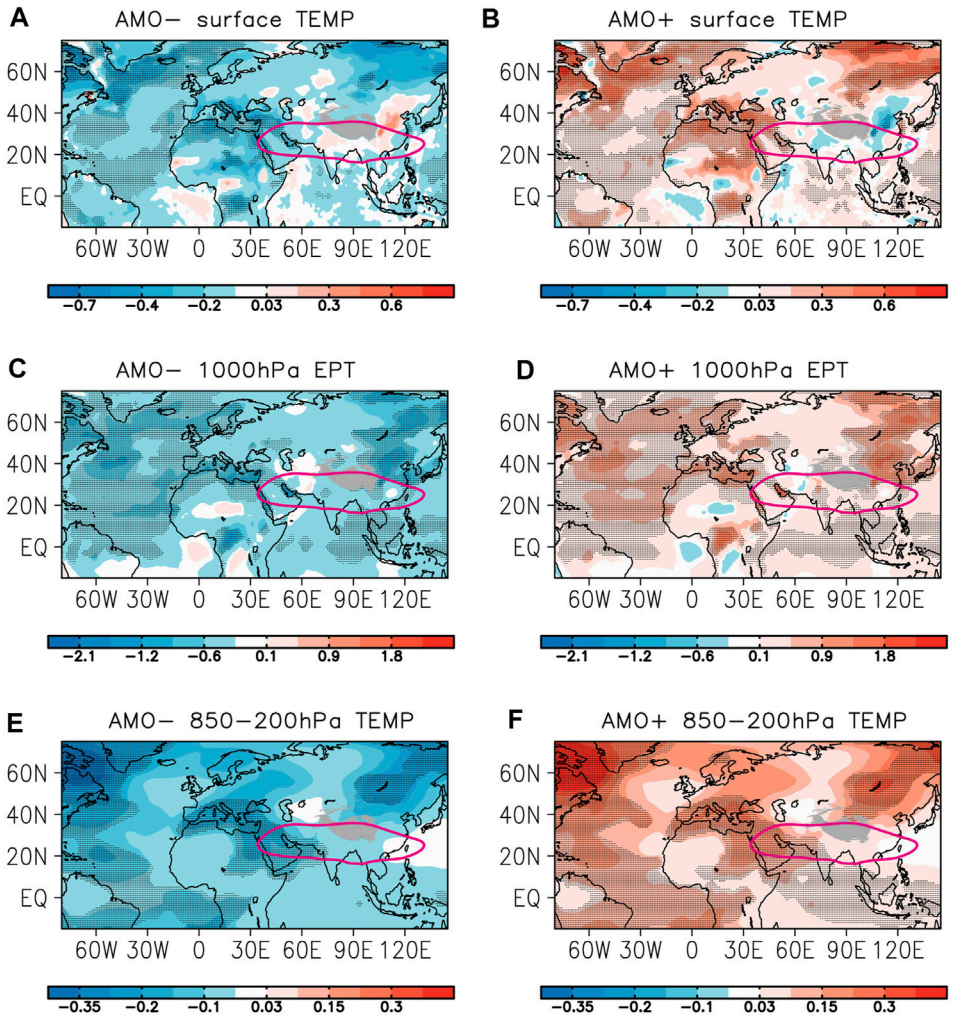

FIGURE 9 | A composite of the summer **(A,B)** surface air temperature anomalies (unit: °C), **(C,D)** equivalent potential temperature anomalies (unit: °C) at 1,000 hPa, and **(E,F)** tropospheric temperature anomalies (unit: °C) during **(A,C,E)** AMO− and **(B,D,F)** AMO+ periods from the ERA-20c dataset during the period 1900–2010. Dots denote values that attained the 90% significance level. Shadings in gray indicate the Tibetan Plateau region. The pink contour denotes the climatological isoline of 12,400 gpm at 200 hPa in summer. AMO, Atlantic Multidecadal Oscillation; ERA-20c, European Centre for Medium-Range Weather Forecasts 20th-century reanalysis.

analysis is performed on the lower and upper atmospheric circulations for the AMO− and AMO+ periods. **Figure 5** illustrates the composites of the SSTAs over the northern Atlantic Ocean and SLP anomalies in summer during the AMO− and AMO+ periods for the ERA-20c dataset during the period of 1900–2010. In the AMO− phase, the negative SSTAs are clearly seen over nearly the whole northern Atlantic Ocean region. Two significant value branches centered over the tropical North Atlantic and Labrador Sea. However, remarkable positive SLP anomalies are located near 20°N and 60°N of the Atlantic Ocean, as well as around the west of the Arabian Peninsula. Clearly, the large-scale negative SLP anomalies appear in Northeast Asia. In the AMO+ phase, the result is well similar to that in the AMO− but with the opposite sign. The tropical and extratropical branches of the SSTAs are coinciding with the location of the SLP anomalies over the northern Atlantic Ocean. It seems that the cold/warm Atlantic Ocean SSTAs could promote/reduce SLP anomalies over the tropical and extratropical Atlantic Ocean because of the atmospheric instability. Significantly, the SLP anomalies around the west of the Arabian Peninsula weaken/enhance the SLP gradient between the tropical Indian Ocean and the continent to its northwest, which will mainly contribute to the decreased/reinforced SMJ strength on the interdecadal timescale as shown in **Figures 3E,F**.

Along the Asian westerly jet, there is a wave train-like teleconnection pattern zonally propagating from Europe to East Asia. This pattern is referred to as the SRP, which is similar to the CGT over the Eurasian continent (e.g., Ding and Wang, 2005; Hong et al., 2018). The SRP, the leading mode of the upper tropospheric meridional wind anomalies in summer (e.g., Hong and Lu, 2016; Kosaka et al., 2009; Sato and Takahashi, 2006; Cen et al., 2020), indicates both a remarkable interannual component and a considerable decadal component (e.g., Enomoto et al., 2003; Lu et al., 2002; Sato and Takahashi,

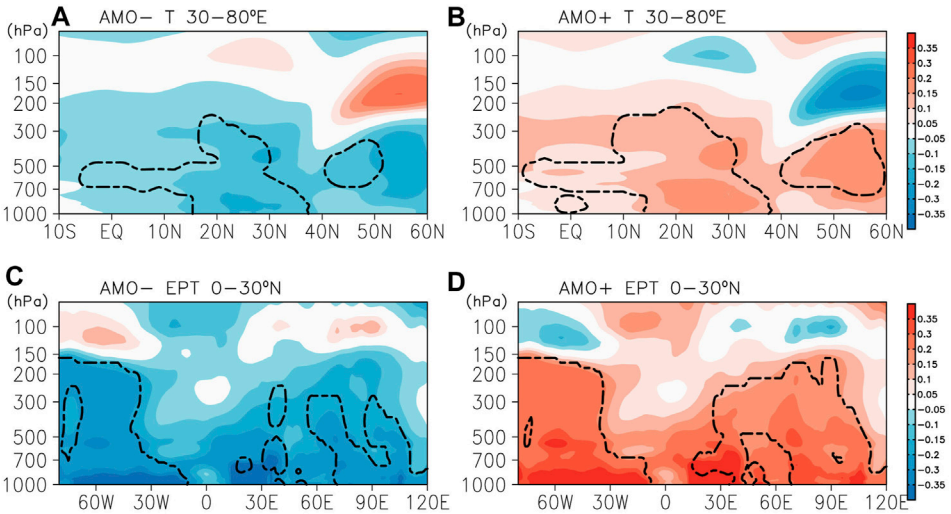

FIGURE 10 | A composite of **(A,B)** the meridional mean (30°–80°E) air temperature anomalies (unit: °C) and **(C,D)** the zonal mean (0°–30°N) equivalent potential temperature anomalies (unit: °C) in summer during **(A,C)** AMO− and **(B,D)** AMO+ periods from the ERA-20c dataset during the period 1900–2010, respectively. Areas covered by dashed contours denote values that attained the 90% significance level. AMO, Atlantic Multidecadal Oscillation; ERA-20c, European Centre for Medium-Range Weather Forecasts 20th-century reanalysis.

2006; Hong et al., 2018; Wang et al., 2017; Lin et al., 2016). The temporal evolution in the interdecadal component of the SRP was found to be synchronous with that in the AMO. Based on sensitivity experiments driven by the specified AMO-related SSTAs in the North Atlantic using five AGCMs, Lin et al. (2016) suggested that ID-CGT pattern should be excited, at least partially, by the AMO-related SSTAs. To confirm this, **Figures 6A,B** illustrate composites of the summer 200-hPa meridional wind anomalies and the summer horizontal wave activity flux during the AMO− and AMO+ phases for 1900–2010. The wind anomalies appear as a clear wave-like pattern characterized by alternate southerly and northerly anomalies along the Asian westerly jet (the blue solid contours in **Figure 6**). The midlatitude wave train is consistent with the interdecadal component of SRP as announced by various previous studies (e.g., Chen and Huang, 2012; Hong and Lu, 2016; Kosaka et al., 2009; Lu et al., 2002; Sato and Takahashi, 2006; Yasui and Watanabe, 2010). For the AMO− period, southerly anomalies are centered over the tropical North Atlantic, Labrador Sea, Caspian Sea, and northeast Asian and northerly anomalies around the East Europe, North Africa, Lake Belga, and east of the Okhotsk Sea (**Figure 6A**). The wave activity flux (Takaya and Nakamura 2001) associated with the AMO− phase emanates from Europe, enters the Asian jet stream near the Caspian Sea, and points continuously eastward toward East Asia along the jet stream, confirming that the wave-like pattern is a Rossby wave train. For the AMO+ period, locations and amplitudes of the anomalous centers tend to be similar but with the opposite phase (**Figure 6B**). To further confirm whether this AMO-related wave-like pattern is similar to the interdecadal SRP, we then compare the regression of the interdecadal component of the summer 200-hPa meridional wind and horizontal wave activity flux anomalies onto the interdecadal component of the summer AMO and SRP indices in **Figures 6C,D**. Clearly, the alternate southerly and northerly anomalous centers along the Asian westerly jet are essentially consistent in **Figures 6C,D**, except for the anomalies over the northern Atlantic Ocean. Both regressions of the horizontal wave activity flux anomalies in **Figures 6C,D** are propagating from East Asian to Europe along the jet stream, which reveals the warm AMO phase corresponding to the negative phase of the SRP. Similar results are obtained by Wang et al. (2017), and they also suggest that the positive (negative) phase of the AMO significantly facilitates the occurrence of a negative (positive) phase of the interdecadal SRP (e.g., figure 9B and figures 11A,B of Wang et al., 2017). The spatial similarity coefficient between the regression of the interdecadal 200-hPa meridional wind onto the AMO index (**Figure 6C**) and that onto the SRP index (**Figure 6D**) in the main SRP region (30°–60°N, 30°–130°E) is as high as 0.72, indicating that the AMO-related wave-like pattern is a SRP-like wave train.

Figure 7 is the same as **Figure 6**, but for the summer 200-hPa geopotential height anomalies (departures from zonal means), 200-hPa relative vorticity anomalies, and horizontal wave-activity flux anomalies. In the AMO− phase, a well-organized wave train between 30°N and 60°N propagates along the Asian westerly jet (the blue solid contours in **Figure 7**) with positive geopotential height/negative relative vorticity anomalies over the northern Atlantic Ocean and east of the Caspian Sea and negative geopotential height/positive relative vorticity anomalies over the Mediterranean Sea, Arabian Peninsula–Iranian Plateau, and Northeast Asia (**Figures 7A,C**). These positive and negative anomalies are consistent with the 200-hPa meridional wind anomalies shown in **Figure 6A**. Actually, this atmospheric wave train originated from the extratropical Atlantic Ocean, which can be confirmed by the wave activity flux (**Figure 7A**). This suggests that in virtue of the strong barotropic instability at the jet exit region over the North Atlantic during the

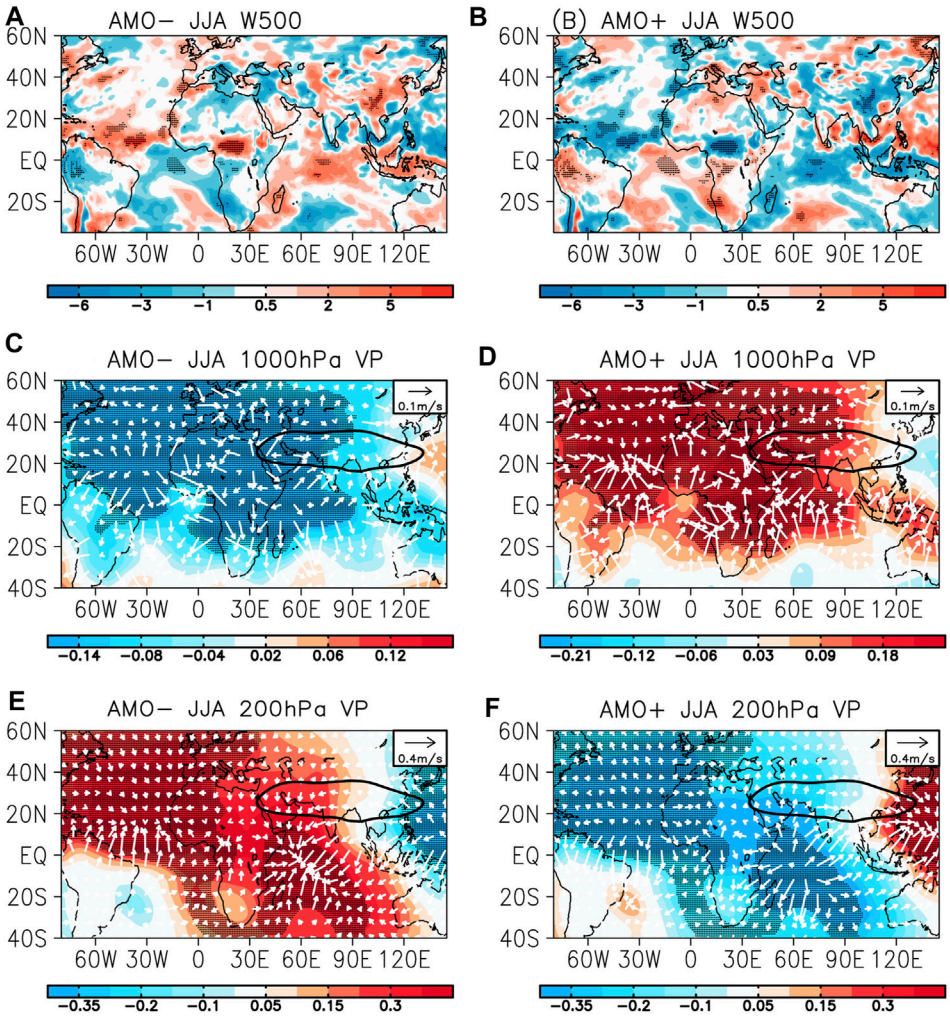

FIGURE 11 | A composite of **(A,B)** the 500-hPa omega (10^{-3} Pa s^{-1}) anomalies, the **(C,D)** 1,000-hPa and **(E,F)** 200-hPa divergent winds (arrow, m s^{-1}), and stream function (shadings, 10^{-4} m^2 s^{-1}) anomalies in summer during **(A,C,E)** AMO− and **(B,D,F)** AMO+ periods from the ERA-20c dataset during the period 1900–2010. Dots denote values that attained the 90% significance level. AMO, Atlantic Multidecadal Oscillation; ERA-20c, European Centre for Medium-Range Weather Forecasts 20th-century reanalysis.

AMO− phase, an anomalous high can be triggered over the extratropical Atlantic Ocean, followed by alternatively positive and negative anomalies further downstream. The consistent positive anomalies over the extratropical Atlantic Ocean and negative anomalies over Northeast Asia in SLP with those in 200-hPa geopotential height reveal a barotropic structure. The barotropic property of the Rossby wave train on interdecadal timescale as suggested by previous studies (Luo et al., 2011; Lin et al., 2016; Hong et al., 2018) also can be revealed by the zonal mean height/relative vorticity from 30°W to 120°E in **Figure 8**. The barotropy of the cyclonic/anticyclonic centers between 0° and 30°E in the AMO−/AMO+ phase is relatively weak in the geopotential height field (**Figures 8A,B**), but it is strong and significant in the relative vorticity field (**Figures 8C,D**). As suggested by Hoskins et al. (1977), the relative vorticity has some advantages over geopotential height in representing the two-dimensional propagation of Rossby waves.

As indicated by the wave activity flux, the interdecadal SRP-like wave train excited by the cold SST anomalies over the extratropical Atlantic Ocean propagates poleward across Europe and then to the equator across Northeast Asia. Specifically, the negative 200-hPa geopotential height/positive 200-hPa relative vorticity anomalies from the Mediterranean Sea to the Arabian Peninsula corresponding to the positive SLP anomalies around the west of the Arabian Peninsula indicate a strong baroclinicity of the local atmospheric circulation, which is favorable to the weakening of the SAH and SMJ. Meanwhile, the strong and significant anomalies over the northwest Pacific Ocean in the geopotential height field (departure from zonal mean) are relatively weak and insignificant in the original geopotential height (**Figures 3G,H**) and relative vorticity fields (**Figures 7C,D**), which suggests that the weakening or strengthening of the summer SAH mainly rely on the low/high anomaly from the Arabian

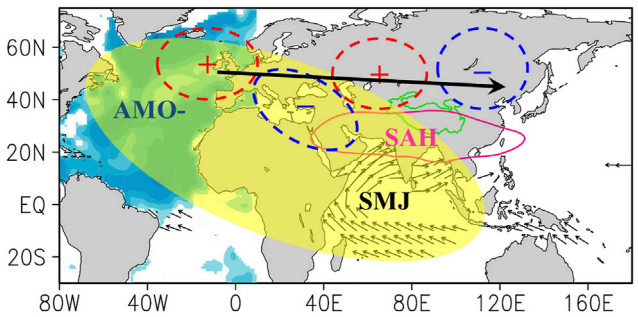

FIGURE 12 | Schematic diagram illustrates modulation mechanism of the summer SAH and SMJ interdecadal variabilities by the AMO− phase *via* the interdecadal Silk Road pattern and Matsuno–Gill-like tropical atmospheric response. Blue shading over North Atlantic denotes the negative SST anomalies related to AMO− phase. Red circle and blue circle respectively represent the positive and negative anomalies of 200-hPa geopotential heights in AMO− phase. The black solid line with an arrow is the propagation path of the interdecadal Silk Road pattern. The pink contour denotes the climatological location of the SAH in summer. The black arrows indicate the summer SMJ. Contour in green indicates the Tibetan Plateau region. SAH, South Asian High; SMJ, Somali jet; AMO, Atlantic Multidecadal Oscillation; SST, sea surface temperature.

Peninsula to the Bay of Bengal (**Figures 3G,H**). In the AMO+ phase, a similar Rossby wave train pattern propagating from the North Atlantic across Northeast Asia is visible (**Figures 7B,D**), but with a quite opposite phase. The above result indicates that a propagating Rossby wave train associated with the AMO−/AMO+ phase leads to reduced/enhanced SAH *via* the anomalous Arabian Peninsula–Iranian Plateau low/high along with its path, and consequently a weakening/strengthening of the SMJ through the weakened/enhanced pressure gradient between the tropical Indian Ocean and the continent, which is caused by the baroclinic structure of the local atmospheric circulation over the Arabian Peninsula–Iranian Plateau (**Figures 5C,D**).

Tropical Atmospheric Response

By now, we have clearly demonstrated the modification of AMO-related SSTAs on the interdecadal variabilities of the SAH and SMJ intensities through the propagation of the interdecadal SRP-like wave train excited by the extratropical heating branch. As diagnosed in **Figures 5A,B**, the tropical heating branch related to the AMO phase cannot be ignored, but how it can exert influence on the interdecadal variabilities of SAH and SMJ intensities is still unclear. To investigate the tropical atmospheric response to AMO-related SST anomalies, we conducted a composite analysis of SAT anomalies, equivalent potential temperature (EPT) anomalies at 1,000 hPa, and tropospheric temperature anomalies (average between 850 and 200 hPa) in summer during the AMO− and AMO+ periods (**Figure 9**). For the summer SAT, significant negative temperature anomalies exist over the tropical and extratropical North Atlantic, as well as the northern African continent and Central Siberia area in AMO−, but there are obvious positive anomalies over these domains in the AMO+. The response of the EPT anomalies at 1,000 hPa is the same as that of the SAT, but with the significant value around the Central Siberia area, which expands southward to the tropical Indian Ocean, which is a result of the Matsunuo–Gill response of the tropical atmosphere. For the tropospheric temperature (average between 850 and 200 hPa), the temperature response exhibits a Matsunuo–Gill-like pattern with uniform negative/positive values zonally extending to the entire tropical region in the AMO−/AMO+ phase. Qian et al. (2002) pointed out that the center of the SAH has the heat preference property, which is usually located over or moving toward an area with larger heating rates. Huang et al. (2011) also indicated that tropical tropospheric temperature variation is closely related to geopotential height anomalies at the upper troposphere and variation of the SAH in terms of both intensity and spatial location. The tropospheric warming over the tropical Indian Ocean is favorable for a positive height anomaly in the south of the SAH location in summer, which results in the strengthening and southward shifting of the SAH. According to the barometric equation, the negative/positive AMO-related tropical SSTAs cool/warm the tropospheric temperature in the south of the SAH location and then lower/elevate the height above it, which is favorable for the weakening/strengthening and northward/southward expansion of the SAH.

Besides, pronounced anomalies are found around the western Atlantic Ocean, northeast Asia, Mediterranean Sea, and Arabian Peninsula, which mainly result from the interdecadal SRP-like wave train triggered by the extratropical AMO-related SST anomalies. Among them, the significant negative/positive temperature anomalies from the Mediterranean Sea to the Arabian Peninsula could decrease/increase meridional gradient of the tropospheric temperature between the tropical Indian Ocean and its north continent. The increased meridional gradient anomalies of the tropospheric temperature over the tropical Indian Ocean associated with the AMO+ could enhance the SMJ. This mechanism coincides with previous works (Goswami et al., 2006; Feng and Hu, 2008; Li et al., 2008; Luo et al., 2011), which viewed that the ISM may be enhanced by the AMO through the increased meridional gradient of the tropospheric temperature between the Indian subcontinent and tropical Indian Ocean. To provide more evidence, the composite of the meridional mean (30°–80°E) air temperature anomalies in summer during the AMO− and AMO+ periods is investigated in **Figures 10A,B**. In AMO−, remarkably significant negative values between 20°N and 30°N could extend to nearly 200 hPa, which reduces the meridional gradient of the

tropospheric temperature between the tropical Indian Ocean and its north continent, as well as consequently weaken the SMJ intensity. The result in the AMO+ phase is exactly opposite to that in AMO−, with stronger positive anomalies at 20°N–30°N from the surface to the upper layer, which mainly contribute to the strengthened SMJ.

Next, how can the AMO-related SSTAs or SAT anomalies over the tropical Atlantic Ocean influence the tropical tropospheric temperature anomalies? Many studies viewed that the moist adjustment process was very important for the tropospheric warming in the tropical atmosphere (Emanuel et al., 1994; Su et al., 2003; Su and Neelin, 2003). As verified by Xie et al. (2009), SST warming in the tropical Indian Ocean could warm the overlying atmospheric column through modifying the EPT and moist static energy in the atmospheric boundary layer, with a Matsunuo–Gill response of the tropospheric temperature anomalies located over the Indian Ocean. A qualitatively similar response of the tropical tropospheric temperature anomalies to the AMO-related SSTAs over tropical North Atlantic is seen from **Figures 9E,F**. Response of the tropospheric temperature to SSTAs in the tropical North Atlantic Ocean exhibits an obvious Matsunuo–Gill-like pattern with the large-scale approximate uniform anomalies covering the whole tropical region. This is also revealed by the zonal mean (0°–30°N) EPT anomalies composed during the AMO− and AMO+ periods in **Figures 10C,D**. In AMO−, the significant negative EPT anomalies can extend from the surface to more than 200 hPa over the tropical Atlantic Ocean (between 80°W and 30°W). An approximate uniform variation of the EPT anomalies from the lower to upper level is also seen between 30° and 90°E. These reveal that the EPT change in the atmospheric boundary layer (seen from **Figures 9C,D**) induced by AMO-related SSTAs is an important pathway through which the lower atmospheric heat can be transferred to the upper layer, modifying the tropospheric thermal variation. In the AMO+, the result is similar to that in AMO−, but with an opposite sign. In brief, the AMO-related tropical SST cooling (warming) induces negative (positive) EPT variation in the atmospheric boundary layer, modulates air temperature of the overlying atmosphere, and further cools (heats) the atmospheric column.

To better understand the AMO modulation on the interdecadal variabilities of the summer SAH and SMJ intensities *via* the tropical atmospheric response, we further focus on the composites of the 500-hPa omega anomalies, divergent wind, and velocity potential anomalies at 1,000 and 200 hPa in summer for the AMO− and AMO+ phases (**Figure 11**). As for the 500-hPa omega anomalies, significant AMO− phase-related subsiding anomalies are found over the northern tropical North Atlantic, southern Sahel, central tropical Indian Ocean, and central East Asia where the reverse signal of vertical velocity can be seen for the AMO+ (**Figures 11A,B**). Among them, the descending motion anomaly over northern tropical North Atlantic and central East Asia in **Figure 11A** is mainly associated with a southward shift and weakening of the climatological Intertropical Convergence Zone (ITCZ), which is in accordance with previous results (e.g., Zhang and Delworth, 2006; Luo et al., 2011), while pronounced descending motion anomalies over the southern Sahel of **Figure 11A** are suggestive of a decreasing Sahel summer rainfall as investigated by Zhang and Delworth (2006). In particular, subsidence motion anomalies over the central tropical Indian Ocean (**Figure 11A**) correspond to a basin-wide divergence in the lower troposphere and convergence in the upper troposphere over the tropical Indian Ocean during the AMO− period (**Figures 11C,E**). The tropical Indian Ocean divergence associated with the AMO− phase in the lower troposphere leads to the weakened SMJ, and the tropical Indian Ocean convergence for the AMO− phase in the upper troposphere is favorable for the decrease and northward displacement of SAH. Here, the extratropical divergence/convergence over the North Atlantic in the lower/upper troposphere is produced by the extratropical North Atlantic heating, and the tropical divergence/convergence extending from North Atlantic to the tropical Indian Ocean in the lower/upper troposphere is suggestive of a Matsunuo–Gill-like pattern trigged by tropical North Atlantic heating in agreement with our above result. For the AMO+ phase, the result is quite opposite, which is conducive to the strengthening of the SMJ and SAH in summer (**Figures 11B,D,F**).

SUMMARY

Based on four reanalysis datasets (JRA-55, NCEP/NCAR, 20CRv3, and ERA-20c), we investigate the interdecadal variation of the SAH and SMJ intensities, as well as their modulation mechanism by AMO phase-related SSTAs in summer. In order to reveal the temporal variation of the summer SAH, 200-hPa geopotential height anomalies in summer (over 15°–40°N; 20°–130°E) are decomposed by an EOF technique. The result shows that the leading spatial pattern of the 200-hPa geopotential height anomalies represents the variation of the SAH intensity. In contrast, the time series of the PC1 is in phase with that of the SMJI on the interdecadal timescale, with almost all of the correlation coefficients between them from different datasets exceeding the 99% confidence level. Regressions of the interdecadal SST component onto the interdecadal SMJI and PC1 component in summer from the different datasets reveal a positive correlation of the AMO with the SAHI and SMJI. Besides, through comparing the time series of the AMO index with that of the PC1 and SMJI, we find that these three indices (PC1, SMJI, and AMO) evolve almost synchronously on multidecadal timescales, with the two AMO cold phases (AMO−) for a period of 59 years (1900–1925 and 1963–1995) corresponding to the weak phases for the SAH and SMJ, and the two warm AMO phases (AMO+) for 52 years (1926–1962 and 1996–2010) corresponding to the strong phases for the SAH and SMJ. The composite analysis of the summer 925-hPa wind and 200-hPa geopotential height anomaly fields in the AMO−/AMO+ phase also supports this result.

The qualitative analysis shows that the interdecadal variabilities of the SAH and SMJ intensities in summer may be modulated by the AMO phase. Next, the tropical and extratropical atmospheric circulations from the Atlantic Ocean to Northeast Asia are examined to investigate the modulation

mechanism of the AMO phase on the summer SAH and SMJ intensities. The modulation mechanism appears to be achieved *via* two ways, which are schematically depicted in **Figure 12**: one is *via* an interdecadal SRP-like wave train propagating from the North Atlantic across Northeast Asia, and the other is *via* a Matsunuo–Gill-like tropical atmospheric response. The former is trigged by extratropical North Atlantic forcing related to the AMO phase, while the latter is tied to the AMO-related tropical North Atlantic heating. On the one hand, as confirmed by the wave activity flux, a cold SST anomaly over extratropical North Atlantic related to the AMO– phase induces an anomalous high over Western Europe due to the strong barotropic instability. The perturbation of geopotential heights gives rise to a well-organized Rossby wave train between 30°N and 60°N propagating along the Asian westerly jet with positive 200-hPa geopotential height anomalies over the northern Atlantic Ocean and east of the Caspian Sea, as well as negative anomalies from the Mediterranean Sea to the Arabian Peninsula–Iranian Plateau and over Northeast Asia. This interdecadal SRP-like wave train over the Eurasian continent excited by the AMO-related SSTAs have been verified by many previous studies (e.g., Li et al., 2008; Luo et al., 2011; Lin et al., 2016). The anomalous Arabian Peninsula–Iranian Plateau low along with the Rossby wave train path leads to a reduced SAH. On the other hand, the AMO-related cold SSTAs over tropical North Atlantic reduce the EPT in the boundary layer. Through the moist adjustment process, the tropical tropospheric atmosphere is continuously cooled and produces a Matsuno–Gill-like atmospheric response covering the tropical Indian Ocean, which lowers the geopotential height above it. Because of the heat preference property in SAH, the SAH will weaken and shift northward. At the same time, superimposed cold anomalies from the Mediterranean Sea to the Arabian Peninsula caused by the interdecadal SRP-like wave train reduce meridional gradient of the tropospheric temperature between the tropical Indian Ocean and its north continent, which is favorable for the weakening of the summer SMJ. This coincides with previous works (Goswami et al., 2006; Feng and Hu, 2008; Li et al., 2008; Luo et al., 2011). Finally, due to a Matsuno–Gill-like response trigged by tropical North Atlantic heating, subsidence motion anomalies over the central tropical Indian Ocean corresponding to a result in increased lower-level divergence and upper-level convergence are produced over the tropical Indian Ocean. The tropical Indian Ocean divergence in the lower troposphere leads to the weakened summer SMJ, and the tropical Indian Ocean convergence in the upper troposphere is favorable for the decrease and northward displacement of SAH in summer.

DATA AVAILABILITY STATEMENT

The original contributions presented in the study are included in the article/Supplementary Material, further inquiries can be directed to the corresponding authors.

AUTHOR CONTRIBUTIONS

WS: Methodology, data curation, manuscript design, and writing—original draft preparation. WS and QW: conceptualization and investigation. ZX: manuscript design and writing—reviewing and editing. WC: writing—reviewing and editing. WD: investigation and data collection.

FUNDING

This work was jointly supported by the Second Tibetan Plateau Scientific Expedition and Research (STEP) program (2019QZKK0105), the National Natural Science Foundation of China (U1902209, 41930972), and the Key Laboratory of Geo-Information Engineering (SKLGIE2019-ZZ-6).

REFERENCES

Ashfaq, M., Shi, Y., Tung, W.-w., Trapp, R. J., Gao, X., Pal, J. S., et al. (2009). Suppression of South Asian Summer Monsoon Precipitation in the 21st century. *Geophys. Res. Lett.* 36 (1), L01704. doi:10.1029/2008GL036500

Bjerknes, J. (1964). Atlantic Air-Sea Interaction. *Adv. Geophys.* 10, 1–82. doi:10.1016/s0065-2687(08)60005-9

Boos, W. R., and Emanuel, K. A. (2009). Annual Intensification of the Somali Jet in a Quasi-Equilibrium Framework: Observational Composites. *Q.J.R. Meteorol. Soc.* 135, 319–335. doi:10.1002/qj.388

Cadet, D., and Desbois, M. (1981). A Case Study of a Fluctuation of the Somali Jet during the Indian Summer Monsoon. *Mon. Wea. Rev.* 109, 182–187. doi:10.1175/1520-0493(1981)109<0182:acsoaf>2.0.co;2

Cen, S., Chen, W., Chen, S., Liu, Y., and Ma, T. (2020). Potential Impact of Atmospheric Heating over East Europe on the Zonal Shift in the South Asian High: the Role of the Silk Road Teleconnection. *Sci. Rep.* 10, 6543. doi:10.1038/s41598-020-63364-2

Chakraborty, A., Nanjundiah, R. S., and Srinivasan, J. (2009). Impact of African Orography and the Indian Summer Monsoon on the Low-Level Somali Jet. *Int. J. Climatol.* 29 (7), 983–992. doi:10.1002/joc.1720

Chen, G., and Huang, R. (2012). Excitation Mechanisms of the Teleconnection Patterns Affecting the July Precipitation in Northwest China. *J. Clim.* 25 (22), 7834–7851. doi:10.1175/jcli-d-11-00684.1

Compo, G. P., Whitaker, J. S., Sardeshmukh, P. D., Matsui, N., Allan, R. J., Yin, X., et al. (2011). The Twentieth Century Reanalysis Project. *Q.J.R. Meteorol. Soc.* 137, 1–28. doi:10.1002/qj.776

Dai, W., and Xiao, Z. N. (2014). Multi–Time Scale Variation Characteristics of Somali Jet and its Contact with Precipitation in China. *J. Trop. Meteorol.* 30 (2), 368–376. doi:10.3969/j.issn.1004-4965.2014.02.018 (in Chinese).

Delworth, T. L., and Mann, M. E. (2000). Observed and Simulated Multidecadal Variability in the Northern Hemisphere. *Clim. Dyn.* 16, 661–676. doi:10.1007/s003820000075

Ding, Q., and Wang, B. (2005). Circumglobal Teleconnection in the Northern Hemisphere Summer*. *J. Clim.* 18 (17), 3483–3505. doi:10.1175/JCLI3473.1

Emanuel, K. A., David Neelin, J., and Bretherton, C. S. (1994). On Large-Scale Circulations in Convecting Atmospheres. *Q.J R. Met. Soc.* 120, 1111–1143. doi:10.1002/qj.49712051902

Enomoto, T., Hoskins, B. J., and Matsuda, Y. (2003). The Formation Mechanism of the Bonin High in August. *Q. J. R. Meteorol. Soc.* 129 (587), 157–178. doi:10.1256/qj.01.211

Enomoto, T. (2004). Interannual Variability of the Bonin High Associated with the Propagation of Rossby Waves along the Asian Jet. *J. Meteorol. Soc. Jpn.* 82, 1019–1034. doi:10.2151/jmsj.2004.1019

Feng, S., and Hu, Q. (2008). How the North Atlantic Multidecadal Oscillation May Have Influenced the Indian Summer Monsoon during the Past Two Millennia. *Geophys. Res. Lett.* 35, L01707. doi:10.1029/2007gl032484

Findlater, J. (1969). A Major Low-Level Air Current Near the Indian Ocean during the Northern Summer. *Q.J R. Met. Soc.* 95 (404), 362–380. doi:10.1002/qj.49709540409

Folland, C. K., and Parker, D. E. (1990). "Observed Variations of Sea Surface Temperature," in *Climate–Ocean Interaction* (Dordrecht: Springer), 21–52. doi:10.1007/978-94-009-2093-4_2

Gastineau, G., and Frankignoul, C. (2015). Influence of the North Atlantic SST Variability on the Atmospheric Circulation during the Twentieth Century. *J. Clim.* 28, 1396–1416. doi:10.1175/jcli-d-14-00424.1

Goswami, B. N., Madhusoodanan, M. S., Neema, C. P., and Sengupta, D. (2006). A Physical Mechanism for North Atlantic SST Influence on the Indian Summer Monsoon. *Geophys. Res. Lett.* 33, L02706. doi:10.1029/2005GL024803

Halpern, D., and Woiceshyn, P. M. (2001). Somali Jet in the Arabian Sea, El Niño, and India Rainfall. *J. Clim.* 14, 434–441. doi:10.1175/1520-0442(2001)014<0434:sjitas>2.0.co;2

He, J., Wen, M., Ding, Y., and Zhang, R. (2006). Possible Mechanism of the Effect of Convection over Asian-Australian "land Bridge" on the East Asian Summer Monsoon Onset. *Sci. China Ser. D* 49 (11), 1223–1232. doi:10.1007/s11430-006-2039-0

Hong, X., and Lu, R. (2016). The Meridional Displacement of the Summer Asian Jet, Silk Road Pattern, and Tropical SST Anomalies. *J. Clim.* 29 (10), 3753–3766. doi:10.1175/jcli-d-15-0541.1

Hong, X.-W., Xue, S.-H., Lu, R.-Y., and Liu, Y.-Y. (2018). Comparison between the Interannual and Decadal Components of the Silk Road Pattern. *Atmos. Oceanic Sci. Lett.* 11 (11), 270–274. doi:10.1080/16742834.2018.1439661

Hoskins, B. J., Simmons, A. J., and Andrews, D. G. (1977). Energy Dispersion in a Barotropic Atmosphere. *Q.J R. Met. Soc.* 103, 553–567. doi:10.1002/qj.49710343802

Hu, J., Zhou, B., and Tao, Li. (2010). Comparative Analysis of the Relation between Characteristic Parameters of South Asia High and Summer Precipitation of China. *Meteorol. Mon.* 36 (4), 51–56. doi:10.3788/HPLPB20102207.1462 (in Chinese).

Huang, Y., and Qian, Y. (2004). Relationship between South Asian High and Characteristics of Precipitation in Mid– and Lower– Reaches of Yangtze River and North China. *Plateau Meteorol.* 23, 70–76. (in Chinese). doi:10.3321/j.issn:1000–0534.2004.01.010

Huang, G., Qu, X., and Hu, K. (2011). The Impact of the Tropical Indian Ocean on South Asian High in Boreal Summer. *Adv. Atmos. Sci.* 28 (2), 421–432. doi:10.1007/s00376-010-9224-y

Jia, J., and Liu, Y. (2020). Spatial–temporal Characteristics of the Asia High Warm Center and Atmospheric Waves Excited by it in Upper Troposphere. *Chin. J. Geophy.* 63 (10), 3626–3639. (in Chinese). doi:10.6038/cjg2020N0162

Joseph, P. V., and Raman, P. L. (1966). Existence of Low–Level Westerly Jet Stream over Peninsular India During July. *Indian J. Meteorol. Geophys.* 17, 407–410.

Kalnay, E., Kanamitsu, M., Kistler, R., Collins, W., Deaven, D., Gandin, L., et al. (1996). The NCEP/NCAR 40-Year Reanalysis Project. *Bull. Amer. Meteorol. Soc.* 77, 437–471. doi:10.1175/1520-0477(1996)077<0437:tnyrp>2.0.co;2

Kerr, R. A. (2000). A North Atlantic Climate Pacemaker for the Centuries. *Science* 288, 1984–1985. doi:10.1126/science.288.5473.1984

Knight, J. R., Folland, C. K., and Scaife, A. A. (2006). Climate Impacts of the Atlantic Multidecadal Oscillation. *Geophys. Res. Lett.* 33, L17706. doi:10.1029/2006GL026242

Kobayashi, S., Ota, Y., Harada, Y., Ebita, A., Moriya, M., Onoda, H., et al. (2015). The JRA-55 Reanalysis: General Specifications and Basic Characteristics. *J. Meteorol. Soc. Jpn.* 93, 5–48. doi:10.2151/jmsj.2015-001

Kosaka, Y., Nakamura, H., Watanabe, M., and Kimoto, M. (2009). Analysis on the Dynamics of a Wave-like Teleconnection Pattern along the Summertime Asian Jet Based on a Reanalysis Dataset and Climate Model Simulations. *J. Meteorol. Soc. Jpn.* 87 (3), 561–580. doi:10.2151/jmsj.87.561

Krishnamurti, T. N., and Bhalme, H. N. (1976). Oscillations of a Monsoon System. Part I. Observational Aspects : Observational Aspects. *J. Atmos. Sci.* 33, 1937–1954. doi:10.1175/1520-0469(1976)033<1937:ooamsp>2.0.co;2

Lei, X., and Yang, X. (2008). Interannual Variation Characteristic of Eastern Hemispheric Crossequatorial Flow and its Contemporaneous Relationships with Temperature and Rainfall in China. *J. Trop. Meteorol.* 24, 127–135. (in Chinese). doi:10.1016/s1872-2075(08)60025-4

Li, S., and Bates, G. T. (2007). Influence of the Atlantic Multidecadal Oscillation on the Winter Climate of East China. *Adv. Atmos. Sci.* 24, 126–135. doi:10.1007/s00376-007-0126-6

Li, S., Perlwitz, J., Quan, X., and Hoerling, M. P. (2008). Modelling the Influence of North Atlantic Multidecadal Warmth on the Indian Summer Rainfall. *Geophys. Res. Lett.* 35, L05804. doi:10.1029/2007GL032901

Lin, J.-S., Wu, B., and Zhou, T.-J. (2016). Is the Interdecadal Circumglobal Teleconnection Pattern Excited by the Atlantic Multidecadal Oscillation? *Atmos. Oceanic Sci. Lett.* 9 (6), 451–457. doi:10.1080/16742834.2016.1233800

Lin, P., Yu, Z., Lü, J., Ding, M., Hu, A., and Liu, H. (2019). Two Regimes of Atlantic Multidecadal Oscillation: Cross-basin Dependent or Atlantic-intrinsic. *Sci. Bull.* 64, 198–204. doi:10.1016/j.scib.2018.12.027

Liu, B., He, J., and Wang, L. (2009). Characteristics of the South Asia High Establishment Processes above the Indo–China Peninsula from April to May and Their Possible Mechanism. *Chin. J. Atmos. Sci.* 33 (06), 1319–1332. doi:10.1016/S1003-6326(09)60084-4 (in Chinese).

Liu, Z. (2012). Dynamics of Interdecadal Climate Variability: A Historical Perspective*. *J. Clim.* 25, 1963–1995. doi:10.1175/2011jcli3980.1

Lu, R.-Y., Oh, J.-H., and Kim, B.-J. (2002). A Teleconnection Pattern in Upper-Level Meridional Wind over the North African and Eurasian Continent in Summer. *Tellus A: Dyn. Meteorol. Oceanogr.* 54, 44–55. doi:10.3402/tellusa.v54i1.12122

Lu, R., Dong, B., and Ding, H. (2006). Impact of the Atlantic Multidecadal Oscillation on the Asian Summer Monsoon. *Geophys. Res. Lett.* 33, L24701. doi:10.1029/2006GL027655

Luo, F., Li, S., and Furevik, T. (2011). The Connection between the Atlantic Multidecadal Oscillation and the Indian Summer Monsoon in Bergen Climate Model Version 2.0. *J. Geophys. Res.* 116, D19117. doi:10.1029/2011JD015848

Mason, R. B., and Anderson, C. E. (1963). The Development and Decay of the 100-Mb. Summertime Anticyclone over Southern Asia. *Mon. Wea. Rev.* 91 (1), 3–12. doi:10.1175/1520-0493(1963)091<0003:tdadot>2.3.co;2

Nan, S., Li, J., Yuan, X., and Zhao, P. (2009). Boreal Spring Southern Hemisphere Annular Mode, Indian Ocean Sea Surface Temperature, and East Asian Summer Monsoon. *J. Geophys. Res.* 114, D02103. doi:10.1029/2008JD010045

Poli, P., Hersbach, P., Tan, D. G. H., Dee, D. P., Thépaut, J. N., Simmons, A., et al. (2013). The Data Assimilation System and Initial Performance Evaluation of the ECMWF Pilot Reanalysis of the 20th–century Assimilating Surface Observations Only (ERA–20C). *ERA Rep. Ser.* 14, 62, 2013 . Available online at: http://www.ecmwf.int/sites/default/files/elibrary/2013/11699–dataassimilation–system–and–initial–performance–evaluation–ecmwfpilot–reanalysis–20th.pdf.

Pu, B., and Cook, K. H. (2010). Dynamics of the West African Westerly Jet. *J. Clim.* 23 (23), 6263–6276. doi:10.1175/2010jcli3648.1

Qian, Y., Wang, O., Dong, Y., and Gong, Y. (1987). Numerical Experiment of Somali Jet. *Chin. J. Atmos. Sci.* 11 (2), 176–184. (in Chinese).

Qian, Y., Zhang, Q., Yao, Y., and Zhang, X. (2002). Seasonal Variation and Heat Preference of the South Asia High. *Adv. Atmos. Sci.* 19 (5), 821–836. doi:10.1007/s00376-002-0047-3

Rayner, N. A., Parker, D. E., Horton, E. B., Folland, C. K., Alexander, L. V., Rowell, D. P., et al. (2003). Global Analyses of Sea Surface Temperature, Sea Ice, and Night Marine Air Temperature since the Late Nineteenth Century. *J. Geophys. Res.* 108 (D14), 4407. doi:10.1029/2002jd002670

Ren, S., Jiang, J., and Xu, J. (2014). Application of Upper Troposphere Circulation Revealed by the Satellite IR3 Channel to Heavy Rainfall Events Analysis in the East Side of South Asia High. *Meteorol. Mon.* 40 (6), 697–705. (in Chinese). doi:10.7519/j.issn.1000-0526.2014.06.006

Sato, N., and Takahashi, M. (2006). Dynamical Processes Related to the Appearance of Quasi-Stationary Waves on the Subtropical Jet in the Midsummer Northern Hemisphere. *J. Clim.* 19 (8), 1531–1544. doi:10.1175/JCLI3697.1

Shi, N., Feng, G., Gu, J., and Gu, D. (2007). The Climatological Variation of Global Cross–Equatorial Flow for the Period of 1948–2004. *J. Trop. Meteorol.* 23 (4), 326–332. (in Chinese). doi:10.3969/j.issn.1004–4965.2007.04.002

Shi, W., Xiao, Z., and Sun, H. (2017). The Correlation of Somali Jet Strength with South Asia High on Interdecadal Timescale. *Chin. J. Atmos. Sci.* 41 (3), 561–577. (in Chinese). doi:10.3878/j.issn.1006–9895.1609.16163

Simpson, G. C. (1921). The South-West Monsoon. *Q.J.R. Meteorol. Soc.* 47 (199), 151–171. doi:10.1002/qj.49704719901

Su, H., and Neelin, J. D. (2003). The Scatter in Tropical Average Precipitation Anomalies*. *J. Clim.* 16, 3966–3977. doi:10.1175/1520-0442(2003)016<3966:tsitap>2.0.co;2

Su, H., Neelin, J. D., and Meyerson, J. E. (2003). Sensitivity of Tropical Tropospheric Temperature to Sea Surface Temperature Forcing*. *J. Clim.* 16, 1283–1301. doi:10.1175/1520-0442-16.9.1283

Sutton, R. T., and Hodson, D. L. R. (2005). Atlantic Ocean Forcing of North American and European Summer Climate. *Science* 309, 115–118. doi:10.1126/science.1109496

Sutton, R. T., and Hodson, D. L. R. (2007). Climate Response to Basin-Scale Warming and Cooling of the North Atlantic Ocean. *J. Clim.* 20, 891–907. doi:10.1175/JCLI403810.1175/jcli4038.1

Takaya, K., and Nakamura, H. (2001). A Formulation of a Phase-independent Wave-Activity Flux for Stationary and Migratory Quasigeostrophic Eddies on a Zonally Varying Basic Flow. *J. Atmos. Sci.* 58, 608–627. doi:10.1175/1520-0469(2001)058<0608:afoapi>2.0.co;2

Ting, M., Kushnir, Y., Seager, R., and Li, C. (2009). Forced and Internal Twentieth-Century SST Trends in the North Atlantic*. *J. Clim.* 22, 1469–1481. doi:10.1175/2008jcli2561.1

Wang, H., and Li, D. (2019). The Impacts of Global Sea Surface Temperature on Decadal Transitions of Summer Precipitation over Eastern China at Global Warming Transition Points. *J. Trop. Meteorol.* 35 (3), 398–408. doi:10.16032/j.issn.1004-4965.2019.037 (in Chinese).

Wang, Y., Li, S., and Luo, D. (2009). Seasonal Response of Asian Monsoonal Climate to the Atlantic Multidecadal Oscillation. *J. Geophys. Res.* 114, D02112. doi:10.1029/2008JD010929

Wang, L., Xu, P., Chen, W., and Liu, Y. (2017). Interdecadal Variations of the Silk Road Pattern. *J. Clim.* 30 (24), 9915–9932. doi:10.1175/jcli-d-17-0340.1

Watanabe, T., and Yamazaki, K. (2014). The Upper-Level Circulation Anomaly over Central Asia and its Relationship to the Asian Monsoon and Mid-latitude Wave Train in Early Summer. *Clim. Dyn.* 42, 2477–2489. doi:10.1007/s00382-013-1888-4

Wei, W., Zhang, R., Wen, M., Rong, X., and Li, T. (2014). Impact of Indian Summer Monsoon on the South Asian High and its Influence on Summer Rainfall over China. *Clim. Dyn.* 43, 1257–1269. doi:10.1007/s00382-013-1938-y

Wei, W., Zhang, R., Wen, M., Kim, B.-J., and Nam, J.-C. (2015). Interannual Variation of the South Asian High and its Relation with Indian and East Asian Summer Monsoon Rainfall. *J. Clim.* 28, 2623–2634. doi:10.1175/jcli-d-14-00454.1

Wu, B., Zhou, T., and Li, T. (2016). Impacts of the Pacific-Japan and Circumglobal Teleconnection Patterns on the Interdecadal Variability of the East Asian Summer Monsoon. *J. Clim.* 29, 3253–3271. doi:10.1175/jcli-d-15-0105.1

Xiao, Z., Shi, W., and Yang, P. (2015). Possible Causes of the Interdecadal Transition of the Somali Jet Around the Late 1990s. *J. Meteorol. Res.* 29 (2), 214–227. doi:10.1007/s13351-015-4103-1

Xie, S.-P., Hu, K., Hafner, J., Tokinaga, H., Du, Y., Huang, G., et al. (2009). Indian Ocean Capacitor Effect on Indo-Western Pacific Climate during the Summer Following El Niño. *J. Clim.* 22, 730–747. doi:10.1175/2008jcli2544.1

Xu, H., He, J., and Dong, M. (2001). Interannual Variability of the Meiyu Onset and its Association with North Atlantic Oscillation and SSTA over North Atlatic. *ACTA Meteorol. Sin.* 59 (6), 694–706. doi:10.11676/qxxb2001.073 (in Chinese).

Yang, G., Li, C., and Tan, Y. (2013). A Study on Interdecadal Variation of South Asian High and its Possible Cause (In Chinese). *J. Trop. Meteorol.* 29 (4), 529–539. doi:10.3969/j.issn.1004–4965.2013.04.001

Yasui, S., and Watanabe, M. (2010). Forcing Processes of the Summertime Circumglobal Teleconnection Pattern in a Dry AGCM. *J. Clim.* 23 (8), 2093–2114. doi:10.1175/2009JCLI3323.1

Zhang, R., and Delworth, T. L. (2006). Impact of Atlantic Multidecadal Oscillations on India/Sahel Rainfall and Atlantic Hurricanes. *Geophys. Res. Lett.* 33, L17712. doi:10.1029/2006GL026267

Zhang, Q., Qian, Y., and Zhang, X. (2000). Interannual and Interdecadal Variations of the South Asia High. *Chin. J. Atmos. Sci.* 24 (1), 67–78. (in Chinese). doi:10.3878/j.issn.1006–9895.2000.01.07

Zhang, Q., Wu, G., and Qian, Y. (2002). The Bimodality of the 100 hPa South Asia High and its Relationship to the Climate Anomaly over East Asia in Summer. *J. Meteorol. Soc. Jpn.* 80, 733–744. doi:10.2151/jmsj.80.733

Zhang, P., Yang, S., and Kousky, V. E. (2005). South Asian High and Asian-Pacific-American Climate Teleconnection. *Adv. Atmos. Sci.* 22, 915–923. doi:10.1007/bf02918690

Zhou, Y., and Zheng, D. (1999). Monte Carlo Simulation Tests of Correlation Significance Levels. *Acta Geod. et Cartographica Sin.* 28 (4), 313–318. (in Chinese).

Zhou, N., Yu, Y., and Qian, Y. (2006). Simulations of the 100-hPa South Asian High and Precipitation over East Asia with IPCC Coupled GCMs. *Adv. Atmos. Sci.* 23 (3), 375–390. doi:10.1007/s00376-006-0375-9

Zhu, Y. (2012). Variations of the Summer Somali and Australia Cross-Equatorial Flows and the Implications for the Asian Summer Monsoon. *Adv. Atmos. Sci.* 29 (3), 509–518. doi:10.1007/s00376-011-1120-6

Conflict of Interest: WS and QW were employed by the company CSSC Marine Technology Co. Ltd.

The remaining authors declare that the research was conducted in the absence of any commercial or financial relationships that could be construed as a potential conflict of interest.

Publisher's Note: All claims expressed in this article are solely those of the authors and do not necessarily represent those of their affiliated organizations, or those of the publisher, the editors, and the reviewers. Any product that may be evaluated in this article, or claim that may be made by its manufacturer, is not guaranteed or endorsed by the publisher.

frontiers in Earth Science

ORIGINAL RESEARCH
published: 05 January 2022
doi: 10.3389/feart.2021.756762

Impact of Solar Activity on Snow Cover Variation Over the Tibetan Plateau and Linkage to the Summer Precipitation in China

Yan Song[1]*, *Zhicai Li*[2], *Yu Gu*[3] and *Ziniu Xiao*[4]

[1]Training Centre, China Meteorological Administration, Beijing, China, [2]Shanxi Climate Center, Taiyuan, China, [3]University of California, Los Angeles, Los Angeles, CA, United States, [4]Institute of Atmospheric Physics, Chinese Academy of Sciences, Beijing, China

Solar activity is one of the main external forcing factors driving the Earth's climate system to change. The snow cover over the Tibetan Plateau is an important physical factor affecting the East Asian climate. At present, insufficient research on the connection between solar activity and snow cover over the Tibetan Plateau has been carried out. Using Solar Radio Flux (SRF), Solar Sunspot Number (SSN), and Total Solar Irradiance (TSI) data, this paper calculated the correlation coefficients with snow indices over the Tibetan Plateau, such as winter and spring snow depth (WSD/SSD) and snow day number (WSDN/SSDN). These snow indices are obtained from the daily gauge snow data in the Tibetan Plateau. Through correlation analyses, it is found that there are significant synchronous or lag correlations between snow indices and solar parameters on multi-time scales. In particular, the Spring Snow Day Number (SSDN) is of significant synchronous or lag correlation with SRF, SSN, and TSI on multi-time scales. It is further found that SSDN over the Tibetan Plateau has more stable positive correlations with SRF by using the 21-year running mean and cross spectrum analyses. Therefore, SSDN can be ascertained to be the most sensitive snow index to the solar activity compared with other snow indices. Moreover, its influence on summer precipitation of China is strongly regulated by solar activity. In high solar activity years (HSAY), the significant correlated area of summer precipitation in China to SSDN is located further north than that in low solar activity years (LSAY). Such impact by solar activity is also remarkable after excluding the impact of ENSO (i.e., El Niño–Southern Oscillation) events. These results provide support for the application of snow indices in summer rainfall prediction in China.

Keywords: solar activity, snow cover over the Tibetan plateau, summer precipitation of China, correlation analyses, East Asian monsoon

OPEN ACCESS

Edited by:
Xiaoming Hu,
Sun Yat-sen University, China

Reviewed by:
Boqi Liu,
Chinese Academy of Meteorological Sciences, China
Yana Li,
City University of Hong Kong, Hong Kong, SAR China

***Correspondence:**
Yan Song
songyan@cma.gov.cn

Specialty section:
This article was submitted to Atmospheric Science, a section of the journal Frontiers in Earth Science

Received: *11 August 2021*
Accepted: *19 November 2021*
Published: *05 January 2022*

Citation:
Song Y, Li Z, Gu Y and Xiao Z (2022) Impact of Solar Activity on Snow Cover Variation Over the Tibetan Plateau and Linkage to the Summer Precipitation in China. Front. Earth Sci. 9:756762. doi: 10.3389/feart.2021.756762

INTRODUCTION

The Tibetan Plateau, which is the largest mountain in the world, has an important impact on the global and regional climate, especially East Asian climate. The thermal and dynamic roles of the plateau are irreplaceable in terms of the onset and maintenance of the East Asian summer monsoon, especially the location of rain belt during flood season in East Asia.

The snow amount over the Tibetan Plateau could affect the thermal difference between Euro-Asian land and the surrounding sea through altering the soil moisture content by snow melting in

spring, which is critical to the onset of the following summer monsoon (Bamzai and Marx, 2000; Qian et al., 2003; Zhao et al., 2007; Wei et al., 2008). Therefore, much attention has been paid to the influence of the Tibetan Plateau on the East Asian summer monsoon and the precipitation on the interannual time scale. However, the snow cover over the Tibetan Plateau has obvious interdecadal oscillation itself (Wang et al., 2018). The decline of the East Asian summer monsoon in recent decades is thought to be related to the continuous increase of snow amount in the plateau (Zhang et al., 2004). The anomalous interdecadal oscillation of snow cover in spring and winter is closely related to the shift of abnormal spatial rainfall pattern in summer in Eastern China (Zhang et al., 2008; Ding et al., 2009; Zhou et al., 2009; Wu et al., 2010; Zhao et al., 2010). However, the relationship between snow and summer precipitation in China is uncertain. Under different interdecadal backgrounds of climate change, the spatial correlations of snow and summer precipitation are quite different (Song et al., 2011). Therefore, there may be some other external forcing factors that could modulate the correlation relationship between snow and summer precipitation.

The climate system on the Earth is driven by various external forcing factors, especially the Sun, where the main energy of the Earth comes from. The solar activity could exert considerable impact on the global and regional climate. The regional climatic response to solar activity is often one order of magnitude greater than the global response, due to more sensitive water cycle in the regions (Lean, 2010). Therefore, the signals of regional precipitation that responded to the Sun are relatively stronger.

Many studies examined the impact of solar activity on the East Asian summer monsoon (Zhao et al., 2011; Zhao & Wang, 2014; Wang et al., 2005; Kerr, 2005; Verschuren et al., 2009). The interdecadal variability of the East Asian summer monsoon precipitation could be affected by solar activity, and the effect varied within different time periods (Wasko and Sharma, 2009). Model simulation results show that during the Little Ice Age, the global monsoon rainfall was reduced with weak solar activity and less sunspot number, while during the Middle Ages, the global monsoon was strong (Liu et al., 2009). In history, during the active period of solar activity, the Hadley Circulation expanded, the subtropical dry area extended northward, and the monsoon region shifted northward in the Northern Hemisphere. Simultaneously, most of the land areas around the world had more precipitation due to the monsoon intensification (Hoyt and Schatten, 1997; Haigh et al., 2005; Kodera, 2004; Haigh, 2003; Kushner and Polvani, 2006; Haigh andB, ackbum, 2006).

Recent studies show that the East Asian monsoon intensity was controlled by the solar cycle (Wang et al., 2005; Tan et al., 2008). The interdecadal change of the latitude of rain belt during onset period of the East Asian summer monsoon depends on the sunspot cycle phase, and the responses of precipitation phases in the south and north of the Yangtze River to the solar cycle are totally opposite (Zhao and Han, 2012). It can be explained by the interdecadal locking phase of the intensity and the northern boundary position of Southwest Monsoon flow with the sunspot cycle (Zhao and Han, 2012). In addition, the generalized Meiyu season in East Asia is just the time period with the highest correlation coefficient between the latitude of rain belt of the East Asian Monsoon and the solar cycle. In the high solar activity years (HSAY), the Meiyu rain belt is 1.2° latitude to the north and has a greater interannual variability (Zhao & Wang, 2014). In addition, some studies show that the impact of ENSO (El Niño–Southern Oscillation) on the East Asian climate, the relationships between Arctic Oscillation and the East Asian winter climate, the relation of spring NAO and the following summer precipitation in East Asia, and the connection of the East Asian winter monsoon to the following summer monsoon can all be regulated by the Sun's 11-year cycle (Chen & Zhou, 2012; Zhou & Chen, 2012; Zhou, 2013 Thesis; Zhou and Chen, 2014). It is demonstrated that the solar cycle affects obviously the interaction between sea and air, as well as among atmospheric internal components. Through the coupling interaction between the Pacific Ocean and the atmosphere, the solar 11-year cycle could affect winter precipitation in Northeast Asia (Song et al., 2019). As we know, there are significant correlations between snow over the Tibetan Plateau and the East Asian summer monsoon, as well as the summer rain belt in Eastern China. Is it possible that such a relationship can be affected by the solar activity? As to the winter and spring snow depths and snow day numbers, which has the most sensitive response to the solar activity? These deserve further study.

Up to now, few studies have focused on the impact of solar activity on snow cover over the Tibetan Plateau and its relationship with summer precipitation in China. Previous studies mainly focused on the influence of different solar irradiance spectrum bands on the snow albedo and snow melting rate (Grenfell et al., 1994; Li et al., 2009; Meinander et al., 2009). Our previous research showed that the winter and spring snow cover over the Tibetan Plateau had significant responses to the Solar Radio Flux (SRF) in the recent 50 years on the interdecadal time scale with significant lag correlations (Song et al., 2016a). The impact of winter snow depth on the following summer precipitation in China was strongly regulated by solar activity (Song et al., 2016b, 2019). The four snow indices are defined as winter and spring snow depth and snow day number, respectively. This paper focuses on detecting the most sensitively responded snow index to the solar activity and the Sun's regulation on spatial correlation patterns between snow and summer precipitation in China.

DATA AND METHODS

Data

In this paper, SRF data (F10.7 cm data) during 1947–2015 are obtained from the National Oceanic and Atmospheric Administration (NOAA) Data Center (http://www.esrl.noaa.gov/psd/data/correlation/solar.data). The F10.7 cm data are expressed in solar flux units (sfu) where 1 sfu = 10^{-22} W m^{-2}·Hz^{-1}. The winter SRF is obtained by the average of the data in December and the subsequent January and February. The Solar Sunspot Number (SSN) data for 1770–2014 used in this paper is collected from the Solar Influences Data Analysis Center (SIDC), which is the solar

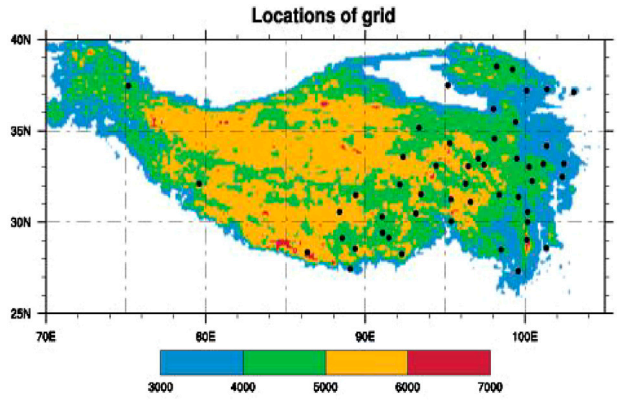

FIGURE 1 | The distribution of observation stations over the Tibetan Plateau (the shaded area means that the elevation altitude is above 3,000 m. Black dots indicate observation stations chosen to calculate snow indices over the Tibetan Plateau).

physics research department of the Royal Observatory of Belgium (http://sidc.oma.be/sunspot-data). The Total Solar Irradiance (TSI) reconstruction data during 1610–2013 is downloaded from Laboratory Atmospheric Space Physics of University of Colorado Boulder (Coddington et al., 2015; Kopp et al., 2016) (http://lasp.colorado.edu/home/sorce/data/tsi-data/). The monthly mean data of atmospheric circulation are the reanalysis data from the National Centre for Environmental Prediction/National Center for Atmospheric Research (NCEP/NCAR) in the United States (Kalnay et al., 1996).

The snow indices used in this study are winter and spring snow depth (WSD/SSD) and snow day number (WSDN/SSDN) from 1951 to 2015 (Song et al., 2011). All of these four indices are daily observational data over the Tibetan Plateau from the China Meteorological Information Center. In order to eliminate data discontinuity, the original data have been chosen carefully and interpolated strictly to obtain continuous monthly data over 51 gauge stations of 1961–2015 (Song et al., 2011). The distribution of the observational stations over the Tibetan Plateau is shown in **Figure 1**, in which black dots indicate gauge stations. The shaded area indicates that the elevation is above 3,000 m. The monthly snow data are the sum of daily snow data in 1 month. SSD and SSDN are obtained by calculating the average of monthly snow depth and snow day number from March to May at each station. Similarly, WSD and WSDN can be defined as the average of snow depth and snow day number from December to January and February of the following year at each station. Thus, we acquire the seasonal snow data of all stations over the plateau.

Summer precipitation data over 160 observation stations in China can be obtained from the National Meteorological Information Center, China Meteorological Administration (http://10.1.64.154/). The strong ENSO events data involving strong El Niño and La Niña events are obtained from the National Climate Center of China, which uses the Nino indices data published by the National Oceanic and Atmospheric Administration to calculate the Nino Z SSTA Index, which is the composite Nino index of the area weighted average for Nino1+2, Nino3, and Nino4 zones in the tropical Pacific Ocean (https://www.esrl.noaa.gov/psd/gcos_wgsp/Timeseries/). The climatological mean of all data sets used in this paper is the 30-year average from 1981 to 2010.

Methods

Monte Carlo significance test method: For different data sets with different time scales, it is necessary to use different significance test methods. For example, the Student's *t*-test method is adopted to test the significance levels of correlation coefficients of raw data sets. However, for data sets after running mean, Monte Carlo method should be used to test the significance levels (Yan et al., 2003; Zhao and Han, 2005; Zhou et al., 2012), because of the decrease in both data number and degree of freedom.

The detailed steps in computing the critical values of correlation coefficients with the Monte Carlo method are as follows:

(1) Produce two random sample sequences, then compute the correlation coefficient of the two sample sequences after running mean; finally, get 5,000 correlation coefficients after calculating 5,000 times repeatedly.
(2) Arrange the 5,000 correlation coefficients from small to large values, and find the correlation coefficients of No. 5,000 × 90%, 5,000 × 95%, and 5,000 × 99%, respectively, with reliability thresholds of 0.1 significant level, 0.05 significant level, and 0.01 significant level.
(3) Repeat the above steps 40 times, and then get 40 correlation coefficient thresholds of 0.1 significant level, 0.05 significant level, and 0.01 significant level. Average the 40 reliability thresholds of correlation coefficients for 0.1 significant level, 0.05 significant level, and 0.01 significant level to be the required reliability thresholds.

See Zhou and Zheng (1999) for the method to calculate the degree of freedom of new sample series after running mean. The raw data set of winter snow depth over the Tibetan Plateau used in this paper is a discrete time series, 55 years in total, i.e., $\{x(n\Delta)\}$ (n = 0, 1, 2, . . . , 55), in which Δ is 1 year. After filtering of the 11-year running mean, the new data set has been changed into $\{x(n\Delta)\}$ (n = 6, 7, 8, . . . , 50), and Δ is 1 year.

So, the bandwidth of the original data set is $f_w = f_n - f_k = \frac{1}{2\times1} - \frac{1}{55\times1} = 0.482$. The bandwidth of the new data set after filtering of the 11-year running mean is $f_p = f_n - f_1 = \frac{1}{12} - \frac{1}{50} = 0.083 - 0.02 = 0.063$. Then, $\frac{1}{\chi} = \frac{f_p}{f_w} = \frac{0.063}{0.48} = 0.13125$.

So, the degree of freedom of the new data set is equal to that of the original sequence multiplied by $\frac{1}{\chi}$, i.e., it is equal to 55*0.13125 = 7.22 ~ 7.

Therefore, the degree of freedom of the new winter snow depth data set for 55 years after the 11-year running mean is changed to approximately 7.

Composite Mean Difference (CMD) method: The CMD used in this paper is an intuitive way to obtain the spatial pattern by calculating the differences between the strong and weak solar activity composites. CMD is often used to deduce the spatial pattern of the solar cycle response (Camp and Tung, 2007). In this

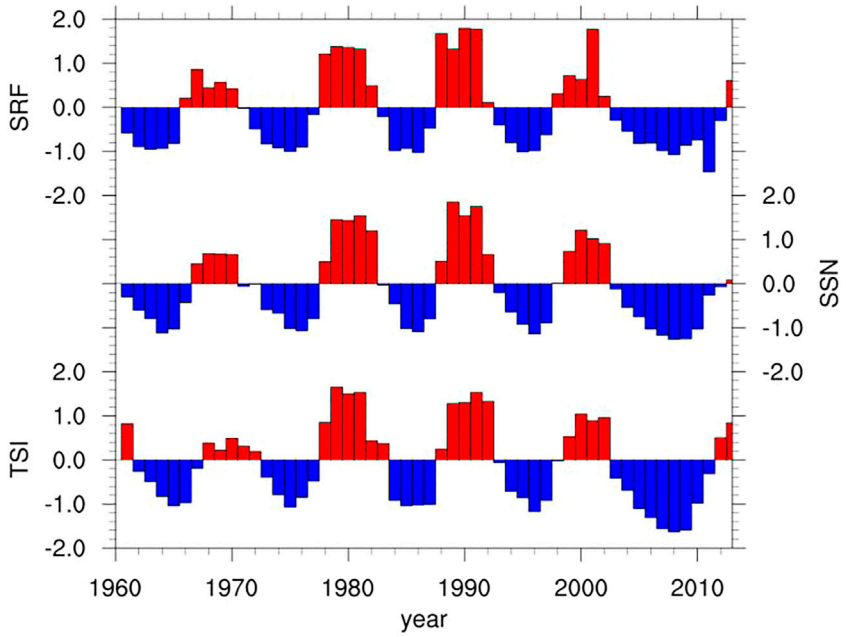

FIGURE 2 | Time series of the normalized SRF, SSN, and TSIduring 1961–2013.

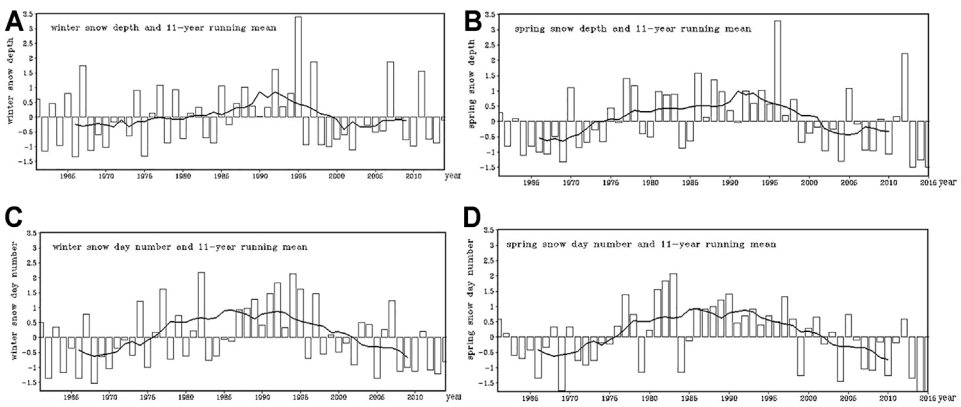

FIGURE 3 | Time series of normalized WSD **(A)**, WSDN **(B)**, SSD **(C),** and SSDN **(D)** and their interdecadal variations after the 11-year running mean.

study, we divide all the data into two groups according to the strong and weak solar activity years [e.g., normalized data values larger than zero are ascribed to HSAY, and those smaller than zero are ascribed to low solar activity years (LSAY)] and then calculate the difference between the two groups to obtain a spatial pattern of solar response. The Student's *t*-test is used to examine the significance level.

Cross Spectral Analyses

1) Continuous Wavelet Transform (CWT)

Geophysical science often needs to decompose one signal into wavelets. The fourier transform is used to decompose a signal into infinite number of terms, which lose most time-localization information. The continuous wavelet transform (CWT) could decompose a time series into time-frequency space and could be used for feature extraction purposes. The CWT method is often used for analyzing localized intermittent oscillations in a time series, especially the time series that are not normally distributed.

2) Cross Wavelet Transform (XWT)

CWT could be used to examine whether two time series are linked in some way. Therefore, two CWTs could be used to construct the Cross Wavelet Transform (XWT) so as to expose their common power and relative phase in time-frequency space.

The cross wavelet spectrum of two time series X and Y with wavelet transform W_n^X and W_n^Y is described as $|W_n^{XY}(S)| = |W_n^X(S) \cdot W_n^{*Y}(S)|$ (Torrence and Compo, 1998), where W_n^{*Y} is

TABLE 1 | Correlation coefficients of WSD and SRF, SSN, and TSI on multi-time scales from 1961 to 2015.

WSD	SRF (raw/9 years/11 years)	SSN (raw/9 years/11 years)	TSI (raw/9 years/11 years)
0	–0.10/0.37/0.646	–0.09/0.36/0.61	0.16/0.55/0.56
-1	–0.08/0.44/0.69	–0.12/0.41/0.64	0.16/0.59/0.58
-2	–0.08/0.50/*0.72	–0.07/0.47/0.68	*0.23/0.61/0.62
-3	–0.00/0.55/*0.77	0.07/0.55/*0.74	0.21/0.60/0.64
-4	0.18/0.60/**0.80	0.18/0.58/*0.77	0.16/0.54/0.62
-5	0.17/0.60/*0.79	0.21/0.61/*0.78	0.10/0.47/0.61
-6	*0.27/0.59/*0.77	*0.29/0.60/*0.76	0.10/0.43/0.59
-7	*0.29/0.54/0.71	0.16/0.55/0.69	–0.08/0.40/0.54
-8	–0.04/0.41/0.58	–0.01/0.46/0.58	–0.06/0.40/0.49
-9	–0.05/0.32/0.46	–0.07/0.37/0.48	–0.00/0.41/0.45
-10	–0.07/0.22/0.33	–0.16/0.28/0.36	–0.06/0.39/0.41

Note.* *indicates higher than 0.1 significance level, ** indicates higher than 0.05 significance level.*

TABLE 2 | Correlation coefficients of WSDN and SRF, SSN, and TSI on multi-time scales from 1961 to 2015.

WSDN	SRF (raw/9 years/11 years)	SSN (raw/9 years/11 years)	TSI (raw/9 years/11 years)
0	0.14/0.53/*0.75	0.17/0.53/*0.73	–0.07/0.38/0.67
-1	0.17/0.57/**0.81	0.15/0.56/**0.77	–0.12/0.42/*0.71
-2	0.14/0.59/**0.82	0.17/0.58/**0.79	–0.01/0.46/*0.744
-3	0.22/0.59/**0.83	0.21/0.59/**0.80	0.08/0.51/*0.74
-4	0.20/0.56/**0.82	0.18/0.56/**0.79	0.16/0.51/0.71
-5	0.11/0.52/*0.79	0.14/0.54/*0.78	0.18/0.48/0.67
-6	0.17/0.50/0.77	0.12/0.53/*0.75	*0.26/0.45/0.63
-7	0.08/0.47/0.70	0.07/0.53/0.69	0.06/0.38/0.56
-8	-0.02/0.43/0.58	0.03/0.50/0.59	–0.12/0.32/0.49
-9	0.01/0.40/0.45	0.01/0.47/0.46	–0.056/0.30/0.42
-10	0.01/0.34/0.29	0.02/0.39/0.31	–0.22/0.27/0.36

Note.* *indicates higher than 0.1 significance level, ** indicates higher than 0.05 significance level.*

TABLE 3 | Correlation coefficients of SSD and SRF, SSN, and TSI on multi-time scales from 1961 to 2015.

SSD	SRF (raw/9 years/11 years)	SSN (raw/9 years/11 years)	TSI (raw/9 years/11 years)
0	–0.10/0.55/**0.80	0.04/0.56/**0.79	0.09/0.63/0.77
-1	–0.08/0.55/**0.82	0.01/0.56/**0.80	0.01/0.65/*0.80
-2	–0.08/0.54/**0.80	0.02/0.56/**0.79	0.04/0.68/*0.81
-3	–0.00/0.53/**0.78	0.13/0.55/*0.77	0.15/0.68/*0.80
-4	0.18/0.51/*0.76	0.18/0.52/*0.75	0.18/0.63/0.77
-5	0.17/0.50/*0.74	*0.24/0.50/0.72	0.24/0.55/0.70
-6	*0.27/0.47/0.67	0.22/0.48/0.65	0.18/0.47/0.60
-7	*0.29/0.44/0.58	**0.31/0.47/0.56	0.23/0.41/0.48
-8	–0.04/0.39/0.45	0.14/0.42/0.42	0.03/0.33/0.34
-9	–0.05/0.30/0.26	–0.02/0.34/0.25	–0.03/0.26/0.20
-10	–0.07/0.22/0.09	–0.10/0.25/0.12	–0.14/0.21/0.13

Note.* *indicates higher than 0.1 significance level, ** indicates higher than 0.05 significance level.*

TABLE 4 | Correlation coefficients of SSDN and SRF, SSN, and TSI on multi-time scales from 1961 to 2015.

SSDN	SRF (raw/9 years/11 years)	SSN (raw/9 years/11 years)	TSI (raw/9 years/11 years)
0	*0.27/**0.69/***0.88	*0.26/**0.70/***0.87	**0.30/*0.69/**0.78
-1	*0.24/*0.69/***0.92	**0.28/**0.71/***0.91	*0.25/**0.73/**0.84
-2	*0.25/*0.67/***0.91	0.22/*0.68/***0.89	0.23/**0.77/***0.88
-4	0.16/0.52/**0.79	0.10/0.53/*0.78	0.14/*0.69/**0.86
-5	0.06/0.43/0.72	0.02/0.45/0.70/	0.06/0.60/*0.79
-6	-0.02/0.36/0.62	0.03/0.40/0.61	0.03/0.52/0.68
-7	0.08/0.32/0.50	0.12/0.38/0.49	0.08/0.47/0.55
-8	0.09/0.27/0.33	0.13/0.34/0.33	0.01/0.41/0.37
-9	0.05/0.21/0.12	0.11/0.26/0.12	0.11/0.34/0.18
-10	0.12/0.13/-0.11	0.05/0.16/-0.09	0.07/0.23/0.03

Note.* *indicates higher than 0.1 significance level, ** indicates higher than 0.05 significance level, *** indicates higher than 0.01 significance level.*

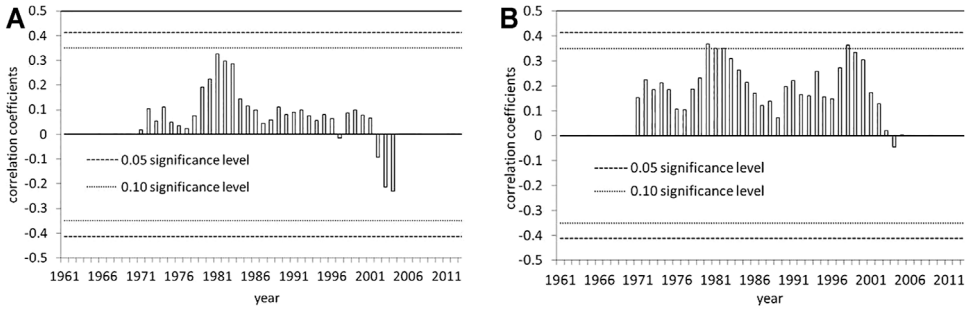

FIGURE 4 | The 21-year running correlation coefficients of snow indices and SRF, **(A)** WSDN and **(B)** SSDN. Rectangles are snow indices. Short dashed lines indicate 0.05 significance levels, and long dashed lines are 0.01 significance levels, respectively.

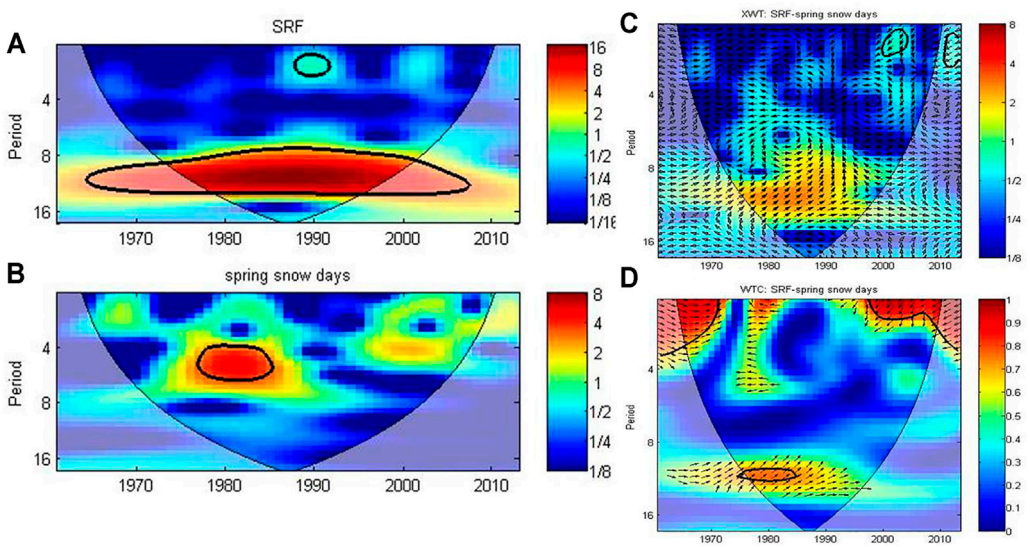

FIGURE 5 | Cross spectral analyses of SSDN and SRF. **(A)** Power spectrum of winter SRF, **(B)** power spectrum of SSDN, **(C)** cross wavelet transforms, and **(D)** square wavelet coherence of SSDN and SRF [thick black contour designates the 0.05 significance level against red noise and the cone of influence (COI) where edge effects might distort thepicture is shown as a lighter shade].

the complex conjugate of W_n^Y and W_n^{XY} is the local relative phase between time series X_j and Y_j. Statistical significance is estimated against a red noise model (Torrence and Webster, 1998). Thus, XWT denotes their common power and relative phase in time-frequency space.

3) Wavelet Coherence (WTC)

In this paper, we used another tool to further identify the significant coherence between two CWTs. Even though the common power is low, Wavelet Coherence (WTC) can exhibit how confidence levels against red noise backgrounds are calculated. Different from the cross wavelet power, coherence detects the intensity of the covariance in time-frequency space with a measure of the common power of two time series.

A red noise to determine the 95% statistical confidence level of the coherence is identified by Monte Carlo method (Torrence and Webster, 1999; Jevrejeva et al., 2003).

RESULTS

Relationship Between Solar Activity and the Tibetan Plateau Snow Cover Variations

Time Series of Solar Activity Parameters and Snow Indices Over the Tibetan Plateau

Figure 2 shows the time series of normalized SRF, SSN and TSI, respectively. It can be speculated that the long-term variations of three solar parameters have an obvious 11-year cycle. They signify different meanings when they represent solar activity. SRF is solar radio flux with a 10.7-cm wavelength. SSN is the sunspot number, which is related to the Sun's magnetic field. TSI is the total solar irradiance of the Sun. If we use different solar parameters to study the impact on climate system, there could be subtle differences.

Figure 3 is the time series of normalized values of four snow indices with the 11-year running mean. They have very distinct

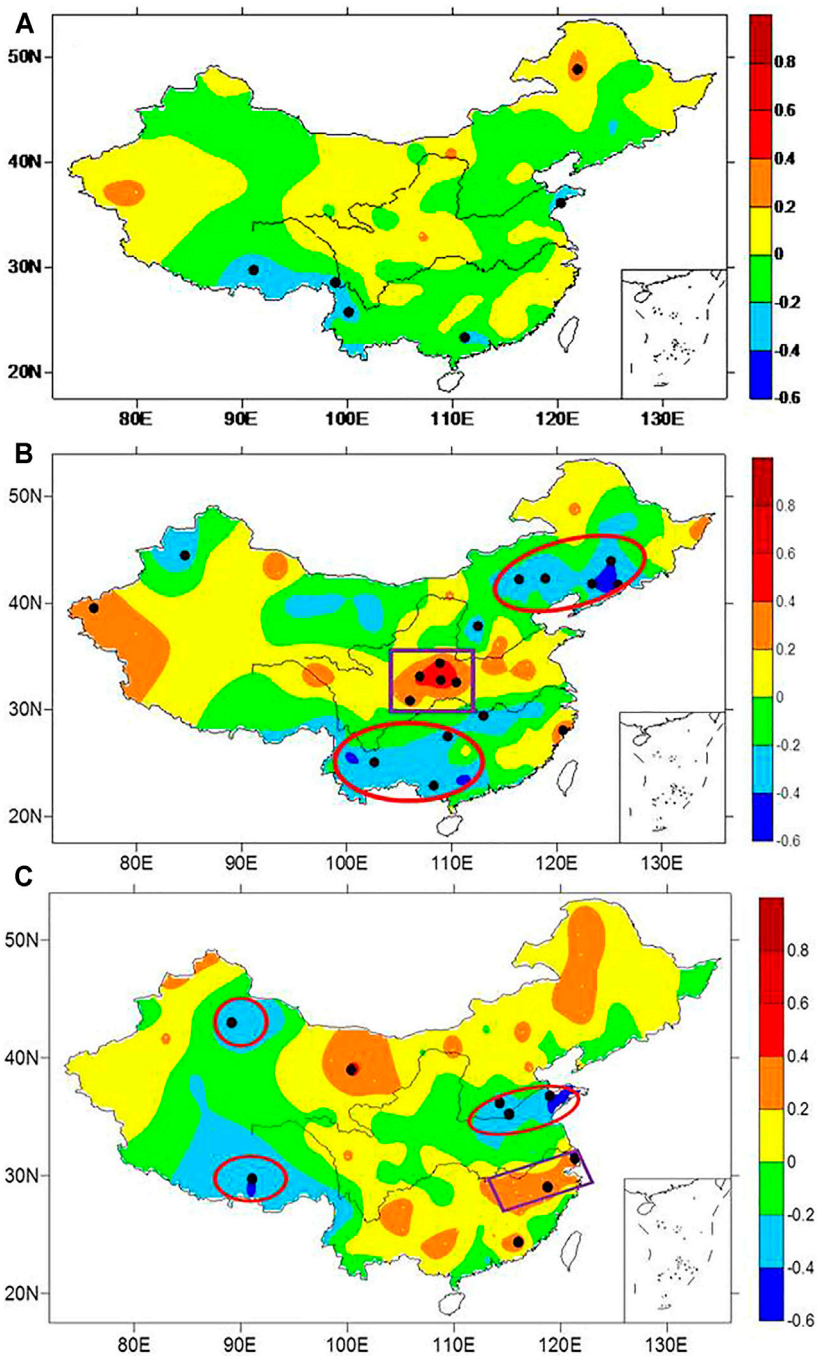

FIGURE 6 | Correlation coefficients of SSDN and summer precipitation of China in **(A)** normal years, **(B)** HSAY, and **(C)** LSAY. (Warm colors indicate the positive correlation coefficients, cold colors indicate the negative correlation coefficients, and black dots indicate gauge stations with high correlations at 0.1 significance levels. Red ellipses indicate negative correlation coefficients, and purple rectangles indicate positive correlation coefficients.)

interannual and interdecadal variabilities. On a long time scale, three obvious interdecadal periods are identified, i.e., less snow before the end of the 1970s, more snow from 1980 to 2003, and less snow after the early 2000s, except for WSD with a longer snow period from 1980 to 1999, ending earlier than other snow indices.

Correlation Coefficients of Solar Activity Parameters and Snow Indices Over the Tibetan Plateau on Multi-Time Scales

In order to detect the response of snow indices to the solar activity, we calculate the contemporaneous and lag correlation

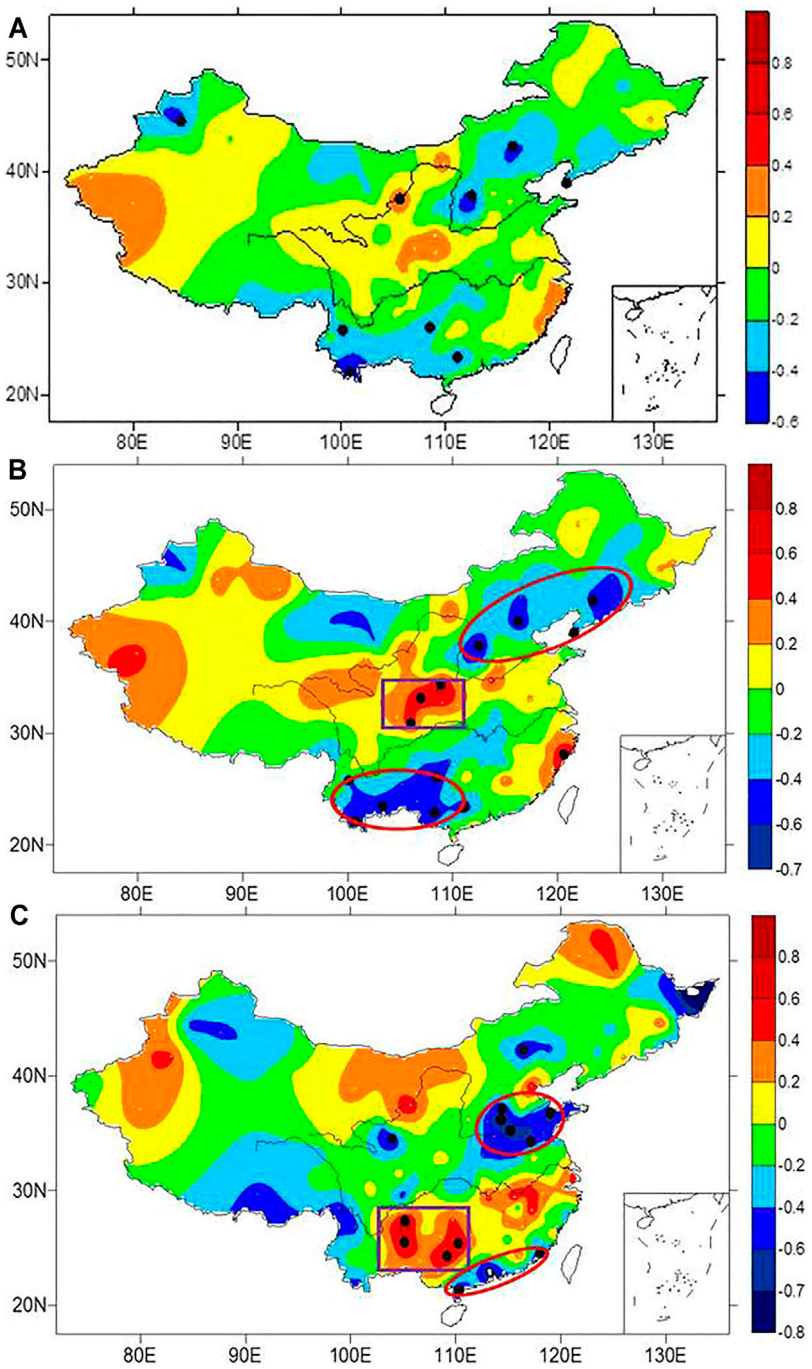

FIGURE 7 | Similar to **Figure 6** but the partial correlation coefficients of SSDN and summer precipitation in China excluding the impact of ENSO events.

coefficients between three solar parameters and four snow indices on multi-time scales, including interannual and interdecadal time scales. On interdecadal time scales, the correlation coefficients are calculated after a 9-year running mean (so as to remove the influence of ENSO) and after an 11-year running mean, respectively. The results are presented in **Tables 1–4**, where *, **, and *** indicate 0.1, 0.05, and 0.01 significance levels, respectively.

Table 1 lists the correlation coefficients between WSD and SRF, SSN, and TSI. In the first column, 0 indicates contemporary, 1 indicates a lag of 1 year, 2 indicates a lag of 2 years, and so on. In the first line, "raw" indicates the raw

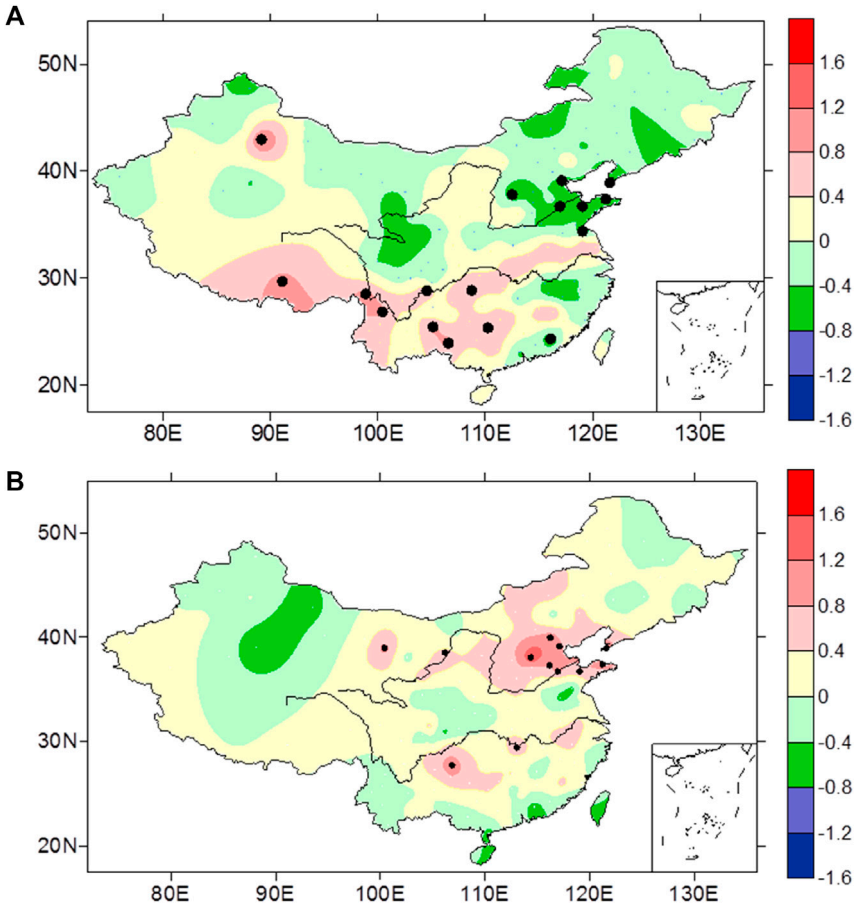

FIGURE 8 | Composites of anomalous summer precipitation in China in **(A)** peak years and **(B)** valley years, respectively. (Warm colors indicate summer precipitation increases, cold colors indicate that summer precipitation decreases, and black dots indicate gauge stations with high correlations at 0.1 significance levels.)

data, "9 years" indicates the 9-year running mean data, and "11 years" indicates the 11-year running mean data. **Tables 2–4** are similar to **Table 1**. It is noticeable that WSD has a significant lag correlation with SRF and SSN after the 11-year running mean. In particular, at a lag of 4 years, the lag correlation coefficient with SRF is above 0.05 significance level. Similarly, **Tables 2–4** also exhibit the correlation coefficients between WSDN/SSD/SSDN and SRF, SSN, and TSI, respectively. It is also found that WSDN, SSD, and SSDN are highly correlated with a time lag with SRF, SSN, and TSI after the 11-year running mean. WSDN not only has a significant lag but also has contemporaneous correlation coefficients with SRF and SSN, especially at a lag of 1–4 years, with correlation coefficient above the 0.05 significance level. It is noteworthy that SSDN has the closest correlations with three solar parameters after the 11-year running mean. Moreover, SSDN has significant correlations with SRF, SSN, and TSI not only after the 9-year and 11-year running means but also for the unfiltered raw data. After the 9-year running mean, SSDN has not only remarkable contemporaneous correlation coefficients with SRF and SSN at 0.05 significance level, but also remarkable lag correlation coefficients with SSN and TSI at 0.05 significance level. After the 11-year running mean, SSDN has remarkable contemporaneous and lag correlation coefficients with SRF and SSN at 0.01 significance level as well as remarkable contemporaneous and lag correlation coefficients with TSI at 0.05 and 0.01 significance levels, respectively.

Based on the above correlation analyses, it can be deduced that SSDN is the most sensitive snow index response to solar activity because it is significantly correlated with both the original data and running-mean data of three solar parameters.

In order to further detect the correlation of snow indices and solar activity, the 21-year running correlations of four snow indices and SRF are investigated, as shown in **Figure 4**. It is seen from the figure that the correlations of snow day numbers in winter/spring and SRF are quite stable and present positive correlation coefficients. In particular, SSDN is the most sensitive response snow index to SRF. Comparatively, the 21-year running correlations between snow depth in winter/spring and SRF vary and have obvious transition from positive correlation coefficients to negative correlation coefficients around 1983 (omitted).

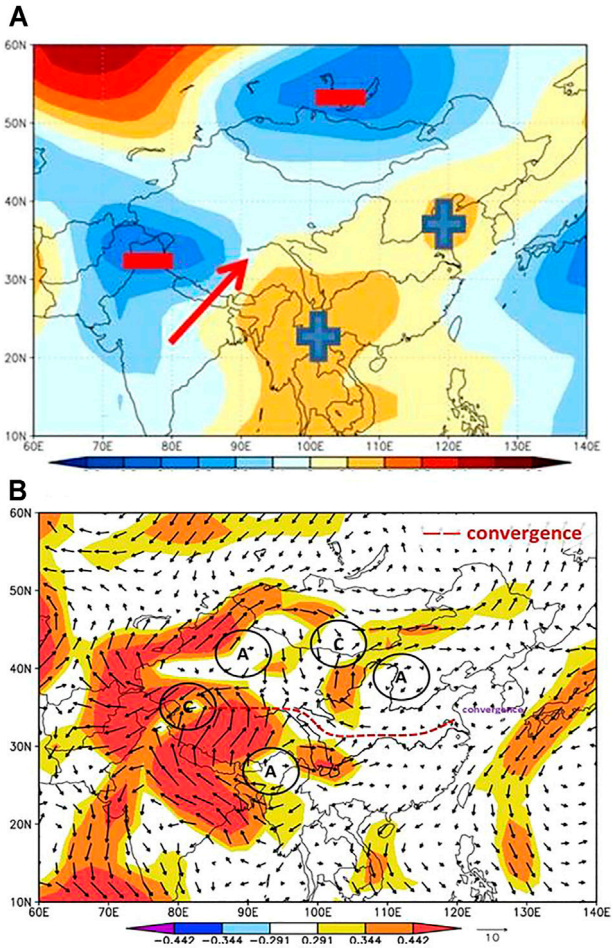

FIGURE 9 | Correlation coefficients of SSDN and **(A)** 500 hPa geopotential height field, **(B)** 850 hPa wind field in HSAY. (In panel a, "+" represents the positive correlation coefficient, "-" indicates the negative correlation coefficient, and the red arrow is the direction of the air flow. In panel b, "A" represents the anomalous anticyclone, "(C)" is the anomalous cyclone, and "——" means convergent zone. The arrows are air flows. The colored shaded areas indicate that the significance level is more than 0.1. The gray shaded areas indicate that the elevation altitudes are above 1500 m.)

Cross Spectral Analyses of Spring Snow Day Number and Solar Radio Flux, Solar Sunspot Number, and Total Solar Irradiance

Figure 5 shows the cross spectral analyses of SSDN and SRF during 1961–2015 as well as SSN and TSI during 1961–2011 to further verify the highly correlated relationship of SSDN and the Sun.

From the power spectrum of winter SRF (**Figure 5A**), SSN, and TSI (figures omitted), it can be speculated that SRF, SSN, and TSI have an obvious 11-year cycle, but SSDN has no such signal (**Figure 5B**). However, on longer time scales, it has obvious coherence with SRF, SSN, and TSI. Cross wavelet transforms show that SSDN has a positive correlation with SRF (**Figure 5C**), SSN, and TSI (figures omitted) on decadal time scales, respectively. From 1980 to 1992, the positive correlation with SSN is significant. Analyses on square wavelet coherence indicate that SSDN has high correlations with SRF (**Figure 5D**) and SSN (figure omitted) from the mid-1970s to the mid-1980s, and with TSI from the end of the 1960s to the early 1980s (figure omitted). It illustrates that SSDN has indeed positive coherence with solar parameters.

THE CORRELATION OF SPRING SNOW DAY NUMBER AND SUMMER PRECIPITATION OF CHINA REGULATED BY SOLAR ACTIVITY

Correlations Between Spring Snow Day Number and Summer Precipitation in China

Figure 6 shows the correlations of SSDN and summer precipitation in China for normal years, HSAY, and LSAY, respectively. HSAY (LSAY) is defined as the year of normalized value of SRF being more (less) than zero. It is seen that there are few highly correlated stations between SSDN and gauge precipitation in China (**Figure 6A**), but in HSAY (**Figure 6B**), the number of stations with significant correlation is more than that of normal years. Most parts of Northeast China and North China, as well as the south of the Yangtze River, have significant negative correlation coefficients, which indicates that when the solar activity is strong and SSDN is larger, these areas get less precipitation and are relatively dry. Between the Yellow River and the Yangtze River, significant positive correlation coefficients are identified, especially in the south of the Hetao area. It means that when the Sun is active and SSDN is larger, the precipitation in these areas increases. LSAY (**Figure 6C**) are accompanied with weakening correlations. However, there are still some stations with significant correlation coefficients in North China, south of the Yangtze River and Southwest China, while the patterns are opposite to those in HSAY. Therefore, solar activity could regulate the correlations between SSDN and summer precipitation in China.

Correlations Between Spring Snow Day Number and Summer Precipitation in China Without El Niño–Southern Oscillation Events

Based on the above analyses, it can be deduced that the correlation between SSDN and summer precipitation in China is regulated by solar activity. However, the data we used could be contaminated by strong ENSO events. As we know, ENSO events would also have strong influence on summer precipitation in China (Zhang et al., 1999; Wu et al., 2003). Therefore, analyses need to be done for HSAY and LSAY years with strong ENSO events (i.e., strong El Niño and La Niña events) excluded.

In order to filter out the impact of ENSO events on summer precipitation in China, the intensity grade of ENSO events issued by the National Climate Center is adopted to calculate partial correlation coefficients of SSDN and summer precipitation in China, as shown in **Figure 7**.

Figure 7 is similar to **Figure 6**, but it excludes the impact of ENSO events. It is apparent that without the contamination of ENSO events, the correlations between SSDN and summer precipitation in China in **Figure 7A** have the same pattern as

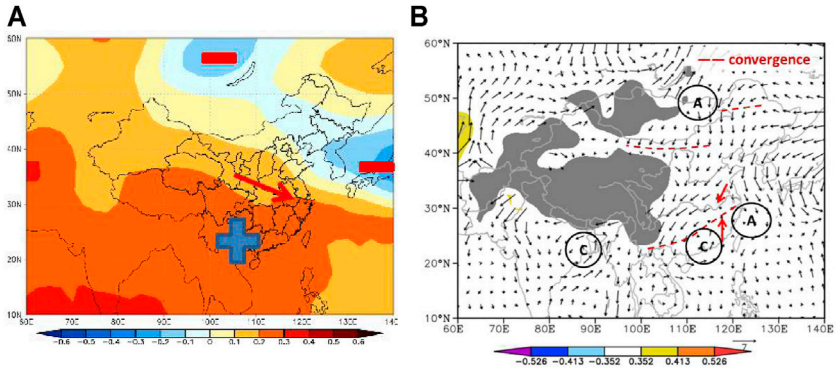

FIGURE 10 | Correlation coefficients of SSDN and **(A)** 500 hPa geopotential height field, **(B)** 850 hPa wind field in LSAY. (In panel a, "+" represents the positive correlation coefficient, "-" indicates the negative correlation coefficient, and the red arrow is the direction of the air flow. In panel b, "A" represents the anomalous anticyclone, "C" is the anomalous cyclone, and "— —" means convergent zone. The arrows are air flows. The colored shaded areas indicate that the significance level is more than 0.1. The gray shaded areas indicate that the elevation altitudes are above 1500 m.)

Figure 6A. In particular, in Shandong Peninsula, Southeast of the Tibetan Plateau, Guangdong province and south of Yunnan province, there are significant negative correlations, while there are remarkable positive correlation coefficients in the Daba Mountain area. In HSAY (**Figure 7B**), the correlation coefficients become more significant than those in normal years (**Figure 7A**). A number of remarkable negative correlation coefficients are seen in Northeast China, North China, Southwest China, Guizhou, and Guangxi areas, which means that, in HSAY, more spring snow over the Tibetan Plateau could cause less precipitation in these areas. There are significant positive coefficients in the south of Hetao Basin, around Shaanxi, the north of Sichuan, Zhejiang, and Fujian provinces, which indicates that, in HSAY, more spring snow could lead to more precipitation in these areas. In LSAY (**Figure 7C**), in Shandong province and east of Henan province, i.e., the north of lower reach of Huaihe River and the south of Yellow River, southeast of the Tibetan Plateau, and the Southeast China, there are obvious negative anomalies, indicating that more spring snow could cause less precipitation in these areas. Meanwhile, the positive anomalies are not obvious in **Figure 7C**. Therefore, in HSAY and LSAY, without the impact of ENSO events, there are obviously different correlation patterns between SSDN and summer precipitation in China, which testifies that the modulation of solar activity to correlation between snow and summer precipitation is valid without the influence from ENSO.

In terms of summer precipitation in China, in order to distinguish the direct influence of solar activity from the indirect influence of snow cover over the Tibetan Plateau, which is caused by solar activity, the composites of summer precipitation in peak years and valley years are investigated, as shown in **Figure 8A** and **Figure 8B**, respectively. Compared with **Figure 7**, the anomaly patterns of summer precipitation in **Figure 8** are obviously different. Here, wintertime solar radio flux peak years are selected as the peak years of solar activity namely 1957/58, 1957/68, 1979/80, 1990/91 and 2001/02, respectively; and wintertime solar radio flux valley years are selected as the valley years of solar activity namely 1963/64, 1975/76, 1986/87, 1995/96 and 2008/09. In peak years, around the middle and south of North China, there are negative anomalies, indicating the decreased precipitation there, while in Guangxi, Guizhou, south of Xizang and west of Yunnan, positive anomalies are found with increased precipitation (**Figure 8A**). In the valley years, less stations can pass the significance test. When SSDN increases, the precipitation in most parts of North China, Shandong Peninsula and a few stations of the Yangtze River Basin increases significantly, and other observation stations can not pass the significance test. The results indicate that, to a certain extent, solar activity could regulate the relationship between snow over the Tibetan Plateau and summer precipitation in China.

SUMMARY

In order to explain the anomalous summer precipitation pattern in China in **Figure 6**, correlation coefficients of SSDN, 500 hPa geopotential height field, and 850 hPa wind field in HSAY are calculated, respectively, as shown in **Figure 9A** and **Figure 9B**. It is seen from **Figure 9A** that a positive correlation coefficient belt is found from northeast to southwest along the east of China, and a negative correlation coefficient belt is identified from Lake Baikal to the west of China. The positive anomaly and negative anomaly present meridional belt distribution. It indicates that much warmer and moister air mass is transported from the Indian Ocean to western China, leading to intensified precipitation over the area. At 850 hPa, there exist two convergent zones in Xinjiang province and south of Hetao area, which correspond to areas with more precipitation in **Figure 6B**, located at Qinling Mountains and the Daba Mountain area.

In LSAY, the correlation coefficients between SSDN and geopotential height field on 500 hPa exhibit a zonal belt distribution of negative-north–positive-south, which is conducive to the invasion of cold air as shown in **Figure 10A** and **Figure 10B**, to the Yangtze River and further south. The correlation between SSDN and 850 hPa wind field shows that there is an anomalous cyclone in the north part of the bay of Bengal, which is farther south and farther west

than that in normal years. This condition is not conducive to the northward penetration of the southwest monsoon flow. There is a pair of vortices in the south of the Yangtze River, i.e., an anomalous cyclone in the north of Guangdong and an anomalous anticyclone over the East China Sea. Between them, there is an obvious southerly anomaly at 115–120oE in the east of South China, while in the north, a northerly anomaly exists in the coastal area, along with a convergence zone of the northeast to southwest direction in the south of the Yangtze River, which corresponds to the rain belt in **Figure 7C**. Shandong Peninsula and its west area are divergent zones, corresponding to the area with reduced precipitation in **Figure 7C**. In addition, the other two convergence zones are located in the north of Hetao and Daxinganling, respectively.

According to the above results, we get the following summary:

(1) Based on the synchronous and lag correlation coefficients of four snow indices over the Tibetan Plateau and three solar parameters on multi-time scales, it is inferred that SSDN is the most sensitive snow index on multi-time scales. SSDN has consistently positive correlations with SRF after the 21-year running mean, which is further verified by cross spectral analyses of SSDN and SRF, SSN, and TSI.
(2) The correlation coefficients between SSDN and summer precipitation in China are more significant when considering intensity variation of solar activity. In HSAY, the correlation of SSDN and summer precipitation is more significant than that in LSAY. Over Northeast China, North China, Southwest China, Guizhou, and Guangxi, there are obvious negative correlation coefficients, while the south of Hetao Basin, around Shaanxi and the north of Sichuan, and Zhejiang and Fujian provinces experience positive anomalies. In LSAY, the south of North China, the lower reach of Huaihe River, and the Southeast China present obvious negative anomalies, while Southwest China shows positive anomaly. When excluding the influence of strong ENSO events, the regulation of solar activity on the correlation between SSDN and summer precipitation in China is still robust. Furthermore, the direct influence caused by solar activity on summer precipitation in China is obviously different from that caused by snow cover over the Tibetan Plateau. Therefore, it is verified that the correlation coefficients between SSDN and summer precipitation are indeed regulated by solar activity.

MAIN FINDINGS

Spring snow day number is the most sensitive snow index of response to solar activity based on correlation analysis on multi-time scales. The relationship between spring snow day number and summer precipitation in China is regulated by solar activity obviously. Excluding the influence of strong ENSO events, the regulation of solar activity on the above relationship is more obvious.

DATA AVAILABILITY STATEMENT

The raw data supporting the conclusions of this article will be made available by the authors, without undue reservation.

AUTHOR CONTRIBUTIONS

YS and ZL designed this manuscript; ZL performed the data analysis; YS drafted the manuscript; YG and ZX performed manuscript review and editing.

FUNDING

This paper is supported by the National Natural Science Foundation of China under Contracts 41575091 and 42075040, the Major National Scientific Research Project of China under Contracts2012CB957803 and 2012CB957800, and the project of Training Center of ChinaMeteorological Administration "Study on Physical Factors to Affect China Climate". ZL is supported by the Key R and D (Social Development) program of Shanxi Province (201803d31219).

REFERENCES

Bamzai, A. S., and Marx, L. (2000). COLA AGCM Simulation of the Effect of Anomalous spring Snow over Eurasia on the Indian Summer Monsoon. *Q.J R. Met. Soc.* 126, 2575–2584. doi:10.1002/qj.49712656811

Camp, C. D., and Tung, K. K. (2007). Surface Warming by the Solar Cycle as Revealed by the Composite Mean Difference Projection. *Geophys. Res. Lett.* 34, L14703. doi:10.1029/2007GL030207

Chen, W., and Zhou, Q. (2012). Modulation of the Arctic Oscillation and the East Asian winter Climate Relationships by the 11-year Solar Cycle. *Adv. Atmos. Sci.* 29, 217–226. doi:10.1007/s00376-011-1095-3

Coddington, O., Lean, J. L., Pilewskie, P., Snow, M., and Lindholm, D. (2015). A Solar Irradiance Climate Data Record. *Bull. Am. Meteorol. Soc.* doi:10.1175/BAMS-D-14-00265.12

Ding, Y. H., Sun, Y., Wang, Z. Y., Zhu, Y. X., and Song, Y. F. (2009). Inter-decadal Variation of the Summer Precipitation in East China and its Association with Decreasing Asian Summer Monsoon. Part II: Possible Cause. *Int. J. Climatol.* 29, 19451955. doi:10.1002/joc.1759

Grenfell Thomas, C., Warren Stephen, G., and Mullen Peter, C. (1994). Reflection of Solar Radiation by the Antarctic Snow Surface at Ultraviolet, Visible, and Near-Infrared Wavelengths. *J. Geophys. Res.*, 18,699–18,684. doi:10.1029/94jd01484

Haigh, J. D., Blackburn, M., and Day, R. (2005). The Response of Tropospheric Circulation to Perturbations in Lower-Stratospheric Temperature. *J Clim.* 18, 3672–3685. doi:10.1175/JCLI3472.1

Haigh, J. D., and Blackburn, M. (2006). Solar Influences on Dynamical Coupling between the Stratosphere and Troposphere. *Space Sci. Rev.* 125, 331–344. doi:10.1007/s11214-006-9067-0

Haigh, J. D. (2003). The Effects of Solar Variability on the Earth's Climate. *Phil. Trans. R. Soc. Lond. Ser. A: Math. Phys. Eng. Sci.* 361, 95–111. doi:10.1098/rsta.2002.1111

Hoyt, D. V., and Schatten, K. H. (1997). *The Role of the Sun in Climate Change*. New York: Oxford University Press, 288.

Jevrejeva, S., Moore, J. C., and Grinsted, A. (2003). Influence of the Arctic Oscillation and El Niño-Southern Oscillation (ENSO) on Ice Conditions in the Baltic Sea: the Wavelet Approach. *J. Geophys. Res.* 108, 214677. doi:10.1029/2003jd003417

Kalnay, E., Kanamitsu, M., Kistler, R., Collins, W., Deaven, D., Gandin, L., et al. (1996). The NCEP/NCAR 40-year Reanalysis Project. *Bull. Amer. Meteorol. Soc.* 77, 437–471. doi:10.1175/1520-0477(1996)077<0437:tnyrp>2.0.co;2

Kerr, R. A. (2005). Changes in the Sun May Sway the Tropical Monsoon. *Science* 308, 787. doi:10.1126/science.308.5723.787

Kodera, K. (2004). Solar Influence on the Indian Ocean Monsoon through Dynamical Processes. *Geophys. Res. Lett.* 31, L24209. doi:10.1029/2004gl020928

Kopp, G., Krivova, N., Wu, C. J., and Lean, J. (2016). The Impact of the Revised Sunspot Record on Solar Irradiance Reconstructions. *Sol. Phys.* 291, 2951–2965. doi:10.1007/s11207-016-0853-x

Kushner, P. J., and Polvani, L. M. (2006). Stratosphere-Troposphere Coupling in a Relatively Simple AGCM: Impact of the Seasonal Cycle. *J. Clim.* 19, 5721–5727. doi:10.1175/JCLI4007.1

Lean, J. L. (2010). Cycles and Trends in Solar Irradiance and Climate. *Wires Clim. Change* 1, 111–122. doi:10.1002/wcc.18

Li, W., Sun, S., Wang, B., and Liu, X. (2009). Numerical Simulation of Sensitivities of Snow Melting to Spectral Composition of the Incoming Solar Radiation. *Adv. Atmos. Sci.* 26, 403–412. doi:10.1007/s00376-009-0403-7

Liu, J., Wang, B., Ding, Q., Kuang, X., Soon, W., and Zorita, E. (2009). Centennial Variations of the Global Monsoon Precipitation in the Last Millennium: Results from ECHO-G Model. *J Clim.* 22, 2356–2371. doi:10.1175/2008jcli2353.1

Meinander, O., Wuttke, S., Seckmeyer, G., Kazadzis, S., Lindfors, A., and Kyroe, E. (2009). Solar Zenith Angle Asymmetry Cases in Polar Snow UV Albedo. *Geophysica* 45 (1-2), 183–198.

Qian, Y. F., Zhang, G. Y., and Zheng, Y. Q. (2003). Impacts of the Tibetan Plateau Snow Anomaly in Winter and Spring on Precipitation in China in Spring and Summer. *Arid Meteorology* 21, 1–7.

Song, Y., Zhang, J., Li, Z. C., and Zhao, P. (2011). Interdecadalchange of winter Snow Cover of Tibetan Plateau and its Effect on Summer Precipitation in China. *Plateau Meteorology* 30, 843–851.

Song, Y., Li, Z. C., Z, N. Xiao., Zhang, J., Li, H. Y., and Zhu, Y. X. (2016b). Analysis on Interdecadal Correlation between Solar Activity and Snow Depth over the Qinghai-Xizang Plateau and East Asian Atmospheric Circulation in winter. *Plateau Meteorology* 35, 1135–1147. doi:10.7522/j.issn.1000-0534.2015.00059

Song, Y., Li, Z. C., Zhang, J., and Xiao, Z. N. (2016a). Review of Researches of Modulation Effects of Solar Activity on the Snow over Tibetan Plateau and East Asian Summer Monsoon. *Adv. Met Sc&T* 6, 148–154.

Song, Y., Li, Z., Gu, Y., Liou, K.-N., Zhang, X., and Xiao, Z. (2019). The Effect of Solar Cycle on Climate of Northeast Asia. *J. Meteorol. Res.* 33, 885–894. doi:10.1007/s13351-019-8132-z

Tan, L., Cai, Y., An, Z., and Ai, L. (2008). Precipitation Variations of Longxi, Northeast Margin of Tibetan Plateau since AD 960 and Their Relationship with Solar Activity. *Clim. Past* 4, 19–28.

Torrence, C., and Compo, G. P. (1998). A Practical Guide to Wavelet Analysis. *Bull. Amer. Meteorol. Soc.* 79, 61–78. doi:10.1175/1520-0477(1998)079<0061:apgtwa>2.0.co;2

Torrence, C., and Webster, P. J. (1999). Interdecadal Changes in the ENSO-Monsoon System. *J. Clim.* 12, 2679–2690. doi:10.1175/1520-0442(1999)012<2679:icitem>2.0.co;2

Torrence, C., and Webster, P. J. (1998). The Annual Cycle of Persistence in the El Nino-Southern Oscillation. *Q. J. R. Meteorol. Soc.* 124. doi:10.1256/smsqj.55009

Verschuren, D., Damste, J. S. S., Sinninghe Damsté, J. S., Moernaut, J., Kristen, I., Blaauw, M., et al.CHALLACEA project members (2009). Half-precessional Dynamics of Monsoon Rainfall Near the East African Equator. *Nature* 462, 637–641. doi:10.1038/nature08520

Wang, Y., Cheng, H., Edwards, R. L., He, Y., Kong, X., An, Z., et al. (2005). The Holocene Asian Monsoon: Links to Solar Changes and North Atlantic Climate. *Science* 308, 854–857. doi:10.1126/science.1106296

Wang, Z., Wu, R., and Huang, G. (2018). Low-frequency Snow Changes over the Tibetan Plateau. *Int. J. Climatol.* 38 (2), 949–963. doi:10.1002/joc.5221

Wasko, C., and Sharma, A. (2009). Effect of Solar Variability on Atmospheric Moisture Storage. *Geophys. Res. Lett.* 36, a–n. doi:10.1029/2008GL036310

Wei, Z. G., Chen, W., and Huang, R. H. (2008). Numerical Simulation of the Influence of the Tibetan Plateau winter-spring Snow Anomalies on the Summer Precipitation in China. *Plateau Mountain Meteorology Res.* 28 (1), 1–7.

Wu, R., Hu, Z.-Z., and Kirtman, B. P. (2003). Evolution of ENSO-Related Rainfall Anomalies in East Asia. *J. Clim.* 16 (22), 3742–3758. doi:10.1175/1520-0442(2003)016<3742:eoerai>2.0.co;2

Wu, R., Wen, Z., Yang, S., and Li, Y. (2010). An Interdecadal Change in Southern China Summer Rainfall Around 1992/93. *J. Clim.* 23 (9), 2389–2403. doi:10.1175/2009jcli3336.1

Yan, H. M., Zhong, M., and Zhu, Y. Z. (2003). The Determination of Degrees of freedom for Digital Filtered Time Series - an Application in the Correlation Analysis between Length of Day Variation and SOI. *ActaAstronomicaSinica* 44 (3), 324–329.

Zhang, R. H., Wu, B. Y., Zhao, P., and Han, J. P. (2008). The Decadal Shift of the Summer Climate in the 1980s over East China and its Possible Causes. *ActaMeterologicaSinica* 66, 697–706.

Zhang, R., Sumi, A., and Kimoto, M. (1999). A Diagnostic Study of the Impact of El Niño on the Precipitation in China. *Adv. Atmos. Sci.* 16, 229–241. doi:10.1007/bf02973084

Zhang, Y., Li, T., and Wang, B. (2004). Decadal Change of the Spring Snow Depth over the Tibetan Plateau: The Associated Circulation and Influence on the East Asian Summer Monsoon*. *J. Clim.* 17, 2780–2793. doi:10.1175/1520-0442(2004)017<2780:dcotss>2.0.co;2

Zhao, J., and Han, Y. B. (2005). Estimation of Correlation Significance Levelsafter Moving Average. *J. Beijing Normal Univ. (Natural Science)* 41, 139–141.

Zhao, J., and Han, Y. (2012). Sun's Total Irradiance Reconstruction Based on Multiple Solar Indices. *Sci. China Phys. Mech. Astron.* 55, 179–186. doi:10.1007/s11433-011-4496-5

Zhao, L., and Wang, J.-S. (2014). Robust Response of the East Asian Monsoon Rainband to Solar Variability. *J. Clim.* 27 (8), 3043–3051. doi:10.1175/jcli-d-13-00482.1

Zhao, L., Wang, J., and Zhao, H. (2012). Solar Cycle Signature in Decadal Variability of Monsoon Precipitation in China. *J. Meteorol. Soc. Jpn.* 901, 1–9. doi:10.2151/jmsj.2012-101

Zhao, L., Xu, Y., Wang, J. S., Ding, Y. H., and Xiao, Z. N. (2011). Progress in Studies on the Influence of Solar Activity on Climate Change during the Last 100 Years. *Adv. Meteorol. Sci. Tech.* 1 (4), 37–48.

Zhao, P., Yang, S., and Yu, R. (2010). Long-term Changes in Rainfall over Eastern China and Large-Scale Atmospheric Circulation Associated with Recent Global Warming. *J. Clim.* 23 (6), 1544–1562. doi:10.1175/2009jcli2660.1

Zhou, Z. J., and Liu, J. P. (2007). Variability of Tibetan spring Snow and its Associations with the Hemispheric Extratropical Circulation and East Asian Summer Monsoon Rainfall: An Observation Investigation. *Journal of Climate* 20 (15), 3942–3955. doi:10.1175/jcli4205.1

Zhou, Q., and Chen, W. (2014). Impact of the 11-year Solar Cycle on the Relationship between the East Asian winter Monsoon and the Following Summer Monsoon and the Related Processes. *Climatic Environ. Res.* 19, 486–496.

Zhou, Q., and Chen, W. (2012). Influence of the 11-year Solar Cycle on the Evolution of ENSO-Related SST Anomalies and Rainfall Anomalies in East Asia. *Chin. J. Atmos. Sci.* 36, 851–862.

Zhou, Q., (2013). *The Impact of 11-year Solar Cycle on Climate in East Asia and its Mechanism*, China; Institute of Atmospheric Physics, Chinese Academy of Sciences, 113.

Zhou, X., Zhao, P., Chen, J., Chen, L., and Li, W. (2009). Impacts of Thermodynamic Processes over the Tibetan Plateau on the Northern Hemispheric Climate. *Sci. China Ser. D-earth Sci.* 52, 1679–1693. doi:10.1007/s11430-009-0194-9

Zhou, Y. H., and Zheng, D. W. (1999). Monte Carlo Simulation Tests of Correlation Significance Levels. *ActaGeodaeticaet Cartographic Sinica* 28 (4), 313–318.

Conflict of Interest: The authors declare that the research was conducted in the absence of any commercial or financial relationships that could be construed as a potential conflict of interest.

Publisher's Note: All claims expressed in this article are solely those of the authors and do not necessarily represent those of their affiliated organizations, or those of the publisher, the editors, and the reviewers. Any product that may be evaluated in this article, or claim that may be made by its manufacturer, is not guaranteed or endorsed by the publisher.

frontiers in Earth Science

ORIGINAL RESEARCH
published: 07 March 2022
doi: 10.3389/feart.2022.834284

Relationship Between Summer Compound Hot and dry Extremes in China and the Snow Cover Pattern in the Preceding Winter

Haoxin Yao[1], *Liang Zhao*[2]*, *Xinyong Shen*[1,3]*, *Ziniu Xiao*[2] *and Qingquan Li*[1,4]

[1]*Key Laboratory of Meteorological Disaster, Ministry of Education/Joint International Research Laboratory of Climate and Environment Change/Collaborative Innovation Center on Forecast and Evaluation of Meteorological Disasters, Nanjing University of Information Science and Technology, Nanjing, China,* [2]*State Key Laboratory of Numerical Modeling for Atmosphere Sciences and Geophysical Fluid Dynamics (LASG), Institute of Atmospheric Physics, Chinese Academy of Sciences, Beijing, China,* [3]*Southern Marine Science and Engineering Guangdong Laboratory (Zhuhai), Zhuhai, China,* [4]*Laboratory for Climate Studies, National Climate Center, China Meteorological Administration, Beijing, China*

OPEN ACCESS

Edited by:
Renguang Wu,
Zhejiang University, China

Reviewed by:
Lisuo Hu,
Second Institute of Oceanography, China
Ge Liu,
Chinese Academy of Meteorological Sciences, China

***Correspondence:**
Liang Zhao
zhaol@lasg.iap.ac.cn
Xinyong Shen
shenxy@nuist.edu.cn

Specialty section:
This article was submitted to Atmospheric Science, a section of the journal Frontiers in Earth Science

Received: *13 December 2021*
Accepted: *10 February 2022*
Published: *07 March 2022*

Citation:
Yao H, Zhao L, Shen X, Xiao Z and Li Q (2022) Relationship Between Summer Compound Hot and dry Extremes in China and the Snow Cover Pattern in the Preceding Winter. Front. Earth Sci. 10:834284. doi: 10.3389/feart.2022.834284

With global warming, the probability of summer compound hot and dry extreme (CHDE) days, which are higher risk compared with single-factor extreme events, increases in some regions. However, there have been few studies on the winter precursor signals of such events. In this study, we found that summer CHDEs have generally increased in the last 20 years, with the increases in the middle and lower reaches of the Yangtze River region and Southwest China being more than double those in other regions of China. The dominant mode of summer CHDEs in China is characterized by more hot–dry days in the Yangtze–Huaihe River Basin (YHRB). Importantly, we found that there is an obvious cross-seasonal relationship between the first mode of winter snow cover in the Northern Hemisphere (NH) and summer CHDEs in China. When the mode of winter snow cover in the NH is in a positive phase with a negative-phase Arctic Oscillation (AO), i.e., more snow cover in Europe, Northeast China, and the northern United States, and less snow cover in central Asia and the midlatitudes in winter, more CHDEs in China in the following summer. Compared with the signals from the AO, these signals from winter snow can be better stored and transmitted into summer through the snow, soil and ocean, inducing a northward shift of the upper-level westerly jet and strengthening of South Asia high. Through the strong dynamic forcing of negative vorticity advection with the change of westerly jet, the subsidence movement in the western Pacific subtropical high (WPSH) region is strengthened, resulting in the stable maintenance of the WPSH in the YHRB. Under the synergy of a remote mid- and high-latitude wave train in summer, which also relates closely to winter snow cover, more CHDEs ultimately occur in the YHRB of China.

Keywords: snow cover, compound hot and dry extremes, EOF analysis, east asian monsoon, arctic oscillation, subtropical highs

INTRODUCTION

According to the sixth Assessment Report of the Intergovernmental Panel on Climate Change (IPCC, 2021), the global average temperature in the past 10 years was about 1.1°C higher than that in 1850–1900, and this will result in a general increase in heat waves and an extension of the warm season. It has also been reported that drought will be more severe in some areas in the future, such as East Asia, Western North America, Western and Central Europe and so on (Leonard et al., 2014; Chen et al., 2018; Sippel et al., 2018; Ribeiro et al., 2020). This means that the probability of multivariate compound extreme events is likely to increase. However, single-variable analyses often underestimate the combined effects of multi-variable anomalies, and compound extreme events have become a major challenge for human beings today and in the future (Dosio et al., 2018; Rasmijn et al., 2018). Compound hot and dry extremes (CHDEs) in summer are becoming more frequent under enhanced greenhouse gas forcing at the global scale, and this trend will continue with higher global warming (IPCC, 2021). The increasingly frequent occurrence of CHDEs not only brings great pressure to transportation, urban water supply, and power supply, but also affects people's daily lives and the safety of property. Therefore, it is not only of scientific significance to study the changes in CHDEs and their early signals, but it also helps to provide a reference for meteorological departments to improve the accuracy of predictions.

Many research results have shown that the occurrence of CHDEs in summer is often associated with local land–atmosphere feedback or remote wave activity/warm advection occurring simultaneously (Haarsma et al., 2015; Duchez et al., 2016; Miralles et al., 2019; Geirinhas et al., 2021). On the one hand, local or regional anticyclonic high-pressure anomalies at mid and upper troposphere have an important influence on the occurrence of CHDEs in summer (e.g., You et al., 2011; Tian et al., 2021). A strengthening and westward extension of the WPSH is conducive to the occurrence of extreme high-temperature weather in summer in southern China (Choi and Kim, 2019). Mid–high-latitude blocking highs associated with previous deceleration of the Atlantic Meridional Overturning Circulation and cold sea temperatures in the Atlantic Ocean have also been pointed out in favor of persistent hot–dry extremes (Haarsma et al., 2015; Duchez et al., 2016). A recent growth in long-lived heatwaves in China was reported because of the joint influence of the South Asia high and the WPSH (Li et al., 2021). On the other hand, remote anomalies of coupled ocean–land–atmosphere systems in distant areas also play an important role. The effects of ENSO, polar vortex, the westerly jets and cross-equatorial flow on hotter and drier summers cannot be ignored (Coumou et al., 2018; Hao et al., 2018; Ting et al., 2018; Lim et al., 2019). Hao et al. (2018) used the results of a logistic regression model to show that El Niño–Southern Oscillation (ENSO) played an important role in the occurrence of CHDEs in the warm season in northern South America, southern Africa, Southeast Asia, and Australia. Lim et al. (2019) found that the promotion of hot and dry extremes in Australia resulted from the downward coupling of a weakened polar vortex to tropospheric levels, where it linked with the low-index polarity of the Southern Annular Mode, an equatorward shift of the midlatitude westerly jet stream, and subsidence and warming in the subtropics. Ting et al. (2018) indicated the possible role of cross-equatorial flows in an extreme high-temperature event in southern China in 2016.

However, there have been few studies on the cross-seasonal precursor signals of compound extreme events. Snow cover and atmosphere–ocean coupled factors are known to possess long persistence and "memory", and therefore have the potential to be used as the source of predictability of extremes (Saito et al., 2004; Wu et al., 2016; Zhao et al., 2016). Snow can affect both atmospheric temperature and soil moisture, thereby potentially relating to subsequent compound anomaly events of temperature and moisture. Anomalies of soil moisture are often able to last for a long period and induce changes of the thermal condition on the land surface, which causes the lagged responses of the atmosphere. Betts et al. (1994) considered that locally large soil moisture increased the surface latent heat flux, which was beneficial to the occurrence of convective precipitation in summer. Through evapotranspiration, soil moisture can significantly affect surface air temperature and precipitation locally and cause transports of dry or wet air from other regions (Douville, 2002; Seneviratne et al., 2010). Over East Asia, some studies reported that wet spring soil in the Yangtze–Huaihe River Basin (YHRB) can lead to a decrease in summer rainfall in eastern China (e.g., Zhang and Zuo 2011; Meng et al., 2014; Liu et al., 2017a,b). Notable is, anomalies of spring and summer soil moisture could be induced by previous anomalies of snow or snowmelt in winter and spring (Vinnikov and Yeserkepova, 1991; Entin et al., 2000; Zhu and Ding, 2009; Lu et al., 2020), denoting that the signals of snow cover may be earlier. Winter snow cover over the Eurasian continent can not only affect the atmospheric circulation over the Eurasian continent (Saito et al., 2004; Matsumura and Yamazaki, 2012; Halder and Dirmeyer, 2016), but can also cause changes in summer precipitation and temperature over the mid and high latitudes of Eurasian continent (Prabhu et al., 2017; Wang et al., 2019).

Some key regions with a large variability of snow could have impacts on climate in the following seasons. For example, more snow cover over Eurasia in winter or spring leads to a delayed increase in surface temperature in spring, resulting in increased soil moisture in spring and summer (Wu and Kirtman, 2007; Halder and Dirmeyer, 2016; Wang et al., 2019). More Siberian snow cover in autumn increase the probability of a strong Siberian high-pressure ridge and upward atmospheric wave energy flux, resulting in large rises in polar geopotential heights, often followed by severe winter weather (Cohen et al., 2020). Snow cover in northern China and southern Mongolia was pointed out to be a bridge between East Asian winter and summer monsoons, impacting on a decrease in summer rainfall in the subtropical China (Lu et al., 2020). Snow cover and soil moisture anomalies in the Tibetan Plateau (TP) region in winter and spring can affect summertime drought and flooding in the East Asia, even remote regions, by regulating local thermal characteristics, hydrological processes and teleconnection response, thereby

regulating the upstream and downstream atmospheric circulation (Chow, et al., 2008; Wu et al., 2016; Qian et al., 2019; Liu et al., 2020). However, if we focus only on one region without considering the synergy between multiple regions, it may lead to inconsistent results. Some studies found that the snow mode with the spatially synchronous changes and reverse changes in different regions could have longer persistent influences than variations of continent-wide or one-region snow cover (e.g., Yim et al., 2010; Zhao et al., 2016). Therefore, the objective of this paper is to comprehensively consider the snow cover in Eurasia and TP, and even the changes of snow cover in the whole northern hemisphere, and to detect whether it has a regular impact on precipitation in China.

Although these studies have found that pre-seasonal signals such as snow cover have important effects on or links with summertime climate anomalies in East Asia, in terms of summer CHDEs in China, the snow signal in the preceding winter has rarely been studied. Accordingly, the objective of the present study was to evaluate the possible relationship between summer CHDEs and preceding-winter snow cover on the interannual timescale. The motivation behind this objective was to help better understand and predict CHDE events.

DATA AND METHODS

Data

We used the fifth major global reanalysis (ERA5) produced by the European Centre for Medium-Range Weather Forecasts (https://apps.ecmwf.int/datasets), including snow cover, geopotential height, wind speed, soil moisture, surface temperature, and relative humidity, with a resolution of 1° × 1° from 1981 to 2020 (Hersbach et al., 2020). Daily air temperature and relative humidity data were used to calculated CHDEs and then monthly CHDEs were obtained. Other variables are monthly data. According to the monthly average data, the seasonal average of each meteorological factor was obtained. The monthly index of the Arctic Oscillation (AO) provided by the Climate Prediction Center of the National Oceanic and Atmospheric Administration of the United States was also employed (https://www.cpc.ncep.noaa.gov/products/precip/CWlink/daily_ao_index/ao.shtml).

Calculation of CHDEs

First, to determine the threshold criterias. The air temperature/relative humidity of the 75th/25th percentile (from small to large) was used as threadholds (Wu et al., 2019). Second, to determine the thresholds for climatological 92 days (from 1 June to 31 August). Samples for calculating threshold.

On one day were 600 days (15 × 40; 40 is number of years; 15 is the sampling window (15 days), corresponding to 7 days on either side of the target date) (Perkins and Alexander, 2013; Deng et al., 2019). By moving the 15-days sampling window forward or backward, we can get consecutive thresholds for climatological 92 days. Third, to calculate CHDEs. The grid was then marked as 1 when the temperature was above the 75% threshold and the relative humidity was below the 25% threshold on one day, which was defined a CHDE day. Finally, it was extended to all grids in China.

Calculation of Wave Activity Flux

Wave activity flux (WAF), proposed by Takaya and Nakamura (1997), was used to indicate the propagation of stationary Rossby waves. The horizontal components of WAF were defined as follows:

$$WAF = \frac{pcos\varphi}{2|U|}\begin{Bmatrix} \frac{U}{\alpha^2 cos^2\varphi}\left[\left(\frac{\partial\psi'}{\partial\lambda}\right)^2 - \psi'\frac{\partial^2\psi'}{\partial\lambda^2}\right] + \frac{V}{\alpha^2 cos\varphi}\left[\frac{\partial\psi'}{\partial\lambda}\frac{\partial\psi'}{\partial\varphi} - \psi'\frac{\partial^2\psi'}{\partial\lambda\partial\varphi}\right] \\ \frac{U}{\alpha^2 cos\varphi}\left[\frac{\partial\psi'}{\partial\lambda}\frac{\partial\psi'}{\partial\varphi} - \psi'\frac{\partial^2\psi'}{\partial\lambda\partial\varphi}\right] + \frac{V}{\alpha^2}\left[\left(\frac{\partial\psi'}{\partial\varphi}\right)^2 - \psi'\frac{\partial^2\psi'}{\partial\varphi^2}\right] \end{Bmatrix}$$

where U and V denote the climatological zonal and meridional wind, respectively; $|U|$ represents the climatological magnitude of winds; p denotes the pressure scaled by 1000 hPa; ψ' is the perturbed geostrophic stream function; and α, λ, and φ are the square of the Earth's radius, longitude, and latitude, respectively.

Calculation of East Asian Winter Monsoon and East Asian Summer Monsoon

There are many calculation methods for the monsoon index. Here, the East Asian Winter Monsoon (EAWM) proposed by Shi et al. (1996) is selected, which is defined as the sum of the zonal standardized sea level pressure difference between 110°E and 160°E in 20°–50°N, and the obtained sequence is standardized again. The East Asian summer Monsoon index (EASM) is defined as the differences of 850-hPa zonal wind between the tropical monsoon trough region (10°–20°N and 100°–150°E) and the East Asian subtropical monsoon region (25°–35°N and 100°–150°E) (Zhang et al., 2003). For specific data, please see **Supplementary Figure S1**.

Statistical Analysis

We performed an empirical orthogonal function (EOF) analysis on the summer CHDEs in China and winter snow cover in the Northern Hemisphere (NH) to derive the spatiotemporal variability. Prior to the analysis, 9-years Lanczos high-pass filter is used to remove the low-frequency interdecadal oscillation and leave the annual oscillation signa. The filtered summer CHDEs, winter snow cover, geopotential height are also used for subsequent correlation analysis. After 9-years Lanczos high-pass filter, the effective degrees-of-freedom of the sample becomes 20 (Pyper and Peterman, 1998). In addition, linear correlation and regression analyses were used to detect the statistical connections between variables. The significance of all the analyses was determined by the standard two-tailed Student's *t*-test.

RESULTS

Spatiotemporal Characteristics of Summer CHDE Events in China

The occurrence of CHDE events requires the temperature and humidity to have a certain degree of opposite change in summer. **Figure 1A** shows the climatology (average from 1981 to 2020) of

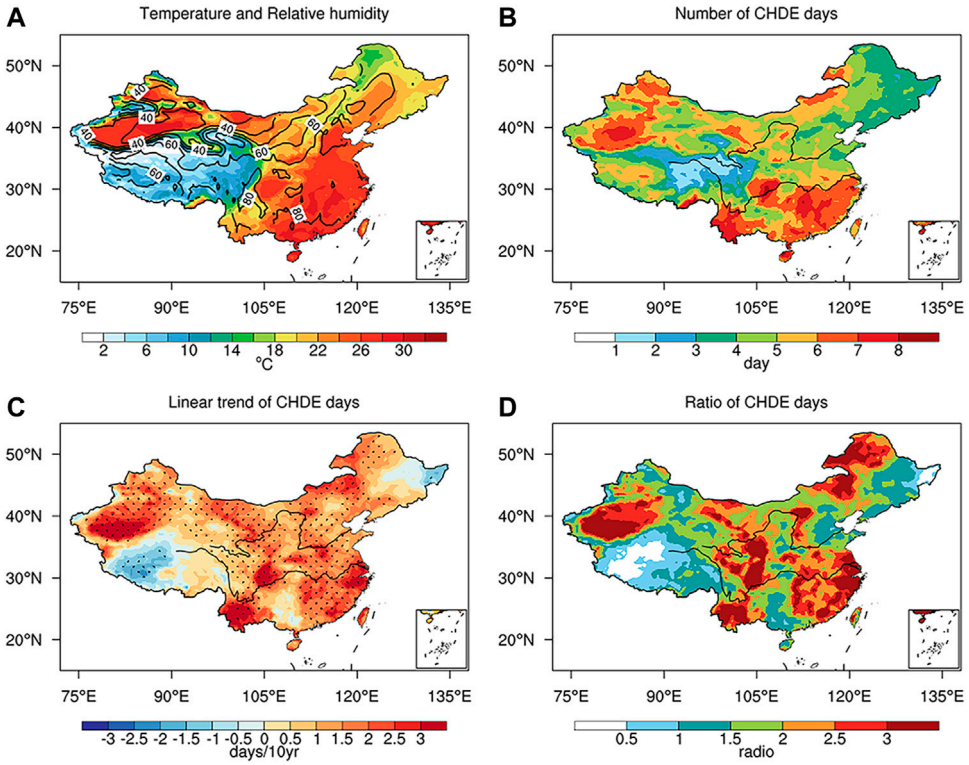

FIGURE 1 | (A) Climatology of average daily temperature (unit: °C) and humidity (unit: %) in summer (June to August) in China from 1981 to 2020. **(B)** Number (unit: day), **(C)** linear trend (unit: day/10 years), and **(D)** ratio (latter 20 years compared to previous 20 years) of summer CHDE days. Dotted areas in **(C)** indicate that the linear trend of CHDEs in these regions exceeds the 95% confidence level.

humidity and temperature in summer in China. It can be seen that, except over the TP, the temperature in summer is mostly above 18°C. Especially in Northwest, East, and South China, the temperature range is 26–32°C. The highest temperature appears in the Tarim Basin of Xinjiang and Guangdong Province. In summer, the high-value area of humidity in China is in the area south of 35°N, showing a spatial distribution pattern of wet in the south and dry in the north. The highest value of humidity appears in Guangdong Province, which exceeds 93%. Notably, the humidity in Xinjiang Province is very low and the temperature is high, that is, dry and high temperature tend to be coupled, which may be related to the semi-arid and desert climate in this region.

Figure 1B shows the summer CHDEs calculated according to the threshold of the 75th percentile of temperature (from small to large) and 25th percentile of humidity (from small to large). Most CHDEs occur in South and Northwest China. This distribution is similar to the temperature field in summer, but it is quite different from the distribution of the humidity field (**Figure 1A**). This means that the frequency of summer CHDEs has a significant positive correlation with the temperature background, but the relationship with the humidity background is more complex. Because of the warm and dry conditions tend to be easily coupled in Northwest China, CHDEs therefore occur frequently. However, Southeast China is also a high-incidence CHDE area, but has a warm and humid background. This suggests that CHDEs in this area based on the percentile thresholds are not caused by the climatological seasonal-mean humidity background field, but instead are related to the subseasonal variation and the coupling between heat and drought.

Figure 1C shows the linear trends of summer CHDEs. In the past 40 years, except over the western TP, the number of CHDEs in most regions of China generally shows an upward trend. The maximum trend of CHDEs exceeds 3 days/10 years, implying a dramatic increase in frequency of CHDE days. The most obvious upward CHDE trend is in South China, Northwest China, and the YHRB. Compared with **Figure 1B**, there is an obvious increasing trend of CHDEs in North China and the YHRB, but they are not areas with high frequency, which is deserving of close attention. Moreover, the spatial pattern of the trend in the TP region is opposite to the multi-year average state of CHDEs (fewer in the east and more in the west; **Figure 1B**). It is worth noting that the eastern TP is the birthplace of many important rivers, and the frequency of CHDEs is increasing, which is worthy of high vigilance. Besides, a significant decrease of CHDEs in the western TP is noted, although it needs to be further confirmed due to less observations there, which is consistent with some studies (e.g., Zhang et al., 2017; Sun et al., 2020).

Figure 1D shows the ratio of CHDEs in the last 20 years (2001–2020) to the first 20 years (1981–2000). It can be clearly seen that in many regions of China, the number of CHDE events in the latter 20 years (2001–2020) has more than doubled

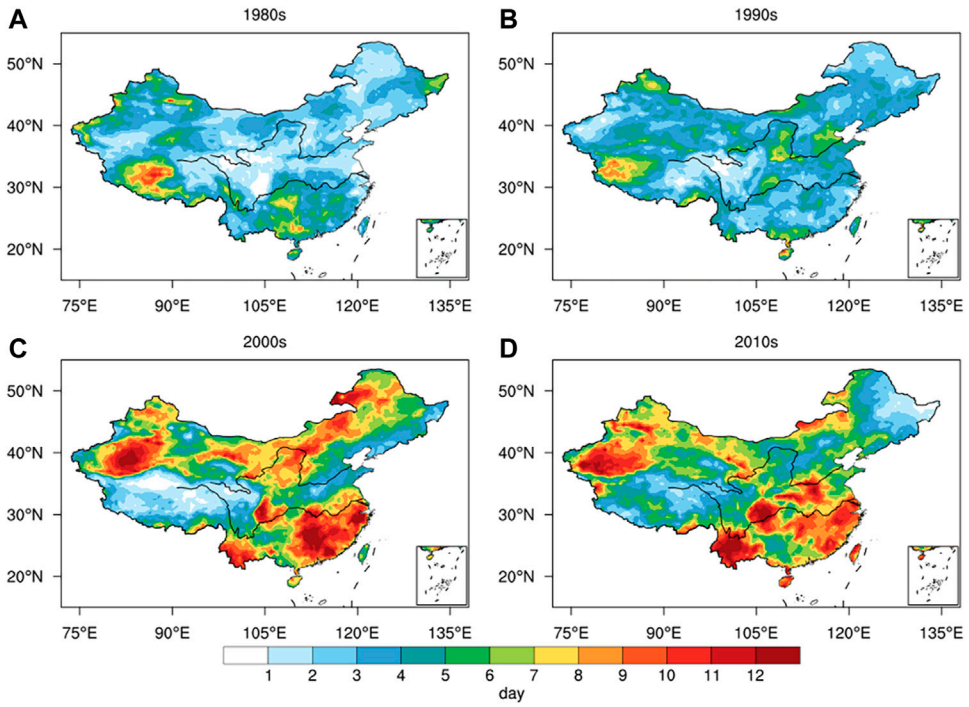

FIGURE 2 | The day numbers of summer CHDEs in the **(A)** 1980s, **(B)** 1990s, **(C)** 2000s, and **(D)** 2010s (units: day).

compared with the previous 20 years (1981–2000). Also, their distribution is similar to that in **Figure 1C**, indicating that the positive long-term linear trend of CHDEs is mainly due to the interdecadal growth of CHDEs after 2000.

The distribution and evolution of occurrence days of CHDEs per decade are shown in **Figure 2**. From the results it was found that before the 21st century there were very few CHDEs in summer, most of which were less than 5 days, and the large-value area was mainly concentrated in the western TP. After the turn of the 21st century, however, CHDEs increased rapidly in North and South China. Then, in the most recent 10 years, high incidence of CHDEs is mainly apparent in the YHRB, southwestern China and Xinjiang Province. Furthermore, it is clear that CHDEs in summer during the last decade can last for more than 12 days, which is more than double that in the 1980s.

Dominant Modes of Summer CHDEs in China and Winter Snow Cover in the NH

Next, we investigated the dominant EOF modes of summer CHDEs (after detrending) in China to better understand the spatial and temporal characteristics. As is shown in **Supplementary Figure S2**, the first EOF mode (EOF1) of summer CHDEs in China is very similar to the linear trends (**Figure 1C**); both show an increasing trend, and the first principal component (PC1) possesses clear characteristics of decadal change, indicating that this mode is likely to reflect the influence of the global warming signal, 9-years high-pass Lanczos filter (Duchon 1979) was applied to all original variables before analyses, to avoid the potential contamination of interannual relationships by decadal signals. Accordingly, we calculated the ratio of variance of CHDEs after 9-years high-pass filter to the variance of the original data (see **Supplementary Figure S3**), the result of which was generally more than 80% in most regions of China. That is, the data after 9-years high-pass filter retained most of the signals, especially those on the interannual scale. However, its driving factors and precursor signals were unclear. Therefore, we next investigated the dominant mode of the detrended CHDEs and their factors of influence.

The EOF1 and PC1 of summer CHDEs in China are shown in **Figures 3A, C**, respectively, accounting for 13.8% of the total variance, which is statistically distinguishable from the remaining higher modes according to the rule of North et al. (1982). This mode shows that the YHRB (the black box in **Figure 3A**, 110°E ~ 122°E, 28°N ~ 34°N) in China is a large positive-phase region, while the western TP and southern South China are primary negative-phase regions. The distributional characteristics are somewhat different from those of the CHDE trend (**Figure 1C**). For example, the anomalies in Yunnan Province and South China are opposite to those in the Yangtze River Basin, which also suggests that the driving factor affecting the mode may not be global warming.

Given that winter snow possesses signal memory, it is one of the key land surface processes affecting climate anomalies (Vinnikov and Yeserkepova, 1991; Entin et al., 2000), and therefore has certain influence on the land surface conditions

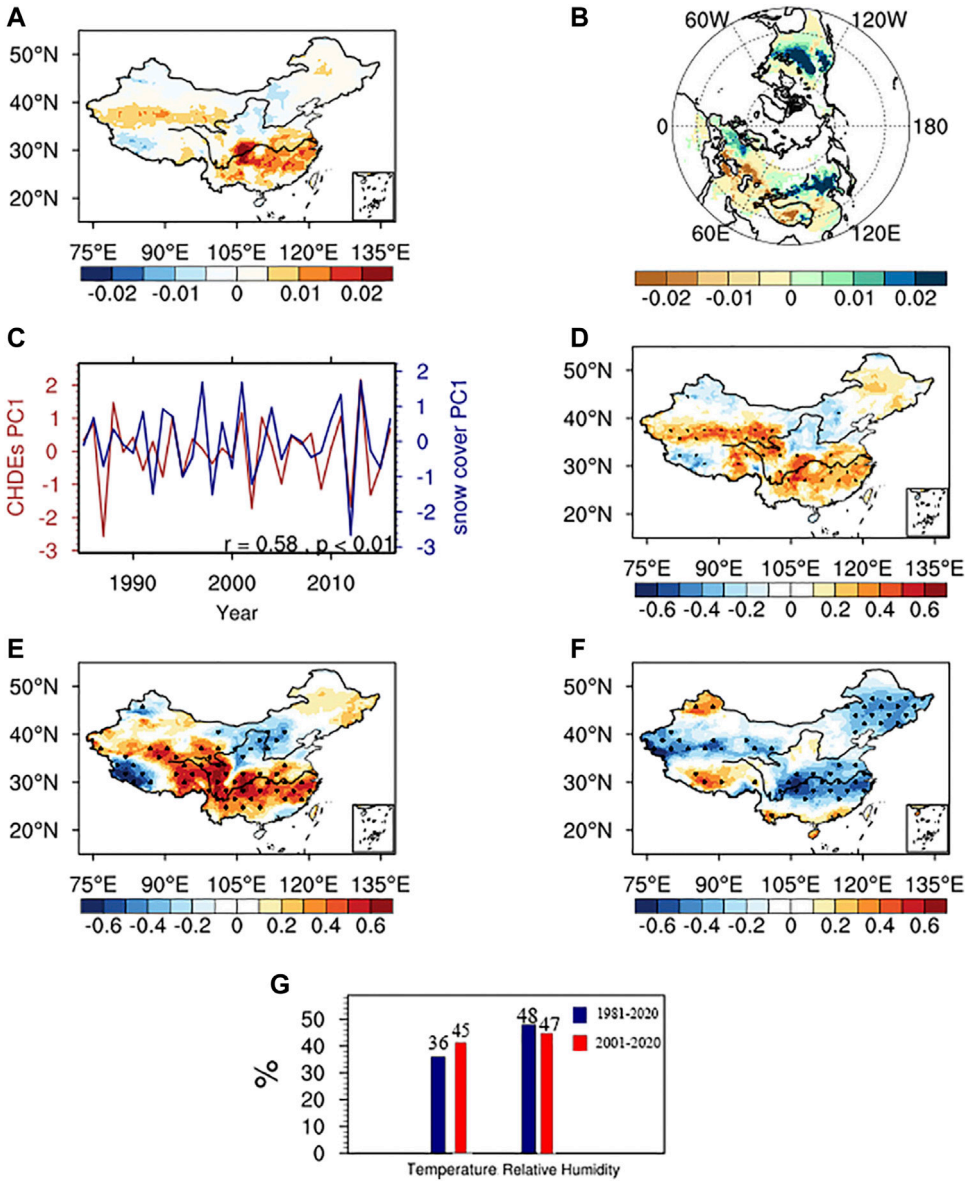

FIGURE 3 | (A) The EOF1 of summer CHDEs in China during 1981–2020. **(B)** The EOF1 of winter snow cover in the NH during 1981–2020. **(C)** The PC1 of summer CHDEs (red line) and winter snow cover (blue line) in the NH. **(D)** Correlation coefficients between the PC1 of winter snow cover and summer CHDEs. Black dots indicate values significant at the 95% confidence level. Correlation maps between the PC1 of CHDEs and **(E)** temperature and **(F)** humidity fields during 1981–2020. **(G)** Contribution ratios of temperature and humidity to the CHDEs in the YHRB during 1981–2020 and during 2001–2020 based on a regression of area-averaged variable over the YHRB (marked by a box in A) against the PC1 of CHDEs.

and atmospheric circulations in spring and summer (Zhao et al., 2016). Whether winter snow cover in the NH is related to summer CHDEs in China—that is, whether the precursor signal can be found in the winter snow cover—is our main concern. Therefore, we performed an EOF analysis to extract the dominant mode of winter snow cover in the NH (after detrending) and examined the possible relationships with following-summer CHDEs in China. The first EOF mode of winter NH snow cover explains 14.7% of the total variance (EOF1, **Figure 3B**), and its spatial distribution shows that when there is more snow cover in Europe, Northeast China, and North America, there is less snow cover in central Asia and the midlatitudes (including the TP region). The EOF1 of NH snow cover is very similar to that in Zhao et al. (2016), who believed that mode may be closely related to the AO anomaly, and its signal may have seasonal transmission. The PC1 of NH snow cover (**Figure 3C**) shows that the typical positive-phase years (greater than one standard deviations) are 1997, 2001, 2011, and 2013, often with dry summers in China; and the typical negative-phase years (less than 1 standard deviations) are 1992, 1998, 2002 and 2012, often with wet summers in China (**Supplementary Figure S4**).

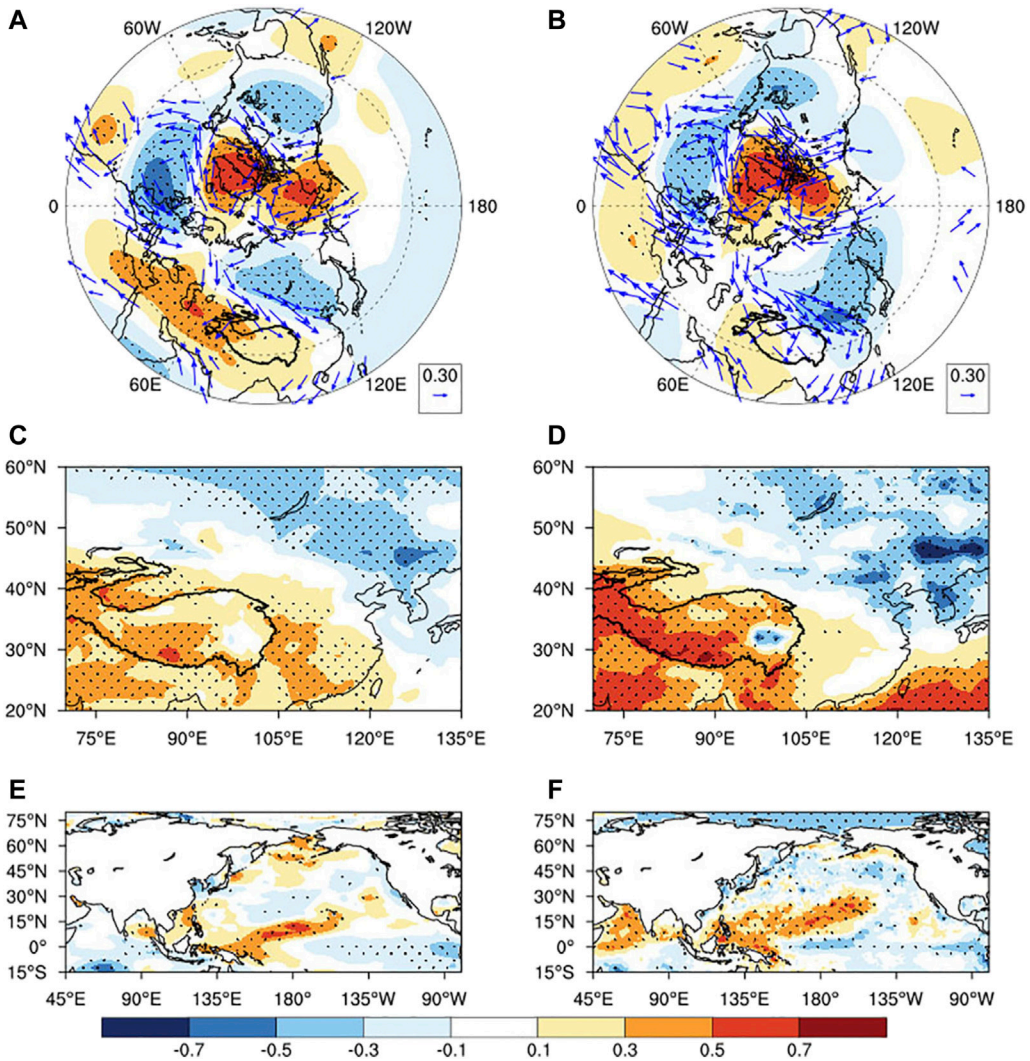

FIGURE 4 | (A,C) Correlation coefficients between the PC1 of snow cover and **(A)** 500-hPa geopotential height (shade) and 500-hPa wind (vector), **(C)** land surface temperature in winter **(B,D)**. As in **(A,C)** but for the PC1 of summer CHDEs. Black dots indicate values significant at the 95% confidence level. A positive correlation for zonal or meridional wind component is denoted by an eastward or poleward arrow, respectively.

TABLE 1 | Correlation coefficients between the PC1s of winter snow cover, summer CHDEs and the AO, EAWM, and ENSO (Niño3.4) indices in winter for 1981–2020. After/represents the correlation coefficient after removing ENSO.

	CHDEs PC1	AO	EAWM	ENSO
Snow-cover PC1	0.58**/0.57**	−0.42**/−0.40**	0.40*/0.38*	−0.21
CHDEs PC1	—	−0.65**/−0.57**	0.39*/0.36*	−0.05

**90% and **95% confidence levels.*

Importantly, the two PC1s of 1snow and CHDEs bear some similarity. It was found that the NH snow cover could explain a significant fraction of the CHDE variance ($r = 0.58$, $p < 0.01$; **Figure 3C**) during the period 1981–2020. Statistically, in years with positive-phase winter snow cover in the NH, the YHRB is prone to CHDEs in summer. The cross-seasonal correlation coefficient between them can reach a high level of significance, indicating that the influence of the first mode of the winter NH snow cover on summer CHDEs is worth noting and studying.

Figure 3D shows the spatial distribution of the correlation coefficient between the PC1 of winter NH snow cover and summer CHDEs, which is similar to the CHDE EOF1 pattern in **Figure 3A**. The spatial correlation coefficient of **Figures 3A,D** is 0.93, and they are both high values in the Yangtze River Basin and southern Xinjiang Province. This also suggests that the first mode of summer CHDEs in China is related to the first mode of winter NH snow cover.

We further studied contribution of higher temperature and lower humidity to more summer CHDEs in the YHRB, respectively, in the last 20 years **Figures 3E,F** show that correlation maps between the PC1 of CHDEs and temperature and humidity fields and **Figure 3G** is contribution ratios of temperature and humidity to the CHDEs in the YHRB. High

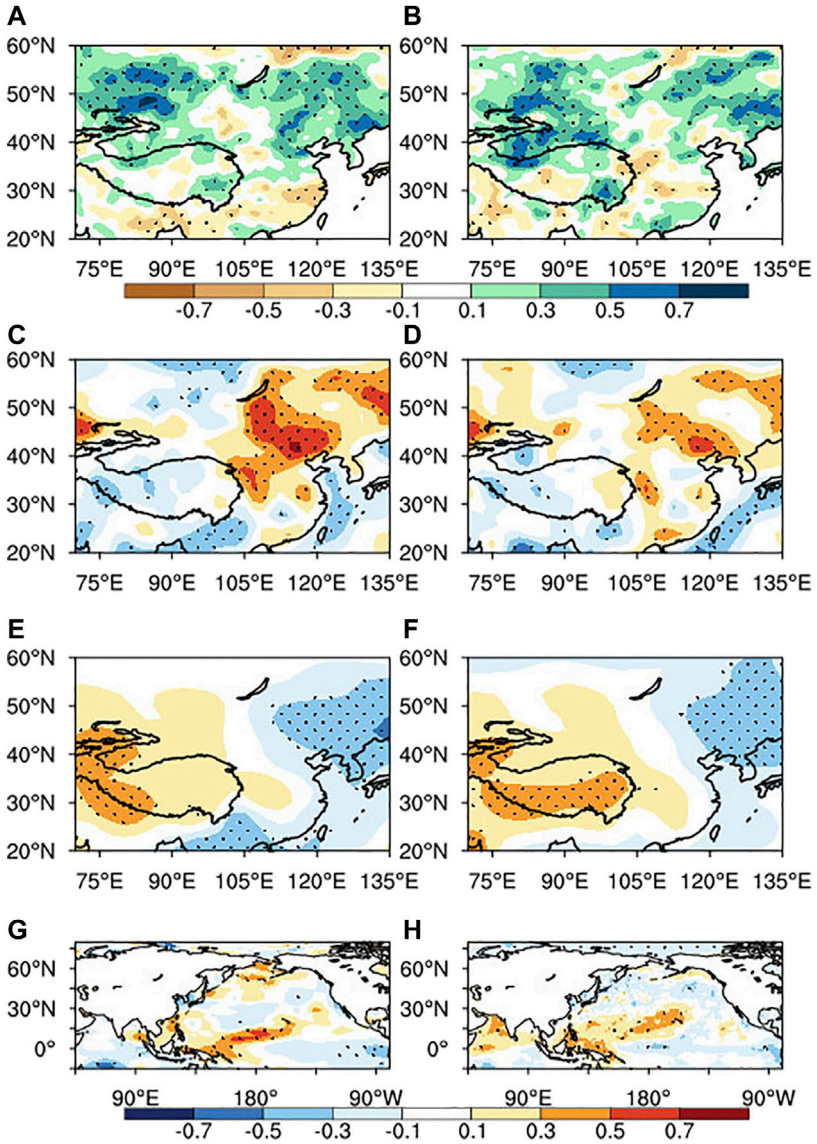

FIGURE 5 | (A,C,E) Correlation coefficients between the PC1 of winter NH snow cover and spring **(A)** soil moisture, **(C)** latent heat flux and **(E)** land surface temperature. **(B,D,F)** As in **(A,C,E)** but for the PC1 of summer CHDEs. Black dots indicate values significant at the 95% confidence level.

TABLE 2 | Correlation coefficients between the EASM index and the PC1s of winter snow cover and summer CHDEs for 1981–2020.

	Winter snow-cover PC1	Summer CHDE PC1
EASM	0.36*	0.38*
Winter snow-cover PC1	—	0.58**

**90% and **95% confidence level.*

correlations in the YHRB region for both temperature and humidity implying the first mode of CHDEs is related to both high temperature and low humidity in the YHRB. For the whole 40 years, temperature/humidity contributed 36%/48% to variation in the PC1 of CHDEs. However, For the last 20 years, temperature/humidity contributed 45%/47% to variation in the PC1 of CHDEs. Contribution from temperature has increased by 9%.

Mechanisms of the relationship between the two dominant modes of winter NH snow cover and summer CHDEs in China.

Climatic Factors in Winter

In order to analyze the mechanism of the relationship between the two dominant modes of winter snow cover and summer CHDEs, we verified whether the winter atmospheric circulation pattern associated with the PC1 of winter snow cover is similar to that of the PC1 of summer CHDEs. **Figures 4A,B** show the relationships between winter 500-hPa geopotential height (shade) and wind (vector), and the PC1s of winter NH snow cover and summer CHDEs, respectively. When

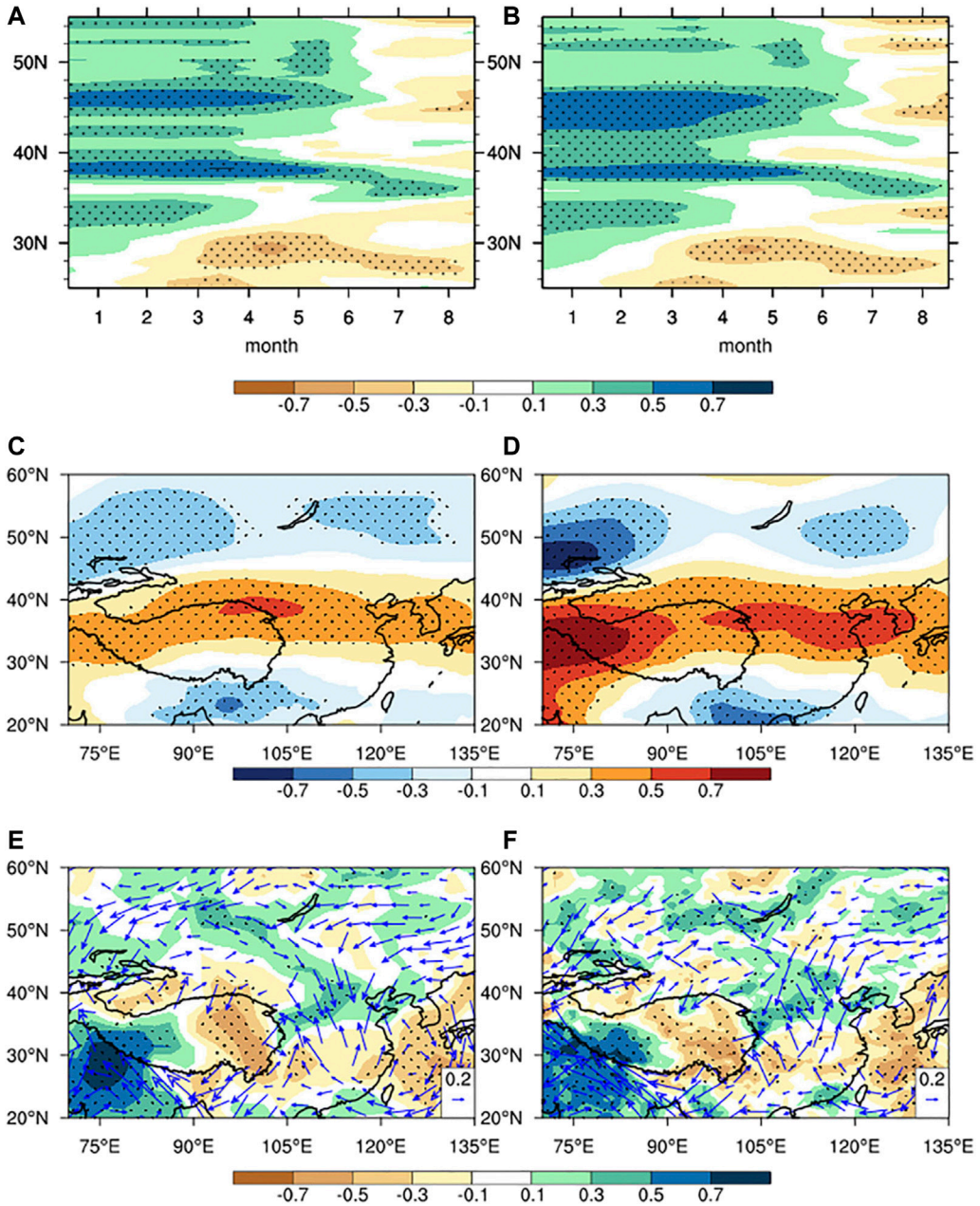

FIGURE 6 | (A,C,E) Correlation coefficients between the PC1 of winter NH snow cover and **(A)** soil moisture with time along 115–120°E, **(C)** summer 200 hPa zonal wind, and **(E)** summer total precipitation (shade); 850 hPa wind (vectors). **(B,D,F)** As in **(A,C,E)** but for the PC1 of summer CHDEs. Black dots in **(A-F)** indicate values significant at the 95% confidence level. A positive correlation for zonal or meridional wind component is denoted by an eastward or poleward arrow, respectively.

the PC1 of winter NH snow cover is positive, there is a large area of high negative anomalies in Europe, northeastern China, and northeastern America, while positive anomalies exist in the Arctic, Central Asia, and the TP (**Figure 4A**), which are the characteristics of a negative AO. During a strong negative AO, there is a weak polar vortex over the Arctic region and a strong East Asian trough, denoting frequent cold-air activity. However, there is less snow and higher temperatures over Central Asia and the TP region because of the anomalous high-pressure system (**Figures 4C,D**). The correlation coefficient (R) between the PC1 of winter NH snow cover and the AO/East Asian summer monsoon is −0.42 ($p < 0.01$)/0.40 ($p < 0.01$). The correlation coefficient between the PC1 of summer CHDEs and the AO/East Asian summer monsoon is −0.65 ($p < 0.01$)/0.39 ($p < 0.01$) (**Table 1**). Therefore, the EOF1 of winter NH snow cover and summer CHDEs are both closely related to the AO and the EAWM. Moreover, the distribution in **Figure 4B** is consistent to that in **Figure 4A** (the

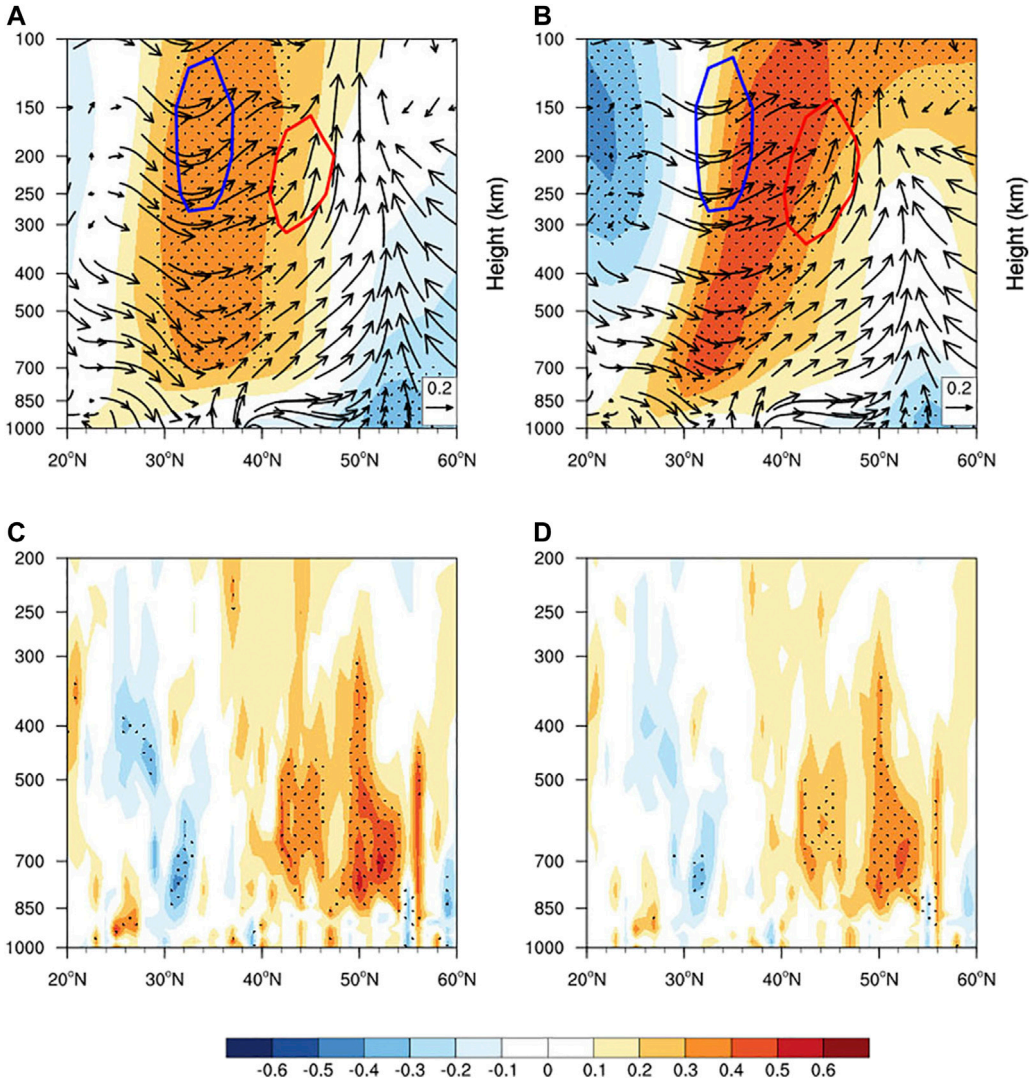

FIGURE 7 | (A,C) Correlation coefficients between the PC1 of winter NH snow cover and summer **(A)** geopotential height (shading) and vertical circulation (vectors), **(C)** relative vorticity along 115°N. **(B,D)** As in **(A,C)** but for the PC1 of summer CHDEs. The red lines in **(A,B)** represent 30 m/s zonal wind, which are regressed by high-value years of the PC1 of winter NH snow cover and summer CHDEs, and the blue lines are regressed by low-value years. Black dots and black vectors indicate values significant at the 95% confidence level. A positive correlation for meridional or upward wind component is denoted by an poleward or upward arrow, respectively.

spatial correlation coefficient of **Figures 4A,B** is 0.88), indicating that the atmospheric circulation in the preceding winter affecting the EOF1 of summer CHDEs is highly consistent with the atmospheric circulation corresponding to the EOF1 of winter NH snow cover, which are both related to the AO and EAWM.

Besides, the correlation coefficient between the PC1s with ENSO is not significant. And after removing ENSO, we recalculated the correlation coefficients and found that they were still significantly indigenous (**Table 1**). Therefore, we believe that the relationship between snow cover and AO/EAWM at the interannual scale is likely not modulated by ENSO. Therefore, in the preceding winter of more summer CHDEs in China, the atmospheric circulation is mainly characterized by a negative AO. The land surface is mainly characterized by more snow cover in Europe and northern East Asia but less snow cover on the TP.

Climatic Factors in Spring

If winter snow cover can affect the summer climate, it is bound to store and transmit signals in spring. **Figures 5A,B** show dry (wet) soil in the YHRB (northeastern China) in spring, which may be related to the lack (abundant) of snowfall and rainfall in winter as in **Figure 3B**. The dry soil in the YHRB causes a decrease in evaporation and latent heat (**Figures 5C,D**), which can promote rising of land surface temperature in spring and higher temperature (**Figures 5E,F**). The wet soil in northeastern China causes an increase in latent heat (**Figures 5C,D**) and delays rising of surface temperature due to cooling effect of

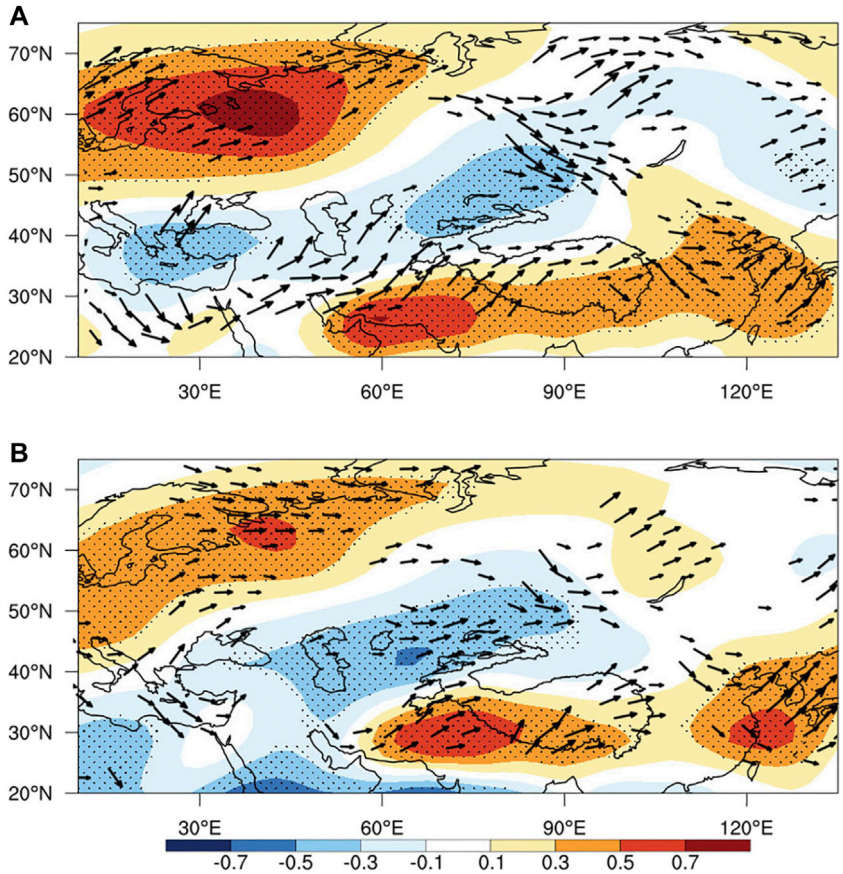

FIGURE 8 | Correlation coefficients between 500-hPa geopotential height and WAF in summer and **(A)** the PC1 of winter snow cover and **(B)** the PC1 of summer CHDEs. Black dots and black vectors indicate values significant at the 95% confidence level. A positive correlation for zonal or meridional WAF component is denoted by an eastward or poleward arrow, respectively.

the latent heat and evaporation, inducing a lower temperature (**Figures 5E,F**). In addition, weakening of the cold-source effect in winter and strengthening of the thermal effect (higher surface temperature) in the spring and summer in the TP are likely related to less snow in winter (Goswami et al., 2006; Feng and Hu, 2008; Ding et al., 2009; Shen et al., 2011). These temperature distribution characteristics lead to an intensification of meridional temperature gradient with cold north China and warm south China in spring, which can strengthen the westerlies. This will cause an anticyclonic anomaly and descending motion in the south side of jet axis, further leading to more dry soil. This is a positive feedback effect resulting in gradual amplification in the domain of influence. Obviously, spring soil could store signals of preceding-winter snow cover, which can enhance thermal contrast between land and ocean and change temperature gradient, further affecting the summer atmospheric circulations, e.g., the summer monsoon and subtropical highs (Yim et al., 2010; Lu et al., 2020).

Climatic Factors in Summer

Sincethe eastern part of China is a monsoon region, the EASM is an important factor affecting severe drought and flood disasters in the YHRB of China. When a strong EASM occurs, the tropical monsoon trough is usually strong but the subtropical mei-yu front is weaker and the WPSH is positioned more to the north, resulting in less monsoon precipitation in the YHRB region of China (Zhang et al., 2003). In this case, CHDE events occur easily in the YHRB, which can be statistically verified (**Table 2**), and the EASM and CHDEs are highly correlated (r = 0.38). Moreover, there is also a significant positive correlation between the EASM and the PC1 of winter NH snow cover (r = 0.36). This suggests that the winter NH snow cover can affect the intensity of the EASM, which is likely related to the previous sea–land thermal contrast and cross-seasonal transmission of the snow signal in soil from winter to summer.

Enhanced land heating due to reductions in snow cover can result in a subsequent anomalously high ridge in the mid–high latitudes (Matsumura and Yamazaki, 2012), causing persistent subsidence and warming. Because the dry (wet) soil leads to stronger (weaker) heating, and the atmospheric temperature rises (decreases). Then an increase of meridional temperature gradient leads to the enhancement of westerly jet, which can cause anticyclonic shear and high-pressure development on the south side of jet axis (**Figure 6**). Soil moisture in the YHRB around 30°N continued to be dry from spring to summer (**Figures 6A,B**). In

TABLE 3 | Correlation coefficients of the PC1 of winter snow cover and the PC2 of spring snow cover with the EASM index and the PC1 of summer CHDEs during 1981–2020.

	EASM	Summer CHDEs PC1
Winter AO	0.20	–0.65**
Spring AO	0.14	–0.09
Winter snow-cover PC1	0.36*	0.58**
Spring snow-cover PC2	0.45**	0.49**

*90% and **99% confidence level.

summer, the range of warm and dry areas was further expanded (**Figure 6**), due to the dry–hot positive feedback effect between land and atmosphere and the thermal difference between sea and land. Due to the enhancement of plateau heat source in spring and the decrease of surface cooling and tropospheric thickness in Northeast China (**Figures 5E, F**), the upper westerly jet will move northward and strengthen (**Figures 6C,D** and **Figures 7A,B**). The westerly jet is northerly than usual, and the zonal circulation is stronger, resulting in the stable WPSH in the northerly position (**Figures 8A,B**), which easily results in CHDE events in YHRB. The northward movement and strengthening of westerly jet are conducive to the formation of abnormal anticyclonic circulation over the YHRB (**Figures 6E,F**), bringing negative vorticity advection (**Figures 7C,D**), resulting in enhanced subsidence over the YHRB and suppressed precipitation (**Figures 6E,F**), which is conducive to the generation of sunny weather and the promotion of ground temperature. In addition, the strengthening of plateau heat source makes the South Asian high extend eastward (Zhu and Ding, 2009). Through the strong dynamic forcing of upper negative vorticity advection in the right side of exit of the westerly jet, the subsidence movement in the WPSH region is strengthened, resulting in the stable maintenance of the subtropical high and clear and high temperature in YHRB. Therefore, sunny weather and strong solar radiation in the YHRB result in the surface absorbing a lot of energy. The dry adiabatic descent in the high-pressure ridge makes the temperature rise in the YHRB, which is therefore prone to CHDEs.

In addition to these local thermal factors causing climatic anomalies, many studies have indicated that the occurrence of compound extreme events is often associated with the combined effect of different factors from local and remote regions (Haarsma et al., 2015; Duchez et al., 2016; Miralles et al., 2019; Geirinhas et al., 2021). **Figure 8A** shows that when the PC1 of the preceding winter snow cover is positive, there is strong WAF propagating to East Asia in the mid and high latitudes of Eurasia, and northern Europe–the southern Barents Sea is the main wave anomaly source. Due to the "+—+" distribution of 500-hPa geopotential height, there is a strong high-pressure anomaly over central and northern East Asia. The features are similar to those in **Figure 8B** for the PC1 of summer CHDEs. Strong anomalous wave trains in the mid and high latitudes are accompanied by pressure anomalies, resulting in significant high-pressure anomalies in northern East Asia. In addition, it is worth noting that, in the two maps, the geopotential height anomalies in East Asia are zonally extended, indicating that the northward and westward WPSH is likely related to the wave train anomaly.

DISCUSSION AND CONCLUSION

With global climate change, the risk of compound extreme events is increasing (Ribeiro et al., 2020), which prompted us to study their precursors and early signals. Some studies have shown that the enhancement of surface heating in the mid–high latitudes associated with the Arctic amplification can significantly affect the midlatitude summer circulation and promote anomalous high pressure in the troposphere through weakening of midlatitude storm tracks, northward movement of jets, and amplification of synoptic-scale quasi-stationary waves (Coumou et al., 2018; Ting et al., 2018). The occurrence of this positive geopotential height anomaly in the mid–high latitudes induces dry and hot weather through subsidence and easterly anomalies of continental origin (Zhang et al., 2021). These links can be partially confirmed in our work. For example, when the Arctic amplification characteristics are obvious, often accompanied by a negative AO, the summertime climate systems in East Asia, such as the subtropical high and westerly jet, are positioned northwards, and an upper-troposphere high-pressure ridge develops. In this case, the midlatitudes of China are prone to a hotter and drier climate.

Different from the conclusions in previous research, we found for the first time that there is a significant relationship between the dominant modes of winter snow cover in the NH and the summer CHDEs in the YHRB of China. The EOF1 of snow cover shows that when there is more snow cover in Europe, Northeast China, and North America, there is less snow cover in central Asia and the midlatitudes. The snow characteristics are coupled with a negative AO (Zhao et al., 2016). Besides, it is also likely that summer CHDEs are related to sea surface temperature anomaly characteristics similar to the La Niña pattern (Hao et al., 2018). However, the contributions of sea surface temperature to the relationship between snow cover and CHDEs in the interannual scale and its mechanism need to be further analyzed. The signals in winter are likely stored and transmitted through snow cover, soil, and ocean, which cause circulation responses in spring and summer, including an enhancing of the westerlies, promotion of the development of mid- and high-latitude high systems, weakening the mei-yu front, resulting in less precipitation in the YHRB of China. At the same time, anomalous planetary waves from the south side of the Barents Sea also play a synergistic role, which propagate southeastwards to induce the WPSH to shift northwards and westwards, thereby controlling the YHRB and its northern region and resulting in high temperatures. The anomalous wave trains are closely related to the EOF1 of winter snow cover, which is consistent with other relevant studies (Francis and Vavrus, 2012; Screen and Simmonds, 2013); plus, our study further finds that this wave train is also closely related to summer CHDEs in the YHRB of China. Therefore, the hot and dry climate in the YHRB in summer can be related to the EOF1 of snow cover and the land–ocean–ice–atmosphere system near the Arctic in the preceding winter. Besides, the opposite trend in the western TP, on one hand, is likely associated with changes of westerlies over the TP (Sun et al., 2020). On the other hand, it could be related anomaly of the Indian summer monsoon (Zhang et al., 2017). The characteristics could be shown in correlation distributions of snow PC1 (**Figure 6** and **Table 2**). Enhance of the upper westerlies can lead to anomalous divergence in the south of

the upper jet entrance (the western TP), resulting in anomalous ascending favoring the wetting in western TP. Meanwhile, the western TP is usually located in the left of the lower jet (usually related to monsoon), which can intensify ascending and rainfall. And enhance of the upper westerlies also leads to anomalous anticyclonic shear in the south of the westerly jet (the eastern TP and the YHRB), strengthening the high-pressure anomaly and descending.

These precursors in winter—especially the snow signal—may have potential value for the prediction of summer heat and drought anomalies. Furthermore, we conducted an EOF analysis of spring snow cover in the NH and found that the EOF2 of spring snow cover (**Supplementary Figure S5**) is likely a continuation of the EOF1 of winter snow cover (**Figure 3B**). They are not only spatially similar, but their PCs are also highly correlated (r = 0.50, $p < 0.01$). Moreover, both the winter and spring snow modes are significantly related to the EASM and summer CHDEs in China. However, by comparison, the AO, as an atmospheric signal, shows no robust interseasonal transmission (**Table 3**). Therefore, the modes of winter and spring snow in the NH are more "memorable" than the AO, and have the potential to be used as predictors for hot and dry climate conditions in summer in China.

Similaritybetween **Supplementary Figure S5** and **Figure 3B** implies not only seasonal continuity of snow signals in some key regions but also the spatial synergy. Both of their spatial distributions show that when there was more snow cover in Europe, Northeast China, and North America, there was less snow cover in central Asia and the midlatitudes (including the TP region). Halder and Dirmeyer (2016) found that although the snow-albedo effect is prevalent over western Eurasia, the delayed hydrological effect is strong and persistent over the eastern part. Yim et al. (2010) found the second EOF mode of spring Eurasia is dominated by an east-west dipole structure and this dipole-pattern snow cover has better persistence and is more closely related to the EASM rainfall than that of continent-wide snow cover, which is similar to our conclusion. To identify the importance of the leading mode of snow cover in the northern hemisphere and the synergy among snow variations in multiple key regions, according to the EOF1 of winter snow cover (**Figure 3B**), we calculated correlation coefficients between three key regions (midwestern Europe: 5°–30°E and 45°–55°N, Northeast China: 110°–135°E and 40°–50°N and northern United States: 85°–115°W and 40°–50°N) of winter snow cover and summer China CHDEs PC1. It was found that although snow in the key regions was all significantly correlated with the summer CHDEs PC1 (correlations are from 0.36 to 0.48; **Supplementary Table S1**), the correlation coefficient was not as large as that of the PC1 of whole winter northern-hemisphere snow cover (r = 0.58). So the synergistic variations of winter snow cover in the northern hemisphere are likely more important than that of in a single region.

Using percentile event thresholds is a simple and robust way of placing the current temperature/humidity conditions in the context of both climatology and variability at a specific location. Though percentile event thresholds are undeniably a meaningful index, one should be careful with its interpretation. Firstly, one disadvantage is the necessity of a robust probability density function on which to base the percentiles (Ford et al., 2016) and it should be noted that this method do not provide a physical indication of Droughts/Heat waves severity. Secondly, this approach may amplify the response of extreme events to climate change (Klein Tank and Können 2003; Donat et al., 2013; Sillmann et al., 2013). For southern China, 25th percentile (from small to large) is still relative humidity value of about 75%. But if we define 50% relative humidity as an absolute threshold, the CHDE events will be hardly happen in southern China. So both the relative and absolute thresholds have weakness. It deserves to be further studied in the future whether it will be better and more reasonable to add an absolute threshold of humidity when calculate the CHDEs.

DATA AVAILABILITY STATEMENT

The original contributions presented in the study are included in the article/**Supplementary Material**, further inquiries can be directed to the corresponding authors.

AUTHOR CONTRIBUTIONS

HY: Methodology, Data curation, Writing-Original draft preparation; LZ: Conceptualization, Writing-Reviewing and Editing; XS: Writing-Reviewing and Editing; ZX and QL: Writing-Reviewing and Editing.

FUNDING

This work is supported by the Second Tibetan Plateau Scientific Expedition and Research Program (2019QZKK0208), the National Natural Science Foundation of China (41790471, 42075040, 41975054 and 41930967), the Strategic Priority Research Program of the Chinese Academy of Sciences (XDA20100304, XDA20060501 and XDA23090102), the National Key Research and Development Program of China (2018YFA0606203 and 2019YFC1510400), the Innovative Development Special Project of China Meteorological Administration (CXFZ2022J039) and Guangdong Major Project of Basic and Applied Basic Research (2020B0301030004).

ACKNOWLEDGMENTS

We thank the reviewers and editor for insightful remarks. We would like to thank the European Centre for Medium-Range Weather Forecasts for providing the ERA5 reanalysis data. The authors acknowledged the Climate Prediction Center of the National Oceanic and Atmospheric Administration of the United States for providing AO index data.

SUPPLEMENTARY MATERIAL

The Supplementary Material for this article can be found online at: https://www.frontiersin.org/articles/10.3389/feart.2022.834284/full#supplementary-material

REFERENCES

Betts, A. K., Ball, J. H., Beljaars, A. C. M., Miller, M. J., and Viterbo, P. (1994). "Coupling between Land-Surface Boundary-Layer Parameterizations and Rainfall on Local and Regional Scales: Lessons from the Wet Summer of 1993," in Fifth Symp. *On Global Change Studies*, 174–181.

Chen, Y., Moufouma-Okia, W., Masson-Delmotte, V., Zhai, P., and Pirani, A. (2018). Recent Progress and Emerging Topics on Weather and Climate Extremes since the Fifth Assessment Report of the Intergovernmental Panel on Climate Change. *Annu. Rev. Environ. Resour.* 43 (1), 35–59. doi:10.1146/annurev-environ-102017-030052

Choi, W., and Kim, K.-Y. (2019). Summertime Variability of the Western North Pacific Subtropical High and its Synoptic Influences on the East Asian Weather. *Sci. Rep.* 9, 7865. doi:10.1038/s41598-019-44414-w

Chow, K. C., Chan, J. C. L., Shi, X., Liu, Y., and Ding, Y. (2008). Diurnal Variations of Circulation and Precipitation in the Vicinity of the Tibetan Plateau in Early Summer. *Clim. Dyn.* 32, 55–73. doi:10.1007/s00382-008-0374-x

Cohen, J., Zhang, X., Francis, J., Jung, T., Kwok, R., Overland, J., et al. (2020). Divergent Consensuses on Arctic Amplification Influence on Midlatitude Severe winter Weather. *Nat. Clim. Chang.* 10, 20–29. doi:10.1038/s41558-019-0662-y

Coumou, D., Di Capua, G., Vavrus, S., Wang, L., and Wang, S. (2018). The Influence of Arctic Amplification on Mid-latitude Summer Circulationfluence of Arctic Amplification on Mid-latitude Summer Circulation. *Nat. Commun.* 9, 2959. doi:10.1038/s41467-018-05256-8

Deng, K., Yang, S., Ting, M., Zhao, P., and Wang, Z. (2019). Dominant Modes of China Summer Heat Waves Driven by Global Sea Surface Temperature and Atmospheric Internal Variability. *J. Clim.* 32 (12), 3761–3775. doi:10.1175/jcli-d-18-0256.1

Ding, Y., Sun, Z., Wang, Z., Zhu, Y., and Song, Y. (2009). Inter-decadal Variation of the Summer Precipitation in China and its Association with Decreasing Asian Summer Monsoon Part Ii: Possible Causes. *Int. J. Climatol.* 29 (13), 1926–1944. doi:10.1002/joc.1759

Donat, M. G., Alexander, L. V., Yang, H., Durre, I., Vose, R., Dunn, R. J. H., et al. (2013). Updated Analyses of Temperature and Precipitation Extreme Indices since the Beginning of the Twentieth century: The HadEX2 Dataset. *J. Geophys. Res. Atmos.* 118, 2098–2118. doi:10.1002/jgrd.50150

Dosio, A., Mentaschi, L., Fischer, E. M., and Wyser, K. (2018). Extreme Heat Waves under 1.5 °C and 2 °C Global Warming. *Environ. Res. Lett.* 13 (5), 054006. doi:10.1088/1748-9326/aab827

Douville, H. (2002). Influence of Soil Moisture on the Asian and African Monsoons. Part II: Interannual Variability. *J. Clim.* 15 (7), 701–720. doi:10.1175/1520-0442(2002)015<0701:iosmot>2.0.co;2

Duchez, A., Frajka-Williams, E., Josey, S. A., Evans, D. G., Grist, J. P., Marsh, R., et al. (2016). Drivers of Exceptionally Cold North Atlantic Ocean Temperatures and Their Link to the 2015 European Heat Wave. *Environ. Res. Lett.* 11, 074004. doi:10.1088/1748-9326/11/7/074004

Duchon, C. E. (1979). Lanczos Filtering in One and Two Dimensions. *J. Appl. Meteorol.* 18 (8), 1016–1022. doi:10.1175/1520-0450(1979)018<1016:lfioat>2.0.co;2

Entin, J. K., Robock, A., Vinnikov, K. Y., Hollinger, S. E., Liu, S., and Namkhai, A. (2000). Temporal and Spatial Scales of Observed Soil Moisture Variations in the Extratropics. *J. Geophys. Res.* 105, 11865–11877. doi:10.1029/2000jd900051

Feng, S., and Hu, Q. (2008). How the north atlantic Multidecadal Oscillation May Have Influenced the Indian Summer Monsoon during the Past Two Millennia. *Geophys. Res. Lett.* 35 (1), 548–562. doi:10.1029/2007gl032484

Ford, T. W., Wang, Q., and Quiring, S. M. (2016). The Observation Record Length Necessary to Generate Robust Soil Moisture Percentiles. *J. Appl. Meteorol.* 55 (10), 2131–2149. doi:10.1175/jamc-d-16-0143.1

Francis, J. A., and Vavrus, S. J. (2012). Evidence Linking Arctic Amplification to Extreme Weather in Mid-latitudes. *Environ. Res. Lett.* 39 (6). doi:10.1029/2012gl051000

Geirinhas, J. L., Russo, A., Libonati, R., Sousa, P. M., Miralles, D., and Trigo, R. M. (2021). Recent Increasing Frequency of Compound Summer Drought and Heatwaves in Southeast Brazil. *Environ. Res. Lett.* 16 (3), 034036. doi:10.1088/1748-9326/abe0eb

Goswami, B. N., Madhusoodanan, M. S., Neema, C. P., and Sengupta, D. (2006). A Physical Mechanism for north atlantic Sst Influence on the Indian Summer Monsoon. *Geophys. Res. Lett.* 33 (2). doi:10.1029/2005gl024803

Haarsma, R. J., Selten, F. M., and Drijfhout, S. S. (2015). Decelerating Atlantic Meridional Overturning Circulation Main Cause of Future West European Summer Atmospheric Circulation Changes. *Environ. Res. Lett.* 10, 94007. doi:10.1088/1748-9326/10/9/094007

Halder, S., and Dirmeyer, P. A. (2016). Relation of Eurasian Snow Cover and Indian Summer Monsoon Rainfall: Importance of the Delayed Hydrological Effect. *J. Clim.* 30 (4), 1273–1289. doi:10.1175/JCLI-D-16-0033.1

Hao, Z., Hao, F., Singh, V. P., and Zhang, X. (2018). Quantifying the Relationship between Compound Dry and Hot Events and El Niño-Southern Oscillation (ENSO) at the Global Scale. *J. Hydrol.* 567 (September), 332–338. doi:10.1016/j.jhydrol.2018.10.022

Klein Tank, A. M. G., and Können, G. P. (2003). Trends in Indices of Daily Temperature and Precipitation Extremes in Europe, 1946-99. *J. Clim.* 16, 3665–3680. doi:10.1175/1520-0442(2003)016<3665:tiiodt>2.0.co;2

Leonard, M., Westra, S., Phatak, A., Lambert, M., van den Hurk, B., McInnes, K., et al. (2014). A Compound Event Framework for Understanding Extreme Impacts. *WIREs Clim. Change* 5, 113–128. doi:10.1002/wcc.252

Li, N., Xiao, Z. N., and Zhao, L. (2021). A Recent Increase in Long-Lived Heatwaves in China under the Joint Influence of South Asia and Western North Pacific Subtropical Highs. *J. Clim.* 34 (17), 7167–7179. doi:10.1175/jcli-d-21-0014.1

Lim, E.-P., Hendon, H. H., Boschat, G., Hudson, D., Thompson, D. W. J., Dowdy, A. J., et al. (2019). Australian Hot and Dry Extremes Induced by Weakenings of the Stratospheric Polar Vortex. *Nat. Geosci.* 12, 896–901. doi:10.1038/s41561-019-0456-x

Liu, D., Yu, Z., and Mishra, A. K. (2017a). Evaluation of Soil Moisture-precipitation Feedback at Different Time Scales over Asia. *Int. J. Climatol.* 37 (9), 3619–3629. doi:10.1002/joc.4943

Liu, L., Zhang, R., and Zuo, Z. (2017b). Effect of spring Precipitation on Summer Precipitation in Eastern China: Role of Soil Moisture. *J. Clim.* 30 (22), 9183–9194. doi:10.1175/jcli-d-17-0028.1

Liu, S., Wu, Q., Schroeder, S. R., Yao, Y., Zhang, Y., Wu, T., et al. (2020). Near-global Atmospheric Responses to Observed Springtime Tibetan Plateau Snow Anomalies. *J. Clim.* 33 (5), 1691–1706. doi:10.1175/jcli-d-19-0229.1

Lu, M., Kuang, Z., Yang, S., Li, Z., and Fan, H. (20202020). A Bridging Role of winter Snow over Northern China and Southern mongolia in Linking the East Asian winter and Summer Monsoons. *J. Clim.* 33.22, 1–50. doi:10.1175/jcli-d-20-0298.1

Matsumura, S., and Yamazaki, K. (2012). Eurasian Subarctic Summer Climate in Response to Anomalous Snow Cover. *J. Clim.* 25, 1305–1317. doi:10.1175/2011jcli4116.1

Meng, L., Long, D., Quiring, S. M., and Shen, Y. (2014). Statistical Analysis of the Relationship between spring Soil Moisture and Summer Precipitation in East China. *Int. J. Climatol.* 34 (5), 1511–1523. doi:10.1002/joc.3780

Miralles, D. G., Gentine, P., Seneviratne, S. I., and Teuling, A. J. (2019). Land-atmospheric Feedbacks during Droughts and Heatwaves: State of the Science and Current Challenges. *Ann. N. Y Acad. Sci.* 1436, 19–35. doi:10.1111/nyas.13912

North, G. R., Bell, T. L., Cahalan, R. F., and Moeng, F. J. (1982). Sampling Errors in the Estimation of Empirical Orthogonal Functions. *Mon. Wea. Rev.* 110, 699–706. doi:10.1175/1520-0493(1982)110<0699:seiteo>2.0.co;2

Perkins, S. E., and Alexander, L. V. (2013). On the Measurement of Heat Waves. *J. Clim.* 26, 4500–4517. doi:10.1175/jcli-d-12-00383.1

Prabhu, A., Oh, J., Kim, I., Kripalani, R. H., Mitra, A. K., and Pandithurai, G. (2017). Summer Monsoon Rainfall Variability over north east Regions of india and its Association with Eurasian Snow, atlantic Sea Surface Temperature and Arctic Oscillation. *Clim. Dyn.* 49 (7-8), 2545–2556. doi:10.1007/s00382-016-3445-4

Pyper, B. J., and Peterman, R. M. (1998). Comparison of Methods to Account for Autocorrelation in Correlation Analyses of Fish Data. *Can. J. Fish. Aquat. Sci.* 55 (9), 2127–2140. doi:10.1139/f98-104

IPCC (2021). "Summary for Policymakers," in *Climate Change 2021: The Physical Science Basis. Contribution of Working Group I to the Sixth Assessment Report of the Intergovernmental Panel on Climate Change [Masson-Delmotte, V.* Editors P. Zhai, A. Pirani, S. L. Connors, C. Péan, S. Berger, N. Caud, et al. (Cambridge University Press). In Press.

Qian, Q. F., Jia, X. J., and Wu, R. (2019). Changes in the Impact of the Autumn Tibetan Plateau Snow Cover on the Winter Temperature over North America in the Mid-1990s. *J. Geophys. Res.* 124, 19. doi:10.1029/2019jd030245

Rasmijn, L. M., van der Schrier, G., Bintanja, R., Barkmeijer, J., Sterl, A., and Hazeleger, W. (2018). Future Equivalent of 2010 Russian Heatwave Intensified by Weakening Soil Moisture Constraints. *Nat. Clim Change* 8, 381–385. doi:10.1038/s41558-018-0114-0

Ribeiro, A. F. S., Russo, A., Gouveia, C. M., Páscoa, P., and Zscheischler, J. (2020). Risk of Crop Failure Due to Compound Dry and Hot Extremes Estimated with Nested Copulas. *Biogeosciences* 17, 4815–4830. doi:10.5194/bg-17-4815-2020

Saito, K., Yasunari, T., and Cohen, J. (2004). Changes in the Sub-decadal Covariability between Northern Hemisphere Snow Cover and the General Circulation of the Atmosphere. *Int. J. Climatol.* 24 (1), 33–44. doi:10.1002/joc.984

Screen, J. A., and Simmonds, I. (2013). Exploring Links between Arctic Amplification and Mid-latitude Weather. *Geophys. Res. Lett.* 40 (5), 959–964. doi:10.1002/grl.50174

Seneviratne, S. I., Corti, T., Davin, E. L., Hirschi, M., Jaeger, E. B., Lehner, I., et al. (2010). Investigating Soil Moisture-Climate Interactions in a Changing Climate: a Review. *Earth Sci. Rev.* 99 (3–4), 125–161. doi:10.1016/j.earscirev.2010.02.004

Shen, C., Wang, Wei-Chyung., and Zeng, G. (2011). Decadal Variability in Snow Cover over the Tibetan Plateau during the Last Two Centuries. *Geophys. Res. Lett.* 38 (10). doi:10.1029/2011gl047288

Shi, N., Lu, J. J., and Zhu, Q. G. (1996). East Asian winter/summer Monsoon Intensity Indices with Their Climatic Change in 1873–1989 (In Chinese). *J. Nanjing Inst. Meteorol.* 19, 168–177.

Sillmann, J., Kharin, V. V., Zhang, X., Zwiers, F. W., and Bronaugh, D. (2013). Climate Extremes Indices in the CMIP5 Multimodel Ensemble: Part 1. Model Evaluation in the Present Climate. *J. Geophys. Res. Atmos.* 118, 1716–1733. doi:10.1002/jgrd.50203

Sippel, S., Reichstein, M., Ma, X., Mahecha, M. D., Lange, H., Flach, M., et al. (2018). Drought, Heat, and the Carbon Cycle: a Review. *Curr. Clim. Change Rep.* 4, 266–286. doi:10.1007/s40641-018-0103-4

Sun, J., Yang, K., Guo, W., Wang, Y., He, J., and Lu, H. (2020). Why Has the Inner Tibetan Plateau Become Wetter since the Mid-1990s? *J. Clim.* 33 (19), 8507–8522. doi:10.1175/jcli-d-19-0471.1

Takaya, K., and Nakamura, H. (1997). A Formulation of a Wave-Activity Flux for Stationary Rossby Waves on a Zonally Varying Basic Flow. *Geophys. Res. Lett.* 24 (23), 2985–2988. doi:10.1029/97gl03094

Tian, F., Klingaman, N. P., and Dong, B. (2021). The Driving Processes of Concurrent Hot and Dry Extreme Events in China. *J. Clim.* 34 (5), 1809–1824. doi:10.1175/jcli-d-19-0760.1

Ting, D., Hui, G., and Weijing, L. (2018). Extreme High-temperature Event in Southern China in 2016 and the Possible Role of Cross-equatorial Flows. *Int. J. Climatol.* 38, 3579–3594. doi:10.1002/joc.5518

Vinnikov, K. Y., and Yeserkepova, I. B. (1991). Soil Moisture: Empirical Data and Model Results. *J. Clim.* 4 (1), 66–79. doi:10.1175/1520-0442(1991)004<0066:smedam>2.0.co;2

Wang, M., Jia, X. J., Ge, J. W., and Qian, Q. F. (2019). Changes in the Relationship between the Interannual Variation of Eurasian Snow Cover and spring SAT over Eastern Eurasia. *J. Geophys. Res. Atmos.* 124 (2), 468–487. doi:10.1029/2018jd029077

Wu, R., and Kirtman, B. P. (2007). Observed Relationship of Spring and Summer East Asian Rainfall with Winter and Spring Eurasian Snow. *J. Clim.* 20 (7), 1285–1304. doi:10.1175/jcli4068.1

Wu, X., Hao, Z., Hao, F., and Zhang, X. (2019). Variations of Compound Precipitation and Temperature Extremes in China during 1961-2014. *Sci. Total Environ.* 663, 731–737. doi:10.1016/j.scitotenv.2019.01.366

Wu, Z., Zhang, P., Chen, H., and Li, Y. (2016). Can the Tibetan Plateau Snow Cover Influence the Interannual Variations of Eurasian Heat Wave Frequency? *Clim. Dyn.* 46, 3405–3417. doi:10.1007/s00382-015-2775-y

Yim, S.-Y., Jhun, J.-G., Lu, R., and Wang, B. (2010). Two Distinct Patterns of spring Eurasian Snow Cover Anomaly and Their Impacts on the East Asian Summer Monsoon. *J. Geophys. Res.* 115 (D22), D22113. doi:10.1029/2010jd013996

You, Q., Kang, S., Aguilar, E., Pepin, N., Flügel, W.-A., Yan, Y., et al. (2011). Changes in Daily Climate Extremes in China and Their Connection to the Large Scale Atmospheric Circulation during 1961-2003. *Clim. Dyn.* 36, 2399–2417. doi:10.1007/s00382-009-0735-0

Zhang, Q., Tao, S., and Chen, L. (2003). The Interannual Variability of East Asian Summer Monsoon Indices and its Association with the Pattern of General Circulation over East Asia (In Chinese). *Acta Meteorologica Sinica* 56, 199–211.

Zhang, R., and Zuo, Z. (2011). Impact of spring Soil Moisture on Surface Energy Balance and Summer Monsoon Circulation over East Asia and Precipitation in East China. *J. Clim.* 24 (13), 3309–3322. doi:10.1175/2011jcli4084.1

Zhang, T., Wang, T., Feng, Y., Li, X., and Krinner, G. (2021). An Emerging Impact of Eurasian spring Snow Cover on Summer Rainfall in Eastern China. *Environ. Res. Lett.* 16 (5), 054012. doi:10.1088/1748-9326/abf688

Zhang, W., Zhou, T., and Zhang, L. (2017). Wetting and Greening Tibetan Plateau in Early Summer in Recent Decades. *J. Geophys. Res. Atmos.* 122, 5808–5822. doi:10.1002/2017jd026468

Zhao, L., Zhu, Y., Liu, H., Liu, Z., Liu, Y., Li, X., et al. (2016). A Stable Snow-Atmosphere Coupled Mode. *Clim. Dyn.* 47 (7-8), 2085–2104. doi:10.1007/s00382-015-2952-z

Zhu, Y., and Ding, Y. (2009). Simulation of the Influence of winter Snow Depth over the Tibetan Plateau on Summer Rainfall in China. *Chin. J. Atmos. Sci.* doi:10.1016/S1003-6326(09)60084-4

Conflict of Interest: The authors declare that the research was conducted in the absence of any commercial or financial relationships that could be construed as a potential conflict of interest.

Publisher's Note: All claims expressed in this article are solely those of the authors and do not necessarily represent those of their affiliated organizations, or those of the publisher, the editors and the reviewers. Any product that may be evaluated in this article, or claim that may be made by its manufacturer, is not guaranteed or endorsed by the publisher.

frontiers | Frontiers in Earth Science

ORIGINAL RESEARCH
published: 14 April 2022
doi: 10.3389/feart.2022.732635

OPEN ACCESS

Edited by:
Sergio Antonio Sejas,
Science Systems and Applications, Inc., United States

Reviewed by:
Catriona Fyffe,
Northumbria University, United Kingdom
Pablo Wainstein,
BGC Engineering, Canada

***Correspondence:**
Luis Felipe Gualco
luis.gualco@epn.edu.ec

†ORCID:
Luis Felipe Gualco
orcid.org/0000-0002-2150-107X
Luis Maisincho
orcid.org/0000-0002-6078-1895
Marcos Villacís
orcid.org/0000-0002-4496-7323
Lenin Campozano
orcid.org/0000-0002-3580-2439
Vincent Favier
orcid.org/0000-0001-6024-9498
Jean-Carlos Ruiz-Hernández
orcid.org/0000-0002-7801-5566
Thomas Condom
orcid.org/0000-0002-4408-8580

Specialty section:
This article was submitted to Cryospheric Sciences, a section of the journal Frontiers in Earth Science

Received: 29 June 2021
Accepted: 23 March 2022
Published: 14 April 2022

Citation:
Gualco LF, Maisincho L, Villacís M, Campozano L, Favier V, Ruiz-Hernández J-C and Condom T (2022) Assessing the Contribution of Glacier Melt to Discharge in the Tropics: The Case of Study of the Antisana Glacier 12 in Ecuador. Front. Earth Sci. 10:732635. doi: 10.3389/feart.2022.732635

Assessing the Contribution of Glacier Melt to Discharge in the Tropics: The Case of Study of the Antisana Glacier 12 in Ecuador

Luis Felipe Gualco[1†], Luis Maisincho[1,2†], Marcos Villacís[1†], Lenin Campozano[1†], Vincent Favier[3†], Jean-Carlos Ruiz-Hernández[1,3,4†] and Thomas Condom[3†]*

[1]Escuela Politécnica Nacional, Departamento de Ingeniería Civil y Ambiental & Centro de Investigación y Estudios en Ingeniería de los Recursos Hídricos, Quito, Ecuador, [2]Instituto Nacional de Meteorología e Hidrología (INAMHI), Quito, Ecuador, [3]University of Grenoble Alpes, IRD, CNRS, Grenoble INP, IGE, Grenoble, France, [4]Sorbonne Université, UMR 7619 METIS, Paris, France

Tropical glaciers are excellent indicators of climate variability due to their fast response to temperature and precipitation variations. At same time, they supply freshwater to downstream populations. In this study, a hydro-glaciological model was adapted to analyze the influence of meteorological forcing on melting and discharge variations at Glacier 12 of Antisana volcano (4,735–5,720 m above sea level (a.s.l.), 1.68 km^2, 0°29′S; 78°9′W). Energy fluxes and melting were calculated using a distributed surface energy balance model using 20 altitude bands from glacier snout to the summit at 30-min resolution for 684 days between 2011 and 2013. The discharge was computed using linear reservoirs for snow, firn, ice, and moraine zones. Meteorological variables were recorded at 4,750 m.a.s.l. in the ablation area and distributed through the altitudinal range using geometrical corrections, and measured lapse rate. The annual specific mass balance (–0.61 m of water equivalent -m w.e. y^{-1}-) and the ablation gradient (22.76 kg m^{-2} m^{-1}) agree with the values estimated from direct measurements. Sequential validations allowed the simulated discharge to reproduce hourly and daily discharge variability at the outlet of the catchment. The latter confirmed discharge simulated (0.187 m^3 s^{-1}) overestimates the streamflow measured. Hence it did not reflect the net meltwater production due to possible losses through the complex geology of the site. The lack of seasonality in cloud cover and incident short-wave radiation force the reflected short-wave radiation via albedo to drive melting energy from January to June and October to December. Whereas the wind speed was the most influencing variable during the July-September season. Results provide new insights on the behaviour of glaciers in the inner tropics since cloudiness and precipitation occur throughout the year yielding a constant short-wave attenuation and continuous variation of snow layer thickness.

Keywords: tropical glacier, melting, albedo, precipitation, energy balance, shortwave radiation, Antisana

1 INTRODUCTION

Tropical glaciers refer to ice bodies found at high elevations in a region where the diurnal temperature variations are more significant than the seasonal ones (Kaser and Osmaston, 2002). These glaciers are characterized by the occurrence of melting all year round because the 0°C isotherm remains continuously near the glacier fronts. Thus minimal energy inputs generate runoff (Francou et al., 2013). This aspect makes tropical glaciers suitable climatical indicators due to their quick mass balance response to temperature and precipitation variations (Ramírez et al., 2001; Francou et al., 2004). The Andes host 99% of tropical glaciers (Kaser and Osmaston, 2002), and they play an important role in the freshwater supply for cities located in the lowlands, especially during seasons with low or scarce precipitation (Chevallier et al., 2011; Buytaert et al., 2017).

Most precipitation in the eastern slopes of the Andes occurs due to dominant easterly winds which transport moisture from the Amazon basin and are forced to rise when encountering this barrier (Espinoza et al., 2020). Also, there is a contribution from the eastern Pacific, which triggers convection and precipitation over western slopes (Segura et al., 2019). These conditions ensure significant precipitation year-round in the Equatorial Andes. However, the rain-snow partitioning relies on temperature variability, conditioning the layer of snow on glaciers (Francou et al., 2004; Sagredo et al., 2014; Campozano et al., 2021), which in turn controls the surface albedo of the glacier (Favier et al., 2004b; Vincent et al., 2005).

Vuille et al. (2000, 2008) estimated that the Andes of Ecuador experienced a warming of 0.1°C per decade since 1950, whereas the projected warming during the 21st century is estimated between 4 and 5°C. To examine the glacier response to current weather and projected scenarios, a monitoring program was initiated in Ecuador by French Development Research Institute (IRD), Instituto Nacional de Meteorología e Hidrología (INAMHI) and Empresa Pública Metropolitana de Agua Potable y Saneamiento de Quito (EPMAPS) in June 1994. This network currently includes rain gauges, water-height gauges in rivers and automatic weather stations (AWS) installed at the ground level between 3,500 and 5,000 m a.s.l. but over different surface states, including paramo, moraine, and glacier surfaces (Villacís, 2008; Maisincho, 2015) around the Antisana Glacier 15 (AG15) (Francou et al., 2000; 2004). Initial results have shown the occurrence of an accelerated glacier retreat since the late 1970s (Cáceres et al., 2006; Rabatel et al., 2013). In addition, various Surface Energy Balance (SEB) modelings have been performed both at one point (Favier et al., 2004a) and at the scale of the entire glacier (Maisincho, 2015). Finally, another SEB modeling has been done over the snow-covered paramo using a coupled ground-snow model (e.g., ISBA/CROCUS, Wagnon et al., 2009).

These studies demonstrated that net short-wave radiation and albedo variations control melting rates in the ablation zone during most of the year. A melting minimum (compared to the mean observed melt during the rest of the year) was shown during the June-September season related to large energy losses associated with high sublimation rates. Likewise, the hydrological balance calculations showed that total glacier melting from AG15 are not directly drained into rivers at lower elevations, because significant amounts of water (>50%) are sunk before the glacier front, contributing to subsurface flows (Favier et al., 2008). The water drained from the watershed is even larger than previously calculated by Favier et al. (2008) because in their study he did not consider that the highest elevations of the glacier receive 60% more snow than the lowest slopes of the western flanks of the volcano (Basantes-Serrano et al., 2016). This increase was initially ignored in surface mass balance calculation on the AG15 (Francou et al., 2000; Francou et al., 2004) suggesting that the glacier-wide climatic balance values published before Basantes-Serrano et al. (2016) presented a significant negative bias.

To better assess the contribution of glaciers to lowland streamflow, the Antisana Glacier 12 (AG12) was monitored since 2004. Over this catchment, discharge modeling has only been done with conceptual and semi-empirical approaches (e.g., Villacís, 2008). The variations of melting with elevation and hence the origin of waters have never been clearly analyzed. This latter scientific concern is analyzed in this paper using a glacier-wide distributed SEB modeling and calculation of the transfer function of flows from each zone of the glacier towards the outlet of the catchment, which may result in more accurate results than statistical approaches (Veettil et al., 2017).

The distributed SEB has been successfully applied in many areas, but it requires a large amount of data to provide accurate results (Gerbaux et al., 2005; Hock and Holmgren, 2005; Anslow et al., 2008; Dadic et al., 2008; Naz et al., 2014; Ren et al., 2018). This glacier-wide modeling has been applied on the Zongo glacier in Bolivia (Sicart et al., 2011) and the Shallap glacier in Peru (Gurgiser et al., 2013a), demonstrating the crucial role of clouds in the longwave radiation budget and the role of solid precipitation in the net short-wave budget. However, these glaciers are not directly comparable to the Antisana Glaciers, which are located in an area with different climate settings (Favier et al., 2004b). The distributed SEB of AG15 has been investigated by Maisincho (2015) proving that the short-wave radiation and albedo exert first-order control on the energy available for melting on this glacier.

Here, we apply and validate this approach to demonstrate the processes that control the mass balance gradient and the corresponding discharge generated by melting at different altitudes. The amounts of melting in each altitude level were used as input for linear reservoirs and finally added to compute the simulated discharge (hereafter referred to as the potential discharge) that should be drained to the river downstream of the glacier if there were no underground losses.

The water discharge was computed over 23 months in 2011–2013. This spatialized computation allowed 1) investigating the variations of energy fluxes controlling the ablation and discharge production and 2) quantifying the water from different sources in the catchment. This paper is organized as follows: In **Section 2** we describe the study site and the available data. The distributed SEB and the reservoir models are described in **Section 3**. In **Section 4**, we validate the coupled model and present results. In **Section 5**, we discuss the

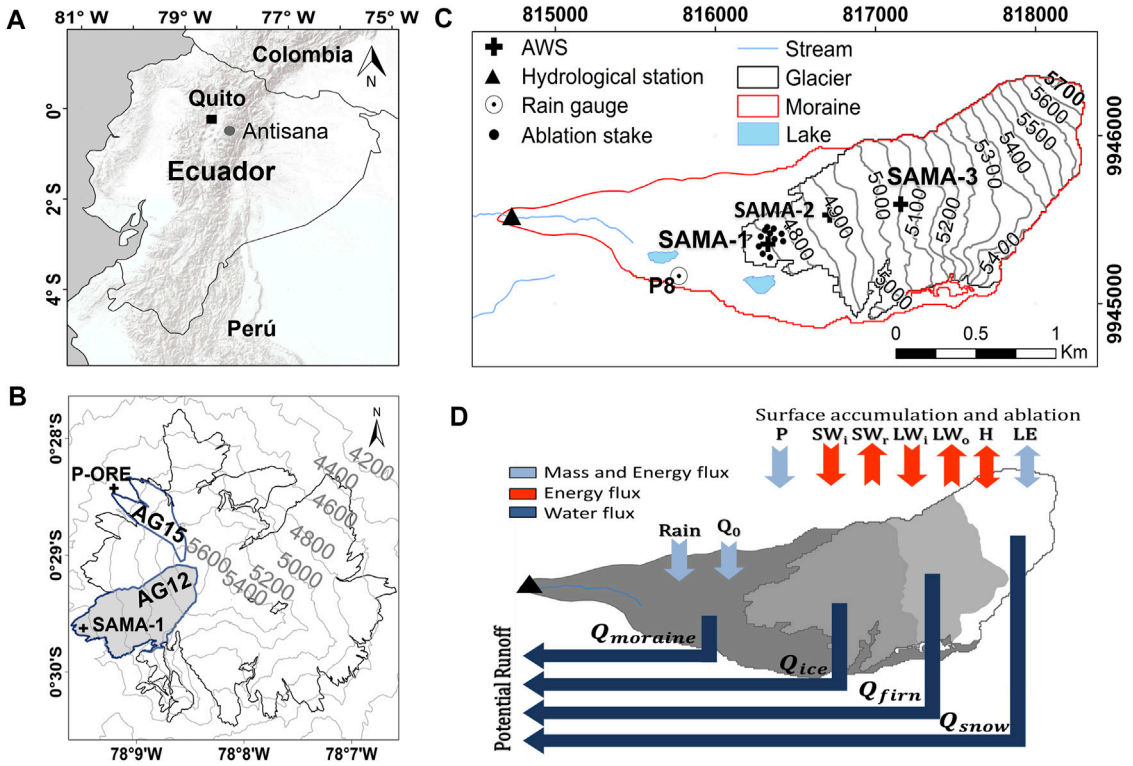

FIGURE 1 | Study area: **(A)** Location of the Antisana volcano south-eastward of Quito, the capital of Ecuador. **(B)** Delineation of the studied glaciers in Antisana icecap: The Glacier 15 (AG15) on the northwest flank and the Glacier 12 (AG12) on the southwest shaded in gray. The location of the P-ORE and AWS SAMA-1 stations are also shown (black crosses). Cap outline and DEM taken from Basantes-Serrano (2015). **(C)** Distribution of monitoring network around Glacier 12 catchment. **(D)** Schema of processes simulated by the coupled glacier-hydrology model illustrating the fluxes of mass and energy between the atmosphere and land surface implemented over snow, glacier ice, and moraine. Arrows indicate P, precipitation; SWi, incident short-wave radiation; SWr, reflected short-wave radiation; LWi, downwelling longwave radiation; LWo, outgoing longwave radiation; H, sensible heat; and LE, latent heat. For moraine zone is also shown the Rain and basal ground flow Q_0.

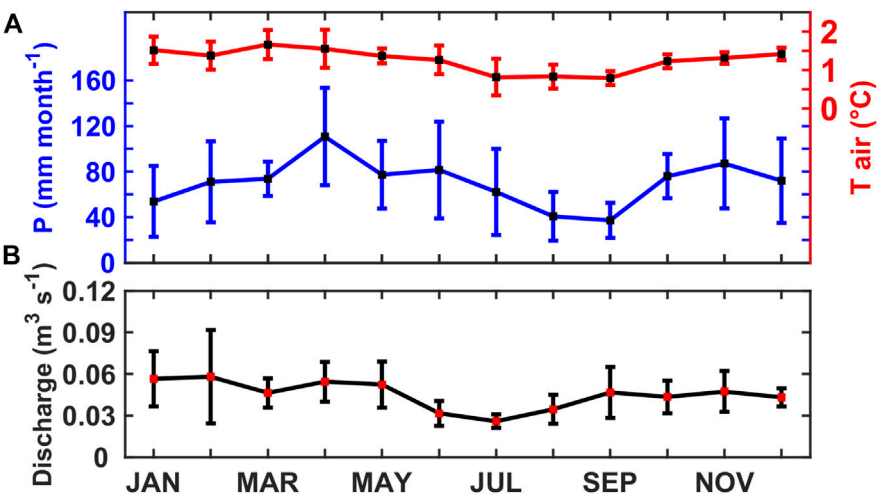

FIGURE 2 | (A) Monthly precipitation values (blue line) measured at P8 rain gauge between 2005 and 2015, vertical bars represent monthly standard deviation. The same for air temperature (red line) measured at SAMA-1 between 2011 and 2015. **(B)** Mean monthly discharge measured (black line) in Los Crespos hydrological station measurements between 2004 and 2014. Only months with data for more than 80% of the time steps were considered for cycles.

model uncertainties and the role of groundwater flow in AG12. Finally, our conclusions are presented in **Section 6**.

2 STUDY SITE AND DATA

2.1 Study Site and Climate Settings

This study was conducted on the Glacier 12 (AG12) located in the "Los Crespos" catchment (2.9 km^2, 57% glacial cover) on the southwest flank of the Antisana volcano (Basantes-Serrano, 2015) in the Eastern Cordillera of Ecuador. AG12 spans from the summit at 5,720 m a.s.l. to glacier snout at 4,735 m a.s.l. covering a surface of 1.65 km^2, with a length of 2.3 km (**Figure 1**). The monthly temperature over the glacier snout remains homogeneous throughout the year at around 1.2°C on average (**Figure 2**). A slight temperature maximum is however observed between February-May (1.7°C) related to the period of higher humidity and cloudiness (Favier, 2004c); while the minimum between June-September (0.8°C) is related to the decrease in cloudiness and increase in wind speed. The 0°C isotherm shifts between 4,800 and −5,100 m a.s.l. (Basantes-Serrano et al., 2016) in accordance with the equilibrium line altitude (ELA) of the glacier around 5,030 m a.s.l. (Jomelli et al., 2009). Daily temperature variations exceed the seasonal ones, and this phenomenon is amplified by the radiative cooling and katabatic winds intensification during the night and early morning; which cause the temperature to drop below 0°C even at the glacier front (Favier et al., 2004b; Sklenár et al., 2015).

Most precipitation at the site occurs due to adiabatic cooling of moist air coming from the Amazon basin. These air masses are pushed by the easterlies and condense as they rise on the slopes of the massif (Espinoza et al., 2020). Thus, a precipitation peak between April and July is associated, whereas a decrease between December and February is expected (Laraque et al., 2007). Likewise, due to its location on the border of the inter-Andean plateau, the area also receives a contribution from the inter-Andean valley regime (with two wet seasons in February-May and October-November) (Ilbay-Yupa et al., 2021; Ruiz-Hernández et al., 2021). During July-September, the minimum precipitation is associated with the strengthened easterlies inhibiting the vertical cloud development (Campozano et al., 2016; Espinoza et al., 2009). As result, the precipitation follows a complex regime with a substantial amount during all months (**Figure 2**) reaching 837 ± 122 mm per year at glacier snout, depending on the El Niño-Southern Oscillation phase (Francou et al., 2004). These conditions justify the large extension of Glacier 12 compared to the others located in the western sector (Basantes-Serrano, 2015).

2.2 Data

2.2.1 Meteorological Data

The data used in this study were collected by an automatic weather station (AWS) SAMA-1 located at 4,753 m a.s.l., near the glacier snout. Records extend for 23 months between 07/02/2011 and 05/16/2013, referred to as the Study Period (SP) hereafter. The station was equipped with sensors calibrated prior to their installation. The station records the 30-min average of air temperature (T), relative humidity (RH), wind speed (Ws), incoming (SWi) and reflected (SWr) short-wave radiation, and incoming (LWi) and outgoing (LWo) longwave radiation measured every 15 s, except for the wind direction which is measured once every 30 min. **Supplementary Table SA1** summarises the technical specifications of all sensors used. Furthermore, the cloud factor (CF-dimensionless-) was included to relate the cloud cover attenuation to the net radiation (Favier et al., 2004b; Azam et al., 2016) by comparing incoming short-wave radiation (SWi) to the theoretical solar radiation at the top of atmosphere (STOA) according to **Eq. 1**.

$$CF = 1.3 - 1.4\left(\frac{SWi}{S_{TOA}}\right) \quad (1)$$

The precipitation was measured by a non-heated rain gauge located on the glacier moraine (at 4,720 m a.s.l.) referred to as P8 in **Figure 1C**. The tropical conditions enhance the melting of snow during the day and a delay of minutes is expected. Whereas snowfall occurring in the late afternoon or night requires to meet melting conditions (temperatures above 0°C or sufficient solar radiation) before being transformed into water droplets reaching the gauge orifice. Therefore, a delay of several hours is expected. This shortcoming could disturb the daily cycle of energy fluxes whereas their seasonality remains unchanged. A scheme based on temperature ranges was used to estimate the phase of precipitation (see **Section 3.1.2**).

Between 29/09/2011 and 30/08/2011 (32 days) and between 31/10/2011 and 29/11/2011 (29 days), a precipitation data gap was filled using measurements from another rain gauge (P-ORE, 4,850 m a.s.l.) located in the AG15 moraine (**Figure 1B**). Correlation between P8 and P-ORE were significant over the study period ($r^2_{P_8-P_{ORE}}$ = 0.63), but not very high because the P-ORE rain gauge was more sheltered from easterly winds by the volcano itself. Nevertheless, P-ORE was located near the ablation zone, making data more relevant for the study of the ablation of the AG12 than other rain gauges around the Antisana volcano.

Air temperature variation with elevation was studied using observation data from stations located above SAMA-1. These stations corresponded to SAMA-2 (4,925 m a.s.l.); SAMA-3 (5,065 m a.s.l.) placed over the glacier (**Figure 1C**). These auxiliary stations exhibit few data gaps due to harsh climatic conditions and power shutdown issues. **Supplementary Appendix 2** summarizes the period with available information and gaps.

TABLE 1 | Mass balance periods retrieved for ablation stakes used for SEB model validation at local point scale.

Period	Duration (days)	Starting/deadline date
MP1	92	30-08-2011/29-11-2011
MP2	28	03-02-2012/01-03-2012
MP3	106	17-01-2013/02-05-2013

2.2.2 Glaciological Data

Point surface mass balance (SMB) measurements have been performed monthly in the ablation zone of the glacier using stakes, which were distributed between 4,735 and 4,797 m a.s.l. Over the study period, a specific focus was made on data from three periods of short duration, hereafter referred to as MP1, MP2, and MP3 (**Table 1**). These periods were selected due to the available continuous mass balance series. Moreover, we use the 2012 mass balance profile computed by Basantes-Serrano (2015) for elevation ranges of 50 m between 4,750 and 5,700 m a.s.l. These values were obtained from direct mass balance measurements on stakes and in snow pits, and from the geodetic approach based on aerial photogrammetry restitutions (for details, refer to Basantes-Serrano et al., 2016). Data were used here to validate the distributed SEB model. The 10-m resolution digital elevation model (DEM) produced by Basantes-Serrano (2015) was also used to compute slope and aspect maps.

2.2.3 Hydrological Data

The "Los Crespos" hydrological station was installed below the frontal moraine at 4,520 m a.s.l. to collect the streamflow from the glacier melting and the surface streams originating from the surrounding paramo and moraine surfaces (Villacís, 2008). Water depth at the gauging station was measured every 30 min with a pressure gauge (**Supplementary Table SA1**) and transformed into streamflow using a stage-discharge curve previously obtained from direct manual discharge measurements performed regularly and using a power-law fit. The employed curve showed a difference of 5% concerning the theoretical hydraulic curve of the trapezoidal section according to Villacís (2008). During the study period, data were characterized by 27% of data gaps related to power shutdowns. Hydrological data were used to calibrate the linear reservoir model and then to validate the variations of simulated discharge at hourly and daily time scales (see **Section 4.2.4**).

2.2.4 Climatological Data

To put in context the meteorological conditions of SP concerning the regional long-term average conditions, we used historical monthly time series of temperature and precipitation. Here we used the 1979–2018 monthly air temperature from ERA-5 single levels reanalysis (https://www.ecmwf.int/en/forecasts/datasets/reanalysis-datasets/era5) from the European Centre for Medium-Range Weather Forecasts (ECMWF), available at a 0.25° resolution (Hersbach et al., 2020). Data were retrieved over the Antisana Massif (0.2–0.8°S, 77.8–78.5°W) at the 600 hPa level. The mean annual cycle was computed over the 1979–2018 reference period. Similarly, the mean annual cycle of precipitation in AG12 was computed from monthly precipitation provided by CHIRPS (Climate Hazards Group Infrared Precipitation with Stations https://data.chc.ucsb.edu/products/CHIRPS-2.0/) product at a 0.05° resolution (Funk et al., 2015). Data from the 1981–2019 period were considered for the closest cell to the Antisana site (78.15°W, 0.45°S).

3 DESCRIPTION OF SEB MODEL

3.1 Modelling Framework

The surface energy balance (SEB) model (Favier et al., 2011) has been widely applied on mountain glaciers (Verfaillie et al., 2015; Azam et al., 2016; Favier et al., 2016) to calculate the energy available at the surface ($E_{surface}$) and the resulting melting of snow and ice according to **Eq. 2**.

$$SWi - SWr + LWi - \left[(1-\epsilon)LWi + \epsilon\sigma T_s^4\right] + LE + H = E_{surface} \quad (2)$$

The fluxes were measured in W m^{-2}, being positive towards the surface and negative outwards from the surface. SWi is the incoming short-wave radiation and SWr is the reflected short-wave radiation. LWi is the incoming longwave radiation and the term in brackets is the outgoing longwave radiation LWo measured in the field. T_s is the modeled surface temperature, ϵ = 0.99 is the surface emissivity, and $\sigma = 5.6710^{-8}$ W m^{-2} K^{-4} is the Stefan-Boltzmann constant. H and LE are the sensible and latent heat fluxes, respectively, which were computed using the bulk method including stability corrections based on the bulk Richardson number (Favier et al., 2011). The heat supplied by precipitation on glaciers is insignificant compared to the other fluxes and is therefore neglected (Johnson and Rupper, 2020). Part of short-wave radiation (S = SWi-SWr) is not available for warming/cooling or melting processes at the surface, because the short-wave flux partly penetrates the ice (Bintanja et al., 1997). Hence, $E_{surface}$ was separated into two terms following **Eq. 3**.

$$E_{surface} = G_0 + (1-a)S \quad (3)$$

Where G_0 (W m^{-2}) is the energy excess or deficit at the surface, a is the fractional amount of short-wave radiation that penetrates the surface layer. When the surface temperature is 0°C, positive G_0 values represent the energy available for melt (mm w.e.). Otherwise, this amount is used to cool/warm the frozen surface and the underlying snow/ice before melting by thermal diffusion. Since Antisana is a temperate glacier, the model does not consider the compaction of the snowpack or the refreezing of liquid water. **Supplementary Material** presents a detailed description of the method used to compute the SEB components.

3.1.1 Precipitation Correction

Due to turbulence associated with high winds during snowfalls, rain gauges do not usually fully collect hydrometeors. Precipitation is therefore underestimated in the field. To correct the rain gauge collection deficit, we apply a 23% increase to P8 values according to Pollock et al. (2018) for cylinder-like rain gauge for wind-exposed sites. This value is within the range of previous corrections, which may reach 50%, as observed for the AG15 rain gauge located on the moraine (Wagnon et al., 2009). At lower elevations, in the paramo zone, 15% had been proposed for correcting rainfall (Padrón et al., 2015).

Furthermore, in a previous study, Basantes-Serrano et al. (2016) demonstrated that mass balance at the upper zone requires 60% more than the precipitation measured at the

AG15 front (after precipitation data correction). This is due to the occurrence of more precipitation at the summit of Antisana than on the leeward slopes (Junquas et al., 2022). Indeed, the general easterly flow generates an important foehn effect associated with a significant drying of humid air masses of Amazonian origin when they descend at the lee of the summit. To account for this effect, a progressive 10% increase of precipitation was applied every 100 m of elevation. We discuss the influence of precipitation correction on the mass balance profile in **Section 5**.

3.1.2 Precipitation Phase Model

In the absence of direct observation of the precipitation phase, a temperature threshold is often applied to distinguish between the occurrence of snowy and rainy precipitation. Several studies carried out in the Antisana region have shown that a threshold value of 1°C allows for the proper separation of snowy events from liquid precipitation (Favier, 2004c; Maisincho, 2015). However, this phase change does not generally occur at a single threshold value, and rather appears gradually. Thus, the percentage of snowfall occurrence (PSO) was set to decrease from 100 to 0% between −1 and 3°C according to L'Hôte et al. (2005) scheme. This means that, between −1 and 3°C, only a fraction of the precipitation corresponds to snowfall and the remaining fraction to rain. This approach gives much more satisfactory results at the study site; especially in the ablation zone, which is a zone more sensitive to changes in the phase of precipitation (Favier et al., 2004a).

3.1.3 Albedo Modelling

We modeled albedo variations as a function of snow aging over time. It takes into account the age of the snow since the last snowfall and the impact of ice when the snow cover disappears (see **Eqs 4–6**) (Sicart et al., 2011; U.S. Army Corps Of Engineers, 1956).

$$\alpha_{snow} = \alpha_{wet\ snow} + \left(\alpha_{fresh\ snow} - \alpha_{wet\ snow}\right)e^{-\frac{n_j}{n^*}} \quad (4)$$

$$\alpha_{ice} = \alpha_{dirty\ ice} + \left(\alpha_{clean\ ice} - \alpha_{dirty\ ice}\right)e^{-\left(\frac{nj_{ice}}{n^*_{ice}}\right)^{\frac{1}{2}}} \quad (5)$$

$$\alpha = \alpha_{snow} + (\alpha_{ice} - \alpha_{snow})\left(1 + \frac{e_s}{e_s^*}\right)^{-3} \quad (6)$$

The measured albedo α results from the contribution of ice (α_{ice}), snow (α_{snow}), and snow cover thickness (e_s). The ice impacts the albedo when the snow depth is lower than a characteristic snow cover thickness (e_s^*) from which the underlying ice is visible and contributes to the surface albedo (Sicart, 2002). Snow albedo evolves as a function of time and decreases rapidly after snowfall ($\alpha_{snow\ fresh}$) to a value corresponding to wet snow ($\alpha_{wet\ snow}$). This decrease follows an exponential function of the number of days since the last snowfall (n_j) and depends on a characteristic time scale (n*). To complete this model Masiokas et al., 2020 added an expression allowing the albedo of the ice (α_{ice}) to vary according to the increase of the dust proportion on the ice surface. The ice changes from clean ice ($\alpha_{clean\ ice}$) to dirty ice ($\alpha_{dirty\ ice}$) as a function of the number of days since the disappearance of the snow cover (nj_{ice}) and of a characteristic time scale of the aging of the ice (n^*_{ice}) (**Eq. 5**). When the surface is covered with fresh snow for more than 6 days, nj_{ice} is forced to 0 and the albedo of the ice α_{ice} becomes equal to $\alpha_{clean\ ice}$ again.

As a starting point, we used parameters from previous work on the AG15 glacier and performed a sensitivity test to calibrate these parameters as best as possible. We first examined the variation of the determination coefficient (r^2) between simulated and measured albedo in 2012 (the entire year achieved for SP) by varying the parameters of the albedo model. Albedo parameters were classified into two groups. Group 1 corresponds to the albedo parameters of dirty ice $\alpha_{dirty\ ice}$, clean ice $\alpha_{clean\ ice}$, fresh snow $\alpha_{fresh\ snow}$ and wet snow $\alpha_{wet\ snow}$ whose initial values were taken from Gurgiser et al., 2013a. The second group of parameters corresponds to the characteristic aging scales of ice (n^*_{ice}) and snow (n*) as well as the characteristic snow depth scale (e_s^*) whose initial values were taken from Maisincho (2015). The ranges of variation of values of these parameters were obtained from Cuffey and Paterson, (2010) and were expressed as relative values with respect to the initial values given in **Table 2**.

3.1.4 Temperature Lapse Rate

To represent the decrease in air temperature as a function of altitude, we determined a temperature lapse rate (TLR) of = −5.5°C $(km)^{-1}$ for the site. This value was obtained by linear regression between the mean values measured at each SAMA stations' location (see **Supplementary Table SA2**). Therefore we ensure to capture the mean spatial variability over the glacier and avoid deviations that could cause the inclusion of values from moraine terrain which experiment large daily variations. The computed gradient matches with the value commonly employed to extrapolate air temperature in the outer tropics (Sicart et al., 2011; Gurgiser et al., 2013a) and was similar to the −5.4°C $(km)^{-1}$ found by Ceballos et al. (2012) for colombian glaciers in the inner tropics.

3.1.5 Roughness Parameters

The aerodynamic (z_{0m}) and scalar (z_{0T}, z_{0q}) roughness lengths play an essential role in the evaluation of turbulent heat fluxes using the bulk method (e.g., Favier et al., 2011). Turbulent heat fluxes are very sensitive to the choice of these parameters (Wagnon et al., 1999; Hock and Holmgren, 2005), and surface roughness lengths are often obtained by calibration using field measurements (e.g. Wagnon et al., 1999, 2003; Favier et al., 2004a). It is often easier to fix the values of equal roughness ($z_{0m} = z_{0T} = z_{0q}$) as considered in several studies in the tropics. In this case, roughness lengths lose their physical meaning. For the AG12 site, we used a value of $z_{0m} = z_{0T} = z_{0q} = 2.9$ mm for the ice, which corresponds to the value calibrated in the ablation zone of AG15 by Favier et al. (2004a). A value of $z_{0m} = 4$ mm was used for snow (Wagnon et al., 1999). In the case of a precipitation event, the roughness length of fresh snow is reduced to 0.29 mm during the current time-step (Gurgiser et al., 2013a).

TABLE 2 | Albedo parameters after calibration completed. The initial snow/ice albedos (initial value) and aging threshold values (final value) were taken from Gurgiser et al., 2013a and Maisincho (2015), respectively.

Group	Parameter	Notation	Initial value	Final value
1: Snow/ice albedo	Snow fresh albedo	$\alpha_{fresh\ snow}$	0.88	0.88
	Wet snow albedo	$\alpha_{wet\ snow}$	0.63	0.69
	Clean ice albedo	$\alpha_{clean\ ice}$	0.46	0.46
	Dirty ice albedo	$\alpha_{dirty\ ice}$	0.16	0.16
2: Aging thresholds	ice aging threshold (days)	n^*_{ice}	82.6	135.4
	renewing ice albedo threshold (days)	$n_{s\ ice}$	1.52	6.71
	snow decay threshold (days)	n^*	0.85	5.79
	Snow cover thickness threshold (mm w.e.)	e^*_s	1.64	2.71

3.2 Distributed SEB Model

Initially, the model was applied locally at the SAMA-1 altitude level, where the model parameters were calibrated. This step was particularly important for the albedo model. Then, the model was distributed over 20 different 50-m altitude bands. For this purpose, the incident short-wave radiation (SWi) was corrected according to the mean slope (β_i) and the mean aspect (Az_i) of the corresponding band. These values were computed from the DEM pixels located between $z_i - 25$ and $z_i + 25$. The representative area (A_i) on which the energy balance was calculated corresponds to the number of pixels in the band multiplied by the individual area of one pixel (100 m^2) and by the cosine of the slope.

Calculations were performed with a 30-min time step for each band (i), following the order of operations described below: 1) we first calculate the incident short-wave radiation $SWi(z_i)$ as a function of surface slope (β_i) and azimuth (Az_i), 2) we extrapolate the air temperature for each band using temperature lapse rate, the air temperature (Tz_{ref}) measured at the SAMA-1 station located at the reference altitude z_{ref} = 4,753 m a.s.l., and the altitude (z_i) of the considered band, 3) using Stephan Boltzmann equation, we correct the LWi values as a function of altitude considering that the variations depend on air temperature only $T(z_i)$ 4) we evaluate the precipitation as a function of altitude z_i, 5) we discriminate the precipitation phase as a function of $T(z_i)$, 6) we model the snow accumulation and the albedo, 7) we evaluate the value of the short-wave radiation reflected by the surface SWr (z_i), 8) we calculate the turbulent fluxes for the corresponding $T(z_i)$, surface roughness length and surface temperature $T_s(z_i)$ value from the preceding calculation time step 9) we compute the available surface energy $E_{surface}$, the available energy for melting G_0 and apply the thermal diffusion to obtain the melting. Thermal diffusion was computed according to an explicit scheme to a depth of 18.2 m, with a 2 cm grid resolution and a 20 s time step. After computing melting, mass balance components (e.g., solid and liquid precipitation, melting, and sublimation) were aggregated to get hourly values corresponding to the current time-step of the linear reservoir model.

3.3 Linear Reservoir Model

The transfer of meltwater and rainfall through the glacier to the outlet of the watershed is modeled using the Baker et al. (1982) model. This reservoir-type model is used to calculate the transfer from the various zones of the watershed. In our case, the watershed has been divided into four zones: three zones correspond to the glacier, which has been divided according to altitude, and a fourth zone corresponds to moraine terrain outside the glacier. Each zone is represented by a linear reservoir (**Eq. 7**) such that the flow rate [Q(t)] depends on a characteristic storage parameter (k) and the inflow rate [R(t)]. R(t) corresponds to the sum of melting (evaluated from the distributed SEB) and liquid precipitation. Consequently, the net discharge at the outlet results from the sum of the individual inflows.

$$Q(t) = Q(t-1)e^{-\frac{1}{k}} + \left(1 - e^{-\frac{1}{k}}\right)R(t) \quad \left(m^3\ s^{-1}\right) \tag{7}$$

In our approach, the "ice reservoir" refers to the lower part of the glacier, corresponding to the ablation zone. Water discharges from the central part, around the equilibrium zone, are modeled using the reservoir called "firn reservoir" hereafter; and in the upper part, where accumulation occurs, we refer to the reservoir as the "snow reservoir". **Figure 1** shows the watershed of Glacier 12 and the distribution of the different reservoirs. The boundary between the ice and firn reservoirs has been set at 5,100 m a.s.l., close to the equilibrium line altitude (Basantes-Serrano, 2015). The boundary between the firn and snow reservoirs was set at 5,300 m a.s.l., due to the change in the observed mean snow density as a function of altitude in this area (Cáceres et al., 2010).

Moreover, a reservoir corresponding to water contribution from the moraine was included in our modeling to account for the area between the glacier snout and the hydrological station (1.5 km downstream). This reservoir is fed by a permanent underground flow of $Q_0 = 0.01\ m^3\ s^{-1}$ estimated from hydrological balances and salt gauging (data not shown) and to which the contribution of rainfall is added and is proportional to precipitation (measured with the rain gauge P8) according to PSO and to the surface area of this zone ($A_{moraine}$). To represent the evaporation/sublimation of this zone, a stream coefficient f_0 = 0.8 was included. Thus, the inflow [$R_0(t)$] for this reservoir was represented by **Eq. 8**.

$$R_0(t) = Q_0 + f_0 * P8_{rain}(t) * A_{moraine} \tag{8}$$

Heavy precipitation sometimes produces a snow cover that can persist from a few hours to a few days over the entire

TABLE 3 | Altitude range, area, and storage constants used for the linear reservoir model. In the approach the altitude for each reservoir were kept fix since most of snowfalls at site are short-lived.

Reservoir	Altitude range (m a.s.l.)	Area (km^2)	Storage constant (h^{-1})
Moraine	[4,550–4,730]	1.28	361
Ice	[4,730–5,100]	0.69	9
Firn	[5,100–5,300]	0.37	282
Snow	[5,300–5,720]	0.59	146

watershed, resulting in short-term water storage. Nevertheless, the parameters for sizing the storage in the reservoir model were considered constant because the snow stored in the lowest part of the watershed was considered negligible, but also because the model is only a conceptual representation allowing to compute the water amount delivered at the hydrological station. Studying the exact origin of the inflow is not a focus here. Thus, the storage corresponding to the snow is indirectly integrated into the calculation of the reservoir parameters when the model is calibrated (Hock, 2005).

The model parameters corresponding to the water storage were calibrated using a Monte-Carlo-type approach carried out on 10^4 simulations for which all the parameters had randomly estimated values. This calibration of the time of responses (k) was performed over the 2012 period, and the validation was carried out over the July-December 2011 plus January-May 2013 period. The optimal values selected are those that maximize the coefficient of determination calculated between the observed and simulated discharges. **Table 3** shows the final parameter values obtained. The ranges of variation of the parameters were defined according to the values applied in linear reservoir models on other glacial basins (Cuffey and Paterson, 2010). A sensitivity analysis was not performed because the simulated discharge using the linear reservoir model is not strongly dependent on the parameters associated with storage (Hock and Noetzli, 1997).

4 RESULTS

4.1 Meteorological Conditions

4.1.1 Observed Values During SP

During SP, the air temperature and specific humidity at SAMA-1 oscillated around the mean values of 1.31°C and specific humidity of 5.8 g kg^{-1}, respectively. They presented a slight maximum between February and May (1.66°C, 6.7 g kg^{-1}) related to the equinox characterized by a higher cloud cover and weaker wind conditions. In contrast, a slight drop in both variables was observed from June to September (0.75°C and 5.2 g kg^{-1}, respectively). These differences are minimal compared to the standard deviation of daily values (1.81°C and 1.2 g kg^{-1}), reflecting the lack of marked thermal seasonality in Ecuador (Kaser and Osmaston, 2002). The cloud factor (CF) showed values above 0.6 during the two periods of heavy precipitation (February-May and October-December); therefore these periods were characterized by lower values of SWi and large values of LWi (**Figure 3**). On the contrary, the mean wind speed was 3.8 m s^{-1} (σ = 2.4 m s^{-1}), with June-September season marked by stronger easterly winds

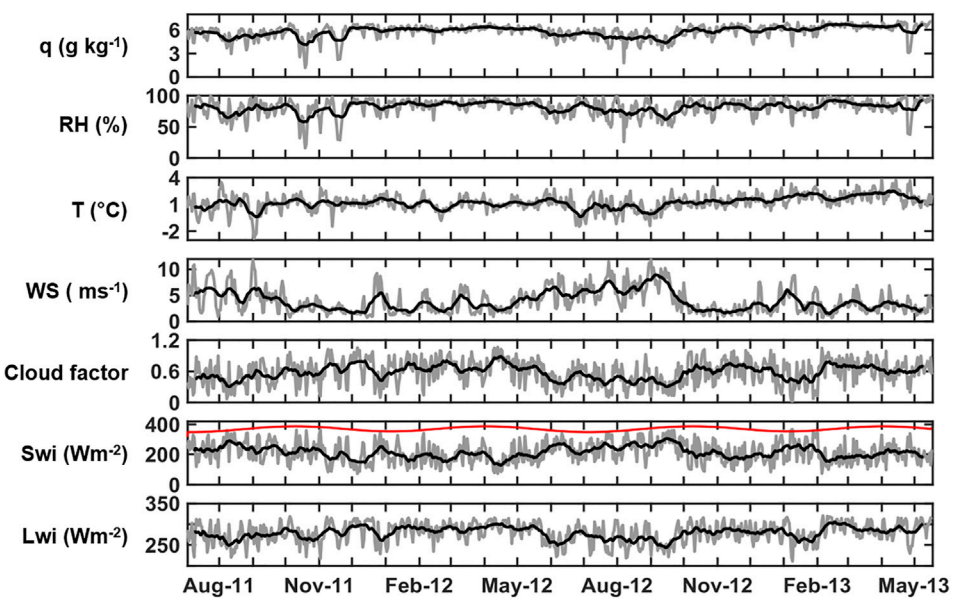

FIGURE 3 | Summary of daily mean (gray line) meteorological conditions measured at AWS SAMA-1 (4,753 m a.s.l.). Thick black lines represent the 15-day running means. The red curve shows theoretical solar radiation at the top of atmosphere (STOA) reduced by 50 Wm^{-2} and represents maximums theoretical radiation on clear days. The cloud factor CF (dimensionless) was calculated as the ratio between the incoming short-wave radiation and STOA according to **Eq. 1**.

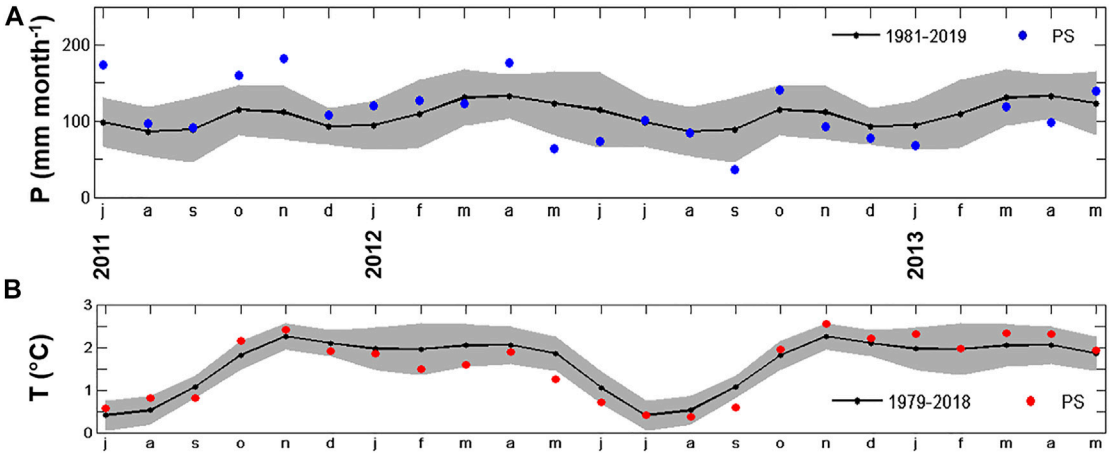

FIGURE 4 | (A) Monthly CHIRPS precipitation (0.05° × 0.05°) values for the study period (blue circles) relative to mean CHIRPS precipitation for 1981–2019 period (black circles) and monthly standard deviations (gray shading) for the grid point nearest Antisana 12 Glacier (78.15°W, 0.45°S). **(B)** Monthly ERA5 air temperature (0.25° × 0.25°) at 600 hPa level, averaged over the Antisana massif region (0.2 to 0.8°S, 77.8 to 78.5°W) for the sudy period (red circles) relative to mean ERA air temperature for 1979–2018 period (black circles) and monthly standard deviations (gray shading).

(mean = 6.7 m s^{-1}, σ = 3.3 m s^{-1}), thus reducing cloud cover leeward the volcano (CF = 0.2) which in turn reduced LWi and increased SWi.

P8 rain gauge collected 1,429 mm and dry days accounted for 28% of the SP. Periods without precipitation never exceeded 10 days. Thus, demonstrating the prevalence of rainy conditions. Using the PSO to separate liquid and solid precipitation (see **Section 3.1.2**), snowfall accounted for 757 mm corresponding to 53% of total precipitation. This value was higher than 681 mm computed using the 1°C threshold, justifying that a higher albedo value is modeled at the SAMA-1 level with the PSO approach than with a constant 1°C threshold (**Figure 5**).

These characteristics in temperature and radiation, as well as the precipitation cycle, affect the melting conditions, and in consequence influence the variations of the monthly discharge measured at "Los Crespos" station. Which presented an average discharge of 0.045 m^3 s^{-1} with a minimum between June and August (0.026 m^3 s^{-1}) (**Figure 2**). On the other hand, two maxima in discharge were observed around 0.058 m^3 s^{-1} in January-May and September-November. These were associated with heavy precipitation during equinoxes and favorable conditions for significant melting (Favier et al., 2004a).

4.1.2 Representativeness of SP

In the study area, the average precipitation provided by CHIRPS was 1,298 mm (standard deviation, σ = 174 mm). The precipitation values from 2011, 2012, and 2013 differed from the mean by +2σ, −0.46σ, and −0.02σ, respectively; suggesting that 2011 was relatively wet while 2012 was slightly dry. Comparing the SP values with the corresponding monthly mean (**Figure 4**), five of 23 months presented values larger than one standard deviation suggesting precipitation excess, whereas 3 months were dry, i.e., with values lower than 1 standard deviation. Therefore, the study period was marked by irregular monthly precipitation with excess from July 2011 to April 2012, followed by a deficit from May 2012 to January 2013, and finally by an alternation between wet and dry months. Similarly, the mean annual temperature from ERA-5 was 1.59°C over the Antisana region (standard deviation σ = 0.74°C). 2011, 2012, and 2013 years were marked by differences with the interannual mean of +0.05σ, −0.21σ, and +0.15σ, respectively. Thus, 2012 was slightly cold, while 2013 was slightly warm. SP presented 10 months with the temperature above the respective monthly mean, and 9 months below. Thus, the study period experienced fluctuating temperatures with increasing temperature between July to November 2011, then a decrease between December 2011 and September 2012, and finally a further increase during the remaining months.

4.2 Model Validation

4.2.1 Validation of Albedo Model

To study the role of each parameter in the albedo model a sensitivity test was carried out. The ice-snow parameters varied from 0.2 to 1.2 times the initial values taken from Maisincho (2015). These variations had an insignificant impact on the resulting albedo, except for the wet snow albedo for which high values led to a better reproduction of the daily measurements (computed between 10:00 and 16:00 local time). On the other hand, changes in the characteristic aging scales (Group 2 of **Table 2**) resulted in relatively random variations of the determination coefficient (**Supplementary Figure S1**). Then, a Monte Carlo approach based on 10^4 simulations was performed to maximize this value computed between the daily simulated albedo and measured values. These parameters' variation span from 0.2 to 6 times the initial values taken from Gurgiser et al., 2013a. The resulting values after calibration were summarized in **Table 2**.

The parameters obtained were representative of rapid snow metamorphism and faster albedo degradation in the inner tropics than in the Alps (Wagnon et al., 2009; Sicart et al.,

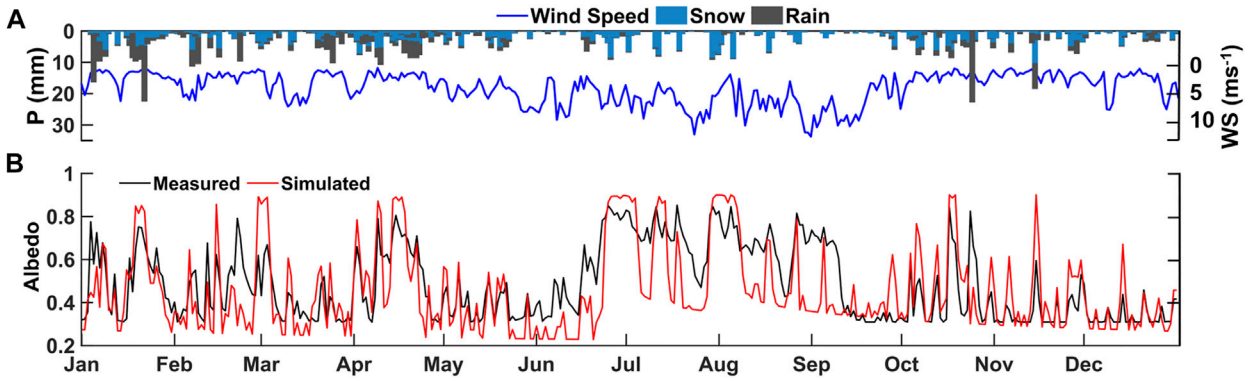

FIGURE 5 | (A) Daily snow and rain values accumulated from 30-min precipitation at P8. Snowfall fraction was discriminated according to PSO scheme depending on temperature ranges (See **Section 3.1.2**). Daily wind speed values (blue line) measured in SAMA-1 were included for comparison purposes. **(B)** Comparison between daily albedo measured at SAMA-1 station (black line) and simulated after setting parameters (red line). Daily values were computed in the daytime between 10:00 and 16:00 h local time.

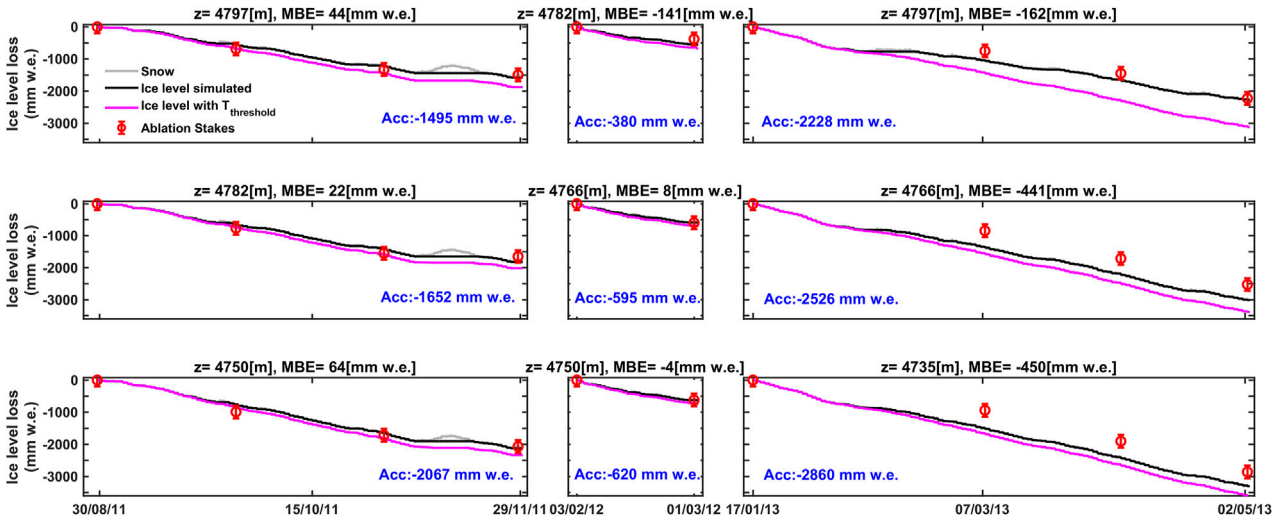

FIGURE 6 | Computed and measured surface height changes for different sites (rows) during MP1, MP2, and MP3 (columns). Ice (black line) and snow (gray line) surface height were computed following the PSO scheme. Surface height measured (red circles) includes 150 mm error bars related to the measurement method. Mean bias error (MBE) between simulated and measured surface height, and cumulated height measured (text in blue) were included for each site. For comparison purposes, surface height computed with a 1°C threshold temperature (pink line) is also shown.

2011). The value of the characteristic snow cover thickness at which the underlying ice surface is visible (e_s^*) is lower at Antisana than in the outer tropics. This point reflects the frequent presence of thin layers of fresh, wet snow due to light snowfalls, which, however, have a significant impact on albedo. Moreover, the addition of a progressive ice-albedo degradation in **Eq. 5** allows taking into account a progressive accumulation of dust particles on the ice surface. This improvement is particularly significant during sporadic precipitation and for dry periods marked by a progressive decrease of the albedo until reaching the dirty ice-albedo value (**Figure 5**). Therefore, calibration allowed us to improve the simulations increasing the determination coefficient between measured and modeled daily albedo data, from $r^2 = 0.13$ ($r = 0.36$, $n = 366$, $p = 0.17$) obtained with the initial values to $r^2 = 0.72$ ($r = 0.85$, $n = 366$, $p < 0.05$) after calibration. The improvement was also significant for 30-min values with $r^2 = 0.65$ ($r = 0.81$, $n = 5{,}124$, $p < 0.01$).

Since albedo controls variations of the net short-wave radiation (Favier et al., 2004a), these changes significantly improved the representation of this energy flux, which controls the energy available at the surface and thus the melt. Over the study period, the determination coefficient between modeled and measured daily melting values reached $r^2 = 0.75$ ($r = 0.87$, $n = 686$, $p < 0.05$), indicating good performance for long time series. There were small differences in simulated albedo

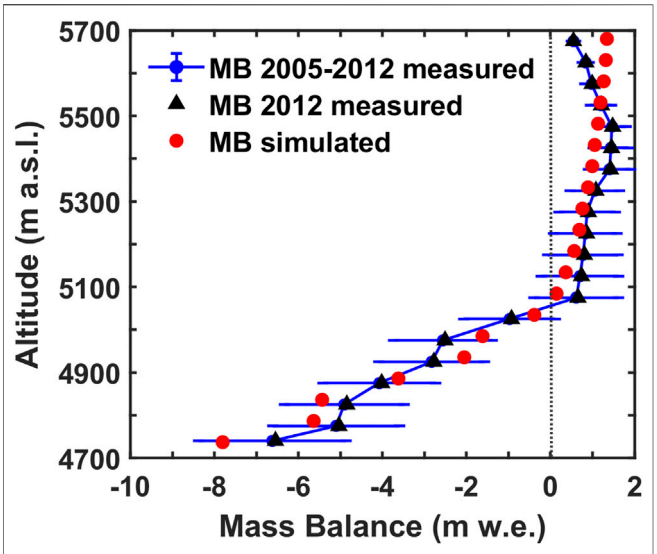

FIGURE 7 | Comparison between measured and computed mass balance profiles. Blue dots represent the mean of 2005–2012 measurements, blue bars represent corresponding standard deviation for each altitude band. Black triangles represent the measurements for 2012, and red dots correspond to mass balance profile simulated. The dashed line represents equilibrium line that cross mass balance profile around 5,100 m a.s.l.

between July and September (**Figure 5**), probably because windy conditions could redistribute the snowpack with increasing snow depth and albedo in patchy areas only. The latter process cannot be represented by the model (Maisincho, 2015).

4.2.2 Validation of Point-Based Melt Modeling

After tunning the albedo parameters, we applied the SEB model over three successive periods, called MP1, MP2, and MP3 (**Table 1**). These periods allowed us to test the evolution of the model quality in the ablation zone for different surface conditions. **Figure 6** shows the simulated cumulative surface elevation changes for different sites around the SAMA-1. The separation between snow and rain was performed using the PSO scheme, but for comparison, the use of 1°C threshold was also tested. To quantify the differences between calculated and measured surface elevation, we compute the mean bias error (MBE) for the ablation stake locations. Since the MP2 period was short compared with MP1 and MP3, only graphical comparisons were carried out.

The MBE of the three points of MP1 was between 22 and 64 mm w.e., which corresponded to 2–4% of measured cumulative ablation, respectively. Thus, the model slightly underestimates ablation. Conversely, during the MP3, the modeled MBE was more negative than observations, with differences ranging between −450 and −162 mm w.e. suggesting that cumulative ablation was overestimated in a range of 7–17%. Using the PSO scheme, the modeled ablation got lower biases than using the 1°C threshold; especially for MP1 and MP3 both with a duration larger than 90 days. This occurred because the PSO improved the consistency between observed and modeled albedo changes due to better reproduction of solid precipitation occurrences for low-intensity events (0.5 mm w.e.) than with the 1°C threshold. This improvement was more significant for MP3 at 4,797 m a.s.l. since solid precipitation was 72 mm w.e. using the 1°C threshold, whereas it was 159 mm w.e. with PSO. This snow surplus produced a reduction in ablation of 852 mm w.e. Therefore, the additional snow was crucial to maintain the albedo above 0.3 and thus to avoid overestimating ablation.

4.2.3 Validation of the Distributed Modelling

The variations of the mass balance with elevation were simulated and compared with those of the observed geodetic mass balance (**Figure 7**). By examining the mass balance profiles with elevation, most of the simulated values were very close to the measurements. The distributed SEB model overestimated 15% of the ablation in the lowest zone (4,735–4,850 m a.s.l.), while it underestimated ablation by 20% between 4,850 and 5,100 m a.s.l. However, the errors in ablation modeling compensated each other, and the glacier-wide mass balance was correctly reproduced. The mass balance gradient with elevation was 22.76 kg m^{-2} m^{-1} y^{-1} close to the 19.32 kg m^{-2} m^{-1} y^{-1} measured, and to the 24.5 kg m^{-2} m^{-1} y^{-1} ±5% generally applied in the inner tropics (Kaser, 2001). Between 5,100 and 5,500 m a.s.l., the model underestimated the measured accumulation by 25%, whereas it overestimated the measured accumulation by 42% in the upper part (between 5,500 and 5,720 m a.s.l.). Despite of these discrepancies in the mass balance profile modeling, the resulting glacier-wide mass balance for 2012 was −0.61 m w.e. y^{-1}, which was close to the measured value in 2012 (−0.58 m w.e. y^{-1}) and to mean rate of −0.57 ± 0.81 m w.e. y^{-1} obtained over the period 2005–2012 (Basantes-Serrano, 2015). The distributed SEB was a priori reasonably representative of the average value observed on a 10-year scale. In **section 5**, we discuss why the distributed SEB could not fully represent the measured profile.

4.2.4 Streamflow Simulation

The calibrations performed on the distributed SEB and the flow transfer models allow to reproduce properly the variability of the measured discharge at a daily (r^2 = 0.54, p < 0.01, n = 423) and hourly (r^2 = 0.58, p < 0.01, n = 11,553) timescales. However, the mean simulated discharge largely overestimates the measured one. Daily mean simulated discharge was 0.187 m^3 s^{-1} (min = 0.03 m^3 s^{-1}, max = 0.6 m^3 s^{-1}) whereas observed discharge was 0.033 m^3 s^{-1} (min = 0.01 m^3 s^{-1}, max = 0.06 m^3 s^{-1}). The potential discharge was on average 5.86 times larger for the SP than the streamflow measured at the hydrological station. It is even possible that this ratio becomes 15 for some days (**Figure 8**). The current difference between both discharges indicates that rain and meltwaters from the glacier likely percolate into the groundwater system above the gauging station so that the streamflow at the gauging station is lower than expected. This occurrence of significant groundwater flow had already been observed in the case of the AG15 (Favier et al., 2008), showing the limits of hydrological measurements to assess the melting and mass balances of the Antisana glaciers.

Furthermore, the average contributions of each reservoir to the potential discharge were: 77% from ice zone, 14% from moraine

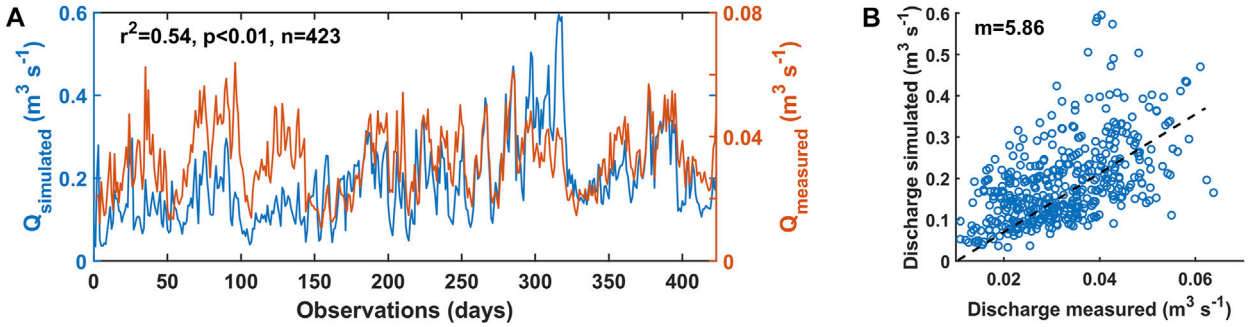

FIGURE 8 | (A) Comparison between simulated (blue line) and measured discharge (orange line). Only days with precipitation and discharge available are presented. **(B)** Scatter plot of measured vs. simulated discharge daily values. Dashed line represents the mean ratio (m = 5.86) between simulated and measured values.

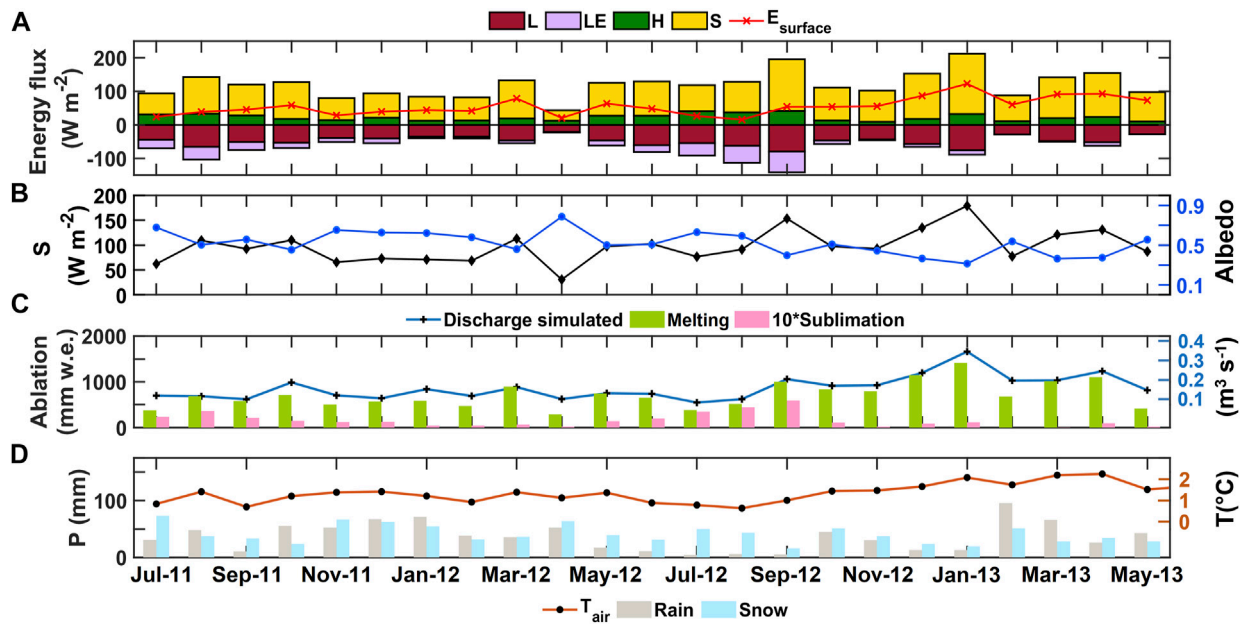

FIGURE 9 | (A) Monthly values of the surface energy balance components and resulting energy available at surface (red line) for the 4,780 m a.s.l. band nearest to SAMA-1. **(B)** Comparison between net short-wave radiation (black line) and albedo (blue line) at 4,780 m a.s.l. **(C)** Monthly discharge simulated (blue line), accumulated melting (green bars) and sublimation (pink bars) at 4,780 m a.s.l. For visualization purposes, sublimation was multiplied by a 10 factor. **(D)** Monthly air temperature measured in SAMA-1 (brown line) and accumulated snow and rain measured in P8. Separation phase was determined through PSO scheme.

zone, 6% from firn zone, and 3% from snow zone. These percentages confirmed that most of the runoff originated within the glacier came from the ablation zone and the nearby moraine. Therefore, the contribution of the accumulation zone was not significant.

4.3 Application of Distributed SEB Model

The model calibration step demonstrated that the coupling between the distributed SEB and water flow transfer allowed us to simulate the variations of ablation and streamflow if we assume the occurrence of significant groundwater flow circulations. Consequently, the model will be used hereafter as an analytical tool to relate weather conditions, the energy balance, and the water flows in the Los Crespos gauging station.

4.3.1 Melting, Sublimation and Discharge Peaks

In the ablation zone, as observed before on AG15 (Favier et al., 2004b), the net short-wave radiation (S = SWi − SWr) was the primary source of energy available at the surface during the study period (**Figure 9**), and it contributed to 53% of the absolute energy exchange. This flux was controlled by albedo variations (r^2 = −0.96, n = 23, p < 0.01), which in turn was related to the phase of precipitation through the snow cover thickness (r^2 = −0.79, n = 23, p < 0.01). Since the ice reservoir was the main provider of meltwater at the outlet, there was also a significant correlation between the potential discharge and the net short-wave radiation (r^2 = 0.80, n = 23, p < 0.01). The correlations between the potential discharge and other components of the SEBs were

not significant (r^2 always lower than 0.4, $p > 0.05$), demonstrating that the outflow was not highly dependent on these other fluxes. However, despite a significant seasonality of the short-wave radiation at the top of the atmosphere (STOA), the presence of cloudiness and precipitation during the study period attenuated the seasonality of SWi (**Figure 3**), and no seasonality was found in the variation of discharge during SP.

Moreover, the location of the Antisana massif in the vicinity of the Amazon basin allows the glacier to continuously receive the moisture transported by the easterlies (Junquas et al., 2022). During SP, this induced the presence of significant cloud cover throughout the year and finally reduced the seasonality in LWi (**Table 3**). Also, the homogeneity of air temperature (**Section 2.1**) allowed the glacier surface to be at the melting point most of the time (Francou et al., 2004), and LWo was regular. As consequence, the longwave radiation also presented no seasonality (**Figure 9**). Since the radiative fluxes (S + L) contributed 80% of mean absolute energy during SP, the $E_{surface}$ and mass balance neither exhibited seasonality in accordance with their low coefficient of variability (CV = 0.5) and low standard deviation (**Table 3**). The lack of seasonality in SWi and LWi also implies that SWr and LWo variations drove S and L and were key in determining the available energy for melting. Considering that SWr are related to albedo and snowpack thickness, it justifies that glaciers in the inner tropics are very sensitive to air temperature through its influence on the precipitation phase (Favier et al., 2004a; Favier et al., 2004b; Francou et al., 2004).

Finally, to illustrate the influence of weather conditions on discharge variations, we related it with the energy fluxes at SAMA-1 during the months of maximum/minimum energy available for melting. During April 2012, the net short-wave radiation (S = 43 W m^{-2}) was minimal (**Figure 9**) due to continuous cloud cover (CF = 0.95) and solid precipitation, SWi was reduced and a significant snow cover (64 mm) was present at the surface leading to an increase in the albedo up to 0.8. With very high SWr, the net short-wave radiation dropped leading to low melting amounts and discharge. Similarly in July 2012, low air temperature and significant precipitation provided fresh snow at the surface, which sustained a high albedo and low S value. In addition, seasonal high wind speed (Ws = 6.62 m s^{-1}) favored a large turbulent latent heat flux, which is an efficient energy sink. Both conditions reduced the available energy to 26 W m^{-2}. Thus, melting and discharge were minimum (around 380 mm w.e. and 0.09 m^3 s^{-1}, respectively), and 47% lower than their respective mean values over SP. Conversely, January 2013 presented low cloud cover (CF = 0.45) and high precipitation deficit yielding high SWi and low SWr, which resulted in maximum short-wave radiation (S = 179 W m^{-2}). Moreover, the air temperature was high (T = 1.85°C), favoring a positive turbulent sensible heat flux (H = 32 W m^{-2}) toward the glacier surface. Then, the available energy was maximal ($E_{surface}$ = 122 W m^{-2}), causing a peak in melting (1,414 mm w.e.) and discharge (Q = 0.37 m s^{-1}) (**Figure 9**) corresponding to overflow of 99 and 119% with respect to their respective mean values.

4.3.2 Variation in Energy Fluxes According to Elevation

Figure 10 shows the dependence of energy fluxes on altitude. A reduction of the net short-wave radiation resulted from the occurrence of greater snowfall amounts at high elevations. Frequent snowfalls maintained the albedo above 0.7 (high SWr). The concave shape of the glacier also contributed to this result because the zenithal angle increases with the slope, thus reducing SWi. The net short-wave radiation decreased from 120 W m^{-2} at the glacier front to 30 W m^{-2} at 5,100 m a.s.l. Above this altitude, its decrease was less significant, reaching 26 W m^{-2} at the summit. In addition, the drop in air temperature induced a reduction of the LWi from 281 W m^{-2} at the front of the glacier to 247 W m^{-2} at the summit. This decrease was partially offset by the reduction in LWo due to the drop in surface temperature (T_s). Thus, the net longwave budget passed from −33 W m^{-2} at 4,735 m a.s.l. to −47 W m^{-2} at 5,100 m a.s.l. This reduction continued almost linearly with the altitude until reach −67 W m^{-2} at the summit.

Since the decrease of T_s was linked to the radiative flux decrease with altitude, the temperature gradient between air temperature above the surface and T_s remained almost constant. In consequence, the sensible turbulent heat was constant with an elevation of around 23 W m^{-2}. Similar behavior occurred with the specific humidity gradient. Therefore, the latent heat did not evolve significantly with elevation and remained around −15 W m^{-2}. The changes in turbulent fluxes between 4,900 and 5,000 m a.s.l. were related to changes in the surface roughness length due to the surface transition from ice and snow. Assuming constant wind speed profile with elevation (measured at SAMA-1) resulted in a slight variation of turbulent fluxes. However, this assumption propagates uncertainties to higher altitudes where stronger wind should drive higher turbulent fluxes values (Dadic et al., 2013).

The variation of SEB components resulted in a decrease of $E_{surface}$ from the glacier snout to the ELA (5,100 m a.s.l.) such that the net short-wave radiation and the turbulent sensible heat flux prevailed in the ablation zone and provided 21 W m^{-2} of energy to the surface for melt, on average. In addition, 64% of the melting occurred directly at the surface, while the remaining 36% occurred in the sub-surface layer. This may explain the observed 5–10 cm deep cryoconite holes in the field. The ablation zone received 74% of total rain and 33% of total snow; but accounted for 91% of melting amount and 46% of sublimation, respectively. Although the highest melting rate occurred at the glacier snout, the largest contribution came from the 4,850 m a.s.l. altitude band (**Figure 10**), in accordance with the major exposure area at the ablation zone. Since the turbulent heat fluxes and net radiation compensated each other in the accumulation zone, there was unimportant melting in this zone. Then, mass losses at high elevation were mainly by sublimation. The highest snow accumulation occurred at the summit, but the zone of maximum accumulation took place at 5,300 m a.s.l. due to the widest surface area at this altitude.

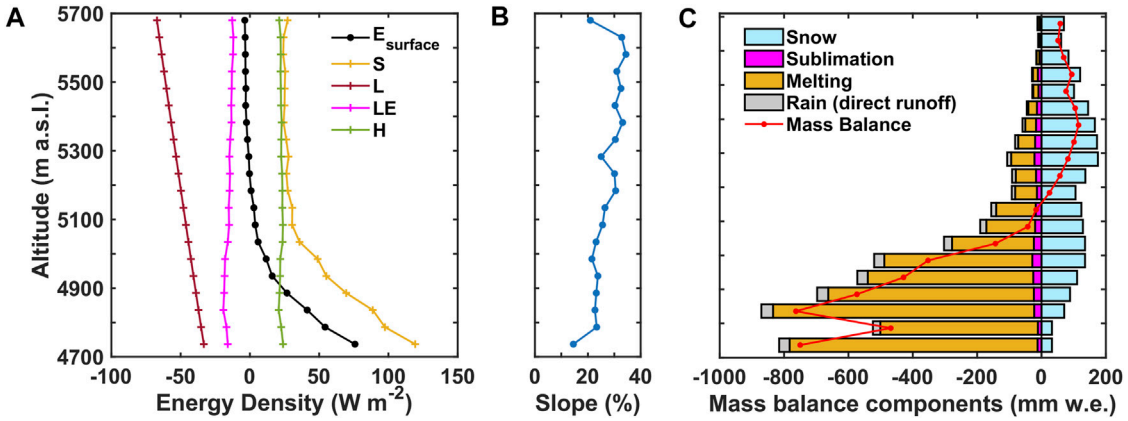

FIGURE 10 | (A) Mean variation of energy fluxes with altitude during SP. **(B)** Variation of surface slope with altitude resulted from the DEM analysis. **(C)** Altitudinal profile of components of specific mass balance for SP.

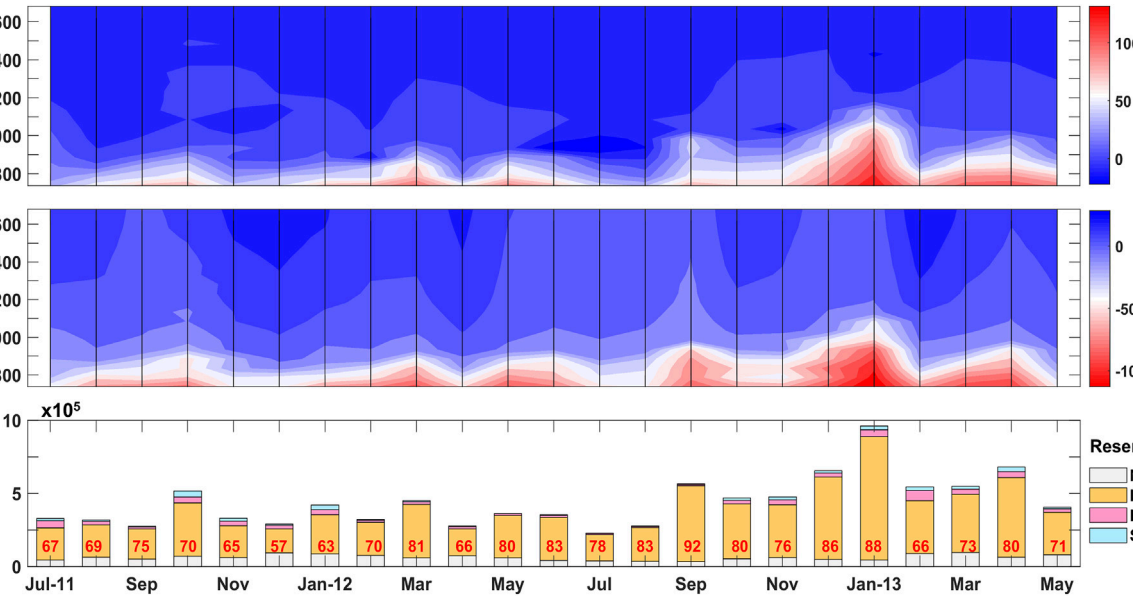

FIGURE 11 | (A) Monthly profile of surface energy available at surface. **(B)** Monthly mass balance profile. **(C)** Monthly discharge cumulated at each reservoir. Numbers in red represents the ice reservoir contribution concerning total discharge.

4.3.3 Relationship Between Mass Balance and Potential Streamflow

Figure 11 shows the monthly variation profiles of $E_{surface}$ and surface mass balance as a function of altitude, as well as the volume of water from each reservoir. During SP, the average monthly ablation was −0.24 m w.e. between 4,735 and 5,100 m a.s.l. (−0.65 m w.e. at the glacier snout), corresponding to a mean discharged volume of 4.38×10^5 m^3 with 77% coming from the ice reservoir. Months with the lowest precipitation (less than 40 mm) like September 2012, December 2012, and January 2013 were associated with a higher mass loss (−0.52 m w.e.) generating larger meltwater volumes around 7.22×10^5 m^3 with 86% of the contribution from ice reservoir. Indeed, September 2012 was characterized by the maximum wind speed (Ws = 6.8 m s^{-1}), and the lowest specific humidity (q = 4.8 g kg^{-1}) that maximized the turbulent fluxes (H = 42 Wm^{-2}, LE = −62 Wm^{-2}). Sublimation (59 mm w.e.) was promoted by dry conditions, but low precipitation (21 mm) led to a low albedo leading to intense ablation.

By contrast, months with precipitation exceeding 90 mm like July, November and December 2011, and April 2012 were marked by limited mass losses (−0.16 m w.e. on average), resulting in 3.1 $\times 10^5$ m^3 volume discharged such that ice reservoir contributed with 64% of the potential discharge. The two latter months were

TABLE 4 | Summary of Mean monthly values of meteorological and SEB variables at SAMA-1 location during SP. Des. Std. and Coef. Var. refer to standard deviation and coefficient of variation, respectively.

Variable (unit)	Mean	Desv. Std.	Max	Min	Coef. Var.
SWi (W m^{-2})	213	33	284	160	0.2
SWr (W m^{-2})	90	21	128	56	0.2
LWi (W m^{-2})	279	12	301	257	0.01
Lwo (W m^{-2})	313	3	315	309	0.01
T air (°C)	1.2	0.5	2.2	0.5	0.4
q (g kg^{-1})	5.8	0.5	6.7	4.9	0.1
Ws (m s^{-1})	3.8	1.6	6.8	1.9	0.4
STOA (W m^{-2})	418	14	434	386	0.01
Cloud factor	0.6	0.1	0.8	0.4	0.2
S (W m^{-2})	123	31	189	59	0.3
L (W m^{-2})	–34	10	–19	–54	0.3
H (W m^{-2})	23	10	42	9	0.5
LE (W m^{-2})	–17	17	4	–62	1
SWi/STOA	0.5	0.1	0.7	0.4	0.1
E surface (W m^{-2})	62	26	122	28	0.3
Melting (mm w.e.)	712	282	1,414	292	0.4
Sublimation (mm w.e.)	15	15	59	2	1
MB (mm w.e.)	–490	222	–128	–1,057	0.5

thus possibly marked by mass gains in the accumulation zone (0.14–0.21 m w.e.). In general, the melting above the ELA was limited because significant sublimation sank $E_{surface}$. Hence, firn and snow reservoirs contributed with the 6 and 3%, respectively, of the potential discharge. Whereas below this altitude, the ice reservoir concentrated most of the melting. In general, the contribution of ice and moraine reservoirs depended on the rain/snow ratio because months with greater snowfall occurrence than rain limited the contribution from the moraine and increased the contribution of the ice reservoir up to 80% (**Figure 11**).

5 DISCUSSION

5.1 Comparison of Antisana Glacier 12 SEB With Other Tropical Glaciers

We compared the meteorological conditions and SEB values at the AG12 (**Table 4**) with those reported at AG15 by Favier et al. (2004a). Slight differences were found. AG12 presented lower SWi and slightly larger LWi than at AG15. Indeed, moisture transported by the wind can condense at the summit and along the upper slopes on the western side of the volcano (Basantes-Serrano et al., 2016), producing a cloud cover on the AG12. Whereas along the northern flank, this air flux preferably passes without producing clouds, and AG15 is more frequently under clear sky conditions. Also, the windy conditions and cooler temperatures in AG15 are explained by the higher location of the AWS (125 m higher than on AG12). Therefore, local features linked to the aspect and morphology of the glacier increased energy losses of AG15 via L and LE and reduce melting and ablation than on AG12.

These differences do not alter the low seasonality of energy fluxes and became less important at the interannual scale. Hence, both glaciers share similar responses and mass balance trends (–0.46 m w.e. y^{-1} for AG15 vs. –0.57 m w.e. y^{-1} for AG12 for 2005–2012 records) rough to the –0.6 m w.e. y^{-1} estimated by Rabatel et al. (2013) to the tropical glaciers. Therefore, results in AG12 can be used as a first proxy to determine the meltwater production and mass balance of Cayambe and Cotopaxi glaciers located in the Eastern Cordillera, which share similar climatic conditions. Conversely, the Chimborazo volcano is located in the Western Cordillera and holds less-humid conditions (550–750 mm/year) with a marked dry season between June-September (Ilbay-Yupa et al., 2021). Thus, Chimorazo's glaciers present more negative mass balance and additional melting reaching 1.5 m w.e. below their ELA (5,050 m a.s.l) according to Saberi et al. (2019).

In addition, the meteorological conditions and SEB components of AG12 were compared with those reported in Artesonraju glacier (Peru) (Juen, 2006) and Zongo glacier (Sicart et al., 2011). The air temperature at all sites presented low seasonal variability characteristic of tropical glaciers. However, the vicinity of AG12 to the moisture sources explains the larger values of specific humidity, cloudiness, and LWi than all the other sites (**Supplementary Table S1**). The wet conditions make the turbulent latent heat flux constant and prevent nocturnal radiative cooling maintaining the surface glacier temperature close to 0°C. Thus, energy balance and melting depend mostly on short-wave radiation, except during the June-September season when strengthen Easterlies increase the sublimation and melting is reduced, similarly as observed on Artesonraju glacier. In addition, the variation of SEB components with altitude modeled in AG12 followed the same behavior of the values at Shallap glacier (Gurgiser et al., 2013a), especially the turbulent heat fluxes. This was expected since Shallap and Antisana glaciers present quite similar conditions. Conversely, Zongo Glacier is characterized by a very marked seasonality of LWi, especially during the June-September season; where very large sublimation amounts are not compensated by the solar radiation and melting is then negligible (Favier et al., 2004b).

5.2 Influence of Temperature Lapse Rate and Precipitation Correction

To analyze the effect of TLR and precipitation factors on the mass balance profile we investigate some schemes to extrapolate these variables over the glacier. The linear regression between mean temperature values at SAMA-1, 2, and 3 leads to a lapse rate of –5.5°C km^{-1} (see **Section 3.1.4.**); also, we try with –5.9°C km^{-1} corresponding to the median value of TLRs computed from 30-min sets measured simultaneously for the three SAMA stations. Concerning precipitation corrections, we tested four configurations: 1) constant precipitation with elevation without including a correction for wind-induced under-catch 2) constant precipitation with elevation including a 23% correction to account for the under-catch of hydrometeors (see **Section 3.1.1**) 3) same as configuration 2 but we added a precipitation gradient with the altitude of 40 mm per 100 m as proposed Basantes-Serrano et al., 2016 to match measured mass balances in the accumulation zone of AG15, and 4) same as configuration 2 but we include a linear increase of 10% every

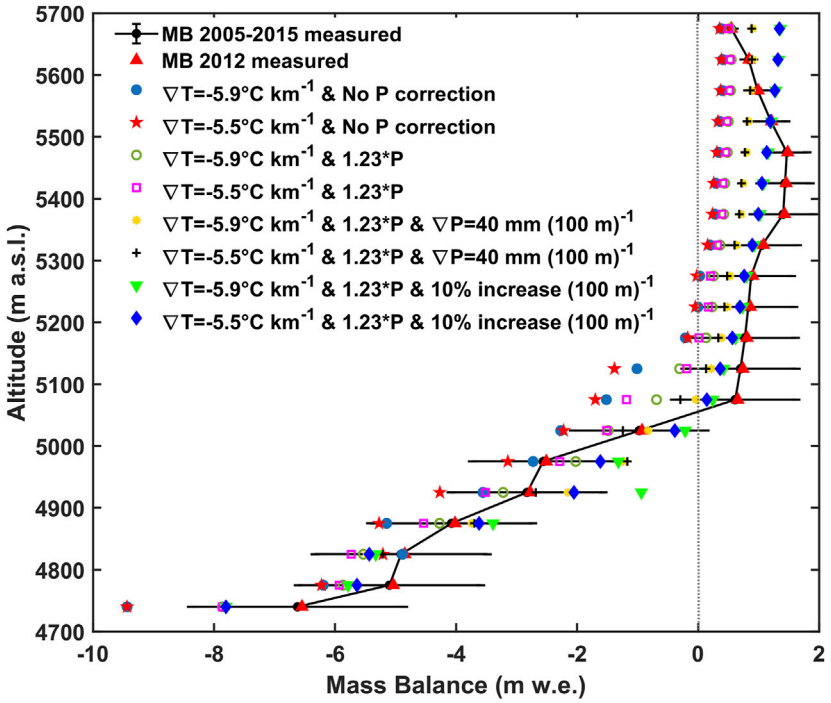

FIGURE 12 | Variation of simulated mass balance 2012 profile to changes in temperature lapse rate and precipitation correction schemes. Scheme with ∇T = −5.5°C km^{-1} and 10% (100 m)$^{-1}$ linear increase of corrected precipitation by 1.23 factor used for simulating distributed SEB got the minimum RMSE.

100 m in altitude. Thus, the 837 mm cumulated annually at P8 would increase to 1,450 mm at the summit (e.g., a 73% factor) with configuration 3; whereas configuration 4 enhances an increase from 837 to 2,059 mm at the summit (e.g., a 146% factor).

All configurations were applied to assess the mass balance simulated during 2012 (**Figure 12**). The schemes employing constant precipitation and with/without correction for under-catch resulted in more significant mass balance losses and located the ELA 300 m above its real altitude. Thus, a vertical increase of precipitation is critical to match the mass balance with measurements. Recently, Junquas et al., 2022 has found the spatial precipitation maximum occurs at the Antisana summit with maximum values preferably on the windward side of the mountain. This reinforces the need of employing a scheme to represent the correction of precipitation with elevation. Adding 40 mm per 100 m^{-1} gives accurate point mass balance in the ablation zone, but underestimated the accumulation between 5,100 and 5,500 m a.s.l. This was not the case with the 10% linear increase, which proposed the best fit with data measured along the entire altitudinal profile.

Concerning the temperature lapse rate, we observed TLR of −5.9°C km^{-1} leads to underestimating ablation with elevation with the largest bias observed between 4,900 and 5,050 m a.s.l. Above this elevation range, both TLR gives similar mass balance because melt becomes negligible. Therefore, TLR of −5.9°C km^{-1} may be less representative because it was derived from a smaller dataset of air temperature measurements (N = 1,224). Conversely, the TLR of −5.5°C km^{-1} produced fewer deviations since this value was derived with a larger dataset available (N = 54,683, 28,713, and 8,297 for SAMA-1, -2, and -3, respectively), thus allowing a better representation of glacier conditions. Overall, the best fit between simulated and observed MB (RMSE = 0.55 m w.e.) is obtained with the value of −5.5°C km^{-1}, and considering that precipitation increases linearly with elevation at a rate of 10% (100 m)$^{-1}$. This temperature lapse rate is close to the value −5.1°C km^{-1} computed by Erazo (2020) for interpolations above 5,500 m a.s.l. in the Ecuadorian Andes. Moreover, this precipitation increase factor used to balance the accumulation has also been used in distributed SEB modeling in the Tropical Andes (Autin et al., 2021; Lozano Gacha and Koch, 2021). However, new accumulation measurements should be necessary to validate this precipitation rate since accumulation is particularly difficult to assess in the accumulation zone of Antisana glaciers (Basantes-Serrano et al., 2016).

In the distributed SEB model, the implementation of refreezing scheme was neglected because the glacier surface in the ablation zone stays at the melting point most of the time (Francou et al., 2004) and because most melt is concentrated under ELA. Finally, here we did not analyze the influence of the variation of wind speed and specific humidity with altitude because the measurements available at SAMAs stations did not overlap during SP. Also, since these variables are prone to local variations, due to the influence of boundary layer effects and topographical disturbances (Zardi and Whiteman, 2013), the resulting relationships with altitude are more complex than linear interpolations used in temperature. Thus, the lack of additional measurements along the altitudinal profile did not

TABLE 5 | Comparisons of hydrological features between Antisana Glacier 12 for 2012 year using distributed SEB plus linear reservoirs and Antisana Glacier 15 for 1995–2005 period using semi empirical approach taken from Favier et al. (2008).

	Glacier 12	Glacier 15
Altitude range (m a.s.l.)	[4,735–5,720]	[4,850–5,720]
Catchment area (km^2)	2.93	1.37
Glacial area (km^2)	1.65	0.71
Ablation area (km^2)	0.69	0.38
Mean melting (mm w.e.)	5,971	1,285
Measured streamflow ($m^3\ s^{-1}$)	0.033	0.017
Simulated streamflow ($m^3\ s^{-1}$)	0.187	0.029
$Q_{simulated}/Q_{measured}$	5.86	1.71

allow us to propose realistic gradients on Antisana volcano. The available measurements show the mean wind speed on SAMA-3 (5,065 m a.s.l.) was 6.2 m s^{-1} (**Supplementary Table SA4**) twice as high as at SAMA-1. Whereas the mean decrease in specific humidity was about 4% between the same stations (**Supplementary Table SA3**). Considering that higher wind speed and lower specific humidity increase turbulent fluxes (Dadic et al., 2013), the use of invariant values of Ws and q along the glacier profile could lead to underestimating turbulent fluxes and sublimation in the upper part.

5.3 Groundwater Flow

Despite simulated discharge values being significantly higher than measured values (**Table 5**), we observed a significant correlation between the two variables. This reflects the close relationship between albedo and discharge fluctuations. A large part of meltwater from the ablation zone (0.69 km^2) likely flows through moulins and crevasses and percolates into subglacial channels that connect with a groundwater flow network. This phenomenon has already been described for ice-covered watersheds (Hayashi, 2020; Somers and McKenzie, 2020; Miller et al., 2021), and is particularly significant at the AG15 as shown by Favier et al. (2008).

The high correlation values between modeled and measured discharges suggest the flow measured at the proglacial gauging station probably originates from a minor proportion of the glacier, which is likely at lower elevations. Indeed, if percolation in the groundwater flow system were significant beneath the entire glacier, it would absorb all meltwater during periods of low melt. Then, the discharge would reflect no diurnal variation during periods of low melt. This is not the case in **Figure 8A**, moreover, meltwater probably flows directly to the gauging station, without entering in a porous medium, as suggested by the short delay between melt onset and peak flow at the gauging station. Perhaps, the circulation of water in a porous medium, within the moraine, would filter the flow response and attenuate flow fluctuations (Wagnon et al., 1998; Flowers, 2008). These observations were already suggested by tracer experiments performed by Favier et al. (2008), but the present modeling approach offers a better understanding of water origins. Retrieving the exact origin of meltwater is, however, a challenging task relying on complex geophysical surveys and water chemical tracing experiments (Harrington et al., 2018; Vittecoq et al., 2019). This would be relevant to accurately characterize the hydrological drainage system on the Antisana.

Direct comparisons had shown the glacier streamflow from Los Crespos gauging station contributes 22% on average (ranging between 10 and 30% according to the season) to the watershed outlet at downstream (Villacís, 2008). However, hydrograph separation based on electroconductivity, and isotopic tracers showed glacier contribution could rise to 40% of streamflow at outlet during precipitation events (Minaya et al., 2021). The calculation of hydrological balances at the scale of the massif would be necessary to find out if the underground flows are effective at lower altitudes. Studies conducted on the Quilcay river, a 3,925 m long study reach between 3,910 and 4,040 m.a.s.l. (Cordillera Blanca, Peru), have shown 49% of the streamflow is exchanged with the subsurface, with the net groundwater contribution to the discharge at the outlet about 29% (Somers et al., 2016). Thus, it is essential to develop hydrogeological studies to better understand the hydrological processes in the Antisana massif.

6 CONCLUSION

The impact of climatic variations on the extent of glaciers in the inner tropics has been of growing interest in recent years because of their quick response to temperature and precipitation variations. In this work, we coupled the distributed surface energy balance with a linear reservoir to quantify the potential discharge produced by melting over the entire glacier including moraine zone. In addition, the variation of discharge was related to meteorological conditions by energy fluxes. The use of precipitation partitioning based on temperature ranges instead of temperature threshold improved the mass balance simulations. Moreover, the sensitivity analysis demonstrated the need of including an increase in precipitation of 10% per 100 m increase in altitude to reproduce correctly the mass balance profile. Therefore, sequential calibrations allowed us to control the SEB model performance and best reproduce the integrated melting at the glacier scale.

It was verified that the net short-wave radiation was the main energy input for melting in the ablation zone, where 91% of the meltwater and 86% of discharge are produced. This explains the significant correlation between this flux and the simulated discharge. The lack of significant seasonality in cloud cover and in the incident short-wave radiation implies that reflected short-wave radiation rules the melting variations. This explains why albedo variations via the snow thickness regulate ablation in the inner tropics. During the July-September season, the strength of Easterlies dissipates cloud cover, and the wind speed and low specific humidity become more relevant to control melt variations due to a high turbulent latent heat flux.

The existence of groundwater flow occurring directly below the glaciers prevents us from directly comparing the amount of simulated meltwater with the measured discharge values at the hydrological gauging station. However, the high correlation

between them at daily and hourly time steps ensures the model could reproduce satisfactorily the main processes influencing discharge variations. Moreover, we propose that the meltwater flowing at the gauging station comes primarily from a limited area in the lowest parts of the glacier. Hydrogeological studies are needed to complete the glacial modeling and define the area of the glacier contributing to downstream flow.

Finally, these results will allow a better understanding of the differences in the behavior between glaciers located along the Andes of Ecuador. An analysis over a longer period would now be interesting to analyze the interannual variations of energy fluxes, and their links with climate variability, in particular with ENSO; which is the main climatic driver in the zone.

DATA AVAILABILITY STATEMENT

The raw data supporting the conclusions of this article will be made available by the authors, without undue reservation.

AUTHOR CONTRIBUTIONS

LG conducted the literature review, results and analysis. LG and J-CR-H wrote the draft of the manuscript. VF and LM performed the model development. MV and LC supervised the work and mentored LG. LM conducted field work and data acquisition. J-CR-H, VF, and TC provided technical contributions and contributed to the manuscript edition. All authors contributed to the article and approved the submitted version.

FUNDING

Financial support received from Escuela Politécnica Nacional (EPN) by the projects EPN-PIMI-14-06 and EPN-PIJ-18-05 for the development of this research. Also, financial support for field survey received by French Research Institute for Development (IRD) through the International Laboratory LMI GREAT-ICE.

ACKNOWLEDGMENTS

The authors thank the Escuela Politécnica Nacional (EPN) and Instituto Nacional de Meteorología e Hidrología (INAMHI) through the project SENACYT-EPN PIC-08-506 for the support provided to install and operate the AWS SAMA-1. To the INAMHI research program Glaciares Del Ecuador and the MsC. Bolívar Cáceres for the glaciological information provided. To the GLACIOCLIM Observation Service for the information on the E-ORE station used, and to Ruben Basantes for the glaciological and geographical information provided. J-CR-H thanks to Secretaría Nacional de Educación Superior, Ciencia, Tecnología e Innovación, SENESCYT for financial support through a PhD scholarship. The authors acknowledge Juan Carvajal for the field data acquisition.

SUPPLEMENTARY MATERIAL

The Supplementary Material for this article can be found online at: https://www.frontiersin.org/articles/10.3389/feart.2022.732635/full#supplementary-material

REFERENCES

Anslow, F. S., Hostetler, S., Bidlake, W. R., and Clark, P. U. (2008). Distributed Energy Balance Modeling of South Cascade Glacier, Washington and Assessment of Model Uncertainty. *J. Geophys. Res.* 113 (2), 1–18. doi:10.1029/2007JF000850

Autin, P., Sicart, J. E., Rabatel, A., and Soruco, A. (2021). Climate Controls on the Interseasonal and Interannual Variability of the Surface Mass Balance of a Tropical Glacier (Zongo Glacier, Bolivia, 16°S): New Insights from the Application of a Distributed Energy Balance Model over 9 Years. *Earth Space Sci. Open Archive*. [Manuscript submitted for publication]. doi:10.1002/ESSOAR.10507310.1

Azam, M. F., Ramanathan, A., Wagnon, P., Vincent, C., Linda, A., Berthier, E., et al. (2016). Meteorological Conditions, Seasonal and Annual Mass Balances of Chhota Shigri Glacier, Western Himalaya, India. *Ann. Glaciol.* 57 (71), 328–338. doi:10.3189/2016AoG71A570

Baker, D., Escher-Vetter, H., Moser, H., Oerter, H., and Reinwarth, O. (19821982). A Glacier Discharge Model Based on Results from Field Studies of Energy Balance, Water Storage and Flow (Vernagtferner, Oetztal Alps, Austria). Hydrological Aspects of Alpine and High-Mountain Areas. *Proc. Exeter Symp.* 138, 103–112.

Basantes-Serrano, R. (2015). Contribution à l'étude de l'évolution des glaciers et du changement climatique dans les Andes équatoriennes depuis les années 1950 [Université Grenoble Alpes, PhD dissertation, 207. Available at: http://theses.fr/2015GREAU009.

Basantes-Serrano, R., Rabatel, A., Francou, B., Vincent, C., Maisincho, L., Cáceres, B., et al. (2016). Slight Mass Loss Revealed by Reanalyzing Glacier Mass-Balance Observations on Glaciar Antisana 15α (Inner Tropics) during the 1995-2012 Period. *J. Glaciol.* 62 (231), 124–136. doi:10.1017/jog.2016.17

Bayas-Erazo, M. (2020). "Understanding Ecuador's Growth Prospects in the Aftermath of the Citizens' Revolution," in *Representing Past and Future Hydro-Climatic Variability over Multi-Decadal Periods in Poorly-Gauged Regions: The Case of Ecuador [Université Paul Sabatier-Toulouse III, PhD Dissertation*, 213–230. https://tel.archives-ouvertes.fr/tel-03124408. doi:10.1007/978-3-030-27625-6_9

Berberan-Santos, M. N., Bodunov, E. N., and Pogliani, L. (1997). On the Barometric Formula. *Am. J. Phys.* 65 (5), 404–412. doi:10.1119/1.18555

Bintanja, R., Jonsson, S., and Knap, W. H. (1997). The Annual Cycle of the Surface Energy Balance of Antartic Blue Ice. *J. Geophys. Res.* 102 (96), 1867–1881. doi:10.1029/96jd01801

Buytaert, W., Moulds, S., Acosta, L., De Bièvre, B., Olmos, C., Villacis, M., et al. (2017). Glacial Melt Content of Water Use in the Tropical Andes. *Environ. Res. Lett.* 12 (11), 114014. doi:10.1088/1748-9326/aa926c

Cáceres, B., Maisincho, L., Manciati, C., Loyo, C., Cuenca, E., Arias, M., et al. (2010). *Glaciares del Ecuador, Antisana 15*. INAMHI. Informe del año 2009. Informe técnico.

Cáceres, B., Francou, B., Favier, V., Bontron, G., Maisncho, L., Tachker, P., et al. (2006). *El Glaciar 15 del Antisana. Diez años de investigaciones glaciológicasMemorias de La Primera Conferencia Internacional de Cambio Climático: Impacto En Los Sistemas de Alta Montaña*.

Campozano, L., Célleri, R., Trachte, K., Bendix, J., and Samaniego, E. (2016). Rainfall and Cloud Dynamics in the Andes: A Southern Ecuador Case Study. *Adv. Meteorology* 2016, 1–15. doi:10.1155/2016/3192765

Campozano, L., Robaina, L., Gualco, L. F., Maisincho, L., Villacís, M., Condom, T., et al. (2021). Parsimonious Models of Precipitation Phase Derived from Random Forest Knowledge: Intercomparing Logistic Models, Neural Networks, and Random Forest Models. *Water* 13 (21), 3022. doi:10.3390/w13213022

Ceballos, J., Rodríguez, C., and Real, E. (2012). *Glaciares de Colombia: más que montañas con hielo*. Bogotá: IDEAM.

Chevallier, P., Pouyaud, B., Suarez, W., and Condom, T. (2011). Climate Change Threats to Environment in the Tropical Andes: Glaciers and Water Resources. *Reg. Environ. Change* 11 (Suppl. 1), 179–187. doi:10.1007/s10113-010-0177-6

Cuffey, K. M., and Paterson, W. S. B. (2010). *The Physics of Glaciers (Fourth Edi)*. Elsevier B.V.

Dadic, R., Corripio, J. G., and Burlando, P. (2008). Mass-balance Estimates for Haut Glacier d'Arolla, Switzerland, from 2000 to 2006 Using DEMs and Distributed Mass-Balance Modeling. *Ann. Glaciol.* 49, 22–26. doi:10.3189/172756408787814816

Dadic, R., Mott, R., Lehning, M., Carenzo, M., Anderson, B., and Mackintosh, A. (2013). Sensitivity of Turbulent Fluxes to Wind Speed over Snow Surfaces in Different Climatic Settings. *Adv. Water Resour.* 55, 178–189. doi:10.1016/j.advwatres.2012.06.010

Denby, B., and Greuell, W. (2000). The Use of Bulk and Profile Methods for Determining Surface Heat Fluxes in the Presence of Glacier Winds. *J. Glaciol.* 46 (154), 445–452. doi:10.3189/172756500781833124

Douville, H., Royer, J.-F., and Mahfouf, J.-F. (1995). A New Snow Parameterization for the Météo-France Climate Model. *Clim. Dyn.* 12, 21–35. doi:10.1007/BF00208760

Espinoza, J. C., Garreaud, R., Poveda, G., Arias, P. A., Molina-Carpio, J., Masiokas, M., et al. (2020). Hydroclimate of the Andes Part I: Main Climatic Features. *Front. Earth Sci.*, 8. Frontiers Media S.A, 64. doi:10.3389/feart.2020.00064

Espinoza Villar, J. C., Ronchail, J., Guyot, J. L., Cochonneau, G., Naziano, F., Lavado, W., et al. (2009). Spatio-temporal Rainfall Variability in the Amazon basin Countries (Brazil, Peru, Bolivia, Colombia, and Ecuador). *Int. J. Climatol.* 29 (11), 1574–1594. doi:10.1002/joc.1791

Favier, V., Agosta, C., Genthon, C., Arnaud, L., Trouvillez, A., and Gallée, H. (2011). Modeling the Mass and Surface Heat Budgets in a Coastal Blue Ice Area of Adelie Land, Antarctica. *J. Geophys. Res.* 116 (3), 1–14. doi:10.1029/2010JF001939

Favier, V., Coudrain, A., Cadier, E., Francou, B., Ayabaca, E., Maisincho, L., et al. (2008). Evidence of groundwater flow on Antizana ice-covered volcano, Ecuador /Mise en évidence d'écoulements souterrains sur le volcan englacé Antizana, Equateur. *Hydrological Sci. J.* 53 (1), 278–291. doi:10.1623/hysj.53.1.278

Favier, V. (2004c). Etude du bilan d'énergie de surface et de la production des écoulements de fonte d'un glacier des Andes d'Equateur : Relation glacier - climat en zone tropicale. 262. [Université Montpellier 2, PhD dissertation. Available at: http://theses.fr/2004MON20200

Favier, V., Verfaillie, D., Berthier, E., Menegoz, M., Jomelli, V., Kay, J. E., et al. (2016). Atmospheric Drying as the Main Driver of Dramatic Glacier Wastage in the Southern Indian Ocean. *Sci. Rep.* 6 (1), 1–12. doi:10.1038/srep32396

Favier, V., Wagnon, P., Chazarin, J. P., Maisincho, L., and Coudrain, A. (2004b). One-year Measurements of Surface Heat Budget on the Ablation Zone of Antizana Glacier 15, Ecuadorian Andes. *J. Geophys. Res.* 109 (18), 1–15. doi:10.1029/2003JD004359

Favier, V., Wagnon, P., and Ribstein, P. (2004a). Glaciers of the Outer and Inner Tropics: A Different Behaviour but a Common Response to Climatic Forcing. *Geophys. Res. Lett.* 31 (16), 1–5. doi:10.1029/2004GL020654

Flowers, G. E. (2008). Subglacial Modulation of the Hydrograph from Glacierized Basins. *Hydrol. Process.* 22 (19), 3903–3918. doi:10.1002/HYP.7095

Francou, B., Rabatel, A., Soruco, A., Sicart, J. E. E., Silvestre, E., Ginot, P., et al. (2013). *Glaciares de los Andes Tropicales: Víctimas del Cambio Climático*. doi:10.13140/RG.2.1.1255.4082

Francou, B., Ramirez, E., Cáceres, B., and Mendoza, J. (2000). Glacier Evolution in the Tropical Andes during the Last Decades of the 20thCentury: Chacaltaya, Bolivia, and Antizana, Ecuador. *AMBIO: A J. Hum. Environ.* 29 (7), 416–422. doi:10.1579/0044-7447-29.7.416

Francou, B., Vuille, M., Favier, V., and Cáceres, B. (2004). New Evidence for an ENSO Impact on Low-Latitude Glaciers: Antizana 15, Andes of Ecuador, 0°28′S. *J. Geophys. Res.* 109 (18), 1–17. doi:10.1029/2003JD004484

Funk, C., Peterson, P., Landsfeld, M., Pedreros, D., Verdin, J., Shukla, S., et al. (2015). The Climate Hazards Infrared Precipitation with Stations-A New Environmental Record for Monitoring Extremes. *Sci. Data* 2 (1), 1–21. doi:10.1038/sdata.2015.66

Gerbaux, M., Genthon, C., Etchevers, P., Vincent, C., and Dedieu, J. P. (2005). Surface Mass Balance of Glaciers in the French Alps: Distributed Modeling and Sensitivity to Climate Change. *J. Glaciol.* 51 (175), 561–572. doi:10.3189/172756505781829133

Gurgiser, W., Marzeion, B., Nicholson, L., Ortner, M., and Kaser, G. (2013a). Modeling Energy and Mass Balance of Shallap Glacier, Peru. *The Cryosphere* 7 (6), 1787–1802. doi:10.5194/tc-7-1787-2013

Harrington, J. S., Mozil, A., Hayashi, M., and Bentley, L. R. (2018). Groundwater Flow and Storage Processes in an Inactive Rock Glacier. *Hydrological Process.* 32 (20), 3070–3088. doi:10.1002/HYP.13248

Hayashi, M. (2020). Alpine Hydrogeology: The Critical Role of Groundwater in Sourcing the Headwaters of the World. *Groundwater* 58 (4), 498–510. doi:10.1111/GWAT.12965

Hersbach, H., Bell, B., Berrisford, P., Hirahara, S., Horányi, A., Muñoz-Sabater, J., et al. (2020). The ERA5 Global Reanalysis. *Q.J.R. Meteorol. Soc.* 146 (730), 1999–2049. doi:10.1002/qj.3803

Hock, R. (2005). Glacier Melt: A Review of Processes and Their Modelling. *Prog. Phys. Geogr. Earth Environ.* 29 (3), 362–391. doi:10.1191/0309133305pp453ra

Hock, R., and Holmgren, B. (2005). A Distributed Surface Energy-Balance Model for Complex Topography and its Application to Storglaciären, Sweden. *J. Glaciol.* 51 (172), 25–36. doi:10.3189/172756505781829566

Hock, R., and Noetzli, C. (1997). Areal Melt and Discharge Modelling of Storglaciären, Sweden. *A. Glaciology.* 24, 211–216. doi:10.3189/s026030550001219210.1017/s0260305500012192

Ilbay-Yupa, M., Lavado-Casimiro, W., Rau, P., Zubieta, R., and Castillón, F. (2021). Updating Regionalization of Precipitation in Ecuador. *Theor. Appl. Climatol* 143 (3–4), 1513–1528. doi:10.1007/s00704-020-03476-x

Johnson, E., and Rupper, S. (2020). An Examination of Physical Processes that Trigger the Albedo-Feedback on Glacier Surfaces and Implications for Regional Glacier Mass Balance across High Mountain Asia. *Front. Earth Sci.* 8, 129. doi:10.3389/feart.2020.00129

Jomelli, V., Favier, V., Rabatel, A., Brunstein, D., Hoffmann, G., and Francou, B. (2009). Fluctuations of Glaciers in the Tropical Andes over the Last Millennium and Palaeoclimatic Implications: A Review. *Palaeogeogr. Palaeoclimatol. Palaeoecol.* 281 (3–4), 269–282. doi:10.1016/j.palaeo.2008.10.033

Juen, I. (2006). *Glacier Mass Balance and Runoff in the Cordillera Blanca, Perú*. Austria: [University of InnsbruckPhD dissertation, 195.

Junquas, C., Heredia, M. B., Condom, T., Ruiz-Hernández, J. C., Campozano, L., Dudhia, J., et al. (2022). Regional Climate Modeling of the Diurnal Cycle of Precipitation and Associated Atmospheric Circulation Patterns over an Andean Glacier Region (Antisana, Ecuador). *Clim. Dyn.* 2021, 1–30. doi:10.1007/S00382-021-06079-Y

Kaser, G. (2001). Glacier-climate Interaction at Low Latitudes. *J. Glaciol.* 47 (157), 195–204. doi:10.3189/172756501781832296

Kaser, G., and Osmaston, H. (2002). *Tropical Glaciers*. Cambridge, United Kingdom: The Press Syndicate.

L'hôte, Y., Chevallier, P., Coudrain, A., Lejeune, Y., and Etchevers, P. (2005). Relationship between precipitation phase and air temperature: comparison between the Bolivian Andes and the Swiss Alps /Relation entre phase de précipitation et température de l'air: comparaison entre les Andes Boliviennes et les Alpes Suisses. *Hydrological Sci. J.* 50 (6). doi:10.1623/hysj.2005.50.6.989

Laraque, A., Ronchail, J., Cochonneau, G., Pombosa, R., and Guyot, J. L. (2007). Heterogeneous Distribution of Rainfall and Discharge Regimes in the Ecuadorian Amazon basin. *J. Hydrometeorology* 8 (6), 1364–1381. doi:10.1175/2007JHM784.1

Lozano Gacha, M. F., and Koch, M. (2021). Distributed Energy Balance Flux Modelling of Mass Balances in the Artesonraju Glacier and Discharge in the Basin of Artesoncocha, Cordillera Blanca, Peru. *ClimateMDPI AG* 9 (9), 143. doi:10.3390/cli9090143

Maisincho, L. (2015). Analyse de la fonte glaciaire et nivale dans les Andes tropicales à partir d'un bilan d'énergie: Glacier de l'Antisana, Equateur (0°28'S). [Université Grenoble Alpes, PhD dissertation. 213 pp]. Available at: http://theses.fr/2015GREAU027.

Masiokas, M. H., Rabatel, A., Rivera, A., Ruiz, L., Pitte, P., Ceballos, J. L., et al. (2020)., 8. Frontiers Media S.A, 99. doi:10.3389/feart.2020.00099A Review of the Current State and Recent Changes of the Andean Cryosphere*Front. Earth Sci.*

Miller, J. B., Frisbee, M. D., Hamilton, T. L., and Murugapiran, S. K. (2021). Recharge from Glacial Meltwater Is Critical for alpine Springs and Their Microbiomes. *Environ. Res. Lett.* 16 (6), 064012. doi:10.1088/1748-9326/ABF06B

Minaya, V., Camacho Suarez, V., Wenninger, J., and Mynett, A. (2021). Runoff Generation from a Combined Glacier and Páramo Catchment within the Antisana Reserve in Ecuador. *J. Ecohydraulics*, 1–16. doi:10.1080/24705357.2021.2005472

Naz, B. S., Frans, C. D., Clarke, G. K. C., Burns, P., and Lettenmaier, D. P. (2014). Modeling the Effect of Glacier Recession on Streamflow Response Using a Coupled Glacio-Hydrological Model. *Hydrol. Earth Syst. Sci.* 18 (2), 787–802. doi:10.5194/hess-18-787-2014

Oke, T. R. (1987). *Boundary Layer Climates*. Second edition. Routledge.

Padrón, R. S., Wilcox, B. P., Crespo, P., and Célleri, R. (2015). Rainfall in the Andean Páramo: New Insights from High-Resolution Monitoring in Southern Ecuador. *J. Hydrometeorology* 16 (3), 985–996. doi:10.1175/JHM-D-14-0135.1

Rabatel, A., Francou, B., Soruco, A., Gomez, J., Cáceres, B., Ceballos, J. L., et al. (2013). Current State of Glaciers in the Tropical Andes: A Multi-century Perspective on Glacier Evolution and Climate Change. *The Cryosphere* 7 (1), 81–102. doi:10.5194/tc-7-81-2013

Ramírez, E., Francou, B., Ribstein, P., Descloitres, M., Guérin, R., Mendoza, J., et al. (2001). Small Glaciers Disappearing in the Tropical Andes: a Case-Study in Bolivia: Glaciar Chacaltaya (16o S). *J. Glaciol.* 47 (157), 187–194. doi:10.3189/172756501781832214

Ren, Z., Su, F., Xu, B., Xie, Y., and Kan, B. (2018). A Coupled Glacier-Hydrology Model and its Application in Eastern Pamir. *J. Geophys. Res. Atmos.* 123 (2413), 613–692. 713. doi:10.1029/2018JD028572

Ruiz-Hernández, J.-C., Condom, T., Ribstein, P., Le Moine, N., Espinoza, J.-C., Junquas, C., et al. (2021). Spatial Variability of Diurnal to Seasonal Cycles of Precipitation from a High-Altitude Equatorial Andean valley to the Amazon Basin. *J. Hydrol. Reg. Stud.* 38, 100924. doi:10.1016/J.EJRH.2021.100924

Saberi, L., McLaughlin, R. T., Ng, G.-H. C., La Frenierre, J., Wickert, A. D., Baraer, M., et al. (2019). Multi-scale Temporal Variability in Meltwater Contributions in a Tropical Glacierized Watershed. *Hydrol. Earth Syst. Sci.* 23 (1), 405–425. doi:10.5194/hess-23-405-2019

Sagredo, E. A., Rupper, S., and Lowell, T. V. (2014). Sensitivities of the Equilibrium Line Altitude to Temperature and Precipitation Changes along the Andes. *Quat. Res.* 81 (2), 355–366. doi:10.1016/j.yqres.2014.01.008

Segura, H., Junquas, C., Espinoza, J. C., Vuille, M., Jauregui, Y. R., Rabatel, A., et al. (2019). New Insights into the Rainfall Variability in the Tropical Andes on Seasonal and Interannual Time Scales. *Clim. Dyn.* 53 (1–2), 405–426. doi:10.1007/s00382-018-4590-8

Sicart, J. E. (2002). Contribution à l'étude des flux d'énergie, du bilan de masse et du débit de fonte d' un glacier tropical: le Zongo, Bolivie [Université Paris 6, PhD dissertation. 347. Available at: http://www.theses.fr/2002PA066505.

Sicart, J. E., Hock, R., Ribstein, P., Litt, M., and Ramirez, E. (2011). Analysis of Seasonal Variations in Mass Balance and Meltwater Discharge of the Tropical Zongo Glacier by Application of a Distributed Energy Balance Model. *J. Geophys. Res.* 116 (13). doi:10.1029/2010JD015105

Sklenár, P., Kuèerová, A., Macková, J., and Macek, P. (2015). Temporal Variation of Climate in the High-Elevation Páramo of Antisana, Ecuador. *Supplementi Di Geografia Fisica e Dinamica Quaternaria* 38 (1), 67–78. doi:10.4461/GFDQ.2015.38.07

Somers, L. D., Gordon, R. P., McKenzie, J. M., Lautz, L. K., Wigmore, O., Glose, A., et al. (2016). Quantifying Groundwater-Surface Water Interactions in a Proglacial valley, Cordillera Blanca, Peru. *Hydrol. Process.* 30 (17), 2915–2929. doi:10.1002/HYP.10912U.S

Somers, L. D., and McKenzie, J. M. (2020). A Review of Groundwater in High Mountain Environments. *WIREs Water* 7 (6), e1475. doi:10.1002/WAT2.1475

U.S. Army Corps Of Engineers (1956). Snow Hydrology: Summary Report of the Snow Investigations. Available at: https://usace.contentdm.oclc.org/digital/collection/p266001coll1/id/4172/.

Veettil, B. K., Wang, S., Florêncio de Souza, S., Bremer, U. F., and Simões, J. C. (2017). Glacier Monitoring and Glacier-Climate Interactions in the Tropical Andes: A Review. *J. South Am. Earth Sci.* 77, 218–246. doi:10.1016/j.jsames.2017.04.009

Verfaillie, D., Favier, V., Dumont, M., Jomelli, V., Gilbert, A., Brunstein, D., et al. (2015). Recent Glacier Decline in the Kerguelen Islands (49°S, 69°E) Derived from Modeling, Field Observations, and Satellite Data. *J. Geophys. Res. Earth Surf.* 120 (3), 637–654. doi:10.1002/2014JF003329

Villacís, M. (2008). Ressources en eau glaciaire dans les Andes d'Equateur en relation avec les variations du climat : Le cas du volcan Antisana [Université Montpellier II, PhD dissertation, 251. Available at: http://www.theses.fr/2008MON20078.

Vincent, C., Ribstein, P., Favier, V., Wagnon, P., Francou, B., Le Meur, E., et al. (2005). Glacier Fluctuations in the Alps and in the Tropical Andes. *Comptes Rendus Geosci.* 337 (1–2), 97–106. doi:10.1016/j.crte.2004.08.010

Vittecoq, B., Reninger, P.-A., Lacquement, F., Martelet, G., and Violette, S. (2019). Hydrogeological Conceptual Model of Andesitic Watersheds Revealed by High-Resolution Heliborne Geophysics. *Hydrol. Earth Syst. Sci.* 23 (5), 2321–2338. doi:10.5194/HESS-23-2321-2019

Vuille, M., Bradley, R. S., and Keimig, F. (2000). Climate Variability in the Andes of Ecuador and its Relation to Tropical Pacific and Atlantic Sea Surface Temperature Anomalies. *J. Clim.* 13 (14), 2520–2535. doi:10.1175/1520-0442(2000)013<2520:cvitao>2.0.co;2

Vuille, M., Francou, B., Wagnon, P., Juen, I., Kaser, G., Mark, B. G., et al. (2008). Climate Change and Tropical Andean Glaciers: Past, Present and Future. *Earth-Science Rev.* 89 (3–4), 79–96. doi:10.1016/j.earscirev.2008.04.002

Wagnon, P., Lafaysse, M., Lejeune, Y., Maisincho, L., Rojas, M., and Chazarin, J. P. (2009). Understanding and Modeling the Physical Processes that Govern the Melting of Snow Cover in a Tropical Mountain Environment in Ecuador. *J. Geophys. Res.* 114 (19), 1–14. doi:10.1029/2009JD012292

Wagnon, P., Ribstein, P., Francou, B., and Pouyaud, B. (19991998). Annual Cycle of Energy Balance of Zongo Glacier, Cordillera Real, Bolivia. *J. Geophys. Res.* 104, 3907–3923. doi:10.1029/1998jd200011

Wagnon, P., Ribstein, P., Schuler, T., and Francou, B. (1998). Flow Separation on Zongo Glacier, Cordillera Real, Bolivia. *Hydrol. Process.* 12 (12), 1911–1926. doi:10.1002/(sici)1099-1085(19981015)12:12<1911::aid-hyp673>3.0.co;2-h

Wagnon, P., Sicart, J. E., Berthier, E., and Chazarin, J. P. (2003). Wintertime High-altitude Surface Energy Balance of a Bolivian Glacier, Illimani, 6340 M above Sea Level. *J. Geophys. Res.* 108 (6). doi:10.1029/2002jd002088

Zardi, D., and Whiteman, C. D. (2013). "Diurnal Mountain Wind Systems," in *Mountain Weather Research and Forecasting*. Editor F. Chow (Springer Atmospheric Sciences), 35–119. doi:10.1007/978-94-007-4098-3_2

Conflict of Interest: The authors declare that the research was conducted in the absence of any commercial or financial relationships that could be construed as a potential conflict of interest.

Publisher's Note: All claims expressed in this article are solely those of the authors and do not necessarily represent those of their affiliated organizations, or those of the publisher, the editors and the reviewers. Any product that may be evaluated in this article, or claim that may be made by its manufacturer, is not guaranteed or endorsed by the publisher.

Advantages of publishing in Frontiers

OPEN ACCESS
Articles are free to read for greatest visibility and readership

FAST PUBLICATION
Around 90 days from submission to decision

HIGH QUALITY PEER-REVIEW
Rigorous, collaborative, and constructive peer-review

TRANSPARENT PEER-REVIEW
Editors and reviewers acknowledged by name on published articles

Frontiers
Avenue du Tribunal-Fédéral 34
1005 Lausanne | Switzerland

Visit us: www.frontiersin.org
Contact us: frontiersin.org/about/contact

REPRODUCIBILITY OF RESEARCH
Support open data and methods to enhance research reproducibility

DIGITAL PUBLISHING
Articles designed for optimal readership across devices

FOLLOW US
@frontiersin

IMPACT METRICS
Advanced article metrics track visibility across digital media

EXTENSIVE PROMOTION
Marketing and promotion of impactful research

LOOP RESEARCH NETWORK
Our network increases your article's readership